GRUPPO NAZIONALE DI GEOFISICA DELLA TERRA SOLIDA

# 33° convegno nazionale

# Bologna

25-27 novembre 2014

Palazzo della Regione

## ATTI

## Tema 3: Geofisica Applicata

ISTITUTO NAZIONALE DI OCEANOGRAFIA E DI GEOFISICA SPERIMENTALE

In collaborazione con

EAGE EUROPEAN ASSOCIATION OF GEOSCIENTISTS & ENGINEERS

SEZIONE ITALIANA

14° Convegno Nazionale

RegioneEmilia-Romagna

GRUPPO NAZIONALE DI GEOFISICA DELLA TERRA SOLIDA

# 33°Convegno Nazionale
## Atti - Tema 3: Geofisica Applicata

**Comitato organizzatore**

D. Slejko
D. Albarello
A. Argnani
F. Bianco
E. Cardarelli
A. Del Ben
D. Di Bucci
M. Dolce
E. Eva
G. Florio
P. Galli
A. Manzella
L. Martelli
P. Mazzucchelli
G. Naso
F. Pacor
R. Petrini
V. Socco
U. Tinivella

A cura di: D. Slejko, A. Riggio, E. Cardarelli, G. Florio, A. Manzella, P. Mazzucchelli, V. Socco, U. Tinivella

Con la collaborazione di: M. Bobbio e P. Giurco

Copertina: M. Sedmach

Impaginazione:
Luglio Fotocomposizioni, Trieste

Stampa: Centro Stampa della Regione Emilia-Romagna, Bologna

Finito di stampare nel mese di novembre 2014

*Ancora in giro per l'Italia. I giorni di Roma sono lontani nel tempo e Trieste è subentrata come sede frequente del convegno del Gruppo Nazionale di Geofisica della Terra Solida (GNGTS) intervallata da altre città che hanno ospitato il congresso. E così, dopo Prato e Potenza, è Bologna che si è offerta per organizzare quest'anno il convegno. Si potrebbe dire che il congresso GNGTS ha trovato una collocazione ideale presso il Servizio Geologico, Sismico e dei Suoli della Regione Emilia – Romagna, sancendo l'interesse che gli studi geofisici rivestono per l'apparato amministrativo.*

*L'ubicazione relativamente baricentrica di Bologna dovrebbe favorire l'affluenza dei ricercatori, anche se i fondi sempre limitati destinati alla ricerca condizionano da anni la partecipazione. I presupposti per una buona riuscita del convegno ci sono, visto l'alto numero di note ricevute per la presentazione e il numero di pre-iscritti che un mese prima del convegno ha già superato le 230 unità.*

*La strutturazione del convegno su 3 temi, proposta negli ultimi anni, é stata mantenuta: ci sembra rispecchi le principali discipline geofisiche e risulta di semplice organizzazione. Pertanto anche quest'anno le presentazioni sono state suddivise nei tre temi generali: Geodinamica, Caratterizzazione Sismica del Territorio e Geofisica Applicata, che sintetizzano i grandi filoni lungo i quali si articola la ricerca geofisica italiana. Ogni tema, poi, si sviluppa in tre sessioni specifiche con apertura sia alla componente geologica che a quella ingegneristica. È doveroso segnalare l'interesse che l'argomento sismologico riveste da alcuni anni e che si manifesta in maniera decisa con l'elevato numero di relative presentazioni che spaziano dall'individuazione di faglie potenzialmente attive e lo studio di particolari terremoti alle stime di pericolosità sismica e di risposta locale per giungere alle ricadute in termini normativi atti a salvaguardare la sicurezza di persone e cose nel caso di terremoto.*

*Anche quest'anno è stata fatta la scelta di raccogliere note estese (ma non troppo) a formare gli atti del convegno. Ricordiamo che questa scelta è stata dettata dalla necessità di produrre un volume utilizzabile per la valutazione ufficiale dell'attività scientifica dei ricercatori e degli enti. Il presente volume raccoglie ben 138 note, delle 234 che verranno presentate al convegno. Si tratta di una percentuale (59%) abbastanza alta che premia la scelta fatta. La produzione di atti di rilevanza scientifica ha determinato la necessità di avviare un processo di referaggio di tutti i testi. I convenor se ne sono fatti carico e, pertanto, risultano responsabili della qualità del*

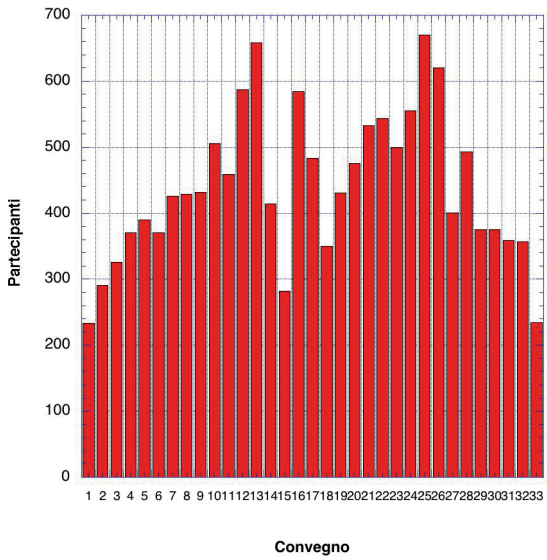


Fig. 1 – Numero di partecipanti ai convegni GNGTS. Il primo convegno si è tenuto nel 1981 e, in seguito, ha avuto cadenza annuale con l'eccezione del 1982. Il numero dei partecipanti all'ultimo convegno è aggiornato ad un mese prima dell'inizio del convegno stesso.

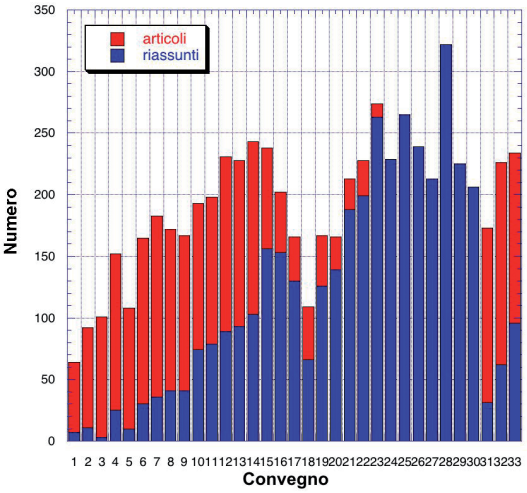


Fig. 2 – Numero di note presentate nei convegni GNGTS. Fino al 2004 è stato pubblicato il volume (dal 1997 sotto forma di CD-Rom) degli atti del convegno contenente in forma estesa le note presentate (barre rosse). In seguito, si è deciso di pubblicare soltanto il volume dei riassunti estesi (barre blu).

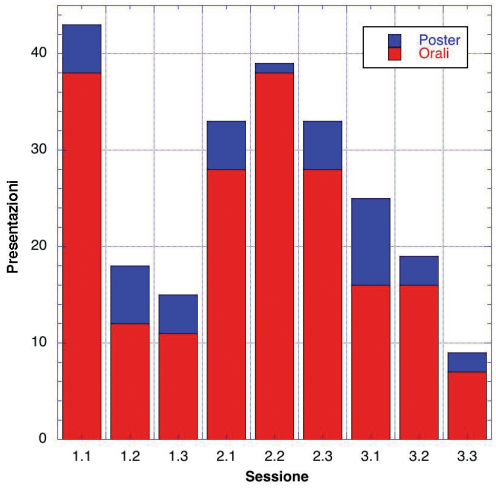


Fig. 3 – Numero di note presentate nelle varie sessioni del 33° convegno. Vengono indicate le comunicazioni orali con il colore rosso e quelle in forma di poster con il colore blu.

*materiale presentato. La notevole mole di materiale da stampare ha fatto confermare la scelta di suddividere gli atti in tre volumi, ciascuno dei quali raccoglie le note relative ad uno dei tre temi. Molte note (83) sono in lingua inglese: ciò permette una diffusione del presente volume anche all'estero. Delle 234 note in programma, ben 194 sono destinate alla presentazione orale.*

*Anche quest'anno alcune sessioni del convegno GNGTS (quelle di Geofisica Applicata) sono state organizzate in collaborazione con la Sezione Italiana EAGE-SEG, che realizza così il suo 14° Convegno Nazionale.*

*Una segnalazione degna di nota va all'Associazione Geofisica Licio Cernobori, che ha scelto anche quest'anno il convegno GNGTS quale sede per l'attribuzione del premio in memoria di un caro collega ed amico prematuramente scomparso anni or sono.*

*Un ringraziamento particolare va ai convenor (Dario Albarello, Andrea Argnani, Francesca Bianco, Ettore Cardarelli, Anna Del Ben, Daniela Di Bucci, Mauro Dolce, Elena Eva, Giovanni Florio, Paolo Galli, Adele Manzella, Luca Martelli, Paolo Mazzucchelli, Giuseppe Naso, Francesca Pacor, Riccardo Petrini, Valentina Socco e Umberta Tinivella), che hanno proposto e organizzato le varie sessioni e hanno curato il referaggio dei testi, ed alla Segreteria Organizzativa (Anna Riggio, Muzio Bobbio, Paolo Giurco), che ha raccolto e preparato tutto il materiale qui stampato. Desideriamo ringraziare, infine e soprattutto, il Presidente dell'OGS, che ha accolto ancora una volta con entusiasmo e con generosità l'idea di finanziare il convegno GNGTS, nonostante le difficoltà economiche con cui tutti gli enti di ricerca devono scontrarsi, la Giunta della Regione Emilia - Romagna, che ha accordato i suoi locali, e Paola Barchiesi, Simonetta Scappini, Francesco Marucci, nonché la segreteria del Servizio Geologico Sismico e dei Suoli, che hanno curato tutti gli aspetti logistici.*

*Dario Slejko e Luca Martelli*

*"...cerco qualcosa: un briciolo di conoscenza in questo nostro piccolo grande pianeta. E in me stesso..." L. C. 1989.*

## PREMIO DELL'ASSOCIAZIONE PER LA GEOFISICA "LICIO CERNOBORI" - 2014

L'**Associazione per la Geofisica Licio Cernobori -AGLC**, nata il 30 ottobre del 2000 per ricordare Licio Cernobori, geofisico prematuramente scomparso, ed il suo entusiasmo contagioso, ha come fine la promozione degli studi geofisici, e soprattutto la formazione scientifica e la crescita dei più giovani.

Tale fine è stato perseguito attraverso l'elargizione di un premio di studio presso l'Università di Trieste, aperto anche a laureandi/laureati in Geofisica Applicata di altre università o strutture scientifiche coinvolte in progetti comuni con l'Ateneo di Trieste. Si ricordano i vincitori degli anni passati Giulio Paoli (2001), Sara Cisilin (2002), Marica Calabrese (2003), Manfredi Scozzi (2004), Ivan Gladich (2006), Manuela Zuliani (2006), Andreika Starec (2008), Sara Ferrante (2009).

Oltre all'attività didattica/divulgativa che i componenti dell'Associazione svolgono in diverse occasioni, sono stati finanziati negli anni diversi convegni, scuole, progetti, iniziative, in Italia e all'estero:

- Copie degli Atti del Convegno TRANSALP (Trieste, Febbraio 2003) per le biblioteche universitarie;
- Agevolazioni per gli studenti al Congresso: STRUCTURES IN THE CONTINENTAL CRUST AND GEOTHERMAL RESOURCES (Siena, 24-27 September 2003);
- Sovvenzione di uno studente, Alberto Gaudio dell'università di Urbino per la Scuola di Processing dati sismici marini (Trieste, ottobre 2004);
- Agevolazioni per studenti del terzo mondo alla partecipazione del Workshop IRIS-Orfeus "Understanding and managing information from seismological networks" (Palmanova (UD), 28 Febbraio - 6 marzo 2005);
- Finanziamento di € 400 Euro ad Andrejka Starec (2006), allora studentessa, per garantirle un altro mese presso il TNO (Paesi Bassi) a conclusione della sua borsa e consentirle la conclusione della tesi sullo stoccaggio geologico della CO2, con la guida di Pascal Winthaegen e del chiar.mo Prof. Rinaldo Nicolich dell'Università di Trieste.
- Finanziamento annuale di € 400 per la partecipazione di un insegnante ai seminari GIFT per gli insegnanti delle scuole elementari e secondarie nell'ambito del convegno dell' European Geosciences Union - Geophysical Information for Teachers (GIFT): Giovanni Banchelli (2007), Pier Paolo Caputo (2008), Giovanni Aglialoro (2009), Francesco Gobbo (2010), Giulia Realdon (2011), Eva Godini (2012), Maria Barbera (2013).

Nell'occasione del decennale (2010) si è istituito un premio per i giovani relatori al Congresso annuale GNGTS, ripetuto nel 2011. Nel 2010 il premio di 2000,00 € è andato alla dottoressa **Marina Pastori**, per il lavoro ***"Crustal fracturing field and presence of fluid as revealed by seismic anisotropy: case-histories from seismogenic areas in the Apennines"***, selezionato tra 40 lavori e 8 finalisti, nel 2011 al dott. **Edoardo Peronace**, per il lavoro ***"Shallow geophysical imaging of the mt. Marzano fault zone; a kaleidoscopic view through ERT, GPR and HVSR analyses"***, selezionato tra 38 lavori e 13 finalisti.

Dal 2012 il premio è stato suddiviso tre premi di 700,00 €, uno per ciascuno dei Temi del convegno: Geodinamica, Caratterizzazione sismica del territorio e Geofisica applicata. I vincitori sono stati:

**Lorenzo Bonini**, per il lavoro: ***"Comprendere la gerarchia delle faglie attive per migliorare la caratterizzazione sismica del territorio: l'esempio del terremoto di L'Aquila del 2009 (Mw 6.3)"***, **Rocco Ditommaso**, per il lavoro ***"Risposta sismica delle strutture: dalla non stazionarietà alla non linearità apparente"***, **Gianluca Fiandaca**, per il lavoro ***"Time domain induced polarization: 2D inversion for spectral information"***, selezionati tra 31 lavori presentati.

Nel 2013 i vincitori sono stati: **Giuseppe Pezzo**, per il lavoro ***"Fault activity measurements from InSAR space geodesy: the fundamental role of geological constraints for correct data interpretation and analytical fault modeling"***, **Giovanni Rinaldin**, per il lavoro ***"Effectiveness of the N2 Method for the seismic analysis of structures with different hysteretic behaviour"*** e **Daniele Sampietro**, per il lavoro ***"Il modello GEMMA: realizzazione, validazione e distribuzione"***, selezionati su 28 candidati.

Quest'anno i lavori presentati sono 18. Purtroppo si è registrato un calo nelle domande per il tema 1, di cui cercheremo di capire le cause. I riassunti e le presentazioni preliminari sono attualmente all'esame delle tre commissioni, che stanno lavorando per scegliere i tre vincitori, che verranno annunciati e premiati nel corso dell'Assemblea del Convegno (26 novembre 2014).

Per altre informazioni, per diventare socio e contribuire a continuare e migliorare le iniziative dell'Associazione per la Geofisica Licio Cernobori –AGLC, scrivere a cernobor@units.it.

# Indice

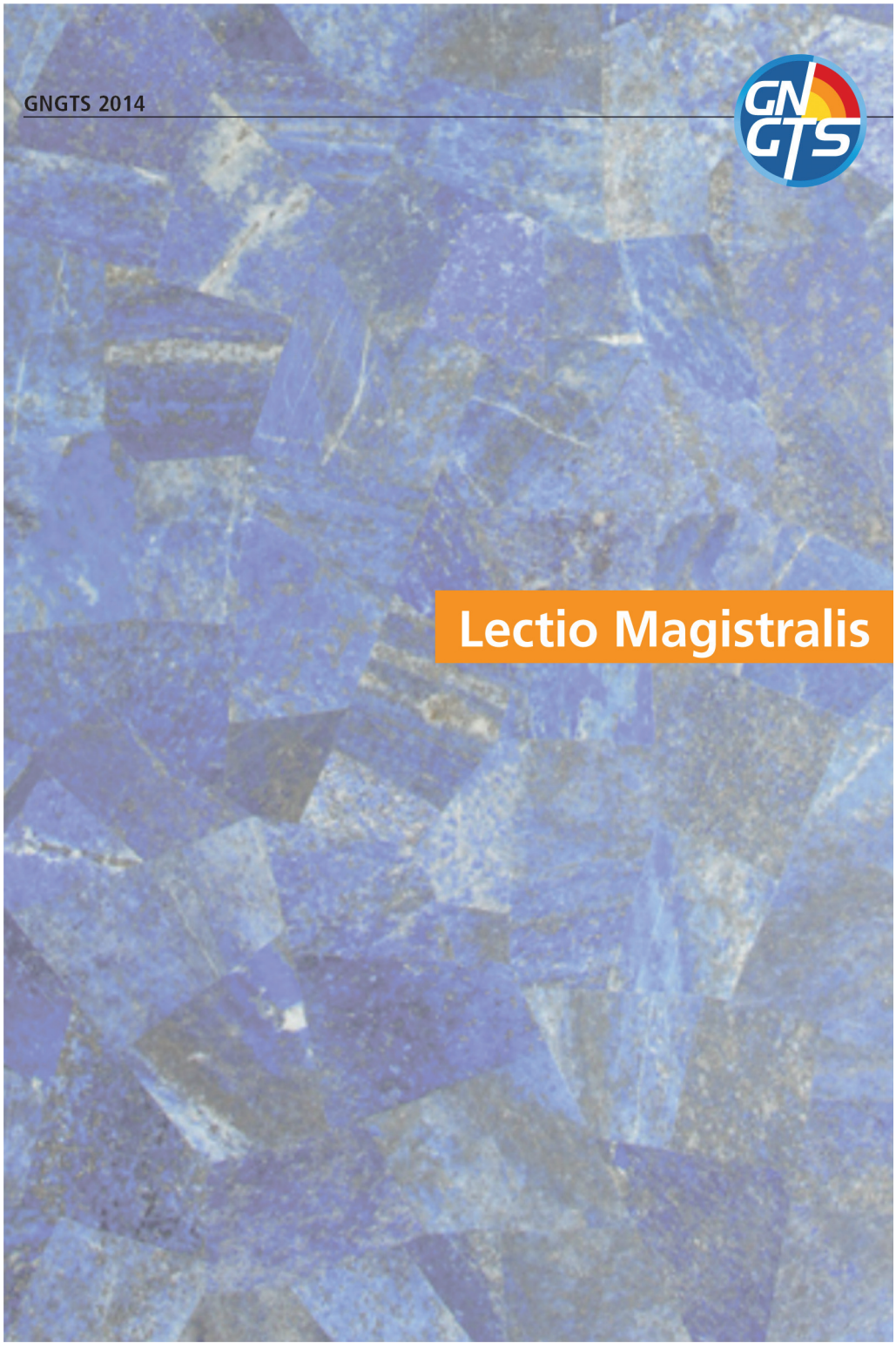

# Lectio Magistralis

# GIUSEPPE MERCALLI *"MAESTRO DOTTO, MODESTO E GENEROSO"*

**Andrea Tertulliani**
*Istituto Nazionale di Geofisica e Vulcanologia, Roma*

Cento anni fa, nella notte tra il 18 e il 19 marzo 1914 Giuseppe Mercalli moriva tragicamente nell'incendio del suo alloggio napoletano. Era in quel momento il Direttore del Regio Osservatorio Vesuviano.

È impossibile in poche righe tracciare in modo esaustivo il ritratto di Giuseppe Mercalli, il ruolo che ha avuto per le scienze della terra e il suo percorso umano e scientifico. Durante tutto questo anno 2014 si sono svolte molte commemorazioni, in tutta Italia, e molte cose sono state scritte [vedi tra le altre Di Vito *et al*. (2014)].

Lo scopo di questa breve Lectio è quindi di ripercorrere la sua biografia per cercare di contestualizzarlo nel suo tempo, in una sintesi, per forza di cose, parziale.

Giuseppe Mercalli era nato a Milano il 21 maggio 1850, in una famiglia di artigiani tessili, terzo di cinque figli. Dopo gli studi in seminario, venne ordinato sacerdote nel 1872.

Scelse il titolo di abate, per poter insegnare ed essere "libero" da compiti pastorali, così poté dedicarsi allo studio e all'insegnamento e come molti altri religiosi prima di lui perpetuò la tradizione di sacerdoti scienziati, molto diffusa tra il XVII e il XIX secolo. Il suo stesso maestro e mentore, l'abate Antonio Stoppani, fu un illustre geologo, docente al Politecnico di Milano.

La formazione spirituale, civile e professionale di Mercalli vennero senz'altro influenzate dal suo aderire alla dottrina rosminiana, a quel tempo oggetto di opposizione da parte di ambienti della Curia, fino ad arrivare alla messa all'indice delle opere del filosofo di Rovereto. Sulla scorta infatti degli insegnamenti liberali di Rosmini, Mercalli e soprattutto il suo maestro Stoppani furono proponenti e protagonisti di un avvicinamento tra progresso scientifico e chiesa cattolica, oltre a vedere un chiaro ruolo sociale e pedagogico dello scienziato soprattutto in vista della formazione della nascente nazione italiana [si veda ad es. Licata (1968) e Rimoldi (1983)].

Per Mercalli, che non viveva in una torre d'avorio, l'insegnamento sarà una regola di vita e un dovere civile.

Sotto la guida di Stoppani divenne insegnante di Scienze Naturali al seminario, e contemporaneamente pubblicò i suoi primi lavori di glaciologia. Tra i suoi allievi e assistenti dobbiamo segnalare Achille Ratti, futuro papa Pio XI, al quale Mercalli chiese di collaborare ad un capitolo di una delle sue opere più famose, *Vulcani e fenomeni vulcanici in Italia*, e cioè alla parte riguardante il catalogo dei terremoti (Fig. 1).

Il terremoto di Casamicciola del 1883 rappresentò il suo primo incontro diretto con il fenomeno sismico: durante le vacanze estive si recò sul posto per studiare direttamente gli effetti del disastro. Studiando il precedente del 1881, Mercalli si era fatta l'idea che i terremoti ischitani fossero l'espressione diretta dell'attività vulcanica del monte Epomeo. Questa ipotesi, che traeva elementi in una visione ancora plutonica, confermava secondo Mercalli il legame strettissimo tra i terremoti e l'attività vulcanica: "*tutti i fenomeni endogeni, diversissimi nelle loro manifestazioni, sono fra di loro intimamente legati per l'armonia colla quale agiscono nell'economia tellurica, quasi una sola forza, ad un unico scopo: la reazione contro l'azione degradatrice e livellatrice degli agenti esterni*" (Mercalli, 1883).

Bisogna dire tuttavia che il Nostro si dimostrò "*parco nella trattazione riguardo l'origine dei terremoti, argomento al quale pur troppo molti hanno dedicato soverchie quanto inutili disquisizioni, affastellando ipotesi destinate presto, prestissimo a tramontare*" (Baratta, 1915), mentre presterà estrema attenzione ai danni subiti dagli edifici, al loro rapporto con la litologia e la morfologia del territorio, ma soprattutto alla grande responsabilità che la qualità delle costruzioni ha nel generare gravi danni. La pubblicazione sui terremoti di Ischia (Mercalli, 1884) riceverà molto apprezzamento (*"il mio terno al lotto"* lo chiamava) anche in ambienti governativi, oltreché scientifici.


Fig. 1 – Carta sismica con la rappresentazione topografica dei terremoti basata sul catalogo pubblicato in *Vulcani e fenomeni vulcanici in Italia* (Mercalli, 1883).

Raggiunta una certa notorietà, nel 1885 venne inviato in missione dal Governo italiano a studiare il terremoto dell'Andalusia, insieme a Torquato Taramelli (altro allievo di Antonio Stoppani). Nel 1887 il terremoto della Liguria occidentale, altra grande tragedia nazionale, fu un'ulteriore occasione di studio, sempre su incarico ministeriale. Da allora quasi ogni terremoto italiano significativo vedrà la presenza e lo studio di Mercalli.

La adesione di Mercalli alle idee rosminiane fu la causa e forse la molla che lo spinse a decidere di andare via da Milano e gli aprì, non senza qualche difficoltà, definitivamente la carriera. Motivo delle sue dimissioni dall'insegnamento al seminario era stata la sua partecipazione ad una sottoscrizione proposta da Stoppani per un monumento a Rosmini da porre dinanzi al Museo Civico di Milano. La polemica fu rovente e la Curia milanese chiese la ritrattazione da parte di Mercalli e degli altri firmatari, pena la decadenza dall'incarico di insegnante. Con risposta cortese ma ferma, Mercalli rassegnò le dimissioni. Siamo alla fine del 1888. Mercalli forse desiderava comunque una destinazione più vicina agli oggetti dei propri studi, i vulcani, siti nel meridione d'Italia, documentata anche dalle sue richieste per insegnare nella scuola pubblica presso sedi come Catania, Napoli o Messina (Redondi, 2014).

Tuttavia il suo primo incarico fu a Reggio Calabria nel 1889, pare per le pressioni di Piero Tacchini, direttore dell'Ufficio Centrale di Meteorologia e Geodinamica, al quale interessava la sua collaborazione per gli studi sulle Eolie. Nel 1892 Mercalli fu trasferito a Napoli, ad insegnare presso il liceo Vittorio Emanuele. E' il coronamento della sua grande passione: il Vesuvio.

Prese casa con vista sul vulcano, un modesto appartamento di due stanze in via della Sapienza, e le mattine, durante il suo periodo napoletano, prima di andare ad insegnare o di salire sul Vesuvio (Figg. 2 e 3), "*diceva messa nella chiesa di S. Agnello Maggiore, e spesso si fermava ivi a pregare e a confessare (testimonianza nella lettera di Luigi Sartorelli, curato di S. Agnello, all'Osservatore Romano del 21 marzo 1914, a risposta delle voci che vedevano il M. aver rinunciato all'abito)"* (Osservatore Romano, 1914).

Fig. 2 – Giuseppe Mercalli sul Vesuvio nel 1907 (Archivio Storico Osservatorio Vesuviano).

Fig. 3 – Giuseppe Mercalli sul Vesuvio nel 1907 (Archivio Storico Osservatorio Vesuviano).

Nel 1903 concorse al posto di Direttore del prestigioso Osservatorio Vesuviano. Matteucci, il suo antagonista nelle polemiche sulla formazione del Colle Umberto nel corso dell'attività del Vesuvio del 1895-98 (polemica fra la teoria dei crateri di sollevamento e la formazione per accumulo, sostenuta dal Mercalli), vinse.

Mercalli si dichiarò deluso al punto di non voler avere più niente a che fare con l'Osservatorio.

Tuttavia alla morte di Matteucci, nel 1911 divenne Direttore dell'Osservatorio Vesuviano, fino al giorno della sua morte. I funerali di Mercalli furono solenni e seguiti da una moltitudine, poiché la sua notorietà, soprattutto a Napoli era immensa. Per i suoi contemporanei fu un vero innovatore, ed una guida per i suoi colleghi e allievi; il giornale La Libertà (1914) scrisse "*Egli fece emergere la vulcanologia dai garbugli delle induzioni e delle mistificazioni della stregoneria*", evidenziando di fatto la sua autorevolezza di scienziato anche in un ambito ben più ampio di quello meramente scientifico.

L'attività di ricerca di Giuseppe Mercalli non è scindibile in vulcanologica e sismologica *tout court*, ma entrambi i filoni di ricerca, essendo considerati come le facce di una stessa medaglia, saranno sempre presenti parallelamente durante tutta la sua avventura scientifica. Lo possiamo annoverare tra gli ultimi scienziati di stampo naturalista, dalla tradizione sette-ottocentesca, per quanto riguarda le scienze della terra, un ponte tra sismologia e vulcanologia osservazionali e quella che sarà la travolgente affermazione degli strumenti di misura. Mercalli era consapevole di questo aspetto, e si tenne abbastanza in disparte, conscio delle sue difficoltà sul piano tecnologico (Malladra, 1914). Ciononostante si fece promotore per l'acquisizione di nuovi e più moderni strumenti di misura per l'Osservatorio Vesuviano.

Ma la sua grande innovazione fu nel metodo: egli capì che la chiave per la comprensione dei fenomeni era la loro osservazione sistematica e la classificazione delle loro caratteristiche, tanto per i vulcani che per i terremoti. A lui si deve il primo vero catalogo dei terremoti, del

1883. Baratta scrisse: "*Con le ricerche del Nostro la cronistoria sismica italiana presenta una ricchezza incomparabile di dati sicuri e l'opera sua è stata ed è tuttora la fonte e la guida per ulteriori ricerche…"*(Baratta, 1915). L'importanza dell'impostazione data da Mercalli alle ricerche sismologiche risalta anche nella dedica che lo stesso Baratta pone all'inizio del suo "I terremoti d'Italia" (Baratta, 1901), caposaldo della letteratura sismologica storica italiana: "*Al professore Mercalli con la riverenza e l'affetto di un discepolo"*.

La stessa spinta innovativa era rivolta allo studio dei vulcani, rinnovando i criteri di classificazione dei vari tipi eruttivi. Mercalli, sulla base dei suoi studi sui vulcani attivi italiani e dei numerosi vulcani spenti, e per la sua vasta conoscenza della letteratura vulcanologica scrisse il trattato "I vulcani attivi della Terra" (Mercalli, 1907). *"Si tratta di un catalogo ragionato dei vulcani attivi del mondo attraverso la morfologia degli apparati, la dinamica delle eruzioni e il chimismo dei prodotti eruttati; si fornisce un testo di vulcanologia impostato sui criteri scientifici più avanzati all'inizio del '900. In quest'opera Mercalli introduce la classificazione dei vulcani per diverse tipologie, secondo il modo di formazione dell'edificio vulcanico"* (Luongo, 2014).

La sua visione della scienza come disciplina didattica e civile fu senz'altro influenzata dalla sua formazione rosminiana. Nei suoi studi sui terremoti sottolineava sempre la necessità che sia l'uomo a cercare di difendersi dai terremoti, rivendicando da una parte il ruolo centrale del sismologo nel prescrivere le indicazioni sui rischi, dall'altra indicando che fosse nella responsabilità di chi governa creare le condizioni per una difesa dai terremoti. Emblematico il titolo di un articolo del 1885, dopo il terremoto di Casamicciola, "Le case che si sfasciano e i terremoti" (Mercalli, 1885), nel quale si evidenzia la straordinaria intuizione, quasi una preveggenza sui mali sismici italiani degli anni successivi: "*Sarebbe quindi molto utile che si compilassero delle storie sismiche municipali, onde le autorità civiche locali sappiano **se e quanto** interessi tener calcolo dell'eventualità di terremoti violenti nel formulare ed applicare i regolamenti edilizi"*.

Fa impressione la sua volontà, espressa nel 1889, di rimanere a insegnare a Reggio Calabria in quanto, secondo lui, la Calabria sarebbe stata la sede del prossimo *parossismo*, e non avrebbe voluto perderselo, da studioso qual'era. La Calabria fu infatti colpita da una ben nota serie di eventi nel 1894, 1905, 1907 e infine 1908.

Purtuttavia anche Mercalli restò vittima, come anche noi oggi ben abbiamo sperimentato, della disillusione propria del ricercatore che non trova ascolto concreto ai suoi ripetuti richiami: *"…nessuno mostrò di dare importanza alle carte sismiche che io ed il mio amico prof. M. Baratta da anni andiamo elaborando, senza alcun aiuto o incoraggiamento ufficiale"* (Baratta, 1915).

Dopo queste brevi e incomplete note sulla biografia e attività di Mercalli mi prendo la libertà di toccare più in dettaglio l'argomento che più mi avvicina (con rispetto parlando) a lui dal punto di vista professionale, e cioè quello per cui è probabilmente più noto nel comune sentire, la Scala Mercalli. O meglio le scale di Mercalli.

Nella seconda metà dell'Ottocento le scale di intensità erano già usate per classificare gli effetti sul territorio dopo un terremoto, ma erano elaborate sul singolo evento ed usate solo dall'autore (*Personal scales*, le chiamerà il Davison) e quindi tutte diverse. Lo stesso Mercalli ne aveva pubblicata una di sei gradi nel 1883. La svolta rivoluzionaria sarà opera di De Rossi (1874) il quale proporrà e renderà operativa una scala con l'intenzione dichiarata di rendere gli studiosi in grado confrontare i terremoti tra loro e classificare gli effetti per le località colpite.

La più usata ed accettata era al tempo di Mercalli, la scala De Rossi-Forel (De Rossi, 1883) in dieci gradi, concordata sulla fusione delle due scale omonime, utilizzate rispettivamente per i terremoti italiani e svizzeri.

Gli studi sul campo sugli effetti dei terremoti, (in special modo quello andaluso del 1884-85 e quello ligure del 23 febbraio 1887) avevano persuaso Mercalli che le scale sino allora in uso, in particolare la De Rossi-Forel, non erano adeguate a descrivere la gradualità del

danneggiamento. Così ne propose una modifica nel 1897, che venne accettata e approvata dalla comunità scientifica e divenne ufficiale nell'uso dal 1900. La De Rossi–Forel, scrisse Mercalli più tardi nelle motivazioni alla sua proposta di modifica (Mercalli, 1902), non aveva la giusta risoluzione per descrivere i danni in quanto squilibrata verso il basso, avendo sei gradi (dal II al VII) per gli effetti sull'uomo, senza danni, e solo tre (VIII, IX e X) per i danni agli edifici: *"mentre è evidente che la differenza di intensità tra un terremoto che fa cadere i fumajoli delle case, e quello che abbatte i muri maestri di solidissimi edifizi, è certamente maggiore è più facile a determinarsi e a graduarsi, che quello che passa tra una scossa sentita da qualche persona (2° grado De Rossi-Forel) e una scossa che cagiona spavento generale e caduta di qualche calcinaccio (VII grado De Rossi-Forel)"*. Alla Seconda Conferenza Internazionale di Sismologia a Strasburgo Adolfo Cancani (1904) propose una variante della scala chiamandola Forel-Mercalli con inclusi i valori di accelerazione per ogni grado, e chiedendo anche di estendere la scala almeno di un grado, per poter descrivere i grandi terremoti giapponesi e americani. Ottenne per questo il benestare di Mercalli, ma la Forel-Mercalli non vide mai la luce ufficialmente. Dopo il terremoto di Messina nel 1908, e aver constatato personalmente l'enorme livello di danneggiamento il Mercalli modificò la sua scala aggiungendo, prima il grado XI (*catastrofe*), e in seguito il XII (*grande catastrofe*). Nel 1912 Sieberg riprese e rielaborò la proposta di Cancani, cominciando a confezionare la Mercalli-Cancani-Sieberg, molto più dettagliata ed efficace negli elementi di diagnosi, rispetto alle prime scale di Mercalli. Nonostante Mercalli non avesse più preso parte a nuove compilazioni di scale, il suo nome è rimasto legato a quasi tutte le scale successive: la Mercalli-Cancani-Sieberg del 1923 (Sieberg, 1923) e poi del 1930 (Sieberg, 1930), la Mercalli Modificata del 1931 (Wood and Neumann, 1931): nelle sue varie versioni.

**Riconoscimenti.** Nella scrittura di questa nota, e soprattutto nella esposizione della Lectio Magistralis, ho attinto dalla letteratura, ma molto anche dalla mia memoria nella quale si sono impressi nel tempo contributi di colleghi che probabilmente e in modo involontario, potrei aver citato senza recuperarne la fonte. Spero che sia considerato peccato veniale. Ringrazio comunque tutti coloro che hanno avuto a che fare con la figura di Giuseppe Mercalli, ed hanno lasciato scritto qualcosa su di lui. La citazione in virgolettato nel titolo è tratta dalla commemorazione di Baratta (Baratta, 1915).

### Bibliografia

Baratta M.; 1901: *I terremoti d'Italia*. A. Forni Editore, Rist. Anast. Bologna, 1979, 951 pp.

Baratta M. ;1915: *L'opera scientifica di Giuseppe Mercalli*. Boll. Soc. Geol. Ital., **34**, 342-419.

Cancani A.; 1904: *Sur l'emploi d'une double èchelle sismique des intensités, empirique et absolue*. In: Emil R., Annexe A 10-Comptes-rendus des séances de la deuxième conférence sismologique internationale réunie à Strasbourg du 24 au 28 juillet 1903, Beiträge zur Geophysik, Ergänzungsband II, Verlag Wilhelm Engelmann Leipzig, 362 pp.

De Rossi M.S.; 1874: *Bollettino del Vulcanismo Italiano*. Anno I, p.i., Roma.

De Rossi M.S.; 1883: *Programma dell'Osservatorio ed Archivio Centrale Geodinamico presso il R. Comitato Geologico d'Italia*. Boll. Vulc. It., **10**, 66-68.

Di Vito M.A., Ricciardi G.P., de Vita S., Cubellis E. e Tertulliani A. (a cura di); 2014: *Giuseppe Mercalli da Monza al Reale Osservatorio Vesuviano: una vita tra insegnamento e ricerca. Contributi presentati per l'inaugurazione dell'Anno Mercalliano*. Miscellanea INGV, 24, Napoli, 166 pp.

La Libertà; 1914: *21-22 marzo 1914*.

Licata G.; 1968: *La "Rassegna Nazionale", conservatori e cattolici liberali attraverso la loro rivista (1879-1915)*. In: Politica e Storia, 20, Edizioni di Storia e letteratura, Roma.

Luongo G.; 2014: *Una riflessione sull'attività scientifica di Giuseppe Mercalli*. In: Di Vito M.A., Ricciardi G.P., de Vita S., Cubellis E. e Tertulliani A. (a cura di), Giuseppe Mercalli da Monza al Reale Osservatorio Vesuviano: una vita tra insegnamento e ricerca, Contributi presentati per l'inaugurazione dell'Anno Mercalliano, Miscellanea INGV, 24, pp. 20-30.

Malladra A.; 1914: *L'attività scientifica di Giuseppe Mercalli*. Rassegna Nazionale, fasc. 1, 200, pp. 42-63.

Mercalli G.; 1883: *Vulcani e fenomeni vulcanici in Italia*. In: Negri, Stoppani e Mercalli (a cura di), La geologia d'Italia, F. Vallardi, parte III, Milano.

Mercalli G.; 1884: *L'isola d'Ischia ed il terremoto del 28 luglio 1883*. Mem. Ist. Lombardo, Scienze Mat. e Nat. **15**, 99-154.

Mercalli G.; 1885: *Le case che si sfasciano ed i terremoti*. Rassegna Nazionale, **21**, 255-264.

Mercalli G.; 1902: *Sulle modificazioni proposte alla scala sismica De Rossi-Forel*. Boll. Soc. Sismol. It., **8**, 184-191.

Mercalli G.; 1907: *I vulcani attivi della terra*. U. Hoepli, Milano, 422 pp.

Osservatore Romano; 1914: *21 marzo 1914*.

Redondi P.; 2014: *Giuseppe Mercalli: storia di una vocazione scientifica*. In: Di Vito M.A., Ricciardi G.P., de Vita S., Cubellis E. e Tertulliani A. (a cura di), Giuseppe Mercalli da Monza al Reale Osservatorio Vesuviano: una vita tra insegnamento e ricerca, Contributi presentati per l'inaugurazione dell'Anno Mercalliano, Miscellanea INGV, 24, pp. 9-19.

Rimoldi A.; 1983: *Le tensioni tomiste-rosminiane a Milano dalla "Aeterni Patris" alla restaurazione della Facoltà teologica (1879-1892)*. In: Fois M., Monachino V. e Litva F. (a cura di), Dalla Chiesa antica alla Chiesa moderna, Univ. Gregoriana, Roma.

Sieberg, A.; 1923: *Geologische, Physikalische und Angewandte Erdbebenkunde*. G. Fischer, Jena.

Sieberg, A.; 1930: *Geologie der Erdbeben*. Handbuch der Geophysik, **2**(4), 552-555.

Wood H.O. and Neumann F.; 1931: *Modified Mercalli Intensity Scale of 1931*. Bull. Seismol. Soc. Am., **21**, 277-283.

# Tema 3

## Geofisica Applicata

# sessione 3.1

## Sismica superficiale e profonda

**Convenor: U. Tinivella e P. Mazzucchelli**

**co-organizzata con Sezione Italiana Eage-Seg**

# 3D INTERPOLATION USING HANKEL TENSOR COMPLETION BY ORTHOGONAL MATCHING PURSUIT

**A. Adamo, P. Mazzucchelli**
*Aresys, Milano, Italy*

**Introduction.** Seismic data are often sparsely or irregularly sampled along one or more spatial axes. Irregular sampling can produce artifacts in seismic imaging results, thus multidimensional interpolation of seismic data is often a key processing step in exploration seismology. Many solution methods have appeared in the literature: for instance in Spitz (1991), Sacchi (2000) it was proposed to perform seismic trace interpolation that handles spatially aliased events using the linear predictors to estimate the missing traces through linear filters in the f-x(y) domain.

Conversely, multidimensional Fourier reconstruction methods exploit a different data representation domain, while still assuming that seismic data consists of a superposition of plane waves: statistical sparsity is assumed in order to retrieve a model that consists of a few dominant wavenumbers representing the observations (Liu, 2004; Sacchi, 2010). In Xu (2004, 2005) and Sacchi (2000) the so-called Antileakage Fourier Transform (ALFT) algorithm was proposed: it tries to resolve, or at least attenuate, the spectral leakage of the irregular Fourier Transform by taking advantage of the compressive sensing framework (data are assumed to be sparse in the frequency-wavenumber domain).

In more recent years, methods based on alternative local transformations, such as curvelet and seislet transforms (Herrmann, 2010; Fomel, 2010), have also been proposed.

Recently, new interpolators have been developed recasting the interpolation problem to a compressive sensing matrix completion problem (Candes, 2009; Yang, 2013; Herrmann, 2014). A matrix with randomly missing entries can be completed by solving the rank minimization problem under the low-rank assumption of the underlying solution, that is in opposition to the fact that the subsampling operator tends to increase the rank of the matrix. Trickett (2010) proposed to apply a Cadzow filtering to solve the trace interpolation problem. The Cadzow algorithm replaces the block Hankel matrix of the incomplete and noisy multidimensional observations: it allows to recover the complete data volume by its low rank approximation and successive averaging along the anti-diagonals of the rank-reduced Hankel matrix.

In recent literature, the low-rank tensor completion technique has become widely used in many areas such as computer vision, signal processing and seismic data analysis. This approach is based on a high order generalization of the low-rank matrix completion problem, and can be approximated by convex relaxation which minimizes the nuclear norm instead of the rank of the tensor. In Trickett (2013) a generalization of Hankel matrices is applied to the tensor to perform an efficient completion.

In order to extend these approaches from matrix to tensor completion, we make use of extended notions on the concept of rank borrowed from linear algebra in conjunction with the high dimensional tensor theory.

Tensor algebra is a mathematical framework that generalizes the concepts of vectors and matrices to higher dimensions. These tools are widely used to address problems of missing data in biomedical signal processing, computer vision, image processing, communication and seismic data processing.

The High Order Singular Value Decomposition (HOSVD; Kolda, 2009) is used in many tensor rank-reduction algorithms. The HOSVD technique can be viewed as a generalization of the classical SVD for tensors. The computation of the HOSVD (De Lathauwer, 2000; Bergqvist, 2010) requires performing SVD as many times as the order of the tensor, over all the possible matrix representations of the tensor. Due to this fact the HOSVD can be expensive in terms of computational time.

In tensor completion, the goal is to fill missing entries of a partially known tensor, under a low-rank condition. Many algorithms have been proposed in literature (Da Silva, 2013; Kreimer,

2012) to solve the low-rank tensor completion problem with global optimization methods.

In this work, we want to introduce a new greedy algorithm, called Orthogonal Rank-One Tensor Pursuit (OR1TP), that extends the Orthogonal Matching Pursuit (OMP) algorithm (Pati, 1993; Davis, 1994) that works in multidimensional tensor space and finds a low rank approximation of a tensor. We present a novel seismic interpolation algorithm based on the rank reduction technique, that solves the low-rank Hankel tensor completion problem in the frequency domain and that is capable to fill missing seismic traces in 3D dataset. Finally, we show experimental results obtained on synthetic data to prove the effectiveness of our method.

**Theory.** A tensor is the generalization of vectors, matrices to higher dimensions. Let $Y \in \boldsymbol{C}^{n_1 \times n_2 \times \ldots \times n_N}$ be a *N*-th order tensor, while $\Omega \subset \{1, \ldots, n_1\} \times \{1, \ldots, n_2\} \times \ldots \times \{1, \ldots, n_N\}$ denotes the indexes of the observed entries of *Y*. The order *N* of a tensor is the number of dimensions, also known as ways or modes.

A second-order tensor is a matrix and a first-order tensor is a vector. Let $P_\Omega$ be the projector onto the space such that the indexes $(i_1, i_2, \ldots, i_N) \in \Omega$.

It is well known that the rank of a matrix coincides with its column and row rank. The rank of a tensor is a much trickier concept. The rank of a tensor *Y* is equal to the minimum number of rank-one tensors that yield *Y* in a linear combination.

Any tensor $Y \in \boldsymbol{C}^{n_1 \times n_2 \times \ldots \times n_N}$ can be written as a linear combination of rank-one tensors, that is

$$Y = \sum_{i=1}^{R} \theta_i (u_1^{(i)} \circ u_2^{(i)} \circ \ldots \circ u_N^{(i)}) = \sum_{i=1}^{R} \theta_i T_i = T(\theta)$$

where $\lambda^{(i)} \in \boldsymbol{R}, u_j^{(i)} \in \boldsymbol{C}^{n_j}$ are rank-one tensors such that $\langle u_j^{(i)}, u_j^{(k)} \rangle = 0 \; \forall i \neq k$ and *r* is the rank of the tensor *Y*.

Rank-One tensor decomposition, also called Canonical Polyadic Decomposition (CPD; Zhang, 2001), gives a compact representation of the underlying structure of the tensor, revealing when the tensor-data can be modeled as lying close to a low dimensional subspace.

The low-rank tensor completion problem aims to minimize the zero-norm of $\theta$ subject to the equality constraint $P_\Omega(T(\theta)) = P_\Omega(Y)$ as follows:

$$\min_\theta \|\theta\|_0 \qquad s.t. \; P_\Omega(T(\theta)) = P_\Omega(Y) \qquad (P0)$$

Unfortunately, direct (P0) norm minimization problem is NP-hard (nondeterministic polynomial time hard

problem) because it is equivalent to a subset selection problem, which is itself an NP-hard combinatorial optimization problem (Donoho, 2004).

**Orthogonal Rank-One Tensor Pursuit.** We can relax the original problem by rewriting (P0) as follows:

$$\min_\theta \left\| P_\Omega(T(\theta)) - P_\Omega(Y) \right\|^2 \qquad s.t. \|\theta\|_0 \leq r \qquad (G0)$$

The main idea is to extend the Orthogonal Matching Pursuit (OMP) procedure (Pati, 1993; Davis, 1994) from the vector field to the tensor field, introducing a novel greedy algorithm called Orthogonal Rank-One Tensor Pursuit (***OR1TP***) that solve (G0) problem in an efficient way. Following the idea proposed by (Wang, 2014), at each iteration a rank-one basis tensor is generated by the vectors that approximate the residual tensor of the data. After that, the weights of the current rank-one tensor bases are updated by performing an orthogonal projection of the

observation tensor on their spanning subspace. The most time consuming step of this method is the computation of the tensor $T = u_1 \circ u_2 \circ \ldots \circ u_N$ that best approximate the residual $R_k = P_\Omega(Y) - \sum_{i=1}^{k-1}(T_i)_\Omega$. This step requires to solve the maximization problem:

$$\max_T \{ \sum_{i_1, i_2, \ldots i_N} T(i_1, i_2, \ldots, i_N) R_k(i_1, i_2, \ldots, i_N) \;\; s.t. \quad rank(T) = 1, \qquad \|T\| = 1 \}$$

In Zhang (2001) iterative methods, based on the Multilinear Rayleigh Quotients, are suggested to find a rank-one approximation of $R_k R_k$ in an efficient way. Differently from the classical Orthogonal Matching Pursuit algorithm, that requires the storage of the entire vectors bases, the proposed algorithm estimates a basis tensor only once, allowing an efficient memory management.

**Orthogonal Rank-One Tensor Pursuit (OR1TP)**

- **Input:** $Y_\Omega$ and a tolerance parameter $\epsilon$
- **Initialize:** $X_0 = 0,\ \theta^k = 0, k = 1$
- Repeat
  - Find a pair of singular tensors $(x_k, y_k, w_k, z_k)$ of the observed residual $R_k = Y_\Omega - X_{k-1}$, set $T_k(i,j,l,k) = x(i)\ y(j)\ w(l)\ z(k)$
  - Solve $\hat{T}_k \theta^k = \hat{y}$, $\hat{m}_I$ reshape of $(T_k)_\Omega$, $\hat{y}$ reshape of $Y_\Omega$
  - Set $X_k = \sum \theta_i^k (T_i)_\Omega$
- Until $\|R_k\| < \epsilon$
- **Output:** $\hat{Y} = \sum \theta_i^k T_i$

Tab. 1. Orthogonal Rank-One Tensor Pursuit (OR1TP) solve the (OMP) by an orthogonal matching pursuit type greedy algorithm using rank-one tensors as the basis. Given a tensor $Y_\Omega$ with missing values, finds a tensor $\hat{Y}$ which is a low-rank approximation of the observed tensor.

**Application to data interpolation problem.** Recently, many trace interpolators based on low-rank tensor completion have been proposed. Our interpolation method considers 3D spatial data in frequency/space domain. We consider the case where seismic traces are attributed to a regular 3D grid through binning. In the case that more than one trace is assigned to a bin, we average them to retain only one observation in each bin. In real situations, mapping seismic traces from an irregular to a regular grid through the binning process, leads to a highly sparse volume with missing traces randomly disposed.

Given a 3D seismic dataset in time-space domain, in order to recover missing traces, we first perform a 1D discrete Fourier transform on the time axis.

A symmetric tensor is a tensor that is invariant under a permutation of its vector arguments $T(i_1, \ldots, i_N) = T(\sigma_1, \ldots, \sigma_N)$ for any permutation $\sigma$. Symmetric tensors form a singular important class of tensors. Hankel tensors are symmetric tensors that originate from applications such as signal processing. Due to the fact that Hankel tensors are symmetric and then well structured, the low-rank assumption is enhanced by the geometrical structure of the data.

To recover the missing samples, each frequency slice of the data in frequency-space domain is rearranged in a 4D Hankel tensor. This tensor can be obtained with an appropriate transformation as described in Trickett (2010). Given a raw 2D frequency slice $\in \boldsymbol{C}^{m\times n}$, to form the 4D Hankel tensor $\boldsymbol{T} \in \boldsymbol{C}^{p\times q\times r\times s}$, we apply the following:

$$T(i,j,k,l) = S(i+j-1, k+l-1)$$

where the four tensor directions have length, respectively, $p = \frac{m}{2}+1$, $q = \frac{m+1}{2}$, $r = \frac{n}{2}+1$ and $t = \frac{n+1}{2}$, with $i \in \{1,\dots,p\}$, $j \in \{1,\dots,q\}$, $k \in \{1,\dots,r\}$ and $l \in \{1,\dots,s\}$.

Once the tensor *T* is obtained, the low-rank tensor completion is performed by the OR1TP algorithm and the interpolated frequency slice is obtained applying the inverse transform.

The interpolation procedure described above is summarized in Tab. 2.

- Take the Discrete Fourier Transform (DFT) of each trace in the grid
- For each frequency within the signal band
  - Form a complex-value Hankel tensor *T*
  - Perform tensor completion on *T* by OR1TP algorithm
  - Recover the interpolated frequency slice from the completed tensor
- Take the Inverse Discrete Fourier Transform (IDFT) of each trace.

Tab. 2. Interpolation procedure by low-rank Hankel tensor completion in frequency domain performed by the OR1TP greedy algorithm.

**Examples.** We chose to test the proposed approach with a portion of the synthetic SEG Advanced Modeling Program (SEAM) 3D dataset to prove the effectiveness of our method. We obtained an irregularly sampled dataset from the (regularly sampled) reference data by removing a randomly selected subset of traces. Two different parameter sets have been tested: in the first experiment (Fig. 1), each 2D frequency slice is of size 7 × 7 samples, that rearranged in a Hankel tensor becomes a 4D volume of size 4 × 4 × 4 × 4. Due to the fact that the maximum rank of our 4D Hankel tensor is $n^3 = 64$, we recovered each tensor by approximating it with a tensor having maximum rank equal $\frac{n^3}{2} = 32$ . In the second experiment, the frequency slice is a window of size 5 × 5 samples that, once mapped to a Hankel tensor, becomes a multidimensional array of order 4 and size 3 × 3 × 3 × 3. Similarly to the experiment previously described, the maximum rank was chosen equal to $\left\lceil \frac{n^3}{2} \right\rceil = 14$.

To better highlight the interpolation capability of the proposed approach, both experiments have being carried out by eliminating half of the traces in the original 3D dataset.

The computation of the rank-one tensor that approximates the residual tensor at each iteration of the OR1TP is performed through the generalized iterative Rayleigh quotient method (Lathauwer, 2000), choosing as stopping criteria either maximum number of iterations *MaxIter* = 20 and tolerance *tol* =1e-3.

Fig. 1 shows the results obtained by OR1TP greedy algorithm with frequency slices of size 7 × 7 samples over a portion of the data containing linear events.

Fig. 2 shows the results obtained by filling the missing traces with OR1TP algorithm. In this case, the frequency slice size is equal to 5 × 5 samples. In this portion of data there is the presence of hyperbolic events with high curvature that does not influence the results of the reconstruction.

To evaluate quantitatively the performance of our interpolation algorithm, we chose to vary the percentage of randomly zeroed traces from 20% to 60% for fixed instances (5×5 and

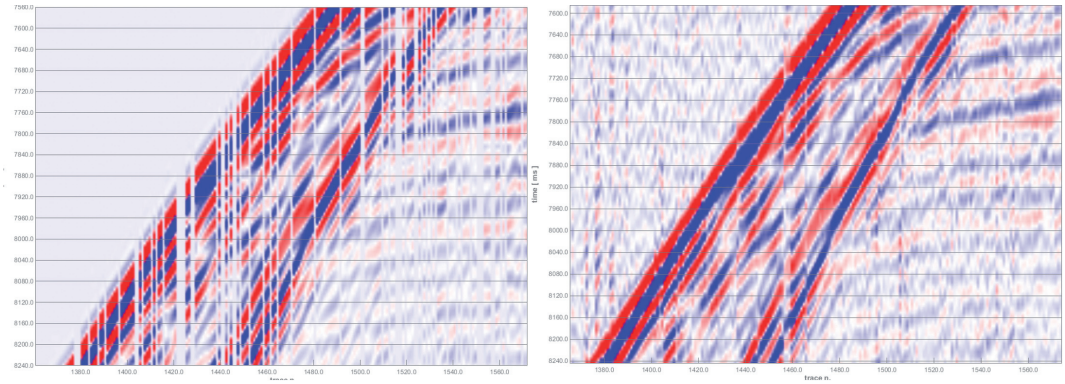

Fig. 1 - Results obtained on a portion of data with presence of linear events. Subset of synthetic data with 50% of missing traces (left), interpolation result obtained by OR1TP algorithm (right).

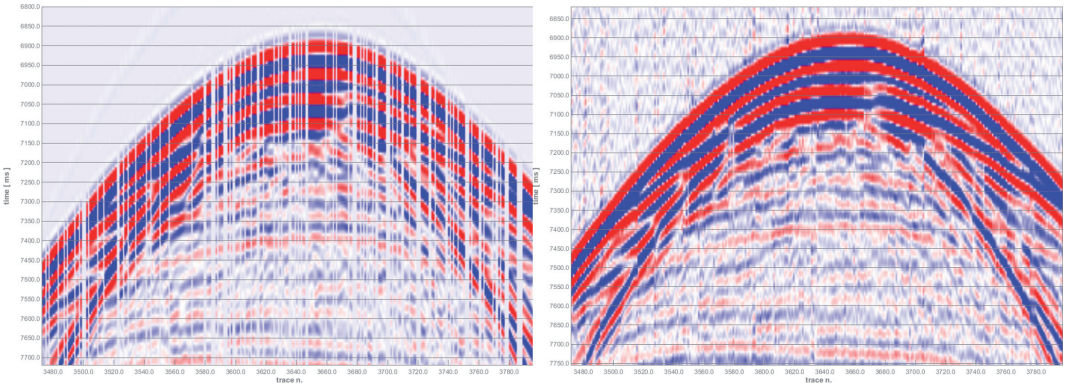

Fig. 2 - Results obtained on a portion of data with presence of hyperbolic events. Subset of synthetic data with 50% of missing traces (left), interpolation result obtained by OR1TP algorithm (right).

7×7 frequency slice size), and to calculate the Signal to Noise Ratio of the recovered data in time domain. Results are showed in Fig. 3. As it was easy to guess, the reconstruction quality decreases as the percentage of censored traces increases, maintaining acceptable values even with high number of missing traces.

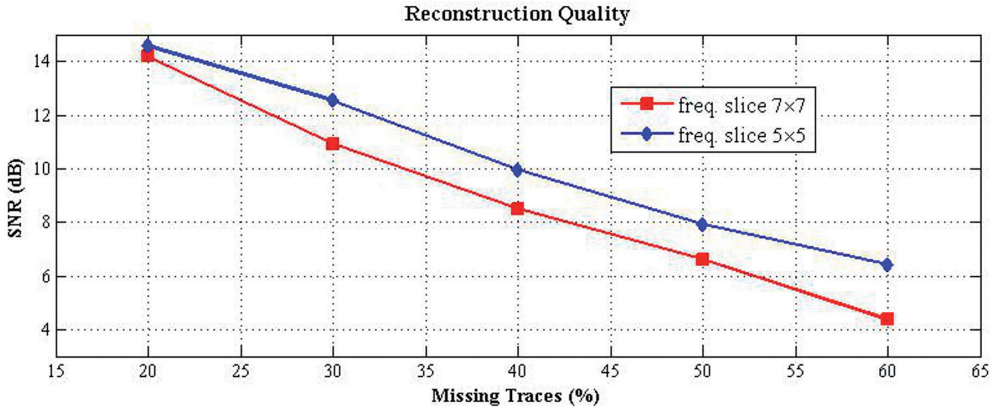


Fig. 3 - Quality reconstruction obtained for 5×5 and 7×7 frequency slice size, varying the number of random censored traces of the 3D data. The quality measure is the Signal to Noise Ratio (SNR) in dB.

The parameters which are required by our interpolation algorithm are the spatial window size and the maximum rank of the tensor. The spatial window size is a crucial parameter that can influence significantly the computational time since it affects the dimensions of the tensors to be completed. There are no known methods in the literature to estimate the optimal rank of each tensor. However, this fact does not influence significantly the reconstruction quality as long as the maximum rank is set to a value comparable to the largest fraction of the energy recalled by the approximating tensor. In all our experiments, it was enough to choose the maximum rank of the approximating tensor equal to half of the maximum rank of the tensor of observations.

It is important to notice that the curvature of the events has not affected the quality of the reconstruction, thus demonstrating empirically that the proposed method turns out to be independent to the shape of the events. This appears to be an important advantage with respect to Spitz-like methods or algorithms based on local transform like seislet or curvelet, requiring proper geometrical assumptions**.**

Similarly to all low-rank tensor completion methods, the interpolation algorithm proposed in this paper cannot handle spatially aliased data, but only dense data in a regular grid with irregularly missing traces.

**Conclusions.** In this work we have extended the greedy Orthogonal Matching Pursuit algorithm to the multidimensional case, making making it applicable to low-rank tensor completion problem.

We have introduced a new method for reconstructing and interpolating missing traces in 3D datasets.

The algorithm operates in frequency-space domain, solving, for each temporal frequency, instances of the low-rank Hankel completion problem by the proposed OR1TP greedy algorithm. At each iteration this algorithm searches for a rank-one tensor approximation of the residual, making the method efficient in terms of time and solution quality.

Synthetic data extracted from the synthetic SEG Advanced Modeling Program (SEAM) dataset, was used to prove the ability of the proposed method to recover missing traces in a 3D irregularly sampled dataset. Since there are no assumptions about the data, the algorithm turns out to be robust with respect to the shape of the events, obtaining good results both in case of linear and curved events.

**Acknowledgements.** The authors would like to thank Nicola Bienati (ENI E&P) for fruitful discussions and valuable suggestions.

## References

G. Bergqvist: *The Higher-Order Singular Value Decomposition:* Theory and an Application // Signal Processing Magazine, IEEE, vol. 27, iss.3, pp. 151-154, 2010

E. J. Candes, B. Recth: *Exact Matrix Completion via Convex Optimization* // Foundations of Computational Mathematics archive, vol. 9, iss. 9, pp. 717-772, 2009

E. J. Candes, and M. B. Wakin: *An Introduction To Compressive Sampling* // IEEE Signal Processing Magazine, vol.21, march 2008.

C. Da Silva , F. J. Herrmann: *Hierarchical Tucker Tensor Optimization - Applications to Tensor Completion* // SAMPTA, 2013

C. Da Silva, F. J. Herrmann: *Low-rank promoting transformations and tensor interpolation: applications to seismic data denoising* // Abstract, European Association of Geoscientists and Engineers, EAGE 2014.

G. Davis, S. Mallat, Z. Zhang: *Adaptive time-frequency decompositions with matching pursuits* // Optical Engineering, 1994

L. De Lathauwer, B. De Moor and J. Vandewalle: *A multilinear Singular Value Decomposition* // SIAM 21, 2000

D. L. Donoho: *For Most Large Underdetermined Systems of Linear Equations the Minimal ℓ1-norm Solution is also the Sparsest Solution* // Comm. Pure Appl. Math, vol. 59, pp. 797—829, 2004

S. Fomel and Y. Liu: *Seislet transform and seislet frame*: Geophysics, vol. 75, pp. V25–V38, 2010

G. Hennenfent, L. Fenelon, and F. J. Herrmann: *Nonequispaced curvelet transform for seismic data reconstruction: A sparsity-promoting approach* // Geophysics, vol. 75, 2010

T. Kolda, Bader, W. Brett: *Tensor Decompositions and Applications* // SIAM Rev. 51: 455–500, 2009

B. Liu: *Multi-dimensional reconstruction of seismic data* // PhD thesis, University of Alberta, 2004.

S. G. Mallat, Z. Zhang: *Matching Pursuits with Time-Frequency Dictionaries* // IEEE Transactions on Signal Processing, December 1993, pp. 3397–3415.
S. G. Mallat, F. Bergeaud: *Matching pursuit of images*, In Proc. // International Conference on Image Processing vol. 1, pp. 53–56 vol.1, 1995.
N. Kreimer, M. D. Sacchi: *A tensor higher-order singular value decomposition for prestack seismic data noise reduction and interpolation* // Geophysics, May 2012, vol. 77, pp. V113-V122, July 9, 2012
Y. Pati, R. Rezaiifar, P. Krishnaprasad: *Orthogonal Matching Pursuit: recursive function approximation with application to wavelet decomposition* // Asilomar Conf. on Signals, Systems and Comput., 1993
M. D. Sacchi and H. Kuehl: *F-X ARMA filters* // 70th Annual International Meeting, SEG, Expanded Abstarcts, pp. 2092–2095, 2000
M. D. Sacchi, D. Trad: *Reconstruction of wide azimuth seismic data: assumptions, methodology and field examples*. SEG Technical Program Expanded Abstracts 2010 // pp. 3825-3828, 2010
M. D. Sacchi, P. M. Zwartjes: *Fourier reconstruction of non-uniformly sampled, aliased data* // 74th Annual International Meeting, SEG, Expanded Abstracts, 1997–2000.
S. Spitz: *Seismic trace interpolation in the F-X domain* // Geophysics, vol. 56, pp. 785–796, 1991
S. Trickett, L. Burroughs, A. Milton, L. Walton, R. Dack: *Rank-reduction-based trace interpolation* // SEG Technical Program Expanded Abstracts: pp. 3829-3833, 2010.
S. Trickett, L. Burroughs: *Interpolation Using Hankel Tensor Completion* // CSPG/CSEG/CWLS GeoConvention, 2013
Z. Wang, M. Lai, Z. Lu, W. Fan, H. Davulvu, J. Ye: *Orthogonal Rank-One Matrix Pursuit for Low Rank Matrix Completion* // arXiv 2014
Xu S., D. Pham: *Seismic data regularization with anti-leakage Fourier transform* // 66th Conference and Exhibition, EAGE, Extended Abstracts, D032, 2004
Xu S., Y. Zhang, G. Lambare: *Antileakage Fourier transform for seismic data regularization in higher dimensions* // Geophysics, 70, WB113–WB119, 2005
Y. Yang, J. Ma, S. Osher: *Seismic data reconstruction via matrix completion* // Inverse Problems and Imaging (IPI), vol. 7, pp. 1379 – 1392, iss. 4, 2013
T. Zhang, G. H. Golub: *Rank-One Approximation to High Order Tensors* // SIAM. J. Matrix Analysis & Applications, vol. 23(2), pp. 534–550, 2001
R. Kumar, A. Y. Aravkin, E. Esser, H. Mansour, F. J. Herrmann: *SVD-free low-rank matrix factorization : wavefield reconstruction via jittered subsampling and reciprocity* // EAGE Conference, 2014
L. De Lathauwer, B. De Moor, J. Vandewalle: *On the Best Rank-1 and Rank-($R_1$,$R_2$,. . .,$R_N$) Approximation of Higher-Order Tensors* // SIAM Journal on Matrix Analysis and Applications, vol. 21, iss. 4, pp. 1324-1342, 2000

## STRATIGRAPHIC ARCHITECTURE OF DEEP SEA DEPOSITIONAL SYSTEMS IN THE SOUTHERN TYRRHENIAN SEA: SOME EXAMPLES IN THE ISCHIA AND STROMBOLI VOLCANIC ISLANDS (SOUTHERN ITALY)

**G. Aiello, E. Marsella**
*Istituto per l'Ambiente Marino Costiero (IAMC), Consiglio Nazionale delle Ricerche (CNR), Napoli, Italy*

The stratigraphic architecture of deep sea depositional systems has been discussed in detail by Galloway (1998). Some examples in the Ischia offshore are here shown and represented. The submarine slope and base of slope depositional systems represent a major component of marine and lacustrine basin fills, constituting primary targets for hydrocarbon exploration and development. The slope systems are characterized by seven basic facies building blocks, including the turbiditic channel fills, the turbidite lobes, the sheet turbidites, the slide, slump and debris flow sheets, lobes and tongues, the fine-grained turbidite fills and sheets, the contourite drifts and finally, the hemipelagic drapes and fills (Galloway, 1998).

The grain size of the supplied sediments is a primary control in the development of the morphology in the channel-lobe systems. The grain size also controls the scale and the importance of slump and debris flow deposits. Siliciclastic slope systems have been divided into two main

families. The constructional (allochtonous) systems include the fans, the aprons and the basin floor channels. They have been built from sediments supplied from delta, shore zone, shelf or glacial systems. The facies architecture of the allochtonous systems is mainly determined by the sediment texture and the pattern of supply at the shelf margin. The point sources of supply create the fans. The line sources have created strike-elongated prisms of slope sediments, called the slope aprons. The shelf margin deltas provide a particularly common intermediate source geometry, which forms onlapping delta-fed aprons. Another type is represented by the autochtonous system, including retrogressive aprons, canyon fills and megaslump complexes, recording the slope reworking and sedimentation.

The variability in the form and growth of sediment waves on turbidite channel levees has been deeply investigated (Normark *et al.*, 2002). Fine-grained sediment waves have been observed in many modern turbidite systems, generally restricted to the overbank depositional elements. The sediment waves have developed on six submarine fan systems and have been compared by using seismic reflection data coupled with sediment cores. Geological data have documented the upslope migration of the wave forms, with thicker and coarser beds deposited on the up-current flanks of the waves. Some wave fields are orthogonal to channel trend and were initiated by large flows whose direction was controlled by upflow morphology, whereas fields subparallel to the channel levees resulted from local spillover. Other studies have been carried out on the youngest channel-levee systems of the Bengal Fan, resulting from digital sediment echosounder data (Hubscher *et al.*, 1997).

Channel levee-systems represent the main architectural elements of submarine fans. Some channel-levee systems of the Ischia continental slope will be shown on seismic profiles. As a result of large input of sediments, the accumulated sediments may be considered as a high resolution record of the climatic history of the earth. The depositional structures reflect all the processes that affect sediment transfer from the hinterland towards the fan, e.g. the sea level and the climatic changes, the mountain uplift and the monsoon activity. The acoustic strata patterns and the downslope development of the channel levee system were examined with the parametric sediment echosounder Parasound. The determination of the age of the sedimentary strata shows turbiditic activity during sea level rise and highstand. The initial formation of the system in the middle fan occurred in the late glacial and outer levee growth stopped with glacial termination. Several vertical, aggradational sediments constitute the inner levees created in the Holocene. The formation of the inner levee segments indicates the construction of a wide channel in discrete phases. The top of the segments form topographic pinnacles, explaining the morphology of other channel-levee systems from other fans. Some cross sections from the lower fan reveal lenticular channel-levee systems with a common reflection characteristics. Prograding distinct reflections on the outer sides of the upper levees terminate with a downlap against an unconformity, which separates the upper part of the overbank deposits from a reflecting lower part. Examples of modern and ancient turbidite systems have been compared and the related problems and concepts have been examined (Mutti and Normark, 1987). The example, selected for the comparison represent depositional systems similar in such characteristics as the type of basin, the size of sediment source, the physical and temporal scales and the stage of development. A conceptual framework for comparing modern and ancient turbidite systems has been presented. Four basic types of turbidite basins have been defined based on size, mobility of the crust, effects of syndepositional tectonic activity and volume of sediment available in the source areas. The difference in physical scale and the great dissimilarities in the type of data available are particularly important in the comparison of modern and ancient deposits. Comparisons have been done for basin-fill sequences or complexes (1$^{st}$ order), for individual fan systems (2$^{nd}$ order), for stages of growth within an individual system (3$^{rd}$ order) or for the scales of specific elements (facies associations and component substages) within a system, i.e. lobes, channel deposits, overbank deposits (4st order; Mutti and Normark, 1987). Individual fan elements have been defined to provide criteria applicable to both modern and ancient settings. These elements are channels, overbank deposits,

lobes, channel/lobe transition features and scours (major erosional non-channel features). The derived characteristics, such as the fan divisions and sedimentation models are considered as secondary points only used as necessary for the discussion. The use of morphologic terms to describe ancient deposits has been also qualified. The primary emphasis remains on detailed, complete field work both on land and at sea in order to provide the characterization of the sediments and rocks assemblages and to ensure that similar features are being compared in terms of both temporal and physical scales (Mutti and Normark, 1987). Turbidite systems and their relationships to depositional sequences have been described in detail (Mutti, 1985). Long term global sea level variations and local tectonic control form the basic framework within which turbidite sediments develop as a response to breaks in the equilibrium between shelf and basin sedimentation. An understanding of the interaction of these processes and resulting types of turbidite deposition requires a precise framework of turbidite sediments within well defined depositional sequences. The volume of the gravity flows enhances the depositional characters of the channels that progressively become the only site of sand deposition where small volume and highly confined flows lose most of their fines through overbank processes. Within the same system, a decrease in the volume of gravity flows determines different stages of growth, that are expressed by distinctive facies associations.

Channel-levee complexes, terminal deep sea fans and sediment wave fields associated with the Toyama Deep Sea Channel System in the Japan Sea have been described in detail (Nakajima *et al*., 1998). The Toyama Deep Sea Channel in the Japan Sea is one of the most prominent deep sea channels in rifted margins. The course and morphology of the channel-fan system are mainly controlled by the basin morphology. Thick, sheet-like sediments, deposited from ponded turbidity currents have accumulated in narrow throughs, whereas extensive levees have formed in more open basins. The distribution of the sediments and the consequent morphology of the channel-levee complexes are also controlled by Coriolis force. The preferential development of the levees is attributed to the Coriolis force tilt effects in the Northern Emisphere. The distribution, form and orientation of the sediment waves are consistent with the effect and direction of inferred spill-over turbidity currents, with a consequent levee growth. The sediment transport may have ceased during the Holocene in the cut and fill tributaries developed in the Quaternary succession on the slope to the through, where a wide shelf separates the canyons from the rivers in the eastern margin of the drainage area.

Important results on the stratigraphic architecture of deep sea depositional systems have been obtained from the GNV Italian project (Chiocci *et al*., 2003). Further constraints have been obtained from the CARG Project (Aiello *et al*., 2010, 2012) and from the Stromboli geophysical experiment (Castellano *et al*., 2008; Aiello *et al*., 2014).

The submarine portions of the Italian volcanoes, their survey and the assessment of the potential volcanic hazards have been deeply investigated with a particular reference to the DTM generation for the Vulcano, Stromboli and the southern Ischia islands (Chiocci *et al*., 2003). Other tasks have included the geotechnical characterization of submarine instabilities and related subaerial phenomena, the geotechnical analysis and modeling of instability phenomena affecting the flanks of the volcanic islands. Some researches on the Ischia submerged flanks have also been carried out, coupled with the reconstruction of the evolutive processes by marine data and with the seismo-stratigraphic analysis. Other objectives have included the understanding of the geological processes active in the Italian submarine areas, the evaluation of the potential risks associated with the volcanic seamounts and with the submerged portions of the volcanic islands of the Tyrrhenian sea. Investigations on the submerged portion of the Mount Etna volcanic edifice have also been carried out in order to ascertain the presence of tectonic lineaments, both extensional and compressional, connected with those on land, due to the absence of buttress towards the sea (Chiocci *et al*., 2003).

High-resolution seismic reflection profiles (Sparker Multitip) offshore southern Ischia island (Naples Bay) have been presented (Aiello *et al*., 2012). New seismo-stratigraphic evidence on

buried volcanic structures and overlying Quaternary deposits of the south-eastern offshore of the Ischia Island have been discussed to highlight their implications on the marine geophysics and volcanology. The Ischia Bank is a large and flat relic volcanic edifice with steep slopes, merging on the continental shelf. The age of this monogenic volcano is unknown, lacking a direct datation of its basement. It represents the eruptive center of the pyroclastic fall cropping out onshore in the eastern sectors of the island, ranging in age from 8 to 6 ky B.P. In the eastern Ischia offshore relict volcanic edifices, mostly formed by hialoclastites, have been investigated through high-resolution seismics. They represent remnants of hydro-magmatic volcanic vents and suggest a subaqueous emplacement. Regional seismic sections in the south-eastern Ischia offshore, across buried volcanic structures, have been presented and discussed (Aiello *et al*., 2012).

In the case of Ischia island, the occurrence of isolated volcanic bodies, such as intrusions, domes, volcanic necks and tabular, acoustically transparent seismic units, makes the sequence stratigraphic approach particularly complex for the geological interpretation of seismic profiles. In the Ischia offshore the volcanic bodies, such as the lava flows, the domes and the intrusions, cannot be investigated in their inner part through the reflection seismics, because they are acoustically transparent. On the contrary, the seismic facies of the pyroclastic edifices and/or the buried pyroclastic deposits may be detected, due to their internal stratification. The marine sedimentation includes both the contribution of alluvial and marine sediments and the input of volcanites and volcaniclastic deposits originated from the eruptions of Ischia and Procida volcanic complexes.

Deep sea depositional systems in Ischia island are well developed in correspondence to the Southern Ischia canyon system (Aiello and Marsella, 2014). The canyon system engraves a narrow continental shelf from Punta Imperatore to Punta San Pancrazio, being limited southwestwards from the relict volcanic edifice of the Ischia bank. While the eastern boundary of the canyon system is controlled by extensional tectonics, being limited from a NE-SW trending (counter-Apenninic) normal fault, its western boundary is controlled by volcanism, due to the growth of the Ischia volcanic bank. Submarine gravitational instabilities also acted in relationships to the canyon system, allowing for the individuation of large scale creeping at the sea bottom and hummocky deposits already interpreted as debris avalanche deposits.

High resolution seismic data (Subbottom Chirp) coupled to high resolution Multibeam bathymetry collected in the frame of the Stromboli geophysical experiment aimed at recording seismic active data and tomography of the Stromboli island are here presented. The Stromboli geophysical experiment has been already carried out based on onshore and offshore data acquisition in order to investigate the deep structure and the location of the magma chambers of the Stromboli volcano. A new detailed swath bathymetry of Stromboli islands is here shown and discussed to reconstruct an up-to-date morpho-bathymetry and marine geology of the area, compared to the volcanologic setting of the Aeolian Arc volcanic complex (Aiello *et al*., 2014). Due to its high resolution the new DTM of the Stromboli island has given interesting information about the submerged structure of the volcano, particularly about the volcano-tectonic and gravitational processes involving the submarine flanks of the edifice. Several seismic units have been identified based on the geologic interpretation of Subbottom Chirp profiles recorded around the volcanic edifice and interpreted as volcanic acoustic basement pertaining to the volcano and overlying slide chaotic bodies emplaced during its complex volcano-tectonic evolution (Fig. 1). They are related to the eruptive activity of Stromboli, mainly poliphasic and to regional geological processes involving the geology of the Aeolian Arc (Aiello *et al*., 2014).

Some new insights about the morphobathymetry, marine geology and seismic stratigraphy of the Stromboli submarine area are discussed through Multibeam and seismic data. New bathymetric maps coupled with seismic interpretation provide new data on the submarine structure of the volcanic edifice of the Stromboli island. Eight subaerial volcanic edifices are located in correspondence to the Aeolian Arc. While the most part of these volcanoes are supplied by fluid magmas genetically related to the Ionian lithospheric slab, other ones

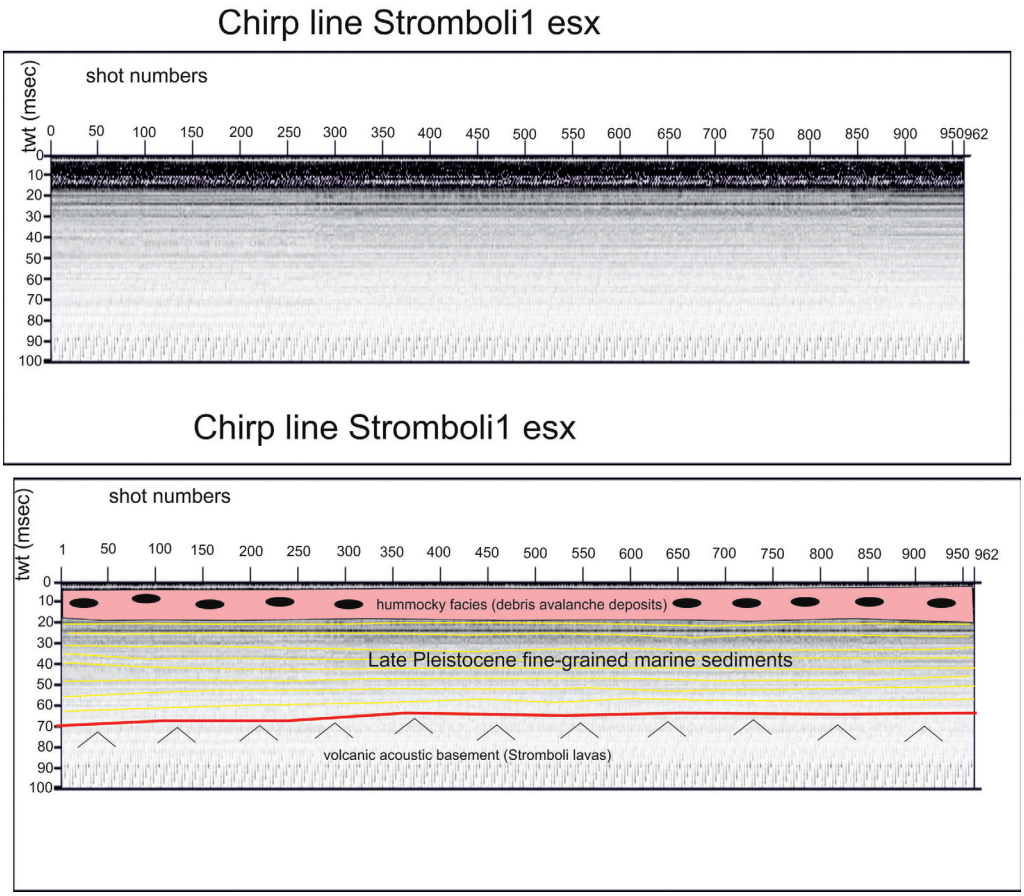


Fig. 1 - Subbottom Chirp line Stromboli esx (a) and corresponding geologic interpretation (b). The line has been processed by using the Seisprho software (licensed by CNR-ISMAR, Istituto per la Geologia Marina, Sezione di Bologna). Note the occurrence of a thick volcanic acoustic basement related to the Stromboli volcanic lavas.

(Vulcano, Lipari and Salina) are aligned along a regional strike-slip fault having a NNW-SSE trending, cutting also the Etna volcano. The submarine volcanic districts of the Tyrrhenian sea have been recently analyzed also as possible geothermal resources, considered the high values of heat flow related to these volcanic structures (Signanini *et al.*, 2006). In the Aeolian Arc the volcanic activity was explicated with four main phases, ranging in age from 1-1.3 My B.P. at the Sisifo seamount and at the Filicudi volcanic island. From 0.8 My B.P. to recent times shoshonitic and calcalkalyine lavas, consisting of basalts, andesitic basalts and rhyolites have been erupted in the volcanic complexes, both subaerial and submarine. The volcanic edifice of the Stromboli island started to form about 110 ky ago. The volcano shows symmetric flanks and a conical shape and has an average elevation of about 927 m above sea level. It represents the emerged part of an important volcanic edifice, high more than 3000 m. The eruptive activity, typically poliphasic, has controlled a stratigraphic architecture characterized by overlapping of different volcanic products (lavas and pyroclastites). The formation of the volcano started about 200 ky B.P. in the north-eastern sector of the island with the growth of a volcanic edifice now completely eroded, whose central neck is represented by the Strombolicchio inlet. About 100 ky B.P. in correspondence to the present-day volcanic edifice, a new volcano started to grow (Paleostromboli I), reaching a height of 400 m; a great part of this volcano was downthrown after

great explosions, leaving at its place a caldera having an elliptical shape. The caldera depression was then infilled by the growth of a new volcano, reaching the height of 700 m (Paleostromboli II). The life of this volcano concluded about 35 ky ago with the downthrowing of a new caldera, having a circular shape. About 34 ky B.P. a new volcano, called Vancori underwent a giant sliding in its upper part and in the western flank. To testify this collapse a large amphitheater remains, which nowadays surrounds the present top of the Stromboli volcano, including the active crater.

The structure of the Stromboli volcanic island has been related to that one of the Campania volcanoes: in both ones a well-developed low velocity layer, having a thickness of 10-15 km occurs under a thin lid, overlain by a thin continental crust (Panza *et al*., 2003). The structural difference among the Stromboli volcano and the proximal volcanoes of Volcano and Lipari is confirmed by the different geochemical characters (Finizola *et al*., 2003; Revil *et al*., 2004).

The geological data here discussed well fit with some previous results obtained on the geology of the Aeolian islands and of the Stromboli canyon (Kidd *et al*., 1998). The basin margins are characterized by slump scars, channels and large debrites on the continental slope off Campania region, not imaged by the data discussed in the present paper. Blocky hummocky avalanche deposits have been recognized on the flanks of the Stromboli volcano (Kidd *et al*., 1998). This hint is in agreement with seismo-stratigraphic data shown by Chirp interpretation. In the Stromboli canyon and in minor deep sea channels sediment transport by turbidity currents generates sediment waves. Between the basin margins and the abyssal plain, the outcropping volcanic basement traps part of the sediment coming from the marginal area (Kidd *et al*., 1998). The volcanic acoustic basement genetically related to the Stromboli lavas has been widely recognized also in the seismic lines study in the present paper. Moreover, the abyssal plain surrounding the volcanic edifice is characterized by low relief lobes and ponded sediments (Kidd *et al*., 1998). Circular high backscatter patches have been recognized through the interpretation of Sidescan Sonar photomosaics (Kidd *et al*., 1998), indicating that volcanic blocks have been transported downslope in the Stromboli canyon. Blocky hummocky facies have been widely recognized in the Chirp lines analyzed in the present paper. The streaked high backscatter patterns at the scarp base are interpreted as coarse-grained sediments transported downslope along the Stromboli canyon (Kidd *et al*., 1998). Coarse-grained units have also been often recovered.

## References

Aiello G., Budillon F., Conforti A., D'Argenio B., Putignano M.L., Toccaceli R.M.; 2010: *Note illustrative alla cartografia geologica marina. Foglio geologico n. 464 Isola d'Ischia*. Regione Campania, Settore Difesa Suolo, III SAL, Geologia Marina, Preprints.

Aiello G., Marsella E., Passaro S.; 2012: *Stratigraphic and structural setting of the Ischia volcanic complex (Naples Bay, southern Italy) revealed by submarine seismic reflection data*. Rend. Lincei, **23 (4)**, 387-408.

Aiello G., Di Fiore V., Marsella E., Passaro S.; 2014: *High resolution seismic data coupled to Multibeam bathymetry of Stromboli Island collected in the frame of the Stromboli geophysical experiment: implications with the marine geophysics and volcanology of the Aeolian Arc volcanic complex (Sicily, Southern Tyrrhenian sea, Italy)*. Springerplus, **3 (232)**, doi:10.1186/2193-1801-3-232.

Aiello G., Marsella E.; 2014: *The Southern Ischia canyon system: examples of deep sea depositional systems on the continental slope off Campania (Italy)*. Rendiconti online della Società Geologica Italiana, in press.

Castellano M., Augusti V., De Cesare W., Favali P., Frugoni F., Montuori C., Sgroi T., De Gori P., Govoni A., Moretti M., Patanè D., Cocina O., Zuccarello L., Marsella E., Aiello G., Di Fiore V., Ligi M., Bortoluzzi G., Ferrante V., Marchetti E., La Canna G., Ulivieri G.; 2008: *Seismic Tomography Experiment at Italy's Stromboli volcano*. EOS Transactions AGU, **89 (30)**, 26, 259-276.

Chiocci F.L., Marani M., Tommasi P., Romagnoli C., de Alteriis G., De Vita S., Senatore M.R., Vezzoli L.; 2003: *The submarine portions of Italian Volcanoes: their survey and assessment of the potential volcanic hazards*. Final Report on the GNV Project, available on the website, 23 pp.

Finizola A., Sortino F., Lenat J.F., Aubert M., Ripepe M., Valenza M.; 2003: *The summit hydrothermal system of Stromboli: self-potential, temperature, CO2 and fumarolic fluid measurements with structural and monitoring implications*. Bulletin of Volcanology, **65**, 486-504.

Galloway W.E.; 1998: *Siliciclastic slope and base-of-slope depositional systems:component facies, stratigraphic architecture and classification*. AAPG Bull., **82 (4)**, 569-595.

Hubscher C., Spiess V., Breitzke M., Weber M.E.; 1997: *The youngest channel-levee system of the Bengal Fan: results from digital sediment echosounder data*. Mar. Geol., **141**, 125-145.

Kidd R.B., Lucchi R.G., Gee M., Woodside J.M.; 1998: *Sedimentary processes in the Stromboli canyon and Marsili Basin, SE Tyrrhenian sea: results from side-scan sonar surveys*. Geomarine Letters, **18**, 146-154.

Mutti E.; 1985: *Turbidite systems and their relations to depositional sequences*. NATO ASI Series, **148**, 65-93.

Mutti E. and Normark W.R.; 1987: *Comparing examples of modern and ancient turbidite systems: problems and concepts*. Marine Clastic Sedimentol., 1987, pp. 1-38.

Nakajima T., Satoh M., Okamura Y.; 1998: *Channel-levee complexes, terminal deep-sea fan and sediment wave fields associated with the Toyama Deep-Sea channel system in the Japan sea*. Mar. Geol., **147**, 25-41.

Normark W.R., Piper D.J.W., Posamentier H., Pirmez C., Migeon S.; 2002: *Variability in form and growth of sediment waves on turbidite channel levees*. Mar. Geol., **192**, 23-58.

Signanini P., Madonna R., Iezzi G., Favali P., Di Sabatino B., Crema G., Antonelli U., Paltrinieri D.; 2006: *I distretti vulcanici sottomarini del Tirreno: una possibile risorsa geotermica?* Giornale di Geologia Applicata, **4**, 195-200.

Panza G.F., Pontevivo A., Sarao A., Aoudia A., Peccerillo A.; 2003: *Structure of the lithosphere-astenosphere and volcanism in the Tyrrhenian sea and surroundings*. The Abdus Salam International Centre for Theoretical Physics, Miramare, Trieste, pp. 1-46.

Revil A., Finizola A., Sortino F., Ripepe M.; 2004: *Geophysical investigations at Stromboli volcano, Italy: proceedings of ODP Leg 107 in the frame of Neogene to recent geology of perityrrhenian areas*. In: Kastens K.A., Mascle J. et al. (Eds.) Proceedings of Ocean Drilling Program, Scientific Results, 107th Edition, pp. 715-730.

## MULTIPLE MULTIBEAM BATHYMETRIC DATASETS IN NAPLES AND SALERNO GULFS (SOUTHERN TYRRHENIAN SEA) CALIBRATED THROUGH MULTICHANNEL SEISMIC PROFILES

**G. Aiello[1], E. Marsella[1], C. D'Isanto[2]**

*[1] Istituto per l'Ambiente Marino Costiero (IAMC), Consiglio Nazionale delle Ricerche (CNR), Napoli, Italy*

*[2] Collaboratore Esterno, Università degli Studi di Napoli "Federico II", Italy*

Multiple Multibeam bathymetric datasets collected in Naples and Salerno Gulfs have been calibrated by high resolution multichannel seismic profiles. The research project is based on the processing and the interpretation of bathymetric data recorded by the IAMC-CNR of Naples through different types of Multibeam lateral echosoundings. An analytic comparison between one of the automatic methods most efficient for the data processing, i.e. the CUBE and the manual processing of swath packages has been attempted. The efficiency of the algorithm has been tested on complex morphologies, such as the Capri continental slope and the related geological structures occurring in the Salerno Gulf.

The Multibeam data processing and interpretation has been carried out for several research projects (D'Isanto, 2007). The first one is the CNR-SGN Convention for the redaction of marine geological maps at the 1:25,000 scale of Naples and Salerno Gulfs (geological maps n. 465 "Procida", n. 466 "Sorrento" and n. 467 "Salerno". The second one is the CARG Project at the scale 1:10.000 of the Campania region (geological maps n. 464 "Ischia", n. 465 "Procida", n. 466 "Sorrento", n. 446-447 "Napoli", n. 484 "Capri", n. 486 "Foce del Sele", n. 502 "Agropoli", n. 519 "Capo Palinuro", n. 520 "Sapri"). The third one is the GEOSED project for the acquisition of bathy-morphological data for the geomorphological and sedimentological study of selected areas of Campania continental shelf (Capri and Ischia islands). The fourth one is the SISTER II oceanographic cruise of morpho-bathymetric acquisition in intermediate and deep sea bottoms through the RESON 8160 Multibeam and finalized to the geological

knowledge of the Sorrento continental slope, the Salerno Valley and the northern and southern Sele highs. A fifth project deals with the morpho-bathymetric surveys committed to the CNR IAMC of Naples by the Authority of the Naples harbor for monitoring the marine pollution of sediments. Dedicated software as the PDS2000 (Thales), the NEPTUNE (Merlin) and the ISIS (Triton Elics) have been used for the cartographic restitution of bathymetric data. The bathymetric maps, both contour isobath maps and shaded-relief maps have been interpreted with the aim of reconstructing the main morphological lineaments occurring at the sea bottom, in particular for the Naples Bay canyons, the continental slope off the Sorrento Peninsula, the sedimentary basin of the Salerno Valley and the related depocenters. Bathymetric profiles have been also produced, allowing to distinguish erosional and depositional areas. The correlation of Multibeam data with some significant seismic profiles recorded in Naples and Salerno Gulfs has completed the geological interpretation.

The Multibeam is a sonar allowing for the high resolution reconstruction of the sea bottom morphology. It is a highly technologic instrument having its development during the last fifteen years, since only the power of modern computers has allowed to manage the large amount of data and related operations (Veen and Buckley, 1988; Krim and Viberg, 1996; Van Trees, 2002 ). The principles of functioning of the instrument are here briefly recalled From the transducer (head) it starts a belt of acoustic signals (beams), perpendicular to the ship's tracking. The times of arrival of each single beam are recorded and corrected based on the head's starting angle and to the sound velocity profile, previously measured. For the known problems on the ship's instability, the data are corrected through an accelerometer, measuring the heave, roll and pitch of the ship. The acquisition system is interfaced with a positioning system, usually a differential GPS. One fundamental advantage of the Multibeam system is that of surveying a belt of sea bottom varying from four to six times the water depth and allowing, due to the data redundancy, the creation of three-dimensional models, namely the Digital Terrain Models (DTM). The large number of points (x, y, z) gives the processing phase very long. The methods of automatic cleaning (statistical filters, gradient filters, beam intersection filters) may provoke the loss of the requested detail and are then applied with large parameters after a first cleaning of the spikes. It starts then a phase of detailed morphological control of the Multibeam data.

The acquisition of Multibeam bathymetric data in the frame of previously mentioned research projects has been carried out by using Multibeam systems used in coastal marine environment and shallow waters (Multibeam Reson 8125, Multibeam Reson 8101) and Multibeam systems of intermediate and deep waters (Multibeam Reson 8111, Multibeam Reson 8160), depending on the finalities of the work. Moreover, the Multibeam Simrad EM3000 has been used for the acquisition of morpho-bathymetric data among water depths of 4 and 50 meters.

Some principles of electroacoustic subaqueous methods and applications to the case studies of Naples and Salerno Gulfs are here resumed. Among all the forms of radiations, the sound is the only which better propagates in the sea. The electromagnetic waves are attenuated in the salt waters of the sea, in a major measurement than the mechanical ones. Due to this characteristic, the sound may be used for many applications in the water exploration and these applications are determined by the use of the sonar, defined as the system which uses the acoustic energy to carry out the measurements in an aquatic environment. Some typical sonar applications include the individuation of banks of fishes, the bathymetric measurements and the stratigraphy and the geomorphology of the sea bottoms. The sonar may be active or passive. An active sonar may use a proper acoustic source, while a passive sonar records the signal generated by the object of interest.

The equation of the sonar has been developed during the Second World's War as an aid in the determination of the maximum distance of functioning of the subaqueous acoustic systems. Starting from that period, the equation has been used to describe the functioning of a wide range of submarine measurement systems. The equation of sonar includes all the factors regarding the generation, propagation and attenuation of the sound in the water; for this reason, it constitutes

a subject of study of the submarine acoustics and is the basic component in order to project systems for geophysic and oceanographic applications.

The sonar, due to its technical characteristics, is used in many applications, both scientific and technologic. It is used for conventional bathymetric measurements or Multibeam bathymetry. By resuming, the acoustic echosoundings measure the travel time of the acoustic pulses and the related echoes to survey the sea bottom. The conventional acoustic survey determines a depth value for each pulse, while the Multibeam system determinates many points of measurement in a cross section. The echo intensity should be used to estimate the nature of the sea bottom.

The acoustic systems as the Subbottom profiler, the Sparker, the Airgun and the Watergun are used in order to carry out stratigraphic surveys on the sea bottom. These systems use the acoustic pulses of minor frequency, with respect to the acoustic echosounders, in order to use the characteristics of penetration, reflection and refraction of the signal. In this category of instruments we find the systems of shallow seismic (Subbottom Chirp, Sparker) and deep seismic (Watergun, Airgun).

Lateral scanning sonar are usually used for the geomorphologic studies. These systems measure the shallow lithology of the sea bottom by using the interferometric principle to survey the cross sections and to record the echo intensity, as a function of the nature of the sea bottom. These instruments are also used in order to survey particular structures or objects at the sea bottom (antropic structures as pipelines or relicts). High frequency fish finders are used for the biological studies, with the function to survey fish banks, accompanied by software for the calculation of biological masses. Moreover, passive sonar are used to track the migratory tracks of the great Cetaceous and for studies of bioacoustics.

The procedures of Multibeam processing applied to the Gulf of Salerno are here briefly mentioned. The treatment for the verification and the processing of the bathymetric data with a high resolution Multibeam technology has been carried out accordingly to several phases. The first phase includes the application of the tidal curve to the data, in order to correct the altimetric variations. This phase of elaboration is performed accordingly to one of the three methods, i.e. the correction through a single mareographic station, the correction through two or more pounded stations, based on the distance from the survey area, the correction through tables of tides for works at a regional scale and at high water depths. The second processing step includes the correction of the GPS navigation. This is carried out by visualizing the tracking with the fix in relationship to the diagram of the HDOP (horizontal dilution of precision), which is one of the more precise methods to estimate the horizontal accuracy of the GPS (latitude and longitude). Some mistakes in the navigation lines will correspond to discontinuities and abrupt increase of the values of HDOP, which will be corrected by manually shifting the mistaken fixes and interpolating the positions. The third processing step includes the applications of the profiles of sound velocity along the water column. Normally it is acquired a sound velocity profile each 4-8 hours, in the survey zone by using velocity profiles or CTD multiparametric probes to measure the temperature, the salinity and the pressure. The fourth processing step is represented by the visualization of the single beam and the manual and statistical elimination of the spikes. This cleaning is carried out through the visualization of 50 swaths for each time, equal to the half of the measured ones, in such a way to guarantee a notable precision and accuracy of the filtering. The processed beams have then been used for the creation of a DTM (Digital Terrain Model), which furnishes a three-dimensional representation of the sea bottom. In the DTM the knots are given from the average of the depth of the beams, which falls in the inner of a dimension cell established from the operator. The DTM is further processed through filters operating on the standard deviation or manually clean from the cells affected by the mistakes. The bathymetric data of the Salerno Gulf have been processed both according to the above described procedure and with a statistic method: Combined Uncertainty Bathymetric Estimator (CUBE), ideated from the University of New Hampshire (U.S.A.). With this second method a time advantage has

been obtained which is of about 60% with the same results of a careful manual cleaning of the spikes.

The main sequences of seismic data elaboration, applied in the multichannel seismic data processing are here also described. There are three main phases, i.e. the deconvolution, the stacking and the migration. A set of auxiliary processes has been added to these phases in order to improve the seismic signal. While for the main phases it is important to maintain a specific processing sequence, for the auxiliary processes the commutative property is valid, such as the order of phases is not important. The seismic signal is recorded in a digital format and then is subject to a discrete sampling during the time. The format is convenient for the recording, but not for the data elaboration. It is necessary to order another time the points of sampling in a trace-sequence way (demultiplexing). All the points of sampling related to each single trace are grouped. The format in which the data are converted is the SEG standard format (Society of Exploration Geophysicists). The most used versions are the SEG-Y and the SEG-D formats. The SEG-D is characterized by a greater flexibility of use. It allows to order the data both in a multiplexed and in a demultiplexed modality and has been projected in such a way to satisfy the increase of the quantity of data for record. Once upon a time the data have been demultiplexed, they must be elaborated in such a way to remove the kill traces. The kill traces eliminated are those ones including no information or that ones with monocyclic waveforms caused by electronic interferences (a sinusoidal wave shape with a constant amplitude and wavelength) or that ones with an excessive noise. The editing consists of the cleaning of the dataset to improve the quality of the remaining data. The data, such as they are recorded, may include a certain quantity of noise, due both to instrumental and environmental factors. In our specific case, the bad quality may be linked to a set of causes mainly due to problems related to the energization or to the seismic cable or to noises due to the instruments of recording.

For what concerns the problems of energization it must be verified the possibility that some shots are lacking in energy or that some replies having a low intensity (autopop) have been produced, which are added to the main pulse. The phenomenon of the autopop must be eliminated during the phase of elaboration with techniques similar to that ones used during the removal of the multiple reflections.

The Salerno Valley, bounding the southern sector of the Sorrento Peninsula, represents an useful laboratory for the study of submarine instabilities related to tectonically-controlled slopes. The individuation of the valley and the activity along the rocky slope bounding it are related to the regional normal or strike-slip fault (Capri-Sorrento fault) bounding southwards the Meso-Cenozoic structural high Capri-Sorrento Peninsula. The Salerno Valley is represented by a deep WSW-ENE trending depression, limited northwards by the normal faults down throwing the Mesozoic carbonates of the Sorrento Peninsula and filled by a Plio-Quaternary sequence thick up to 3300 m (Mina 1 well; Agip, 1977). Multibeam bathymetric survey has evidenced the high steepness of the slope and the occurrence of strong erosional processes, partly active, where a dense network of channellised erosional morphologies has been detected. The analysis of seismic reflection profiles has evidenced the tectonic activity of the fault slope as a triggering cause for gravity instability processes during the Late Pleistocene – Holocene. This has been evidenced also by slumping deposits, characterized by a chaotic seismic facies, interstratified in the distal filling of the Salerno Basin. On the contrary in the distal areas of the valley, where the deposition prevails, the shallower sector appears in intense erosion (Salerno canyon) and shows recent tectonic deformations, as antiformal structures and high angle normal faults, interpreted in the regional geological framework as hints of a strong extensional tectonics, lasted up to recent times. A three-dimensional restitution DTM (Digital Terrain Model) covering an area of 1600 square kilometers extending from north-west to the southern slope of the Capri island to south-east to the Sele river mouth has been produced (Fig. 1). The geologic interpretation of Multibeam bathymetry has evidenced a pronounced asymmetry of the continental shelf proceeding from north to south, reflecting the different structural domains

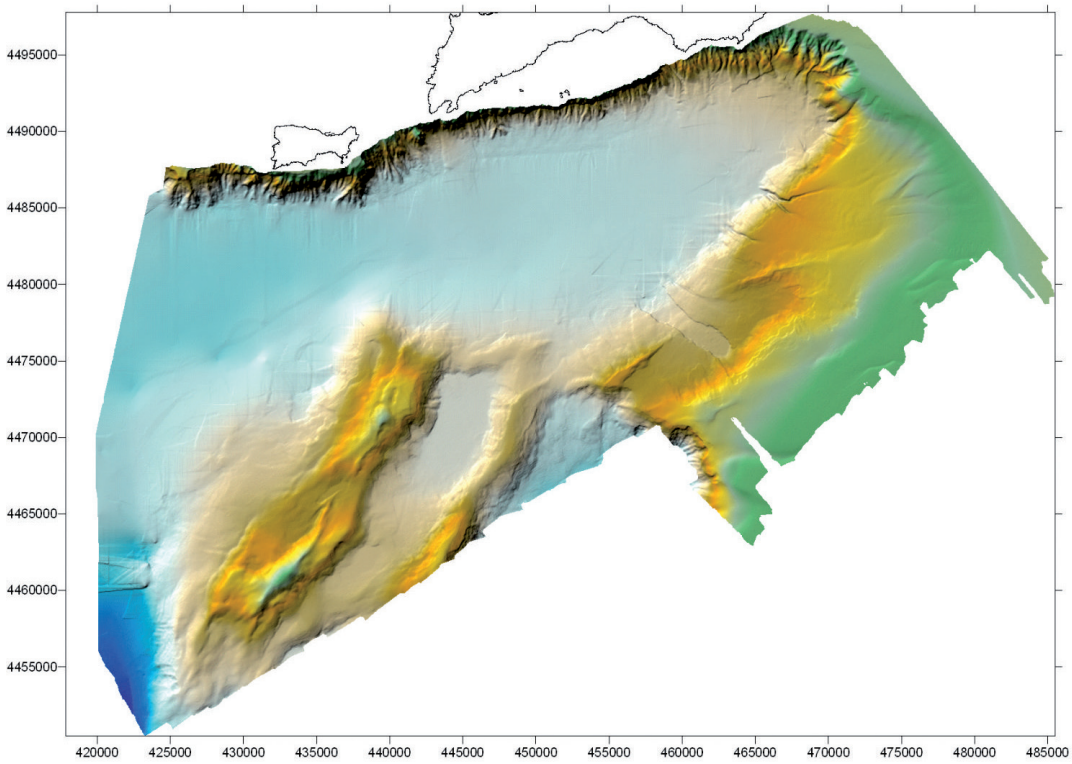


Fig. 1 – Digital Terrain Model south of the Sorrento Peninsula covering the northern sector of the Salerno Bay. Note the occurrence of a dense network of submarine gullies resulting from the prolongation of the drainage system occurring onshore in the Sorrento Peninsula. Note also the occurrence of a wide basin known as the Salerno Valley and two morpho-structural highs known as the northern and southern Sele highs.

of this segment of the eastern Apenninic margin. This variability in the extension, of the depth of the shelf break and of the average slopes are in fact controlled by the structural and geologic setting of the marginal areas (Bartole *et al*., 1984; Sacchi *et al*., 1994), more than of the glacio-eustatic variations during the Pleistocene (Trincardi and Field, 1992; Ferraro *et al*., 1997; Buccheri *et al*., 2002; Aiello *et al*., 2009). The continental slope surrounding the Salerno Gulf is characterized by structural depocenters having an Apenninic trending, originated by the extensional phases related to the Tyrrhenian Basin (Trincardi and Zitellini, 1987; Malinverno and Ryan, 1986) alternating to morpho-structural highs, adjacent to intra-slope basins, where the gravity instabilities are frequent and tectonically-controlled. The Multibeam interpretation has evidenced the occurrence of two morpho-structural highs having a complex nature with a NE-SW trending. The highs appear to be complicated from a morpho-structural point of view and are bounded, on the western flank, by a wide intra-slope basin, located at 700 m of water depth, having a NE-SW trending.

## References

Agip; 1977: *Temperature sotterranee. Inventario dei dati raccolti dall'Agip durante la ricerca e la produzione di idrocarburi in Italia*. Agip, Milano.

Aiello G., Marsella E., Di Fiore V., D'Isanto C.; 2009: *Stratigraphic and structural styles of half-graben offshore basins in Southern Italy: seismic stratigraphy and morpho-bathymetry of the Pleistocene sedimentary basin of the Salerno Valley.* Quaderni di Geofisica, **77**, 1-34.

Bartole R., Savelli D., Tramontana M., Wezel F.C.; 1984: *Structural and sedimentary features in the Tyrrhenian margin off Campania, southern Italy.* Mar. Geol., **55**, 163-180.

Buccheri G., Capretto G., Di Donato V., Esposito P., Ferruzza G., Pescatore T.S., Russo Ermolli E., Senatore M.R., Sprovieri M., Bertoldo M., Carella D., Madonia G.; 2002: *A high resolution record of the last deglaciation in the southern Tyrrhenian sea: environmental and climatic evolution*. Mar. Geol., **186**, 447-470.

D'Isanto C.; 2007: *Acquisizione, elaborazione ed interpretazione geologica di datasets batimetrici Multibeam e correlazioni con profili sismici multicanale. Applicazioni al Golfo di Salerno (Tirreno meridionale)*. Tesi di Dottorato di Ricerca in Scienze ed Ingegneria del Mare, Università degli Studi di Napoli "Federico II".

Ferraro L., Pescatore T.S., Russo B., Senatore M.R., Vecchione C., Coppa M.G., Di Tuoro A.; 1997: *Studi di geologia marina del margine tirrenico: la piattaforma continentale tra Punta Licosa e Capo Palinuro (Tirreno meridionale)*. Boll. Soc. Geol. Ital., **116**, 473-485.

Malinverno A. and Ryan W.B.F.; 1986: *Extension in the Tyrrhenian sea and shortening in the Apennines as a result of arc migration driven by sinking of the lithosphere*. Tectonics, **5**, 227-245.

Krim H. and Viberg M. (1996) *Two decades of array signal processing research*. IEEE Signal Processing Magazine, 67-94.

Sacchi M., Infuso S., Marsella E.; 1994: *Late Pliocene-Early Pleistocene compressional tectonics in the offshore of Campania*. Boll. Geof. Teor. Appl., **36**, 141-144.

Trincardi F. and Field M.E.; 1992: *Geometry, lateral variation and preservation of downlapping regressive shelf deposits: Eastern Tyrrhenian sea margin, Italy.* Journ. of Sedimentary Petrology, **61**, 775-790.

Trincardi F. and Zitellini N.; 1987: *The rifting of the Tyrrhenian basin*. Geomarine Letters, **7**, 1-6.

Van Trees H.L. (2002) *Optimum Array Processing*. Wiley New York, 2002.

Veen B.D.V. and Buckley K.M. (1988) *Beamforming: a versatile approach to spatial filtering*. IEEE ASSP Magazine, 4-24, April 1988.

## THE REGIONAL GEOLOGICAL STRUCTURE OF THE CAMPANIA CONTINENTAL MARGIN INFERRED BY DEEP MULTICHANNEL SEISMIC PROFILES

**G. Aiello[1], E. Marsella[1], V. Di Fiore[1], A.G. Cicchella[2]**

*[1] Istituto per l'Ambiente Marino Costiero (IAMC), Consiglio Nazionale delle Ricerche (CNR), Napoli, Italy*

*[2] Collaboratore Esterno, Università di Napoli "Federico II", Italy*

New seismostratigraphic data on the regional geological structure of the Campania continental margin based on deep multichannel seismic profiles are here presented. Regional geological sections have been constructed along the Ischia-Capri-Volturno structural elongment of the Campania continental margin (Aiello *et al*., 2011). While a large amount of densely spaced seismic surveys of the Naples Bay continental shelf have been previously performed, these sections have furnished a geologic framework of main sedimentary basins and interposed structural highs of the whole continental margin at a regional scale. A new seismostratigraphic setting is furnished for some lineaments, previously not described in detail, as the Capri and Volturno basins, the Capri structural high and the Ischia volcanic structural high. A correlation with the land geology has been attempted to obtain a better geological comprehension of the interpreted structures. Quaternary volcanism of the Campania margin has been discussed, since a large volcanic edifice buried below Quaternary volcanites, previously known only for its magnetic signature.

The Naples Bay lies in the Campania Plain, located between the eastern side of the Tyrrhenian sea and the southern Apenninic chain and produced from the back-arc extension that accompanied the NE-verging accretion of the Apenninic thrust belt during the roll-back of the subducting foreland plate (Malinverno and Ryan, 1986; Faccenna *et al*., 1996). The western sector of the Naples Bay is surrounded by the Phlegrean Fields volcanic district, where volcanism has been active for at least 50 ky. The present-day physiography of the volcanic district has been mainly controlled by volcano-tectonic events occurred after the emplacement of the Campanian Ignimbrite (CI), a huge pyroclastic flow erupted 35 ky B.P., when the area experienced a first

phase of calderization (Barberi *et al*., 1978). In the eastern sector, the sedimentary processes related to the Sarno-Sebeto coastal plain controlled the deposition of marine and coastal seismic units during Late Pleistocene and Holocene, often interlayered with volcanic deposits related to Somma-Vesuvius (Milia *et al*., 1998; Aiello *et al*., 2001). The Capri island represents a key sector for the comprehension of the paleogeographic setting of the southern Apennines during the Mesozoic and the Cenozoic (Barattolo and Pugliese, 1987). In fact, it represents one of the few areas where the inner margin of the Apenninic platform is preserved (Mostardini and Merlini, 1986). The recognized and distinguished units are numerous and include a wide stratigraphic interval ranging between the Early Jurassic and the Miocene. Due to the complex tectonic setting of the island, determined from the Oligo-Miocene Apenninic deformation e then from the Plio-Quaternary neotectonics, the vertical and horizontal relationships among the different units are often very complex, not preserved or unaltered. In particular, this happens in the eastern sector of the island, where the geologic situation is complicated by an intense urbanization and by the wide occurrence of Quaternary deposits. The main formations are represented by the Cala Ventroso dolomites (Lias), the Grotta Delle Felci bioclastic limestones (Middle-Upper Lias),the Torina oolitic limestones (Aalenian-Bathonian), the Migliara cherty limestones (Middle Lias-Kimmeridgian), the Ellipsactinia limestones (Callovian-Valanginian), the Limmo white limestones (Aptian), the Tiberio rudites (Aptian-Turonian p.p.), the Scaglia di Punta Carena (Upper Turonian-Coniacian), the Faro conglomerates (Maastrichtian).

Deep seismic sections on the Southern Tyrrhenian continental margin and in the Tyrrhenian bathyal plain have been collected. Three regional seismic profiles have been processed and interpreted, for an overall length of 160 km. The acquisition parameters are represented by the type of seismic source (N.2 Airguns, G/I gun SI/Sodera), by the record length (5 s, TWT), by the shot interval (25 m) and by the hydrophones interval (12.5 m). The software used for the seismic processing are the “Promax2D” (Landmark Ltd.) and the “Seismic Unix” (Colorado School of Mines). Some advanced processes have been applied to a basic flux of elaboration to improve the useful signal occurring in the seismic data. The seismic data have been promoted to produce stacked sections, which have been interpreted.

The Fourier analysis has been carried out on the seismic traces to identify the frequency content of the signal in several seismograms after the application of a band-pass filter. This enabled to recognize the frequency interval in which the useful signal was concentrated. The gain application consisted of the compensation of the delay of the signal due to absorption, scattering and decay of the amplitude. A large amount of the lost signal has been restored in order to obtain levels of amplitude similar throughout all the seismic data. The corresponding process is the Automatic Gain Control (AGC). The first stacked seismic sections have been produced through the velocity analysis on sorted seismic traces in CMP-gathers. The Common MID Points Gathers (CDP) represent the in-phase sum of the seismic traces coming from the same CDP. The same process has been repeated after applying different processes of elaboration to the seismic data, trying to understand if the same processes have produced or not significant improvements of the seismic signal. The reflection hyperbola alignment obtained using different velocity values have been calculated. The NMO correction has been obtained using previously estimated correct velocity values. The signal/noise ratio was increased through the stacking, reducing the casual noise included in the data. During the stacking, the coherent signal has increased its width by constructive interference of a factor equivalent to the coverage of the data; on the other side, the casual signal has been added to another noise by slightly increasing its width.

The applied filter resulted to be enough conservative (0-20-50-70 Hz) allowing to eliminate the occurring high-frequency noise. A frequency spectrum before and after the band-pass filter has also been constructed.

The procedure of multiple attenuation consisted of both stacking and predictive deconvolution. The move-out between the primary reflections and the multiple ones was discriminated through

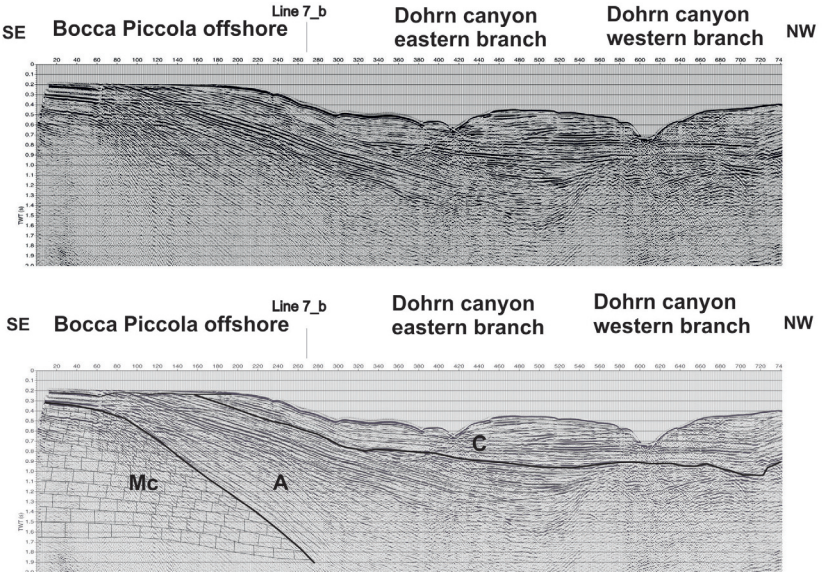


Fig. 1 – Deep multichannel seismic profile showing the seismic stratigraphy of the Campania continental margin between the Bocca Piccola offshore (Capri island) and the Dohrn canyon. Mc: Mesozoic carbonate unit. A: Middle-Late Pleistocene prograding wedge. C: Late Pleistocene prograding wedge. The two wedges constitute the bulk of the stratigraphic architecture of the Naples Bay.

the stacking, defining a correct velocity function of the primary reflections and relieving the mistaken coherent noise. The predictive deconvolution has been carried out on the seismic data in order to eliminate or further reduce the multiple signals which characterize the same section, allowing to get back the high frequencies and reconstruct the waveform. The seismic signals on the sections appear more compressed and consequently, it was simpler to identify the seismic reflectors during the geologic interpretation.

In the Ischia-Capri-Volturno alignment of the Campania continental margin several important morpho-structures have been identified: the Banco di Fuori, a morpho-structural high of Meso-Cenozoic carbonates, bounding southwards the Naples Bay; the Dohrn canyon, separating the eastern side of the Naples Bay, where sedimentary sequences crop out, from the western one, where volcanic seismic units prevail; the Capri structural high, having a sedimentary nature and is related to the regional uplift of Meso-Cenozoic carbonates along the Capri-Sorrento alignment; the Magnaghi canyon, eroding the Mg volcanic seismic unit southwards of the Procida island; the Capri basin, which is a deep basin located southwards of the Naples Bay, filled by Pleistocene-Holocene sediments overlying the Meso-Cenozoic carbonate unit; the Salerno Valley, a half-graben filled by three seismic units corresponding to Quaternary marine deposits, overlying chaotic sequences related to the Cilento Flysch; the Volturno basin, filled by four marine to deltaic seismic sequences, frequently alternating with volcaniclastic levels, overlying deep seismic units, correlated with Miocene flysch deposits (sands and shales) and Meso-Cenozoic carbonates.

The seismic profile Sister4_2, NE-SW trending, extends for a length of 66 kilometers on the Campania continental margin. It starts on the continental slope offshore Bocca Piccola, namely a saddle located between the Sorrento Peninsula and the Capri island and crosses the Dohrn and the Magnaghi canyons, reaching the structural high of the Ischia volcanic complex. The seismic sections ends on the continental slope of the Northern Campania continental margin in the Volturno Basin. Three physiographic and depositional domains have been distinguished through the seismic interpretation. The first domain is represented by the continental slope surrounding the Capri island and the Bocca Piccola offshore. The second domain is represented

by the Magnaghi canyon. The third domain is represented by the Ischia offshore and the Volturno Basin. While in correspondence to the Sorrento Peninsula and the Volturno river a good reflectivity of the seismic signal has been observed, on the contrary, the central sectors of the profile, where the Magnaghi canyon and the Ischia volcanic complex occur, are characterized by a poor reflectivity of the seismic signal, due to the occurrence of levels of volcanites and buried seismic units.

An area of poor penetration of the seismic signal, related to the occurrence of Meso-Cenozoic carbonates (MC unit) has been recognized at the south-eastern corner of the seismic line. This area represents the offshore prolongation of the Capri structural high. In the corresponding emerged sector, Meso-Cenozoic carbonate rocks, related to the western margin of the Campania-Lucania carbonate platform extensively crops out (D'Argenio *et al*., 1973; Barattolo and Pugliese, 1987).

Two seismic units have been identified in the Capri structural high, unconformably overlying Meso-Cenozoic carbonates. They are interpreted as two relict prograding wedges. The oldest prograding wedge (A seismic unit), probably Early-Middle Pleistocene in age, is characterized by continuous and strongly inclined reflectors, truncated close to the sea bottom by an erosional unconformity. The youngest prograding wedge (C seismic unit) is characterized by continuous seismic reflectors, probably dating back to the Late Pleistocene. Along the continental slope it is incised by the Dohrn canyon branches.

The continental slope between the Magnaghi canyon and the structural high of the Ischia volcanic complex shows an acoustically transparent seismic facies, genetically related to the volcanites and to the volcaniclastites of the Ischia volcanic complex (Isch seismic unit).

The southern Procida offshore is characterized by volcanic deposits, lacking of internal reflectivity and deeply incised by the Magnaghi canyon. A volcanic edifice, mounded-shaped, corresponds to a buried volcanic edifice, previously unknown and interstratified with the volcanites of the Mg unit under the canyon itself.

The Volturno Basin is characterized by four main seismic units. The lithologies of the seismic units have been qualitatively calibrated using the lithostratigraphic data of the Castelvolturno 2 exploration well (Ippolito *et al*., 1973) and the onshore seismic section of Mariani and Prato (1988). The oldest unit of the basin fill (D1 unit) is characterized by parallel and continuous seismic reflectors, interpreted as Pleistocene coastal shales alternating with volcaniclastic sediments. The D1 unit overlies the Ff seismic unit showing discontinuous chaotic reflectors and correlating with Miocene flysch deposits, composed of alternating sands and shales and widely cropping out in Central Apennines ("Flysch di Frosinone" Auct.; Parotto and Praturlon, 1975). The overlying seismic unit (D2 seismic unit) is characterized by moderate amplitudes and marked reflectors with high lateral continuity. It has been interpreted as Pleistocene and marine deltaic sediments. This geological interpretation has been supported by the lithostratigraphic data of the Castelvolturno 2 deep borehole and by the onshore seismic sections in the Volturno plain (Mariani and Prato, 1988). The onshore sections suggest the occurrence of a seismic unit composed of discontinuous reflectors with high amplitude and sigmoidal pattern, composed of alternating sands and shales, Pleistocene in age. This unit is genetically related to the D2 unit in the Volturno Basin. In the Volturno Plain lithostratigraphic well data show a thick sequence (about 1000 m) of Pleistocene alternating deltaic sands and shales, interlayered with pyroclastites and lavas. The D3 seismic unit shows parallel to sub-parallel seismic reflectors having a high amplitude. It is formed by alternating sands and shales of deltaic environments, Pleistocene in age, similar to the onshore section (Mariani and Prato, 1988).

The main regional morpho-structures of the Ischia-Capri alignment of the Campania continental margin are here discussed based on seismic interpretation. The Banco di Fuori is a morpho-structural high of the Meso-Cenozoic carbonate substratum, bounding the southern sector of the Naples Bay. Its flanks and top are overlain by the Pleistocene deposits of the Late Quaternary depositional sequence. Acoustically transparent seismic facies, genetically related

to Meso-Cenozoic carbonates have been recognized. The regional geological setting and the seismic interpretation have confirmed that the Banco di Fuori represents a major morpho-structure high, separating the Dohrn canyon from the Magnaghi canyon. It is formed by a Mesozoic carbonate block resulting from the uplift and tilting of the carbonate basement. The carbonatic nature of the structural high is confirmed by its location along the Capri-Sorrento structural alignment and by the lack of significant magnetic anomalies (Aiello *et al*., 2005).

The interpreted seismic data have been compared with previous structural interpretations on the Banco di Fuori area (Milia and Torrente, 1999). The Banco di Fuori high is bounded southwards by a set of normal faults, N to NE trending, down throwing the Meso-Cenozoic substratum many hundred of meters to the SE and characterized by variable cross-section geometries. The top of the acoustic substratum is downthrown towards SE. The appraisal of the corresponding fault varies from 1300 to 1000 m, while on the eastern profile is 600 m. The variations in the displacement have been interpreted according to the model of Walsh and Watterson (1988), evidencing the fault displacement changes along the strike. It is commonly greatest at the centre of the fault, decreasing to zero at the eastern fault tip in the central part of the Naples Bay, where this structure is buried by younger sediments.

One of the main morpho-structures of the Naples Bay is represented by the Dohrn canyon, separating the eastern gulf, where sedimentary seismic units crop out from the western gulf, where the volcanic seismic units prevail. The canyon is articulated into two main branches, the eastern one and the western one, merging in a thalweg having a NE-SW (counter-Apenninic) direction, bounded southwards by the Capri basin. It erodes the Pleistocene relict marine units of the prograding wedges (A and C in the interpreted seismic sections) overlying the Meso-Cenozoic carbonates. Our seismostratigraphic data suggest the occurrence of Meso-Cenozoic carbonates under the canyon thalweg, in the bathyal plain westwards of the Capri island. The carbonatic unit below the Banco di Fuori – Dohrn canyon – Salerno Valley alignment has not been previously pointed out by seismostratigraphic papers on the Naples Bay, suggesting its distribution only in the eastern continental shelf of the Naples Bay, as offshore prolongation of the NW dipping Capri-Sorrento monoclinalic structure (Fusi, 1996).

Another main structure is represented by the Capri structural high, whose southern flank is deeply downthrown by the Capri-Sorrento master fault. Its stratigraphic setting is composed of two relict prograding wedges, the A and C seismic units. The Capri structural high is bounded by the Dohrn canyon structure to the NW and by the Salerno Valley to the SE. The regional structure of the Capri structural high is related to the Capri-Sorrento Peninsula structural alignment (D'Argenio *et al*., 1973; Perrone, 1988). The southern flank of the structural high is controlled by the Capri-Sorrento master fault.

The following structure is represented by the Magnaghi canyon, draining the volcanic and volcaniclastic input coming from the eruptive activity of the Ischia and Procida islands during the Late Quaternary. The canyon erodes the deposits of the Mg unit, characterized by seismic reflectors having a chaotic distribution. A volcanic nature of the Mg unit, genetically related to the Procida volcanic complex, may be assumed. The Magnaghi canyon basin is a sedimentary basin adjacent to the Magnaghi canyon and representing a depositional area, where Pleistocene-Holocene deposits drained by the canyon in its initial thalweg have accumulated. This depositional area, previously unknown, has not been mentioned by previous papers dealing on the seismic stratigraphy of the area (Fusi *et al*., 1991; Milia and Torrente, 1999).

Another main structure is the Capri Basin, which is a deep basin localized in the Tyrrhenian bathyal plain southwards of the Dohrn canyon. It is filled by Pleistocene-Holocene sediments, thick about 0.7 s (twt), unconformably overlying Meso-Cenozoic carbonates. The basin filling is characterized by parallel and laterally continuous seismic reflectors, overlying an acoustically-transparent seismic facies, interpreted as the Meso-Cenozoic carbonates. The seismic stratigraphy of the Capri Basin is relatively unknown, excluding the paper of Milia and Torrente (1999), identifying seven depositional sequences in the basin filling. Two lowstand

units have been related to main tectonic pulses. Mass flow deposits that flowed into the basin directly from the contiguous narrow shelf and steep slope have also been recognized.

Another important structure is represented by the Salerno Valley, a half-graben basin filled by three main seismic units, corresponding to Quaternary marine and continental sediments. These units grade laterally into the chaotic deposits related to the "Flysch del Cilento" Auct. (Bonardi *et al*., 1988). The deepest seismic unit has been interpreted as Meso-Cenozoic carbonates due to the poor penetration of the seismic signal. The tectonic setting of the valley is controlled by the Capri regional fault, downthrowing the Meso-Cenozoic carbonates from the Capri structural high under the basin itself.

The last investigated structure is represented by the Volturno Basin, hosting the northern sector of the Campania Plain and the surrounding offshore and showing a sedimentary filling consisting of four main marine and deltaic seismic sequences, alternating with volcaniclastic levels and overlying deep seismic units, related to Miocene flysch deposits (sands and shales) and Meso-Cenozoic carbonates. New seismo-stratigraphic data have evidenced that the Volturno Basin represents a half-graben, characterized by blocks down thrown along normal faults, involving the top of the Miocene acoustic basement.

## References


Aiello G., Budillon F., Cristofalo G., de Alteriis G., De Lauro M., Ferraro L., Marsella E., Pelosi N., Sacchi M., Tonielli R.; 2001: *Marine geology and morpho-bathymetry in the Bay of Naples*. In: Faranda F.M., Guglielmo L., Spezie G. (Eds.) *Structures and Processes of the Mediterranean Ecosystems*, pp. 1-8, Springer, Italy.

Aiello G., Angelino A., Marsella E., Pelosi N., Ruggieri S., Siniscalchi A. (2005) *Buried volcanic structures in the Gulf of Naples (Southern Tyrrhenian sea, Italy) resulting from high resolution magnetic survey and seismic profiling*. Annals of Geophysics, **48 (6)**, 1-15.

Aiello G., Marsella E., Cicchella A.G., Di Fiore V.; 2011: *New insights on morpho-structures and seismic stratigraphy along the Campania continental margin (Southern Italy) based on deep multichannel seismic profiles*. Rend. Lincei, **22**, 349-373.

Barattolo F. and Pugliese A.; 1987: *Il Mesozoico dell'Isola di Capri*. Quaderni Accademia Pontaniana, **8**, 1-36, 66 tavv.

Barberi F., Innocenti F., Lirer L., Munno R., Pescatore T., Santacroce R.; (1978): *The Campanian Ignimbrite: a major prehistoric eruption in the Neapolitain area (Italy)*. Bull. Volcanol., **41 (1)**, 1-22.

D'Argenio B., Pescatore T., Scandone P. (1973) *Schema geologico dell'Appennino meridionale (Campania e Lucania)*. Atti del Convegno "Moderne vedute sulla geologia dell'Appennino", Accademia Nazionale dei Lincei, Quaderno **183**, 49-72.

Faccenna C., Mattei M., Funiciello R., Jolivet L. (1996) *Styles of back-arc extension in the Central Mediterranean*. Terra Nova, **9**, 126-130.

Fusi N. (1996) *Structural settings of the carbonatic basement and its relationship with magma uprising in the Gulf of Naples (southern Italy)*. Annali di Geofisica, **39 (3)**, 493-509.

Fusi N., Mirabile L., Camerlenghi A., Ranieri G. (1991) *Marine geophysical survey of the Gulf of Naples (Italy): relationships between submarine volcanic activity and sedimentation*. Memorie della Società Geologica Italiana, **47**, 95-114.

Ippolito F., Ortolani F., Russo M. (1973) *Struttura marginale tirrenica dell'Appennino campano: reinterpretazione di dati di antiche ricerche di idrocarburi*. Memorie della Società Geologica Italiana, **12**, 227-250.

Malinverno A. and Ryan W.B.F. (1986) *Extension in the Tyrrhenian sea and shortening in the Apennines as a result of arc migration driven by sinking of the lithosphere*. Tectonics, **5**, 227-245.

Mariani M. and Prato R. (1988) *I bacini neogenici del margine tirrenico: approccio sismico-stratigrafico*. Memorie della Società Geologica Italiana, **41**, 519-531.

Milia A. and Torrente M.M. (1999) *Tectonics and stratigraphic architecture of a peri-Tyrrhenian half-graben (Bay of Naples, Italy)*. Tectonophysics, **315**, 301-318.

Milia A., Mirabile L., Torrente M.M., Dvorak J.J.; 1998: *Volcanism offshore Vesuvius volcano (Italy): implications for hazard evaluation*. Bull. Volcanol., **59**, 404-413.

Mostardini F. and Merlini S.; 1986: *Appennino centro-meridionale: sezioni geologiche e proposta di modello strutturale*. Mem. Soc. Geol. Ital., **35**, 177-202.

Parotto M. and Praturlon A. (1975) *Geological summary of central Apennines*. Quaderni de La Ricerca Scientifica, CNR, **90**, 257-311.

Walsh J.J. and Watterson J. (1988) *Analysis of the relationship between displacements and dimensions of faults*. Journal of Structural Geology, **10**, 239-247.

# THE IMPORTANCE OF THE VP/VS RATIO IN DETERMINING THE ERROR PROPAGATION AND THE RESOLUTION IN LINEAR AVA INVERSION

**M. Aleardi, A. Mazzotti**
*Earth Sciences Department, University of Pisa, Italy*

**Introduction.** The Amplitude-Versus-Angle (AVA) method exploits the variation in seismic reflection amplitude with increasing incidence angle to infer the contrast in seismic velocities and densities at the reflecting interfaces (Castagna, 1998). For this characteristic the AVA technique has been extensively used worldwide for lithology and fluid prediction in deep hydrocarbon exploration (e.g., Ostrander, 1984; Rutherford and Williams, 1989; Mazzotti, 1990, 1991).

The AVA method is based on the Zoeppritz equations (Zoeppritz, 1919) which describe the variation in seismic amplitude with increasing angle of incidence for a plane wave incident on an idealized interface separating two semi-infinite half spaces. The system of equation formulated by Zoeppritz is so algebraically complex that many different approximated formulas have been derived to simplify and linearise the inversion process. These simplified equations, valid under certain assumptions, are those frequently used in AVA inversion and interpretation (Ursenbach and Stewart, 2008; Wang, 1999).

Performing linear AVA inversion a *Vp*/*Vs* ratio equal to two is usually assumed (Castagna, 1998). This ratio is a good approximation of the true value in case of classical deep sediments exploration (hydrocarbon exploration), but generally it is an underestimation of the true ratio in case of shallow or seabed sediments. This may constitute a problem because, in addition to the classical deep exploration, the AVA inversion can also be useful for characterizing shallow layers (Riedel and Theilen, 2001) and, thus can be of help for shallow hazard assessment and well site analysis.

While performing linear AVA inversion the importance of the *Vp*/*Vs* ratio is usually underrated and its value is set without worrying too much. Therefore, in this work we want to point out that the assumed *Vp*/*Vs* ratio plays a crucial role in determining the expected resolution and the uncertainties associated with each inverted parameter. To this end we have considered the well known three terms Aki and Richards (Aki and Richards, 1980) equation and the two terms Ursenbach and Stewart formula (Ursenbach and Stewart, 2008), which are analyzed making use of the sensitivity analysis tools applied to the inversion kernel. We have first studied how the *Vp*/*Vs* value influences the condition number, the amplitude of the eigenvalues (not shown here for the lack of space) and the orientation of associated eigenvectors in model space. Moreover, also applying the classical truncated SVD method and studying the resolution and the covariance matrices, we have analyzed how the *Vp*/*Vs* ratio determines both the expected resolution of each inverted parameter and the error propagation from data space to model space.

**Inverse problems, sensitivity analysis and SVD decomposition.** A seismic inverse problem aims to estimate model parameters ($m$) from collected data ($d$) minimizing the misfit between predicted and observed data (Tarantola, 2005). If we assume that the fundamental physics are adequately understood, a function, $G$, may be specified relating $m$ and $d$:

$$d = G(m)$$

The simplest and best understood inverse problems are those that can be represented by an explicit linear equation $d = Gm$ in which $G$ takes a matrix form. Many important seismic inverse problems are linear, such as the AVA inversion performed by applying approximations of the Zoeppritz equations.

One commonly used measure of the misfit in solving an inverse problem is the $L_2$ norm of the residuals. A model that minimizes this $L_2$ norm is called a least-squares solution. The least-squares solution for linear inverse problems can be derived using the following equation (also called the normal equations solution):

$$m_{L2} = (G^T G)^{-1} G^T d$$

where the superscript $T$ indicates the transpose. In a compact form the solution of a linear inverse problem can be written as follow:

$$m = G^{-g} d$$

where $G^{-g}$ is called the generalized inverse. For a common overdetermined least-squares problem, this matrix is equal to:

$$G^{-g} = (G^T G)^{-1} G^T$$

However, to resolve an inversion problem, one must not only find a solution that best fits the observed data but should also investigate the relation between the estimated model and the true model or, in other words, analyze which properties of the true model are resolved in the estimated model. This problem can be approached with the sensitivity analysis method. For linear inverse problems, this analysis essentially consists in computing the model covariance and model resolution matrices.

On one hand the model resolution matrix ($R$) describes how well the predicted model matches the true one. It can be demonstrated (Aster *et al.,* 2005) that the resolution matrix for a linear inverse problem can be computed as follows:

$$R = G^{-g} G$$

On the other hand, to understand how an error in the data propagates as an error in the estimated model, it is useful to define the model covariance matrix $C_{m.}$ If the data are assumed to be uncorrelated and all have equal variance, the covariance matrix (unit covariance matrix) is given by:

$$C_m = G^{-g} G^{-gT}$$

Another useful tool in approaching inverse problems is the Singular Value Decomposition (SVD). According to this method the matrix $G$ be broken down into the product of three matrices:

$$G = USV^T$$

where $S$ is a diagonal matrix of singular values, $V$ is the matrix of eigenvectors in model space and $U$ contains the eigenvectors in data space. The SVD decomposition is essential in sensitivity analysis because it permits to get a better understanding of the physical meaning of the $G$ matrix. Moreover, the SVD method is also a powerful tool for solving ill-conditioned least-squares problems. In these problems, the process of computing an inverse solution is extremely unstable and a small change in the measurements can lead to a large change in the estimated model. In these cases the $G$ matrix is characterized by a high condition number, which is the ratio between the highest and the smallest singular values of the $G$ matrix. Therefore, in order to stabilize the inversion, the truncated SVD method (T-SVD) can be applied. This method is aimed at eliminating the smallest singular values of the $G$ matrix and at reducing the condition number. We pay a price for this stability in that the regularized solution has a decreased resolution. Very detailed information about geophysical inverse problems can be found in Aster *et al*. (2005) and Tarantola (2005).

**The Aki and Richards and Ursenbach and Stewart approximations.** Starting from the Zoeppritz equations, Aki and Richard (1980) provided approximation for P-P wave reflection coefficients that is valid for small physical contrasts and small incidence angles (generally less than 30-35 degrees). This equation can be written as

$$R_{pp}(\vartheta) = \frac{1}{2\cos^2\vartheta}\frac{\Delta\alpha}{\alpha} - 4\gamma^2\sin^2\vartheta\frac{\Delta\beta}{\beta} - \frac{1}{2}\left(4\gamma^2\sin^2\vartheta - 1\right)\frac{\Delta\rho}{\rho}$$

where the P-wave reflection coefficient is $R_{pp}$, $\vartheta$ is the average of incidence and P-wave transmission angles across the interface, and the P-wave velocity, S-wave velocity and density are indicated by $\alpha$, $\beta$, and $\varrho$, respectively. In this equation $\Delta x/x$ denotes the relative contrast for a particular property between the overlying and underlying media, whereas $\gamma$ is inversely correlated with the background $Vp/Vs$ ratio:

$$\gamma = \frac{\beta_1 + \beta_2}{\alpha_1 + \alpha_2}$$

where the subscripts 1 and 2 refer to the overlying and underlying media, respectively.

The Aki and Richards equation is inverted to retrieve the relative contrasts at the reflecting interface that can be conveniently written as

$$\frac{\Delta\alpha}{2\alpha} = R_p; \qquad \frac{\Delta\beta}{2\beta} = R_s; \qquad \frac{\Delta\rho}{2\rho} = R_d$$

In this form $R_p$, $R_s$ and $R_d$ indicate the P-wave, S-wave and density reflectivity, respectively.

To reduce the physical ambiguity inherent to the AVA method (Drufuca and Mazzotti, 1995) and to stabilize the inversion process the number of unknowns can be reduced. To this end two-term approximations of the Zoeppritz equations are frequently used. In particular in this work we consider the Ursenbach and Stewart equation (Ursenbach and Stewart, 2008):

$$R_{pp}(\vartheta) = \left(1 + \frac{4\gamma^2\cos^2\vartheta - 1}{5}\sin^2\vartheta\right)\frac{R_I}{\cos^2\vartheta} - 8\gamma^2\sin^2\vartheta R_J$$

where the density term is incorporated into the P and S impedance contrasts expressed by $R_I$ and $R_J$, respectively.

These linear approximations of the Zoeppritz equations enable the description of the relationship between the observed AVA response ($R_{pp}$) and the model parameters ($m$) in a linear, compact, matrix form:

$R_{pp}(\vartheta) = Gm$

In this form the $G$ matrix contains the three- or the two-term equation, whereas the vector $m$ contains the inverted parameters (elastic or impedance contrast at the reflecting interface).

The singular value decomposition of the $G$ matrix splits the reflectivity $R_{pp}(\vartheta)$ into three orthogonal components in both data space and model space. It is interesting to consider the physical meaning of the decomposition. The eigenvectors $V$ are a basis in the model space. The eigenvalues represent the reflected energy due to medium perturbations along the eigenvectors in model space. The amplitude versus angle effects of the reflections are described by the eigenvectors in data space, which are three orthogonal functions (De Nicolao *et al.*, 1993).

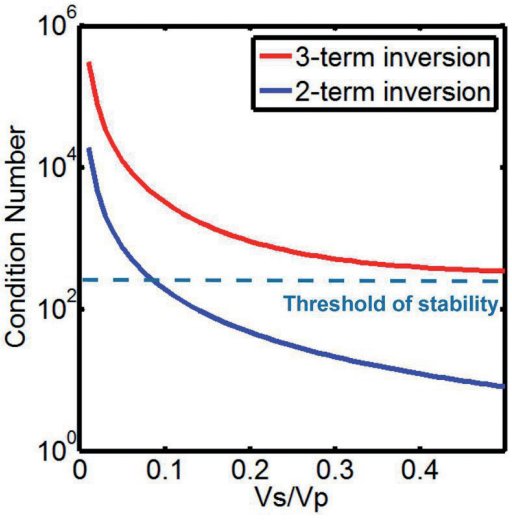


Fig. 1 – Condition number for the three-term Aki and Richards equation (red line) and the two-term Ursenbach and Stewart equation (blue line) for varying background *Vs*/*Vp* ratios. The dotted line represents the assumed threshold of stability for the linear AVA inversion.

**Condition number and eigenvectors in model space.** We now compare the condition number for the three- and the two-term inversions by varying the background *Vp*/*Vs* ratio. We remind that high condition numbers indicate an ill-conditioned problem. Based on previous experience with linear AVA inversion, we can fix the threshold of stability for the linear AVA inversion between 200 and 500. Therefore, we can determine how the *Vp*/*Vs* ratio influences the stability of the inverse problem (Fig. 1). Specifically, if *Vp*/*Vs* is equal to 2 (or *Vs*/*Vp*=0.5), as is often assumed in deep

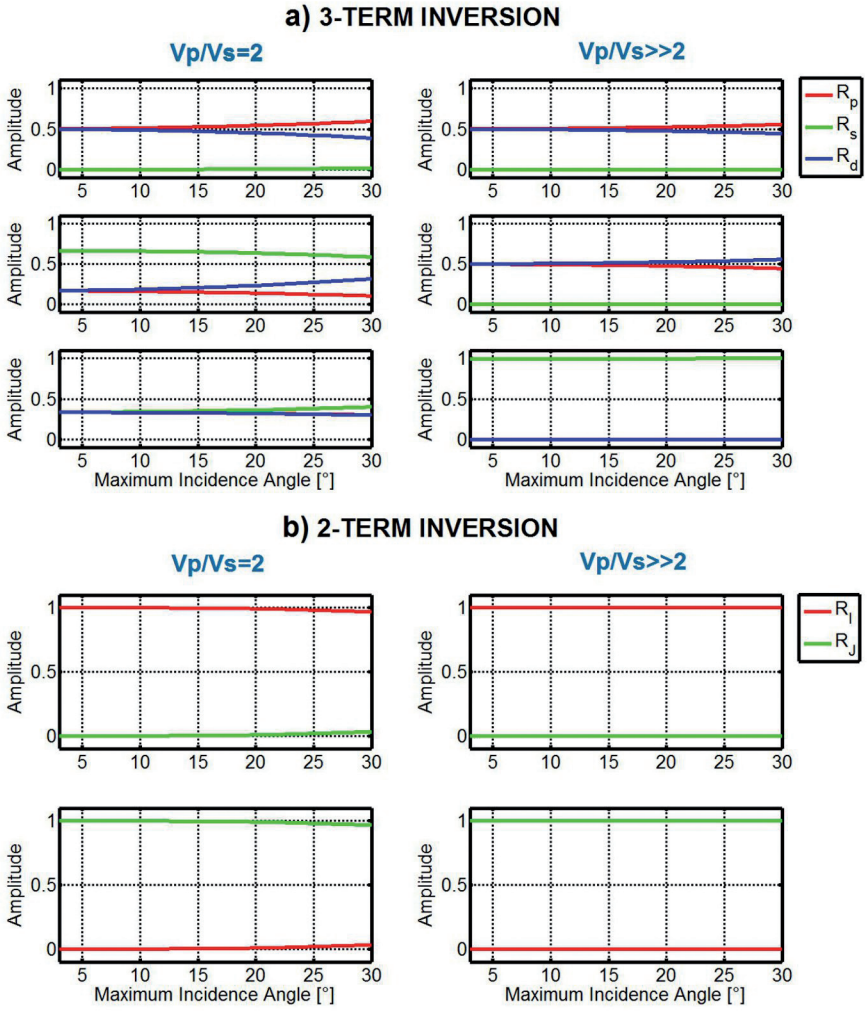


Fig. 2 – a) Eigenvectors in model space versus the maximum observation angle for three-term inversion. The *Vp*/*Vs*=2 and *Vp*/*Vs*>>2 are represented on the left and on the right, respectively. For each case, the first, second and third eigenvectors are shown from top to bottom, respectively. b) Eigenvectors in model space versus the maximum observation angle for the two-term inversion. The left column represents the *Vp*/*Vs*=2 case, whereas the right column displays the *Vp*/*Vs*>>2 case. For each case, the first and second eigenvectors are shown at the top and bottom, respectively.

sediment exploration, the inverse problem becomes stable as we pass from the three- to the two-term approximation. Conversely, when the *Vp*/*Vs* ratio is very high (or *Vs*/*Vp* approaches 0), as it occurs for shallow or seabed sediments, the inverse problem is ill-conditioned even if a two-term approximation is considered. Therefore, in the case of linear AVA inversion with very high *Vp*/*Vs* ratios, the application of a regularization method (i.e the T-SVD method) is needed to stabilize the inversion process.

Now we move to describe the orientation of the eigenvectors in model space for the three- and two-term inversions. We first analyze the Aki and Richards equation and assuming a *Vp*/*Vs* ratio of two (Fig. 2a, left column). For low angles, the $R_p$ and $R_d$ components are equal and $R_s$ is zero. Therefore, the vector points in the direction of P-impedance perturbations. This result is obvious: it is known that the zero-offset reflection coefficient depends only on the acoustic impedance contrast at the reflecting interface. The $R_s$ component becomes significant for

higher angles. The second eigenvector points, approximately, in the direction of S-impedance perturbations, whereas the third eigenvector does not have any particular physical meaning.

In the *Vp*/*Vs*>>2 case (Fig. 2a, right column), both the first and second eigenvectors, associated with the first and second singular values, point toward the P-impedance. Conversely, only the third eigenvector, associated with the smallest singular value, points entirely in the $R_s$ direction. This fact indicates that this component spans the null-space of the *G* matrix. This result illustrates that for high *Vp*/*Vs* ratios, the S-wave velocity plays a very minor role in determining the AVA response. Moreover, by comparing the first and second eigenvectors for *Vp*/*Vs*=2 and *Vp*/*Vs*>>2, we can see that an increased *Vp*/*Vs* ratio increases the cross-talk between $R_p$ and $R_d$: a smaller distance is observed between the $R_p$ and $R_d$ components as the *Vp*/*Vs* ratio increases. This trend makes an independent estimation of these two parameters more problematic in the case of high *Vp*/*Vs* values. These observations allow us to draw some important conclusions. First, the difficulty of achieving a reliable $R_s$ estimation with increasing *Vp*/*Vs* values; second, the cross-talk between $R_p$ and $R_d$ also increases as the *Vp*/*Vs* ratio increases.

Now, we briefly consider the eigenvectors in model space for the two-term approximation (Fig. 2b). In the case of *Vp*/*Vs*=2 (Fig. 2b, left column), the first eigenvector points toward the P-impedance for small angles, whereas the $R_J$ component is not-null only if large incidence angles (grater than 20 degrees) are considered. Conversely, if we increase the *Vp*/*Vs* ratio (Fig. 2b, right column), the first eigenvector points toward the P-impedance regardless of the considered angle range. In this case, the $R_J$ parameter spans the null space of the *G* matrix, indicating that, for a reliable estimation of the $R_J$ term, a sufficiently high *Vp*/*Vs* ratio is needed. Note that the two-term inversion is stable only for sufficiently low *Vp*/*Vs* values (see Fig. 1), and in these cases, use of the second eigenvector allows the inversion to extract the $R_J$ parameter. In the *Vp*/*Vs*=2 case, this eigenvector can be used in the inversion and the $R_J$ information can be recovered with a good degree of accuracy. Instead, in cases of *Vp*/*Vs*>>2, a regularization method (for example, the T-SVD method) is needed to stabilize the inversion. In these cases, the truncation of the second singular value (and the associated eigenvector) renders a reliable estimation of the $R_J$ value impossible.

**Model resolution and unit covariance matrices.** Here, we describe the model covariance and resolution matrices. The former describes how the error in the data space propagates in the model space. The latter describes how the true parameters influence the estimated ones. We start by analyzing the unit covariance matrix (computed by assuming an identity data covariance matrix) for the least-squares inversion, for which the model resolution matrix is equal to an identity matrix (see Aster *et al*., 2005 for a rigorous mathematical demonstration).

Fig. 3a shows the unit covariance matrices computed for both *Vp*/*Vs*=2 and *Vp*/*Vs*>>2 and for both the three- and two-term approximations. From this figure, we can see that the order of magnitude of the errors decreases from the three- to two-term inversion (independent of the *Vp*/*Vs* value) and from the *Vp*/*Vs*>>2 to the *Vp*/*Vs*=2 case (independent of the parametrization). It is worth noting that the *Vp*/*Vs* ratio determines the error propagation from the data to the model space. In fact, for high *Vp*/*Vs* values, the parameters most contaminated by noise are those associated with the *Vs* values ($R_s$ and $R_J$, respectively). Instead, if the *Vp*/*Vs* is equal to two, the error is more homogeneously distributed among the parameters although, even in this case, the error most strongly affects $R_s$ and $R_J$.

Now we eliminate the smallest singular value of the *G* matrix (applying the T-SVD method) and recompute the unit covariance and the model resolution matrices. Let us first consider the model resolution matrices (Fig. 3b). For the three-term inversion, it is clear that for the *Vp*/*Vs*>>2 case, we obtain a null resolution for the $R_s$ parameter and a good resolution for both $R_p$ and $R_d$ (note that the resolution is expressed by the diagonal terms). In the case of *Vp*/*Vs*=2, the three parameters can be recovered with almost the same resolution, even if the lowest resolution capability is always related to $R_s$. If we reduce the dimension of the model space considering the two-term equation, we can see that for both cases, the $R_I$ parameter is characterized by the

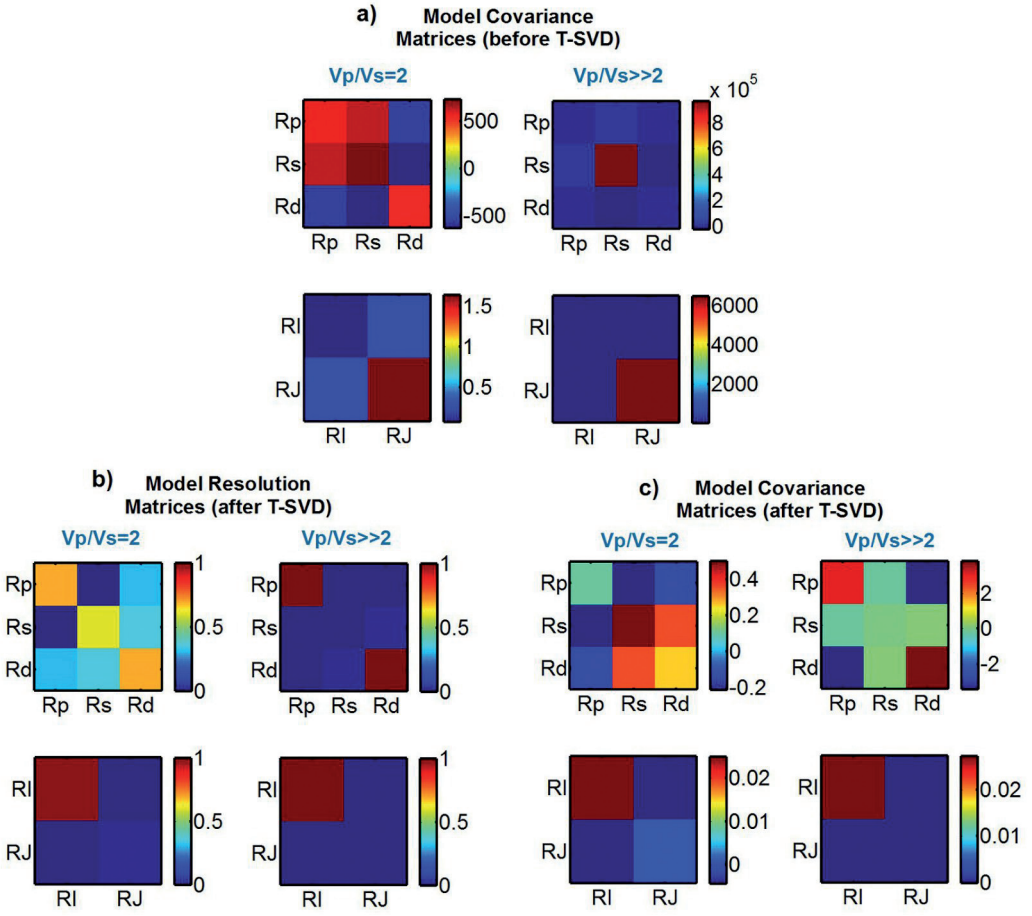


Fig. 3 – a) Unit covariance matrices in the case of a least-squares inversion. b) Model resolution matrices after applying the T-SVD method. c) Unit covariance matrices after applying the T-SVD method. In all cases both the *Vp*/*Vs*=2 and *Vp*/*Vs*>>2 (left and right columns, respectively) and the three- and two-term inversions (top and bottom rows, respectively) are considered.

highest resolution. Also in this case, the resolution of the *Vs*-related parameter $R_J$ decreases with the increasing *Vp*/*Vs* ratio.

Now we describe the unit covariance matrix, which is obtained after applying the T-SVD method (Fig. 3c) to eliminate the smallest singular value of the *G* matrix and to stabilize the inversion. We start with the three-term inversion. For high *Vp*/*Vs* ratios, the error is mapped onto the $R_p$ and $R_d$ parameters because the third eigenvalue, pointing toward the $R_s$ parameters, has been eliminated by the truncation. We also observe a strong negative covariance (expressed by the off-diagonal terms and indicating a correlation) between $R_p$ and $R_d$, which confirms the strong cross-talk between these two unknowns and the difficulties of achieving an independent estimation. As expected, both the correlation between $R_p$ and $R_d$ and the error magnitude decrease if we consider a *Vp*/*Vs* ratio equal to two. In this case, the error is more homogeneously distributed among the three parameters. Also by observing the unit covariance matrix for the two-term inversion, we see that the error magnitude decreases from the *Vp*/*Vs*>>2 case to the *Vp*/*Vs*=2 case. Moreover, the truncation of the second singular values (in the case of *Vp*/*Vs*>>2) results in the error being mapped entirely onto the $R_I$ parameters, whereas in the case of *Vp*/*Vs*=2, the error also affects the $R_J$ values. Finally, by comparing Fig. 3a and 3c, we can see that

in any case the T-SVD method reduces the order of magnitude of the error associated with each parameter estimation.

**Conclusions.** The sensitivity analysis highlights the strong influence of the *Vp*/*Vs* ratio on both the stability of the linear AVA inversion and on the physical meaning expressed by the *G* matrix. Specifically, we have analyzed how the *Vp*/*Vs* value influences the condition number, the orientation of eigenvectors in model space, the resolution for each inverted parameter and the error propagation from data to model space. From the analysis of the condition number we note that if *Vp*/*Vs* is equal to 2 the inverse problem becomes stable as we pass from the three- to the two-term approximation. Conversely, when the *Vp*/*Vs* ratio is very high (as occurs for shallow seabed sediments), the inverse problem is ill-conditioned even if a two-term approximation is considered. Therefore, in the case of linear AVA inversion with very high *Vp*/*Vs* ratios, the application of a regularization method (i.e the T-SVD method) is needed to stabilize the inversion process. Moreover, the orientation of the eigenvectors in model space shows that for high *Vp*/*Vs* ratios the eigenvectors associated with the *Vs*-related parameter ($R_s$ and $R_J$) span the null-space of the inversion kernel. This fact, combined with the observation of the resolution matrices, highlights that the determination of the *Vs* contrast (or the S-impedance contrast) for shallow sediments or at sea bottom becomes a hopelessly non-unique problem in the case of high *Vp*/*Vs* values. Finally, we observe that for increasing the *Vp*/*Vs* values the error propagation from data to model space becomes more and more severe. The same happens to the cross-talk between $R_p$ and $R_d$ making it impossible their independent estimation.

## References


Aki K. and Richards P. G.; 1980: *Quantitative seismology: Theory and methods*. WH Freeman and Co.

Aster R. C., Borchers B. and Thurber C. H.; 2005: *Parameter estimation and inverse problems*. Elsevier Academic Press.

Castagna J. P., Swan H. W. and Foster, D. J.; 1998: *Framework for AVO gradient and intercept interpretation*. Geophysics, 63(3), 948-956.

De Nicolao A., Drufuca G. and Rocca F.; 1993: *Eigenvalues and eigenvectors of linearized elastic inversion*. Geophysics, 58(5), 670-679.

Drufuca G., and Mazzotti A.; 1995: *Ambiguities in AVO inversion of reflections from a gas-sand*. Geophysics, 60(1), 134-141.

Mazzotti A.; 1990: *Prestack amplitude analysis methodology and application to seismic bright spots in the Po Valley, Italy*. Geophysics, 55, 157-166.

Mazzotti A.; 1991: *Amplitude, Phase and Frequency versus Offset Applications*. Geophysical Prospecting. 39, 863-886.

Ostrander W.; 1984: *Plane-wave reflection coefficients for gas sands at non-normal angles of incidence*. Geophysics, 49(10), 1637-1648.

Riedel M. and Theilen, F.; 2001: *AVO investigations of shallow marine sediments*. Geophysical Prospecting, 49(2), 198-212.

Rutherford S. R. and Williams R. H.; 1989: *Amplitude-versus-offset variations in gas sands*. Geophysics, 54(6), 680-688.

Tarantola A.; 2005: *Inverse problem theory and methods for model parameter estimation*. Siam.

Ursenbach C. P. and Stewart R. R.; 2008: *Two-term AVO inversion: Equivalences and new methods*. Geophysics, 73(6), 31-38.

Wang Y.; 1999: *Approximations to the Zoeppritz equations and their use in AVO analysis*. Geophysics, 64(6), 1920-1927.

# L-SHAPED ARRAY REFRACTIONS MICROTREMORS (LeMi)

**J. Boaga[1], C. Strobbia[2], G. Cassiani[1]**
*[1] Dipartimento di Geoscienze, Università degli Studi di Padova, Italy*
*[2] Total S.A., Pau, France*

**Introduction.** Surface wave methods are nowadays the main testing tools for the site characterization concerning engineering applications. Their use has been growing in past years especially due to the increasing interest in shear wave velocity measurement, which is essential in geotechnical earthquake engineering applications (Beavers, 2002; Chaillat *et al*. 2009). One of the reasons is the progression of several internationals a-seismic building codes that propose simplified seismic scenario based on Vs classification (e.g. Vs30 parameter as in Moss, 2008; EC8, 2003). Surface wave methods based on dispersion properties studies are nowadays widely adopted in local subsoil Vs characterization: different frequencies involve different soil thicknesses, and consequently travel at different velocities. Dispersion properties of surface waves are then used to define vertically heterogeneous media (Thomson, 1950; Tokimatsu, 1995; Foti, 2003, 2011; Socco and Strobbia, 2004; Strobbia and Cassiani, 2011), and they represent by now the most diffused techniques for Vs modeling. Surface wave methods are free from many practical and theoretical limitations of the classical body-wave analyses and they are free from the logistical effort of drilling (Boaga *et al*., 2010, 2011; Vignoli *et al*. 2010, 2012; Foti *et al*., 2011). The technique requires an accurately recorded Rayleigh/Love wavefields to be analyzed for its dispersive properties, and the consequent inversion of the dispersion curve (e.g. phase velocity versus frequency). Surface wave methods can be divided in active methods, relying on the use of controlled sources, and passive methods, basing on the analysis of ambient noise, or microtremors. The active (controlled source) surface wave methods retrieve dispersion properties using several procedures: linear array methods as MASW (Park *et al*., 1999), coupled receivers methods as SASW (Nazarian *et al*., 1983) or single receiver methods as FTAN (Levshin *et al*., 1972; Nunziata *et al*., 1999; Boaga *et al*., 2010). Active methods basing on the use of controlled sources are accurate, but have limited exploration depth linked the ability of generating low frequencies with adequate sources. Passive methods have no control of the sources but, with the same array geometry, can reach deeper investigation depth thanks to the low frequency content of seismic noise and microtremors. The standard approaches for passive surface wave methods in shallow engineering applications derive for the seismological array processing. In seismological applications microtremors techniques use mainly 2D arrays of low frequency receivers in various and irregular geometries (Aki, 1957; Frosh and Green 1966; Tokimatsu *et al*., 1992; Okada, 2003). 2D arrays deployment identifies in fact the source direction and it is required in order to identify the velocity and the direction of a wavefield which is not controlled and comes from unknown directions (Bonnefoy-Claudet *et al*., 2006). In exploration seismology common passive arrays techniques are: i) beamforming methods as F-K, ii) spatial autocorrelation SPAC (Aki, 1957), iii) extended Spatial autocorrelation ESAC (Ohori *et al*., 2002), iv) high resolution arrays like MUSIC (Schmidt, 1981) and v) cross-correlation methods (Sabra *et al*., 2005; Shapiro *et al*., 2005). The logistic constraints of typical engineering applications often do not allow deploying large 2D arrays. Moreover, the required processing techniques, despite their relative simplicity, are often not available to the 'practitioners' community. This is the main reason for the success of the simple linear array passive method called ReMi (Refraction Microtremors: Louie, 2001). A linear array in a diffused wavefield has a response which is not function of its direction, but only of its size (length and receiver spacing). An averaged kinematics spectrum, such as the spectral density in the frequency wavenumber domain f-k, can be used to estimate the local propagation properties. The most important limitation of the ReMi approach is related to the basic assumption that the recorded data consist of a uniform wavefield. When this is not the case, the ReMi spectrum depends on the unknown source distribution, and its interpretation or

inversion is not possible. This induces to an overestimation in retrieving shear wave velocities, that can be dangerous for seismic hazard evaluation. The proposed data processing method, based on refraction microtremors L-shaped arrays (LeMi), can easily and appropriately solve the problem.

**Refractions Microtremors with L-shaped arrays.** The processing of passive data on two dimensional arrays is well known and widely discussed in the literature (Okada, 2003). Some of the processing techniques can be considered extensions of the transform-based methods typically used in active multichannel surface wave testing. As conventional MASW data are transformed from T-X to F-K (or F-P, F-V), with two dimensional arrays the data are transformed from T-X-Y into the F-Kx-Ky domain. The transforms can be FKK transforms or other 2D beamformers. In the following we show the results obtained with different 2D arrays in processing non-uniform wavefield for engineering practice both for synthetic and real cases. The objective of this work is not the evaluation of optimal arrays for passive surface wave testing, but simply suggest 2D array procedure consisting of two linear-arrays evenly spaced receivers. In our proposal the array geometry consists of two straight branches, to simplify the deployment of receivers and cables and the surveying: the use of evenly spaced arrays is chosen to simplify the processing, and to allow the use of the spectral analysis methods typically available in commercial software. An L-shaped array has the advantage of allowing the acquisition of active multichannel data with a limited extra effort. A far-field linear plane wave propagating across a dual-linear array is detected with two different apparent wavenumbers by the two branches: each identifies the apparent velocity and apparent wavenumber in its direction assuming that a single plane wave is recorded simultaneously. If the two directions are orthogonal, and they correspond to a local reference systems x-y, the true wavenumber can be determined simply as

$$K_{true} = \mathrm{sgrt}\,(kx^2 - ky^2) \quad (1)$$

In the case of passive measurements, this allows to overcome the trouble issue of oriented noise source, not easy detectable on site. If a source direction is strongly dominant on the recorded data, then the two averaged measurements represent the same direction and can be combined as in Eq. (1) to retrieve the true wavenumber $K_{true}$. From true wavenumber we can define the surface wave phase velocity versus frequency dispersion property and then, after the inversion process, the shear wave profile. In the synthetic case of Fig. 1a it is visible how a predominant unknowns orientated source make impossible the common ReMi linear array detection of the true wavenumber (and then of the true seismic velocity). In this peculiar case, considering the *y* branch linear orientation could bring to an over-estimation of the seismic velocity of 10-20% because the array is almost perpendicular to the main noise source (Fig. 1b). Since orientation noise source is unknown, one operator can potentially consider to use only a linear array as the x branch, leading to a huge misleading over-estimation of the velocity (Fig. 1b) that can have serious consequence in seismic hazard studies.

The use of an L-shaped array can on the contrary retrieve the true wavenumber (and then the true velocity) starting from any orientation of the perpendicular branches (Fig. 1b). The combination of the results of two linear arrays can overcome the limitations of ReMi in cases of strongly directional sources. If the sources are stationary, the acquisition of the two arrays could even be done separately, one after the other, processing the arrays separately for the best *k* resolution. Since common seismograph channels numbers adopted in engineering practice is increasing, it is however recommended to acquire the arrays simultaneously. This ensures the absence of variation of the dominant sources, and allows, if needed, a proper 2D processing as beamformer analysis (Capon, 1969). We do not propose complex theoretical approach but provide a simple modification of the ReMi procedure that can be successfully implemented by practitioners in the field and still be rigorous enough to provide useful estimates of true shear wave velocity.

**Real data L-shaped array test.** The test site was located in Badia Polesine (Ro), N-E Italy, in the southern part of the 'Po' river plain. The site was selected for its geological conditions,

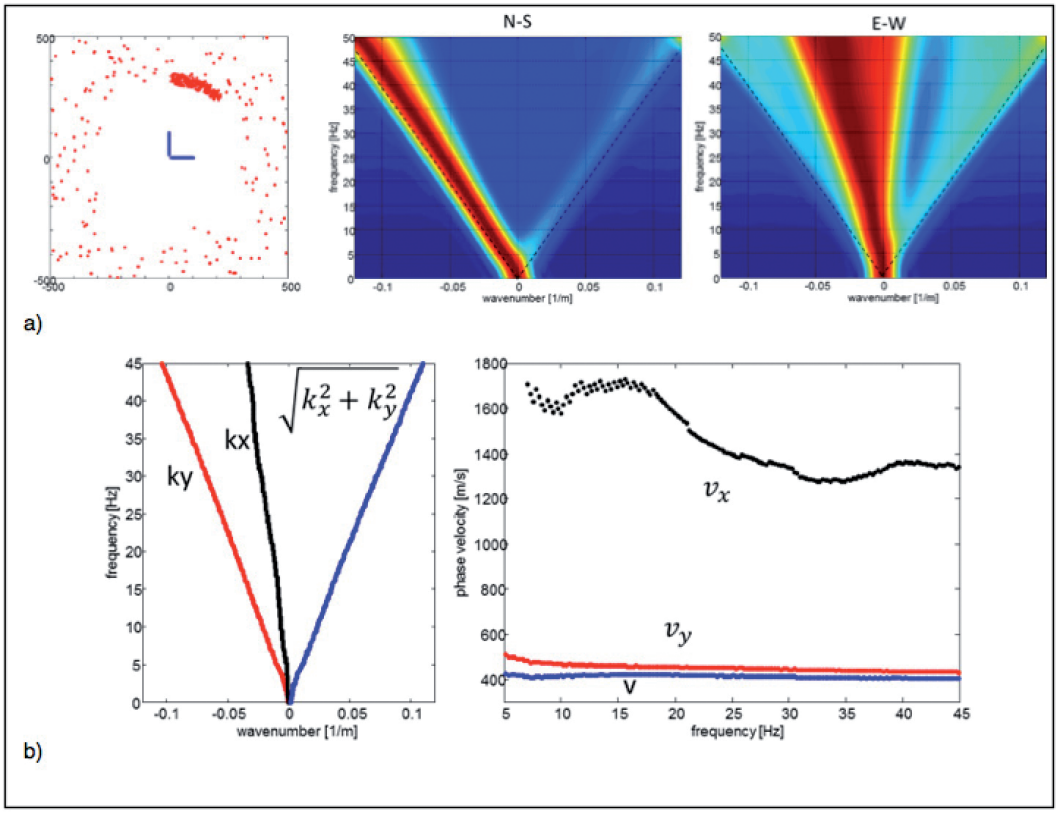


Fig. 1 – a) Synthetic example of ReMi spectra on two orthogonal arrays with a concentration of source in a sector. Left: plan view of the simulated geometry, with sources in red, receivers in blue. Centre: ReMi f-k spectrum on the y (N-S) array branch. Right: ReMi f-k spectrum of the x (E-W) array branch. b) Picking of the wavenumber for the case of Figure1a and phase velocity/frequency transform. Kx (black) refers to the x direction and Ky (red) refers to the y direction. In blue the combination to estimate the true wavenumber from LeMi procedure. Note as in this case the blind orientation of a linear array can lead to great overestimation of the phase velocity while the L-shaped array allows to retrieve the true phase velocity.

which can be well assimilated to 1D profile, being characterized by deep spatial homogeneous alluvial deposits (Fontana *et al.*, 2008). It is expected that in such environment passive linear arrays retrieve same results for any orientation the operator can choose, being on not laterally variable environment. The acquisition has been performed using an L-shaped array: a linear array of 24 receivers (4.5 Hz natural frequency) along the E-W (x) direction and a perpendicular linear array of 24 receivers (4.5 Hz natural frequency) along the N-S (y) direction. The receiver spacing was 4m for both branches, sampling rate was 2 ms. Controlled source records were acquired besides the passive data, to test the validity of LeMi approach, using a seismic gun as source with record lengths of 2 s. For the passive analysis record lengths was 30 s for each noise window. One of the main advantage of the proposed L-shaped array stays in fact in the possibility to locate a shot point at the vertex of the L-shaped array, in order to simultaneously provide two active tests along the 2 directions with common multichannel analysis of surface wave. Active data results to be used as benchmark are plotted in Fig. 2.

Fig. 3 summarizes the advantage of application of the passive LeMi approach in the Badia test site. As it could be seen from data, despite the strictly geological 1D conditions confirmed by several boreholes, the Kx and Ky wavenumbers referred to the two branches of the L shaped passive array present different values. This implies the site was afflicted by

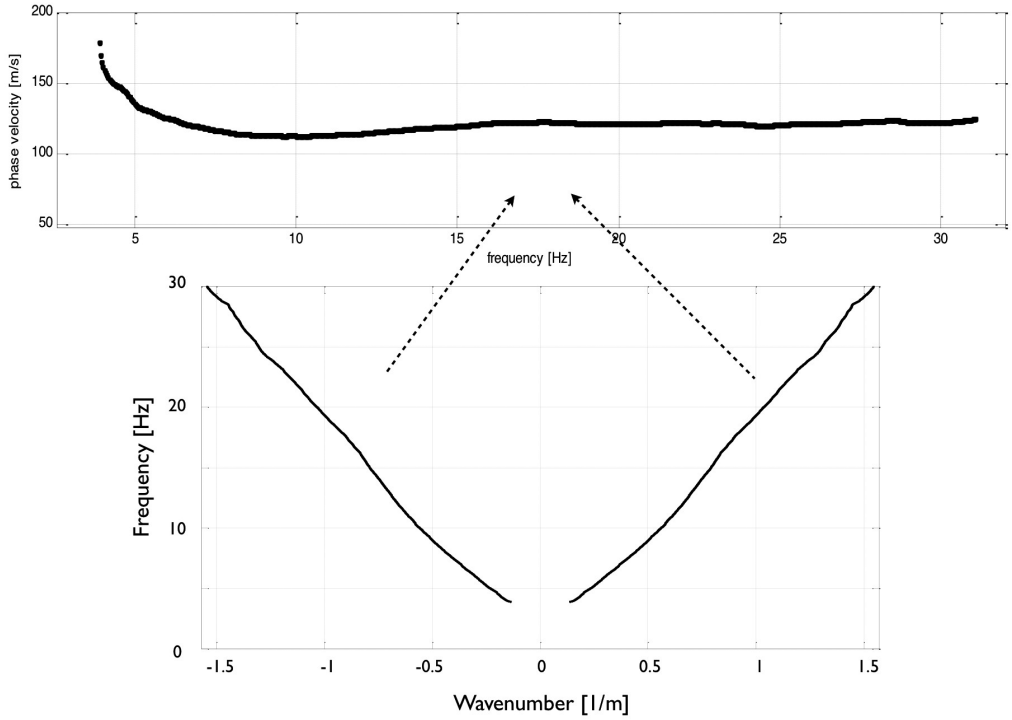


Fig. 2 – Controlled source f-k spectrum for the L shaped array, (branch x and y) and dispersion curve obtained averaging the results of the two branches, for the real dataset collected in Badia Polesine (Ro).

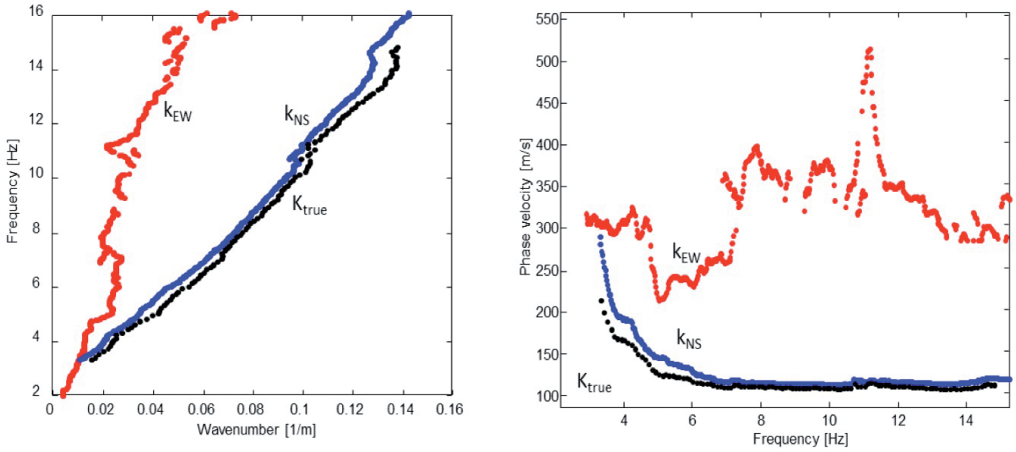


Fig. 3 – F-k maxima picking for the N-S (y) branch (blue); E-W (x) branch (red) and combination of the two apparent wavenumbers (EW and NS) to estimate the Ktrue values. In right panel are visible the relative dispersion curves in the Phase velocity/ frequency.

an unknown orientated noise source (in this case toward y direction), which does not admit common linear array ReMi treatment. The combination of the results of two L-shaped linear arrays can overcome the limitations of ReMi in cases of these strongly directional sources. The use of LeMi L-shaped array approach allows to detect the orientation of the predominant source and correctly estimate Ktrue and the related phase velocities (Fig. 3). In this test site L-shaped array results proved to be in agreement with the controlled source test results of

Fig. 2, in the common range of frequency, retrieving the K true and overcoming the difficult orientated noise source condition. The use of two linear arrays allows the identification of the true propagation direction, and the correction for the error that a single array would produce. For the Badia Polesine case these passive results were supported by the controlled source test and by the geotechnical local informations (personal communication of Dr. F. Marinoni). For the presented real case we tested with success also the response of the L-shaped array with use of classical beamforming techniques thus identifying true velocity and direction of events, independently on the source distribution been more or less spatially polarized.

**Conclusion.** ReMi is based on the hypothesis of a uniform wavefield, and only in this case the results can be considered representative of the local propagation properties. The properties of the spectrum should be analyzed and tested to verify the validity of the basic hypothesis site by site. To overcome the limitations, an alternative and quick acquisition solution consist in L–shaped arrays practice. The proposed LeMi combination of two linear evenly spaced arrays presents the advantages of practical fieldwork, allowing the acquisition of simple multichannel data on the same spread. The use of LeMi approach allows: i) the detection of predominant orientated noise source; ii) the identification of the true wavenumber, overcoming the error that a single array would produce. It must be underlined that combining 2 arrays simultaneously practically limits the number of available receivers and consequently the f-K resolution. Narrow directional source admits theoretically LeMi treatment even if record of the 2 L-shaped branches are not simultaneously but the issue can become critical with a more complex source distribution (different than uniform or narrow directional noise sources). If LeMi data are based on the simultaneous analysis of the data of the two arrays, the proposed acquisition scheme allows in any case more advanced 2D treatment approaches as beamformer. These should be adopted in the cases where there are evidences of more variable source distribution.

In conclusion the passive LeMi methods, characterized by easy deployment and treatment, can considerable improve the correct estimation of seismic velocity for site characterization fronting narrow oriented and variable source orientation. This avoids the overestimation of the subsoil velocities, typical of linear passive array as ReMi, in the current case of oriented noise source. This can play a relevant role in all the seismic hazard characterization studies, since the overestimation of parameter as Vs can lead to totally misleading seismic response estimation.

**Acknowledgments.** Authors thank the geologist F. Marinoni for the Badia Polesine site geological and geotechnical information. Jacopo Boaga work is supported by the European FP-7 project CLIMB:' Climate Induced Changes on the Hydrology of Mediterranean Basins'.

## References

Aki, K. ,1957, Space and time spectra of stationary stochastic waves, with special reference to microtremors, Bull. Earthq. Res. Inst., 35, 415–457

Beavers J. , 2002, A review of seismic hazard description in US design codes and procedures Progress in Structural Engineering and Materials Volume 4, Issue 1

Boaga J, Cassiani G., Strobbia C, Vignoli G. ,2013, Mode mis-identification in Rayleigh waves: ellipticity as a cause and a cure, Geophysics, v. 78 ,3,.

Boaga J, Vignoli G, Cassiani G. ,2011, Shear wave profiles from surface wave inversion: the impact of uncertainty onto seismic site response analysis. Journal of Geophysics and Engineering 8 ,2011, 162–174 doi:10.1088/1742-2132/8/2/004

Boaga J., Vaccari F., Panza F.G. ,2010,, Shear wave structural models of Venice Plain, Italy,from Time Cross-Correlation of seismic Noise. Engineering Geology n.116, 2010

Bonnefoy-Claudet, S., Cotton, F., Bard, P.-Y., ,2006,. The nature of noise wave!eld and its applications for site effects studies — a literature review. Earth-Science Reviews 79 ,3–4,, 205–227.

Capon, J., 1969. High-resolution frequency–wavenumber spectrum analysis. IEEE 1408–1419.

Chaillat S., Marc Bonnet and Jean-Franc¸ois Semblat ,2009, A new fast multi-domain BEM to model seismic wave propagation and amplification in 3D geological structures Geophys. J. Int., vol. 177.

Eurocode 8, EN 1998-1 ,2003, – General rules, seismic actions and rules for buildings. CEN European Committee for Bruxelles, Belgium

Fontana, P. Mozzi, A. Bondesan, 2008, Alluvial megafans in the Venetian–Friulian Plain (north-eastern Italy): Evidence of sedimentary and erosive phases during Late Pleistocene and Holocene, Quaternary International, 189 (2008), pp. 71–90.

Foti S., Parolai S., Albarello D., Picozzi M. ,2011,, Application of Surface wave methods for seismic site characterization, SURVEYS IN GEOPHYSICS, Springer, pp. 49, 2011, Vol. 32

Levshin, A., V. F. Pisarenko, and G. A. Pogrebinsky, ,1972,, On a frequency- time analysis of oscillations: Annals of Geophysics, 28, 211–218.

Louie, J. N., ,2001,, Faster, better: shear-wave velocity to 100 meters depth from refraction microtremor arrays: Bulletin Seismological Society of America, 91, 347–364.

Moss E., ,2008,. Quantifying Measurement Uncertainty of Thirty-Meter Shear Wave Velocity, Bulletin of the Seismological Society of America, 98, 1399-1411

Nazarian, S., K. H. Stokoe II, and W. R. Hudson, ,1983,, Use of spectral analysis of surface waves method for determination of moduli and thicknesses of pavement systems: Transportation Research Record, 930, 38–45.

Nunziata, C., G. Costa, M. Natale, and G. F. Panza, 1999, FTAN and SASW methods to evaluate Vs of neapolitan pyroclastic soils: 2nd International Conference on Earthquake Geotechnical Engineering, Pro- ceedings, 15–19.

Ohori, M., A. Nobata, and K. Wakamatsu, ,2002, A comparison of ESAC and FK methods of estimating phase velocity using arbitrarily shaped microtremor analysis: Bulletin of the Seismological Society of America, 92, 2323–2332.

Okada, H., ,2003,. The Microtremor Survey Method. Geophys, Monograph Series, SEG, 129

Park, C.B., R. D. Miller and J. Xia, 1999, Multichannel analysis of surface waves: Geophysics, 64, no. 3, 800-808.

Sabra, K.G., Gerstoft, P., Roux, P., Kuperman, W.A., Fehler, M.C., 2005. Extracting time- domain Greens function estimates from ambient seismic noise. Geophys. Res. Lett. 32, L03310.

Schmidt, R.O., 1981. A signal subspace approach to multiple emitter location and spectral estimation. Ph.D. thesis, Stanford University, California, USA.

Shapiro, N.M., Campillo, M., Stehly, L., Ritzwoller, M.H., 2005. High resolution surface-wave tomography from ambient seismic noise. Science 307 (5715), 1615–1618

Socco, L.V. and C. Strobbia, 2004, Surface Wave Methods for near-surface characterization: a tutorial: Near Surface Geophysics, 2, 165-185.

Strobbia, C. and G. Cassiani, 2011, Refraction Microtremors ,ReMi,: data analysis and diagnostics of key hypotheses: Geophysics, 76, no.3, 1-20.

Strobbia, C., A. Laake, P.L. Vermeer and A. Glushchenko, 2011, Surface Waves: Use Them Then lose them. Surface wave analysis, inversion and attenuation in land reflection seismic surveying: Near Surface Geophysics, 9, 845-857.

Thomson, W.T., 1950, Transmission of Elastic Waves Through a Stratified Soil Medium: Journal of Applied Physics, 21, 89-93.

Tokimatsu, K., 1995, Geotechnical Site Characterisation using Surface Waves Proceedings of IS Tokyo 1995: eds Balkema, 1333-1368

Vignoli G. and G. Cassiani, 2010, Identification of lateral discontinuities via multi-offset phase analysis of surface wave data, Geophysical Prospecting, 58

Vignoli, G., G. Cassiani, M. Rossi, R. Deiana, J. Boaga and P. Fabbri, 2012, Characterization of a small pre-alpine catchment using surface waves, Journal of Applied Geophysics, 80.

# FIRST RESULTS FROM MICROSEISMIC MONITORING OF A ROCKSLIDE AT MADONNA DEL SASSO (VERBANIA, ITALY)

**C. Colombero[1], C. Comina[1], A. Fiaschi[2], G. Saccorotti[3], S. Vinciguerra[1,4,5]**
*[1] Dipartimento di Scienze della Terra, Università degli Studi di Torino, Italy*
*[2] Fondazione Prato Ricerche, Prato, Italy*
*[3] Istituto Nazionale di Geofisica e Vulcanologia, Pisa, Italy*
*[4] Department of Geology, University of Leicester, Leicester, UK*
*[5] British Geological Survey, UK*

**Introduction.** The hazard mitigation of rockslides and the understanding of their time evolution are a main task particularly when a pre-existing fracture system affects the rock mass. Instability can rapidly accelerate to failure without clear precursory warnings. Traditional monitoring techniques (inclinometers, tiltmeters, extensometers, ...) may be inadequate to forecast the dynamics of evolution and provide quantitative elements for the development of an early warning system. Since a persistent fracture system originates from the genesis, growth and progressive coalescence of microcracks, it is key to constrain the initial stages of rupture. The energy release, in the form of elastic waves, associated with the formation of microcracks can be detected by a microseismic monitoring network. The location of the microseismic events and the monitoring of their time and spatial evolution with particular reference to potential destabilizing factors, such as rainfalls and temperature changes, can provide information with respect to the understanding of the unstable sectors within the rock mass and the prediction of the possible acceleration to the failure.

To understand the failure processes and to search for precursory patterns to failure, the microseismic technique has been extensively used in rock samples at the laboratory scale and at intermediate scales in quarries, mines or tunnels. Conversely, only a few applications exist at the landslides/rockslides scale, and thus it is a priority testing the ability of microseismic monitoring in giving interesting insights into gravitational instability and, in very few cases, in providing precursory patterns for failure forecasting and hazard assessments. Interesting applications on unstable rock slopes and rockfalls have been developed by Spillman *et al.* (2007), Amitrano *et al.* (2010), Helmstetter and Garambois (2010) and Levy *et al.* (2011), studies on rocky cliff instabilities (Amitrano *et al.*, 2005) and mudslides (Amitrano *et al.*, 2007) are also reported.

In this paper we present the first results from a microseismic monitoring network installed at Madonna del Sasso (NW Italy) to monitor rock instability phenomenon highlighted by neat and long lasting episodes of slow deformation recorded by standard monitoring devices (topographic measurements, borehole inclinometers, crackmeters and extensometers).

A detailed geophysical and geomechanical characterization of the site has been preliminarily undertaken in order to define the overall geometry and the fracturing state of the instable rock mass and to establish the best position of the nodes for the monitoring network. Furthermore the definition of the seismic velocity field inside the rock mass is a fundamental parameter for the processing of the recorded microseismic signals, in order to localize the microseismic events. We also analyzed the signals acquired during the first six months of monitoring. We present the first results, and we aim to develop objective and automatic procedures for signal classification and event localization.

**The test site.** The cliff of Madonna del Sasso (45° 79' N, 8° 37' E) is located in NW Italy, on the western shore of the Orta Lake. It is a high massive granite outcrop bordered on three sides (N, E and S) by roughly vertical walls, with a height of about 200 m (Fig. 1a). The top of the relief is located at an altitude of approximately 650 m a.s.l. and it is occupied by a panoramic square, in front of the XVIII-century sanctuary from which the place takes its name.

From a geological point of view, the area is totally characterized by a granitic rock mass, known as Granito di Alzo. The actual morphology has been heavily affected from intense mining activity carried out until a few decades ago. A preliminary geomechanical characterization

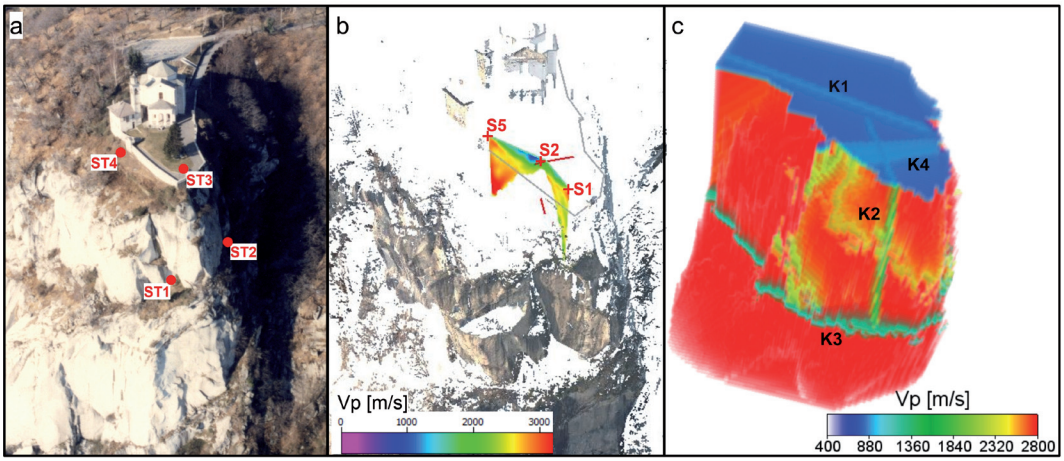


Fig. 1 – Building of a 3-D seismic velocity model for microseismic event localization. a) The cliff of Madonna del Sasso (NW Italy) with the location of the four triaxial geophones of the monitoring network. b) The point cloud obtained from a previous laser-scanner survey with the results of the cross-hole seismic tomography between the inclinometric boreholes S1, S2 and S5. c) Rendering of the 3-D velocity model for P waves obtained from DSM, cross-hole tomography results, geological and geomechanical observations and measurements.

(Lancellotta *et al*., 1991) led to the identification of four main joint sets (dip direction/dip): K1 (110/75), K2 (0/80), K3 (150/15) and K4 (50/75). These discontinuities tend to isolate the north-western frontal portion of the cliff which increases its instability as a function of the rock joints along the fractures and its foot edge. A volume of about 12,000 $m^3$ has been estimated forming the instable sector. Particularly along a K4 discontinuity there is a clear evidence of movement: a decimetric step dislocates the lawn and the confining walls of the panoramic square.

**Geophysical investigation.** Focusing on the gravitative processes that affect the studied rock mass, a good knowledge of the fracturing state is an important requirement for the stability analysis, with particular reference to orientation, spacing, opening and persistence, filling and hydraulic conditions of the discontinuities. With this aim, we extended a previous cross-hole seismic tomography (Colombero and Comina, 2014) realized in the yard in front of the sanctuary, in order to obtain a tomographic image between three available inclinometric boreholes (Fig. 1b). To perform the tests a Borehole Impacter Source by Geotomographie GmbH was used as in-hole source in the S2 borehole, with three different locations till a depth of about 6 m (after this depth an obstruction of the hole casing inhibited deeper measurements) while a sledge hammer, impinging both vertically and horizontally on a steel rod, was employed as surface source in different locations along the lines connecting the three holes.

A prototype borehole string equipped with 8 three-component geophones (10 Hz) at 1 m spacing, stiffly connected by a PVC bar that permits to control geophone orientation, was progressively lowered (with a 2-geophone superposition each subsequent positioning) in the S1 and S5 soundings, till the maximum available depth (respectively of 27 and 21 m). On the lawn surface 4 three-component geophones (2 Hz) were placed along the lines connecting the three boreholes, with a reciprocal spacing of 2.5 m (along S1-S2) and 4 m (along S2-S5).

First break manual picking was performed on the acquired seismic traces, on the pertaining components, to allow for both P- and S-wave velocities imaging. Data were inverted to obtain a tomographic image between the investigated volume with the use of GeoTomCG software, which performs three-dimensional tomographic analysis with source and receiver positions in any configuration within a 3-D grid. The software allows for curved-ray calculations which have been observed to be more accurate in case of strong velocity contrasts. Curved ray tracing is performed with a revised form of ray bending, derived from the Um and Thurber (1987)

method. Inversions are performed with the simultaneous iterative reconstruction technique (SIRT, Lytle *et al.*, 1978; Peterson *et al.*, 1985).

Given the test disposition (reduced ray coverage due to difficulties in lowering the in-hole source) and the hole casing (possible interference of tube waves) the resulting seismic sections have to be considered with particular precautions. Nevertheless in both seismic sections (an example for P wave is reported in Fig. 1b) a shallow coverage of low velocity materials of about 2 m (top soil and highly altered/fractured granite, as also resulting from S1 and S2 core logs) is evidenced. A clear refraction boundary is noticed below this zone revealing an interface with a high-velocity but non-homogeneous formation. Intact granite velocity reaches about 2.9-3.1 km/s for P waves and 1.6-1.8 km/s for S waves. Estimated velocities appear to be quite low for an intact granite formation; direct measurement on rock samples are planned in this respect to obtain a direct verification. Two main low-velocity zones (about 2.2-2.4 km/s for P waves and 1.2-1.4 km/s for S waves) are also evidenced in both seismic sections within the massive granite formation. The position and dip of these zones agree with the fractures of the K4 system (50/75) whose traces are directly visible on the yard in front of the sanctuary. Low seismic velocities depths quite well compare with the outcomes of the stratigraphic log along the S1 sounding, enabling to associate the reduction in velocity values to zones of the rock mass with clear evidence of recrystallized fractures and fractures with alteration patinas. Given the accordance of all these evidences, the geophysical survey reveals a non-uniform (in shape, opening and velocity values) sliding plane probably associated with the presence of rock bridges whose ruptures could be the main cause of instability and which are the subject on which we focus the microseismic monitoring campaign.

**The microseismic monitoring network.** The microseismic network has been installed at Madonna del Sasso in November 2013. It consists of four triaxial geophones (4.5 Hz) connected to a multichannel acquisition system (Granite - Kinemetrics, Inc.). Geophone location is reported in Figure 1a.The first two geophones are placed on sheltered areas of the high walls of the cliff, at a height of about 50 m below the top yard, on the south-eastern (ST1) and northern (ST2) side of the instable volume. The other two stations are placed in shallow manholes accessible from the panoramic square: ST3 is located in the lawn, near the inclinometric borehole S1, and ST4 is outside this unstable area, SE from the sanctuary.

In the first operative weeks we managed to set up the best acquisition parameters for signal recording. We used a continuous recording at 250 Hz sampling frequency (later changed to 1 kHz in March 2014 for improving the first arrival time picking and obtain wider frequency content information) and a trigger recording based on a STA/LTA (Short Time Average over Long Time Average) detection algorithm.

The STA/LTA ratio is continuously calculated and if it exceeds the user defined STA/LTA trigger threshold level, for any channel of the monitoring network, trigger is declared on the whole network. The network de-triggers if the STA/LTA ratio falls below another preset value (STA/LTA de-trigger threshold level). All calculations are made for every data sample in each of the twelve channels connected to the recorder, ensuring minimal time delay between the microseismic event and the triggering. Since these parameters of seismological interest are mainly used for the detection of earthquakes, we made several attempts to find threshold values suitable for the microseismic monitoring. We set a small STA window duration (0.3 s) since the shorter it is, the more sensitive to short and high frequency signals the STA/LTA trigger should be, and a LTA window duration of 30 s, with a STA/LTA Trigger Threshold Level of 6. We also set a low value of STA/LTA de-trigger threshold (10%) to preserve complete coda waves for further analysis.

Each channel was assigned a number of votes that it may cast towards getting the system to trigger. We selected the number of votes each channel would contribute (when it is triggered) to the total number of votes required to trigger the system (12). We gave zero votes to the six channels of ST3 and ST4 that we didn't want to affect the triggering since they are located in

shallow manholes, easily influenced by human presence and activity on the square. We assigned 3 votes to all the other channels.

During November 2013 - March 2014 we recorded more than 2000 events with different waveforms, duration and frequency content. Our first aim is therefore to analyze and classify these signals and to extract only the ones with a possible relation with fracture processes. Their localization and time evolution can give important information in respect to the most active zones in the rock mass and their progression to failure.

**First results of signal analysis and classification.** The identification and classification of the recorded seismic signals is a major task for the monitoring of the stability at Madonna del Sasso. Each type of signal is related to different source processes, among which we would like to focus on those related to fracturing processes. Only after this classification the spatial localization and temporal distribution of the microseismic events could be used as an objective element to realize an early warning system. In order to achieve this goal, the classification of the recorded events should be done as close to real time as possible, with automatic procedures of analysis and classification of data. For these reasons, researches are involved in the development of automatic robust seismic event discrimination algorithms, enabling to reduce subjectivity and time of analysis and to concentrate only on a reduced number of signals.

Many efforts have been made in past years for the automatic recognition of seismo-volcanic events: the recent trend is to complement the human work with automatic recognition systems providing support in early warning (Aspinall *et al.*, 2006) or continuous volcano monitoring (Cortés *et al.*, 2009) scenarios. Several authors have successfully applied Hidden Markov Models (HMMs) to continuous volcano-seismic event recognition (Benítez *et al.*, 2007; Beyreuther *et al.*, 2008) rivalling in popularity with other techniques such as Artificial Neuronal Networks (ANNs) (Falsaperla *et al.*, 1996; Scarpetta *et al.*, 2005) and Support Vector Machines (SVMs) (Masotti *et al.*, 2006; Giacco *et al.*, 2009).

We are currently analysing manually the recorded events and characterizing them in time and frequency domains (Fig. 2), in order to identify the key parameters on which make reliable distinctions among the nature of each signal and to devise an automatic classification procedure. The considered parameters are signal shape (in terms of amplitude, duration, kurtosis) and frequency content (range of maximum frequency content, frequency distribution in spectrograms). Particularly the kurtosis of the envelope was found to be a crucial parameter for the description of a signal shape (Hilbert *et al.*, 2014). Kurtosis parameter ($k$) is a quantitative measurement of the flatness or peakedness of a random-variable distribution compared to a normal distribution. For a random variable, it can be expressed as the ratio between the fourth central moment and the fourth power of the standard deviation of the expected distribution:

$$k = \frac{E\,(x-\mu)^4}{\sigma^4} \qquad (1)$$

where $\mu$ is the mean of $x$, $\sigma$ is the standard deviation of $x$ and $E(y)$ represents the expected value of the quantity $y$. In this way the kurtosis of a normal distribution is 3. Distributions that are flatter than normal have kurtosis values lower than three, sharper-distribution kurtosis is higher than 3.

As a first result, we can clearly distinguish four main classes of recorded signals: microseismic events, regional earthquakes, electrical noises and calibration signals, still unclassified events (probably grouping rockfalls, quarry blasts, other anthropic and natural sources of seismic noise).

Microseismic events (Fig. 2a) show impulsive and short duration signals which envelope has a triangle shape with a clear coda. The spectrogram has a specific aspect with a sharp energy increase followed by an exponential decay of the high-frequency content with time. These features are in good agreement with those reported by several authors (Burlini *et al.*, 2007; Helmstetter and Garambois, 2010; Levy *et al.*, 2011). As a result, they show very short duration (0.8-4 s) and very high kurtosis values (>10). Unlike the high frequency content expected for

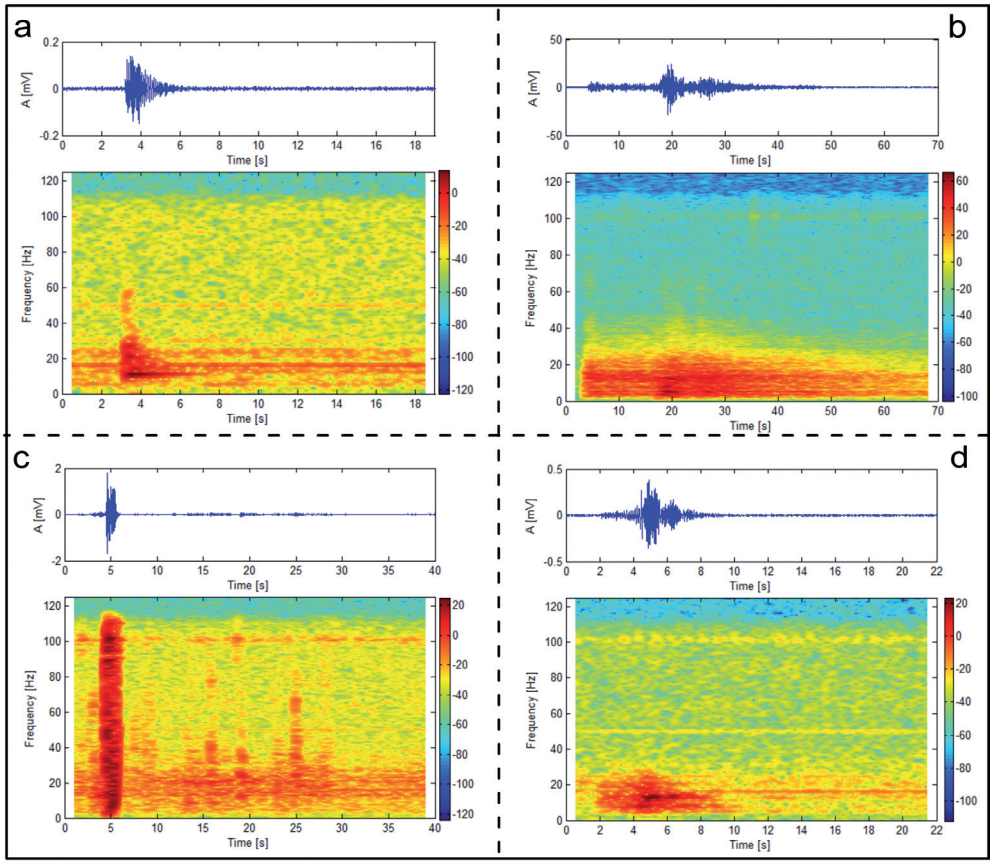


Fig. 2 – First classification of different types of signal: a) a microseismic event; b) an earthquake (Northern Italy, $M_L$=3.8, 2013-11-21 10:36:49.0 UTC, 44.91N 9.03E); c) electrical transient and d) still unclassified events.

this kind of signals, the ones recorded at Madonna del Sasso have the highest frequency content in the band 20-30 Hz. The lower frequency may be related to bigger source dimension, since it is known that the frequency content of the signal emitted by the fracture mechanism is a scale-dependent parameter (Amitrano *et al*., 2010). On a series of 5-month monitoring data (over 2000 events) only 93 signals show these features (~4.5%).

Regional earthquakes (Fig. 2b) show lemon-shape envelope and long duration (30-60 s). Most of them are characterized by quite well separated impulsive P- and S-wave onsets. Their kurtosis values are always lower than 10. The maximum energy content is in the frequency range between 1 and 20 Hz, depending on the epicentral distance. Comparing the date and time of earthquake national and international catalogues, we surely identify 25 signals relative to this source mechanism.

Noise transients generated by electrical disturbances (Fig. 2c) are impulsive spike-like signals, with very short duration and high energy content (50-100 Hz). They are probably caused by atmospheric electrical discharges and other electrical disturbances due to the length of the connecting cables between the stations and the acquisition instrument, according with what observed by Spillman *et al*. (2007). Not by chance, most of this type of signals affect only ST1 and, in smaller amounts, ST2 which are located on the cliff walls with connection cables of more than 50-meters length. A high number of these signals was detected (~100).

At the present stage of this study, we grouped all the other events in an unclassified class (Fig. 2d). It may include rockfalls, quarry blasts and other sources of natural or anthropic

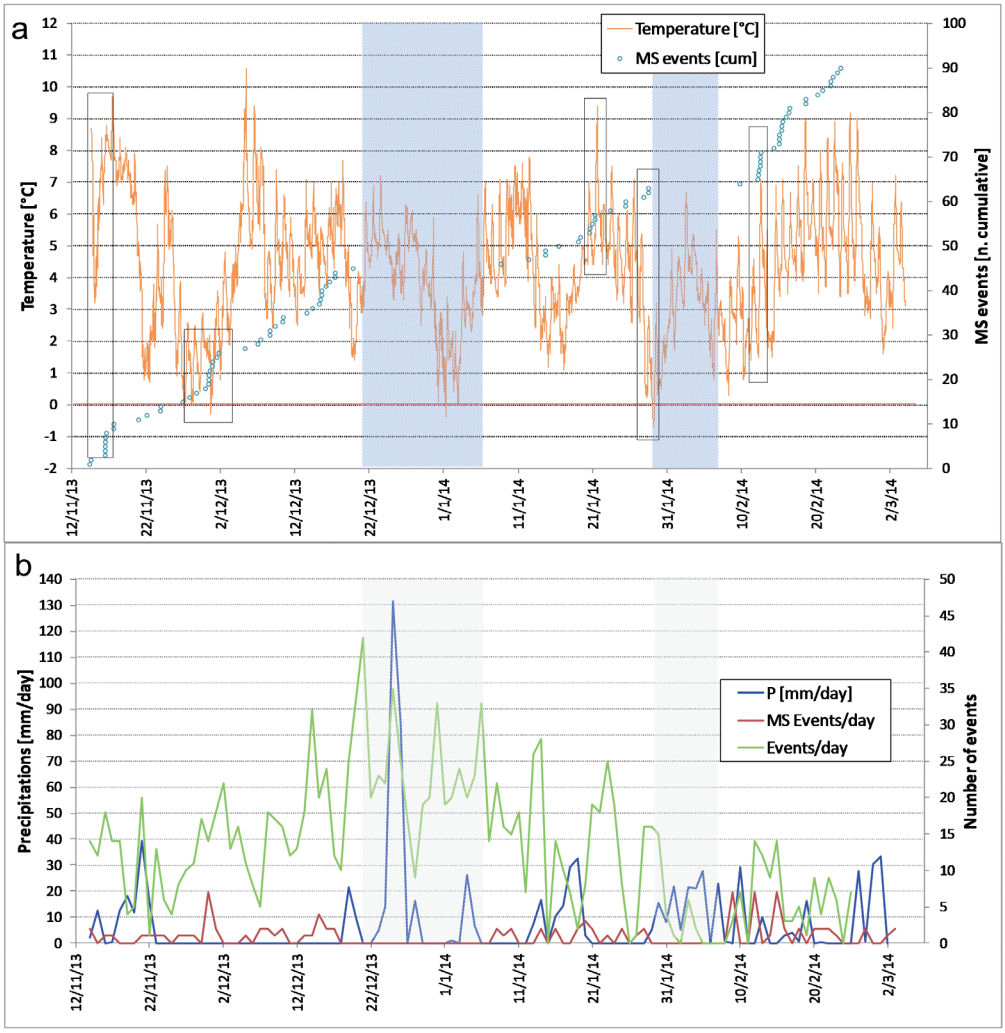


Fig. 3 – First comparisons between event rate and meteorological data for the period November 2013 - February 2014. (a) Temperature recorded by a probe on the southern cliff of Madonna del Sasso and probable microseismic event cumulative curve. Black rectangles point out the steeper parts of the cumulative curve in agreement with abrupt temperature changes. (b) Daily rainfalls measured at the Arpa Piemonte station of Cesara (VB) compared with the daily total number of events and the daily number of probable microseismic events. The coloured rectangles overlap periods in which signal recording was lacking and only event count was available.

disturbances. As we want to focus the study on microseismic events related to fracture processes we temporarily don't deepen the distinction and the research of their specific source mechanisms.

The comparison between event rate and meteorological data can give further information about microseismic source mechanisms and related temporal distribution. The correlation between temperature recorded by an automatic data logger placed on the southern cliff of Madonna del Sasso and the cumulative curve of probable microseismic events is shown in Fig. 3a. At a first sight a relationship between sudden accelerations in the number of microseismic events and abrupt changes (negative or positive) in the air temperature values can be observed. The largest number of probable microseismic events in a day (7) was recorded on 30 November 2013, when temperatures rapidly decreased under 0°C.

Unfortunately, in other periods of winter frost the monitoring network was not correctly working. Conversely rainfalls (obtained from a near monitoring station of ARPA Piemonte) seem not to affect the rate of probable microseismic events. However, it is somehow appreciable in Fig. 3b that rainfalls affect the total number of recordings. Water flow and seepage, entrainment of debris in the fracture zones near the geophones can trigger the system to record a larger number of events.

**3-D velocity model.** After identifying microseismic signals among the large and various number of recordings we located them within the rock mass to constrain the most unstable zones subjected to fractures and understand the evolution related to source position identification along a fracture zone.

At the current state, determining the hypocenter locations has been really challenging for several reasons: many channel recordings are very noisy and first arrival time picks are either lacking or inaccurate for some stations; even if we are monitoring a small volume, the seismic velocity inside the rock mass is highly heterogeneous, as it resulted from the geophysical characterization; there is no evidence of separated p and s onsets in the signals.

To try to overcome the problem we have built a three-dimensional P-wave velocity model joining the DSM (Digital Surface Model) of the cliff obtained from a laser-scanner survey, the results of the cross-hole seismic tomography, the geological observations and the geomechanical measures of the most pervasive fracture planes (Fig. 1c). To do this the original DSM point cloud has been cleaned from vegetation and man-made structures, to obtain a rough DTM (Digital Terrain Model) of the granite cliff. The point cloud has been then resampled to a geometric cubic grid of points at 0.5 m spacing. The air velocity (338 m/s) was assigned to the points having an elevation higher than the DTM, and a constant velocity to the intact granitic rock mass (the higher velocity found from cross-hole tomography). With a GPS measurement survey, we then accurately georeferenced the geophysical test lines and the major fracture traces directly accessible from the yard. We extrapolated in depth the trend of the discontinuities either from the tomographic inversion (for the K4 system) or from the mean dip and dip direction of the systems. The equation of the planes that best fitted these points located on the discontinuities has been found and we gave to those surfaces the lower velocity obtained from cross-hole tomography.

Now we have a quite accurate 3-D velocity model to be used for event localization (Fig. 1c). Tests with known seismic sources in accessible locations above the cliff are also planned in order to obtain a further direct verification of the used seismic velocities. Accordingly, to estimate the hypocenters of the microseismic events we will try to use the NonLinLoc (Non-Linear Location) software package of Lomax *et al*. (2000) for probabilistic, global-search earthquake location in 3D media.

**Conclusions.** This paper shows the first results of an ongoing work concerning the geophysical characterization of an instable rock mass and the signals acquired from the microseismic monitoring network.

The seismic survey allowed investigating in depth the fracturing state of the granite mass, in order to better understand the instability mechanism and to design the monitoring system. The outcomes allowed us to better investigate the presence and geometry of discontinuities, revealing a non-uniform sliding plane, with associated heterogeneous P and S-wave velocities, probably suggesting the presence of rock bridges whose ruptures could be the main cause of instability and can be monitored by the monitoring network. The obtained 3-D velocity model is the basic requirement for the processing and location of the microseismic signals. From the observation of the first months of monitoring data, first steps towards an adequate signal analysis and classification have been made obtaining a preliminary classification of recorded events.

In the near future we will proceed to the localization of event sources, to the improvement and automation of data analysis procedures and to search for correlations between event rates and meteorological data, for a better global understanding of rock mass instability phenomena.

**Acknowledgments.** Geophysical tests of this study have been funded within Progetto d'Ateneo 2012 - SAFER: "Detecting Slow Deformation Signals Preceding Dynamic Failure: A New Strategy For The Mitigation Of Natural Hazards" (Università degli Studi di Torino), supervised by dr. Sergio Vinciguerra. Authors are indebted with Politecnico di Torino for the use of seismic instrumentation and interpretation software.

## References

Amitrano D., Grasso J.R. and Senfaute G.; 2005: *Seismic precursory patterns before a cliff collapse and critical-point phenomena*. Geoph. Res. Let., **32** (8), L08314, doi:10.1029/2004GL022270.

Amitrano D., Gaffet S., Malet J.-P. and Maquaire O.; 2007: *Understanding mudslides through micro-seismic monitoring: The Super-Sauze (South French Alps) case study*. B. Soc. Geol. Fr., **178** (2), 149-157, doi:10.2113/gssgfbull.178.2.149.

Amitrano D., Arattano M., Chiarle M., Mortara G., Occhiena C., Pirulli M. and Scavia C.; 2010: *Microseismic activity analysis for the study of the rupture mechanisms in unstable rock masses*, Nat. Hazards Earth Syst. Sci., **10** (4), 831-841.

Aspinall W., Carniel R., Jaquet O., Woo G. and Hincks T.; 2006: *Using hidden-multistate Markov models with multi-parameter volcanic data to provide empirical evidence for alert level decision-support*. Journal of Volcanology and Geothermal Research, **153** (1), 112–124.

Benítez C., Ramírez J., Segura J.C., Ibáñez J., Almendros J., García-Yeguas A. and Cortés G.; 2007: *Continuous HMM-based seismic-event classification at Deception Island, Antarctica*. IEEE Transactions on Geoscience and Remote Sensing, **45** (1), 138–146.

Beyreuther M., Carniel R. and Wassermann J.; 2008: *Continuous hidden Markov Models: application to automatic earthquake detection and classification at Las Cañadas caldera, Tenerife*. Journal of Volcanology and Geothermal Research, **176** (4), 513-518.

Burlini L., Vinciguerra S., Di Toro G., De Natale G. and Burg J.-P.; 2007: *Seismicity preceding volcanic eruptions: new experimental insights*. Geology, **35** (2), 183-186.

Colombero C. and Comina C.; 2014: *Geophysical characterization of an instable rock mass*. In: Alejano L., Perucho A., Olalla C. and Jiménez R. (Eds): *Rock Engineering and Rock Mechanics: Structures in and on Rock Masses*. Eurock 2014 proceeding papers, Vigo (Spain), Taylor & Francis Group, London, 978-1-138-00149-7,

Cortés G., Arambula R., Gutiérrez L., Benítez C., Ibáñez J., Lesage P., Álvarez I. and García L.; 2009: Evaluating robustness of a HMM-based classification system of volcanoseismic events at Colima and Popocatepetl volcanoes. Geoscience and Remote Sensing Symposium, 2009 IEEE International, IGARSS, **2**, 1012 pp.

Falsaperla S., Graziani S., Nunnari G. and Spampinato S.; 1996: *Automatic classification of volcanic earthquakes by using multi-layered neural networks*. Natural Hazards, 13 (3), 205-228.

Giacco F., Esposito A.M., Scarpetta S., Giudicepietro F. and Marinaro M.; 2009: *Support vector machines and MLP for automatic classification of seismic signals at Stromboli volcano*. In: Apolloni B., Bassis S. and Morabito F.C. (Eds.), WIRN, *Frontiers in Artificial Intelligence and Applications*, **204**, IOS Press, pp. 116-123.

Helmstetter A. and Garambois S.; 2010: *Seismic monitoring of Sechilienne rockslide (French Alps): Analysis of seismic signals and their correlation with rainfalls*. J. Geophys. Res., **115** (F3), F03016.

Lancellotta R., Gigli P. and Pepe C.; 1991: Relazione tecnica riguardante la caratterizzazione geologico-strutturale dell'ammasso roccioso e le condizioni di stabilità della rupe. *Private communication*.

Levy C., Jongmans D. and Baillet L.; 2011: *Analysis of seismic signals recorded on a prone-to-fall rock column (Vercors massif, French Alps)*. Geophys. J. Int., **186**, 296-310.

Lomax A., Virieux J., Volant P. and Berge C.; 2000*: Probabilistic earthquake location in 3D and layered models: Introduction of a Metropolis-Gibbs method and comparison with linear locations*. In: Thurber C.H. and Rabinowitz N. (Eds.): *Advances in Seismic Event Location*, Kluwer, Amsterdam, pp.101-134.

Lytle R.J., Dines K.A., Laine E.F. and Lager D.L.; 1978: *Electromagnetic Cross-Borehole Survey of a Site Proposed for an Urban Transit Station*. UCRL-52484, Lawrence Livermore Laboratory, University of California, 19 pp.

Masotti M., Falsaperla S., Langer H., Spampinato S. and Campanini R.; 2006: *Application of support vector machine to the classification of volcanic tremor at Etna, Italy*. Geophysical Research Letters, **33**.

Peterson J.E., Paulson B.N.P. and McEvilly T.V.; 1985: *Applications of Algebraic Reconstruction Techniques to Crosshole Seismic Data*. Geophysics, **50**, 1566-1580.

Scarpetta S., Giudicepietro F., Ezin E., Petrosino S., Del Pezzo E., Martini M. and Marinaro M.; 2005: *Automatic classification of seismic signals at Mt. Vesuvius volcano, Italy, using neural networks*. Bulletin of the Seismological Society of America, **95** (1), 185-196.

Spillmann T., Maurer H., Green A.G., Heincke B., Willenberg H. and Husen S.; 2007: *Microseismic investigation of an unstable mountain slope in the Swiss Alps*. J. Geophys. Res., **112**, B07301.

Um J. and Thurber C.; 1987: *A Fast Algorithm for Two-Point Seismic Ray Tracing*. Bull. Seismol. Soc. Am., **77**, 972-986.

# REPROCESSING, DEPTH MIGRATION AND INTERPRETATION OF SEISMIC PROFILES IN THE NORTH-WESTERN MEDITERRANEAN SEA

**M. Dal Cin[a], A. Del Ben[a], F. Accaino[b], A. Birch-Hawkins[c], P. Conn[c], D. Chisari[c], R. Geletti[b], W. Toson[b], M. Tyrrell[c]**

[a] *Dipartimento di Matematica e Geoscienze (DMG), Università di Trieste, Italy*
[b] *Istituto Nazionale di Oceanografia e di Geofisica Sperimentale (OGS), Trieste, Italy*
[c] *TGS, Surbiton, Surrey, United Kingdom*

**Introduction**. The geological genesis, evolution and depositional settings of the Mediterranean Sea have been studied for decades by the scientific community which, for some aspects, combines research with the Petroleum Industry to enhance hydrocarbon exploration.

It is in these circumstances that the geophysical study hereafter described was conceived. Two research bodies and a multi-client geophysical company have been involved in this project: the Department of Mathematics and Geosciences of the University of Trieste (DMG), the Italian National Institute of Oceanography and Experimental Geophysics (OGS) and TGS Geophysical Company ASA.

The paper presents a geophysical analysis, based on interpretation of ten 2D multichannel seismic reflection profiles located in the eastern Sardo-Provençal basin of the north-western Mediterranean crossing domains from the outer west Sardinian shelf to the deep basin (Figs. 1A, 1B). The post-stack time migrated lines have a total length of 1545 km and cover an area of about 35.000 km$^2$. The profiles belong to three distinct datasets (WMR, WS, CROP, location on Fig.1A) recorded by different geophysical projects, each of them using specific acquisition parameters. The five WMR (West Mediterranean Regional) profiles were provided by TGS. The three WS (West Sardinia) profiles were acquired by their owner OGS. The two CROP (CROsta Profonda) lines, provided by the DMG, were originally sponsored by AGIP-ENI, CNR & ENEL.

The presence of the Messinian rock salt, that within a sedimentary sequence produces halokinesis and scatters most of the acoustic energy, suggested the reprocessing in time domain of a part of a CROP seismic profile in order to improve the imaging of those reflections that are strongly deformed or masked. To enhance image accuracy assessing size and location of geological structures beneath the Messinian salt, a pre-stack depth migration (PSDM) was executed using the Kirchhoff algorithm.

The processing outcomes were useful not only to enhance and better define the entire seismic interpretation on the available datasets, but also allowed the evaluation of the peculiar lithologic/stratigraphic conditions of the basin. The integration of the three datasets gave better coverage of the study area and supplied complementary information thanks to different resolutions. On the whole, the work presented hereafter aimed at better knowledge of the depositional history, starting from the Messinian Age, of the North-Western Mediterranean basin.

**Geological setting.** According to Gennesseaux and Vanney (1979) and Rehault *et al.* (1984), the western Mediterranean Sea can be classified into four main morphological domains (Fig.1B). On the bathyal plain (or deep basin), on average, the water column is 2700 m thick. The Corso-Sardinian shelf has a minor extension compared with that of the Gulf of Lion and the Corso-Sardinian slope is steeper than the French-Spanish mainland slope. This last is overlapped by large amounts of sediments from the Rhône river, which contribute to the large deep-sea fan of the Gulf of Lion.

The back arc basin of the north-western Mediterranean Sea is confined to the east by the passive margin of the Corso-Sardinian block and to the northwest by the conjugate continental margin of the Gulf of Lions and Provence, to the SW by the Valencia basin and the Balearic promontory and to the south by the Algerian and Alboran basins. The actual isolated position of the Corso-Sardinian block is the result of a NE-SW striking rifting stage due to extensional field stress induced since Late Eocene-Oligocene by the north-westward subduction of the Tethys

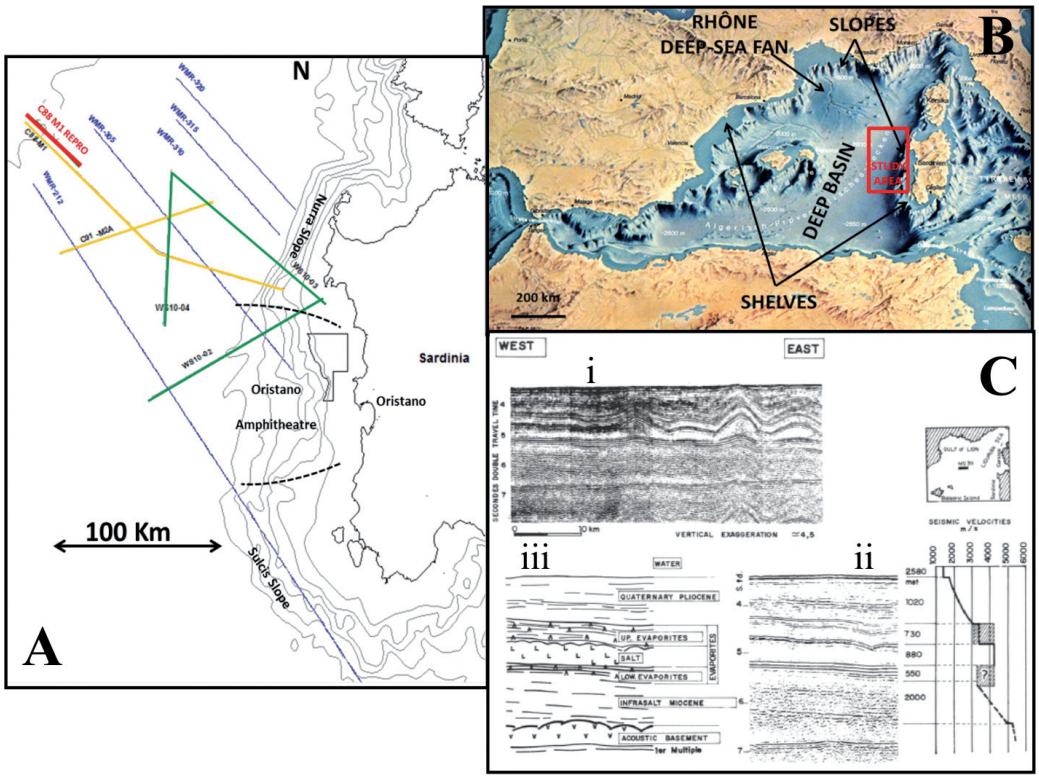


Fig. 1 – A) Position of the analysed seismic reflection lines in the Sardo-Provençal basin of the north-western Mediterranean Sea: WMR profiles (by TGS) in blue; WS profiles (by OGS) in green; CROP profiles in orange. Red segment: reprocessed C88M1 REPRO, part of CROP C88M1. B) Morphology of the western Mediterranean Sea. Study area bounded by the red polygon. C.i) Seismic line recorded in the deep basin domain of the north-western Mediterranean (Finetti and Morelli, 1973). C.ii) Seismic velocities (Montadert *et al*., 1978) that permitted C.iii) the identification of the Messinian Trilogy (modified, Rehault *et al*., 1984).

oceanic lithosphere. The process progressively evolved into a south-eastward slab rollback and was responsible for the spreading stage that lead to the opening of the North-Western Mediterranean as a back-arc basin, during the Miocene (Carminati *et al*., 2012). This occurred in association with the formation of oceanic crust (Carminati and Doglioni, 2005) and the rotation of the Corso-Sardinian block until its collision with the NW Adria plate (Finetti *et al*., 2005).

The oldest units of the sedimentary sequence of the north-western Mediterranean basin and related slopes, comprise rift and post-rift Oligo-Miocene sediments. They correspond, respectively, to discontinuous reflectors with variable amplitude, related to probable continental syn-extensional clastic deposits and to more continuous reflectors possibly related to pelagic deposition (Rehault *et al*., 1984; Geletti *et al*., 2014).

During the Messinian age an extreme and relatively brief geological event occurred in the Mediterranean basin and surrounding areas in response to about 1500 m sea level drop principally due to a closure of the gateway between the Atlantic and Mediterranean Sea (Clauzon *et al*., 1996; Krijgsman *et al*., 1999; CIESM, 2008). This event, known as the Messinian Salinity Crisis (MSC), is generally accepted to have onset 5.96 My ago (Krijgsman *et al*., 1999; CIESM, 2008; Krijgsman and Meijer, 2008). In the western Mediterranean basin the MSC deposits consist of evaporite lithologies with an average thickness ranging between 1600-2100 m (Geletti *et al*., 2014) that have not been sampled by boreholes except for the uppermost part. These units were

interpreted for the first time on a seismic reflection line (Fig. 1C.i), recorded in the offshore domain by the OGS (Finetti and Morelli, 1973).

Seismic velocities (Fig. 1C.ii, Montadert *et al*., 1978), allowed the definition of three seismostratigraphic units that were named, starting from the bottom, by Rehault *et al*. (1984) as: Lower Evaporites, Messinian Salt and Upper Evaporites (Fig. 1C.iii). These three seismic units have been identified together with the name of Messinian Trilogy. Lofi *et al*. (2011) proposed a new global terminology for Messinian surfaces and depositional units that is based on seismic facies and/or geometrical relationships: Mobile Unit (MU) is the intermediate salt layer (halite according to Ryan *et al*., 1973), Lower Unit (LU) the layer beneath the MU, Upper Unit (UU) the one laying above the MU. The MSC units are hereafter referred to this terminology.

The LU has a seismic facies corresponding to a group of continuous high amplitude and low frequency reflections, recognized only in the deep basin (Rehault *et al*., 1984; Lofi *et al*., 2011). Due to its position, immediately below the salt layer, the acoustic energy does not always penetrate deeply enough and thus the LU cannot be well imaged (Lofi *et al*., 2011; Geletti *et al*., 2014). According to Montadert *et al*. (1978), the interval velocity is uncertain, ranging between 3200 and 4200 m/s (Fig. 1C.ii). The LU, never calibrated, may be lithologically constituted of carbonates and evaporitic sediments (Ryan *et al*., 1973; Rehault *et al*., 1984), but it could also contain a large part of detrital sediments eroded from the continental slopes and shelves during the sea-level falling stage of MSC (Lofi *et al*., 2005; Sage *et al*., 2005).

In the western Mediterranean, the MU is characterised by a transparent seismic facies and an associated ductile deformation that generates dome and diapiric structures (Rehault *et al*., 1984; Sage *et al*., 2005; Lofi *et al*., 2011; Geletti *et al*., 2014). Halokinesis is observed at lower slope of the western margin, where diapirs generally distort reflectors at the base of the post-MSC sediment cover only (Sage *et al*., 2005). Growth faults demonstrate Pliocene activity (Lofi *et al*., 2011), even though locally some growth strata in the UU indicate late Messinian salt tectonics (Geletti *et al*., 2014). In some places of the deep basin the MU forms diapirs that disrupt the uppermost part of the overlying sediments (Sage *et al*., 2005; Lofi *et al*., 2011; Geletti *et al*., 2014).

In the western Mediterranean the UU has an interval velocity of 3500 m/s (Montadert *et al*., 1978; Rehault *et al*., 1984; Lofi *et al*., 2011; Geletti *et al*., 2014) and it is characterised by an alternation of high amplitude reflectors and transparent layers thicker in the deep basin than that in the lower slope. Where the thickness is greater, a lower less reflective seismic package is present. One of the uppermost transparent layers is particularly thick and it was interpreted as an autochthonous salt layer, labelled with "s" (Geletti *et al*., 2014).

The UU sampled within the western Mediterranean basin was described as composed of marly beds, dolomitic or gypsiferous layers (Ryan *et al*., 1973; Rehault *et al*., 1984).

Five MSC surfaces were defined within the Mediterranean basin by Lofi *et al*. (2011), on the basis of their relationship with downslope Messinian units. These surfaces are labelled as: BS/BES (Bottom Surface/ Bottom Erosion Surface), IES (Intermediate Erosion Surface) and TS/TES (Top Surface /Top Erosion Surface). BS/BES correspond respectively to the bottom non-erosional/erosional surface at the base of the MSC units. IES is a term that identifies all those intermediate unconformities present within the MSC depositional units. TS/TES correspond respectively to the uppermost non-erosional/erosional boundary of the MSC deposits.

In the upper continental slope the Messinian units are generally absent and the main seismic feature is a strong reflector which truncates the top-lapping pre-Messinian reflectors (Geletti *et al*., 2014) evidencing an angular discordance between pre-MSC and Plio-Quaternary deposits (Lofi *et al*., 2011). It is interpreted by Lofi *et al*. (2011) as a time equivalent of the entire MSC units and surfaces of the deep basin. In the West Sardinian margin this unconformity may be the result of the last erosional events linked to the MSC and superimposed on probable earlier erosional surfaces (Geletti *et al*., 2014). This unconformity is known as Margin Erosion Surface, MES (Lofi *et al*., 2011; Geletti *et al*., 2014).

The end of the MSC event probably coincided with the marine re-flooding of the Mediterranean basin at the Miocene/Pliocene boundary, 5.33 Ma ago (Krijgsman *et al*., 1999; CIESM, 2008). This is testified by pelagic sediments draping the cored margins (Ryan *et al*., 1973; Rehault *et al*., 1984) and extending throughout the entire north-western basin. The Lower Pliocene unit in the north-western Mediterranean basin has a typical semi-transparent acoustic facies. It lies beneath a more reflective facies (Rehault *et al*., 1984; Sage *et al*., 2005; Geletti *et al*., 2014) representing the Upper Pliocene-Quaternary turbiditic bodies of coarser clastic sediments transported by the Rhône (Rehault *et al*., 1984; Aslanian *et al*., 2012). On the contrary, the unit is often absent or very thin on the Sardinian slope where sediment supply has been minor: the PQ units are 1200-1600 ms TWT thinner at the foot of the Western Sardinian slope than that in the north-western sector of the deep basin (Geletti *et al*., 2014).

**Reprocessing in time domain.** In general, the available seismic dataset is affected by several problems, that can be summarized as follows:

- structural complexity characterizing part or all the sedimentary cover of the Messinian salt, due to the halokinesis generating domes, diapirs, faults, etc; this produces intense lateral lithological changes, implying strong lateral velocity variations for the seismic wavelets that propagate through the subsurface.
- Pre-salt geological features are mostly unidentifiable, except on some of the WMR and CROP data, due to salt presence.
- Salt-related pull up events.
- Sea bed multiple (at about 7 s TWT) that may overlap primary reflections.
- Over-migration of deep seismic reflectors.
- Out of plane effects, which are commonly related to salt diapirism. Only accurate migration of a 3D seismic dataset will solve this geophysical problem (Yilmaz, 2001).

The reprocessed part of the CROP C88M1 line, using the Focus (Paradigm Inc., 2007) software, is named C88M1 REPRO (location in Fig. 1A). It is 56.6 km long and it extends from the Western Sardinian slope to the north-western part of the eastern Sardo-Provençal deep basin. It was selected because of the investigation depth reached by the CROP survey itself and because it represents one the best examples of the geological and structural setting within the explored sedimentary basin, as identified by a first stage of interpretation. It contains also several different shaped salt diapirs, widely disrupting the MU overburden and causing high lateral velocity variation. A wide salt diapir is also present reaching the sea bed and generating a suspected (considering the first seismic interpretation) pull up event of about 0.6 s TWT for the underlying reflectors.

Starting from raw data, the processing flow comprises: trace editing, multiple attenuation, normal-move out-correction, gain, spike deconvolution, stack, migration. Because of strong lateral velocity variability, the velocity function (named VELGEOD and executed using the GeoDepth software -Paradigm Inc., 2008) was determined by iterative analyses on semblance panels derived from CDP gathers chosen alternately within a small sedimentary basin and in correspondence to a salt structure. The velocity picking was overall based on the amplitude response displayed on semblance panels, carefully evaluated beside the correspondent best dynamic correction (normal-move-out) of mayor reflection hyperbolas displayed on each CDP gather. The preliminary seismic interpretation was consulted in case of ambiguity (e.g., doubtful velocity inversions, primary reflections) in order to respect geological and geophysical constraints. However, the computation was hampered due to the lack of calibrations by well data.

After the reprocessing in time domain a geological interpretation was done. A detail is shown Fig. 2A, where the wide salt diapir was newly interpreted as connected to the mother layer, since the reflector (affected by pull up) that was present inside the structure and that was interpreted as the top of the UU, is not visible in the new outcome. Somewhere in the reprocessed data, the thickness of the UU resulted higher than what was preliminarily interpreted, this is due the

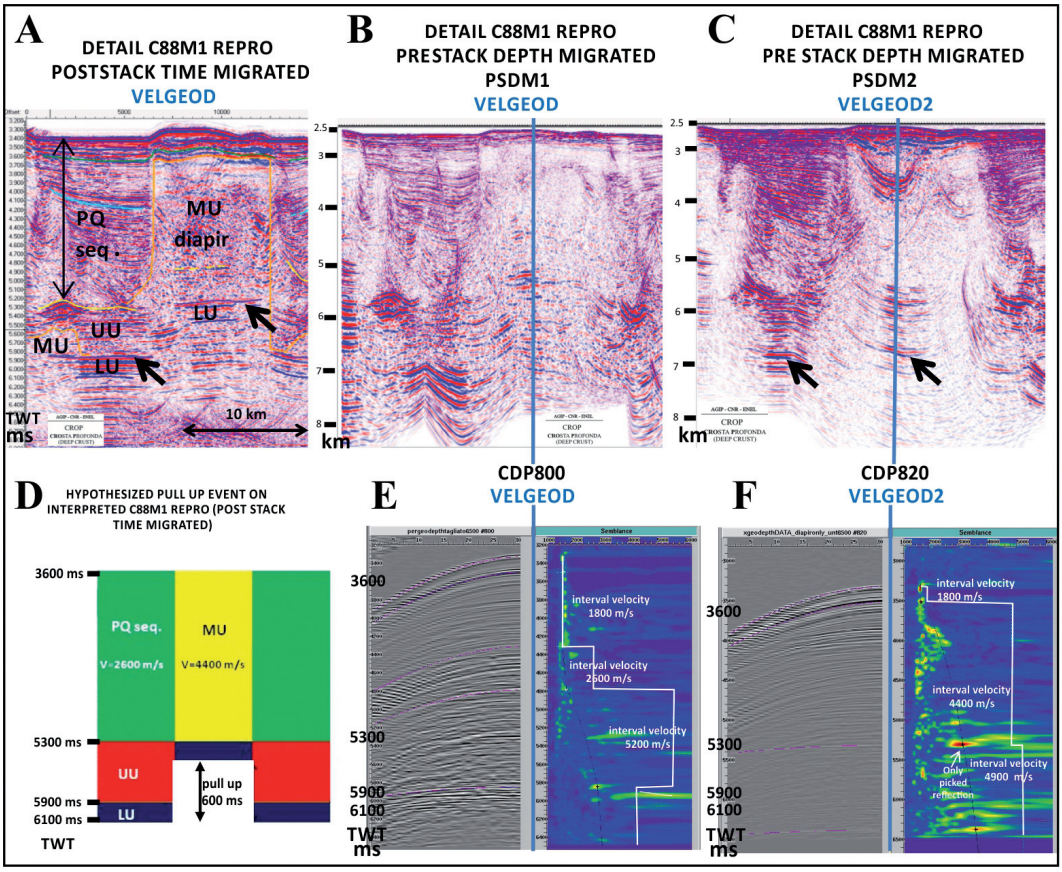


Fig. 2 – A) Interpretation of a detail of C88M1 REPRO reprocessed in time domain and characterised by wide salt diapir generating pull up event. Results on the corresponding detail of pre stack depth migration outcomes: B) PSDM1 and C) PSDM2. (D) Schematized pull up event interpreted on C88M1 REPRO reprocessed in time domain. (E) Velocity Spectra on Semblances related to CDP800 of VELGEOD–PSDM1 and (F) CDP820 of VELGEOD2-PSDM2.

presence of reflectors having a similar seismic facies to that of the UU interpreted in the entire dataset. Furthermore, in some areas evidences of sub parallel reflectors beneath the MU at a time of 5.6-6 s TWT were interpreted as LU.

**Pre stack depth migration (PSDM).** PSDM processing was twice tested, on the same segment chosen for the reprocessing in time domain, to better image the complex structural conditions of the investigated media. Two velocity fields were separately applied to perform PSDM1 and PSDM2: the VELGEOD and the VELGEOD2, respectively. The first is described above. The latter was determined on semblance panels (generated by the GeoDepth software-Paradigm Inc., 2008) computed from different CDP gathers chosen so that the lateral velocity variations could be constrained by the vertical borders that define the transition from a small sedimentary basin to a salt structure. In this way, the software could perform the velocity model by smoothing velocity values within the same structure, that are assumed to have the similar velocity trend. Furthermore, VELGEOD2 was picked focusing only on few, deep and strong primary reflections. Their identification was primarily based on the seismic interpretation conducted, on the basis of new evidence, on the reprocessed section.

Comparing PSDM1 and PSDM2, some differences can be pointed out. The wide salt diapir (around CDP 800), interpreted as connected to the mother layer, generates a suspected pull up

event of about 0.6 s TWT for the underlying reflectors, that are probably related to the LU (Fig. 2A). The hypothesized scenario is represented in the scheme of Fig. 2D and takes in account mean interval velocities of 2600 m/s and 4400 m/s for the Plio-Quaternary sequence and for the MU, respectively. They were chosen on the basis of both literature works and determined velocity function discussed above. In Figs. 2B and 2C are reported, for comparison, the details of the outcomes of PSDM1 and PSDM2 in correspondence to the pull up event and the related velocity functions picked on semblance panels derived from CDP 800 (VELGEOD–PSDM1) and 820 (VELGEOD2-PSDM2) gathers (Figs. 2E, 2F). It can be noticed that in the first outcome (PSDM1) no evidence of pull up flattening is present, while in the second outcome (PSDM2) the pull up seems to be restored. A strong reflection in correspondence with the salt diapir of the detail of PSDM2 is present at 6.8-6.9 km of depth (Fig. 2C). Its seismic facies is similar to that of the bottom MU interpreted in correspondence of the little sedimentary basin on the left side of the line. Although the PSDM2 is affected by artefacts (probably due to large lateral velocity variations), the information given around the CDP 820, in correspondence of 6.8-6.9 km depth, could confirm the interpretation of the pull up event previously done on the post stack time migrated data. Furthermore, the resultant size of the salt diapir is almost 4 km high.

**Seismic interpretation and mapping.** Among the interpreted dataset, in the deep basin the MSC units and the Plio-Quaternary (PQ) sequence were generally recognised with the same acoustic characters defined by literature, although some variabilities in the seismic response are locally present. Furthermore, different numbers of reflections characterise the UU and the PQ units among the analysed dataset. This is because the WMR dataset offers relatively a medium-high vertical resolution which is higher than that of the CROP dataset (aiming at a deep crustal investigation) and lower than that of the WS dataset (supplying in any case a medium-high resolution). Thus, for example, the autochthonous salt layer "s" is imaged on the WMR and WS data, but it is not detected by the CROP profiles (Fig. 3A).

Halokinesis is particularly intense and generates high diapirs that often intrude the UU and the lower part of the PQ sequence (Fig. 3A), but sometimes reach the sea bed (Figs. 2A, 2B, 2C). The UU is locally characterized by growth strata. This demonstrates that the halokinetic movements started during the late stage of the MSC event, as suggested by Geletti *et al*. (2014). This could be due to the increasing of the sedimentary and water column loading related to several cycles (Krijgsman and Meijer, 2008) of inflow water during the deposition of the UU. However, growth strata are frequently present within the lower and middle Pliocene units, testifying that the halokinesis developed further and more intensely during the Pliocene, when the complete reflooding of the Mediterranean was reached, accompanied by relatively thick sedimentation of pelagic deposits.

In the part of the basin which is adjacent to the toe of the slope, coalescent salt diapirs almost completely disrupt the UU, which is disarticulated in numerous small packages: sometimes they are difficult to recognize, either because they may be little over the limit of resolution or because, being incorporated into the salt as it moved vertically, their seismic responses are attenuated.

At the toe of the slope and on the lower slope, roll over structures are often present. They are sometimes associated with growth strata of the UU and/or the PQ sequence (whose thickness is considerably reduced in respect to the north-western part of the basin). Halokinetic normal and listric faults bound the dislocated blocks of the overburden and in some cases they also affect the sea bed. This intense halokinesis may be related to a local sliding of the salt toward the basin on the inclined West Sardinian lower slope. The process produced local compressive stresses that acted on the adjacent part of the basin, also deforming of the post-Messinian salt sedimentary sequence.

MU shows the minimum thickness (less than 200 ms) on the sector adjacent to the Western Sardinian lower slope, where it flowed inside or above the UU as allocthonous salt bodies. In correspondence of the lower slope, the thickness of MU is further reduced and the unit pinches

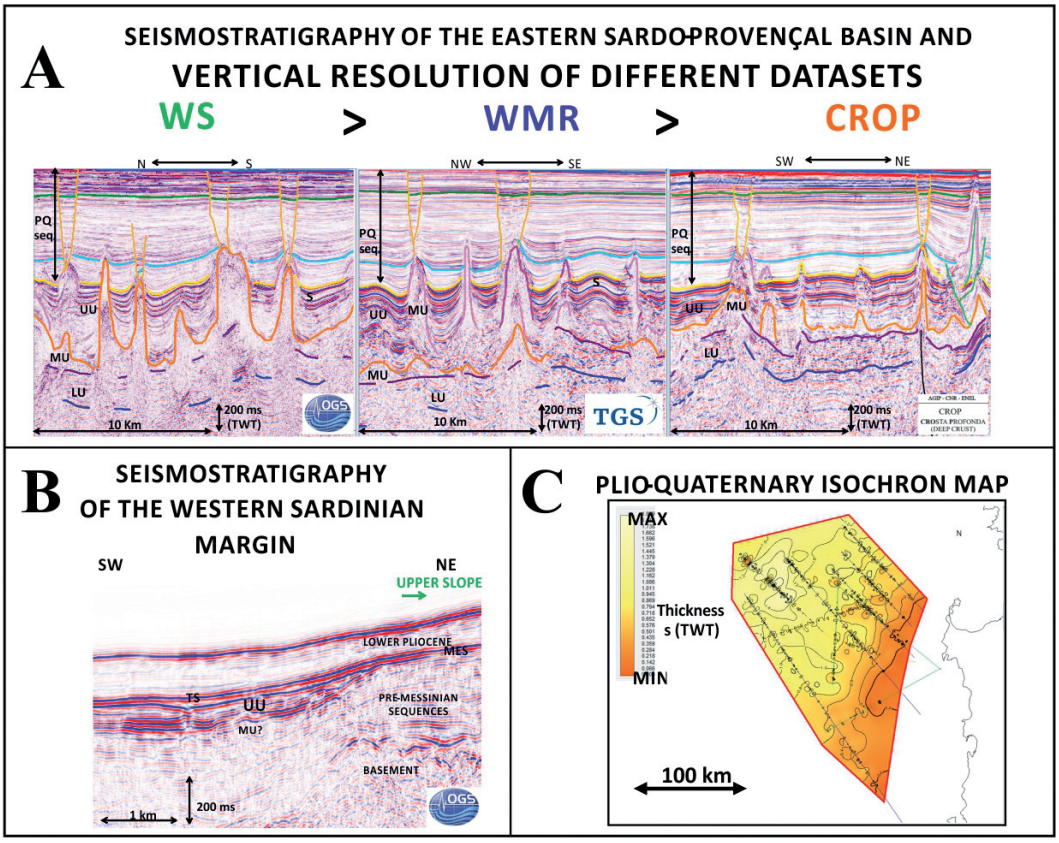


Fig. 3 – A) Comparison among vertical resolutions of WS, WMR, CROP seismic data and seismostratigraphy of the eastern Sardo-Provençal basin. B) Seismostratigraphy of the Western Sardinian Margin. C) Isochron map of the Plio-Quaternary sequence.

out at 4 s TWT depth. Vertical load by the sedimentary overburden and seawater column produced a great amount of diapirs in the deep basin.

In the upper slope LU, MU, UU are no more present and the lower unit (Lower Pliocene) of the PQ sequence directly overlays the pre-MSC sequences clearly depicted by the MES angular unconformity (Fig. 3B).

The Plio-Quaternary isochron map (Fig. 3C) shows a time-thickness that increases toward the north-western basin, where locally it reaches the maximum value of 1.7 s TWT (in correspondence of increased accommodation space for the presence of weld). The Plio-Quaternary sediment supply has been much higher in the Gulf of Lion than that in the eastern part (Aslanian *et al.*, 2012; Geletti *et al.*, 2014). In this way, at the end of the Messinian salinity crisis event, the depo-centre of the study area moved in the eastern sector of the north-western Mediterranean deep basin.

**Conclusion.** This work analysed the Messinian to recent geological evolution of the eastern sector of the Sardo-Provençal basin. The reprocessing of a selected part of the seismic profiles has been very useful to improve the imaging of the deep reflections below the salt layer. The depth migration is particularly useful as it reduces the pull up velocity effects when salt layers are present. Several velocity analyses were conducted on CMP gathers and related semblance panels (in time domain). On the basis of different trial methods however, all exhibit strong lateral velocity variations, due to the dense presence of salt diapirs in the investigated area.

The main feature involving the sedimentary sequences of the studied area is the presence of the evaporite units (Messinian Trilogy) deposited in the deep basin during the Messinian post-drifting phase. The salt tectonics developed due to the lower density of salt in relation to loaded adjacent sediments and differential compaction of adjacent and overlying sediments due to the incompressibility of the salt. This process forms domes, diapirs, sliding on deepening basement and compressive deformations. Halokinetic deformation developed mainly during the Lower Pliocene, but continues until Present, as testified by some circular structures piercing the sea bottom.

Some growth strata have been evidenced also in the UU, testifying that local halokinetic processes started as early as the late Messinian, probably due to the UU load and the start of the re-flooding. As shown by the generated structural maps, the favourable conditions for halokinetic tectonics are: large thickness of salt, sedimentary (and water) loading, deepening of the underlying basement and the presence of faults (which make only a local contribution).

Integration of the different seismic datasets used in this work allowed identification of the probable presence of a halite layer within the UU in the deep basin.

The deep basin reaches its maximum depth at the toe of the West-Sardinian slope, but the deep horizons show that the original basin depocentre was in a western position: this is due to the abundant sedimentary supply from the Rhône river, unlike the sparse input from the Sardinia Isle.

**Acknowledgements.** We would like to thank TGS and OGS for permission to disclose seismic data.

**References**

Aslanian D., Moulin M., Schnurle P., Klingelhoefer F., Leroux E., Rabineau M., Gailler A., Bache F. Gorini, C.

Carminati E., Lustrino M. and Doglioni C.; 2012: *Geodynamic evolution of the central and western Mediterranean: Tectonics vs igneous petrology constraints*. Tectonophysics, doi:10.1016/j.tecto.2012.01.026.

Carminati E. and Doglioni C.; 2005: *Mediterranean Geodynamics: Encyclopedia of Geology*. Elsevier, 135–146.

CIESM; 2008: *The Messinian Salinity Crisis from Mega-Deposits to Microbiology- A consensus report*. In:Briand, F. (Ed), CIESM Workshop Monographs, 33, 168.

Clauzon G., Suc J.P., Gautier F., Berger A., Loutre M.F.; 1996: *Alternate interpretation of the Messinian Salinity Crisis: controversy resolved?*. Geology 24, 363–366.

Finetti I.R., Del Ben A., Fais S., Forlin E., Klingelé E., Lecca L., Pipan M. and Prizzon A.; 2005: *Crustal tectono-stratigraphic setting and geodynamics of the Corso-Sardinian Block from new CROP seismic data*. In: Finetti I. R. (Ed.): *CROP PROJECT: Deep Seismic* Exploration *of the Central Mediterranean and Italy*. Atlases in Geoscience, 1, Elsevier B.V., 430-446.

Finetti I.R. and Morelli C.; 1973: *Geophysical Exploration of the Mediterranean Sea*. Bollettino di Geofisica Teorica ed Applicata, 15, 263-341.

Geletti R., Zgur F., Del Ben A., Buriola F., Fais S., Fedi M., Forte E., Mocnik A., Paoletti V., Pipan M., Ramella R., Romeo R. and Romi A.; 2014: *The Messinian Salinity Crisis: new seismic evidence in the West-Sardinian Margin and Eastern Sardo-Provençal Basin (West Mediterranean Sea)*. Marine Geology, 351, 76-90.

Gennesseaux M. and Vanney J.R.; 1979: *Cartes bathymetriques du Bassin Algero- Provençal*. Somm. Soc. Geol. Fr., 4, 191-194.

Krijgsman W. and Meijer P.Th.; 2008: *Depositional environments of the Mediterranean "Lower Evaporites" of the Messinian Salinity Crisis: constraints from quantitative analyses*. Marine Geology, 253, 73-81.

Krijgsman W., Hilgen F.J., Raffi I., Sierro F.J., Wilson D.S.; 1999: *Chronology, causes and progression of the Messinian Salinity Crisis*. Nature, 400, 652–655.

Kuroda, J. Eguchi, N., Droxler A., Alain K., Roure F. and Haq B.; 2012: *Structure and evoultion of the Gulf of Lions: The Sardinia Seismic Experiment and the GOLD (Gulf of Lions Drilling) project*. The Leading Edge - Special Section: Mediterranean Region, 786-792.

Lofi J., Déverchère J., Gaullier V., Gillet H., Gorini C., Guennoc P., Lonke L., Maillard A., Sage F. and Thinon I.; 2011: *Atlas of the Messinian seismic markers in the Mediterranean and Black Seas*. Mem. Soc. Geol. Fr., n. s. 179 and World Geological Map Commission, 72.

Lofi J., Gorini C., Berné S., Clauzon G., Dos Reis A.T., Ryan W.B.F. and Steckler M.S.; 2005: *Erosional processes and paleo-environmental changes in the Gulf of Lions (SW France) during the Messinian Salinity Crisis*. Marine Geology, 217, 1-30.

Montadert L., Letouzey J. and Mauffret A.; 1978: *Messinian event: seismic evidence*. In: Hsü K. J., Montadert L., et al. (Eds), Initial Reports of the Deep Sea Drilling Project, 42, part I, US Government Printing Office, 1037-1050.

Rehault J. P., Boillot G. and Mauffret A.; 1984: *The Western Mediterranean Basin Geological Evolution*. Marine Geology, 55, 447-477.

Ryan W.B.F., Hsü K.J., Cita M.B., Dumitrica P., Lort J., Maync W., Nesteroff W.D., Pautot, G. Stardner, H. Wezel, F.C.; 1973: *Boundary of Sardinia slope with Balearic Abyssal Plain - Sites 133 and 134*. In: Ryan et al. (Ed.): Init. Rep. DSDP, 13, 465–514.

Sage F., Von Gronefeld G., Déverchère J., Gaullier V., Maillard A. and Gorini C.; 2005: *Seismic Evidence for Messinian Detrital Deposits at the Western Sardinia Margin, Northwestern Mediterranean*. Marine and Petroleum Geology, 22, 757-773.

Yilmaz O.; 2001: *Seismic Data Analysis: Processing, Inversion and Interpretation of Seismic Data*. Stephen M. Doherty – SEG.

## SEPARATION AND IMAGING OF WATER-LAYER MULTIPLES FOR VSP SURVEYS

**S. Fiorentino, M. Codazzi, P. Mazzucchelli**
*Aresys, Milano, Italy*

**Introduction.** Vertical Seismic Profile (VSP) surveys allow to obtain information about the subsurface structure thanks to (multi-component) geophones in the borehole, that record the transmitted and reflected energy originating from a seismic source at the surface. Such surveys can provide data with higher resolution compared to surface seismic acquisitions, although their coverage is limited around the well area. In this paper the focus will be on the walkaway VSP (WVSP) offshore surveys in which the vessel, equipped with an air-gun, moves progressively along a line (or in an area for 3D surveys) at the sea surface and an array of receivers is held at fixed depths in the well. WVSP surveys, compared to Zero-offset VSP acquisition geometries, provide a continuous illumination of a wider area close to the well. WVSP surveys are usually performed to improve the knowledge of the subsurface, and in particular to refine the estimates of AVO (Amplitude Versus Offset) and anisotropic parameters. However, it must be noted that also WVSP surveys have a limited fold of coverage if compared to surface seismic (thousands of traces vs. millions of traces): thus, the stacking power of imaging algorithms is of little help in attenuating the coherent noise that contaminates recorded data. A meticulous pre-processing phase is mandatory prior to seismic imaging and any quantitative analyses: either techniques typical of VSP borehole data standard processing and approaches borrowed from surface data processing should be applied to WVSP surveys. Among all the spurious wavefields that can contaminate reflection data, multiple arrivals can be the most energetic source of coherent noise that can hide information recorded at target level. While surface related multiple arrivals are ubiquitous in marine data recordings and their effect must be always addressed, energetic internal multiple reflections (which can be tougher to be separated) are related to the presence of sharp variations in the subsurface (i.e., salt-dome flanks), thus their effect can be neglected in areas with limited geological complexity.

**Multiple reflections in walkaway VSP data.** The conventional multiple removal technique for the (Zero-Offset) VSP data is the "up-by-down" deconvolution: after up- and down-going wavefield separation, a predictive deconvolution is applied to the up-going wavefield using an operator built with the down-going wavefield. Although this approach gives good results in case of zero/near-offset VSP when the subsurface model can be considered 1D (i.e., horizontally layered model), more sophisticated techniques are needed for multiple elimination in Walkaway VSP data, because of the extended acquisition geometry.

Similarly, (surface-related) multiple elimination plays a fundamental role in marine data processing and nowadays data-driven convolutional methods, as SRME (Verschuur and Berkhout, 1992), have become the de-facto standard procedure for multiple removal for

surface seismic. SRME algorithm has some manifest advantages with respect to other multiple elimination techniques: in particular its accuracy and its fully data-driven nature that allows the application in the early stages of processing propose it as the benchmark for surface related multiple estimation and elimination.

SRME approach is sketched in figure 1b: multiple reflection ray-paths can be divided into two (or more) reflected ray-paths (color-coded in Fig. 1b), each of which have been recorded by a different trace. Thus, for each input trace *s-r*, practical implementation of SRME involves the convolution of couples of traces *s-n* and *n-r*, where *n* is any possible Downward Reflection Point (DRP) belonging to a regularly sampled surface $\varphi$. The subsequent stack of the so-called Multiple Contribution Gather (MCG) allows to estimate the surface related multiples *m(t)* recorded by trace *s-r*:

$$m_{sr}(t) \approx w^{-1} \sum_{\Phi} d_{sn}(t) * d_{nr}(t) \tag{1}$$

The term $w^{-1}$ represents the deconvolution by the source wavelet (which is often neglected in practical implementation). Then, an adaptive subtraction step allows to separate the interfering wavefields.

3D SRME limitations are mainly related to its computational cost, requiring appropriate strategies for data regridding (Dragoset *et al*., 2010) and for Multiple Contribution Gather (MCG) aperture optimization (Bienati *et al*., 2012). Moreover, it must be noted that the model independency of 3D SRME comes from a strict dependency on acquisition completeness, that cannot be satisfied by any practical acquisitions.

SRME technique cannot be directly applied to WVSP acquisition geometries, as no data is recorded at sea-surface, therefore preventing the correct construction of the Multiple Contribution Gather. Different approaches have been presented to overcome this limitation. Ma *et al*. (2011) proposed to use legacy surface data to complete WVSP acquisition geometries: however, a marine acquisition with the required coverage and orientation around the well cannot be always available. Moreover, such an acquisition, if it exists, have been recorded with different data resolution and in different environmental conditions. Conversely, Hokstad and Sollie (2005) proposed to model the missing surface data, by the mean of the information recorded by WVSP survey only. In particular their purpose is to simulate the ocean-bottom primary reflection only, using an approximation based on the DMO formula.

Indeed, different multiple predictions based on Wave Equation Modeling (WEM) have been proposed to handle incomplete data acquisition for surface acquisitions (Wiggins, 1988; Pica *et al*., 2005). Wang (2011) has shown how a Model-based Water-layer Demultiple (MWD) algorithm (based on the accurate knowledge of the bathymetry only) can outperform SRME data-driven approaches especially for shallow water environment, because of missing near-offset data and the poor quality of water layer primary reflections in the recorded data (as they are weak at large angles and often contaminated by other arrivals such as direct and refracted waves).

In the present work, we similarly substitute the *s-n* trace recorded at sea-surface, that is mandatory for SRME convolutional formulation but missing in WVSP survey, with the Green's function of the Water Layer Primary reflection only (dotted blue ray-paths in Fig. 1b): it can be easily and accurately computed when water velocity and bathymetry are known. Although only a subset of surface related multiples can be predicted, Water Layer Multiples *w.l.m* amplitudes may be significantly higher either than the reflection signals (which are attenuated during the propagation through the subsurface) or other surface-related multiples, lying in the same time window. Furthermore, hard seafloor and high structural attenuation in the subsurface exacerbate these effects. The surface-related multiple estimation procedure described in Eq. (1) is re-written as:

$$w.l.m_{sr}(t) \approx \sum_{\Phi} \delta(t - \tau_{sn}) * d_{nr}(t) = \sum_{\Phi} d_{nr}(t - \tau_{sn}) \tag{2}$$

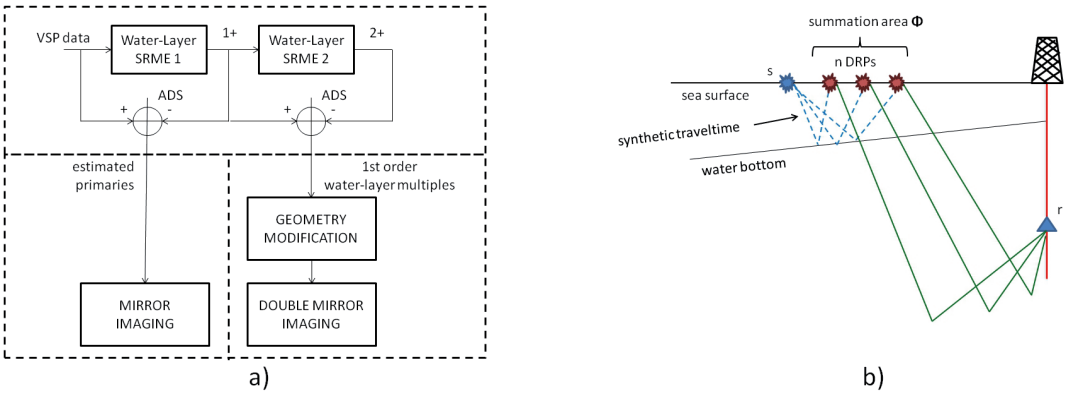


Fig. 1 – a) double mirror migration flowchart. Top-row: a two-step iteration of SRME separate first order only water-layer multiple reflections; bottom-left: data after multiples removal are imaged by receiver mirror migration; bottom-right: first order water-layer multiples are imaged after simple source geometry transform. b) model-based water-layer SRME approach: dotted blue lines in the water-layer represent the synthetic ray-paths s-n while green ray-paths n-r are extracted from WVSP data.

The convolution with missing surface data is replaced by a simple time-shift by the water layer primary reflection traveltime $\tau_{sn}$. The adaptive subtraction step is still required to separate the interfering wavefields, however no explicit source wavelet deconvolution is needed once again.

**Imaging of multiple energy.** Until few years ago, multiple energy has been considered as noise, thus multiple reflection wavefields have been discarded after the separation process. However, multiple reflections contain a wealth of information of the subsurface, that can be used in seismic processing to improve the resolution of reservoir images (Berkhout, 2006). Indeed, recently the geophysicists' mind-set about multiples has changed: an increasing interest actually exists in finding new methods for the exploitation of such an information. Wavefield extrapolation imaging techniques can be adapted to correctly handle both primary and multiple seismic reflections, and recent results proved how non-linear imaging can take advantage of internal multiples, too (when a detailed velocity model that matches the sharp discontinuities at multiple generators is available).

In O'Brien (2013) the imaging of "half order" multiple arrivals (i.e., source-injected energy, after being reflected in the subsurface, is then downward reflected by sea surface, and reaches the receiver array in the borehole as a transmitted wave) proves how the use of "multiple noise" can improve subsurface illumination for WVSP survey, solving at the same time the lack of lateral and shallow illumination. Jiang *et al*., (2007) discuss different approaches to image multiples, with different complexity and sensitivity to velocity model knowledge: among them, a clever "receiver-mirror imaging" technique (i.e., a new acquisition geometry is built by reverting receiver depths $z_r'=-z_r$, and imaging is performed with a double-vertical-size velocity model mirrored in respect of the free-surface, as shown in Fig. 2a) allows to migrate such data without the need to modify standard imaging engines, but only applying simple modification to acquisition geometry. "Half-order" (i.e. mirrored receiver) multiple arrivals and primary reflections do not interfere, because of the difference in ray-path lengths. However, extended recording time must be taken into account when acquiring data.

When more than one reflection is considered in the subsurface, such techniques may fail because of the inability to separate the interaction between primary and multiples from different interfaces or from different multiple orders (i.e., number of reflections in the subsurface) (Fortini *et al*., 2013). In fact, such a cross-talk can be hard to be attenuated after the imaging step, especially for WVSP acquisitions because of their low fold of coverage. Thus, modified imaging algorithms must be implemented to (at least partially) overcome these problems (Zhang *et al*., 2014).

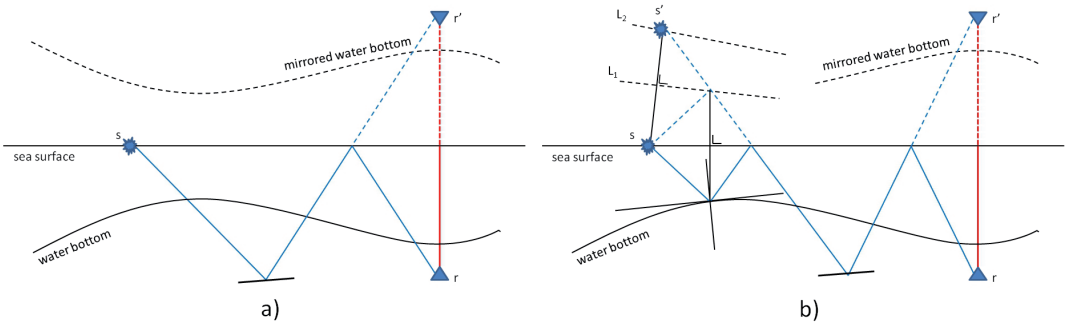


Fig. 2 – a) receiver mirror migration geometry: a new acquisition geometry is built by reverting receiver depths; b) double mirror migration geometry: in addition to the receiver depths transform, the source location is modified unfolding water-layer ray-path.

**Water-layer multiple separation and imaging.** After the subtraction of water layer multiples has been performed according to eq. 2, and subsequent adaptive subtraction, WVSP data $D_{all}$ is split into two different sets: "primary" wavefield $D_1$ and "multiple" wavefield $D_2$:

$D_{all} = P + nonwlM_{1...N} + wlM_{1...N} + IM$

$D_1 = P + nonwlM_{1...N} + IM$

$D_2 = wlM_1 + wlM_2 + \ldots + wlM_N$

where $P$ stands for the primary reflections, $wlM_{1...N}$ for the water layer multiples of order $1\ldots N$, $nonwlM_{1...N}$ for the other types of surface-related multiples of order $1\ldots N$ and $IM$ for all the internal multiples.

Primary reflections cannot be completely isolated, as only a subset of surface-related multiples has been predicted. However, as water layer multiples can be the most energetic subset of interfering wavefield, such a partial noise attenuation is still beneficial (as proved by the comparison of results shown in figure 3a and 3b, described in the next section).

Then first order only water-layer multiple reflections $wlM_1$ can be nicely identified by iterating the previously described SRME prediction and subtraction procedure on $D_2$ subset, as sketched in figure 1a. By eliminating higher order water layer multiple reflections, we obtain a new subset $D_{wlm1}$ that contains only the recorded multiple events that are reflected only one time over water-bottom (from source side).

Thus, multiple estimation iteration allows to isolate a single multiple generator (i.e., water-bottom): migration of $D_{wlm1}$ naturally avoids any cross-talk which degrades the final image, and no post-imaging cross-talk attenuation needs to be applied.

A simple source geometry transform allows to perform the migration of $D_{wlm1}$ multiple reflections without the need of any modification of standard migration tools, analogously to "receiver mirror migration".

Source geometry is modified accordingly to the ray-paths of the first-order multiples traveling in the water-layer. A two-stage mirroring is performed (Fig. 2b): the first mirror moves the water-bottom from its original position to the reverse position $L_1$ (in the z-negative half-plane); then second mirror moves the sea surface from its original position to a symmetrical position $L_2$ in respect of the ghost water bottom $L_1$ (that is assumed to be planar – constant dip, at least locally around source position), allowing to compute virtual source position $S'$ (lying on mirrored sea-surface $L_2$).

Migration velocity model is then extended for negative depths with constant water velocity, and then any standard migration code can be applied. Source-side double mirror transform can be obviously combined with receiver-side mirrored migration, to widen subsurface illumination. It must be noted that in this case two different velocity models (source-side: $v(-z)=V_{water}$, receiver-side: $v(-z,x,y)=v(z,x,y)$ ).

Water layer multiple migration does not provide wider illumination, however the increased fold of coverage promotes better signal-to-noise ratio in the same region where the conventional VSP imaging works. Moreover, the reflection angles of recorded multiples are mostly smaller than those of the corresponding primaries: smaller reflection angles provide higher vertical resolution and can sometimes be less prone to defocusing.

The complete flowchart describing the whole procedure is shown in figure 1a: the ability of imaging water layer multiples through a simple source geometry transform compares favorably to approaches explicitly or implicitly based on interferometric or redatuming techniques (Jiang *et al.*, 2007), although the locally planar sea-bottom hypothesis may be not completely fulfilled.

As first order water layer multiples add a round-trip to corresponding primary reflection ray-paths, a lower signal-to-noise ratio is expected because of greater geometrical spreading. However, other attenuation losses can be safely ignored because the additional ray-path is confined in the water-layer only.

Furthermore, the effects on recorded amplitudes of the reflection at sea-bottom has been ignored so far, which implies that a constant sea-bottom reflection coefficient is implicitly assumed. Thus, imaging results should be considered kinematically correct but one should not trust on retrieved amplitudes.

It must be also noted that in principle the proposed approach can be applied to higher-order water-layer multiple reflections by iterating the procedure.

**Synthetic data example.** The proposed procedure has been tested with a simulated 2D Walkaway VSP dataset. The velocity model has been extracted from the BP2007 benchmark model (software.seg.org): the model extends 20 km laterally and 11.25 km vertically, with a spatial sampling of $\Delta x$=6.25 m (corresponding acoustic impedance is shown as colour-coded background in Fig. 3). Seismic data have been computed by a finite difference isotropic acoustic simulation (using both velocity and density models), with staggered grids. Output time sampling is $\Delta t$=1 ms while trace duration is $T$=16 seconds. The dataset geometry consists of a single geophone, placed at $z_r$=4000 m depth in the well, that is illuminated by 1601 sources at sea-surface with inter-source distance $\Delta s$=12.5 m each other (acquisition geometry is partially sketched in Fig. 3b). Density model is selected to simulate a hard water-bottom interface (mean water layer depth is $w_d$=450 m).

As the subsurface illumination is both laterally and vertically extended by the previously described receiver mirror imaging technique, results comparison is shown for "receiver mirror-imaged" results only, although the analysis and comparison of "conventional" (non mirrored-receiver) results lead to the same conclusions. Pre-stack depth migration is performed by a ray-based Kirchhoff migration, using a smooth velocity model. Receiver mirror-migrated result of WVSP data after Water Layer Multiple subtraction (shown in Fig. 3b) proves how imaging step succeeds to correctly recover most of the subsurface interfaces. This result, compared to the mirror-migrated image of WVSP raw data (i.e., before any interfering wavefield separation), shown in figure 3a, proves how migration stacking power cannot properly attenuate water layer multiple interference.

Finally, in the proposed source double-mirror imaging result is shown in Fig. 3c. The comparison of Fig. 3c with Fig. 3b (water layer multiple free benchmark) proves that first order water layer multiple data can be coherently migrated and carries full subsurface illumination. Multiple migration residuals, highlighted by arrows and in the circled area on the migrated panels, are clearly visible on raw data migration result (Fig. 3a), while they are highly attenuated in both results shown in Figs. 3b and 3c. However, a globally lower SNR of multiple migration result suggests that multiple migration can complement, and not replace primary migration.

**Conclusions.** In this work we have presented a simple and straightforward procedure to estimate, separate and finally image a subset of multiple reflections (water layer multiples) for WVSP surveys. Results on simulated data prove how migration of such surface-related multiple subset can be easily performed by a simple transformation of source point geometry.

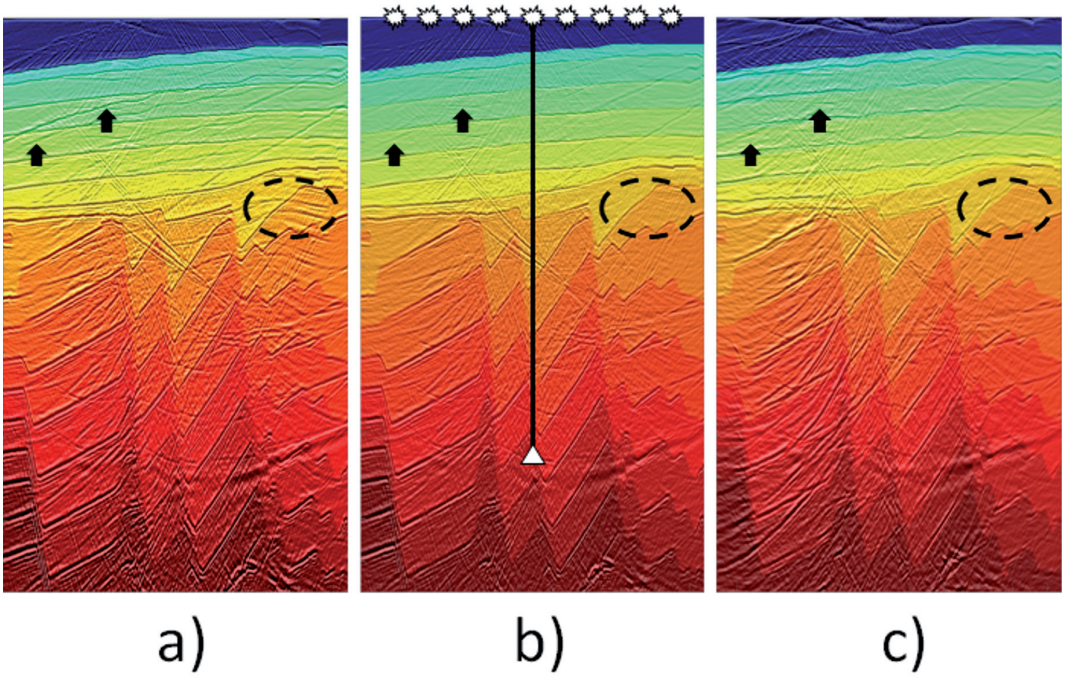


Fig. 3 – a) receiver mirror migration of the simulated raw data; b) receiver mirror migration of the data after adaptive subtraction of the estimated water-layer multiples with the WVSP acquisition geometry superimposed; c) double mirror migration of the first order water-layer multiples. Arrows and circles highlight cross-talk artifacts that corrupt raw data migration but have been attenuated in either primary reflections migration and first water-layer multiple migration.

Source double-mirror migration relies on the local planarity of the water bottom, as ghost sources *S'* positioning errors can deteriorate imaging result: however, complex bathymetry can still be correctly taken into account by minor changes to the migration algorithm, freeing the imaged section from all these artifacts due to the over-approximated positions of the sources. It must be emphasized that the quality of the final results mainly depends on the ability to separate multiples from primaries. The proposed approach, thanks to its ability to cope with any acquisition geometry, can be applied to any marine acquisition geometry, while any imaging technique can be exploited after the proposed source geometry transform.

**Acknowledgements.** The authors would like to thank Francesco Miranda (eni) for fruitful discussions and valuable suggestions.

## References

A.J. Berkhout, and D.J. Verschurr, 2006, Imaging of multiple reflections: GEOPHYSICS, VOL. 71, NO. 4 (July-August 2006), P.SI209-SI220, 19FIGS.

N. Bienati, P. Mazzucchelli, and M. Codazzi, 2012, 3D-SRME Antialiasing in the Multiple Contribution Gather Domain: 74th EAGE Conference & Exhibition incorporating SPE EUROPEC 2012 Copenhagen, Denmark, 4-7 June 2012

B. Dragoset, E. Verschuur, I. Moore, R. Bisley, 2010, A perspective on 3D surface-related multiple elimination: GEOPHYSICS,VOL. 75, NO. 5 (SEPTEMBER-OCTOBER 2010); P. 75A245–75A261, 19 FIGS., 1TABLE.

C. Fortini, V. Lipari, 2013, Imaging of Multiple reflections: 32° Convegno Nazionale GNGTS 2013 Sessione 3.1

K. Hokstad, and R. Sollie, 2005, Surface-Related Multiple Elimination Applied To Walkaway VSP Data: 67th Conference and Exhibition, EAGE, Extended Abstracts, I023.

Z. Jiang, J. Sheng, J. Yu, G.T. Schuster, B.E. Hornby, 2007, Migration methods for imaging different-order multiples: Geophysical Prospecting, 2007, 55, 1-19.

J.T. Ma, F.C. Yao, X.H. Chen, and Y. Liu: VSP Multiple Attenuation Theory Using SRME Technique, 73rd EAGE Conference & Exhibition incorporating SPE EUROPEC 2011 Vienna, Austria, 23-26 May 2011

Pica, A., G. Poulain, B. David, M. Magesan, S. Baldock, T. Weisser, P. Hugonnet, and P. Herrmann, 2005, 3D surface-related multiple modeling, principles and results: 75th Annual International Meeting, SEG, Expanded Abstracts, 2080-2083.

J. O'Brien, B. Farmani, B. Atkinson, 2013, VSP Free-Surface Multiple Imaging - A Detailed Case Study: 75th EAGE Conference & Exhibition incorporating SPE EUROPEC 2013 London, UK, 10-13 June 2013

D.J. Verschurr , and A.J. Berkhout, 1992, Adaptive surface-related multiple elimination: GEOPHYSICS, VOL. 57, NO. 9 (September 1992), 10.1190/1.1443330

P. Wang, H. Jin, S. Xu, and Y. Zhang, 2011, Model-based Water-layer Demultiple: 2011 SEG San Antonio Annual Meeting

Wiggins, J. W., 1988, Attenuation of complex water-bottom multiples by wave-equation-based prediction and subtraction: Geophysics, 53, 1527–1539

D. Zhang and G. T. Schuster, 2014, Least-squares reverse time migration of multiples: GEOPHYSICS,VOL. 79, NO. 1 (January-February 2014), 10.1190/geo2013-0156.1

## SEISMIC INTERPOLATION VIA CONJUGATE GRADIENT PURSUIT

**L. Fioretti[1], P. Mazzucchelli[1], N. Bienati[2]**
[1] *Aresys, Milano, Italy*
[2] *eni E&P, San Donato Milanese, Italy*

**Introduction.** Seismic processing methods often assume data to be regularly and densely sampled in space, but acquisition techniques, in particular in marine environments, rarely achieve this requirement in practice. Thus, during the years, a large number of interpolation algorithms have been developed based on different strategies.

One class of methods is related to the integral of continuation operators (Canning and Gardner, 1996; Bleistein and Jaramillo, 2000; Stolt, 2002; Fomel, 2003), but, despite the connection with the physics of wave propagation, in case of complex geological structure the accuracy is strongly affected. Moreover, this kind of algorithms suffers from coarse sampling, introducing strong artifacts that need to be removed via post-processing.

One of the most popular approaches of the last years is based on the convolution filters (Spitz, 1991; Abma and Claerbout, 1995; Mazzucchelli *et al*., 1998). This kind of algorithms works very well when input data are regularly sampled, but the regularity assumption is a heavy limitation to their usage.

Fourier theory provides another way for handling this problem (Sacchi and Ulrych, 1995; Duijndam *et al*., 1999). Algorithms from this class first estimate Fourier coefficients from input data, then recover data on any desired grid. Again, these methods are effective in interpolating from regularly sampled data, but when irregularities show up, the orthogonality of Fourier basis falls bringing to the so-called 'spectral leakage' effect: the energy of one spectral component 'leaks' onto others, introducing erroneous contributes to the spectral representation.

A new Fourier-based approach was proposed in the last years for facing the spectral leakage problem (Xu and Pham, 2004; Zwartjes and Sacchi, 2004; Xu *et al*., 2005a, 2005b; Özbek *et al*., 2009), the earliest one was the Antileakage Fourier Transform (ALFT): given the input data, estimate its Fourier representation, then pick the most energetic Fourier coefficient and subtract its contribution from residual data, and so on iteration by iteration, until some stopping criterion is met. This method exploits the assumption that seismic data can be sparsely represented in the Fourier domain. Based on the same assumption, a similar strategy has been proposed for improving efficiency (Nguyen and Winnett, 2011): it precomputes the matrix of Fourier components once for all and then, at each iteration, the data is simply projected onto the

dictionary. This alternative approach can be viewed as a mere application of the well-known Matching Pursuit (MP) algorithm first proposed by Mallat and Zhang (1993).

We bring here the contribution of Blumensath and Davies (2009) to the MP approach for handling the data interpolation problem. We apply the so-called Conjugate Gradient Pursuit (CGP) with the Stagewise selection strategy instead of the simple MP for estimating the Fourier components. The usage of this engine in the seismic data processing context has been inspired by the work of Adamo *et al*. (2014). The CGP differs from MP for the fact that, at each iteration, all so far collected components are updated for being *conjugate* to components at previous step. Moreover, the Stagewise selection strategy suggests picking a number of new components per iteration instead of a single one. This leads to a reduction of the final number of iteration needed to get to convergence. On the other hand, the MP, in which the same component is selected again and again until its energy is exhausted, needs a lot of iterations. We make a comparison among the two approaches, and show that they produce comparable results in terms of accuracy but CGP converges much faster than MP as expected.

**Fourier representation of seismic data for interpolation.** An interpolation algorithm, in this context, aims to estimate the Fourier spectrum from irregularly sampled seismic traces while avoiding wavenumber energy leakage. Since seismic data is usually well-sampled in the time direction, it is efficient and accurate to use the FFT for representing data in the *f-x* domain. Then, for each temporal frequency the algorithm estimates the spatial Fourier components (in the *f-k* domain), and uses the expansion for reconstructing data at any desired spatial location. For this reason, to illustrate the concept of the method, we consider the interpolation problem of a single frequency slice of a seismic data set.

Let us consider the complex-valued function $f(x)$ defined in the interval [0,1[ and sampled at a set of $N_x$ points $x_l$. The sampled function $f(x_l)$ represents the temporarily transformed seismic data at a given frequency and spatial position $x_l$. We compute Fourier transformation of irregularly sampled data by direct evaluation of trigonometric sums:

$$\hat{f}(k) = \sum_{l=0}^{N_x-1} f(x_l) e^{-2\pi i k x_l}, \tag{1}$$

while the input data expansion is computed as:

$$f(x_l) = \sum_{k=-\frac{N_k}{2}}^{\frac{N_k}{2}-1} \hat{f}(k) e^{2\pi i k x_l}. \tag{2}$$

In matrix notation, we write data samples $f(x_l)$ as the vector $f$ and Fourier coefficients $\hat{f}(k)$ as the vector $\hat{f}$. The exponential wave functions $e^{2\pi i k x_l}$, are represented by the vectors $\Phi_k$ which constitutes the columns of the matrix operator $\Phi$ of size $N_x \times N_k$. Thus, Eq. (2) can be rewritten in the form

$$f = \Phi \cdot \hat{f} \tag{3}$$

which represents an undetermined system when $N_k > N_n$.

**Interpolation via Matching Pursuit.** The basic assumption which makes this kind of approaches possible (MP, ALFT, and similar ones), is that seismic data have a sparse representation in the Fourier domain, which means that the input data can be accurately approximated by few dominant wavenumbers. It is by this hypothesis that the usage of greedy algorithms is legitimate: Mallat and Zhang (1993) firstly suggest to handle sparse representation problems by using the MP algorithm. This simple approach has already proved to be effective when applied to seismic data regularization and interpolation problems, as Nguyen and Winnett (2011) demonstrated. We here recall first the MP approach, in order to underline afterward our upgrade by the application of CGP.

The MP method approximates the representation of $f$ by choosing one vector $\Phi_k$ per iteration. In practice, at each iteration $n$, the algorithm selects the vector $\Phi_k$, which provides the highest contribution when correlated to the input data:

$$\hat{f}_{k^{[n]}} = \max_{k=-\frac{N_k}{2}\ldots\frac{N_k}{2}-1} |\langle \boldsymbol{\phi}_k, \boldsymbol{f} \rangle| \quad (4)$$

then the algorithm subtracts its contribution from residual data, and iterates this process until some stopping criterion is met.

This approach has proved to be as accurate as the ALFT reference method while more efficient. By the way, it still has a drawback. As already observed, due to the irregularities in the input data sampling, the *f-k* representation of the data shows some energy leakage from true wavenumber components onto near components. This fact leads the algorithm, iteration after iteration, to pick the same component until all its leaked energy is consumed, which increases enormously the total number of iterations. Since the spectral leakage phenomenon is due to the non-orthogonality of the Fourier basis in case of irregular sampling, adding an orthogonalization step at each iteration would do the job. This method goes under the name of Orthogonal Matching Pursuit, OMP (Tropp and Gilbert, 2007) and has been applied in this context by Hollander *et al*. (2012). By the way, this approach leads to performing, at each iteration, an orthogonal projection of the input data onto the components selected so far, which is a very expensive procedure and highly increases the cost of a single iteration.

The work of Blumensath and Davies (2009) addresses the challenge of finding a trade-off among number of iterations and cost per each iteration that would make this kind of approach even more efficient than the already explored MP.

**Interpolation via Stagewise Conjugate Gradient Pursuit.** The proposed approach introduces two main improvements (Blumensath and Davies, 2009), which both bring advantages in reducing computational costs: the Stagewise strategy, which selects more than a single coefficients at each iteration, and the Conjugate Gradient Pursuit which updates at each iteration the coefficient selected so far by a conjugate direction.

For what concerns the stagewise selection, the generalization is straightforward. While both ALFT and MP propose to select, at each iteration, a single Fourier component, this method proposes to take *a number* of components. Apart from the different number of coefficients selected per iteration, the selection strategy is the same as in MP: the wavenumbers which provide the highest energy contribute are taken and added to the set of components collected so far.

For what concerns the update direction, Blumensath and Davies (2009) recall that the usage of a conjugate gradient direction offers significant advantages in terms of computational costs if compared to OMP, while still providing convergence guarantees. Thus, at each iteration, after that the set of new components is selected and the respective contribute to the data representation evaluated, an updating constant is computed such that consecutive directions are conjugate. Of course, being not an exact orthogonalization performed at each iteration, same coefficients can be re-selected iteration after iteration.

Blumensath and Davies (2009) underline that this method has an intrinsic mechanism that senses how orthogonal all previously selected components are with respect to the residual. If they are far from orthogonal, the inner products will give a large result in magnitude and a component will be re-selected. Otherwise, if after a single updating step the components are nearly orthogonal to the residual, then the algorithm will not re-select the same components.

**Practical issues.** Some discussion is due about the actual implementation of the presented interpolation tool.

For what concerns the number of Fourier components selected at each iteration, experiments suggest tuning this parameter depending on the amount of irregularity which affects the input data sampling. In fact, the more irregular the sampling is, the more the amount of leaked energy is, and the lower the number of components selected per iteration should be.

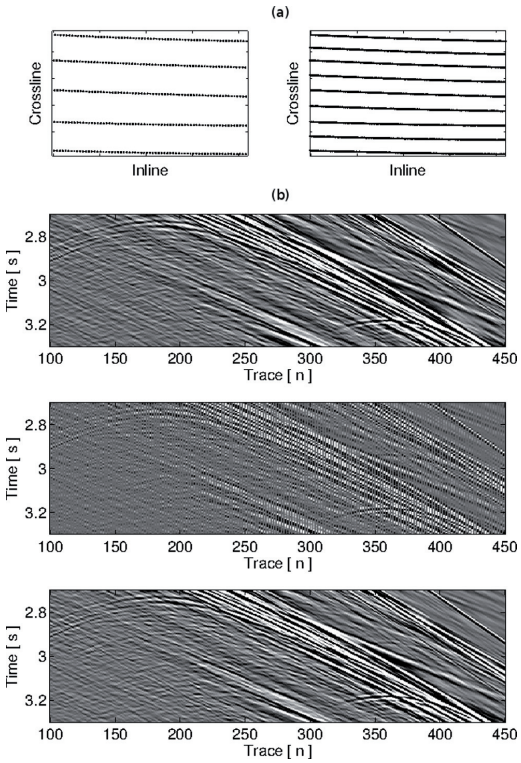


Fig. 1 – Soft upsampling example: a) geometry description: sampling before (left) and after (right) processing; b) results of the interpolation, inline visualization, from top to bottom: MP result, input data, CGP result.

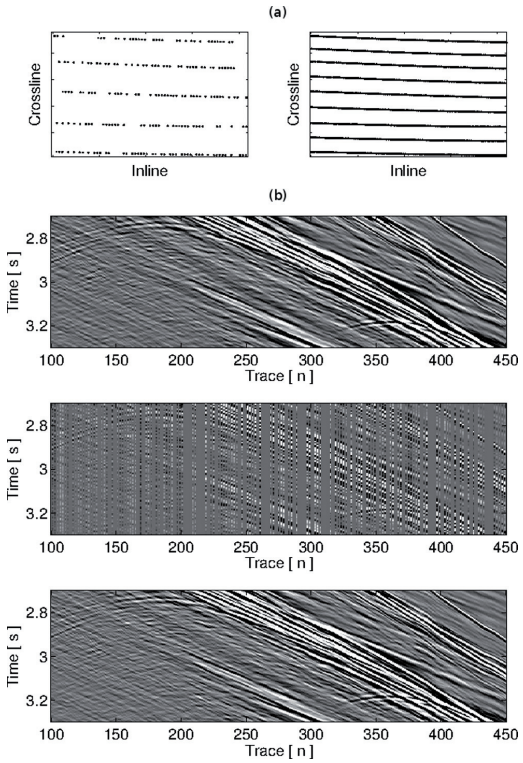


Fig. 2 – Soft upsampling and missing traces infilling example: a) geometry description: sampling before (left) and after (right) processing; b) results of the interpolation, inline visualization, from top to bottom: MP result, input data, CGP result.

We also specify that both our implementations of MP and CGP make use of three different stopping criteria: the maximum number of iterations, and a tolerance both on the norm of the residual and on the norm of the coefficient contribution. The tolerances on the two norms have fixed value which are the same for both algorithms. Instead, as already observed, the maximum number of iteration is a parameter of the algorithm, which, together with the number of components selected at each iteration, is to be tuned depending on the input sampling irregularity.

**Numerical examples.** We compare MP and CGP interpolation results on a marine seismic data set. The 3D data set is sorted by Common Shot Gather and indexed by the two-dimensional offset vector. Time sampling rate is 2 ms. Nominal spatial sampling is 12.5 m along inline direction and 100 m along crossline direction. As the time sampling is regular, the interpolation schemes is applied in the space-frequency domain in frequency slices on both spatial directions simultaneously. Once the Fourier coefficients are obtained, the spectrum is back-transformed to the below specified grids.

Results of reconstruction on three different grids are reported. In all those processing examples an NMO correction is previously applied to input data and afterward removed. Moreover, the interpolation method is applied by overlapping windows.

The three processing settings are described by the top two graphics of Fig.1 to Fig.3. In first example (see Fig. 1) the input grid shows only minor irregularities, which are intrinsically due to the marine acquisition. In this first case a double upsampling along both inline and crossline direction is performed. The second example aims to underline the robustness of the

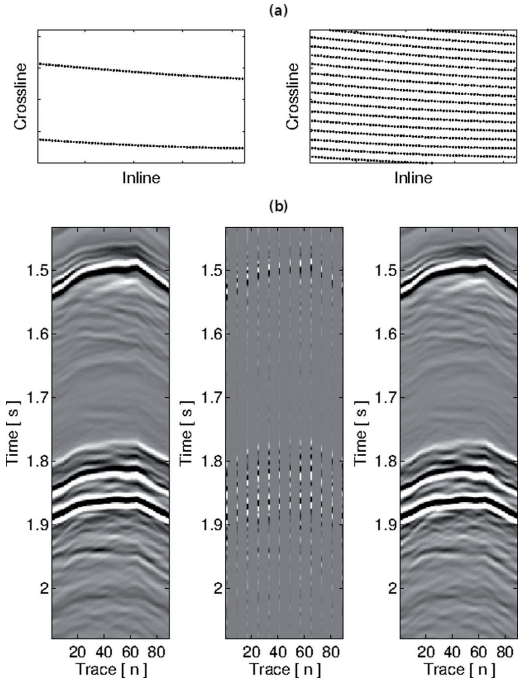


Fig. 3 – Hard upsampling example: a) geometry description: sampling before (left) and after (right) processing; b) results of the interpolation, crossline visualization, from left to right: MP result, input data, CGP result.

approach to irregularities, for this reason, a manual trace decimation is made: one third of traces is randomly selected and discarded. After this procedure the input dataset sampling shows strong irregularities. In this case the reconstruction method is applied for both filling gaps and upsampling, as Fig. 2 shows. The last example performs a strong upsampling along crossline direction: since input sampling is very coarse along crossline direction, the algorithm upsamples input data by a factor 8, in order to obtain a crossline sampling spacing which is comparable to the inline sampling spacing.

All three figures report the comparison among the result of the MP approach ((b), first panel) and the one of the CGP approach ((b), last panel), together with the input data ((b), middle panel). Figures show how CGP produce comparable results in terms of accuracy in all three examples, both in case of almost regular input sampling and strongly irregular input sampling.

Once the reconstruction capability of the CGP method is ascertained, the next step is to show what big improvement this approach represents in terms of computational costs. For obtaining such a high accuracy on all three results, the MP method needs to perform 1000 iterations. This leads to very high computational costs, which even increase when the performed upsampling (as in third example) is by a large factor. On the other hand, the CGP approach needs very few iterations, in particular in the first and third example, in which the input geometry is almost regular: at each iteration half of the components can be selected and 2 total iterations are enough to get to the same result as with MP. Also for CGP an hard upsampling needs more time for being performed than a soft one, but anyway CGP execution times are negligible if compared to the MP ones. The only case in which the number of iteration needs to be high is when the input geometry shows strong irregularities, as in the second example, in this situation, as already discussed in the technical sections, only few components per iterations can be selected due to the spectral leakage phenomenon: in our example we pick 0.1% of total components per iteration which means a single component in most of temporal frequency slices. With such a configuration, the number of iterations needed for getting to a result which is as accurate as the MP is equal to 40, thus we see that even with the same number of components selected at each iteration, the updating step leads CGP approach to gain a lot in terms of number of iterations over the MP. Even if the CGP iteration is more complex than MP one, the final CGP execution time is again much lower than MP time. Tab. 1 reports a summary of all execution times.

**Conclusion.** We have presented a data interpolation algorithm belonging to the class of sparsity promoting Fourier methods. It differs from already presented methods (such as ALFT, MP and similar ones) for making use of the novel Conjugate Gradient Pursuit method with the Stagewise selection strategy. The algorithm operates iteratively, as the above mentioned ones, but selects a number of dominant components instead of a single one per each iteration. Moreover, after the coefficients selection, all so far collected components are recalculated by

a conjugate direction updating. We applied the algorithm on a 3D marine seismic data set. Numerical experiments show that our CGP method gives results which are comparable, in terms of accuracy, to the ones of a well-acquainted method as the MP is, both on complex geologic seismic data and strongly irregularly sampled data. On the other hand, performed experiments have demonstrated a large gain in efficiency of the new method when compared to the MP.

Table 1 - Algorithms setting and performances.

| | | number of components per iteration | maximum number of iterations | execution time |
|---|---|---|---|---|
| soft upsampling | MP | 1 | 1000 | 3 h 13 m |
| | CGP | 50% | 2 | 5 m |
| soft upsampling and missing traces infilling | MP | 1 | 1000 | 2 h 8 m |
| | CGP | 0.1% ≈ 1 | 40 | 36 m |
| hard upsampling | MP | 1 | 1000 | 7 h 2 m |
| | CGP | 50% | 2 | 19 m |

**Acknowledgements.** We would like to thank eni E&P Division for the permission to show data and to publish this paper.

**References**

Abma R., and J. Claerbout, 1995, Lateral prediction for noise attenuation by t-x and F-X techniques: Geo- physics, 60, 1887–1896.

Adamo A., P. Mazzucchelli, and N. Bienati, 2014, Weak orthogonal matching pursuit with geophysical atom selection: 76th Conference and Exhibition, EAGE, Extended Abstracts, P0113.

Bleistein N., and H. Jaramillo, 2000, A platform for kirchhoff data mapping in scalar models of data acquisition: Geophysical Prospecting, 48, 135–161.

Blumensath T., and M. E. Davies, 2009, Stagewise weak gradient pursuit: IEEE Transaction on Signal Processing, 57, 4333–4346.

Canning A., and G. H. F. Gardner, 1996, Regularizing 3-D data sets with DmO: Geophysics, 61, 1103–1114. (Discussion and reply in GEO-62-4-1331).

Duijndam A. J. W., M. A. Schonewille, and C. O. H. Hindriks, 1999, Reconstruction of band-limited signals, irregularly sampled along one spatial direction: Geophysics, 64, 524–538.

Fomel S., 2003, Seismic reflection data interpolation with differential offset and shot continuation: Geophysics, 68, 733–744.

Hollander Y., D. Kosloff, Z. Koren, and A. Bartana, 2012, Seismic data interpolation by orthogonal matching pursuit: 74th Conference and Exhibition, EAGE, Extended Abstracts, B032.

Mallat S. G., and Z. Zhang, 1993, Matching pursuit with time-frequency dictionaries: IEEE Transaction on Signal Processing, 41, 3397–3415.

Mazzucchelli P., F. Rocca, U. Spagnolini, and S. Spitz, 1998, Wavefield Interpolation - Continuation or Prediction Filter Techniques?: 60th Conference and Exhibition, EAGE, Extended Abstracts, 02–51.

Nguyen T., and R. Winnett, 2011, Seismic interpolation by optimally matched fourier components: 81st Annual International Meeting, SEG, Expanded Abstracts, 3085–3089.

Özbek A., A. K. Özdemir, and M. Vassallo, 2009, Interpolation by matching pursuit: 79th Annual International Meeting, SEG, Expanded Abstracts, 3254–3258.

Sacchi M. D., and T. J. Ulrych, 1995, High-resolution velocity gathers and offset space reconstruction: Geophysics, 60, 1169–1177.

Schonewille M., A. Klaedtke, and A. Vigner, 2009, Antialias anti-leakage fourier transform: 79th Annual International Meeting, SEG, Expanded Abstracts, 3249–3253.

Spitz S., 1991, Seismic trace interpolation in the F-X domain: Geophysics, 56, 785–794.

Stolt R. H., 2002, Seismic data mapping and reconstruction: Geophysics, 67, 890–908.

Tropp J. A., and A. C. Gilbert, 2007, Signal recovery from random measurements via orthogonal matching pursuit: IEEE Transaction on Information Theory, 53, 4655–4666.

Xu S., and D. Pham, 2004, Seismic data regularization with anti-leakage fourier transform: 66th Conference and Exhibition, EAGE, Extended Abstracts, D032.

Xu S., Y. Zhang, and G. Lambare, 2005a, Antileakage fourier transform for seismic data regularization in higher dimensions: Geophysics, 70, WB113–WB119.

Xu S., Y. Zhang, D. Pham, and G. Lambare, 2005b, Antileakage Fourier transform for seismic data regularization: Geophysics, 70, V87–V95.

Zwartjes P. M., and M. D. Sacchi, 2004, Fourier reconstruction of non-uniformly sampled, aliased data: 74th Annual International Meeting, SEG, Expanded Abstracts, 1997–2000.

## NON LINEAR IMAGING WITH INTERNAL MULTIPLES

**C. Fortini, V. Lipari**

*Dipartimento di Elettronica, Informazione e Bioingegneria, Politecnico di Milano, Italy*

**Introduction.** Conventional seismic imaging algorithms are based on single-scattering hypothesis (*linear imaging*). The reverberations that generate during wavefield propagation in the subsurface (*multiple reflections*) are usually considered as unwanted noise. Even though the most energetic reverberations (especially in marine seismic acquisition) are the so called *surface-related* multiples, in areas of high structural complexity we usually record also strong *internal* and *intra-salt multiples*. The most common approach used to handle with the presence of multiple reflections (both surface and internal) in the acquired seismic data is to try to eliminate them. First, a model of the multiples is built by means of either *model-based* or *data-driven* methods and then the noise model is adaptively subtracted from the original data (Verschuur, 2006; Verschuur *et al*., 1992; Lipari *et al*., 2012). However, the multiply scattered recorded events had interacted with the subsurface discontinuities and thus carry useful information about it. When properly imaged, these events can enhance the seismic image and may provide additional illumination in those areas poorly imaged by conventional approaches.

Recently, researches on multiples have shifted their focus on the exploitation on what has been often considered only as noise: both surface-related and internal multiples have been proved to carry useful information about the subsurface discontinuities. Berkhout and Verschuur (2006) showed that the multiple reflections can be used to re-create the associated primaries and then exploited for imaging purposes. They also proved that multiples carry useful information and can thus enhance the overall understanding of the subsurface structure. Various authors showed that WE (Wavefield Extrapolation) migration algorithms can be effectively used for the imaging of the multiple reflections (examples can be found in Guitton (2002), Muijs (2007), Alkhalifah (2011)). However, in scenarios characterized by the presence strong reflective interfaces (carbonates layers, salt-bodies,…) we expect to record also relatively strong internal multiples. Recently various authors have proposed new *non-linear imaging* methods (Ravasi and Curtis, 2013; Vasconcelos and Hornby, 2008; Fleury, 2013; Malcolm *et al*., 2009; showing that these techniques help in reducing the image artifacts and improve the resolution and illumination of the subsurface image provided by conventional techniques. The main advantage of these new techniques resides in the use of the internal multiples events.

Here, we propose a technique based on non-linear *wavefield datuming* and *seismic interferometry* that allows us to separately exploit the information coming from the internal multiples recorded in a conventional seismic acquisition. Wavefield datuming is a means of extrapolating a recorded seismic data from one surface to another. From a numerical point of view, it can relocate the source and receiver locations while keeping the propagation features. The seismic data recorded at the original (actual) acquisition surface are used to generate a new seismic dataset with a new (virtual) acquisition geometry deployed at an arbitrary position in the subsurface (Liu and Xu, 2011; Berryhill, 1979, 1984). For the specific applications presented in this paper, the original wavefield is used as input to reconstruct a new virtual seismic

experiment with sources and receivers placed underneath the formations mainly responsible of the multiply scattered events. This new dataset is constructed using both the linear and non-linear components of the Green's function, thus accounting for the multiple reflections. We show examples on the synthetic dataset Sigsbee2b.

**Non-linear datuming.** Fig. 1a shows the acquisition setting of a conventional marine seismic experiment. *S, R, A* and *B* indicate, respectively, the coordinates of the zero-depth original sources and receivers (($x_S$, $y_S$, $z_S = 0$), ($x_R$, $y_R$, $z_R = 0$)) and those of the sources and receivers on a virtual datum surface (($x_A$, $y_A$, $z_A$) and ($x_B$, $y_B$, $z_B$)).

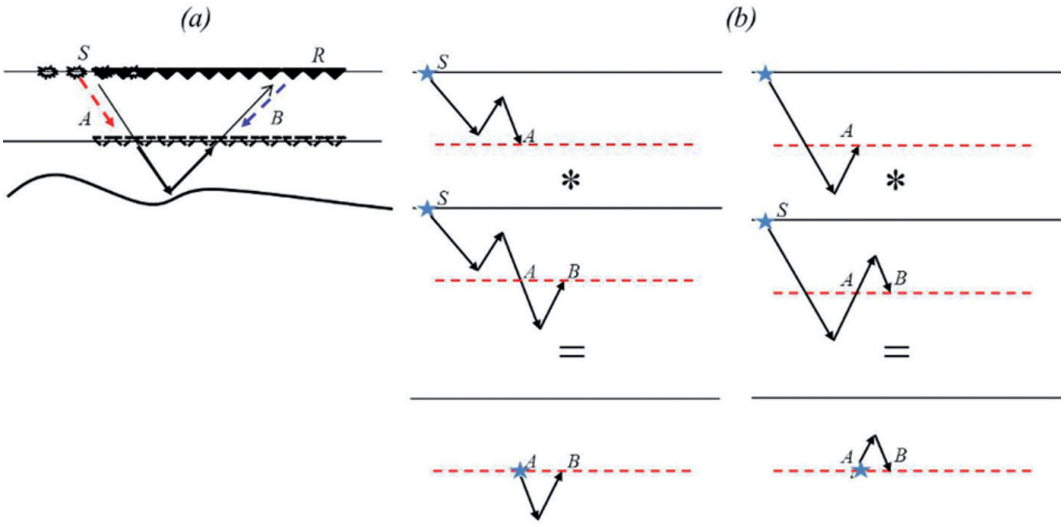


Fig. 1 – a) Scheme of the wavefields datuming. Red arrow: source datuming. Blue arrow: receivers datuming. b) Interferometric composition of different types of events. The dotted lines indicate the depth of the virtual receivers.

Note that in the example of Fig. 1a, $z_A = z_B$, even if all the following derivations also hold in the more general case of $z_A \neq z_B$. Moreover, in the following, with *d(y|x)* we indicate a wavefield recorded at *y* and generated by a source placed at *x* while with capital letters we indicate the same data after a Fourier transformation on the time axis for a selected temporal frequency (e.g. *D(y|x)*). We can the re-locate the data recorded by receivers at depth $z_B$ (receivers datuming) by means of a *backward-in-time* and *downward-in-space* wavefield extrapolation expressed by the following equation:

$$D(B|S) = \int \overline{W(B|R)} * D(R|S)\, dR \qquad (1)$$

where *R* indicates the zero-depth original receivers surface and *W(B|R)* is the Green's functions between each couple of points *R* and *B*. The over-line indicates the complex conjugation operation. The receivers datuming expressed in Eq. (1) is actually the backward-in-time receivers wavefield propagation implemented in the Reverse Time Migration (RTM) imaging algorithms.

Once *D(B|S)* is retrieved, we can proceed and re-locate also the sources (sources datuming). It is possible to perform this step by applying the following equation:

$$D(B|A) = \int D(B|S) * \overline{W(A|S)} dS \qquad (2)$$

where *W(A|S)* indicates the complex conjugate of the Green's function between all the points on the surfaces *S* and *A*. We can consider the Green's functions *W(A|S)* in Eq. (2) to be composed of two different terms: a linear scattered term (first-order Born scattering), $W_l(A|S)$, and a non-linear scattered component, $W_{nl}(A|S)$ (higher orders Born terms). Eq. (2) can thus be re-written as follows:

$$D(B|A) = \int D(B|S) * \overline{W_l(A|S)} dS + \int D(B|S) * \overline{W_{nl}(A|S)} dS \quad (3)$$

We can then express the datumed wavefield as follows:

$$D(B|A) = D_l(B|A) + D_{nl}(A|B) \quad (4)$$

$D_l(B|A)$ contains the primary reflections of the interfaces below the datum level as they would have been recorded with the new virtual acquisition geometry. $D_{nl}(B|A)$ contains the additional primary events retrieved by non-linear datuming with sources and receivers placed on the same datum surface. These events contain different information with respect to $D_l(B|A)$ because they have interacted with the subsurface discontinuities with different incidence angles. Moreover, the use of $D_{nl}(B|A)$ can increases the overall illumination. The linear component of the Green's functions can be obtained by using the smooth background velocity model while, in order to compute $W_{nl}(A|S)$ we need the detailed information of the subsurface discontinuities.

We can implement the source datuming expressed in Eq. (2) by means of an interferometric procedure using $D(A|S)$ in place of $W(A|S)$ (Schuster, 2010). The following equation relates these two quantities:

$$D(A|S) = F * W(A|S) \quad (5)$$

where $F$ indicates the Fourier spectrum of the seismic source. The field $D(A|S)$ is what is computed as the source wavefield in RTM by forward propagating the source impulse. The cross-correlation expressed in Eq. (2) can thus be implemented after substituting $W(A|S)$ with $D(A|S)$, leading to the following formula:

$$D(B|A) \approx \int D(B|S) * \overline{D(A|S)} dS \quad (6)$$

The only difference between Eqs. (2) and (6) is a multiplication of the retrieved signal by the source spectrum $F$. The additional multiplication by $F$, though, will not affect the kinematics of the reconstructed events. Using the approximation of Eq. (6) we have:

$$D(B|A) = \int D(B|S) * \overline{D_l(A|S)} dS + \int D(B|S) * \overline{D_{nl}(A|S)} dS \quad (7)$$

being $D_l(A|S)$ the wavefield composed of the first arrivals recorded at $A$ by a source impulse placed at $S$. $D_{nl}(A|S)$ contains the multiply scattered events generated by the same source in $S$ (see Fig. 1b).

**Internal multiples imaging.** In geological settings characterized by the presence of strong reflective interfaces (salt bodies, carbonates, etc…) we can expect to measure strong internal multiples. They can be generated by the downward bounce occurring, for instance, at the salt edges, either at the bottom of the saline formation or at its top. In a scenario like the one just described we expect to record the types of events that followed the paths drawn in Fig. 1b. If we place our datum level below the salt body and we perform the non-linear datuming procedure explained in the previous section, we reconstruct either up-going and down-going events. The second term in Eq. (4) corresponds to the events composition shown in the panels of Fig 1b. The figures show two examples for the case of, respectively, an intra-salt multiple and an internal multiple event generated by a downward bounce at the bottom of the salt (or more generally at an interface above the datum level). The primary events retrieved as in the left-hand-side panel of Fig. 1b give information about the subsurface region below the datum depth ($D_{nl}^{below}(B|A)$). On the contrary, events of the type of the right-hand-side panel of Fig. 1b, give information about the region above the new virtual acquisition surface ($D_{nl}^{above}(B|A)$). Before applying the interferometric primaries reconstruction shown in Fig. 1b we need to apply a wavefields separation procedure to separate the up-going and down-going components of the wavefield. In order to do so, we first re-locate the receivers at two different datuming surfaces and then we apply a separation technique similar to the one proposed by Neut *et al*. (2013).

**Examples.** For the following examples we used the 2D synthetic dataset Sigsbee2b. The Sigsbee2b dataset simulates a conventional marine experiment with a geology similar to those commonly found in the Gulf of Mexico environment, characterized by the presence of big salt bodies. The dataset, originally built for the purpose of testing multiples prediction algorithms, contains both surface related and internal multiple events. For the following tests, we extracted 219 CSGs (Common Shot Gathers) of the original dataset. The sources go from $xs = 6027$ m to $xs = 16000$ m and the receivers offset from 0m to 8000 m. Both sources and receivers are placed at zero-depth, at the interface between air and water.

Fig. 2 (left-hand-side panel) shows a close-up of the original stratigraphic model. In Fig. 2 (right-hand-side panel) it is possible to see the image generated by the migration of the of the new virtual datasets $D_{nl}^{below}(B|A)$ (see Fig. 1b). Sources and receivers $x$-coordinates are the same as the original dataset while the depth of the new acquisition surface is $z_{datum} = 5000$ m. The receivers datuming procedure has been performed using the (smooth) migration velocity model being the salt interfaces the only detailed information. As expected the main contribution of the non-linear term can be noticed beneath the salt body, where the strongest intra-salt multiples generate.

The panels on the top of Fig. 3 show another area of the Sigsbee2b stratigraphic model and the corresponding RTM image obtained from the original dataset. In order to test the effectiveness of the imaging of wavefields of the type $D_{nl}^{above}(B|A)$, we performed two different tests. We first modeled a seismic experiment generated with sources at depth $z = 0$ and the receivers placed at datum depth $z_{datum} = 5000$ m. For the FD modeling we used the Sigsbee2b stratigraphic model. Fig. 3 (bottom left panel) shows the result of the internal multiple migration: the yellow arrows point to those interfaces better imaged by the internal multiples with respect to the results of RTM fed with the original data. In a more realistic scenario, however, we have at our disposal only the data recorded at the surface. We thus retrieved $D_{nl}^{above}(B|A)$ by performing the receivers datuming pro-cedure explained in the previous sections, followed by the up/downgoing wavefield separation and the Interferometric sources datuming. The receivers datuming procedure was performed using the stratigraphic velocity model. Fig. 3 (bottom right panel) shows the results. Some of the interfaces are well imaged (bottom of the salt, seabed, etc...) and there are some little improvements with respect to the RTM image (the interfaces pointed by the red arrows in Fig. 3). However, compared with both the images in Fig. 3 (top right and bottom left) the results are worse, especially in the region near the side of the salt body and the additional information provided with respect to the RTM image is not so significant as for the previous case.

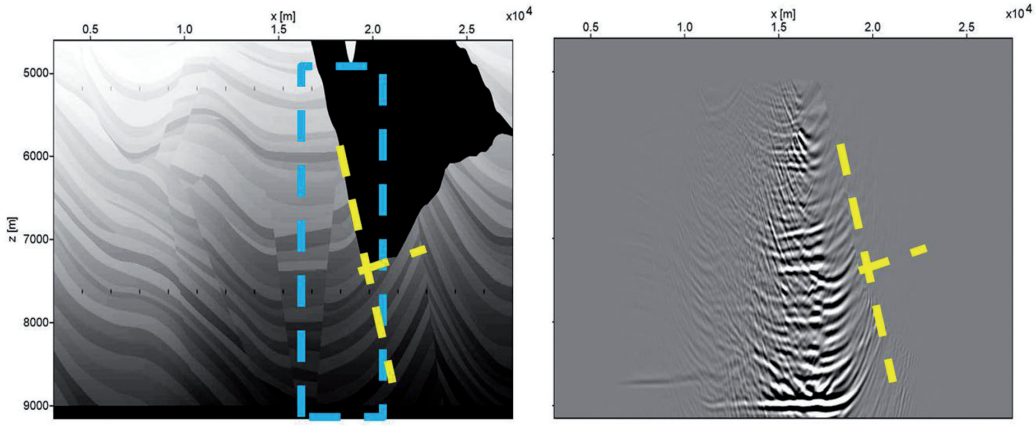


Fig. 2 – Left: Sigsbee2b stratigraphic model. Right: migration result of the intra-salt multiples. The blue box highlights the area where the internal multiples provide illumination. The illumination provided by the multiples can be useful to complement the image coming from a conventional migration.

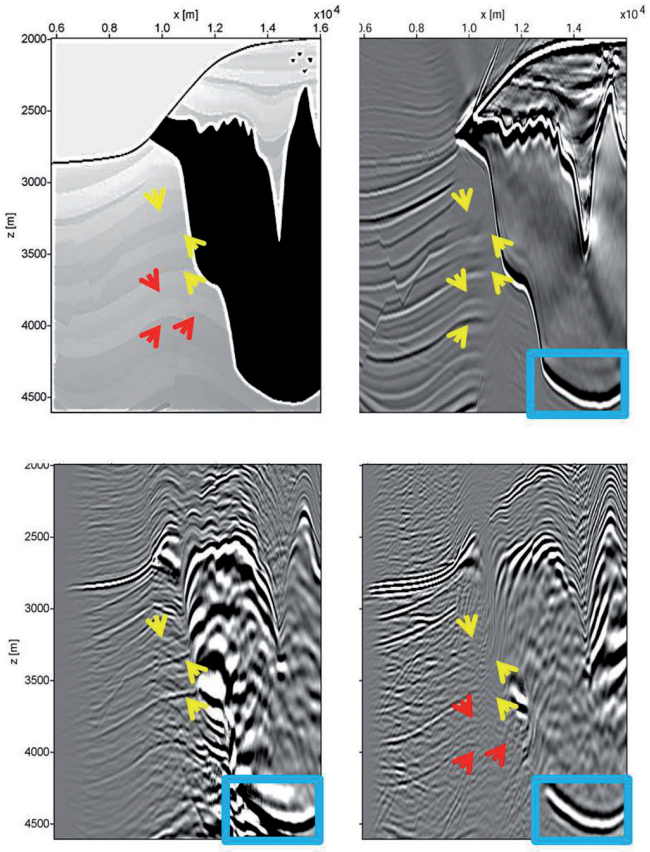


Fig. 3 – Top left: Sigsbee2b stratigraphic model and RTM image obtained from the original dataset (top right). The yellow arrows indicate some of the interfaces not well imaged by conventional RTM and that benefit from the migration of the downgoing internal multiples. Migration of $D_{nl}^{above}(B|A)$ by using data obtained with FD modeling (bottom left) and RTM receivers datuming (bottom right). The yellow and red arrows point to those interfaces better imaged by the multiples. The blue boxes highlight the bottom of the salt body.

**Final remarks.** We have shown here a technique able to exploit the multiply scattered events contained in the seismic recordings, proving that this kind of events can be a source of valuable information about the subsurface discontinuities. Moreover, we have also shown that these events can enhance the overall quality of the seismic image, providing additional information and illumination in those areas poorly imaged by conventional migration algorithms. In more realist scenarios, though, the information coming from the non linear component of the recorded wavefield can be little as shown in the last example of this paper. The last example also suggests that the deployment of acquisition devices into the subsurface can significantly improve the imaging of the subsurface.

**Acknowledgements.** The authors wish to the SMAART JV consortium for releasing the Sigsbee2b dataset.

## References

Alkhalifah, T., Zuberi, M.; 2011: *Imaging by Forward Propagating the Recorded Data - An Analysis*. 73rd EAGE Conference & Exhibition incorporating SPE EUROPEC 2011 Vienna, Austria, 23-26 May 2011

Berkhout, A.J., Vershuur, E.; 2006: *Imaging of multiple reflections*. Geophysics, 71, no. 4, SI209-SI220.

Berryhill, J., 1979, *Wave-equation datuming*: Geophysics, 44, 1329–1344.

Berryhill, J., 1984, *Wave-equation datuming before stack*: Geophysics, 49, 2064–2066.

Fleury, C., 2013, *Increasing illumination and sensitivity of reverse-time migration with internal multiples*: Geophysical Prospecting, 61.

Guitton, A.; 2002: *Shot-profile migration of multiple reflections*. Stanford Exploration Project, Report 111.

Lipari, V., Fortini, C., Spadavecchia, E., Bienati, N.; 2012: *Prediction of surface-related and inter-bed multiples via Kirchhoff extrapolation*. Istanbul 2012 - International Geophysical Conference and Oil & Gas Exhibition: pp. 1-4.

Liu, W., and F. Xu, 2011, *Wave-equation global datuming*: SEG Technical Program Expanded Abstracts 2011.

Malcolm, A. E., B. Ursin, and M. V. de Hoop, 2009, *Seismic imaging and illumination with internal multiples*: Geophysical Journal International, 176, 847–864.

Muijs, R., Robertsson, J. O. A., Holliger, K.; 2007: *Prestack depth migration of primary and surface-related multiple reflections: Part I – Imaging*. Geophysics 72, S59-S69.

Neut, J., A. Bakulin, S. Aramco, and D. Alexandrov, 2013, *Acoustic wavefield separation using horizontal receiver arrays deployed at multiple depths on land*: SEG Technical Program Expanded Abstracts 2013, 4601–4607.

Ravasi, M., and A. Curtis, 2013, *Nonlinear scattering based imaging in elastic media: theory, theorems and imaging conditions*: GEOPHYSICS, 78.

Schuster, G. T., 2010, *Seismic interferometry*: Cambridge University Press.

Vasconcelos, I. Snieder, R., and B. Hornby, 2008, *Imaging internal multiples from subsalt vsp data examples of target-oriented interferometry*: GEOPHYSICS, 73.

Verschuur, E., Berkhout, A.J., Wapenaar, C.P.A.; 1992: *Adaptive surface-related multiple elimination*. Geophysics 57, 1166-1177.

Verschuur, E.; 2006: *Seismic multiple removal techniques - past, present and future*. EAGE publications, ISBN 90-73781-51-5.

## ACQUISITION OF GEOPHYSICAL DATA IN SHALLOW-WATER ENVIRONMENTS USING AUTONOMOUS VEHICLES: STATE OF THE ART, PERSPECTIVES AND CASE HISTORIES

**L. Gasperini[1], F. Del Bianco[2], G. Stanghellini[1], F. Priore[3]**

*[1] ISMAR, Istituto di Scienze Marine, U.O. Geologia Marina, CNR, Bologna, Italy*

*[2] Consorzio Proambiente, Bologna, Italy*

*[3] Dip. di Fisica e Scienze della Terra "Macedonio Melloni", Università degli Studi di Parma, Italy*

**Introduction.** We present some examples of geophysical data acquisition carried out in different shallow-water environments, including a lake, a coastal lagoon an artificial channel and a river stream, by means of an Unmanned Surface Vehicle (USV) equipped with geophysical sensors that were designed and built for the purpose. First tests indicate that these technologies and methods can be employed to collect densely-spaced grids of high-resolution data, quickly, efficiently, and at a very low-cost, allowing for execution of repeated surveys even in those area not accessible through conventional systems. The intensive use of "open" technologies and software packages for data acquisition and processing has the potential of widening the application of these methods to an increasing audience of earth scientist that study geological processes in these rapidly evolving environments.

A number of underwater natural or artificial environments, including harbours, coastal areas, river streams, natural and artificial lakes, and coastal lagoons, are particularly affected by anthropic pressures. For this reason, they would require periodical monitoring to evaluate whether they are in a state of "equilibrium" from the geo-biological point of view. In fact, it is rather common that unbalances in environmental variables, caused by either human activity or natural process, could produce dramatic crises.

To date, geo-environmental studies of shallow-water environments are not a consolidated practice, because they require a multidisciplinary knowledge and special instruments. Furthermore, the high costs of such complex technologies and methods are out of the budgets of local environmental protection agencies or private consulting enterprises. As a result, such "transitional" zone between the underwater environment and the "onshore" is poorly investigated through geophysical techniques, that most often represent the basis of each geo-environmental study. This lacking is due to several causes, including: 1) shallow-water environments are difficultly accessed by conventional vehicles such as small boats; 2) the narrow water-column constitute an efficient waveguide for acoustic and ultrasonic signals, and limit their penetration

in the substratum; 3) the shallow-water enhances the effect of noise due to propellers or other natural and artificial causes.

However, the economic and societal importance of such environments call for the development of new technologies and scientific methods that could open their study to a wider spectrum of users, on one side simplifying and better standardizing the survey procedures; on the other side, reducing the costs.

The ongoing research and developments in the field of robotics could represent an interesting opportunity. In fact, the relatively recent availability of miniaturized although accurate sensors, such as gyroscopes, GPS receivers, compass, motion sensors, etc., as well as innovative "open" hardware architectures (*Arduino*, *Raspberry*, etc.) facilitate the design and the development of Unmanned Surface Vehicles (USV), that could operate in extremely shallow, difficultly accessed environments, such as small rivers, channels, lakes and coastal lagoons. This is the case of SWAP (Shallow-WAter Prospector) developed by ISMAR-CNR and Consorzio Proambiente (Tecnopoli dell'Emilia Romagna) a small, highly flexible vehicle that could be employed in a variety of subaqueous environments. Parallel to the development of the USV, it is also important to test new methods and instruments for the geophysical prospection in such a peculiar conditions, which could be employed on board small-size platforms.

We present some example of geophysical surveys carried out with different instruments and techniques in shallow water environments, including a coastal lagoon, a river stream, an artificial channel and a lake.

**Methods.** *The Unmanned Surface Vehicle*. SWAP (Fig. 1) is an USV based on a trimaran framework, i.e., a multihulled boat consisting of a main hull and two smaller outrigger hulls, attached to the main hull with lateral bars.

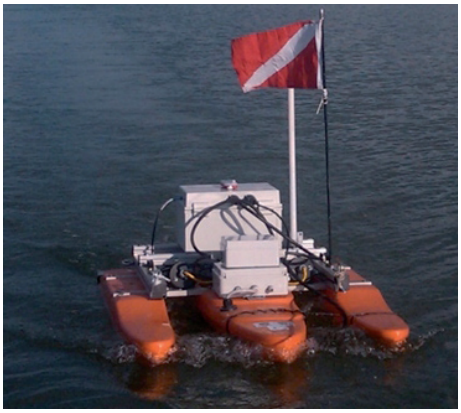

Fig. 1 – The Unmanned Surface Vehicle SWAP (Shallow-Water Prospector), designed and built at ISMAR-CNR in cooperation with Consorzio Proambiente (Tecnopoli dell'Emilia Romagna).

The main hulls hosts the batteries, that supply two brushless engines, controlled by a hybrid speed controller driven by an *Arduino Due* board. The maximum speed reached by SWAP is 3.5-4 knots during a test session carried out in a small lake. Quality check of the data is obtained via sub-sampling of the collected time-series, which are packed and transmitted to a host computer onshore through radio transmission. Although the architecture of the system is modular and could be easily expanded to other USB-based digital sensors, three basic devices were installed on each prototypes: 1) a DGPS receiver; 2) a high-resolution single beam echosounder; and 3) a chirp-sonar subbottom profiler. These are considered "basic sensors" that will be likely employed in most of the survey carried out in shallow-water areas. The vehicle is equipped with a differential GPS system that provide and accuracy of < 1 m in the x-y positioning. NMEA-183 format strings are transmitted to the host computer onshore to monitor continuously the position of the vehicle and errors in the execution of the mission-related profiles. A HMC5883L magnetometer, an ADXL345 accelerometer, and a ITG3200 gyroscope, interfaced to the ARDUINO-DUE board constitute the basic system for inertial navigation and correction of geophysical data for pitch, roll, heave and heading.

*Geophysical sensors*. Ecosounder. A vertical incidence 200 kHz pinger has been mounted onboard of SWAP. Such sensor is particularly suitable for shallow-water environments because is characterized by high operating frequency, narrow beam width (8°, conical), a short pulse length (350 $\mu$s). This configuration lead to a minimum depth range around 0.5 m. However,

since our target is shallow and ultra-shallow waters, we are able to control the echosounder pulse length from 50 to 500 $\mu$s via software. This would widen the use of the system to both shallow and ultra-shallow environments and to deeper areas, such as the coastal zones. Moreover, we implemented a robust bottom detection/depth of the echographic signal [see Gasperini (2005) for further details]. In this way, the shallow-depth limit was reduced to 0.1 m. In order to carry out estimates on the seafloor reflectivity, the echosounder signal is sampled with constant time windows, and the data (the echograms) stored in SEG-Y format (Barry *et al*., 1995) files using a specific acquisition system based on a *Raspberry-Pi* board.

Subbottom Profiler. A typical chirp-sonar subbottom profiling (SBP) system, operating with standard magnetostrictive transducers, at high-voltage (hundreds to thousands of volts) is not suitable for operating on board of SWAP, either for the heavy weight of the transducers and for the power consumption. For this reason, we developed an innovative SBP system based on electromagnetic resonators (*$\mu$Chirp,* ISMAR-CNR) that show interesting performances in the shallow-water environment, and, due to its lightweight, it is easily installed on the vehicle. The system is composed by: 1) a digital generator of frequency-modulated signals based on an *Arduino Due* board; 2) a 600W RMS power amplifier; 3) an array of waterproof magnetic resonators composed of four 4Ω MONACOR transducers; 4) an acquisition system based on a hydrophone array, a signal amplifier, and an *Arduino Due* board used as analog-to-digital-converter (ADC). A *Raspberry-Pi* is employed to store the digital data in SEG-Y format on a SD memory card.

Side-Scan Sonar. We employed a Starfish 450F Side-Scan sonar system, interfaced to a PC board trough an USB port. The system is powered by a 450 kHz CHIRP transmission, to provide a wide range sonar coverage up to 100 m per channel (200 m total swathe) with good, clear image definition.

All data, including echograms, seismic lines and side-scan sonar records were converted processed and interpreted using the open-source package SeisPrho (Gasperini and Stanghellini, 2009).

**Case studies.** *The Valli di Comacchio Coastal Lagoon*. The Valli di Comacchio coastal lagoons are shallow, brackish water environments connected to the Adriatic Sea, which extends south of the Po river between Comacchio and the Reno River. These lagoons (Valli) formed around the tenth Century as a consequence of subsidence and were originally fresh water basins supplied by river floods (Bondesan, 1986). The hydrodynamics of the Valli di Comacchio is controlled by the inflow of freshwater from several sources, but the tidal cycle is a major controlling factor on water circulation in the lagoon, causing water-depth excursions of over 1 m. Because the average depth of the Valli is < 2 m, most of the lagoon areas are not accessible to geophysical surveys performed using conventional vehicles. For this reason, we carried out a combined high-resolution seismic reflection and morphobathymetric survey of the lagoon using the chirp-sonar system and the 200 kHz echosounder mounted onboard of SWAP. The acquisition of the entire echosounder sweep at each sounding point, rather than the simple depth estimate, gave us the opportunity to calculate the bottom reflectivity. Propagation and scattering of high frequency acoustic sound at or near the bottom is controlled by a number of factors, including biological, geological, biogeochemical and hydrodynamic processes operating at the benthic boundary layer (Richardson and Briggs, 1996). However, experimental measurements of compressional wave attenuation suggest that the single most important geotechnical property related to acoustic attenuation is the mean grain size of the insonified sediment (e.g., Shumway, 1960; McCann and McCann, 1969, 1985; Dunlop, 1992). Moreover, a quantitative ground-thruting of relationships between floor reflectivity and mean grain size has been carried out in Valle Fattibello, N of the main lagoon (Gasperini, 2005). Using the reflectivity pattern calculated at each surveyed point of the lagoon floor enabled us to map the distribution of sediments in the Valli di Comacchio lagoon. We note a different distribution of sediments E and W of the Poscoforte Peninsula, that cuts in the N-S direction the lagoon. This could be due to the fact that

water (and sediment) inputs are localized mainly in the W sector of the Valli di Comacchio, and that the peninsula could act as a sill for sediment supply. Moreover, the W part of the lagoon, close to the Adriatic shoreline, is probably supplied probably by aeolian deposits from the coast, which are sheltered by the presence of the peninsula. If this hypothesis is correct, while in the E side the limited circulation could cause anoxia or hypoxia due to the limited water circulation, the W part is more prone to overfeeding of sediment, that could eventually alter the hydrological and ecological equilibrium the lagoon. We note how relatively basic geophysical surveys could give interesting insights for understanding the complex geological processes regulating the equilibrium of such sensitive environments.

*The Lake Trasimeno***.** Lake Trasimeno is located in the Umbria Region of Central Italy is the broadest lake of Central Italy. The extremely low depths, the flat bottom morphology, and the absence of natural outflows and dams along its shorelines caused wide lake-level oscillations and periodical floods since ancient times, only partially attenuated by creation of an artificial outflows. Lake Trasimeno is an interesting geological site for the its peculiar formation (Cattuto and Gregori, 1993), and for the sedimentary succession found below its floor, which records the deformation history of this portion of the Central Apennine since the late Pliocene (Bortoluzzi *et al*., 2005; Gasperini *et al*., 2010). Due to its location, the lake area has been a natural crossroad since proto-historical times. Several Neolithic settlements were found along the lake shores (Moroni Lanfredini, 2003) and important historical events took place in the vicinity of the lake, such as the famous Trasimeno battle (217 B.C.), when the Romans were defeated by the Hannibal's army during the Second Punic War (Brizzi and Gambini, 2007). For this reason, the Lake Trasimeno area is an important archeological/historical site, and was surveyed using different geophysical techniques including a close spaced grid of high resolution seismic reflection lines (Gasperini *et al*., 2009). However, some sectors of the lake, close to the N shore, too shallow to be accessible using conventional vehicles, were surveyed using SWAP. Prior the survey, to test the quality of the data collected by the chirp-sonar mounted onboard of the USV, we performed a comparison with an industry standard chirp-sonar system, the Teledyne Benthos Chirp-III. Result of this benchmark is reported in Fig. 2, where the shallowest part (first 15-20 msec TWT) of the Trasimeno sedimentary sequence is imaged with similar vertical resolutions and penetration by both seismic reflection systems.

*The Cavo Napoleonico artificial channel*. The *Cavo Napoleonico* an artificial channel connecting the Po and the Reno rivers in the Po plain. The channel is oriented perpendicularly to the thrust-and-fold belt, named *Pieghe Ferraresi*, falling in the area undergoing the maximum superficial deformation after the earthquake. For this reason, it is the site of geophysical data acquisition, to image the surface and the subsurface in search for coseismic deformation of the 2012 Emilia earthquakes and seismogenic structures at depth (Priore *et al*., 2013). Among other data acquisition, we carried out a side-scan sonar survey of the channel using a Strarfish SSS system in search of possible earthquake-related structures, such as fractures, fissures or sediment fluidization. First analysis of side-scan sonar mosaics, combined with results of high-resolution seismic reflection survey indicate a correlation between channel-floor disturbances maximum co-seismic deformation. In particular, we observe the presence of such features in correspondence of paleo-channel incisions imaged by chirp-sonar seismic sections, in agreement with observations carried out on land.

*The Reno River.* Reno is the river that forms a wide alluvial fan on which the western edge of the town of Bologna (Central Italy), lays. In such part of its course, the river is particularly prone to periodical flows, close to the connection between the alluvial plain (the southern Po plain) and the Apennines. For this reason, the regime of the river has been artificially regulated since the Roman times and the Middle Age (Barbieri, 2003). We investigated a segment of the river stream close to a major bridge, the *Pontelungo* bridge, whose piers are affected by base erosion. A bathymetric and a reflectivity map (Fig. 3) were compiled using data collected by a 200 kHz echosounder onboard of SWAP. These maps highlight the presence of a deep

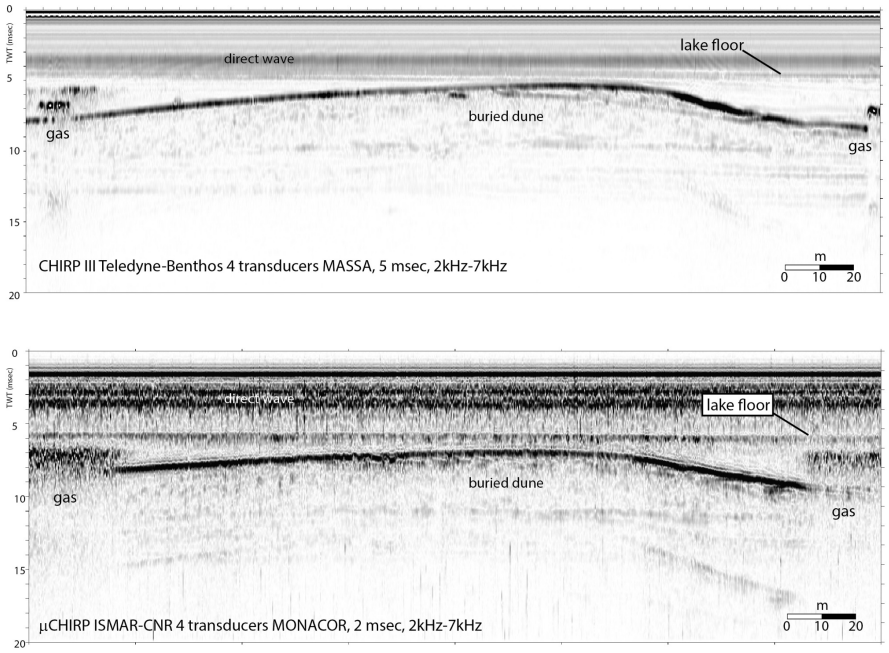


Fig. 2 – Example of seismic reflection profiles collected with two different systems (Chirp III Teledyne-Benthos, Top; ISMAR-CNR µChirp, Bottom) along the same track in Lake Trasimeno. We note that lake deposits are penetrated down to 15-20 msec below the lake floor, with high vertical resolution (tens of cm) that enable us to analyze the fine details of the sedimentary structure.

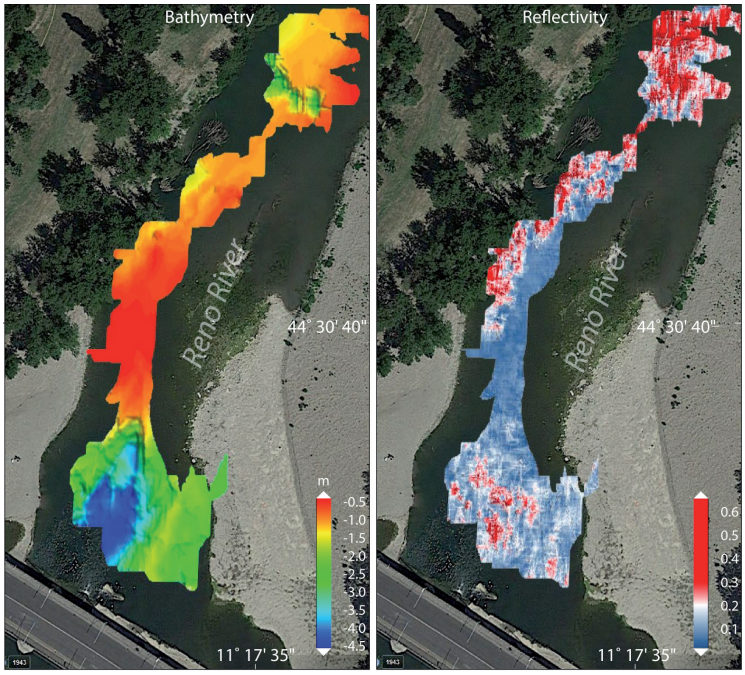


Fig. 3 – Left: morphobathymetric map of the Reno River segment immediately N of the *Pontelungo* bridge (Bologna); blue color indicate maximum depth. We note the presence of a large depression aligned along the river course at the base of the bridge. Right: normalized reflectivity of the river floor obtained by the analysis of the 200 kHz reflected signal. Red colors indicate high reflectivity.

depression (up to 4-5 m of depth) close to the bridge piers, that is probably due to active erosion. We note that areas of prevailing erosion, such as the wide depression immediately N of the bridge, and the external flank of the meandering river towards N, are marked by high-reflectivity patterns, suggesting that this parameter could be useful to study erosional processes in such environments.

**Future Improvements.** The geophysical instruments payload presently installed onboard of SWAP is not exhaustive of all possible geological processes that could be eventually analyzed in shallow-water areas. In fact, the possibility of installing onboard of SWAP other instruments, such as multibeam echosounders or electromagnetic devices (Ground-Penetrating Radars, Magnetometers, Resistivity-meters, etc.) could represent a dramatic improvement in data collection potential. The peculiar design of the hull is suitable for installing ADCP current-meters, that find a wide range of application in hydraulic and physical oceanographic studies. Furthermore, some basic chemical sensors, such as oxygen, nitrates, PH, etc., now available in small and light containers, could represent interesting payloads to carry out rapid assessment of the surface water quality.

**Conclusion.** We presented some case studies of geophysical surveys carried out in different shallow-water environments using an Unmanned Surface Vehicle (USV). The possibility of carrying out such kind of surveys quickly, and at a fraction of the cost of conventional surveys, opens the use of these techniques to a wide range of users. Moreover, it allows planning repeated surveys that could give a time-variant perspective to the study of natural process in these rapidly evolving environments.

**Acknowledgments.** Most figures were compiled using GMT software package (Wessel and Smith, 1991). Part of this work was supported by Consorzio Proambiente, Tecopoli dell'Emilia Romagna.

**References**

Barbieri M., 2003. Brevi note storico-geografiche sul Reno, in BARBIERI Magda (a cura di), *Reno, campi e uomini, Rivista periodica della pianura*, Anno I, n. 1, giugno-dicembre 2003, www.pianurareno.org

Barry, K.M., Cavers, D.A. and Kneale, C.W., 1975, Recommended standards for digital tape formats. Geophysics, **40**, 244-352.

Bortoluzzi, G., Gasperini, L., Bellucci, L.G., Ligi, M., 2005. Ricerche Geofisiche nel Lago Trasimeno, ISMAR-CNR Bologna, Rapporto Tecnico N.97, Novembre 2005, Bologna, pp.49.

Bondesan, M., Favero, V. and Vignals, M.J., 1995, New evidence on the evolution of the Po-delta coastal plain during the Holocene, *Quaternary International*, **29/30**, 105-110.

Brizzi G., Gambini E., 2007. Di nuovo sulla battaglia del Trasimeno qualche ulteriore considerazione. Rivista storica dell'antichità, ISSN 0300-340X, Nº. 37, 77-100.

Cattuto, C., Gregori L., 1993. Origine ed evoluzione del Lago Trasimeno. *Conferenza Auditorium Urban*i. 15 Marzo (Assessorato della cultura - Passignano S.T. Università degli Studi di Perugia).

Dunlop, J.I., 1992, Measurement of acoustic attenuation in marine sediments by impedance tube, *Jour. Acoust. Soc. Am.*, **91**, 460–469.

Gasperini L., 2005. Extremely Shallow-Water Morphobathymetric Surveys: The Valle Fattibello (Comacchio, Italy) Testcase. *Marine Geophysical Researches*, p.26:97-107, 2005.

Gasperini L. and Stanghellini G., 2009 - SeisPrho: an interactive computer program for processing and interpretation of high-resolution seismic reflection profiles, *Computers and Geosciences*, 35,1497-1504.

Gasperini L., 2009 Il rilievo Geofisico-Geologico del Lago Trasimeno (F. 310 Passignano sul Trasimeno) Mem. Descr. Carta Geol. d'It. LXXXVIII (2009), pp. 57 - 60

Haynes, R., Huws, D.G., Davis, A.M., Bennell, J.D., 1997, Geophysical sea-floor sensing in a carbonate sediment regime, *Geo-Marine Letters*, **17**, 253-259.

McCann, C. and McCann, D.M., 1969, The attenuation of compressional waves in marine sediments, Geophysics, **34**, 882-892.

McCann, C. and McCann, D.M., 1985, A theory of compressional wave attenuation in noncohesive sediments, *Geophysics*, **50**, 1311–1317.

Moroni Lanfredini, A. 2003. Il neolitico antico sul lago Trasimeno : il sito di Panicarola (la Lucciola) : l'industria litica. in: Rassegna di archeologia. A, Preistorica e protostorica. Firenze : All'insegna del giglio, c2002- 20A (2003), p. [87]-118

Priore F., Dal Passo E., Del Bianco F., Gallerani A., Stanghellini G., Gasperini L., 2013. Technical Report on the Seismostratigraphic survey of the Cavo Napoleonico, across the epicenter of the 2012 Emilia earthquake-Rapporto Tecnico N.105, Novembre 2005, Bologna, pp.49. Bologna, June 2013.

Richardson, M.D. and Briggs, K.B., 1996, In situ and laboratory geoacoustic measurements in soft mud and hard-packed sand sediments: implications for high-frequency acoustic propagation and scattering, *Geo-Marine Letters*, **16**, 196-203.

Shumway, G., 1960, Sound speed and absorption studies of marine sediments by a resonance method, *Geophysics*, **25**, 451-467.

Wessel, P., and Smith W.H.F., 1991, Free software helps map and display data, *EOS Trans. **Amer. Geophys. U.***, 72, **41**, 445-446.

## WED EQUATION DATUMING APPLIED TO CRUSTAL LAND DATA: REPROCESSING OF CROP PROFILES ACROSS THE GEOTHERMAL PROVINCE OF TUSCANY

**M. Giustiniani[1], U. Tinivella[1], R. Nicolich[2]**

*[1] OGS - Istituto Nazionale di Oceanografia e di Geofisica Sperimentale, Trieste, Italy*

*[2] Dip. Ingegneria e Architettura, Università di Trieste, Italy*

**Introduction.** Reflection seismic profiles, programmed within the Italian CROP (CROsta Profonda) project for the investigation of the deep crust, where acquired across the two main structural domes and geothermal fields of Larderello and Mt. Amiata during 1993-1995.

The transect CROP-18, split into two lines, identified as CROP 18-A and CROP 18-B, was designed to study the continuity of crustal structures from the Larderello to the Mt. Amiata areas, following a NW-SE direction roughly parallel to the Apennine structural trends. CROP-03 was recorded across the Northern Apennine Arc, with nearly E-W direction, from Tyrrhenian to the Adriatic Seas. The profiles allowed exploring the crust to understand the origin of the main heath flow anomalies, looking also for hidden resources and new exploitable geothermal reservoirs (i.e., Della Vedova *et al*., 2008).

The first processing of these lines was focused on illuminating the deep crustal features (Accaino *et al*., 2005, 2006), starting from the major reflector that characterizes the geothermal fields, the K-horizon, based on previous seismic surveys (Batini *et al*., 1978; Liotta *et al*., 1998; Brogi *et al*., 2003, 2005).

On the contrary, our purpose was to reprocess the first 4 s reflection times (6 s for the profile CROP-03), with the aim of better highlighting the upper crust and getting images directly comparable with the drilling information and the industrial seismic profiles, which are of limited extension and designed to inspect specific objectives (Cameli *et al*., 1993, 2000).

In order to reach the above-mentioned goals, we applied advanced techniques improving signal/noise ratio and extracting information previously hidden by approximate static corrections and near surface noise. In fact, the seismic acquisition did not included techniques to better resolve the shallow subsurface, such as down-hole velocity measurements or refraction profiles, and the group distance of 60 m was chosen to detect reflected energy from deep interfaces ignoring the near surface complexities. Moreover, near surface high-velocity formations, alternate to sub-basins filled with Neogene and Quaternary deposits, did not favor the penetration and the focusing of the seismic energy.

Surprisingly, in contrast with the non-reflective and dispersive, or not resolved upper highly deformed nappes, the area turns out to be characterized by the occurrence of high amplitude reflecting horizons with good lateral continuity in the deeper parts. The reflectivity was attributed by several authors to the degree of metamorphism and to thermal alterations. The origin of possible presence of fluids is still debated and it can be of great importance for the recovery of geothermal fluids of industrial interest.

In this study, we have applied the wave equation datuming (WED) technique to remove the effects of topography, the near surface velocity variations and source generated noise on seismic data, moving shots and receivers to a given datum plane. Moreover, WED has contributed to attenuate ground roll, enhance higher frequencies, increase the resolution and improve the signal/noise ratio. After WED, the sections were completed with standard processing steps, such as predictive- and fx-deconvolution, trimmed mean-dynamic filtering and post-stack time migration.

**The re-processing of the CROP seismic data.** The transect CROP-18A&B was acquired in 1995, mostly along strike of the Apennine structural trends. The total length of the reprocessed part is 123 km subdivided in two lines: CROP-18A long 48 km and CROP-18B with 74 km. CROP-03 was recorded in 1993; we processed of this profile only the Tuscany segment crossing the Inner Northern Apennines domain with a length of 63 km, from the Tyrrhenian Sea to the town of Pienza. The main acquisition parameters are reported, for example, in Accaino *et al*. (2005).

The first step of the re-processing consisted of picking all first arrivals. Thetomographic inversion of first breaks, by an iterative method of ray-tracing and travel times calculations, created a near surface velocity model for the upper sequences, where significant complexities in the structural setting characterised by variable lithologies and velocities are present.

To perform the inversion, an initial model was built with square cells 30 m wide, corresponding to half receivers distance. We adopted the commercial software TomoPlus® (GeoTomo LLC: www.geotomo.com), which is based on the minimization of the difference between calculated and observed travel times. The forward ray-tracing modeling was carried out attaining the final representation after 50 iterations. This first output was re-entered in the tomography process as a new initial model, submitted again to 25 iterations before the final result.

A pre-processing was applied to the seismic data to increase the signal to noise ratio with amplitude recovery and to balance the shot and receivers responses. The trace editing removed the noisy parts. Then, we proceeded with the wave equation datuming application in order to move all shots and receivers at the same surface, removing time shifts related to topography and near-surface velocity variations, and to improve the signal/noise ratio. The Kirchhoff integral solution to the scalar wave equation [using both near-field and far-field terms; Berryhill (1979, 1984)] can provide a basis computation to deal with irregular surfaces (Wiggins, 1984; Bevc, 1997) and variable velocities. In the pre-stack domain, WED is applied in two steps: (i) common-source and (ii) common-receiver domains. Operating on a common-source gather has the effect of extrapolating the receivers from one datum to another, and, because of reciprocity, operating on a common-receiver gather changes the datum of the source.

Recalling the main principles of the theory, it is important to distinguish between migration and WED (e.g., Barison *et al*., 2011). Migration involves computing the wave-field at all depths from the wave-field at the surface, i.e. it can be intuitively explained as a succession of downward continuation steps, with the elevation moving ever deeper into the sub-surface. In addition to downward continuation, migration requires imaging principle. WED produces an unmigrated time section at a specified datum plane (Yilmaz and Lucas, 1986). In this respect, WED is an ingredient of migration, when migration is applied as a downward-continuation process. Basically, WED is the process of upward or downward continuation of the wave-field between two arbitrarily-shaped surfaces. For details, see Barison *et al*. (2011) and references therein.

The application of WED requires a regular geometry, i.e., constant distance (equal to 60 m in our case) between receivers in each common shot gather and constant distance (equal to 120 m) between shots in each common receiver gather. So, we added shots with zero traces and the missed traces near the shots by developing home codes. For CROP-18A and CROP-18B, the chosen datum was equal to 0 m.s.l., while for CROP-03 the chosen datum was equal -50 m b.s.l., because the elevations of the shots charges were below 0 m.s.l. in the proximity of the coastline.

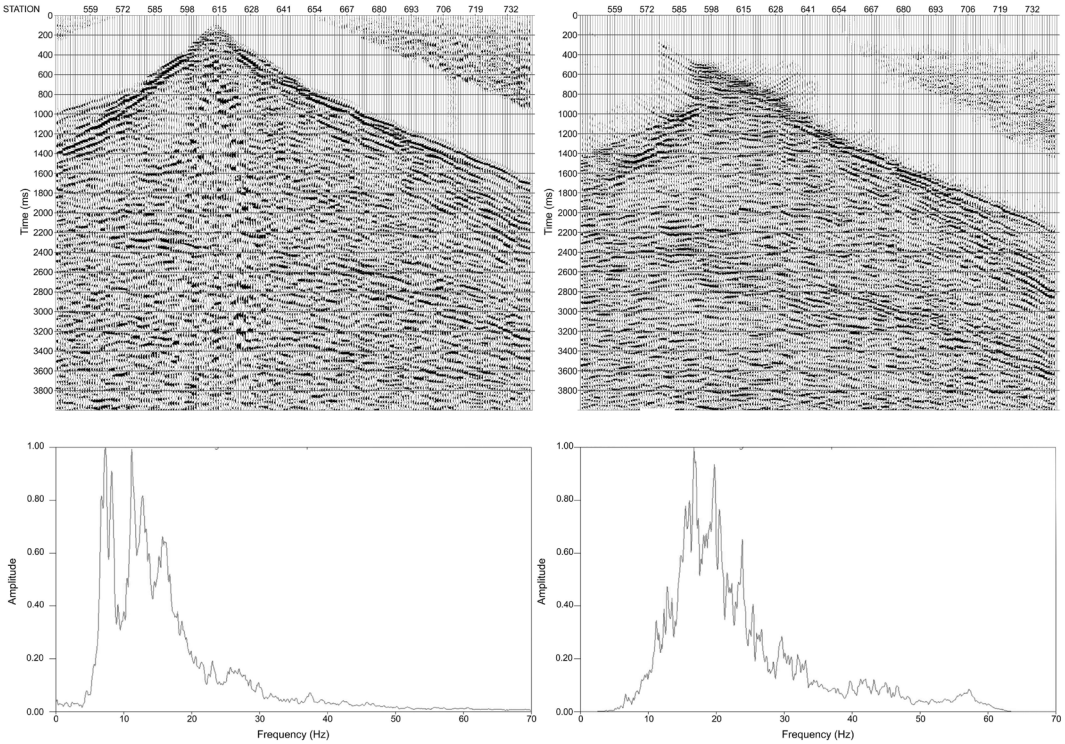


Fig. 1 – Shot gather from the line CROP-18A and its amplitude spectrum computed in the time window of 3800 ms: before (left) and after WED (right). The time shift of 500 ms (right) was applied before WED computation to preserve the data. The smiles in proximity of the source point are due to WED migration and were muted before stack.

In fact, as mentioned before, WED is the process of upward or downward continuation and the datum surface must be totally below or above the topography.

WED was carried out using Seismic Unix package (SU), free software developed at the Colorado School of Mines and home codes which were developed to integrate SU. The code (written by Salinas and based on Liu (1995)) adopts a far field approximation of the original formula formulated by Berryhill for post-stack and pre-stack corrections (Berryhill, 1984). The velocity field used to evaluate the travel time table was the tomographic velocity; the datuming aperture was considered equal to 3500 m. It is worth to mention that heavy computations are called for WED application and long-lasting times are required by using PC based work stations.

After WED, the zero traces introduced to have a regular distance between receivers and shots were removed.

The rapid variation of the topography and velocity in the CROP-18B was a problem in order to complete WED along the whole line. In a part of the line, the problems were mainly related to ray tracing computation that miss. In fact, in several common shot and receiver gathers the topography variation is too steep to be modeled and we carried out several tests in order to avoid these errors. For example, we designed a floating datum instead of a flat datum, we smoothed the velocities and the recording surface, but the ray tracing miss still remained. Finally, we considered each trace as a common shot and receiver gather constituted by a single receiver and shot, respectively. The result was a re-datuming supposing a narrow aperture.

A shot gather and its amplitude spectrum extracted along the CROP-18A is shown in Fig. 1 in order to demonstrate that WED enhances higher frequencies, increasing resolution, and improves the signal/noise ratio.

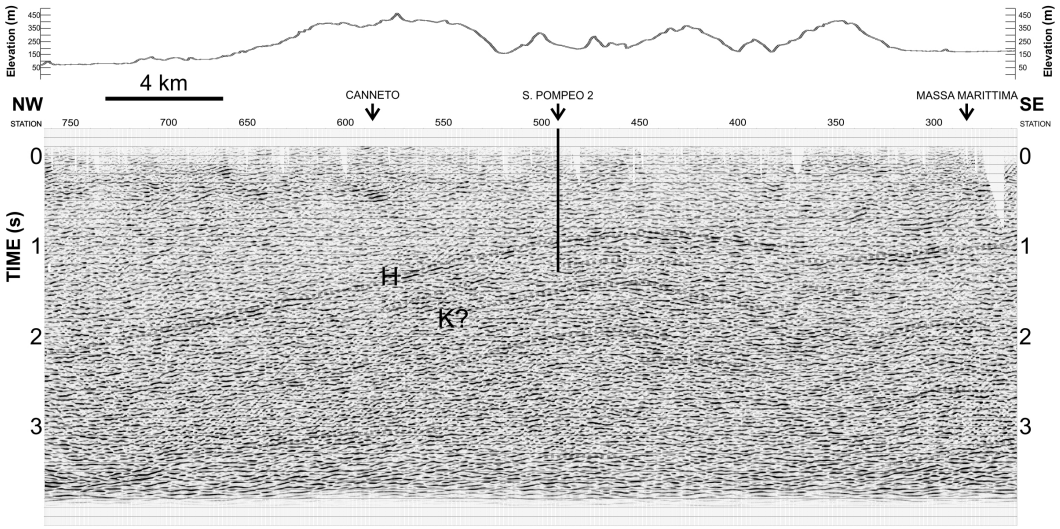


Fig. 2 – Part of the CROP-18A post-stack time-migrated section. Interpreted reflections are highlighted by gray dotted lines. The well S. Pompeo-2 indicates the position of the H horizon at about 1 s TWT (after Batini *et al*., 1983). It can be followed almost over the whole section. The datum plane is fixed at the sea-level for all the sections given in the paper.

After the datuming we applied a gapdeconvolution on CROP-18A and -18B with an operator length of 140 ms and a lag of 12 ms. On CROP-03, an operator length of 70 ms, lag of 4 ms, was used in the window from 0 to 1600 ms TWT, and an operator length of 160 ms, lag of 12 ms, in the window from 1600 to 6500 ms TWT.

We applied a trimmed mean-dynamic filter and fx-deconvolution on the CROP-03 and CROP-18B data. After sorting the data in CDP gather, we interactively performed the velocity analysis for dynamic corrections and residual statics applications. We applied a time-variant filter and a time-variant trace mixing for enhancing identified signals, defining a lateral window of 5 traces weighted by a symmetrical weighting function towards the central trace on the stacked data. At the end, a post-stack Kirchoff time migration was applied for all seismic lines, smoothing and reducing stacking velocities and limiting the aperture.

**Results and discussion.** Our study points out that the application of advanced techniques allows obtaining better seismic images, also for old data.

The presence in the upper crust of more horizons with large difference in acoustic impedance (high reflectivity) is confirmed in all the seismic sections. These reflections are sometimes bright as the previously recognized K-horizon, considered as the principal marker of the investigated area. The new images set give constraints to more precise interpretation procedures of the underground structures. The length of the profiles will help in the construction of new geological models of the geothermal province. In the following part, we present the sections to which an overly has been added to underline the continuity of the main reflecting markers adding transparency and leaving visible the seismic data in the background.

Part of CROP-18A migrated profile is presented as example in Fig. 2. The profile shows a rather continuous horizon, which we marked with dots from Massa Marittima, at around 1 s TWT, to the NW-termination where it reaches 2.2 s. It corresponds to the H-horizon, drilled by the well S. Pompeo-2, positioned in the section according to Batini *et al*. (1983). The improvement obtained with the new processing can be recognized by comparison with the old published profile CROP-18A.

In conclusions, improving the signal to noise ratio and preserving the reflection amplitudes, the distinct seismic units were differentiated, offering a direct image of the variable lithology and petrophysical properties characterizing the upper crust of the Tuscany Geothermal Province.

**Acknowledgments.** The reprocessing of the CROP profiles was partially supported by Geoenergy s.r.l. - Pisa.

**References**

Accaino, F., Nicolich, R., Tinivella, U., 2006. Highlighting the crustal structure of southern Tuscany by reprocessing of the CROP03 NVR profile. Boll. di Geof. teor. ed appl. 47 (3), 425-445.

Accaino, F., Tinivella, U., Rossi, G., Nicolich, R., 2005. Geofluid evidence from analysis of deep crustal seismic data. J. Volcanol. Geotherm. Res. 148, 46-59.

Barison, E., Brancatelli, G., Nicolich, R., Accaino, F., Giustiniani, M., Tinivella, U., 2011. Wave equation datuming to marine OBS data and to land high resolution seismic profiling. J. of Appl. Geophys. 73 (3), 267-277.

Batini, F., Bertini, G., Bottai, A., Burgassi, P.D., Cappetti, G., Giannelli, G., Puxeddu, M., 1983. S. Pompeo 2 deep well: a high temperature and high pressure geothermal system. In: European Geotherm. Update, 3rd Int. Seminar on EC, R.&D. Projects, 341-353.

Batini, F., Burgassi, P.D., Cameli, G.M., Nicolich, R., Squarci, P., 1978. Contribution to the study of the deep lithosphere profiles: "deep" reflecting horizons in Larderello-Travale geothermal field. Mem. Soc. Geol. It. 19, 474-484.

Berryhill, J. R., 1984. Wave-equation datuming before stack. Geophysics 49, 2064-2066.

Berryhill, J. R., 1979. Wave-equation datuming. Geophysics 44, 1329-1344.

Bevc, D., 1997. Flooding the topography: wave equation datuming of land data with rugged acquisition topography. Geophysics 62, 1558-1569.

Brogi, A., Lazzarotto, A., Liotta, D., Ranalli, G., Accaino, F., Batini, F., Bertini, G., Ceccarelli, A., Nicolich, R., Rossi, G., Tinivella, U., 2005b. Crustal structures in the geothermal areas of southern Tuscany (Italy): Insights from the CROP 18 deep seismic reflection lines. J. Volcanol. Geotherm. Res. 148, 60-80.

Brogi, A., Lazzarotto, A., Liotta, D., Nicolich, R., Ranalli, G., 2003a. L'orizzonte K nella crosta di Larderello (Campi geotermici della Toscana Meridionale). Boll. Soc. Geol. It. 122, 103-116.

Cameli, G.M., Ceccarelli, A., Dini, I., Mazzotti, A., 2000. Contribution of the seismic reflection method to the location of deep fractured levels in the geothermal fields of southern Tuscany (Central Italy). Proc. World Geotherm. Congr., Kyushu-Tohoku (Japan), 1025-1029.

Cameli, G.M., Dini, I., Liotta, D., 1993. Upper crustal structure of the Larderello geothermal field as a fracture of post-collisional extensional tectonics. Tectonophysics 224, 413-423.

Della Vedova, B., Vecellio, C., Bellani, S., Tinivella, U., 2008. Thermal Modellig of the Larderello geothermal field (Tuscany, Italy). Int. J. of Earth Sci. 97 (2), 317-332

Liotta, D., Cernobori, L., Nicolich, R., 1998. Restricted rifting and its consistence with compressional structures: results from CROP-3 traverse (Northern Apennines, Italy). Terra Nova 10, 1, 16-20.

Liu, Z., 1995: Migration velocity analysis, PhD thesis, CWP, 168, Center for Wave Phenomena, Colorado School of Mine, Golden Co. USA.

Wiggins J. W., 1984. Kirchhoff integral extrapolation and migration of nonplanar data. Geophysics 49, 1239-1248.

Yilmaz, O., Lucas, D., 1986. Prestack layer replacement. Geophysics 51, 1355-1369.

## SH-WAVE REFLECTION SEISMIC SURVEY AT THE PATIGNO LANDSLIDE: INTEGRATION WITH A PREVIOUSLY ACQUIRED P-WAVE SEISMIC PROFILE

**E. Lauriti[1], L. Meini[1], A. Tognarelli[1], A. Ribolini[1] and E. Stucchi[2]**

*[1] Department of Earth Sciences – Geophysics, University of Pisa, Italy*

*[2] Department of Earth Sciences – Geophysics, University of Milan, Italy*

**Introduction.** Seismic investigation on landslide is hampered by several factors that could prevent the use of the reflection seismic method to characterize the subsurface architecture (Jongmans and Garambois, 2007). Moreover, acquisition and processing of reflection seismic data are more time consuming compared with other geophysical techniques such as refraction seismic and electrical resistivity tomography (ERT), leading inevitably to higher costs. Notwithstanding these difficulties, recently some attempts to delineate the deep slip surface of large landslides have been carried out using P-wave reflection seismic surveys (Apuani *et al*., 2012; Stucchi and Mazzotti, 2009; Stucchi *et al*., 2014;). P-wave reflection seismic method is effective in imaging the slip surface at a depth sufficiently greater than the seismic wavelength, whereas, for very shallow horizons, it suffers from the limited resolution that can be obtained

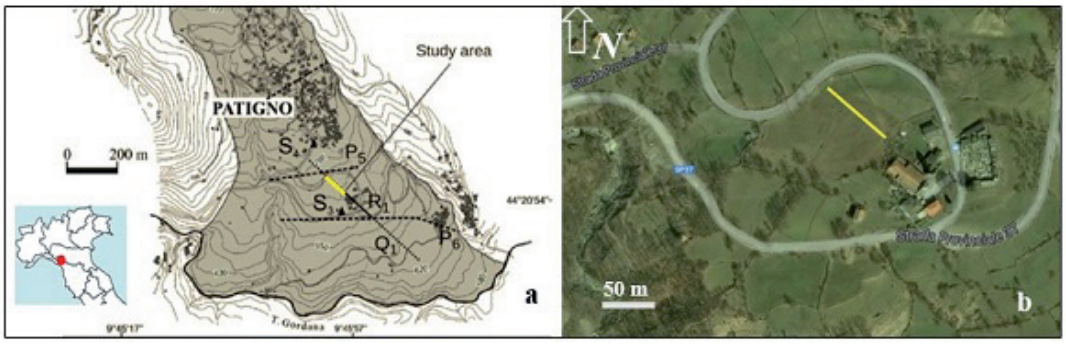


Fig. 1 – a) Location of the P-wave reflection seismic line R1 (from Stucchi *et al*., 2014 ) with overlapped the SH-wave reflection seismic profile in yellow. $S_3$ and $S_4$: boreholes; $Q_1$: ERT line; $P_5$ and $P_6$ refraction seismic lines; b) close-up showing the SH profile.

by the use of compressional waves. In this regards, SH-waves can be used to overcome this limitation (Deidda and Balia, 2001; Guy, 2006; Pugin *et al*., 2006), but they require a specifically-designed energy source for waves generation, geophones measuring horizontal components of particles motion and an accurate choice of acquisition parameters. On the contrary, due to attenuation, the depth of investigation for SH-waves can be lower than for P-waves (Pugin *et al*., 2006). Therefore the geological understanding of a mass movement can take advantage of a combined use of both these geophysical methodologies.

This is the case of the Patigno landslide (Federici *et al*., 2000), a great landslide located in the upper basin of Magra River, in the Northern Appennines, Italy (Fig. 1), where a P-wave study carried out in the last years (Stucchi *et al*., 2014) was able to image the deepest discontinuity of the landslide body at around 40-50 m depth, but no description of the shallower layers can be inferred. Because these surface layers are the slip surfaces of quick reactivation movements of the landslide, an SH high-resolution reflection seismic survey was planned along the previous P-wave profile (Fig. 1). This new survey associated to the P-wave investigation allows a more robust description of the landslide body, from the deepest discontinuity up to the very shallow portions of the landslide.

This work describes the planning, acquisition and processing of the SH reflection seismic survey, and also gives a possible combined interpretation of both P and SH seismic images.

**Acquisition and processing.** The SH seismic survey was acquired using 48 10-Hz horizontal component geophones and a source specifically designed and built for this work, which consisted of a swinging weight of 16 kg striking a baseplate firmly anchored on the ground. The total length of the seismic line was 85 m in NW-SE direction, overlapping part of the previously acquired P-waves seismic profile (Fig. 1).

To obtain an accurate data record it is important to pay attention at the correct positioning of equipment because to generate SH wave is required to energize the ground in transversal direction respect to line acquisition direction; also the appropriate positioning of the geophones along the seismic line is of fundamental importance; in fact, S-waves generated by the source are divided into a vertical (SV) and a horizontal component (SH). In order to record only the SH waves is therefore necessary to exclude from registration SV waves, positioning geophones with the direction of oscillation perpendicular to the acquisition line. The eventuality to also record events related to P converted waves is at least theoretically excluded a priori, since the geophones do not records vertical components. A geometry acquisition was planned to obtain the best advantage from the survey, with the purpose to better manage the equipment supplied in function of the complex geological context to investigate. With the aim of obtaining a sufficiently high fold coverage and a good lateral continuity as required in a landslide context, receiver interval was set at 0.75 m and source interval at 1.5 m.

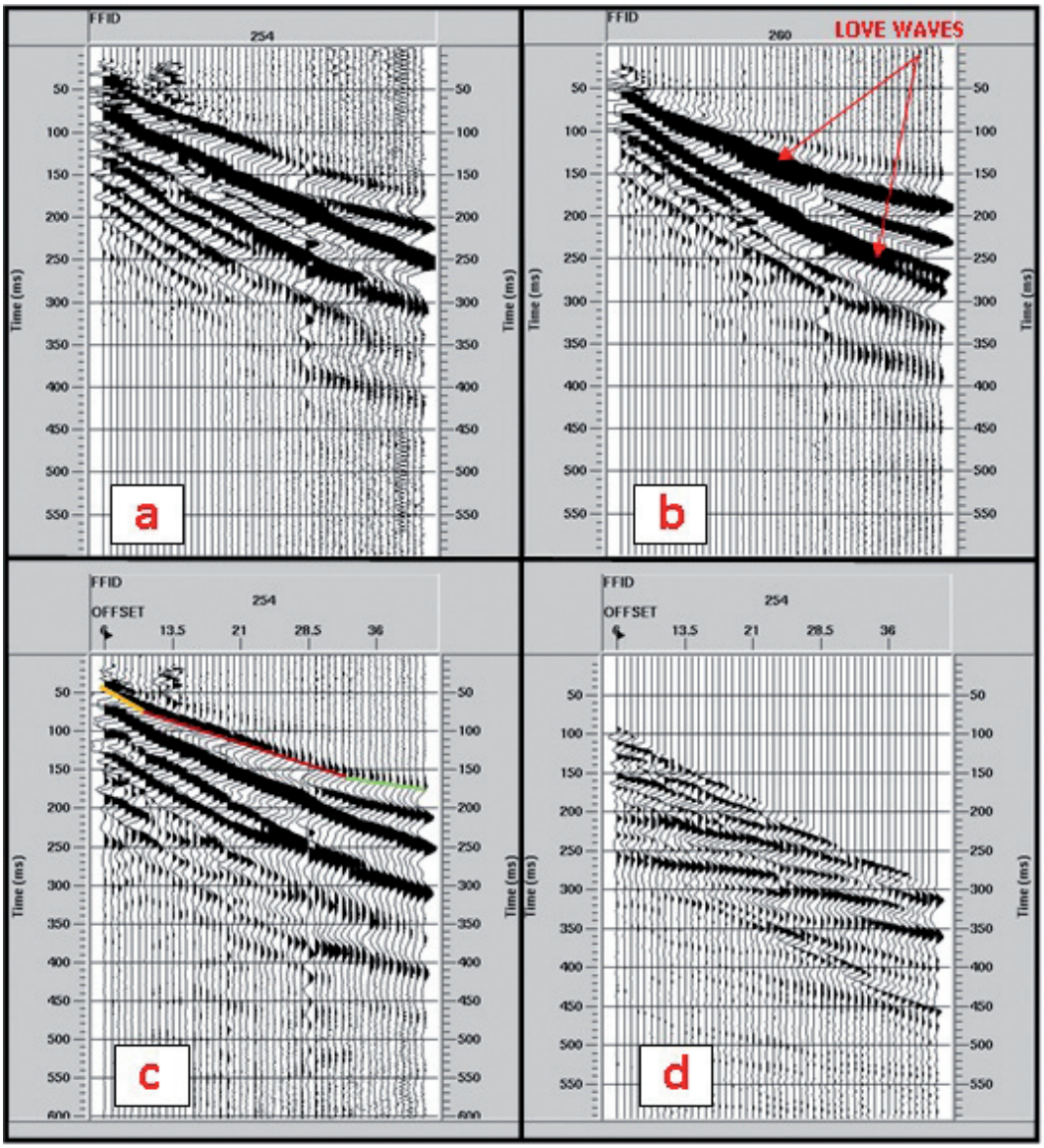


Fig. 2 – a) Raw shot gather acquired with NE-SW polarization; b) raw shot gather with SW-NE polarization, belonging to the same location of the shot displayed in a); c) shot resulting from an optimized sum of shot in a) and shot in b) whose polarity was reversed. In orange, red and green are indicated the direct arrivals and the arrivals from the first refractor and the second refractor respectively; d) shot in c) after the following processing steps: static correction, band pass filter 5-15-100-120 Hz, eigen filter, F-K filter, top mute .

The survey was composed by 6 patterns; in the first pattern the source was originally located in the first station, with a 6 m as minimum offset, and it represented the beginning of the seismic line at 687 m m.s.l. The subsequent shots were done shifting progressively the source of 1.5 m along the line, obtaining a gradual decrease of minimum offset (which become equal to zero at the fifth shot) and a transition to a split-spread shot from an off-end shot for the last two.

At this point of the work, the source was left in its position and the geophones were instead shifted downwards of 8.25 m along the line, passing to the second pattern, where the entire procedure was repeated until the reach of the last pattern in which the source was progressively

shifted upwards until the end of the line, at station 115. Using this scheme the maximum nominal coverage was 24, further doubled in the processing phase applying an interleaving procedure.

To exploit the polarization of SH waves, each shot point was acquired using both directions of energisation and in the processing lab these two records were appropriately summed to enhance the SH-waves while attenuating other unwanted phases in case they were recorded.

To increase the signal to noise ratio 6 shots were done for each polarity (i.e. directions of energisation). In the processing lab, these 6 shots with NE-SW polarization were added together and the same operation has been done for the 6 shots belonging to the same station but with SW-NE polarization, after reversing the polarity of these traces. The two resulted shots were then summed together to enhance the SH-waves while attenuating other unwanted recorded phases. Figs. 2a and 2b show an example of a raw shot gather before the vertical stacking for each direction of energisation (NE-SW and SW-NE respectively) and Fig. 2c shows the resulting shot after vertical stacking and appropriate polarization summation.

The SH events identified on the seismogram in Fig. 2c are: the direct waves in orange, the refracted waves in red and green and strong event with a characteristic dispersion trend corresponding to the Love waves. No reflections can be observed at this stage but they are evident after the de-noising procedure aimed at attenuating the various types of noise present. This is clearly shown in Fig. 2d which displays the same gather as in Fig. 2c at the end of the processing steps applied to reduce the noise.

Taking advantage of the symmetry of the path trajectory in case of SH-SH reflection, for the processing of the SH wave data we can use the same software and algorithms developed for the P-P reflection seismic data, tailoring the parameters accordingly to the required needs. The main additional and different step required in the sequence consists in a calibrated difference between the records of the sources at the same location with opposite polarization, as described before. Besides the conventional steps of database building and cmp (common mid point) gathering (with interleaving), kill of anomalous traces, static corrections, band-pass filter, velocity analysis, normal move out, residual static application and stack, some dedicated operations are applied to remove the Love waves. They constitute a particular type of coherent noise that is characterized by high energy, dispersion behaviour, recording time and frequency band coincident with those of the desired signal. With an accurate design of directional (frequency-wavenumber) and eigenvalues filters applied on the shot domain, it was possible to attenuate these wave modes early in the processing, thus increasing the signal to noise ratio at the pre-stack level as shown in Fig. 2d.

The resulting stack section was depth migrated by means of the Kirchhoff algorithm using as the velocity model a smoothed and Dix converted version of the stacking velocity field. The migrated seismic section exhibits a good signal to noise ratio from the very shallow layers up to 40 m in depth, with many continuous events displaying a trend in accordance to the expected geomorphological and geological setting. This image and the depth converted P-wave seismic section in Stucchi et al. (2014) are the ones used for a combined interpretation.

**Comparison between SH- and P-waves seismic sections.** The main feature that induces to use the SH-wave reflection seismic compared to P-wave reflection seismic is the higher resolution that can be achieved with SH-waves at very shallow depths (Guy *et al.*, 2003; Guy, 2006). Accepting as threshold for the vertical resolution a quarter of the dominant wavelength ($\lambda/4$) (Sheriff and Geldart, 1982; Yilmaz, 2001; Sheriff, 2002), it is easy to deduce that SH seismic method benefits of a higher resolution than P seismic method. In fact, if we consider for the Patigno case a mean velocity of ~280 m/s and a dominant frequency of 25 Hz for SH waves, a resolution around 3 m results at the slip surface depth, compared to approximately 10 m for P-waves (using 2000 m/s and 50 Hz for velocity and dominant frequency respectively). Then the shorter wavelength provides a higher resolution for the SH-waves, but at the same time it causes an earlier signal attenuation because of increased absorption.

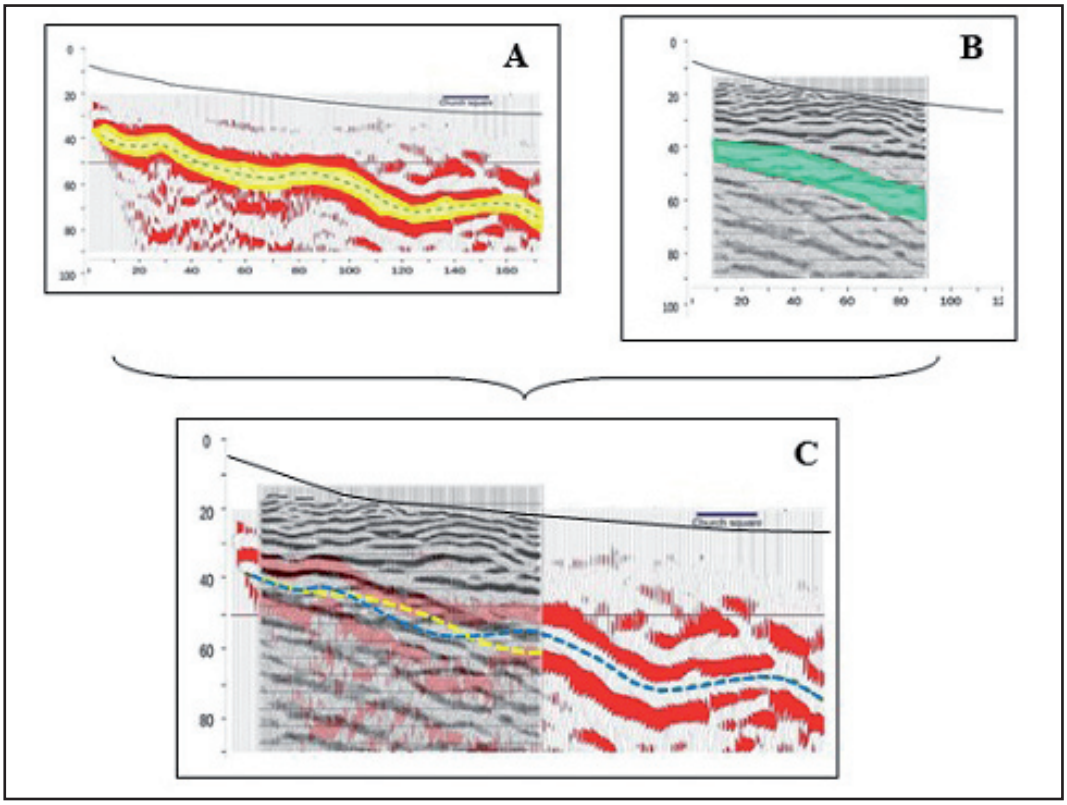


Fig. 3 – a) P- wave reflection seismic section. In yellow is highlighted the reflector related to the main slip surface; b) SH-wave seismic section. In green is highlighted the region related to the main slip surface; c) overlap of the two seismic sections.

On the basis of this considerations, to better characterize the internal structure of the landslide in the investigated area and to exploit the differences and the potentials of the two seismic methods, the resulting P-wave and SH-wave seismic sections have been analyzed and compared separately and then overlapped. Fig. 3a shows that P-waves seismic method is effective in locating the deepest slip surface, recognized as the main reflector in the P-wave seismic image in Stucchi *et al.* (2014) (dashed line in Fig. 3a). This reflector appears as a continuous and well defined event that slightly deepens along the line with two small upwards concavities. At shallower depth, above this event, no information is provided by the P-wave seismic image, therefore the internal structure of the geological body is not resolved by this method.

On the contrary, the SH-wave reflection seismic technique gives the best results in the shallower portion of the subsurface, where many continuous events are visible with a good signal to noise ratio (Fig. 3b). The trend shown by these events is in accordance to the expected geomorphological setting, therefore they can be interpreted as reflectors and related to the small reactivation slip surfaces delineating minor landslides that dismantled the main complex landslide. The main slip surface can also be observed on the SH section, even though it has a lower amplitude due to the progressive decrease in signal to noise ratio with increasing depth. It marks the different trends between the near surface layers and the dipping layers at depth (green band in Fig. 3b).

**Conclusion**. This work demonstrates that high-resolution SH reflection seismic method can be used to study complex landslide bodies highlighting the main geological-geomorfological characteristics of the mass movement. The procedural choices adopted concerning acquisition

and data processing, allow to obtain a depth migrated image with a good signal to noise ratio up to a depth of approximately 40 m, that is relevant for this type of investigation. An added value to these outcomes is that Patigno landslide represents a kind of destabilization phenomena commonly affecting the Apennine slopes, i.e. complex deep landslides, reactivated by surface movements that often are the most destructive.

The combined use of both P-waves and SH-waves offers the possibility to obtain detailed insights of the whole landslide body, overcoming the limitation due to the low resolution of P-waves method for imaging shallow horizons and the low investigation depth of SH method.

Both the seismic methodologies discussed in this work can be used to study large landslide and the choice of which to prefer mainly depends by the purpose of the work. If it is merely the individuation of the main deep slip surface at sufficient depth compared with the propagating wavelength, is preferable to use the P-wave reflection seismic method because it allows a quickly data acquisition, requires standard processing steps and devices. If the aim is instead the reconstruction of the internal architecture of the mass movements, the higher resolution of the SH-waves method offers greater guarantees of success.

Taking into account the results obtained in this work it is possible to conclude that SH-wave seismic reflection methodology has revealed excellent potentialities that makes it applicable in contexts in which it is generally underestimated due to difficulty of acquisition, complexity of data processing and high costs. Notwithstanding these difficulties, SH-wave seismic reflection methodology provides many information about the shallow part of the subsurface and the union of these data with deeper P-wave seismic data gives a more robust description of the whole landslide body from the deepest discontinuity up to the very shallow portions of the landslide. In this regards, the complete knowledge of the landslide internal setting is fundamental to plan adequate and effective defence strategies.

**Acknowledgements.** We gratefully acknowledge the support of Landmark/Halliburton for the use of the seismic software ProMAX and Prof. Mazzotti for his useful suggestion. Geophisical equipment was supplied by So.Ge.T. snc (www.sogetsnc.eu) and Geostudi Astier (www.geostudiastier.com) which are gratefully acknowledged.

## References

Apuani T., Arosio D., De Finis E., Stucchi E., Zanzi L. and Ribolini A.; 2012: *Preliminary seismic survey on the unstable slope of Madesimo (Northern Italy)*. 25th Symposium on the Application of Geophysics to Environmental and Engineering Problems (SAGEEP), Tucson, Arizona, USA, 452-459.

Deidda G.P. and Balia R.; 2001: *An ultrashallow SH-wave seismic reflection experiment on a subsurface ground model*. Geophysics, **66** (4), 1097–1104.

Guy D.E.; 2006: *High-Resolution P- and S-wave Seismic Reflection Investigation of a Shallow Stratigraphic Sequence*. Electronic Journal of Geotechnical Engineering, 11, 37 pp.

Guy E.D., Nolen-Hoeksema R.C., Daniels J.J. and Lefchik T.; 2003: *High-resolution SH-wave seismic reflection investigations near a coal mine-related roadway collapse feature*. Journal of Applied Geophysics, **54**, 51 – 70.

Federici P.R., Puccinelli A., Chelli A., D'Amato Avanzi G., Ribolini A. and Verani M.; 2000: *La Grande Frana di Patigno di Zeri (Massa Carra*a). Memorie della Accademia Lunigianese di Scienze, **70**, 3-51.

Pugin A.J.M., Sargent S.L., Hunt L.; 2006: *SH and P-wave seismic reflection using landstreamers to map shallow features and porosity characteristics in Illinois*. Symposium on the Application of Geophysics to Engineering and Environmental Problems (SAGEEP).

Sheriff R.E., 2002; *Encyclopedic Dictionary of Applied Geophysics*. Society of Exploration Geophysicists, Tulsa, Oklahoma, U.S.A., 376 pp.

Sheriff R.E. and Geldart L.P.; 1982*: Exploration Seismology*: Vol. 1. History, Theory, and Data Acquisition. Cambridge Univ. Press., 628 pp.

Stucchi E. and Mazzotti A.; 2009*: 2D seismic exploration of the Ancona landslide (Adriatic Coast, Italy)*. Geophysics **74**(5), B139.

Stucchi E., Ribolini A. and Anfuso A.; 2014: *High-resolution reflection seismic survey at the Patigno landslide, Northern Apennines, Italy.* Near Surface Geophysics, **4**, 559-571

Yilmaz, O.; 2001: *Seismic Data Analysis: Processing, Inversion, and Interpretation of Seismic Data*. Society of Exploration Geophysicists, 2024 pp.

# APPLICATION OF SEISMIC REFRACTION TOMOGRAPHY TO DETECT ANTHROPOGENIC BURIED CAVITIES IN PROVINCE OF NAPLES (CAMPANIAN PLAIN, ITALY)

**S. Maraio[1], P.P.G. Bruno[2], G. Testa[3], P. Tedesco[3], G. Izzo[4]**
*[1] Dipartimento di Scienze della Terra e Geologico-Ambientali, Università di Bologna, Italy*
*[2] INGV, Istituto Nazionale di Geofisica e Vulcanologia, Sezione Roma 2, Italy*
*[3] Dipartimento di Scienze e Tecnologie, Università degli studi del Sannio, Benevento, Italy*
*[4] Studioizzo Geologia, GIS & Ambiente, Airola (BN), Italy*

**Introduction.** The presence of near-surface buried cavities often poses serious hazards for human safety and infrastructures. Underground voids develop naturally in karst territories while are produced by human activities the cavities such as underground mines, tunnels, buried passage-ways, etcetera (Del Prete, 2008). The sudden collapse of the vault of these cavities is a recurring problem in landscape management and it is a main origin of sinkholes. If the collapses originate from man-made cavities, these phenomena can be classified as *"anthropogenic sinkholes"* (Guarino *et al*., 2012). Therefore, identification of these underground voids is an essential prerequisite for both minimization of risks arising from their presence, and for optimal planning of land use. The geophysics technologies are often the most convenient way to gather information aimed at the characterization of the subsurface and the search for underground voids. Up-to-date different geophysical prospecting methods have been tested for underground voids detection and their success is strongly influenced by local conditions and their ability in terms of penetration and resolution. The main difficulties in finding cavities using geophysical methods are generally related to the size and shape of the voids, and the subsurface lateral velocity variations that can create responses similar to those of underground voids (Riddle *et al*., 2010). The applications on synthetic models (Mandell, 2005a; Sheehan *et al*., 2005a, 2005b), in laboratory experiments on physical models (Grandjean and Leparoux, 2004; Grandjean, 2006) and the application on real data (Sheehan *et al*., 2005c; Cardarelli *et al*., 2010), have shown that the seismic refraction tomography represents a powerful tool for the detection of subsurface cavities. It has the advantages of being a non-invasive technique, of having a good penetrating power while maintaining a good resolution, and of allowing a three-dimensional reconstruction of the underground cavities. In this work we used a densely spaced grid of 2D seismic refraction profiles processed with first-arrival traveltime tomography to detect man-made cavities and to create a three-dimensional model of the subsurface in Casamarciano, in province of Naples. After modelling, some core-drillings have been made to compare and validate the seismic results.

**Geologic contest and underground cavities.** The area of present work is located in the central sector of the Campanian Plain. This latter occupies the bottom of a large structural depression (graben) oriented in NW-SE direction and bounded by carbonate ridges of Mt Massico to NW, of M.ti Lattari to SE and M.ti of Caserta and Partenio to NE and to E. The Campanian Plain graben began to form in the Late Pliocene as a result of tectonic activity that characterized the Apennines orogenic uplift (Bartole *et al*., 1984). The area was affected by intense volcanic activity and the graben was filled by the products of the nearby volcanism, i.e. pyroclastic deposits and lava, and by alluvial and marine deposits. Generally the stratigraphic series of the study area consist of volcanic deposits dating back to Upper Pleistocene - Holocene, such as the Neapolitan Yellow Tuff fm. (NYT: 12 ky b.p.) and the Campanian Ignimbrite fm. (CI; 37 ky b.p.) (Orsi *et al*., 1992, 1996). The stratigraphic series is completed to the top by loose pyroclastic deposits related to the subsequent post-Yellow Tuff activity (<10.5 ky b.p.) (Guarino *et al*., 2012; Di Vito *et al*., 2008; De Vivo *et al*., 2001; Bellucci, 1994).

Part of the survey area was investigated by four core drillings that reveal the stratigraphy down to depth of about 19 m. The stratigraphic series of the area consists of the following lithotypes (from top to bottom): pyroclastic deposits rich in yellow pumices down to depth of 6.5 m; between 6.5 and 11.5 m in depth there are alluvial gravel deposits in a grey pyroclastic

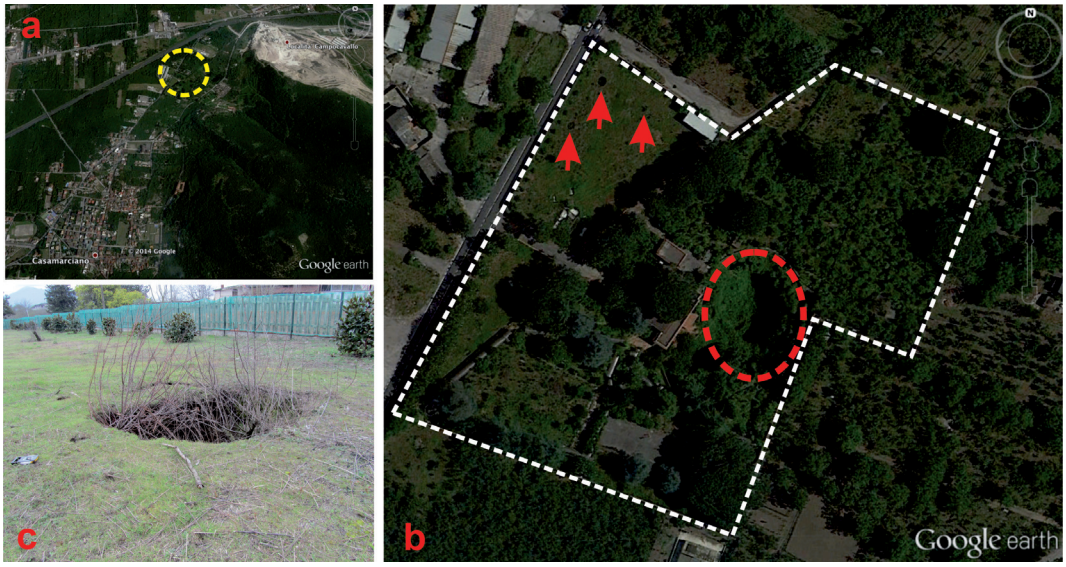


Fig. 1 – a) Aerial photography with location of the survey area by Google Earth (yellow dotted line); b) survey area on Google Earth aerial photography (white dashed line) with some surface evidences of sinkhole (red arrows) and larger sinkhole in the area (red dashed line); c) photo of some surface evidences of sink-hole.

matrix and from 11.5 m to the bottom (19 m) the well shows the Campanian Ignimbrite formation.

The NYT and CI fm. outcrops are associated to a high number of underground excavations (ancient aqueducts, tunnels, tombs, etc.). Good physical and mechanical properties of these tufa formations, wide distribution of these deposits, at depths and easy access, together with limited means of transportation available in the past centuries represented additional reasons that led ancient the communities not only to use the material quarried but also to take advantage of the excavations carried out accordingly (Vallario, 1992). The artificial caves were dug into the layers of pumice and tuff to reduce the cost of construction of the buildings, until the beginning of 1900. The building material was extracted widely from underground vertical shafts that reach the layers of loose pumice and the underlying tuff. Sub-horizontal tunnels were instead excavated within the layers of pumice. Once reached the tufa through vertical wells, sub-horizontal cavities of varying height and width (~ 4-8 m) were dug. After the extraction of the building material, voids were usually used as foodstuffs deposits and wine cellars. The vertical wells of the cavities, located outside of the towns such as the study area, usually were closed; therefore the knowledge about their presence in the subsoil was lost. The loss of maintenance of the cavities and water infiltration within them can result in instantaneous or progressive collapse.

**Data acquisition and method.** The investigated area, of ~10,000 $m^2$, is a private property and its aerial photography is shown in Figs. 1a and 1b.

Some surface evidences of sinkholes are clearly visible from aerial photography (red arrows in Fig. 1b and Fig.1c). For instance one the larger sinkholes in the area (red dashed line in Fig. 1b) has about 50 m in diameter and 20 m in depth. The analysis of visible evidences of sinkholes, together with the measurement of an accessible cavity, has allowed us to define the target of the investigation, namely the search of voids with lateral dimensions of about 10 m and heights of about 8-9 m located within 20 m of depth. In order to determine the optimal acquisition parameters and to test the accuracy of tomographic technique for the identification of these cavities into geologic contest investigated, we used the results of seismic refraction

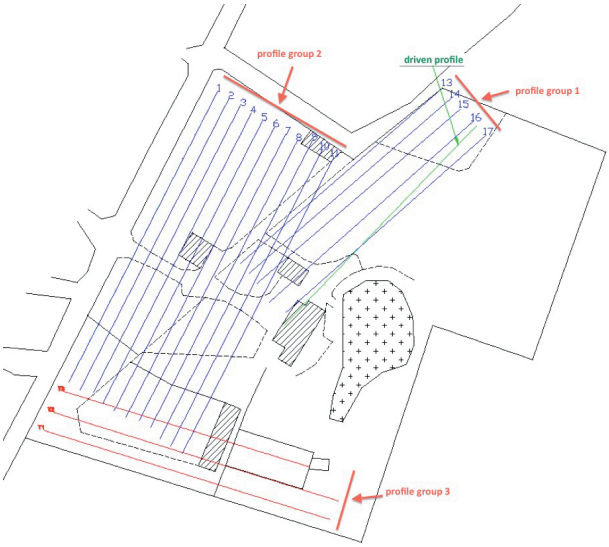


Fig. 2 – Profiles location on the survey area planimetry.

analysis of a synthetic model made by Cardelli *et al.* (2010), moreover we acquired a pilot profile, above a cavity with known size and position. The final velocity model resulting from the pilot profile (Fig. 3a) shows that in correspondence of the cavity there is an anomalous negative distribution of Vp velocity associated to the top of the tuff basement (about 1250 m/s) that is coherent whit the size of the known cavity. Model resolution is assessed by *a posteriori* checkerboard test (Hearn and Ni, 1994), using an input perturbation values of ± 10 m/s in the cell with horizontal size 20 m and vertical size 10 m. Checkerboard test gives information on how data and the method used are spatially sensitive to the velocity variation in the final tomographic model (Improta *et al.*, 2002). The anomalous velocity of Vp associated to the known cavity is in the resolved region of the model. After this test, we acquired 20 seismic profiles with a total profile length of about 2 km. The profiles are located as shown in figure 2 in the survey area. The employed acquisition system consists of two Geometric's GEODE seismographs equipped with vertical geophones with a 40 Hz eigenfrequency, for a total of 48 channels. Seismic data were collected using an 8 kg sledgehammer. At each shot point we stacked 3 recordings to increase the signal and simultaneously to reduce random noise already in acquisition processing. Data were recorded by geophones placed at 2 m intervals, covering a distance of 96 m for each profile. Source move-up was 4 m along all profiles, in order to obtain a dense network of seismic rays and consequently a high spatial resolution. In order to increase the turning ray depth the penetration of the refracted waves offline shot were also acquired.

**Data processing.** After installing the geometry into trace header, a simple pre-processing aimed at improving the signal to noise on first arrivals was applied at recording data. This consisted of a frequency filtering, necessary to eliminate low-frequency noise caused by vehicular traffic, and a manually checking trace by trace to remove dead or very noisy traces. The main and longer part of refraction processing was the picking of the first arrivals, performed on the entire dataset, through the commercial Landmark software named ProMAX 2D.

The quality control on the readings was performed plotting time-distance curves and using the rules of parallelism and reciprocity described by Ackermann *et al.* (1986). The readings of the direct and refracted phases, after being checked for consistency, were inverted using a commercial software that is part of the package SeisImager®, distributed by Oyo Coroporation Ltd. and set on the work of Hayashi and Takahashi (2001). The inversion times algorithm is based on a tomographic technique of iterative reconstruction of image, known as "SIRT" [Simultaneous Iterative Reconstruction Technique; Gilbert (1972)]. The SIRT method requires an initial velocity model that was obtained by conventional procedures of refraction analysis (e.g. Burger, 1992). During inversions, ray tracing and SIRT are applied to the velocity model, until the root mean square (RMS) error on the difference between the observed and calculated travel times is minimized. Horizontal cell size was 2 m. Velocity increased with depth from 200 m/s at the surface to 1500 m/s at a depth of 30 m. On average 20 to 30 iterations of ray tracing and traveltime inversions were conducted. Running the inversions with 3 nodes, we obtained

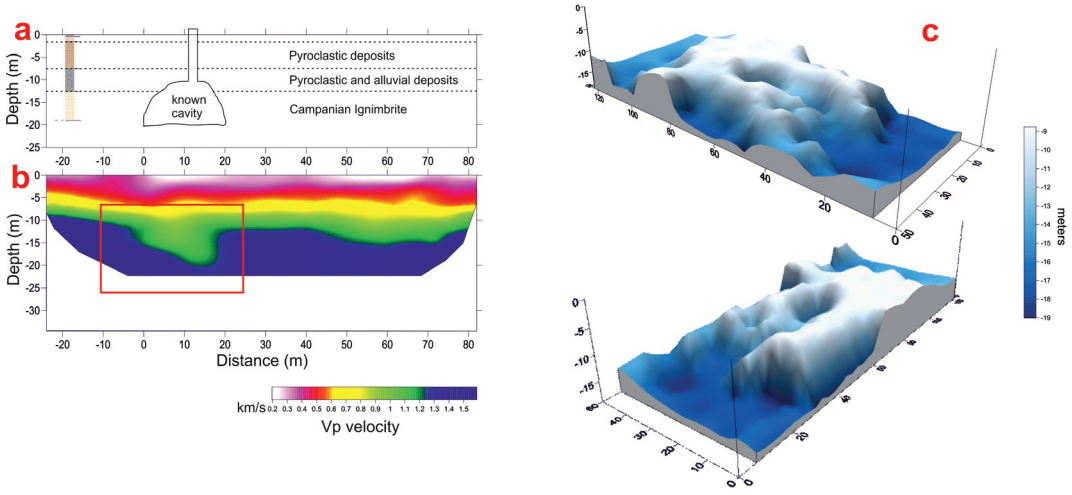


Fig. 3 – a) Syntetic geological model of pilot profile site, from core-drilling analysis; b) tomographic velocity model of pilot profile shows an anomalous velocity associated with known cavity (red box); c) 3d model of the top of CI basement from the profile of group 2.

a final velocity models that are characterized by an average RMS traveltime error of about 2.5 ms. Larger residuals, between 3 and 4 ms, are occasionally observed on some profiles with a smaller signal to noise ratio, as the profiles near the road. These profiles, contaminated by low-frequency random noise, are consequently characterized by a greater uncertainty on the first arrivals picking. Final tomographic velocity models, for each seismic line, were exported as ASCII files and velocity values were interpolated in the 3D space defined at the surface by the profile location. The ray coverage allowed determining the areas of the subsurface effectively resolved by the seismic inversion. All areas of the tomographic models outside the ray coverage have been blanked (Fig. 3).

**Results.** The resulting tomographic models (e.g. Fig. 2) show P-wave velocities that vary from a minimum of about 200 m/s at the surface and increase up to about 1500 m/s at the bottom where the CI basement is reached. It is evident the presence of many velocity lateral variations, which are generally located mainly at depths between 10-20 m from topographic surface. The profiles of group 1 and group 2 (see Fig. 2) show a very articulated CI basement, characterized by an average velocity of 1250 m/s. The velocity anomalies found in the basement, according with the anomalies found on the pilot profile, suggest the presence of underground cavities; in addition, they are consistent on adjacent profiles and appropriate in terms of location.

The tomographic models of group 3 (see Fig. 2) were acquired with a different azimuth (approximately WNW - ESE) are oriented approximately 90° to the direction of the profiles of the group 2. The tomographic sections related to these three profiles differ from the others by the absence of major and evident lateral variations of velocity. These profiles, in fact, show a sub-parallel velocity distribution, with a tendency of the faster layer (i.e. the top of the CI) to widen towards the end of the profiles. On this set of profiles, there is no evidence of voids in the CI tuff, as found on the other sets of profiles.

Spatial interpolation of the velocity information has allowed us to build a three-dimensional model the top of CI fm. (Fig. 3c), which clearly shows both location and dimensions of the voids. Four core-drillings were done in the area covered by the profiles of group 2, in order to validate the tomography results. These logs explorations are in perfect agreement with our results.

## References


Ackermann H. D., Pankratz L. W. and Dansereau D. (1986). *Resolution of ambiguities of seismic refraction traveltime curves*. Geophysics, Vol. 51, N. 2; P. 223-235.

Bartole, R., Savelli, D., Tramontana, M., Wezel, F., 1984. *Structural and sedimentary features in the Tyrrhenian margin of Campania, Southern Italy*. Marine Geol. 55, 163–180.

Bellucci F. *Nuove conoscenze stratigrafiche sui depositi vulcanici del sottosuolo del settore meridionale della Piana Campana*. Boll. Soc. Geol.It. 113 (1994), 395-420.

Burger H. R. (1992). *Exploration Geophysics of the Shallow Subsurface*. Prentice-Hall, Inc., Englewood Cliffs, New Jersey, 489 pp.

Cardarelli E.,Cercato M., Cerreto A. and Di Filippo G. 2010. *Electrical resistivity and seismic refraction tomography to detect buried cavities*. Geophysical Prospecting, **58**, 685–695.

De Vivo, B., Rolandi, G., Gans, P.B., Calvert, A., Bohrson, W.A., Spera, F.J., Belkin, H.E., 2001. *New constraints on the pyroclastic eruptive history of the Campanian volcanic Plain (Italy)*. Min. Pet. 73 (1–3), 47–65.

*Del Prete S., 2008, Geologi – Bollettino trimestrale dell'Ordinedei Geologi della Campania, n. 25, 2008*

Di Vito, M. A., Sulpizio, R., Zanchetta, G., & D'Orazio, M. (2008). *The late Pleistocene pyroclastic deposits of the Campanian Plain: new insights into the explosive activity of Neapolitan volcanoes*. Journal of Volcanology and Geothermal Research, 177(1), 19-48.

Gilbert P. (1972). Iterative methods for the three-dimensional reconstruction of an object from projections. J. Theor Biol 1972;36:105±17.

Grandjean G. 2006. Imaging subsurface objects by seismic P-wave tomography: Numerical and experimental validation. *Near Surface Geophysics* **4**, 279–287.

Grandjean G. and Leparoux D. 2004. *The potential of seismic methods for detecting cavities and buried objects: Experimentation at a test site*. Journal of Applied Geophysics **56**, 93–106.

Guarino, P. M., & Nisio, S. (2012). *Anthropogenic sinkholes in the territory of the city of Naples (Southern Italy)*. Physics and Chemistry of the Earth, Parts A/B/C, 49, 92-102.

Hayashi K. and Takahashi T. (2001). *High Resolution Seismic Refraction Method Using Surface and Borehole Data for Site Characterization of Rocks*. International Journal of Rock Mechanics and Mining Sciences, Vol. 38, pp. 807-813.

Hearn T. M. and Ni J. F. (1994). *$P_n$ velocities beneath continental collision zones: The Turkish_Iranian Plateau*. Geophys JInt. – v. 117, pp. 273-283.

Hubral, P., 1983. *Computing true amplitude reflections in a laterally inhomogeneous earth*.Geophysics 48 (8), 1051–1062.

Improta, L., A. Zollo, A. Herrero, M. R. Frattini, J. Virieux, and P. Dell'Aversana, *Seismic imaging of complex structures by non-linear traveltime inversion of dense wide-angle data: Application to a thrust belt*, Geophys. J. Int., 151, 264–278, 2002.

Orsi, G., D'Antonio, M., de Vita, S., Gallo, G., 1992. *The Neapolitan Yellow Tuff, a large-magnitude trachytic phreatoplinian eruption; eruptive dynamics, magma withdrawal and caldera collapse*. J. Volcanol. Geotherm. Res. 53 (1–4), 275–287.

Orsi, G., de Vita, S., Di Vito, M., 1996. *The restless, resurgent Campi Flegrei nested caldera (Italy):constraints on its evolution and configuration*. J. Volcanol. Geotherm. Res. 74, 179–214.

Riddle, G. I., Riddle, C. J., & Schmitt, D. R. *ERT and Seismic Tomography in Identifying Subsurface Cavities*. GeoConvention 2010, Calgary, Alberta, Canada, May 10-14, 2010

Sheehan J.R., Doll W.E. and Mandell W.A. 2005a. *An evaluation of methods and available software for seismic refraction tomography analysis*. Journal of Environmental and Engineering Geophysics **10**, 21–34.

Sheehan J.R., Doll W.E., Mandell W.A. and Watson D. 2005b. Cavity detection using seismic refraction tomography: Can it be done? Near Surface meeting, Palermo, Italy, Expanded Abstracts, C004.

Sheehan J.R., Doll W.E., Watson D. and Mandell W.A. 2005c. Application of Seismic Refraction Tomography to karst cavities. US Geological Survey Karst Interest Group Proceedings, Rapid City, South Dakota, 12–15 September 2005, 29–38.

# APPLICAZIONE DEL RILEVAMENTO DEL MICROTREMORE SISMICO PER LA RICERCA DI CAVITÀ URBANE: IL CASO DEGLI INSEDIAMENTI TROGLODITI DI PICENZE (L'AQUILA, ABRUZZO)

**A. Moretti, G. Ferrini, A.M. Mari**
*MeSVA, Università dell'Aquila*

**Introduzione.** Il problema della presenza di sistemi ipogei, tanto naturali quanto artificiali, nel sottosuolo di molti centri urbani d'Italia torna regolarmente alla ribalta delle notizie di cronaca con i frequenti, spesso tragici, episodi di crollo sotterraneo che troppo spesso interessano i nostri centri storici, ed altrettanto regolarmente viene ignorato dai servizi pubblici fino al successivo evento calamitoso. Anche nell'area colpita dal terremoto del 6 aprile 2009 sono numerosi i centri urbani interessati da complessi sistemi di caverne, e spesso da fenomeni di instabilità che pongono seri problemi alla ricostruzione delle aree terremotate. In effetti il problema non è di facile soluzione, visto che molti dei cunicoli sotterranei sono accessibili solo da speleologi esperti con notevole rischio personale, talvolta assolutamente inaccessibili e di molti si è finanche persa completamente memoria.

Tra i molti paesi del contado aquilano interessati dal fenomeno, gli scriventi hanno studiato in dettaglio la situazione presente nel paese di Picenze, dove hanno censito e rilevato circa 50 cavità, delle quali almeno 20 di volumetria superiore ai 500 $m^3$ e lunghezza fino a 30-40 m dall'ingresso. La struttura relativamente regolare di molti ipogei, comune anche ad altre città troglodite in diverse parti del mondo, ci ha permesso di ipotizzare la presenza e l'andamento di ampie porzioni di sotterranei, attualmente inaccessibili ma estese sotto ampie porzioni di fabbricati, strade o piazze; altre indicazioni derivano direttamente dal rilevamento speleologico, dove ampi tratti di galleria sono ostruite da crolli o da sbarramenti antropici facendo ragionevolmente presumere la prosecuzione delle caverne; molte informazioni derivano anche dalla memoria degli anziani del paese, che ricordano come molte cavità, attualmente non più visibili, fossero ancora in uso nel secondo dopoguerra. Per confermare o meno la presenza di questi cunicoli (che in ogni caso dovranno essere definite in dettaglio tramite perforazioni e con il rilevamento speleologico), è indispensabile rivolgersi in prima istanza a metodi geofisici non invasivi. Escludendo la tomografia sismica e geoelettrica, possibile solo lungo le vie perimetrali degli aggregati edilizi e peraltro già eseguita con scarso successo da operatori commerciali, abbiamo pensato di rivolgerci allo studio dei microtremori naturali, verificando in primo luogo la possibilità di utilizzare questa tecnica per la ricerca delle cavità. Sono stati quindi studiati alcuni casi in cui la presenza della cavità è certa e geometricamente definita.

Nello specifico sono stati analizzate due cavità, posizionate la prima sotto il piano stradale di un vicolo all'interno dell'abitato, la seconda sottostante un gruppo di edifici attraversato, per la sua totalità, da un ampio complesso ipogeo (*Ju' Rotton de 'Ciatt*) con accesso dai due aggregati adiacenti e quindi sottratto all'osservazione dei più diretti interessati. Per poter individuare e valutare le variazioni negli spettri di risposta microsismica dovuti alla presenza in sottosuolo di vuoti e cavità, è stato preventivamente necessario definire con la massima accuratezza la geologia, la stratigrafia ed i caratteri microsismici dell'area (vedi Moretti e Ferrini, in questo volume). In particolare nei depositi della copertura sedimentaria sono stati distinti 4 termini litostratigrafici locali, solo in parte coincidenti con quanto riportato nelle mappe di microzonazione e nella nuova cartografia d'Italia in scala 1:50.000.

Nel corso delle indagini sono state eseguite oltre 100 misure di microtremore sismico, con tempo di acquisizione di 30 min. e frequenza di campionamento di 256 Hz, utilizzando il sismografo digitale TROMINO della ditta Micromed, ed il relativo *software* dedicato GRILLA. Tra tutte le misure eseguite ne sono state selezionate 47 con sufficiente qualità e buon accoppiamento con il suolo, ed utilizzate per definire la risposta sismica locale media ed il modello sismostratigrafico di riferimento tramite l'inversione dei dati del rapporto H/V (Fig.1). Le misure sono state eseguite in parte in sottosuolo, a diretto contatto con il pavimento

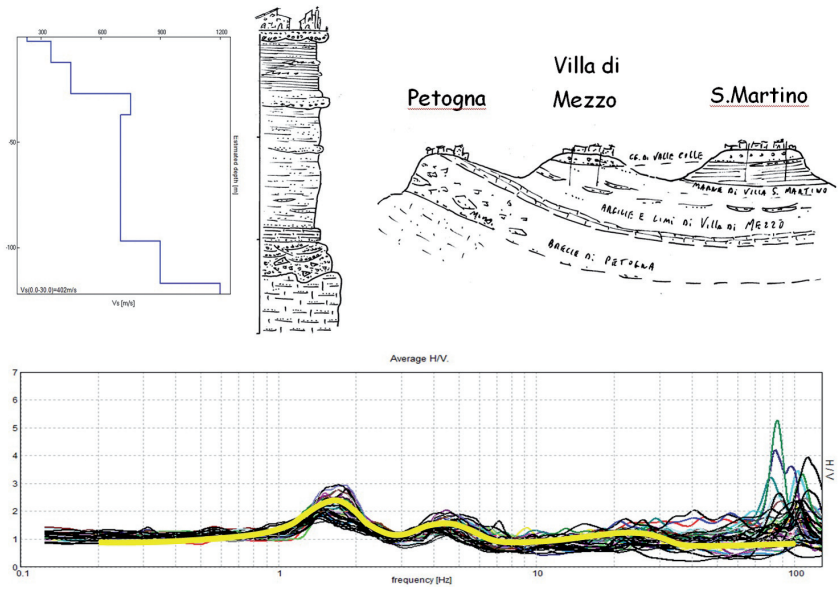


Fig. 1 – In alto: schema stratigrafico dell'area studiata, e miglior modello di velocità delle onde S, ricavato invertendo i dati del microtremore sismico. - In basso: curva sintetica corrispondente al modello di velocità scelto, sovrapposta alle tracce del rapporto H/V delle 47 misure selezionate. La discontinuità sismica più profonda, corrispondente al picco a circa 1.8 Hz, è relativa all'interfaccia tra le brecce basali (Brecce di Petogna) e la successione argilloso-pelitica (Argille e Limi di Villa di Mezzo).

calcareo-marnoso, in parte nei locali interrati degli edifici, nelle corti e nei vicoli circostanti. In linea di massima tutte le misure sono confrontabili tra loro e la risposta microsismica è, in generale, abbastanza uniforme in tutta l'area indagata, rivelando, nonostante la prossimità del sito al sistema delle faglie neogenico-quaternarie che bordano il *graben* dell'Aterno, una buona uniformnità della stratigrafia di sottosuolo. Nel grafico di Fig. 1, in basso, vengono riportati gli spettri complessivi del rapporto H/V delle 47 misure selezionate, tanto in sottosuolo che al suolo. Si evincono facilmente due picchi principali: il primo, ben marcato, alla frequenza di 1.8 Hz ed un secondo, meno marcato, tra 4 e 5 Hz. Si nota una evidente dispersione del segnale spettrale a frequenze maggiori di 50-60 Hz, per l'effetto degli strati antropici superficiali (pavimentazione stradale od edile, solette in cemento, detriti, tubature, fognature ecc.); come è lecito aspettarci, la dispersione è notevolmente inferiore nelle misure eseguite negli ipogei, anche a causa del migliore accoppiamento dello strumento con la roccia in posto.

Nella Fig. 1 è riportato anche il modello di velocità che meglio approssima la dispersione osservata, accompagnato da una colonna litostratigrafica sintetica ricavata dall'integrazione dei dati geofisici con quelli geologici rilevati in campagna, in sottosuolo ed estrapolati da numerosi sondaggi.

La velocità di partenza delle onde sismiche, necessaria alla costruzione del modello e relativa all'intervallo più superficiale, è stata stimata, in prima approssimazione, in base ai primi arrivi delle onde P misurata in tre profili sismici attivi eseguiti in sottosuolo, a diretto contatto con le marne calcaree. Una volta stimata la velocità delle onde S nel primo strato e calcolata la profondità della discontinuità relativa, è stato possibile ricavare le velocità e le profondità degli strati più profondi confrontando, con approssimazioni successive, lo spettro sintetico con la media di quelli osservati. Infine, il modello ottenuto è stato verificato confrontando le velocità stimate per lo strato sedimentario più profondo con quelle ricavate dalla sismica attiva per i corrispondenti litotipi affioranti a poca distanza presso la frazione di Petogna (vedi schema geologico in Fig.1).

**Ricerca delle cavità – casi di studio.** Dopo aver ridefinito la geologia locale è stato possibile interpretare le curve H/V, sperimentali e sintetiche, in funzione delle informazioni stratigrafiche per meglio vincolare alla stratigrafia il modello di velocità del sottosuolo. È stato quindi possibile riferire il primo dei due picchi maggiori (~ 1.8 Hz) al top della formazione delle brecce di base, il secondo (~5 Hz) al limite tra le argille e le marne calcaree, rispettivamente alla profondità di circa 100 e 20 m. La notevole dispersione del segnale, e del conseguente rapporto H/V, a frequenze superiori a 50-60 Hz è da correlare con i livelli più superficiali e prevalentemente antropici del suolo (pavimentazioni, riempimenti, fognature ecc.): è quindi tra questi ultimi due intervalli di frequenza che vanno ricercate le dispersioni e le inversioni del segnale sismico dovute alle eventuali cavità antropiche.

Come è noto infatti, la presenza di strati lenti o grosse cavità in sottosuolo produce, nel rapporto HVSR, il cosiddetto fenomeno dell'inversione sismica, cioè la maggiore ampiezza della traccia relativa alla componente verticale del moto del suolo rispetto a quelle orizzontali. La frequenza, o meglio l'intervallo di frequenze cui l'inversione si verifica è determinato dalla profondità dello strato o della cavità, secondo la nota formula $F=4h \cdot V$; sappiamo anche che per avere effetto sulla propagazione delle onde elastiche un qualunque corpo, o viceversa cavità, deve avere dimensione almeno paragonabile alla metà della lunghezza dei treni di onda che la attraversano. Considerando la velocità delle onde S circa 500 m/s, ne deriva che cavità di ampiezza di alcuni metri (5-10, come nel nostro caso) sono sensibili a frequenze uguali o superiori a 25-50 Hz.

Il primo caso studiato è costituito da un piccolo ipogeo che si estende sotto due diversi aggregati edilizi, incrociando la sede di uno stretto vicolo pavimentato a selci e fortunatamente interdetto al traffico. La camera centrale dell'ipogeo, dell'originaria volumetria di circa 200 $m^3$, ha subito un vistoso crollo dei conglomerati di volta (circa 50 $m^3$) in corrispondenza dell'incrocio con il vicolo, fino ad esporre le tubature dei servizi urbani che corrono lungo la via soprastante (foto in Fig.2). Sovrapponendo la pianta dell'ipogeo, rilevata in sottosuolo dagli scriventi, con le planimetrie catastali è stato possibile individuare con buona approssimazione il tratto di strada interessato. Sono state quindi eseguite lungo il vicolo 11 misure microsismiche, distanziate tra loro di 1 m, in modo da intercettare la traccia dell'ipogeo sottostante. Le misure hanno avuto tempo di acquisizione di 10 minuti, tranne la n. 00, con tempo di acquisizione di 30 minuti; non sono state riscontrate significative differenze tra le relative tracce.

I risultati dell'indagine sono sintetizzati in Fig. 2. Il grafico in alto riporta le tracce complessive del rapporto H/V delle 11 misure, assieme a due misure di riferimento (23SM e 7SM) eseguite in sottosuolo a diretto contatto con il substrato. Si notano chiaramente i due massimi "stratigrafici" a 1.8 ed a 5 Hz, corrispondenti alle due principali discontinuità situate, come detto, alle profondità di circa 100 e 20 m; sulla destra, a frequenze superiori a 50 Hz, compaiono i picchi relativi all'effetto della pavimentazione stradale. A frequenze intermedie (5-50 Hz) si trova il campo di interesse per gli intervalli di profondità interessati dalle cavità (1-10 m). Nella parte centrale della figura sono riportati gli spettri di risposta delle 5 stazioni centrali, che come si può vedere sono chiaramente interessati dal fenomeno dell'inversione (la traccia della componente verticale supera in ampiezza quelle delle componenti orizzontali) nell'intervallo di frequenze di interesse. Il fenomeno è ovviamente più accentuato nelle tre stazioni centrali, posizionate in corrispondenza della volta della cavità. L'inversione del segnale sismico può essere messo in maggiore evidenza utilizzando una routine già disponibile nel programma Grilla, originariamente studiata per l'analisi della vibrazione armonica in edifici, che permette di confrontare tra loro le tracce rilevate delle diverse componenti spaziali (nel nostro caso la componente verticale), sottraendo a ciascuna lo spettro di frequenza di una stazione di riferimento, nel nostro caso una di quelle rilevate in sottosuolo. Il diagramma (Fig. 2, in basso) mette in evidenza un forte e netto picco di amplificazione della componente verticale (fino a 10 volte la misura di riferimento) delle stazioni direttamente sovrastanti la cavità. La costanza della frequenza del picco (circa 20 Hz) in tutte le stazioni interessate suggerisce come questo

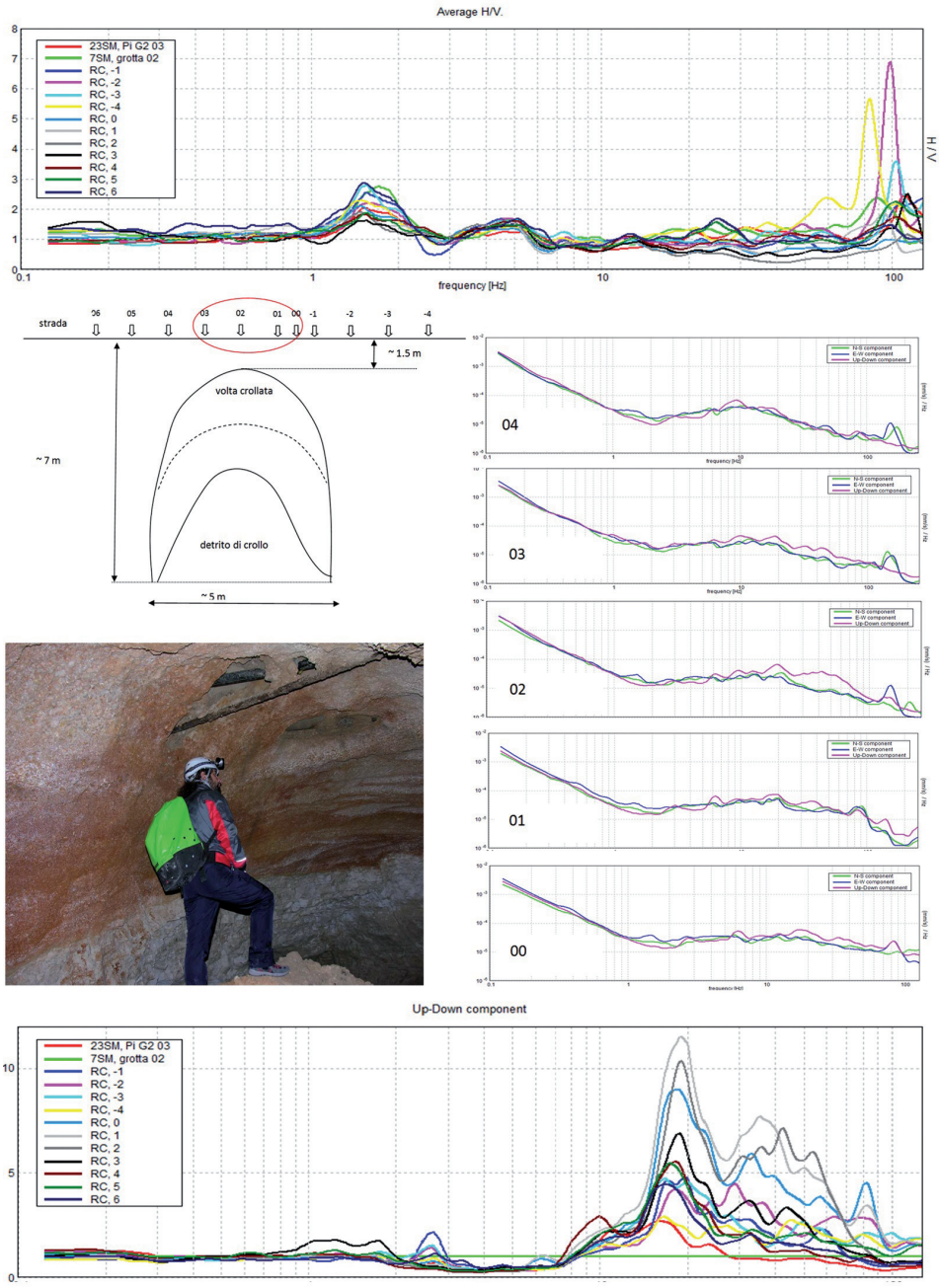


Fig. 2 – Studio dei microtremori rilevati nell'area soprastante una cavità di crollo (nella foto le condutture di acqua e gas sulla volta della caverna rivelano il tracciato stradale). - In alto: tracce cumulative dei grafici H/V nelle quali riconoscono i due picchi caratteristici della stratigrafia locale a 1.8 e 5Hz. - Al centro: esempi di grafici spettrali delle tre componenti del microtremore sismico rilevato in corrispondenza della cavità (l'ubicazione dei punti di misura è riportata nella sezione). Nelle misure eseguite in corrispondenza della volta la traccia rossa, relativa alla componente verticale, è più elevata di quelle delle componenti orizzontali. - In basso: l'amplificazione sulle componenti verticali è messa in maggior evidenza sottraendo a ciascuna traccia quella relativa ad una stazione di riferimento (grotta 02) rilevata nel sotterraneo a contatto con il bedrock. I picchi più pronunciati sono relativi alle stazioni più prossime alla volta della cavità, mentre la relativa frequenza (circa 20 Hz) rimane costante.

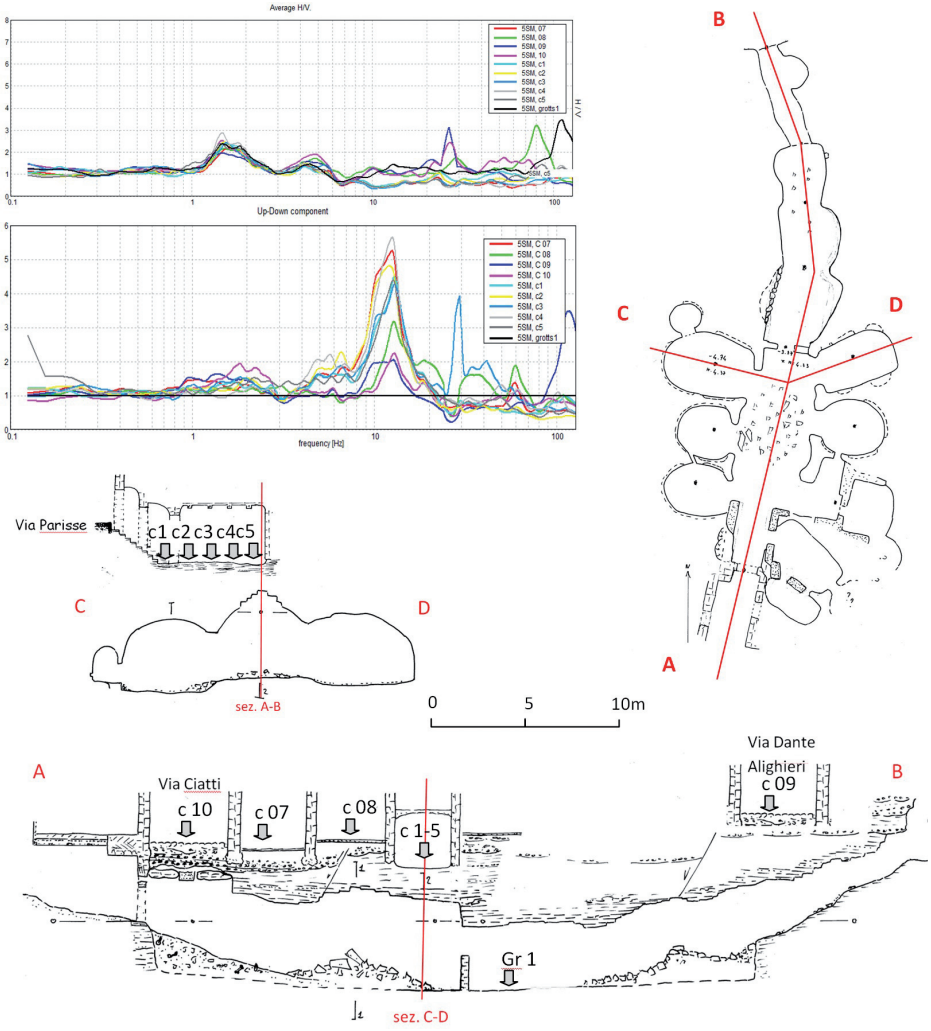


Fig. 3 – Studio dei microtremori rilevati nei locali seminterrati di un aggregato edilizio soprastante una ampia galleria artificiale. Le amplificazioni sulla componente verticale rispetto alla stazione di riferimento Gr 1 sono maggiormente pronunciate nei punti di misura soprastanti la porzione centrale (c 01-c 08), mentre sono poco accennate nelle due stazioni c 09 e c 10, eseguite lungo le vie perimetrali ai due opposti estremi della galleria. Anche in questo caso, pur variando l'ampiezza dei picchi in funzione della posizione dei punti di misura rispetto al sotterraneo, al frequenza (circa 15 Hz) rimane costante.

sia determinato principalmente dalle caratteristiche della cavità piuttosto che dalla posizione relativa della stazione di misura rispetto a questa.

Il secondo caso studiato è relativo ad un ampio ed articolato ipogeo (*Ju' rotton de 'Ciatt*), ricavato probabilmente dalla fusione di più ambienti originari, che si estende per oltre 100 m lineari attraversando un'ampia porzione del paese (nella sezione di Fig. 3 ne è riportata solo la parte meridionale). Il tracciato del sotterraneo si interrompe in corrispondenza della piazza principale del paese, dove il crollo della volta ha causato l'apertura di una voragine nel suolo. Nel suo percorso l'ipogeo attraversa per tutta la sua lunghezza un gruppo di edifici, dai quali peraltro non è possibile accedere ne avere alcun controllo sulla cavità. Per indagare la situazione di sottosuolo dell'aggregato edilizio sono state quindi eseguite numerose misure di microtremore in molti dei locali seminterrati od interrati degli edifici, tanto nell'area certamente

attraversata dall'ipogeo quanto nella restante porzione, dove si sospetta la presenza di cavità analoghe ma non accessibili. Nella più profonda delle cantine interrate, sul cui pavimento affiora direttamente il substrato marnoso, sono state eseguite 5 misure di microtremore (c1-c5), di cui una (c3) con tempo di acquisizione di 30 min, le altre di 10 min.

I risultati sono sintetizzati in Fig. 3, dove è riportata la pianta e le sezioni longitudinale e trasversale di parte dell'ipogeo, ricavati dal rilevamento speleologico eseguito dagli scriventi; nelle sezioni è riportata anche la localizzazione dei punti di misura microsismica. Nel diagramma spettrale in alto, nel quale sono riportate le tracce dei rapporti H/V delle misure relative, si rilevano i due picchi caratteristici a 1.8 e 5 Hz. Nella parte destra del diagramma appaiono le dispersioni del segnale dovute agli strati superficiali; come era lecito aspettarci, le tracce maggiormente disperse alle alte frequenze sono quelle rilevate su pavimentazione stradale (c9 e c10). Nel secondo diagramma, analogamente all'esempio precedente, sono riportati i rapporti spettrali tra la componente verticale delle diverse tracce rispetto ad una misura di riferimento (Gr1) rilevata sul suolo roccioso dell'ipogeo. È evidente il netto picco che appare alla frequenza di circa 15 Hz nelle tracce relative ai punti di misura sovrastanti la cavità. Nelle due misure eseguite sulle sedi stradali (c9 e c10), il picco è poco accentuato, fino ad essere difficilmente riconoscibile, sia per la pavimentazione a ciottoli sia per la ridotta ampiezza della cavità sottostante. Nonostante la differenza di ampiezza dei picchi, la frequenza media (~15 Hz) rimane costante in tutti i siti di misura e significativamente differente da quella caratteristica dell'ipogeo precedente (~20 Hz), di volumetria nettamente inferiore.

In ultimo sono state analizzate e confrontate con lo stesso metodo tutte le tracce delle misure microsismiche rilevate nella restante porzione del gruppo di edifici: tra queste, alcune presentano picchi e morfologia simile a quelli di Fig 3. Analizzando poi separatamente i grafici delle tre componenti spettrali delle relative stazioni di misura, è stato possibile osservare in citato fenomeno dell'"inversione sismica", confermando la probabile presenza di ulteriori cavità ipogee non esplorate sotto parte degli edifici.

**Conclusioni.** Il rilevamento microtremore sismico, attraverso l'analisi spettrale della componente verticale del moto del suolo e del rapporto tra questa e le componenti orizzontali, può essere un utile strumento per individuare cavità nel sottosuolo urbano ove non siano applicabili altre tecniche geofisiche (georadar, tomografia elettrica, microgravimetria ecc.). Al fine di interpretare correttamente il segnale sismico rilevato è tuttavia necessario conoscere *a priori* e con sufficiente dettaglio, la geologia, la stratigrafia e la risposta sismica caratteristica del substrato roccioso interessato dallo sviluppo delle gallerie. Di particolare importanza è la scelta di una o più stazioni di riferimento, rappresentative della risposta microsismica media del substrato indeformato, cioè non interessato da cavità né, per quanto possibile, da coperture antropiche, suoli ecc. L'intervallo di frequenze sensibile alle perturbazioni del moto del suolo indotto dalla presenza delle cavità dipende in prima approssimazione dall'ampiezza delle cavità stesse: nei casi studiati sembra che ogni cavità abbia una sua frequenza caratteristica, e che a volumi maggiori corrispondano frequenze più basse. Stazioni di misura posizionate a diverse distanze dalla volta degli ipogei hanno riportato frequenze simili, ma ampiezze diverse. Poiché la profondità dell'indagine dipende essa stessa dalla frequenza del microtremore sismico secondo la nota formula $F=V\cdot 4h$, se ne deduce che i migliori risultati si raggiungono quando la profondità delle cavità rispetto al suolo è confrontabile con l'ampiezza delle cavità stesse. Ipogei con estensione planimetrica inferiore a poche decine di $m^2$ non sono hanno rivelato significative evidenze microsismiche, mentre i risultati più evidenti sono stati ottenuti con cavità di oltre 100 $m^2$ e larghezza minima superiore a 4-5 m.

Riconoscimenti. Il presente lavoro è stato possibile grazie alla collaborazione ed al lavoro della dott. Carmelina Derose, attualmente in ruolo come geologo presso il Comune dell'Aquila. Si ringraziano gli abitanti del paese di Picenze per le utili ed interessanti indicazioni sulla localizzazione degli accessi, sui tracciati e sulla storia dei "rottoni", in particolare di quelli non più accessibili all'esplorazione diretta.

# GEOSTRUCTURAL AND GEOPHYSICAL SURVEYS FOR THE STABILITY ANALYSIS ALONG A ROCK SLOPE IN THE CULTURAL HERITAGE SITE OF ISPICA (SOUTH-EASTERN SICILY)

**G. Pappalardo[1], S. Imposa[1], S. Mineo[2] , S. Grassi[1]**
*[1] Dipartimento di Scienze Biologiche, Geologiche e Ambientali, Università degli Studi di Catania, Italy*
*[2] Dip. di Scienze della Terra, dell'Ambiente e delle Risorse, Università degli Studi Federico II di Napoli, Italy*

**Introduction.** The aim of this study is to evaluate the degree of fracturing and the stability conditions of the calcareous rock cliff on which the cultural heritage site of Ispica lies. Ispica is a 16.000 inhabitants village belonging to the Ragusa district. It is located in the southeastern coastline of Sicily, where tectonics affects the geology and morphology, as well as the seismicity. Indeed, from a geological point of view, the studied sector is a calcareous horst, with direction NE-SW, bordered by the Gela-Catania foredeep to the west and to the Malta Escarpment to the east (Fig.1a).

The main structural element is represented by a NE-SW fault system, known as Pozzallo-Ispica-Rosolini system (Ghisetti and Vezzani, 1980; Lentini *et al.*, 1987; Grasso *et al.*, 2000). In the study area, this system is named "Ispica fault system" and shows strike slip motion. Faults are sub-vertical, with maximum throws of 80-100 m. This system mainly adjoins the marls and calcarenites of the Ragusa Formation (lower Miocene) to the west with the blue clays of the Tellaro Formation (middle Miocene) to the east (Grasso *et al.*, 1992).

The seismic activity related to this faults is historically known, with the 1727 and 1903 earthquakes (M>5) (Azzaro and Barbano, 2000). Moreover, on 11 January 1693, Ispica village was destroyed by a M <= 7.4 earthquake (Table 1), which is the strongest shaking ever occurred in the area.

Table 1 - historical earthquakes at Ispica village (http://emidius.mi.ingv.it/DBMI04/).

| Number of events: 12 | | | | | |
|---|---|---|---|---|---|
| Effects | Earthquakes | | | | |
| Is | Year Mo Da Hr | Epicentral area | Np | Ix | Mw |
| 10 | 1693 01 11 13 30 | Eastern Sicily | 181 | 11 | 7.41 |
| 3-4 | 1727 01 07 | Noto | 14 | 7-8 | 5.37 |
| 7-8 | 1818 03 01 02 45 | Iblean Mountains | 24 | 7-8 | 5.63 |
| 5-6 | 1848 01 11 | Augusta | 33 | 8-9 | 5.48 |
| 5-6 | 1903 02 10 08 04 | Noto | 10 | 6 | 4.83 |
| 2 | 1905 09 08 01 43 | Calabria | 827 | 10-11 | 7.06 |
| NF | 1908 12 10 06 20 | Novara di Sicilia | 64 | 7 | 5.00 |
| 6 | 1949 10 08 03 08 | Noto | 32 | 7 | 5.18 |
| 3 | 1959 12 23 09 29 | Catania Plain | 108 | 6-7 | 5.23 |
| 2-3 | 1978 04 15 23 33 | Gulf of Patti | 332 | 8 | 6.06 |
| 5-6 | 1980 01 23 21 | Modica | 122 | 5-6 | 4.63 |
| 6 | 1990 12 13 00 24 | South-eastern Sicily | 304 | 7-8 | 5.68 |

The cultural heritage site comprises several worship constructions such as the Friars Minor Monastery, which had been a Franciscan Friary since 1515 A.D. and now is the headquarter of Friars Minor. The cloister is one of the oldest constructions of the village, so an important tourist attraction.

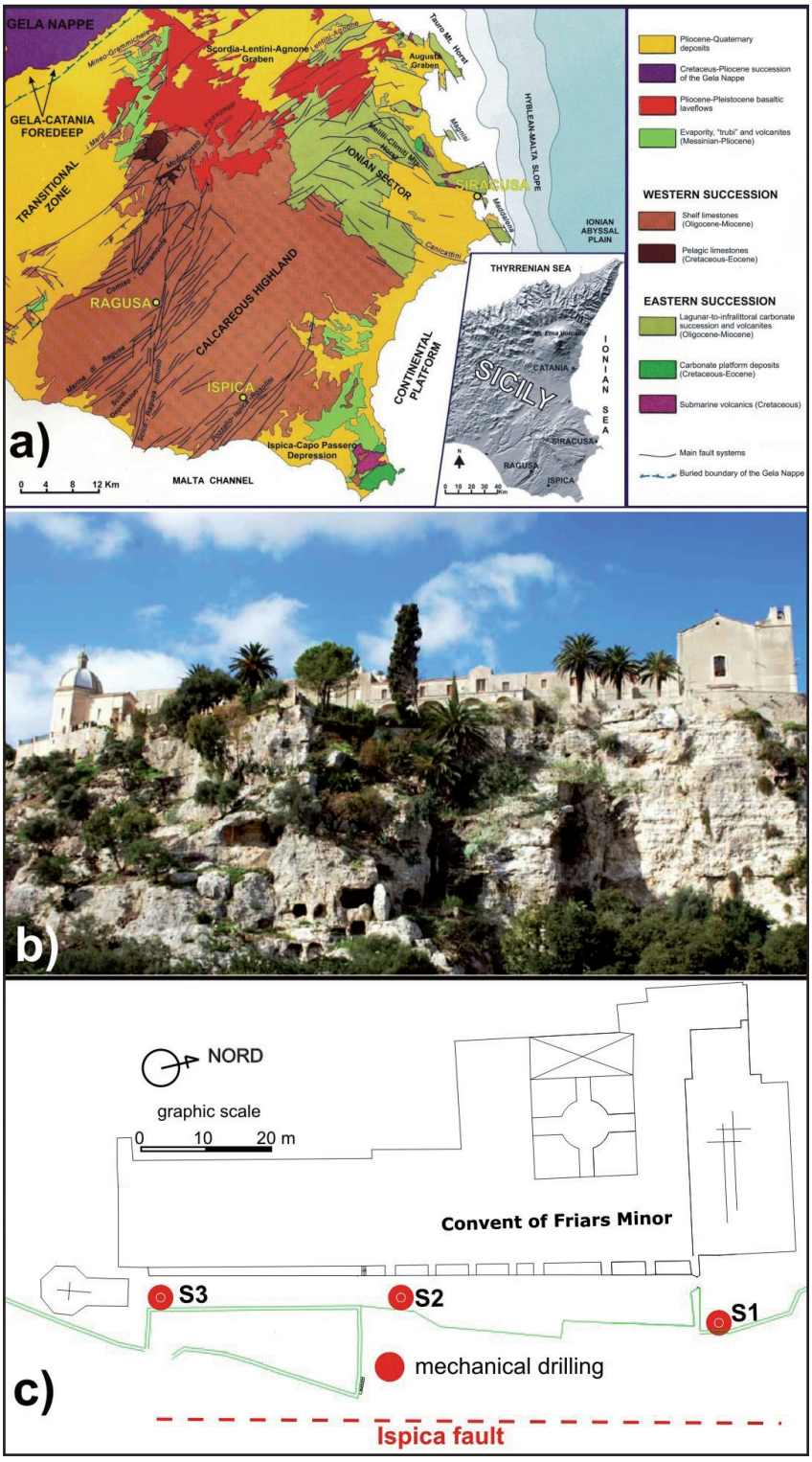


Fig. 1 – a) Geological map of south-eastern Sicily (Lentini *et al.*, 1987); b) convent of Friars Minor photo; c) map of the mechanical drilling location.

This site stands on the top of a 35 m high calcareous cliff (Fig. 1b), located in the eastern sector of Ispica village, showing instability conditions since the presence of deep fracturing and karst, as well as of several blocks about to fail. For the reconstruction of the stratigraphic succession, 3 geognostic mechanical drillings were performed in front of the monastery (Fig. 1c).

The resulting stratigraphy is represented by a succession of calcarenites with different degree of fracturing; particularly, under a thin talus level, 5 meters of intensely fractured calcarenites are present; between 5 and 20 m b.g.l. the succession shows a lower degree of fracturing; from 20 to 30 m b.g.l. intensely fractured calcarenites were drilled.

Deep fracturing, especially close to important tectonic structures, is one of the main causes of slope instability (Barbano *et al.*, 2014; Pappalardo, 2014). Furthermore, the high seismic activity of the study area (category II according to the Italian Ordinance OPCM 3274) may be regarded as one of the potential triggers for rockfalls.

A geophysical survey has been performed to obtain information on the degree of fracturing of the deep rock mass and to estimate the resonance frequency of the site.

Geostructural surveys, kinematic and stability analysis allowed us to better understand the main instability features, as well as to evaluate the safety factors for the most unstable blocks.

**Methodologies.** The study of the environmental microtremors (noise), through passive seismic recordings of single-station H/V (or HVSR), is a non-invasive technique for the investigation of the underground. It allows highlighting the frequencies at which the ground motion is amplified by stratigraphic resonance. The spectral ratios of the vertical and horizontal components of the ground motion, recorded at each measurement station, are taken into account by this technique (Nogoshi and Igarashi, 1970; Nakamura 1989). The amplitude ratio associated with the resonance frequencies of the site is an indicator of the "minimum" amplification expected at the site in case of earthquake.

In a simple two-layer system, characterized by two different speeds ($V_1$ and $V_2$) and by two different densities ($\varrho_1$ and $\varrho_2$), the equation linking the resonance frequency "f" to the thickness "H" of the resonating layer, depends on the shear waves velocity, as shown by:

$$f = nVs/4H \quad (1)$$

where n (= 1, 3, 5 ...) indicates the order of the mode of vibration (fundamental, first superior etc.), Vs and H represent the shear waves velocity and the thickness of the resonating layer respectively.

Eq. (1) allows understanding how the H/V technique can also provide information on stratigraphic characters. Indeed, starting from a noise measurement providing f, once known the Vs of the coverage, the depth of the main seismic reflectors or vice versa can be easily estimated (Ibs-von Seht and Wohlenberg, 1999); each peak in the H/V graph corresponds to a possible reflector (seismostratigraphic level) that presents an impedance contrast compared to the neighbor level; the greater the impedance contrast, the greater the amplitude of the peak would be. However, this report does not follow a linear trend.

The measurements of environmental microtremors were carried out through the use of a portable digital tromograph TROMINO (Micromed S.p.A.), equipped with three electrodynamic orthogonal sensors (velocimeters) responding in the band 0.1 ÷ 1024 Hz. Seismic noise has been acquired with sampling frequency of 128 Hz, and recorded for 20 minutes at 3 measurement stations (N1-N2-N3) (Fig. 2).

These were placed close to the previous drilled boreholes (S1-S2-S3), to verify if such a survey could detect any difference in the physical-mechanical properties of the lithology (i.e. changes in the degree of fracturing), already pointed out by the stratigraphy successions (Fig. 2).

The instruments were located on the ground, with the major axis oriented toward north. Recordings were processed through the software Grilla, to evaluate the relationship between the spectral components of the ground motion.

Data were then processed by dividing the acquired traces in 20 seconds time-windows. Then, a triangular smoothing of 10% was applied, and the signal was "cleaned", eliminating

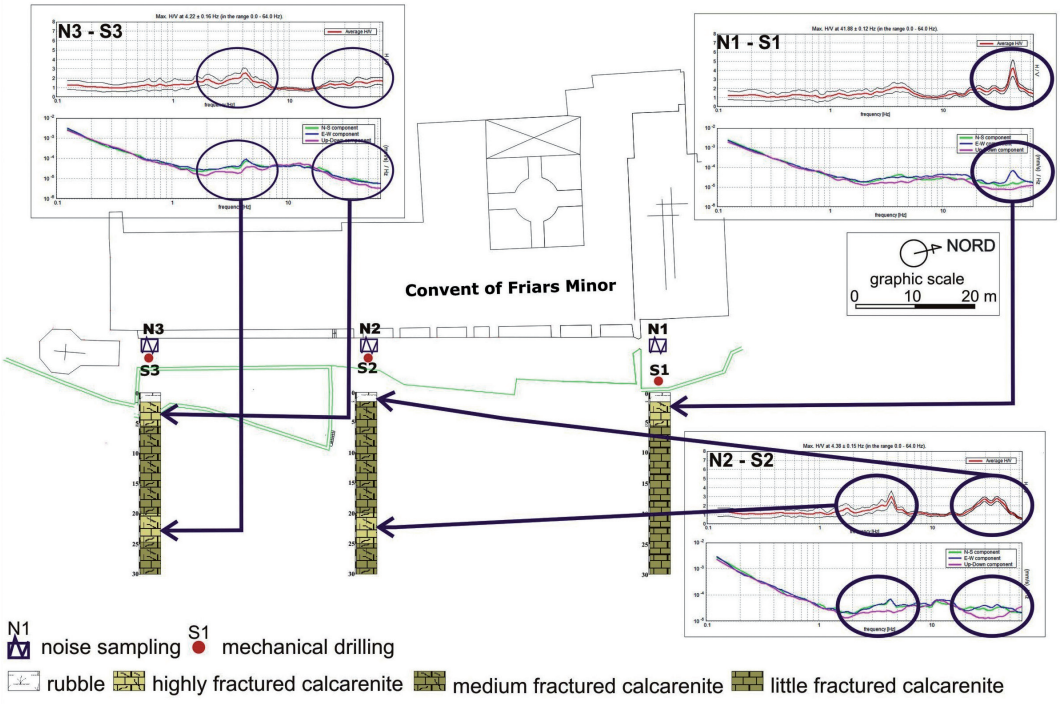


Fig. 2 – Map of the geognostic and geophysical surveys location and the relative stratigraphic sections and H/V spectral ratios.

the transients, (i.e. anthropogenic disturbances). For the analysis, only the stationary portion of the signal has been taken into account. The final functions HVSR of each measurement are represented by frequency (x-axis the 0 to 64Hz) - amplitude H/V spectral ratios (y-axis) graphs.

For each station the outcome of the statistical tests (guidelines SESAME, 2005) showed that all measurements have met the 3 criteria experiencing the reliability of the H / V curve and the goodness of implementation of the measure. For 2 of the 3 recordings also the main peaks of resonance were significant and clear for all the six criteria analyzed; only the recording N3 does not meet the first of the 6 parameters assessing the clarity of the peak.

In order to obtain stratigraphic information from the H / V spectra, which could be compared with those obtained previously by mechanical drillings, the average velocity of shear waves in the investigated sector had to be estimated. It was obtained by down-hole prospecting, performed in correspondence of the drillings. In this way, the inversion of equation 1 allowed obtaining information on the depth of the impedance contrast causing the peak observed in the spectra of our recordings.

Geostructural surveys have been performed at two measurement stations (SL-1 and SL-2) located in the SE portion of the cliff (Fig. 3), according to ISRM (2007) recommendations. Scan lines were placed at the most fractured portions of the slope and inside a karst cave. For each discontinuity dip-immersion, spacing, persistence, opening, in-filling, roughness, uniaxial compressive strength (UCS) and hydraulic conditions have been measured.

Moreover, several unstable blocks, with volumes ranging between 2 and 460 $m^3$, have been surveyed along the southeastern portion of the slope. All the surveyed factors were used for the Bieniawski (1976) classification, to assign a quality class to the rock mass, as well as to calculate its main geomechanical parameters. Bieniaswki's Rock Mass Rating (RMR) system

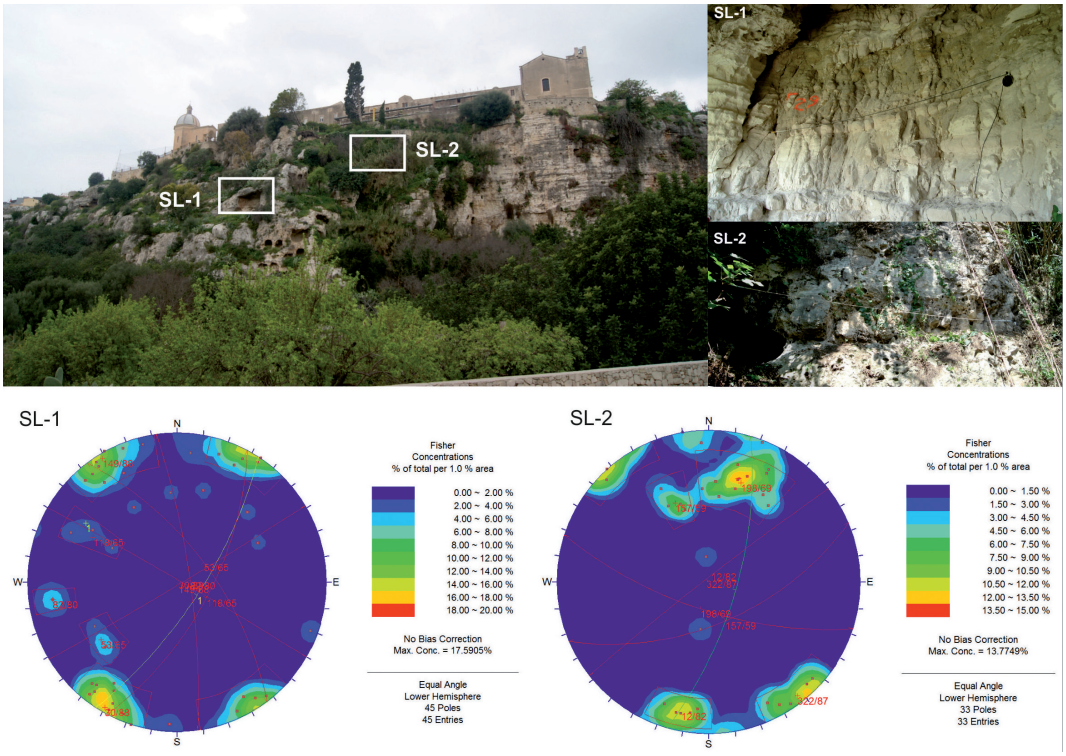


Fig. 3 – Location of geostructural measurement stations with corresponding stereoplots showing the pole density with respect to the surveyed discontinuity sets.

(1976) is a a geomechanical classification system for rock masses, which takes into account 6 parameters: Uniaxial Compressive Strength (UCS) of rock material; Rock Quality Designation (RQD); Spacing of discontinuities; Condition of discontinuities; Groundwater conditions; Orientation of discontinuities.

In particular, UCS is one of the most important parameters since it depends on physical properties of the rock (i.e. porosity, micro fracturing, texture) (Pappalardo *et al.*, 2013). Spacing of discontinuities affects the degree of fracturing, while their orientation plays a significant role in the stability analysis. Each of the six parameters is turned into a value corresponding to the characteristics of the rock. These values are derived from field surveys and laboratory tests.

The sum of the six parameters is the "RMR value", which lies between 0 and 100 and identifies 5 classes of quality, from "very good" to "very poor". Furthermore, on the basis of RMR, mean cohesion and internal friction angle of the rock mass can be calculated (Bieniawski, 1976) through:

$$c' = 5RMRb \quad (2)$$

$$\phi = 0.5RMRb + 5. \quad (3)$$

Stereographic projections of the discontinuity poles allowed grouping all the surveyed discontinuity into sets for the kinematic and stability analysis (Fig. 3).

Kinematic analysis, according to Hoek and Bray (1981), is a graphical procedure allowing the identification of the main failure mechanisms with respect to the geometric relationship between the discontinuity and the slope. If the discontinuity has the same orientation of the slope (±20°) but a lower inclination, planar sliding is the possible failure mechanism; if the discontinuity has the same orientation of the slope (±20°), but an opposite immersion, toppling may occur; if two discontinuities intersect, with a plunge of the intersection lower than the dip angle of the slope face, wedge sliding may be the potential failure mode.

On the basis of these stereonets, Markland Test (1979) allows identifying the unstable mechanisms, with respect to the internal friction angle of the rock mass. In fact, the graphical representation of the discontinuities (as poles or cyclographics), slope (as a cyclographic) and friction angle (as a circle) leads to the delineation of "critical areas" in the stereogram. Each discontinuity, whose pole falls inside of these areas, is to be considered unstable.

Safety factors have been calculated, for the main unstable mechanism, by the limit equilibrium analysis, where the full shear strength is assumed to be mobilized simultaneously (Hoek *et al*., 1973):

$$FS = \frac{3}{\gamma H}(c_A X + c_B X) + \left(A - \frac{\gamma_w}{2\gamma} X\right) = tan\,\varphi_A + \left(B - Y\,\frac{\gamma_w}{2\gamma}\right) = tan\,\varphi_B \qquad (4)$$

where $C_A$ and $C_B$ are the cohesive strengths of planes A and B along the base of the rock wedge; $\varphi_A$ and $\varphi_B$ are the internal friction angles of planes A and B along the base of the rock wedge; $\gamma$ is the unit weight of the rock mass; $\gamma_w$ is the unit weight of water; H is the total height of the rock wedge; X, Y, A and B are dimensionless factors depending upon the geometry of the rock wedge and the slope.

**Results.** The spectrum of the noise recording N1, located in the northern sector of the cultural site, shows a clear peak at a high frequency (41.88 Hz) with an amplitude of the H/V spectral ratio greater than 4. On the contrary, the spectra of the recordings N2 and N3, respectively located in the central and southern portions of the site, show two peaks at different frequencies. The first has an amplitude of the H/V ratio of about 3, at frequencies between 4 and 4.5 Hz; the other has an amplitude ranging between 2 and 3 at frequencies around 40 Hz.

The comparison of the results obtained from noise measurements and the stratigraphic succession (Fig. 2) indicates the presence of one peak in the N1 spectrum, corresponding to transition between low fractured calcarenites and medium fractured calcarenites. On the other hand, spectra N2 and N3 show a low frequency peak (4 Hz) corresponding to the transition between intensely fractured and low fractured calcarenites (Fig. 2). These results are comparable with the stratigraphic succession reconstructed through mechanical drilling S1-S2-S3 (Imposa *et al*., 2010, 2014).

Thus, it can be stated that noise survey, followed by H/V analysis can give information on the stratigraphy (Amorosi *et al*., 2008), since it allows detecting the depth of impedance contrast related to lithological transitions, if the shear wave velocity is known.

Results of geostructural analysis allowed identifying 5 main discontinuity sets at SL-1 and 4 systems at SL-2. These showed a close spacing, modest aperture and slight roughness. Sometimes discontinuities are filled with soft material. Geomechanical classification, according to Bieniawski (1976), allowed the estimation of the RMR index, which classifies the rock mass as "Fair Rock" (III class). Calculated values of cohesion and internal friction angle range between 200 and 300 kPa and 25° to 35° respectively.

Kinematic analysis and Markland Test (1979) showed that planar sliding, wedge sliding and toppling are to be considered potential failure mechanisms. In particular planar sliding are mainly possible at SL-1, at those discontinuities with direction matching to the slope. The main unstable mechanism, at both stations, is the wedge sliding, occurring along two intersecting discontinuities, with a plunge of the intersection lower than the dip angle of the slope face.

Calculated safety factors (FS) for the main failure mechanism (wedge sliding) are lower than 1, both in static and pseudostatic conditions, highlighting the high instability of the slope. It has to be noted that the pseudostatic conditions are the most reliable in this case, since the high seismic activity of the study area.

**Conclusions.** This study aims to evaluate the degree of fracturing, as well as the stability of a rock cliff in an area with a high seismic activity. The Convent of Friars Minor, considered among the cultural heritage sites of Ispica Village, stands on the top of the cliff, which is bordered by an important tectonic alignment striking NE-SW. Several rockfalls occurred in

the past years, threatening the stability of the rock cliff, as well as the static of the cultural heritage site.

From the analysis and the interpretation of the seismic noise, it is clear that the adopted geophysical methodology allows highlighting the presence of a different degree of fracturing in the rock mass. Indeed, it is function of the spectral response. These results, however confirmed by the stratigraphy obtained by mechanical drillings, allow us to say that the Convent of Friars Minor stands on a fairly fractured area and the resonance frequency has values of 4 Hz (S2 and S3) and 41.88 Hz (S1).

Geostructural analysis pointed out the presence of several discontinuity systems. One of them shows an orientation matching with the direction of the NE-SW main fault system. Geomechanical properties of the rock mass are to be considered poor, according to the RMR classification. Moreover, stability analysis highlighted a widespread instability, with planar sliding and wedge as possible failure mechanisms. The limit equilibrium analysis led to the calculation of FS whose values are lower than 1 both in static and pseudostatic conditions. Furthermore, the main instability conditions are related to the southeastern portion of the surveyed slope, where several karst caves are also present.

**Acknowledgments.** This paper was undertaken with the financial support of the University of Catania (PRA n. 20104001082, Scientific Supervisor: S. Imposa).

## References

Amorosi A., Castellaro S., Mulargia F.; 2008: *Single-Station Passive Seismic Stratigraphy: an inexpensive tool for quick subsurface investigations*. Geoacta, **7**, pp. 29-39

Azzaro F., Barbano M.S.; 2000*: Analysis of seismicity of Southeastern Sicily: proposal of a tectonic interpretation*. Annali di Geofisica, **43** (1), pp. 1-18

Barbano M.S., Pappalardo G., Pirrotta C., Mineo S.; 2014: *Landslide triggers along volcanic rock slopes in eastern Sicily (Italy)*. Nat. Hazards, **73**, pp. 1587–1607, DOI 10.1007/s11069-014-1160-1

Bieniawski Z.T.; 1989: *Engineering Rock Mass Classification*, John Wiley & Son, 251

Ghisetti F., Vezzani L.; 1980: *The structural features of the Iblean Plateau and of the Mont Judica ares (southeastern Sicily): a microtectonic contribution to the deformational history of the Calabrian Arc*. Boll. Soc. Geol. It., **99**; pp. 57-102

Grasso M., Reuther C.D., Tortorici L.; 1992: *Neotectonic deformations in SE Sicily: the Ispica fault, evidence of late Miocene-Pleistocene decoupled wrenching within the central Mediterranean stress regime*. J Geodyn., **16** (1/2), pp. 135–146

Grasso M., Pedley H.M., Maniscalco R., Ruggieri R.; 2000: *Geological context and explanatory notes of the "Geological Map of central-southern sector of the Hyblean Plateau"*. Mem. Soc. Geol., Italy, **55**, pp. 45–52

Hoek E., Bray J.W.; 1981: *Rock Slope Engineering*, Third Edition, The Institution of Mining and Metallurgy, London, 368 pp.

Ibs-von Seht, J. Wohlenberg; 1999: *Microtremor measurements used to map thickness of soft sediments*. Bulletin of the Seismological Society of America, **89** (1), pp. 250-259

Imposa S., Corrao M., Barone F., Coco G., Occhipinti R., Mozzicato P.; 2010: *Geostructural and geognostic survey for a stability analysis of the calcareous cliff of Ispica (Hyblean plateau, southeastern Sicily)*. Bull. Eng. Geol. Environ., **69**, pp. 247-256

Imposa S., Corrao M., Mele G., Coco G.; 2014: *Geophysical survey of a calcareous cliff in the area of Ispica (southeastern Sicily)*. Bull. Eng. Geol. Environ, (in press)

ISRM; 2007: *The complete ISRM suggested methods for rock characterization, testing and monitoring*: 1974-2006. R. Ulusay and J.A. Hudson (eds.), Suggested Methods Prepared by the Commission on Testing Methods, International Society for Rock Mechanics, Compilation Arranged by the ISRM Turkish National Group, Kozan Ofset, Ankara, Turkey, 628 pp.

Lentini F., Carbone S., Grasso M.; 1987: *Carta geologica della Sicilia sud-orientale*. Scala 1:100.000. S.EL.CA. Firenze

Markland J.T.; 1972: *A useful technique for estimating the stability of rock slopes when the rigid wedge sliding type of failure is expected*, Imp. Coll. Rock Mech. Res. Rep., 19, 10

Nakamura Y.; 1989: *A method for dynamic characteristics estimation of subsurface using microtremor on the ground surface*. Quarterly Report of Railway Technical Research Institute. Rept., **30**, pp. 25–33

Nogoshi M., Igarashi T.; 1970: *On the propagation charactestics of the microtremors*. Journal of the Seismological Society of Japan, **24**, pp. 24-40.

Pappalardo G., Mineo S., Marchese G.; 2013: E*ffects of cubical specimen sizing on the uniaxial compressive strength of Etna volcanic rocks (Italy).* Italian Journal of Engineering Geology and Environment, **2**, pp. 45-54. **DOI:** 10.4408/IJEGE.2013-02.O-03

Pappalardo G.; 2014: *Correlation Between P-Wave Velocity and Physical–Mechanical Properties of ntensely Jointed Dolostones, Peloritani Mounts, NE Sicily.* Rock Mech Rock Eng, DOI 10.1007/s00603-014-0607-8

SESAME; 2005: *Guilines for the implementation of the H\V spectral ratio technique on ambient vibrations* – European Research Project.

## TOMOGRAFIA SISMICA MARINA MULTICANALE AD ALTA RISOLUZIONE: ESEMPIO DI APPLICAZIONE PRESSO IL "PORTICCIOLO DELLA TONNARA", CAPO GRANITOLA (TP)

**M. Punzo[1], V. Di Fiore[1], G. Cavuoto[1], D. Tarallo[1], N. Pelosi[1], G. Tranchida[2], S. Mazzola[1,2]**
*[1]IAMC - Istituto per l'Ambiente Marino Costiero, CNR Napoli*
*[2]IAMC - Istituto per l'Ambiente Marino Costiero, CNR Capo Granitola, (TP)*

**Introduzione.** Le zone di transizione marino-costiere, le aree alluvionali o vulcaniche sono generalmente caratterizzate dalla presenza di terreni sciolti e forti variazioni geometriche latero-verticali, che si ripercuotono sul campo di velocità del sottosuolo in questi casi estremamente variabile.

La tomografia sismica multicanale a rifrazione è una tecnica di prospezione sismica che permette di definire un modello bi-dimensionale del sottosuolo, grazie l'individuazione delle anomalie di velocità di propagazione delle onde sismiche. Questa metodologia possiede un potere risolutivo nettamente superiore agli altri metodi convenzionali a rifrazione [es: Metodo Reciproco Generalizzato (GRM), metodo del tempo di ritardo (*delay time*), metodo del tempo intercetto], i quali si basano su un modello di sottosuolo costituito da strati regolari e con proprietà elastiche costanti, e che di conseguenza risultano inadeguati quando si è in presenza di forti variazioni laterali della velocità o inversioni di velocità con l'aumentare della profondità, cioè in presenza di situazioni geologicamente complesse.

Il metodo sismico multicanale a rifrazione, grazie alla sua versatilità, è uno dei metodi geofisici più comunemente utilizzati per l'esplorazione del sottosuolo. Tale tecnica permette, infatti, di ricostruire in maniera dettagliata le morfologie sepolte e definire la presenza di eventuali discontinuità in sottosuolo (faglie, fratture). La tomografia sismica viene ampiamente adoperata a terra a scopi ingegneristici; invece in mare ha un'applicazione limitata, in particolare nelle zone costiere e di transizione come porti, lagune e baie. Recentemente, è stato dimostrato che le indagini sismiche a rifrazione in ambiente marino superficiale, possono fornire contributi importanti per la caratterizzazione degli strati del sottosuolo in termini di spessore e di velocità delle onde compressive $V_P$ (Whiteley e Stewart, 2008). La velocità delle onde P, infatti, è legata alla rigidità dei materiali e costituisce, quindi, un parametro importante per individuare il bedrock sismico ed i rapporti stratigrafici tra questo ed i sedimenti di copertura. La ricostruzione accurata del tetto della morfologia del bedrock sismico e quindi la valutazione della variazione degli spessori delle unità più superficiali è indispensabile nei progetti inerenti lo sviluppo di un'area portuale come ad esempio la costruzione di ponti o banchine e soprattutto nella stima degli interventi di dragaggio e ripascimento (MacGergor *et al*., 1994, Young Ho Cha *et al*., 2003).

Al fine di dimensionare un intervento di dragaggio da eseguirsi nello specchio d'acqua del "Porticciolo della Tonnara" di Capo Granitola, a Campobello di Mazara (TP), l'Istituto per l'Ambiente Marino Costiero del CNR di Napoli ha eseguito un test di sismica marina multicanale a rifrazione. Sono stati realizzati 4 profili sismici, di cui tre seriati e paralleli alla costa ed incrociati da un quarto profilo, al fine di ottenere dati di tomografia sismica da elaborare mediante tecniche 2D e 3D.

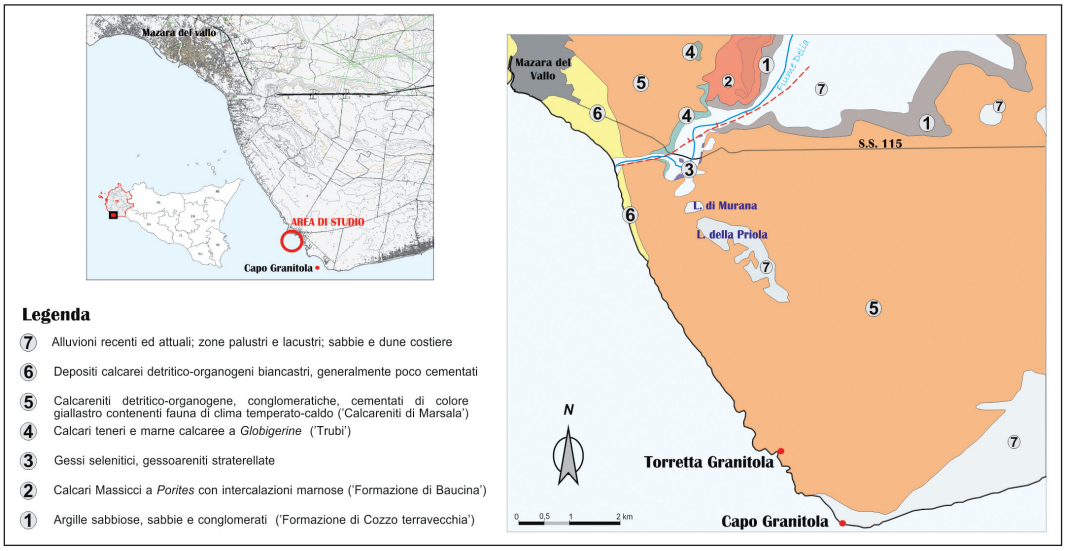


Fig. 1 – Carta geologica del tratto di costa a SW di Mazara del Vallo [stralcio modificato del Foglio 617 "Marsala", D'Angelo e Vernuccio (1992)].

L'indagine ha interessato la fascia batimetrica compresa tra -1 e -3 m e ha previsto il posizionamento di un cavo idrofonico d'acquisizione (bay-cable) direttamente sul fondale del porticciolo allo scopo di elaborare modelli di velocità bidimensionale delle onde P ed S.

La sperimentazione di tale tecnica ha consentito di dedurre utili informazioni dei depositi marini antichi e recenti, sia in termini di geometrie che di caratteristiche elastiche.

**Assetto geologico e geomorfologico.** Il Porticciolo della Tonnara è ubicato nella parte sud-occidentale della Sicilia, nel settore costiero a sud di Mazara del Vallo compreso fra l'abitato di Torretta Granitola e il capo Granitola. Le litologie affioranti nel territorio a sud di Mazara del Vallo sono costituiti prevalentemente da sedimenti marini di tipo calcarenitico, ben stratificati e disposti a monoclinale e immergenti di pochi gradi (5°-10°) verso SW, conosciuti in letteratura come "Calcareniti di Marsala".

Questa successione, datata al tardo Pleistocene inferiore, poggia trasgressivamente su di un basamento di depositi più antichi (di età variabile dal Miocene superiore al Pliocene inferiore), affioranti esclusivamente a NW di Mazara del Vallo sulle ripe del fiume Delia (Fig. 1).

Dal punto di vista tessiturale, i depositi calcarenitici sono caratterizzati dalla presenza di abbondanti bioclasti (Ostree, Pecten, Gasteropodi) e rari livelli argilloso-sabbiosi di spessore decimetrico. Localmente sono ricoperti da pochi metri di depositi superficiali, costituiti prevalentemente da sabbie di spiaggia recente o da luoghi fossilizzati da una debole copertura eluvio-colluviale pedogenizzata con dispersi frammenti di calcareniti, scarsamente coesiva di colore rossastro (Ruggieri *et al.*, 1977; D'Angelo e Vernuccio, 1992, 1994).

Dal punto di vista geomorfologico, il settore in cui ricade l'area in studio è caratterizzato da un esteso tavolato costiero debolmente inclinato verso mare che risulta bruscamente interrotto, in corrispondenza della linea di costa, da tratti di falesia generalmente acclivi ed elevati di pochi metri (circa 3-10 m) sul livello del mare. La linea di costa si sviluppa in senso NW-SE con un suo profilo di erosione pressoché rettilineo con modesto sviluppo di spiagge sabbiose e ciottolose.

Questo implica una generale bassa sinuosità della linea di costa fino all'abitato di Torretta Granitola, dove l'andamento della linea di costa è molto più articolato dal succedersi di piccole baie, spiagge di fondo baia (*pocket beach*) e promontori isorientati impostatesi, generalmente, lungo le linee principali di fratturazione (circa NW-SE e NE-SW) del banco roccioso che è

interessato da cavità, crolli e a luoghi presenta anche aree e segni di intensa attività estrattiva. Infatti, nonostante le Calcareniti di Marsala abbiano caratteristiche di ridotta resistenza, per l'elevato rapporto resistenza/peso dell'unità di volume e per la ridotta conducibilità termica, sono state nel passato e recentemente utilizzate come materiale da costruzione.

**Strumentazione.** La strumentazione utilizzata per l'acquisizione del profilo sismico si compone in 4 unità principali: a) unità d'acquisizione dati, b) sistema di trasduzione, c) unità di immagazzinamento dati e d) sistema di energizzazione.

Il sistema di acquisizione dati (a) è costituito da sismografi modulari GEODE della Geometrics da 24 canali; il sistema di trasduzione (b) è costituito da tre cavi sismici marini (bay cable) da 24 canali equipaggiato con idrofoni frequenza naturale d'oscillazione di 10 Hz; il sistema d'immagazzinamento dati (c) è rappresentato da un PC che, collegato tramite rete locale Ethernet ai Geodi, svolge il compito di archiviare i dati digitalizzati provenienti dai Geodi, di gestire i parametri d'acquisizione e di valutare interattivamente la qualità dei dati acquisiti; il sistema di energizzazione (d) è costituito da una sorgente sismica marina Watergun SODERA Modello S-15 di 0.24 l. di volume.

La sorgente, costituita da due camere ed alimentata da bombole ad aria compressa, immette energia in mare attraverso una prima fase di espulsione dell'acqua dalla camera inferiore ed una successiva implosione con conseguente generazione dell'impulso acustico.

E' stata utilizzata una piccola imbarcazione come supporto della sorgente e di aiuto nella fase di stendimento dei cavi, mentre la strumentazione di registrazione è stata collocata a riva. Gli idrofoni sono stati allineati sul fondale grazie all'utilizzo di una "linea di fede", utilizzando una fune tesa fra le due sponde del porticciolo. Dato che il sistema di acquisizione e quello di energizzazione sono stati installati su due siti differenti, il sistema di trigger ha avuto luogo attraverso una trasmissione radio. In corrispondenza di ciascun punto di scoppio, la camera del Watergun è stata riempita alla pressione di 100 bar.

Durante l'indagine sono state impiegate tre squadre; una ha operato alla stazione di controllo alla quale viene inviato l'input per lo *shot* e in cui si controllano e si registrano i dati ricevuti; un'altra ha agito sull'imbarcazione per la gestione dell'energizzazione e del posizionamento sul punto di scoppio; la terza (subacquea) ha curato il corretto allineamento ed accoppiamento del cavo idrofonico col fondale.

**Geometria d'acquisizione.** La geometria d'acquisizione per i profili 1, 2 e 3 ha previsto l'impiego di un unico stendimento di 24 idrofoni; per questi tre profili sono state svolte sia energizzazioni esterne allo stendimento idrofonico regolarmente spaziate ogni 2,5 m che energizzazioni interne alla stesa idrofonica. Per l'acquisizione della linea n. 4, invece, i tre cavi idrofonici sono stati uniti in modo tale da realizzare un'unica linea idrofonica da 67 canali complessivi e sono state realizzate energizzazioni ogni 5 m (Fig. 2).

In Tab. 1 sono specificati i principali parametri d'acquisizione delle linee sismiche.

Tab. 1 - Principali parametri di acquisizione delle linee sismiche.

| | Linea 1 | Linea 2 | Linea 3 | Linea 4 |
|---|---|---|---|---|
| Lunghezza | 70 m | 85 m | 67.5 m | 167.5 |
| Sorgente | Watergun S-15 | Watergun S-15 | Watergun S-15 | Watergun S-15 |
| Pressione d'esercizio | 100 bar | 100 bar | 100 bar | 100 bar |
| Distanza idrofonica | 2.5 m | 2.5 m | 2.5 m | 2.5 m |
| Spaziatura Sorgenti | Variabile | Variabile | Variabile | 5 m |
| Numero Energizzazioni | 13 | 22 | 24 | 35 |
| Numero Canali | 24 – 10 Hz | 24 – 10 Hz | 24 – 10 Hz | 67 – 10 Hz |
| Massimo Offset | 70 m | 85 m | 90 m | 167 m |
| Finestra temporale | 2 sec | 2 sec | 2 sec | 2 sec |
| Campionamento temporale | 0.5 ms | 0.5 ms | 0.5 ms | 0.5 ms |


Fig. 2 – Immagine di Google Earth dell'area di Capo Granitola (TP) e localizzazione delle linee sismiche acquisite. Con i punti gialli sono rappresentati le posizioni degli idrofoni della linea n. 1, con i punti verdi quelli delle linea n. 2 e con i punti rosa quelli della linea n. 3. Gli idrofono del profilo n. 4, perpendicolare ai tre precedenti, è rappresentato dai punti blu. La posizione di tutti gli shot point eseguiti è raffigurata dai punti rossi.

La geometria d'acquisizione utilizzata, consentendo un fitto campionamento spaziale e temporale in un ampio intervallo di offset, ha permesso una ricostruzione di dettaglio delle geometrie del bedrock sismico e dell'accumulo di sedimenti di copertura all'interno dell'area indagata. Gli idrofoni sono adagiati sul fondo del mare ad una profondità che varia da 1 metro a 2.8 m. Le energizzazioni sono state eseguite ad una profondità di 0.5 m dalla superficie del mare.

**Metodologia.** La prima fase dell'elaborazione a rifrazione è stata la lettura dei tempi relativi alle onde dirette e rifratte. La lettura dei tempi di primo arrivo è stata eseguita su tutte le tracce dei profili sismici acquisiti. Il controllo sulla qualità delle letture è stato ottenuto graficando i primi arrivi in funzione della posizione sul terreno (dromocrone) ed utilizzando le regole di parallelismo e reciprocità descritte da Ackerman (1986). Le letture delle fasi dirette e rifratte, dopo essere state accuratamente verificate, sono state poi invertite sulla base di un modello iniziale di velocità 1D che viene discretizzato in piccole celle a velocità o gradiente costante. La stima iniziale delle velocità del sottosuolo è stata ottenuta mediante le procedure tradizionali di analisi di rifrazione (e.g. Burger, 1992). La dimensione delle celle della maglia e, di conseguenza, la risoluzione del modello di velocità dipende dalla geometria di acquisizione (numero di energizzazioni e numero di ricevitori) e dalla copertura del raggio. Maggiore è il numero di raggi che si incrociano maggiore è la probabilità di ottenere una soluzione stabile. Poiché la copertura del raggio diminuisce con l'aumentare della profondità, anche la significatività del modello di velocità diminuisce con la profondità (Stefani, 1995). Generalmente, la massima profondità che può essere investigata dal metodo tomografico è pari a 1/3 – 1/4 della lunghezza del profilo. Il modello di velocità iniziale viene iterativamente corretto per determinare la migliore distribuzione velocità sulla base del confronto tra i tempi di arrivo misurati e quelli teorici basati sul modello di velocità "a priori" del sottosuolo. Tramite il modello di velocità in ingresso, vengono creati i tempi di arrivo teorici per ciascuna coppia sorgente-geofono via

raytracing. Il programma d'inversione utilizzato per ottenere il tomogramma si basa su un algoritmo il cui scopo è di ricavare il tempo minimo di percorrenza dei raggi tra sorgente e ricevitore per ogni coppia sorgente-ricevitore, attraverso il calcolo del percorso dei raggi e della lentezza (*slowness*). Essendo entrambe le variabili incognite il problema è sottovincolato; l'algoritmo, procedendo in maniera iterativa non-lineare con il metodo dei minimi quadrati (Scales, 1987), utilizza lo scarto tra il tempo misurato e quello calcolato per modificare le velocità nelle celle interessate dal raytracing finché l'errore RMS (Root-Mean Square) relativo alla differenza tra i tempi di percorso osservati e calcolati viene minimizzato.

Il risultato è una immagine bidimensionale che mostra la distribuzione delle velocità sismiche del sottosuolo.

I modelli tomografici sono stati, inoltre, verificati eseguendo alcuni test sintetici (checkerboard, restore resolution test) utilizzando la metodologia descritta in (Zelt, 1998) e (Zelt *et al*., 2006). I valori di velocità del modello tomografico sono stati "perturbati" del ±10 % schematizzando il sottosuolo in celle regolari di dimensioni di 10x10 m. Le dromocrone sono state quindi ricalcolate sul modello di velocità perturbato ed invertite utilizzando il modello di velocità della tomografia iniziale. Il risultato finale rappresenta la capacità dell'inversione tomografica nel risolvere le celle di perturbazione e fornisce un'indicazione della risoluzione superficiale del modello.

**Analisi e interpretazione dei dati.** Sulla base delle velocità individuate dall'analisi delle dromocrone, è stato scelto per il nostro profilo un modello iniziale multi-stratificato con un aumento graduale di velocità con la profondità da 900 m/s a 5000 m/s.

I modelli 2D di velocità ottenuti risaltano la presenza di significative differenze nei valori di $V_P$ ottenuti e mostrano l'articolazione dei vari sismostrati.

In maniera esemplificativa verrà descritto il modello 2D più completo ossia quello ottenuto dal profilo n. 4 (Fig. 3) in quanto raggiunge le massime profondità di investigazione ed illustra le geometrie dei sismostrati in maniera più dettagliata e completa.

Il sismostrato più superficiale è sempre caratterizzato dai più bassi valori di velocità con un gradiente che varia da 900 m/s in superficie fino a 1400-1500 m/s. Nella sezione n.4 esso è contenuto all'interno di due concavità a differente ampiezza, di cui quella verso terra (NE) accoglie gli spessori maggiori valutabili in 5-8 m. Al suo interno possono essere distinte piccole lenti caratterizzate da velocità inferiori a 1000 m/s.

Il secondo sismostrato è caratterizzato da valori di velocità più elevati ed un gradiente che varia da 2060 m/s a 3800 m/s; tra le progressive 45-110 m presenta una profondità della superficie di base all'incirca costante (circa -12/-13 m) ed una morfologia di tetto alquanto articolata a differenza di quanto rilevato tra le progressive 120 e 160 m.

Il terzo sismostrato è marcato da valori più elevati di velocità, in genere maggiori di 4000 m/s. Il suo limite superiore si approfondisce da SW verso NE, dove raggiunge le massime profondità attestandosi tra i -15/-20 m di profondità.

La taratura e l'interpretazione stratigrafica del profilo è stata eseguita sia con l'ausilio di osservazioni dirette del fondale che dall'osservazione della porzione emersa della falesia antistante il porto. Il campo di velocità del primo elettrostrato, può essere riferito a sedimenti prevalentemente sabbiosi, da parzialmente saturi a saturi e di spessore molto variabile. Le zone con i valori velocità più bassi sono da legare alla presenza di sedimenti aggregati in lenti con granulometria e porosità relativamente diverse rispetto allo strato inglobante. Il rilievo diretto ha potuto verificare che localmente livelli alternati di sabbie e di residui di posidonia completamente saturi e/o sabbie limose fini sono accumulate in maniera differenziale all'interno di piccole concavità contenute in sedimenti sabbiosi più grossolani e/o meno saturi.

Il consistente aumento della rigidità dei materiali che occorre al passaggio tra il primo e il secondo elettrostrato è probabilmente correlabile al passaggio tra i sedimenti sabbiosi e la porzione più superficiale dell'ammasso calcarenitico (e.g. Calcareniti di Marsala), che spessa

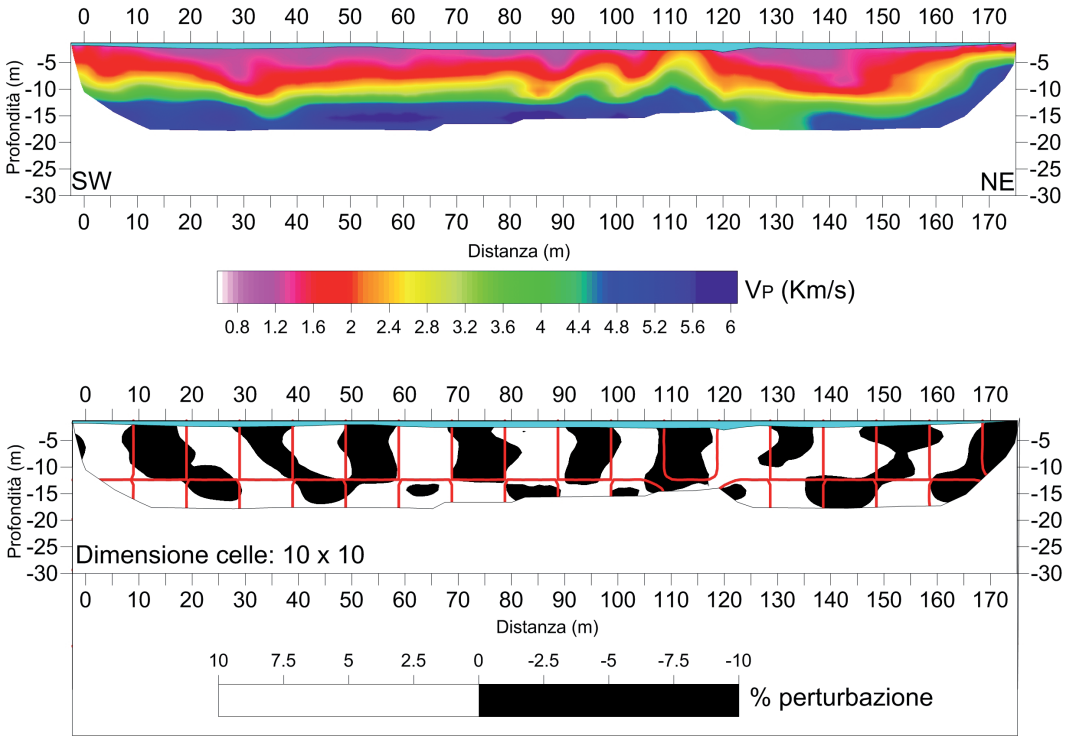


Fig. 3 – Modello di velocità delle onde P relativo al profilo n. 4; l'area non campionata dai raggi è bianca. È ben evidente il forte contrasto di velocità tra i sedimenti di copertura ed il "bedrock sismico", quest'ultimo caratterizzato da valori di VP maggiori di 4000 m/s. L'RMS dopo 20 iterazioni è di 2.82 m/s. Sotto: La perturbazione del modello tomografico, ottenuta dopo un "a posteriori" checkerbord resolution test con celle di dimensioni 10x10 ed una velocità di perturbazione del ±10%, mostra che il modello fornisce una stima robusta delle velocità i primi 10 metri di profondità.

in media 5 m, raggiunge velocità delle onde P maggiori di 3000 m/s.

Le ondulazioni asimmetriche presenti tra le progressive 25 e 100 m, sono probabilmente da porre in relazione a linee di fratturazione ad andamento NW-SE analoghe a quelle esposte lungo la porzione della falesia posta in prossimità del molo di sottoflutto.

La metodologia utilizzata si è dimostrata efficace nel mettere in luce i rapporti stratigrafici tra i sedimenti superficiali ed il *bedrock* sismico. L'immagine tomografica, infatti, mostra, con una buona risoluzione, le variazioni di velocità delle onde compressive nei primi 15 m di profondità e le geometrie sepolte dei sismostrati individuati.

La possibilità di elaborare i dati acquisiti con tecniche 3D consente, quindi, di ottenere una stima di massima dei volumi dei sedimenti per dimensionare le future operazioni di dragaggio del fondale.

**Ringraziamenti.** Gli autori ringraziano il Dr. Mario Sprovieri e Vincenzo Di Stefano per la loro disponibilità durante le fasi di acquisizione. Si ringrazia, inoltre, il C.U.GR.I. (Consorzio Inter-Universitario per la Prevenzione dei Grandi Rischi) Fisciano (SA) per il supporto tecnologico nelle attività di ricerca.

## Bibliografia

Ackermann H. D., Pankratz L. W. and Dansereau D.; 1986: *Resolution of ambiguities of seismic refraction traveltime curves*. Geophysics, Vol. 51, N. 2; P. 223-235.

Berryman J.G.; 1990: *Stable iterative reconstruction algorithm for nonlinear traveltime tomography*. Inverse Problems 6, 21-42.

Burger, H. R.; 1992: *Exploration Geophysics of the Shallow Subsurface*. Prentice-Hall, Inc., Englewood Cliffs, New Jersey, 489 pp.

D'Angelo U., Vernuccio S.; 1992: *Carta geologica del Foglio 617 "Marsala" scala 1:50.000*. In Bollettino Società Geologica Italiana, Vol. 113, Roma.

D'Angelo U., Vernuccio S.; 1994: *Note illustrative della Carta Geologica del Foglio 617 "Marsala"* (scala 1:50.000). Boll. Soc. Geol. It., CXIII, 55-67.

MacGregor F., Fell R., Mostyn G.R., Hocking G. and McNally G.; 1994: *The estimation of rock rippability*. Quarterly Journal of Engineering Geology and Hydrogeology, v. 27, p. 123-144,

Ruggieri G., Unti A., Unti M. e Moroni M.A.; 1977: *La calcarenite di Marsala (pleistocene inferiore) e i terreni contermini*. Estratto dal Bollettino Società Geologica Italiana, 94,1623-1655, 2 ff. Roma.

Scales, J.A.; 1987: *Tomography inversion via conjugate gradient method*. Geophysics 52, 179-185, doi: 10.1190/1.144.2293.

Stefani, J. P.; 1995: *Turning-ray tomography*. Geophysics. 60, 1917-1929.

Whiteley R.J., Stewart S.B.; 2008: *Case studies of shallow marine investigations in Australia with advanced underwater seismic refraction (USR)*. Exploration Geophysics 39(1) 34–40.

Young Ho Cha, Churl-Hyun Jo, and Jung Hee Suh; 2003: *Water Bottom Seismic Refraction Survey for Engineering Applications*. Geosystem Eng., 6(2), 40-45.

Zelt C.A.; 1998: *Lateral velocity resolution from three-dimensional seismic refraction data*. Geophysical J. Int., 135, 1101-1112.

Zelt C.A., Azaria A. and Levander A.; 2006: *3D seismic refraction traveltime tomography at a ground water contamination site*. Geophysics, 71, H67-H78.

## A SEISMIC SURVEY AT ADVENTDALEN, SVALBARD ISLANDS, (NORWAY), FOR PERMAFROST STUDIES: THE IMPERVIA PROJECT

**G. Rossi[1], F. Accaino[1], J. Boaga[2], L. Petronio[1], R. Romeo[1], W. Wheeler[3]**

*[1] OGS - Istituto Nazionale di Oceanografia e di Geofisica Sperimentale, Trieste, Italy*

*[2] Dipartimento di Geoscienze, Università di Padova, Italy*

*[3] Centre for Petroleum Research (CIPR), University of Bergen, Norway*

**Introduction.** Climate warming and permafrost thawing would allow the release into the atmosphere of any greenhouse gasses trapped beneath. Research to date has focussed mainly on the upper fifteen meters of the permafrost as this reacts most rapidly to changes in air temperature. Little focus is given to the deeper permafrost, which may be a good long-term climate indicator. Knowledge of the fluids (waters or gases) present within and beneath the permafrost allows evaluation of the impact of atmospheric release upon thawing.

Svalbard archipelago is an ideal natural peri-arctic laboratory for such a kind of studies. The fluid circulation and permafrost characteristics are constrained by a series of pingos (periglacial mounds of Earth-covered ice), shallow (< 50 m) and a few deep (to 970 m) wells. Near Longyearbyen, in the Adventdalen (Advent Valley), where the Longyearbyen CO2Lab is located (Braathen *et al.*, 2012), deep-target 2D reflection and borehole seismic data are available (Oye *et al.*, 2013). However, no studies targeted full-thickness permafrost characterization, or determining its relation with regional hydrology are available.

These considerations motivated the present study, done within the PNRA project IMPERVIA - Integrated Methods to study PERmafrost characteristics and Variations In an Arctic natural laboratory (Svalbard). The project is led by OGS (Istituto Nazionale di Oceanografia e di Geofisica Sperimentale, Trieste, Italy), in collaboration with CIPR (Centre for Petroleum Research, Bergen University, Norway), UNIS (University Centre in Svalbard, Longyearbyen, Norway), and the Department of Geosciences, University of Padua, Italy. The aim is to combine exploration geophysical tools (2D and 3D) to image and characterize the mid- to lower permafrost, to determine the aquifer architecture (bedrock and fluvio-glacial deposits). Such information can be useful to state permafrost capability of acting as additional cap-rock to future injected $CO_2$. Since the fluid flow from pingos indicates significant fluid circulation

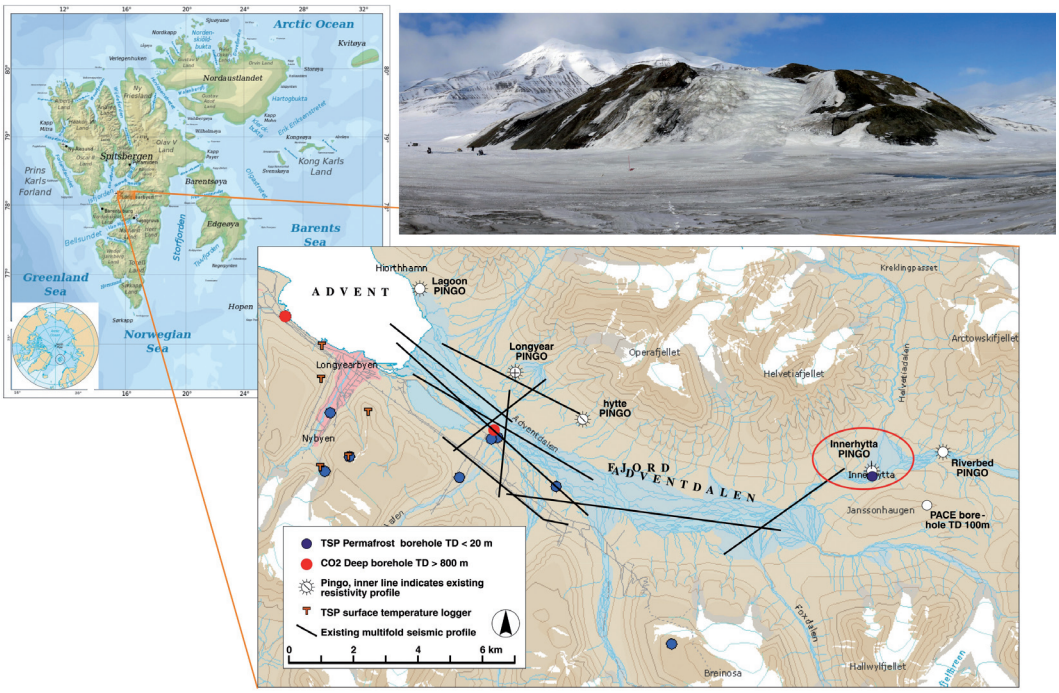


Fig. 1 – Map of Adventdalen in Svalbard Archipelago, with location of Innerhytta Pingo (red ellipse), and the existing seismic lines (black lines) and boreholes (blue and red circles). Above: a view of the Innerhytta pingo.

which likely affects permafrost thickness even away from the pingos, the experiment is done in the vicinity of the Innerhytta (or Innerhytte) Pingo, a well-known giant pingo (Fig. 1).

**The study area.** Pingos are oval dome-shaped hills which form in permafrost areas when the hydrostatic pressure of freezing groundwater causes the raising of frozen ground. They can reach even 90 m altitude and over 800 m of diameter. In open system pingos, artesian pressure builds up under the permafrost layer, and as the water rises and pushes up the overlying material, it freezes in a lens shape. Innerhytta (Inner hut) pingo is located about 16 km east of Longyearbyen (Spitzbergen, Svalbard Islands) in the valley bottom in Adventdalen, a valley about E-W oriented, ending into Adventfjorden, nearby Longyearbyen, on the Spitzbergen Island of Svalbard Archipelago (Fig. 1). It has been first studied in detail by Piper and Porritt (1966), who produced a topographical map.

The pingo is 410 m wide in E-W direction and 200 m in N-S direction. The height above the valley floor is 28 m, above the recognized maximum Holocene marine limit (Ross *et al.*, 2005). It is developed within, and uplifts, Jurassic shales of the Agardhfjellet formation (Major *et al.,* 2000). A mineralized spring generates a noticeable icing covering the pingo summit and southern flank in the late winter, before the active-layer summer thawing (Fig. 1).

In the area, both GPR and resistivity survey were done (Ross *et al.*, 2005; 2007), and continuous temperature monitoring is on-going (Christiansen *et al.*, 2010). Ross *et al.* (2005), from GPR measurements, hypothesized that a southwards migration of the water uprising occurred, so that the actual pingo activity is limited to the area around its apex. According to them, furthermore, the NE part of the structure would be an erosional remnant of bedrock due to the fluvial incision of the overlying relief of Janssonhaugen. The results of the successive resistivity tomographic experiment, however, were not resolutive. They were, in fact, compatible both with the hypothesis of the existence of a ground-ice body at depth (Piper and Porritt, 1966), as well as with the bedrock remnant, without massive ice-body (Ross *et al.*, 2007). The

TSP NORWAY IPY Innerhytta borehole stratigraphy provided information on the presence of ice and of its characteristics in the first 20 meters below the topographic surface (Juliussen *et al.*, 2010), not sufficient to clarify the doubts about the deeper internal structure.

IMPERVIA project experiment, hence, was designed to try to add seismic information to the other existing ones, so to contribute to distinguish between massive-ice and iced-bedrock response, by applying near-surface seismic methods, surface wave information, and tomographic inversion of direct, reflected and refracted arrivals. The combination of different arrivals in a tomographic approach can be successful in overcoming the difficulties of building a near-surface velocity model in permafrost regions, due to near surface high velocity, strong lateral velocity variations and negative velocity gradients present in these regions.

**The spring 2014 seismic experiment.** The experiment of spring 2014 was aimed to verify the capability of a low-environmental impact(?) near-surface seismic survey in the arctic environment to image the permafrost architecture and characteristics, completing the available information from GPR and electric resistivity measurements. The Svalbard Environmental Protection Act, aimed to safeguard virtually untouched area in Svalbard, regulate the research activities in this delicate environment. In particular, authorities strongly discourage research activities that may set marks in the terrain. Geophysical surveys, therefore, are generally done in late-winter to early-spring times, when work can be carried out on snowy, frozen ground, limiting the damages.

IMPERVIA survey took place between April 29 and May 6, 2014. Apart the above mentioned environmental protection issues, this period was chosen since the use of sledges and snowmobiles facilitated equipment transport from Longyearbyen, reducing logistical efforts and costs. However, in order to ensure a good geophone and sources ground coupling, we ought to dig snow pits through the snow coverage, which on the leeward side of pingos reached the two meters. The seismic equipment was composed of conventional vertical geophones, 4.5 Hz and 14 Hz, and a 24 channel gimballed 14 Hz mini snow-streamer, 115 m long with 5 m takeout spacing. Five 24 channel seismographs (Geode, Geometrics) enabled the recording of the signals. To reduce the possible noise due to the frequent strong wind, we buried the geophones and covered with snow the snow-streamer sensors and connecting cables.

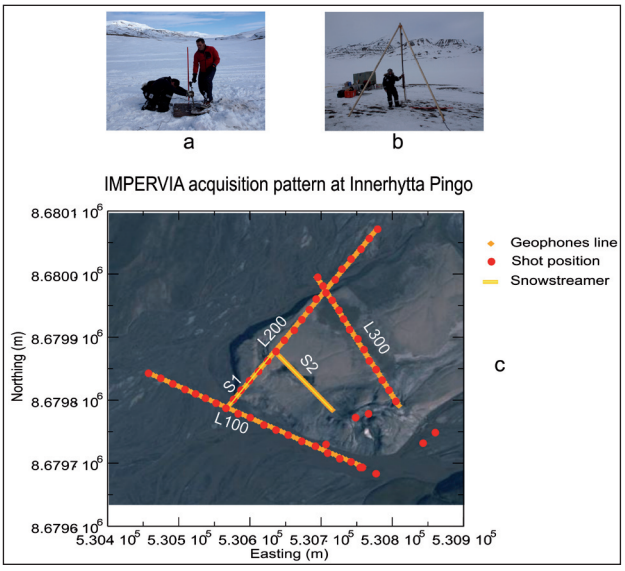


Fig. 2 – a) Seisgun acquisition; b) one of the weight drops used for the surface wave experiments, suspended at the tripod; c) map of the acquired seismic lines (orange), the snowstreamer (orange-yellow lines) and of the shots positions, overimposed to an orthophoto of the Inerhytta pingo (from toposvalbard.npolar.no).

Also for the choice of the sources, the low-impact on the environment is an issue. We used sledge hammer on a steel plate, seisgun with 12-gauge shotgun shell, firecrackers in shallow drilled boreholes. Firecrackers are allowed as self-protection devices against polar bears. The list was completed by two different weight drops, falling from a tripod from an approximate height of 2.5 m. The latter source was aimed to provide low-frequency source to record surface waves, to complement the higher frequency 2D lines (e.g., Boaga *et al.*, 2011). In Fig. 2 the seisgun and one of the weight drops are shown (a, b), together with a map of the seismic survey pattern,

overlapped on an orthophoto of Innerhytta pingo (c). The source and the receiver points were positioned with DGPS.

We acquired three lines for reflection/refraction seismic in a tomographic inversion perspective. We used five 24-channels Geode seismographs, sampling rate 0.250 ms, for a total recording window of 2 s. The vertical 14 Hz geophones were listening, together with the snow streamer. Seisgun, sledgehammer and firecrackers were used as sources. To increase the coverage of the tomographic experiment, while acquiring the 2D lines, we recorded also cross-line, using both the snow-streamer and the geophones, or shooting offline.

The design of the seismic lines was done taking into account the needs of illuminating the different parts of the pingo area, reducing the possible effects of the rough topography and optimizing acquisition costs and duration.

Line L100 is traced at the foothill of the pingo, on the bottom of the above the Adventelva (Advent River) floodplain. Line L200 is traced from L100 across the NE corner of the pingo, while L300 starts from about half of L200 toward a saddle to the East of the pingo's apex. This pattern implied a high coverage above the pingo apex and the areas where the highest lateral variability in depth is expected. Summarizing (see Fig. 2 c):

L100 – 91 channels: 67 channels inline and 24 channels cross-line (snowstreamer S1), 21 shot points;

L200 – 120 channels: 72 channels inline (48 geophone + 24 channels S1 snowstreamer) and 48 channels cross-line (L300), 18 shot points;

L300 – 120 channels: 48 channels inline and 72 channels cross-line (L200: 48 geophone + 24 channels S2 snowstreamer), 24 shot points.

In addition to this, two experiments of surface-wave recording were done, one along L100 and the second one along L200 using two 24-channels Geode seismographs, sampling rate 0.250 ms, for total recording window of 2 s. The sensors were vertical 4.5 Hz geophones, and the sources were sledge-hammer in the case of L100 and the two different weight drops on L200.

**The data and data analysis.** Since one of the goals of the IMPERVIA spring 2014 experiment was to test the capability of the seismic method for near-surface, high-resolution targets in extreme conditions as Svalbard, analyses were carried out both on the field and after the survey, in order to state the efficiency of the different sources for our goals.

In Fig. 3 a comparison between a shot gather when the source is the seisgun (a) and the firecrackers (b), respectively. It is evident the higher resolution due to the latter source, more impulsive and with stronger energy with respect to the seisgun. The sledge-hammer did not provide comparable results. A better quality could be obtained through several shots repeated and stacked, what would, however, imply too long times and more problems in ground coupling, with respect to the other two sources.

As regards as the surface wave experiments, the preliminary data analysis state that the best results were provided using the weight-drops (the heaviest one) with respect to the sledge-hammer, seisgun and firecrackers.

The data processing and data analysis are on-going: it encompasses both standard processing of the reflection data, tomographic inversion of reflected and refracted arrivals, and surface wave inversion. Due to the strong velocity variations and the presence of negative gradients conventional reflection processing can be difficult. The velocity field provided by a tomographic inversion, exploiting all the arrivals generated throughout the experiment (e.g. Vesnaver *et al*., 1999) can be the input for a correct move-out data correction and successive stack, or as input for a depth data migration.

In particular, we started the tomographic analysis of the first line L100, considering both the inline, as well as the cross-line snow-streamer traces. We use the method described in detail by Vesnaver *et al*. (1999) and Rossi *et al*. (2007), with a minimum time ray-tracing modified from Böhm *et al*. (1999) and the iterative inversion SIRT process (van der Sluis and van der

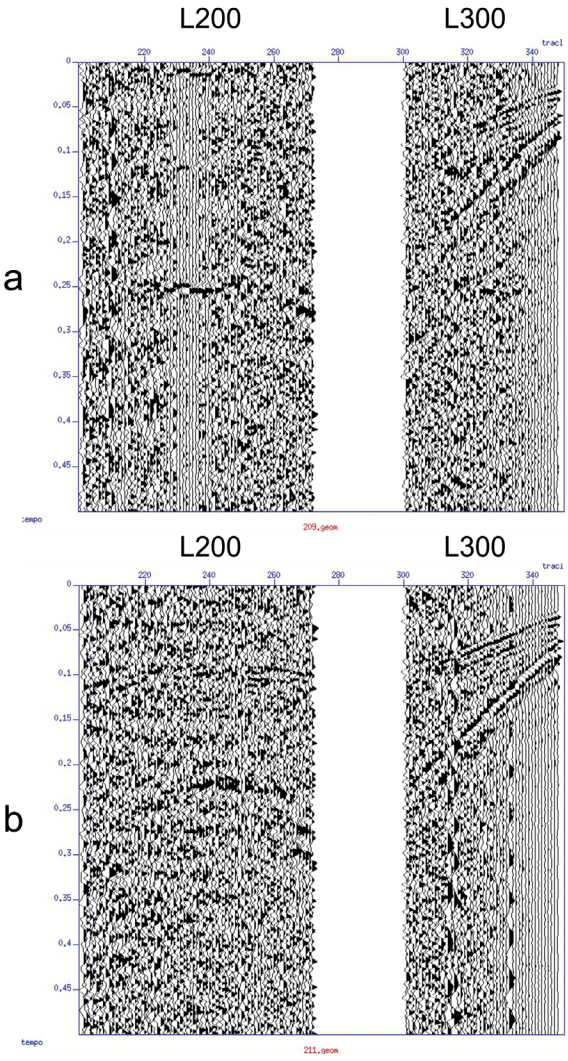


Fig. 3 – a) An example of shot gather from L300 (inline) and L200 (crossline) usig the Seisgun as source. b) The same using firecrackers as source.

Vorst, 1987). The space is discretized into layers, with dipping or curved separating interfaces, constituted by pixels (voxels in 3D), with homogenous velocity.

Through a minimization of the time residuals, it is possible to invert the data both for velocities and for the interface position and shape (e.g. Vesnaver *et al.*, 2000; Rossi *et al.*, 2007). Reflected events provide information on the velocity of the layer above the reflected interface, whereas the refracted arrivals give information also on the velocity of the layer underlying the refracting interface, in correspondence of the ray-path part travelling along the interface. For both reflected and refracted arrivals, it is possible to exploit the time-residuals, converted to depth, to reconstruct the interface depth and shape (e.g., Rossi *et al.*, 2001, 2007).

About line L100, for the moment, we identified reflected and refracted arrivals from three different interfaces. The results obtained are still preliminary, since they have to be confirmed and integrated with the data from the other two lines. They are, however, promising.

As said, the model is constituted by four layers, separated by three interfaces. The approximate depth of the latter is about 15 m, 30 m and 55 m below the topographic surface respectively. Velocities lie within the 1.55 to 4.6 km/s interval, in agreement with the observations from borehole measurements and 2D seismic lines in the same Adventdalen valley, near CO2Clab (Oye *et al.*, 2013). There is evidence of strong velocity variations, both laterally as well as in depth, as it is expected across the pingo.

**Conclusions.** From the very first results of the analysis of the data acquired during the IMPERVIA spring 2014 experiment, we can conclude that seismic method can be applied also for near surface, high resolution targets in presence of permafrost. The observations and the results of the field tests on the sensors and sources and of the successive analysis of the outcoming data can provide guidelines for successive surveys in similar areas. In particular, it is necessary to guarantee a good ground coupling, for both sources and receivers, by digging snow pits. It is also important to reduce the noise, due to the frequent strong wind, by burying the sensors, and covering with snow also the streamer connecting cables (e.g. Lecomte *et al.*, 2014). The choice of the source has to be done, so to have energy also at the long distances required for a correct velocity retrieval. Off-end shooting and cross-line recording can help to

improve the coverage necessary at a relative low acquisition cost.

New contributions for optimizing the acquisition pattern will come from the conclusion of the data processing that presently is analyzing the recorded data amplitude spectra for the different sources and geophones and the overall data quality.

Also from the very first results of the tomographic analysis on the single L100 line, the possibility of jointly invert both reflected and refracted arrivals enables to improve the ray coverage, and, therefore, the inversion reliability, while exploiting at the best the seismic experiment information. In the next months, both velocities and interface depth and shape will be refined by jointly inverting the other two lines and the offline shots, providing a more extended and detailed model of the velocities below and around Innerhytta pingo.

**Acknowledgements.** The project IMPERVIA is a PNRA project (PdR 2010/A2.14 "IMPERVIA"). We are grateful to Hanne Christiansen for the full support given to the project and the useful discussions before and during the field work, we are also indebted with Sara Mollie Cohen and to Mark Mulrooney of the UNIS Geoscience department and to the UNIS Logistic department staff for the assistance, patience and support for the whole field work duration. We thank, furthermore, all the UNIS and Norwegian Polar Institute personnel for the kind help that gave to us.

## References

Boaga J., Vignoli G. and Cassiani G.; 2011: *Shear wave profiles from surface wave inversion: the impact of uncertainty on seismic site response analysis*, J. Geophys. Eng. 8 162-174, doi:10.1088/1742-2132/8/2/004.

Böhm G., Rossi G. and Vesnaver A.; 1999: *Minimum time ray-tracing for 3-D irregular grids*. Journal of Seismic Exploration 8, 117–131.

Braathen, A., Bælum, K., Christiansen, H.H., Dahl, T., Eiken, O., Elvebakk, H., Hansen, F., Hanssen, T.H., Jochmann, M., Johansen, T.A., Johnsen, H., Larsen, L., Lie, T., Mertes, J., Mørk, A., Mørk, M.B., Nemec, W., Olaussen, S., Oye, V., Rød, K., Titlestad, G.O., Tveranger, J. and Vagle, K.; 2012: *The Longyearbyen CO2 Lab of Svalbard, Norway—initial assessment of the geological conditions for CO2 sequestration*. Norwegian Journal of Geology, 92, 353–376.

Christiansen H.H., Etzelmüller B., Isaksen K., Juliussen H., Farbrot H., Humlum O., Johansson M., Ingeman-Nielsen T., Kristensen L., Hjort J., Holmlund P., Sannel A.B.K., Sigsgaard C., Åkerman H.J., Foged N., Blikra L.H., Pernosky M.A., Ødegård R.; 2010: *The thermal state of permafrost in the Nordic area during IPY 2007–2009*. Permafrost and Periglacial Processes 21, 156–181.

Juliussen H., Christiansen H.H., Strand G.S., Iversen S., Midttømme K., Rønning J.S.; 2010: *NORPERM, the Norwegian Permafrost Database – a TSP NORWAY IPY legacy*. Earth System Science Data Discussions 3, 27–54.

Lecomte I., Polom U., Sauvin G., Ruud B.O. *Shear-wave Reflection-seismic Pilot Study at the UNIS CO2 Lab site, Longyearbyen, Svalbard,* EAGE 72 meeting Extended abstracts, DOI: 10.3997/2214-4609.20141243.

Major H., Haremo P., Dallmann W.K. and Andresen A.; 2000: Geological Map of Svalbard 1 : 100,000 Sheet C9G Adventdalen (revised after Major 1964). Temakart No. 31. Norwegian Polar Institute, Tromsø.

Oye V., Braathen A., Polom U.; 2013: *Preparing for CO2 storage at the Longyearbyen CO2 Lab: microseismic monitoring of injection tests*, First Break, 31,

Ross, N., Brabham P.J., Harris C. and Christiansen, H.H.; 2007: *Internal Structure of Open System Pingos, Adventdalen, Svalbard: The Use of Resistivity Tomography to Assess Ground-Ice Conditions*. Journal of Environmental & Engineering Geoscience, 12, 113-126.

Ross N., Harris C., Christiansen H.H and Brabham P.; 2005: *Ground penetrating radar investigations of open system pingos, Adventalen, Svalbard*. Norsk Geografisk Tidsskrift - Norwegian Journal of Geography, 59, 129-138.

Rossi G., Gei D., Böhm G., Madrussani G. and Carcione J.M.; 2007: *Attenuation tomography: an application to gas-hydrate and free-gas detection*, Geophys. Prosp., 55, 655 – 669.

Rossi, G., Corubolo P., Böhm G., Ceraggioli E., Dell'Aversana P., Morandi S., Poletto F. and Vesnaver A.; 2001: *Joint 3-D inversion of SWD and surface seismic data*, First Break, 19, 453-459.

van der Sluis A. and van der Vorst H.A.; 1987: *Numerical solution of large sparse linear algebraic systems arising from tomographic problems*. In: Seismic Tomography (ed. G. Nolet), pp. 49–83. Reidel Publishing Co., Dordrecht.

Vesnaver A., Böhm G., Madrussani G., Petersen S. and Rossi G.; 1999: *Tomographic imaging by reflected and refracted arrivals at the North Sea*. Geophysics 64, 1852–1862.

Vesnaver, A., Böhm G., Madrussani G., Rossi G. and Granser H.; 2000: *Depth imaging and velocity calibration by 3D adaptive tomography*, First Break, 18, 303-312.

Zhu, T., Yan Y., Downton J.; 2011: *Near-surface velocity model building and statics in permafrost regions*, 2011 CSEG Convention.

# COMPARISON BETWEEN SPARSE RADON TRANSFORMS TOWARDS AN MPI IMPLEMENTATION

**Z. Xing[1], E. Stucchi[2], A. Mazzotti[1], A. Tognarelli[1]**
[1] *Department of Earth Sciences, Geophysics, University of Pisa, Italy*
[2] *Department of Earth Sciences, Geophysics, University of Milan, Italy*

**Introduction.** In exploration geophysics the linear Radon transform projects seismic data from time-offset (*t-x*) domain into intercept time-ray parameter (τ-*p*) domain while the parabolic Radon transform maps *t-x* domain seismic data into intercept time-curvature (τ-*q*) domain.

Seismic reflections can be approximated as hyperbolae when the dips are gentle and the spread is small (Yilmaz, 2001). Ideal linear Radon transform maps a hyperbolic seismic event in an ellipse with the center at (0.0) and the vertical and horizontal radii equal to the intercept time τ and the reciprocal of the root mean square velocity *1/v*, respectively. Normal moveout (NMO) correction approximates hyperbolic seismic events as parabolas that become points when an ideal parabolic Radon transform is applied to the seismic gather.

In Radon transform domain Random noise is mapped destructively while seismic reflections are projected constructively and separately. This makes Radon transform methods useful in enhancing signal to noise ratio, doing trace interpolation and attenuating multiples in seismic data processing, especially for marine seismic data. In this work we focus our attention mainly on the parabolic Radon transform.

Two main problems that arise in the Radon transform computation are *i)* the artifacts generated in the transform domain and *ii)* the long computing time.

The artifacts originate from two sources. One is related with a too coarse transform domain sampling rate or a too wide sampling range, the other is related with the limited offset range in *t-x* domain. Different sampling criterions can be used to deal with the limits of the sampling rate and range (Turner, 1990; Schonewille and Duijindam, 2001). A common statement of the sampling criterions is that a higher frequency coincides with a more stringent limit of sampling rate and range. So we can relieve these requirements by doing a filtering before Radon transform. But we should only filter out the frequencies between the maximum useful frequency of the signal and the Nyquist frequency to avoid degrading the resolution of the seismic data.

The limited offset range in *t-x* domain makes NMO corrected seismic events be projected into butterfly structures instead of points in τ-*q* domain. This fact causes the inverse parabolic Radon transform to be unable to reconstruct the original data faithfully and leads to the difficulty in doing multiple attenuation with the Radon transform method. To deal with this difficulty different authors developed various sparse Radon transform algorithms to compress the butterfly structures. Sacchi and Ulrych (1995) proposed the frequency domain sparse Radon transform (FDS-RT). Trad *et al*. (2003) presented the time-frequency domain sparse Radon transform (TFDS-RT). Lu (2013) formulated the iterative shrinkage sparse Radon transform (ISS-RT). We developed our code according to different standard and sparse Radon transform algorithms and compared their performances in the reconstruction of the original data and in the demultiple processing. We also compared our results with the outcomes of the ProMAX® software for what concerns the ability of multiple attenuation.

To deal with the long computing time problem, we used Open MPI to parallelize the Radon transform algorithms. Open MPI is a Message Passing Interface (MPI) library project. MPI allows users to simultaneously use multiple processors to perform a calculation.

**Radon transform.** To avoid too heavy computing, generally the Radon transform is evaluated as an inverse problem in frequency domain (Yilmaz, 2001). Various approaches can be used to solve the system of equations leading to the transform coefficients. They are the damped least squares, the singular value decomposition and the conjugate gradient methods. The damped least squares is a well known method (Yilmaz, 2001). The singular value decomposition calculates eigenvalues and eigenvectors to get the Radon transform domain data, this makes

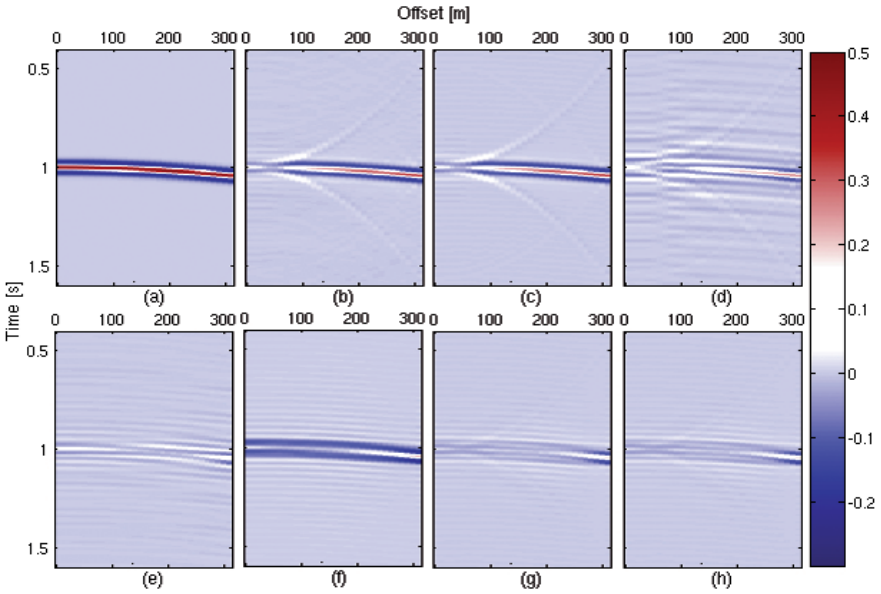


Fig. 1 – a) Synthetic seismogram with only one parabolic event. This parabola represents a multiple after NMO correction. (b) to (h) show the differences between the data in (a) and the data derived from forward and inverse parabolic Radon transform applied to the data in (a) by using different Radon transform methods. (b) to (d) are sequentially related with standard parabolic Radon transform with (b) damped least squares method, c) singular value decomposition method, d) conjugate gradient method; (e) to (h) are sequentially related with sparse parabolic Radon transform methods: e) FDS-RT, f) TFDS-RT, g) ISS-RT with the standard parabolic Radon transform calculating the initial model, h) ISS-RT with FDS-RT calculating the initial model.

it the most stable method. "Stable" means that if we change an entry in the transformation matrix slightly or add some noise to the dataset, the calculated model will not change largely. The conjugate gradient method constructs Radon transform results with iterations. In this algorithm the generalized cross validation (GCV) function can be used as the stopping criterion (Trad *et al*., 2003). In both damped least squares and singular value decomposition methods the Lagrange multiplier $\beta$ is used to balance the data misfit and the model misfit. In conjugate gradient method this balance is done by GCV function. Generally the Lagrange multiplier $\beta$ is chosen according to the maximum curvature of the L-curve. This choice coincides more or less with the minimum in the GCV curve, except that this minimum point slightly overfits the data (Oldenburg and Li, 2005).

By using the conjugate gradient we can get a more compressed butterfly structure in the Radon transform domain compared with the other two methods. After the forward and inverse parabolic Radon transform, the reconstructed t-x domain data have a lower signal to noise ratio and more vertical artifacts, but along the offset axis the attenuation of the amplitudes of the seismic event is lower compared with that presented in data reconstructed by the other two methods. Figs. 1a to 1d show this effect. Fig. 1a displays a synthetic seismogram with only one parabolic event in the time window [0.4 s 1.6 s]. This parabolic event can represent a multiple after NMO correction. Figs. 1b to 1d show the differences between the data in Fig. 1a and the reconstructed data using these standard different Radon transform methods.

Both FDS-RT and TFDS-RT compress the butterfly structures by adding a model weight in the objective function of the inverse problem. The model weight is expressed as

$$\left[W_m\right]_{ii} = \frac{1}{\sqrt{m_i}} \qquad (1)$$

where $[W_m]_{ii}$ is the $i_{th}$ diagonal entry of the diagonal model weight matrix $W_m$, $m_i$ is the $i_{th}$ element of the model vector m. m is in frequency-curvature (f-q) domain for FDS-RT while for TFDS-RT it is in τ-q domain. This indicates that FDS-RT and TFDS-RT compress the butterfly structures in frequency domain and in time domain, respectively. As a consequence FDS-RT has a degraded vertical resolution while TFDS-RT needs a heavy computing time. As the weight is related with the model, we need to resolve nonlinear inverse problems to calculate these two sparse Radon transforms. In our code we use iteratively reweighted least squares to calculate the final model and in each iteration the conjugate gradient is used. ISS-RT also compresses the butterfly structures iteratively. It uses the initial model computed with any Radon transform method, then in each iteration it applies the shrinkage operator to refine the result.

The tests done show that among the three sparse Radon transform methods, the FDS-RT has the drawback of giving τ-q domain data with the lowest signal to noise ratio and the lowest resolution, but it preserves at best the amplitudes of weak seismic events and causes the smallest amplitude attenuation along the offset axis for each seismic reflection in the reconstructed t-x domain data. This will make it the most suitable method for demultiple. On the contrary, TFDS-RT gives τ-q domain data with the highest signal to noise ratio and the highest resolution, but cannot preserve weak seismic events and causes very strong amplitude attenuation along the offset axis in the reconstructed t-x domain data. ISS-RT gives τ-q domain data with a moderate signal to noise ratio and a good resolution. At the same time it is able to reconstruct in t-x domain the weak seismic events but causes some amplitude attenuation along the offset axis even if this attenuation is lower than that of TFDS-RT. If we consider the demultiple processing as a multiple estimation process followed by a subtraction of the estimated multiples, Fig. 1 illustrates the demultiple ability of the different Radon transform methods. The FDS-RT appears to be the most efficient in this context.

Message Passing Interface. For accelerating the Radon transform algorithms proper filtering, use of the conjugate symmetric property of FFT, selective use of the zero padding before FFT and the exploitation of the characteristics of the circulant matrices should be considered (Strang, 1986). However, recent developments of parallel computing suggest to use personal computer clusters to help further speed-up the calculation of the Radon transform coefficients. We parallelized our ISS-RT code by exploiting two for loops in the algorithm. To do the parallelization we used the MPI package from Octave-Forge. This package allows us to connect Octave with Open MPI. Although the current MPI package (Version 1.2.0) cannot be used to send structures or complex numbers properly, by using cell arrays we circumvent this problem.

In the parallel computing code the master node divides the input into pieces. At the beginning it sends each slave node one piece. When a slave node has finished calculating and has sent the results back to the master node, the latter will send a new piece to the former if there are still pieces of input left.

Parallel computing is not always faster than direct calculation. For example in the ISS-RT algorithm one step that calculates a 2D averaging filter is needed. This step is not in the two for loops, so it is outside of the parallelized portion of the code. When we used the damped least squares method to calculate the initial model of ISS-RT, the 2D averaging filter occupied a large percent of the whole computing time. In this case the parallel computing was not faster than the direct calculation according to Amdahl's law. When we used FDS-RT (which can be parallelized) to calculate the initial model of ISS-RT, the acceleration by using MPI on the whole computation time required by ISS-RT was evident. This was tested on a parallel computer system made by three Fujitsu Siemens Esprimo P5720 computers. With 6 processors we achieved a 3.17 times speedup when we set the iteration in the FDS-RT part as 200 and split the frequencies into 25 parts.

We parallelized the ISS-RT code as an example, the parallel computing by using MPI can be applied to other Radon transform algorithms in the same manner.

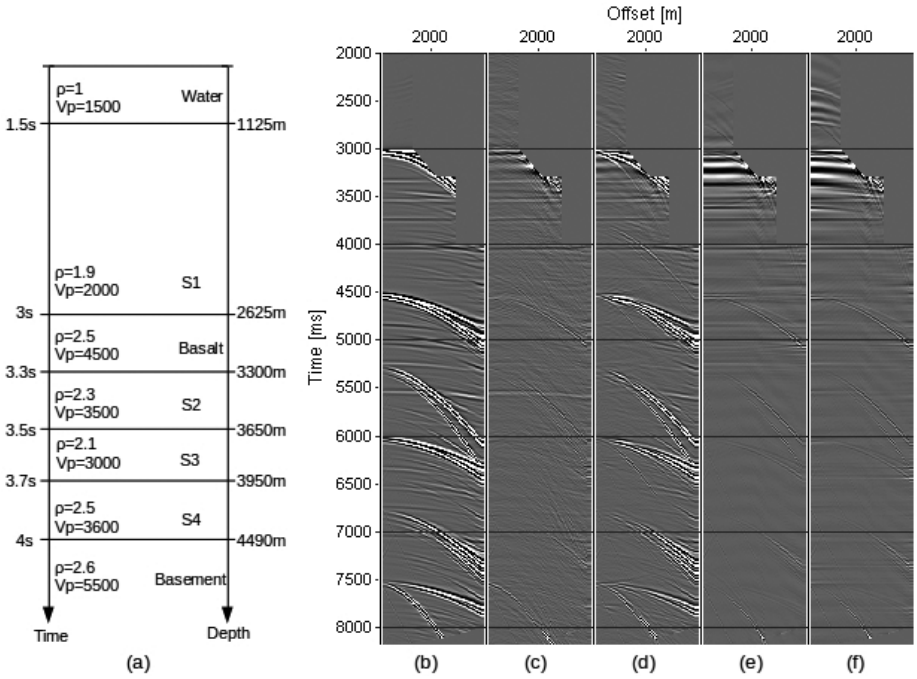


Fig. 2 – a) Synthetic Earth model to test the abilities of different Radon transform methods to attenuate multiples. Densities ϱ are in *g/cm3*, P-wave velocities $V_p$ are in *m/s*. b) Synthetic seismic data derived from the model in (a); muting, NMO correction and spherical divergence correction have been applied to this data by using ProMAX. (c) to (f) show the demultiple results and are sequentially related with: c) our FDS-RT code, d) the FDS-RT code from ProMAX, e) the standard parabolic Radon transform code from ProMAX, f) the standard hyperbolic Radon transform code from ProMAX. To show the differences of the demultiple results better, the seismic data are displayed in the [2000 ms, 8190 ms] time window.

**Synthetic example.** To compare our FDS-RT code and the existing codes on ProMAX according to their abilities on demultiple operation, we used the synthetic data computed on the earth model in Fig. 2a. Fig. 2b shows the data which is characterized by the presence of very strong multiples due to the high velocity basalt layer at 2625 m depth. Muting, NMO correction and spherical divergence correction have been applied to the data by using ProMAX in Fig. 2b. To show the differences of the demultiple results better, the seismic data in Fig. 2 are displayed in the [2000 ms, 8190 ms] time axis window.

The synthetic data are made by 162 traces. The offset ranges from 200 m to 4225 m. The time sampling rate is 2 ms. The strong reflection of the water bottom is at 1.5 s. The top basalt reflection is at 3 s. The first multiple of the water bottom at 3 s makes the top basalt reflection indistinguishable. The primaries after 3 s have weak amplitudes.

To attenuate the multiples by using Radon transform, we first do a forward Radon transform to the NMO corrected seismic data, then in transform domain we do a muting to the primaries, next we do an inverse Radon transform to the multiples, finally we subtract the multiples from the original NMO corrected data. Muting the multiples in the Radon transform to get directly the primaries is not advisable as we would like to preserve the primaries faithfully. Moreover, as a practical procedure, we can mute the data at times lower than the first observed multiple in the seismogram before the forward Radon transform.

On ProMAX the horizontal axis in parabolic Radon transform domain is the moveout Γ instead of the curvature q. The relationship between Γ and q can be described by the equation:

$$\Gamma = qx^2 \qquad (2)$$

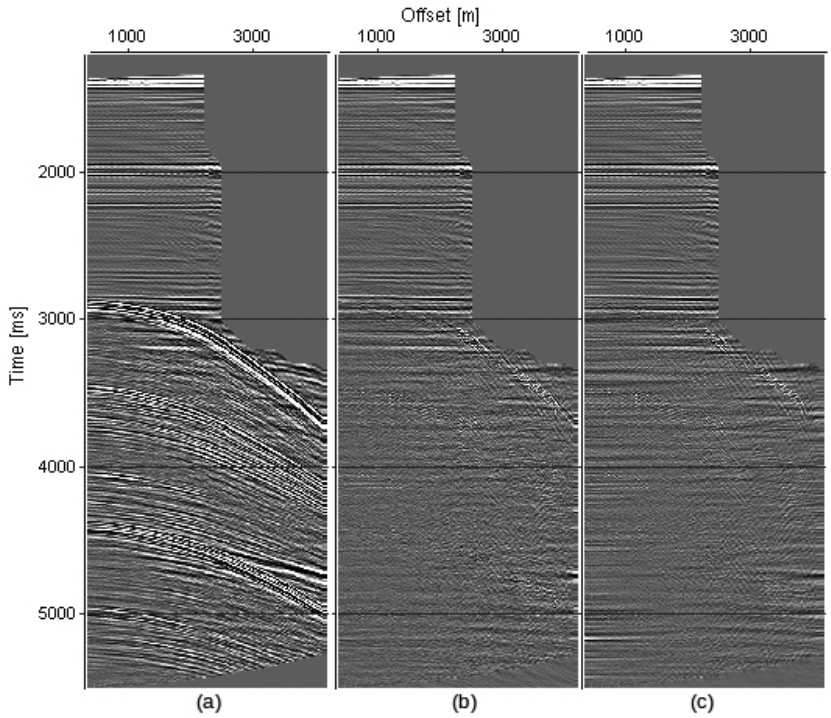


Fig. 3 – a) Real marine data. Muting, bandpass filtering (3-12-60-95 Hz), NMO correction and spherical divergence correction have been applied to the data. b) Our FDS-RT code applied to the data in (a). c) The standard parabolic Radon transform from ProMAX applied to the data in (a).

In $\tau$-$\Gamma$ domain the FDS-RT code from ProMAX gives a better vertical resolution than our FDS-RT code, while the latter gives a better horizontal resolution than the former. We tested also the standard parabolic and hyperbolic Radon transform code from ProMAX.

Fig. 2c shows the demultiple result by using our FDS-RT code while Fig. 2d to Fig.2f show the demultiple results by using ProMAX. From Fig. 2d we see that FDS-RT from ProMAX is less suitable for multiple attenuation because most of the multiple energy remains. The parabolic and hyperbolic Radon transform from ProMAX (Figs. 2e and 2f, respectively) can attenuate multiples quite efficiently but they create some artifacts, in particular between 2 s and 4 s, which over-impose to the primaries between 3 s and 4 s. These artifacts, which are stronger in the hyperbolic case, can cause difficulties in the seismic data interpretation. The FDS-RT code written by us (Fig. 2c) is slightly less efficient in multiple attenuation compared with the standard parabolic or hyperbolic Radon transform from ProMAX, especially at far-offset, but very few artifacts can be observed. Indeed in Fig. 2c the multiples appear well attenuated and the primaries between 3 s and 4 s can be clearly seen. Both our FDS-RT code and the standard parabolic Radon transform code are less efficient in demultiple at the end points when there is an abrupt ending of the multiples in the seismogram.

Real data application. We used both our FDS-RT code and the standard parabolic Radon transform code from ProMAX to attenuate the multiples in a real marine data.

Fig. 3a shows the marine data. Muting, bandpass filtering (3-12-60-95 Hz), NMO correction and spherical divergence correction have been applied to the data by using ProMAX. The data is made by 154 traces. The offset ranges from 375 m to 4200 m. The maximum time is 5500 ms. The time sampling rate is 4 ms. The water bottom is at about 1.5 s. Fig. 3 shows the seismic data in the time window [1200 ms, 5500 ms]. The data are muted at time lower than 2.8 s before forward Radon transform.

The demultiple results using the two best performing Radon transform algorithms tested are displayed in Figs. 3b and 3c. As already observed on the synthetic data, we see that the standard parabolic Radon transform from ProMAX is more efficient in attenuating far-offset multiples, but it seems to create more artifacts at near-offset.

**Conclusion.** Two existing problems in the Radon transform computation are the artifacts generated in the transform domain and the long computing time. The limited offset range in t-x domain leads to far-from-ideal, low-resolution Radon transforms with butterfly structures, that make less effective this algorithm in attenuating the multiples on seismic data.

Different ways of computing the standard Radon transform and different sparse Radon transform methods are compared in this work according to their performances in giving a high resolution transform and in the demultiple operation. For what concern the standard Radon transform, the conjugate gradient method is more efficient in the multiple attenuation than the damped least squares or the singular value decomposition methods. Concerning the sparse Radon transforms, although in $\tau$-q domain FDS-RT provides a lower signal to noise ratio and a worse vertical and horizontal resolution than TFDS-RT and ISS-RT, in t-x domain it better preserves the weak seismic events and causes the smallest amplitude attenuation along the offset axis. The experiments that we carried out on both synthetic and real data show that our implementation of FDS-RT is the most suitable algorithm in the multiple attenuation between all the Radon transform algorithms tested.

To deal with the long computing time problem, the MPI package from Octave-Forge can be used to parallelize the Radon transform algorithms. Taking the ISS-RT code as an example, with 6 processors we achieved a 3.17 times speedup when we set the iteration in the FDS-RT part as 200 and split the frequencies into 25 parts.

As a final remark note that the number of parameters required by the aforementioned algorithms is very different, varying from 3 for the TFDS-RT up to 10 for the ISS-RT with FDS-RT calculating the initial model. This could have a great impact on the processing of seismic data.

**Acknowledgments.** We would like to thank Dr. Angelo Sajeva and Dr. Mattia Aleardi for the beneficial discussions during the work. We would like to thank Signal Analysis and Imaging Group from Department of Physics, University of Alberta for their SeismicLab package. We gratefully acknowledge Landmark Graphics Corporation for the use of their ProMAX® software.

## References

Lu W. K.; 2013: An accelerated sparse time-invariant Radon transform in the mixed frequency-time domain based on iterative 2D model shrinkage. Geophysics, vol. 78, issue 4, p. V147-V155.

Oldenburg D. W. and Li Y. G.; 2005: Inversion for applied geophysics: a tutorial. Investigations in geophysics, 13, 89-150.

Sacchi M. and Ulrych T.; 1995: High-resolution velocity gathers and offset space reconstruction. Geophysics, 60, 1169-1177.

Schonewille M. A. and Duijndam A. J. W.; 2001: Parabolic Radon transform, sampling and efficiency. Geophysics, 66, 667-678.

Strang G.; 1986: Introduction to applied mathematics. Wellesley-Cambridge Press.

Trad D., Ulrych T. and Sacchi M.; 2003: Latest views of the sparse Radon transform. Geophysics, 68, 386-399.

Turner G.; 1990: Aliasing in the tau-p transform and the removal of spatially aliased coherent noise. Geophysics, 55(11), 1496-1503.

Yilmaz Ö.; 2001: Seismic data analysis. Society of Exploration Geophysicists.

# sessione 3.2

## Metodi elettro-magnetici e gravimetrici

**Convenor: A. Manzella e G. Florio**

**co-organizzata con Sezione Italiana Eage-Seg**

# TIME-LAPSE MONITORING OF THE HYPORHEIC ZONE OF AN ALPINE RIVER USING NON-INVASIVE METHODOLOGIES

**L. Busato, J. Boaga, M.T. Perri, G. Cassiani**
*Dipartimento di Geoscienze, Università degli Studi di Padova, Italy*

**Introduction.** The hyporheic zone (HZ) is the area located beneath and adjacent to rivers and streams, where the interactions between surface water and groundwater take place (Reidy and Clinton, 2004; Westhoff *et al*., 2011). Therefore, this domain allows the transport of several substances (e.g., water, nutrients, and pollution) (Boulton *et al*., 1998) from a stream to the unconfined aquifer below, and vice versa, thus playing a fundamental role in the river ecosystem.

The importance of the hyporheic zone in such a complex environment makes its characterization a goal shared by several disciplines, which range from applied geophysics to biogeochemistry, from hydraulics to ecology (Bridge, 2005): Regardless of the field of study, the main aim is always to completely describe the structures and the processes that distinguish this zone. Furthermore, flow and transport models are nowadays key instruments to efficiently characterize the HZ, given their ability of simulating surface water-groundwater exchange phenomena at a local scale (Constantz, 1998; Bianchin *et al*., 2010).

In order to achieve this common purposes, almost all these disciplines offer many invasive techniques that permit punctual *in situ* surveys and/or sample analysis (Bridge, 2005); on the other hand, applied geophysics supplies a few non-invasive methodologies (e.g., Electrical Resistivity Tomography – ERT – and Distributed Temperature Sensing – DTS), which allow a high resolution characterization of the hyporheic zone, overcoming the critical problem of measurements under riverbeds. In fact, ERT is a state-of-the-art technique for this kind of surveys, although it is commonly applied in a cross-well configuration or with a superficial electrodes deployment (Acworth and Dasey, 2003; Crook *et. al*, 2008); conversely, the DTS usage in hydrogeophysics has been developing since the last decade, revealing a wide applicability to the typical issues of this field of study: Based on Raman scattering, this methodology employs heat as tracer and uses a fiber-optic cable to acquire temperature (T) values (Boulton *et. al* 1998; Anderson, 2005; Selker *et al*., 2006; Lane *et al*., 2008).

In this work, we present the preliminary results (first year) regarding the characterization of the hyporheic zone of an alpine river (Vermigliana creek), obtained combining ERT and DTS time-lapse measurements. The typical ERT superficial data collection benefits from an innovative instrumentation deployment, which consists of both an ERT multicore cable and a DTS fiber-optic located in two separated boreholes drilled under the watercourse and perpendicular to it. These acquisition schemes led to high quality data capable to highlight some of the dynamics taking place in the HZ, which, however, still need to be coupled with a flow and transport model, in order to completely describe the domain of interest.

The site and the results here described are part of the EU FP7 CLIMB (Climate Induced Changes on the Hydrology of Mediterranean Basins) project.

**Creek and site description.** The Vermigliana creek is the main watercourse of the Upper Val di Sole, Northern Italy, originates from the Presena Glacier (Presanella Group) and is one of the main tributaries of the Noce creek. Being the Vermigliana an alpine river, it presents a nivo-glacial regime, which entails higher flow rates during the summer (due to snow and glacial melting) and lower flow rates during the winter season. A variation in terms of discharges takes place also daily, since morning flow rates are on average higher than those in the late afternoon.

The whole valley bottom, where the Vermigliana flows, is entirely filled with heterogeneous glacial till and quaternary slope deposits, made up of material whose granulometry ranges from clays to boulders.

Our site is located near the small village of Vermiglio (TN), 1165 meters above mean sea level.

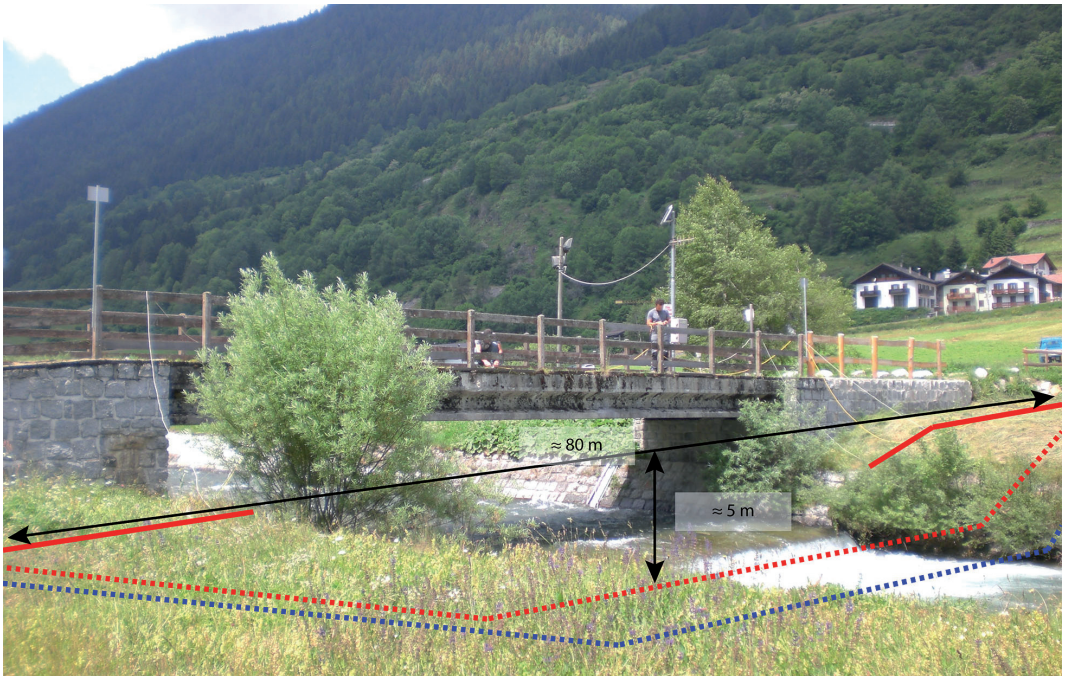


Fig. 1 – Vermigliana creek site (1165 m above sea level). The red solid line represents the superficial ERT deployment on both levee surfaces, the red dotted line represents the ERT borehole deployment (under the Vermigliana creek, inside the hyporheic zone) and the blue dotted line represents the DTS fiber-optic under the watercourse. The DTS borehole is a few meters downstream from the ERT borehole and parallel to it.

**Set-up and acquisitions.** In order to characterize the HZ in our site, we combined two different methodologies, ERT and DTS.

The former has been widely applied for this kind of surveys in many different sites, commonly using cross-well configurations and/or superficial cables (Acworth and Dasey, 2003; Crook *et al.*, 2008). Even if all these typical deployments lead to the acquisition of excellent data, we attempted to improve them by positioning part of the 72 total electrodes used inside the hyporheic zone (Fig. 1): this was possible thanks to the horizontal directional drilling technology, which allowed the remote-guided drilling of a horizontal borehole under the Vermigliana riverbed. The result consists of an 80 m long perforation under the watercourse that permitted the placement of a multicore cable with 48 brass electrodes, spaced 1m, inside the HZ; these electrodes have a diameter of 30 mm and a length of 60 mm. The choice of brass electrodes is due to both economical and technical issues: on the one hand, brass is less expensive than graphite and stainless steel, but offers a lower resistance to water over time; on the other hand, this instrumentation will not be removed from the Vermigliana site and therefore an amortization of its high costs, with an usage in other case studies, will not be possible. To ensure a higher data reliability, we deployed also a superficial survey line of 24 stainless steel electrodes (12 on each river levee) spaced 1 m, in vertical correspondence to the horizontal borehole (Fig. 1). Given the need of creating a single superficial deployment perpendicular to the river and the availability of a non-waterproof multicore cable for superficial surveys, 4 take-outs allowed the connection of the 4 electrodes nearest to the watercourse to the cable itself, which was partly located over the bridge upstream.

Each ERT survey is performed with an IRIS Syscal Pro resistivity meter using all 72 electrodes, with a “skip 0” dipole-dipole scheme and duration of circa 30 minutes. The acquisition of both direct and reciprocal measurements (i.e., exchanging current electrodes with

potential electrodes) permits the error assessment: in fact, each ERT sequence is made up of 4885 measurements, comprising both direct and reciprocal values.

The latter, DTS (Distributed Temperature Sensing), has been employed in hydrogeophysics only for the last dozen of years. This methodology is based on the Raman effect, one of the scattering phenomena arising from the interaction between light photons and the noncrystalline structure of fiber-optic: Such an interaction generates a backscattered signal, whose intensity is temperature dependent (Selker *et al*., 2006). Therefore, with an appropriate data processing, it is possible to compute how temperature varies along the whole fiber-optic cable. The usage of this methodology enables then to exploit heat as a natural tracer, showing its temporal and spatial changes in the domain of interest. Given our aim of characterizing the hyporheic zone of the Vermigliana creek, also for this technique we opted for an innovative deployment, which consists of a 200 m long fiber-optic located in a horizontal borehole a few meters downstream from the ERT perforation and parallel to it: Thus, also the fiber-optic is placed inside the HZ (Fig. 1). For a better comprehension of the site geometry, it is necessary to underline that the DTS perforation has a 100 m linear length. Therefore, the fiber-optic is folded, creating the "double-ended" configuration required (i.e., both ends are connected to the DTS instrument).

For every DTS survey we used the AP Sensing N4386A Distributed Sensing system with a double-ended fiber-optic configuration, a sampling interval equal to 1 m and a spatial resolution equal to 1 m. In each survey, we acquired three single traces with update time and measurement time both equal to 30 s (i.e., every 30 s a new trace acquisition begins and lasts 30 s) and then averaged the three temperature values thus obtained for every sampling point: The result consists of a single profile with 200 temperature values, spaced 1 m one from the other.

The ERT time-lapse monitoring started in July 2013 and still is being carried out approximately once or twice a month, mostly according to the weather conditions. On the other hand, we have been performing the DTS time-lapse monitoring since June 2014 approximately once a month.

Because of the typical continental climate characterizing the Upper Val di Sole, the time-lapse monitoring (both ERT and DTS) can be performed only from spring to autumn, given the absence of snow and of seasonally frozen ground that would lead to high resistivity values and noisy data.

**Data processing, results and discussions.** The ERT data at our disposal call for two different types of inversion. First of all, from each dataset (one from every survey) the correspondent absolute resistivity ($\varrho$) cross-section is obtained with an appropriate inverse modelling, in order to represent the state of the hyporheic zone at the measurement time. After the error calculation based on the combination of each direct measurement with the correspondent reciprocal one, every dataset is refined applying an error threshold equal to 10%, which reduces each sequence to 1400 measurements on average. Despite 10% may seem a quite high error limit, it is perfectly compatible with the heterogeneous material whereof the investigated domain is composed [i.e., clay, tonalite boulders, gravelly-sand and silty deposits, as described by Dal Piaz *et al*. (2007)]. Then, we performed the ERT data inversion thanks to the R2 code (Lancaster University, UK), fixing an error equal to 10% and using a triangular mesh with 5039 nodes and 9729 triangular elements.

An example of the result of such a processing is the resistivity cross-section depicted in Fig.2, representing the acquisition carried out on August 30, 2013. The resistivity distribution here illustrated is largely comparable to those of the other ERT surveys.

A very low resistivity domain characterizes the area beneath the Vermigliana creek and extends till a depth of 4 m below ground level, with an average resistivity value of 50 Ωm. At first glance, the presence of such a domain may be justified by the seepage process, which allows the –total or partial– sub-riverbed saturation with the consequent overall resistivity modification (as expeted, according to Archie's law). If we focus on resistivity values instead, a discrepancy emerges: An average resistivity of 50 Ωm is incompatible with the values characterizing both

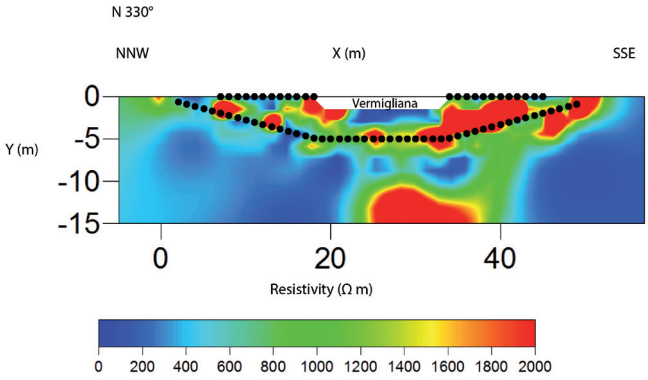


Fig. 2 – Example of resistivity cross-section resulting from the ERT survey conducted in Vermiglio on July 30, 2013. The cross-section is facing downstream. A low resistivity domain is located under the Vermigliana creek, while the riparian zones show, on average, higher resistivity values. The black dots represent the electrodes position both on the levee surface (24 stainless steel electrodes) and inside the perforation drilled under the Vermigliana creek (48 brass electrodes).

deposits and waters of the Vermigliana creek, whose resistivity have orders of magnitude of 1000 Ωm and 100 Ωm respectively. In order to explain the features of this domain, whose existence in the HZ has also been confirmed by two auxiliary ERT surveys, we hypothesized the presence of a high clay fraction coming from the glacial moraines and transported by the creek itself, which not only increases the electrical conductivity in the sub-riverbed, but also reduces its hydraulic conductivity.

On the other hand, if we focus on the areas adjacent to the river, also referred to as "riparian zones", it is possible to highlight a difference between the left and the right bank (Fig. 2), since the former has an average electrical conductivity slightly lower than the latter.

Finally, albeit being outside our domain of interest (i.e., the area between the surface electrodes and the borehole electrodes), the resistivity cross-section in Fig. 2 also shows the bedrock, identified by the very high resistivity domain at a depth of 10 m below ground level.

The second inversion technique is strongly related to the ERT time-lapse monitoring currently in progress in the Vermigliana site and aims at highlighting how resistivity varies over time. As already described by Perri *et. al* (2012), this approach is based on the following equation:

$$R = \frac{R_i}{R_0} R_{\text{hom}}$$

where $R_i$ is the transfer resistance measured at time $t$, $R_0$ is the background (i.e., time 0) transfer resistance and $R_{\text{hom}}$ is the transfer resistance for a homogenous resistivity distribution model; all these transfer resistance values are referred to the same quadripole. Once $R$ is computed for every electrodes quadripole common to all the available datasets, the ERT data inversion with an error equal to 3% is performed, as already described above. The results consist of T–1 cross-sections (with T = total number of ERT acquisitions) displaying the resistivity variation over time expressed as percentage, with respect to the background survey (100% indicates no changes, higher values imply an increase in resistivity, and lower values are related to a decrease). Although the time-lapse monitoring began in July 2013, for this work we consider only the acquisitions carried out from May 5, 2014 onwards, because of the nature of the observed phenomena.

In order to better analyse the outcome of this second inversion technique, it is useful to divide the domain of interest into three parts: sub-riverbed, left bank, and right bank.In the first part, between May 14 and July 16, 2014 an increase in resistivity variation takes place (up to 150%), followed by a rapid decrease to 100%. Such behaviour may be due to a glacial water pulse, which is poor in ions and therefore characterized by a high resistivity. On the other hand, the left bank is characterized by a constant decrease in resistivity variation, from values higher than 120% to values around 60% (on average). This variation is probably related to the presence of an effluent of two small lakes upstream, whose waters are presumably more conductive. Finally, the last part shows a slight increase in resistivity variation over time (values are always, on average,

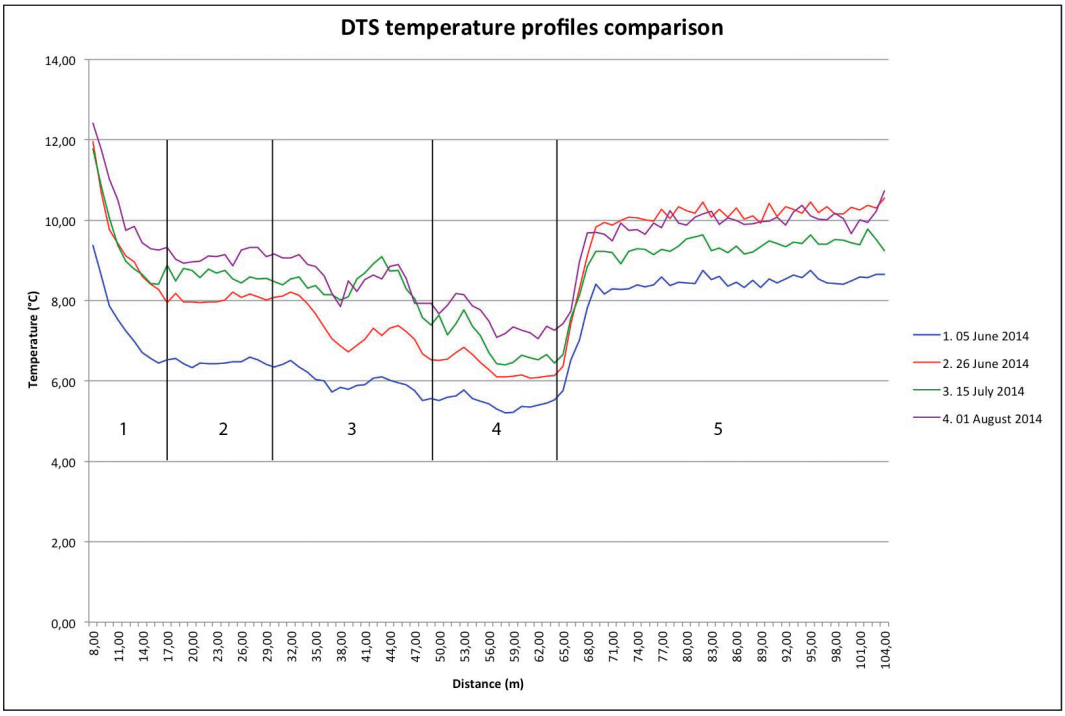


Fig. 3 – Comparison between DTS temperature profiles acquired in the Vermigliana site. In each profile five segments can be identified: 1, initial part influenced by the lakes' effluent and the surface temperature; 2, left bank of the Vermigliana creek (comparable with the left bank of the ERT cross section); 3, Vermigliana creek; 4, right bank of the Vermigliana creek (comparable with the right bank of the ERT cross section); 5, fiber-optic cable rolled at 0.5 m below ground level. All the temperature profiles show the same trend, with higher temperatures in the left bank and lower values in the right one, while the hyporheic zone below the Vermigliana creek is characterized by a variable trend that sharpens over time.

higher than 100%). Therefore, the right bank has constantly a higher resistivity with respect to the background, which may be caused by a constant flux of new glacial water poor in ions.

Al already mentioned in a previous chapter, together with the ERT technique we applied also the DTS methodology: Given the double-ended configuration chosen, it is necessary to lead back the temperature profile to the effective length of the borehole perforation and this has been achieved by averaging each "onward" temperature value with the correspondent "backward" value. Hence, each ultimate temperature profile has a length equal to 96 m with 97 temperature values (4 meters at each fiber-optic end have been removed since they are located outside the borehole).

The four temperature profiles available so far are displayed and compared in Fig. 3, where also the relative positions of both Vermigliana creeks and riverbanks are indicated. All these profiles show a common trend, which can be detected in each trace and analysed according to the partitioning in Fig. 3:

- Part 1: These segments are characterized by the highest temperature values, since here the fiber-optic cable is rather shallow. Therefore, there is a strong influence of the superficial temperature, which is probably also combined with the effect of the waters from the effluent nearby;
- Part 2: In this portion, the trend of each T profile is fairly linear and the temperature values are relatively high. Also here, there may be an influence from the effluent of the lakes upstream;

– Part 3: These segments correspond to the sub-riverbed of the Vermigliana creek. Here the trend is more variable than the other parts and sharpens over time, given the complexity of the processes taking place (e.g., mixing between glacial water and rain water with ground water);
– Part 4: This part of the traces is relative to the right bank and is clearly characterized by the lowest temperature values, probably due to the flux of glacial water;
– Part 5: This portion represents the part of the fiber-optic cable in excess that has been rolled and located at a depth of 0.5 m below ground level.

A time-lapse analysis of the profiles in Fig. 3 highlights a temperature increase over time: In fact, from the first to the last survey, the mean temperature augments of 2.09 °C. This temperature variation is not constant along the whole fiber, since the left bank warms up a little bit more than the right bank (i.e, mean increase for the left bank = 2.67 °C vs. mean increase for the right bank = 2.12 °C): this is also confirmed by the T variation computed for each sampling point. Therefore, not only we can assume that such temperature variation over time is instrument independent, but also we can hypothesize that the left and right riverbanks behave in two different ways, or, more likely, that are subject to different phenomena (i.e., flux of lacustrine and glacial water, respectively).

Finally, what needs to be strongly highlighted is the relation existing between DTS and ERT data, well proven by the comparison of Fig. 3 with the results of the time-lapse inversion. The relatively higher temperature values characterizing the left bank of the Vermigliana creek well fit the decrease in resistivity described before, since both this two effects may be caused by a sub-superficial flow of lacustrine water, which is hotter and richer in ions with respect to glacial water. On the contrary, a sub-superficial flux of glacial water may explain the overall lower temperature of the right bank and its relatively higher resistivity, given the lower ions contents.

**Future work.** The data acquired so far need to be coupled with a flow and transport model, in order to completely describe the structures and the processes characterizing the HZ of the Vermigliana creek. To achieve this future goal, we will use the CATHY (CATchment HYdrology) model combined with data assimilation methods, thanks to whom it is possible to assimilate both ERT and DTS data inside the numerical model itself.

Furthermore, the time-lapse monitoring of the hyporheic zone of the Vermigliana creek will continue in the next years, given the need of analysing more in detail the applicability of these two non-invasive methodologies in such a unique domain.

**Conclusions.** One of the main problems in the HZ characterization is the obvious need of investigating a domain located under a riverbed. In order to overcome such a problem, we applied two non-invasive methodologies, ERT and DTS, with an innovative instrumentation deployment: Both a multicore cable and a fiber-optic cable are located into two horizontal perforations drilled below the Vermigliana creek. Thus, the instruments are inside the HZ, our domain of interest. These two methodologies not only allowed fast surveys, but also supplied several high-quality datasets, comprising both resistivity values and temperature profiles that permitted a time-lapse analysis of the investigated area. The comparison between these different data highlighted a complex domain, characterized by the interaction of waters with different origin (e.g., glacial, superficial, and groundwater). Therefore a combined application of ERT and DTS measurements can lead to a deeper characterization of the hyporheic zone, given the strong correlation existing between the physical parameters analysed. Hence, the preliminary results presented in this work already show their high potential, which, however, will be fully expressed only through an appropriate hydrological modelling.

**References**

Acworth R. I. and Dasey G. R.; 2003: *Mapping of the hyporheic zone around a tidal creek using a combination of borehole logging, borehole electrical tomography and cross-creek electrical imaging, New South Wales, Australia*. Hydrogeology Journal, **11**(3), pp. 368-377.

Anderson M. P.; 2005: *Heat as a ground water tracer*. Groundwater, **43**(6), pp. 951-968.

Bianchin M., Smith L. and Beckie, R.; 2010: *Quantifying hyporheic exchange in a tidal river using temperature time series*. Water Resources Research, **46**(7).

Boulton A. J., Findlay S., Marmonier P., Stanley E. H. and Valett, H. M.; 1998; *The functional significance of the hyporheic zone in streams and rivers*. Annual Review of Ecology and Systematics, pp. 59-81.

Bridge J.W.; 2005: *High resolution in-situ monitoring of hyporheic zone biogeochemistry*. Environmental Agency Science Report.

Constantz J.; 1998: *Interaction between stream temperature, streamflow, and groundwater exchanges in alpine streams*. Water resources research, **34**(7), pp. 1609-1615.

Crook N., Binley A., Knight R., Robinson D. A., Zarnetske, J. and Haggerty, R.; 2008: *Electrical resistivity imaging of the architecture of substream sediments*. Water Resources Research, **44**(4).

Dal Piaz G.V., Castellarin A., Carton A., Daminato F., Martin S., Montresor L., Picotti V., Prosser G., Santuliana E. and Cantelli L.; 2007: *Note Illustrative della Carta Geologica d'Italia alla scala 1: 50.000, Foglio 042 Malè*. Provincia Autonoma di Trento, Servizio Geologico. APAT, Servizio Geologico d'Italia, Roma.

Lane J.W., Day-Lewis F.D., Johnson C.D., Dawson C.B., Nelms D.L., Eddy-Miller C.A., Wheeler J.D., Harvey C.F. and Karam H.; 2008: *Fiber-optic distributed temperature sensing: a new tool for assessment and monitoring of hydrologic processes*. Symposium on the Application of Geophysics to Engineering and Environmental Problems.

Perri M.T., Cassiani G., Gervasio I., Deiana R. and Binley, A.; 2012. *A saline tracer test monitored via both surface and cross-borehole electrical resistivity tomography: comparison of time-lapse results*. Journal of Applied Geophysics, **79**, pp. 6-16.

Reidy C. A. and Clinton S.M.; 2004: *Delineation of the hyporheic zone*. University of Washington Water Center.

Selker J. S., Thevenaz L., Huwald H., Mallet A., Luxemburg W., Van De Giesen N., Stejskal M., Zeman J., Westhoff M. and Parlange M. B.; 2006: *Distributed fiber-optic temperature sensing for hydrologic systems*. Water Resources Research, **42**(12).

Westhoff M. C., Gooseff M. N., Bogaard T. A. and Savenije H. H. G.; 2011: *Quantifying hyporheic exchange at high spatial resolution using natural temperature variations along a first-order stream*. Water Resources Research, **47**(10).

## OTTIMIZZAZIONE DEL CAMPIONAMENTO DEL TRANSIENTE ELETTROMAGNETICO PER DATI AEM

**D. Di Massa[1], G. Florio[1], A. Viezzoli[2]**

*[1] Dipartimento di Scienze della Terra, dell'Ambiente e delle Risorse, Università Federico II, Napoli*

*[2] Aarhus Geophysics ApS, Aarhus, Denmark*

La capacità di descrivere in maniera accurata e quantitativa il modello geologico del sottosuolo in termini di conducibilità elettrica a partire dall'analisi di dati elettromagnetici *airborne* nel dominio del tempo rappresenta la principale sfida in numerose applicazioni: da quelle idrogeofisiche a quelle ambientali, dall'esplorazione mineraria a quella petrolifera.

L'accuratezza dei modelli inversi 1D è influenzata da una serie di parametri che descrivono il sistema nel calcolo del modello diretto (Christiansen *et al*., 2011). Variazioni nella modellizzazione dei suddetti parametri possono portare alla definizione di modelli inversi più o meno differenti tra loro. Un'accurata misura di tali parametri si rende quindi necessaria per ottenere risultati soddisfacenti.

Nel presente lavoro l'attenzione è posta sul metodo di campionamento del transiente elettromagnetico e viene mostrato come l'utilizzo di diversi metodi di campionamento possa influenzare i risultati dell'inversione, in termini di resistività e spessore degli elettrostrati.

Il decadimento del transiente elettromagnetico viene campionato in finestre temporali (*gates*).

L'ampiezza dei *gates* rappresenta un punto cruciale nell'analisi dei dati elettromagnetici. Questo perchè essa influenza due caratteristiche del segnale che controllano contemporaneamente i risultati dell'inversione: il *noise* sui dati e la capacità di risoluzione del modello. In genere il rapporto segnale/rumore tende ad aumentare al crescere dell'ampiezza mentre al contrario la capacità di risoluzione del modello tende a migliorare per *gates* più piccoli. Un corretto campionamento deve tener conto del giusto *trade-off* tra queste due componenti.

Tipicamente il campionamento del transiente elettromagnetico viene fatto utilizzando dei *gates* la cui ampiezza cresce logaritmicamente (*log-gating*). Il *log-gating* presenta il doppio vantaggio di migliorare il rapporto segnale/rumore ai *late times*, quando il segnale elettromagnetico comincia a confondersi con il noise naturale di fondo e di riuscire a garantire una buona risoluzione del modello agli *early times*.

Come è noto il metodo elettromagnetico nel dominio del tempo mostra elevata sensitività per gli strati ad alta conducibilità elettrica. La sensitività è inversamente proporzionale alla velocità di diffusione della corrente che risulta essere maggiore per strati fortemente resistivi. Dal decadimento del transiente elettromagnetico possono essere desunte alcune informazioni sull'andamento della conducibilità con la profondità. Nel caso più semplice di un semispazio omogeneo, infatti, il segnale misurato come *db*/*dt* mostra ai *late times* un decadimento proporzionale a $t^{-5/2}$ in un grafico log-log. Per un modello, invece, orizzontalmente stratificato il decadimento del segnale sarà più veloce o più lento a seconda della conducibilità elettrica degli strati attraversati. Queste variazioni di velocità di decadimento si traducono, praticamente, in variazioni di pendenza del transiente che indicano le interfacce di contrasto tra due elettrostrati.

Le variazioni di pendenza rappresentano la base di partenza per un "*adaptive-gating*" che consiste in un riarrangiamento delle ampiezze dei *gates* con i quali viene campionato il segnale, al fine di migliorare la risoluzione (e quindi diminuire l'ampiezza dei *gates*) in corrispondenza delle aree di variazioni di pendenza.

L'*adaptive-gating* come metodologia per migliorare la risoluzione degli strati nel sottosuolo segue l'avanzamento tecnologico delle strumentazioni di acquisizione *airborne*, le quali sono in grado, attualmente, di registrare il campo elettromagnetico secondario anche ogni 2 $\mu$s. Questo permette di avere a disposizione una mole considerevole di dati per i quali la scelta dell'ampiezza dei gates (*binning*) può essere eseguita o seguendo l'approccio classico (*log-gating*) o attraverso nuove metodologie di adattamento del *gating* in funzione di alcune proprietà derivanti dallo studio del transiente misurato. Il presente lavoro intende dare un contributo in questo senso.

I risultati che di seguito vengono presentati fanno riferimento a un test che utilizza dati sintetici eseguito considerando le specifiche tecniche di un sistema da elicottero e un modello geologico orizzontalmente stratificato a tre strati. I dati sono stati invertiti utilizzando l'algoritmo em1dinv sviluppato presso il Gruppo di Idrogeofisica dell'Università di Aarhus in Danimarca.

Nelle Tabb. 1 e 2 sono riportate le specifiche tecniche del sistema *airborne* utilizzato e le proprietà fisiche del modello geologico considerato:

Tab. 1 - Specifiche tecniche del sistema airborne utilizzato nella simulazione.

| Campo secondario | dB/dt (V/m2), componente verticale z |
|---|---|
| Altezza di volo | 30 m |
| Momento magnetico | 16000 $Am^2$ |
| On-time | 7000 µsec |
| Off-time | 9990 µsec |
| Numero gates | 21 (7 per decade temporale tra $10^{-5}$ e $10^{-2}$ s) |

Tab. 2 - Modello geologico utilizzato nella simulazione.

| Resistività (Ohm*m) | Spessore (m) |
|---|---|
| 10 | 30 |
| 50 | 70 |
| 500 | ∞ |

Lo studio è stato condotto a partire dalla soluzione del *forward problem* per il modello geologico considerato assumendo che il transiente fosse campionato ad intervelli regolari per ogni decade temporale dell'*off-time*.

Nello specifico, tenendo conto del *trade-off* tra ampiezza dei *gates* e *noise*, si è deciso di campionare il transiente ogni 2 $\mu$s tra $10^{-5}$ e $10^{-4}$ s, ogni 20 $\mu$s tra $10^{-4}$ e $10^{-3}$ s e ogni 200 $\mu$s tra $10^{-3}$ e $10^{-2}$ s per un totale di 136 *gates*. Il calcolo dei dati sintetici è stato condotto inizialmente in assenza di *noise*.

La scelta di tenere in considerazione e di eseguire lo studio anche su dati privi di *noise*, per quanto non abbia applicabilità nei casi reali, ci è servita in questa fase come validazione dei risultati ottenuti dai dati con *noise*.

Ad ogni gate è stato successivamente assegnato il *noise* in funzione della propria ampiezza. La *standard deviation* del *noise* per ogni gate ($\sigma_i$) tiene conto di un contributo "moltiplicativo"($\sigma^2_{0,i}$), uniforme su tutti i *gates*, pari al 3% del segnale e dovuto principalmente a complessità geologiche non tenute in considerazione in un approccio di interpretazione 1D e a disallineamenti nel sistema trasmettitore-ricevitore e di un contributo "additivo" ($\sigma^2_{noise,i}$), derivante da un modello di *noise* che può essere approssimato a una retta con pendenza $t^{-1/2}$ in un grafico log-log, assumendo che a 1 ms il valore del *noise* sia pari a 3 nV/m$^2$ (Munholm, 1996). Questo termine rappresenta il rumore "bianco" di fondo che si può ridurre agendo sulla larghezza dei *gates* e sullo *stacking*.

$$\sigma_i = \sqrt{\sigma^2_{0,i} + \sigma^2_{noise,i}} \tag{1}$$

Le zone di variazione di pendenza all'interno del transiente elettromagnetico sono state studiate calcolando la derivata prima del transiente stesso. La presenza di *noise* nei dati, tuttavia, non ha consentito una facile individuazione delle zone di variazione dove riadattare il *gating*, ecco perchè si è deciso di eseguire previamente un *denoising* sui dati utilizzando la trasformata discreta di wavelet (DWT).

La trasformata discreta di wavelet permette di effettuare un filtraggio locale o globale di un segnale (Fedi e Quarta, 1998).

Per ogni funzione $f \in L^2(R)$, la trasformata continua di wavelet (*Continuous Wavelet Transform*, CWT) è definita dall'integrale:

$$\widetilde{W}(a,b) = \frac{1}{\sqrt{a}} \int_{-\infty}^{+\infty} f(x)\overline{\Psi}\left(\frac{x-b}{a}\right) dx \tag{2}$$

Dove $\overline{\Psi}$ è il complesso coniugato di una funzione $\Psi \in L^2(R)$, chiamata ondina madre.

$\widetilde{W}$ si costruisce traslando e dilatando $\Psi$. La coppia di parametri $(a,b)$ controlla la dilatazione e la traslazione dell'ondina: il parametro $a$ è relativo alla scala e il parametro $b$ alla posizione (o tempo). Per una data scala il parametro $b$ fornisce la localizzazione spaziale (temporale) delle caratteristiche del segnale analizzato a quella scala.

Va sottolineato che l'utilizzo del termine "continua", in questa trasformata, è legato alla variabilità nel continuo per i valori di scala e di posizione spaziale (o temporale).

Nel caso discreto, sono usati valori discreti per a e b. In particolare, i valori assumibili dal parametro di scala sono potenze di 2 ($a = 2^m$), mentre i valori assumibili dal parametro di

posizione sono $b = a \cdot n$, con $m, n \in ZxZ$ .

La trasformata discreta di wavelet (*Discrete Wavelet Transform*, DWT) può quindi essere definita come (Fedi e Quarta, 1998):

$$\hat{W}_{m,n}(a,b) = \int_{-\infty}^{+\infty} f(x)\,\Psi_{m,n}(x)dx \qquad (3)$$

dove $\Psi_{m,n} = 2^{-m/2}\,\Psi\,(2^{-m}\,x - n)$

Tra i vari tipi di *wavelets*, le più utili sono quelle dotate di speciali proprietà matematiche, come le ondine ortogonali o bi-ortogonali.

Ondine ortogonali formano una base ortonormale per qualsiasi funzione $f \in L^2(R)$, quindi $f$ può essere espressa come:

$$f(x) = \sum_m \sum_n \hat{W}_{m,n}\Psi_{m,n}(x) \qquad (4)$$

Dato che il concetto di scala può essere associato a quello di frequenza, piccole scale sono in relazione con strutture del segnale ad alta frequenza e grandi scale con quelle a bassa frequenza (Daubechies e Paul, 1987).

Quindi, le caratteristiche di flessibilità dell'analisi di wavelet la rende ottimale per l'analisi di segnali non stazionari composti da piccole lunghezze d'onda sovrapposte a grandi lunghezze d'onda (Fedi e Quarta, 1998).

La scomposizione del segnale in basi di ondine ortonormali può essere interpretata come un'analisi a multirisoluzione del segnale, cioè un processo che correla un segnale $f$ con la sua approssimazione a diverse scale. $f$ sarà decomposta in una somma di approssimazioni del segnale a bassa risoluzione e di diversi dettagli del segnale ad alta risoluzione.

Tale analisi non è univoca (Foufoula e Kumar, 1994) in quanto dipende dalla scelta dell'ondina $\Psi$. Questa scelta è funzione delle caratteristiche del segnale, a differenza della trasformata di Fourier.

Grazie alla proprietà della DWT di fornire una rappresentazione spazio-scala dell'anomalia analizzata è possibile eseguire *denoising* localizzato, ovvero filtrare determinate frequenze solo in alcune porzioni del segnale lasciando inalterata la parte non filtrata. Ciò rappresenta un'ulteriore differenza rispetto alla trasformata di Fourier, per la quale è possibile realizzare solo un *denoising* globale, in quanto il supporto delle funzioni analizzanti della trasformata di Fourier risulta essere infinito nel dominio spaziale.

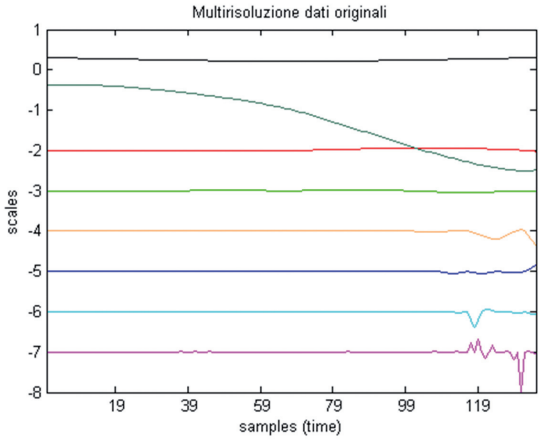


Fig. 1 – Multirisoluzione del transiente elettromagnetico.

Il segnale sul quale è stato eseguito il *denoising* consiste in 136 dati (tanti quanti erano i *gates* calcolati inizialmente dal *forward model*) che sono stati interpolati in modo equispaziato.

Il vettore di dati è stato poi estrapolato ai bordi fino ad ottenere un vettore di 256 campioni. L'ondina utilizzata è stata la "*Interpolating*". L'analisi a multirisoluzione ha fornito la scomposizione del segnale in 7 dettagli e un'approssimazione del segnale a bassa risoluzione (Fig. 1, linea nera, nella parte più in alto del grafico).

Il rumore dà evidenze su diverse scale, e soprattutto alle scale -4, -5, -6 e

-7, e inoltre alle posizioni intorno a x=40 e x=120. Per rimuoverlo sono stati quindi azzerati i coefficienti della DWT corrispondenti a queste scale e il segnale è stato poi ricostruito mediante l'Eq. (4).

Nella ricostruzione del segnale sono stati rimossi i dettagli -5, -6 e -7 e sono stati considerati i dettagli dall' -1 al -4.

La multirisoluzione del segnale è un' analisi non univoca, ma dipendente dal tipo di ondina scelta e dal *noise* contenuto nei dati, che può variare da caso a caso. Nella ricostruzione del segnale, come in tutte le operazioni di filtraggio, deve essere tenuto in considerazione il giusto compromesso tra la rimozione del *noise* e la preservazione dell'informazione contenuta nei dati.

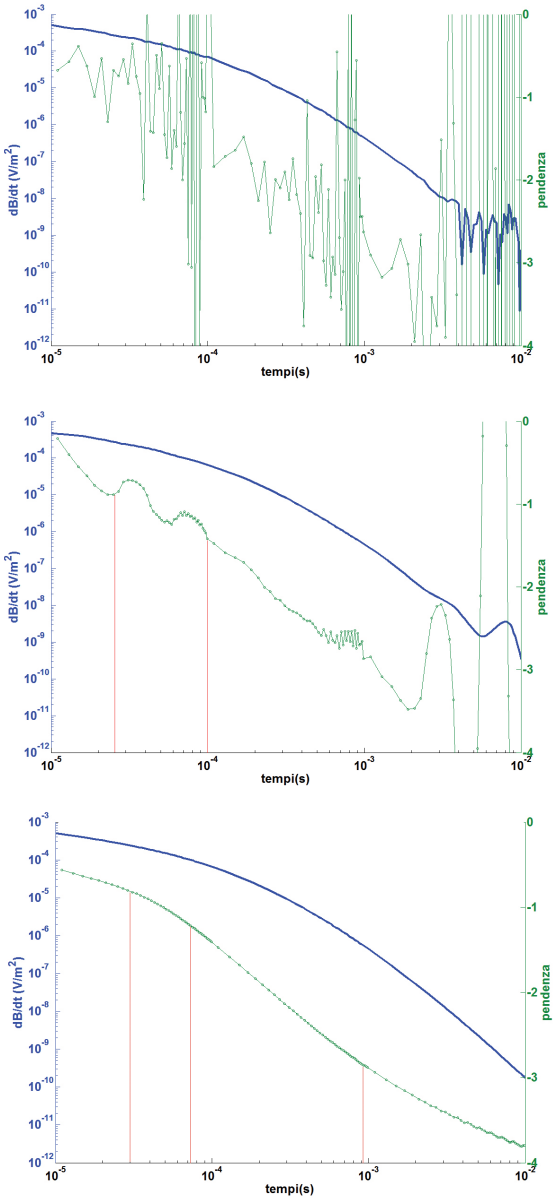


Fig. 2 – In alto derivata prima (curva verde) del transiente (curva blu) senza filtraggio; al centro derivata prima (curva verde) del transiente (curva blu) dopo DWT; in basso dervata prima (curva verde) del transiente (curva blu) per dati senza noise.

Nella Fig. 2 è mostrato come dal calcolo della derivata prima (pendenza, curva verde) del transiente elettromagnetico (curva blu) è possibile individuare un'area di brusca variazione di pendenza ascrivibile a un eventuale cambiamento di conducibilità elettrica nel sottosuolo.

Nello specifico, nel grafico in alto è mostrato il calcolo della pendenza per un transiente sul quale non è stato eseguito il *denoising* con la DWT: in questo caso la presenza di *noise* rende impossibile l'individuazione di un'area di variazione della pendenza.

Nel grafico al centro è mostrato, invece, lo studio condotto sul transiente elettromagnetico filtrato con la DWT: in questo caso risulta possibile individuare un intervallo temporale compreso tra $3*10^{-5}$ e $1*10^{-4}$ s dove è evidente una notevole variazione di pendenza. In questo intervallo temporale è stato quindi definito un *adaptive-gating*. Lo stesso intervallo temporale può essere individuato con maggiore precisione anche nel grafico in basso dove è mostrato lo studio eseguito sul transiente privo di *noise*. In questo grafico è possibile individuare un' ulteriore variazione di pendenza intorno a $1*10^{-3}$ s che segna, presumibilmente, il passaggio tra il secondo e il terzo strato. Tale variazione risulta accennata anche nel grafico mostrato al centro.

In corrispondenza di questa variazione di pendenza non è stato definito un *adaptive-gating* in quanto nell'intervallo di tempo in cui è localizzata, il *noise* comincia ad avere un ruolo predominante

sulla forma del transiente e pertanto risulta impossibile ottenere un aumento di risoluzione nel modello, riducendo l'ampiezza dei *gates*, senza avere un pari incremento del *noise* che comprometterebbe i risultati dell'inversione.

Nella Tab. 3 vengono riportate le informazioni in termini di ampiezza e centro dei *gates* dall'inizio *dell'off-time* utilizzati per invertire i dati, sia in configurazione *log-gating* che in configurazione *adaptive-gating*.

L'*adaptive-gating* ha tenuto conto delle variazioni di pendenza individuate nella precedente fase dello studio e localizzate tra $3*10^{-5}$ e $1*10^{-4}$ s. In corrispondenza di questo intervallo sono stati distribuiti 6 *gates* da 14 $\mu$s. Lo stesso intervallo è coperto nella configurazione *log-gating* da 4 *gates* ad ampiezza variabile.

Tab. 3 - Ampiezza e centro dei *gates* per le configurazione *log-gating* e *adaptive-gating*.

| LOG-GATING | | ADAPTIVE GATING | |
|---|---|---|---|
| Ampiezza gate (μs) | Centro gate (μs) | Ampiezza gate (μs) | Centro gate (μs) |
| 3.9 | 12 | 20 | 20 |
| 5.4 | 17 | 14 | 37 |
| 7.5 | 23 | 14 | 51 |
| 10.5 | 32 | 14 | 65 |
| 14.5 | 45 | 14 | 79 |
| 20.2 | 62 | 14 | 93 |
| 28 | 86 | 14 | 107 |
| 39 | 120 | 39 | 134 |
| 54.1 | 166 | 54.1 | 180 |
| 75.2 | 231 | 75.2 | 245 |
| 104.5 | 321 | 104.5 | 335 |
| 145.2 | 446 | 145.2 | 460 |
| 201.7 | 619 | 201.7 | 633 |
| 280.3 | 860 | 280.3 | 874 |
| 389.5 | 1195 | 389.5 | 1209 |
| 541.2 | 1660 | 541.2 | 1674 |
| 752 | 2361 | 752 | 2375 |
| 1044.9 | 3205 | 1044.9 | 3219 |
| 1451.9 | 4454 | 1451.9 | 4468 |
| 2017.4 | 6188 | 2017.4 | 6202 |
| 2803.1 | 8599 | 2803.1 | 8613 |

L'utilizzo di *gates* con ampiezza minore ha richiesto, per controllare il *trade-off* tra ampiezza dei *gates* e *noise*, un incremento dell'ampiezza dei *gates* al di fuori dell'intervallo temporale di interesse. In questo caso i primi tre *gates* della configurazione *log-gating* sono stati sostituiti da un unico *gates*, nella configurazione *adaptive-gating*, con ampiezza simile. La scelta di inserire un primo gate con ampiezza maggiore dei sei successivi è stata avvalorata dall'analisi eseguita attraverso lo studio sulle variazioni di pendenza presenti nel transiente. Se la variazione di pendenza, che indica il passaggio tra 2 strati a diversa conducibilità elettrica, è individuata a partire da $3*10^{-5}$ s, è lecito considerare che a tempi inferiori la corrente si trovi completamente nello strato superiore e pertanto risulta vantaggioso, per ridurre il *noise* presente nei dati da invertire, campionare il segnale con un unico gate più largo.

I *gates* successivi (dal numero 7 al numero 21) sono considerati della stessa ampiezza in entrambe le configurazioni.

L'inversione dei dati è stata eseguita utilizzando l'algoritmo di inversione em1dinv (Gruppo di Idrogeofisica dell'Università di Aarhus in Danimarca).

Nella Fig. 3 sono riportati i risultati grafici delle inversioni e nella Tab. 4 sono riassunti i risultati in termini di resistività e spessori dei modelli inversi, e i fattori di *standard deviation* (STDF) ottenuti da un'analisi di sensitività sui parametri ottenuti.

Il fattore di *standard deviation* per ogni parametro ($m_s$) è calcolato a partire dalla covarianza del parametro definita nella matrice di covarianza ($C_{est}$)

$$STDF(m_s) = exp\left(\sqrt{C_{est(s,s)}}\right) \quad (5)$$

Questa espressione deriva dal fatto che i parametri del modello sono rappresentati come logaritmi. In base ai valori di STDF un parametro risulta perfettamente risolto per un STDF=1, ben risolto per 1<STDF<1.2, moderatamente risolto per 1.2<STDF<1.5, poco risolto per 1.5<STDF<2 e non risolto per STDF>2 (Auken e Christiansen, 2004).

Come si può osservare, l'utilizzo di un *adaptive-gating* consente di ottenere un buon miglioramento, dell'ordine del 10%, nella stima delle resistività e degli spessori degli strati. Il *misfit* tra i dati calcolati e quelli reali è invece in entrambi i casi ottimo.

Il miglioramento è evidente anche nel fattore di *standard deviation* per la resistività e lo spessore del primo strato. Lo stesso non può essere detto per la resistività e lo spessore del secondo strato, dove si osserva un aumento del STDF. I suoi valori (prossimi o maggiori di 2), in entrambe le configurazioni sono comunque indice di un parametro non risolto correttamente e ciò è dovuto al particolare modello di strati considerato in questo lavoro: un modello a tre strati con la resistività che aumenta con la profondità, modello intrinsecamente difficile da risolvere con questo metodo. Lo stesso valore di resistività del terzo strato risulta enormemente sovrastimato.

Tabella 4 - Valori di resistività e spessori e relativi STDF ottenuti dall'inversione 1D dei dati in configurazione *log-gating* e *adaptive-gating*.

| Log-gating | | | | Adaptive-gating | | | |
|---|---|---|---|---|---|---|---|
| Resistività (Ohm*m) | STDF_resistività | Spessore (m) | STDF_spessore | Resistività (Ohm*m) | STDF_resistività | Spessore (m) | STDF_spessore |
| 9,7 | 1,1098 | 25,4 | 1,4357 | 9,8 | 1,1035 | 27,1 | 1,3934 |
| 33,7 | 2,0152 | 63,2 | 1,9322 | 39,4 | 2,1442 | 70 | 2,1569 |
| 4000 | -1 | | 0 | 8000 | -1 | | 0 |

**Conclusioni**. In questo lavoro è stato mostrato come il *gating* eseguito sul transiente elettromagnetico controlli il *noise* e la capacità di risoluzione, e come un *adaptive-gating* che tenga conto delle massime variazioni di pendenza presenti nel transiente possa portare a un miglioramento dei risultati dell'inversione. Sono stati confrontati i risultati ottenuti a partire dai dati di un transiente campionato con *gates* in configurazione *log-gating* e quelli ottenuti a partire dai dati di un transiente campionato con un *adpative-gating* per un modello a tre strati con resistività che aumenta con la profondità.

L'*adaptive-gating* è stato definito per mezzo di uno studio sulle variazioni di pendenza presenti all'interno del transiente elettromagnetico e messe in evidenza grazie a una tecnica di *denoising* (DWT) applicata sui dati. I risultati mostrano che l'uso dell'*adaptive-gating* porta a un miglioramento nella definizione delle resistività e degli spessori veri del modello geologico considerato.

Eventuali sviluppi futuri previsti su questo studio sono diretti verso la conferma del metodo su altri modelli geologici, anche più complessi, e sulla messa a punto di una tecnica automatizzata

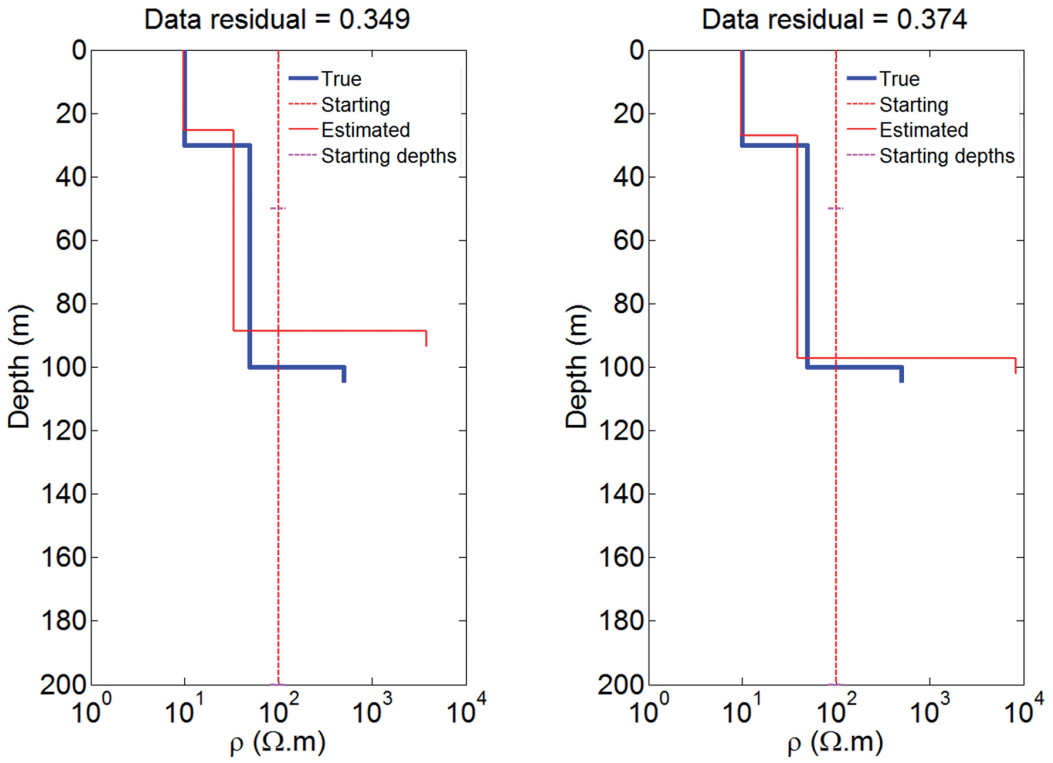


Fig. 3 – Confronto tra il modello inverso ottenuto con campionamento del transiente in configurazione log-gating (a sinistra) e quello ottenuto con campionamento in configurazione adaptive-gating (a destra).

di individuazione di zone all'interno del transiente dove adattare il *gating*. Anche se si tratta di lavori in corso, i risultati ottenuti finora suggeriscono la validità del nostro approccio per il campionamento e *pre-processing* dei dati AEM ottenuti da sistemi *airborne* EM moderni, capaci di campionare i transienti ad altissima frequenza. Invece di definire a priori il tipo di *gating* (ad esempio *log-gating*) e le caratteristiche di *gating* dei diversi canali (tempi di centro, larghezza) a prescindere da variazioni geologiche e di segnale nell'area, sarebbe invece vantaggioso definire solo il massimo numero di canali da utilizzare, e applicare il *gating* adattivo, transiente per transiente, ottenendo la massima capacità di risoluzione delle variazioni 3D della resistività del sottosuolo.

## Bibliografia

Auken E., Christiansen A. V. [2004] Layered and laterally constrained 2D inversion of resistivity data. Geophysics, 69, 3, 752-761.

Christiansen A. V., Auken E., Viezzoli A. [2011] Quantification of modeling errors in airborne TEM caused by inaccurate system description. Geophysics, 76, 1, F43-F52.

Daubechies I., Paul T. [1987] Wavelets - some applications. Proceedings of the International Conference on Mathematical Physics, 675-686, in eds. M. Mebkhout and R. Seneor, World Scientific, Marseille, France.

Fedi M., Quarta T. [1998] Wavelet analysis for the regional-residual and local separation of potential field anomalies. Geophysical Prospecting, 46, 507-525.

Foufoula G. E., Kumar P. [1994] Wavelets in Geophysics. Academic Press, Inc.

# GEOPHYSICAL AND HYDROGEOLOGICAL CHARACTERIZATION OF SIRINO LAKE (BASILICATA, ITALY)

**V. Giampaolo[1], L. Capozzoli[1], E. Rizzo[1], S. Grimaldi[2]**
*[1] CNR-IMAA. Laboratorio Hydrogeosite, Marsico Nuovo (PZ), Italy*
*[2] Università degli Studi della Basilicata, Potenza, Italy*

**Introduction.** The presence of natural or artificial lakes and reservoir that can empty due to natural phenomena such as landslides, flood and piping is a serious hydrogeological problem because it can generate catastrophic events affecting urban and agricultural areas settled below the source area.

This is the case of the Sirino Lake affected, in the last century, by many pipings as a result of sudden openings of sinkholes which resulted in the almost total lake depletion (Fig. 1). Moreover, the hydraulic instability combined with the geomorphological and seismic risks recognize the entire area as exposed to potential flood and landslide risk due to new episodes of siphoning.

In order to mitigate this hydrogeological risk it is necessary to solve some fundamental questions regarding for example the thickness of the impermeable layer und the lake, the flow pathways and the presence of possible water escape routes. Therefore, scientific community has devoted considerable attention to some geophysical methods, such as electrical resistivity tomography (ERT), Ground Penetrating Radar (GPR), and self-potential (SP) because these methods are relatively time and cost effective when working on large area and are reasonably user-friendly for geomorphologists (Naudet *et al*., 2008).

The electrical resistivity method is an important tool in the hydrogeological applications (Kosinski and Kelly, 1981; Daily *et al*., 1992; Slater *et al*., 1997; Binley *et al*., 2002; Dam and Christensen, 2003; Darnet *et al*., 2003; Rizzo *et al*., 2004; Binley and Kemna, 2005; Straface *et al*., 2007).

One of the electrical resistivity surveys skill is the evaluation of subsurface condition in water-covered area (stream, river, wetland, lake, and see) for hydrogeological and environmental purposes. Surveys in water-covered areas includes conventional surveys using multi-electrodes resistivity system where part of the survey line crosses a river or a lake, and surveys conducted entirely within a water-covered environment (Loke and Lane, 2004). However, while on dry land the geoelectrical method is well known, the method in water-covered areas is not widespread. Still less common are electrical resistivity measurements in wetlands, ponds and lakes. Examples of applications have been reported by Mansoor and Slater (2007) who performed aquatic electrical resistivity imaging to predict spatial and temporal patterns of pore-fluid conductivity in wetland soils using fixed floating electrodes, Baumgartner (1996) who used electrodes located underwater and orientated vertically, and Yang *et al*. (2006) who integrated GPR and resistivity image profiling methods at the water surface. Inversion algorithms generally used for inverting apparent electrical resistivity measurements in water covered areas are commonly iterative, nonlinear least squares methods, with regularization based on discretized first or second spatial derivative filters, to produce a flat or smooth tomogram, respectively. One strategy to improve the resolution of electrical resistivity tomograms in water covered areas is to incorporate constraints on the water-column resistivity and thickness (Loke and Lane, 2004).

Ground penetrating radar (GPR) is a high resolution geophysical electromagnetic technique (10 MHz ÷ 2 GHz) designed primarily to investigate the shallow subsurface of the earth, building structures, roads, and bridges. However, GPR was used successfully to locate and characterize risk of subsidence of a sinkhole collapse in carbonate crock outcrops (Gómez-Ortiz and Martín-Crespo, 2012), to assess karst collapse hazard (Nuzzo *et al*., 2004), to identify geological hazard for exploitation (Zayc *et al*., 2014) in flyschoid rocks, to detect water surface of geological structures beneath rivers, ponds, and swamps (Yang *et al*., 2006) and to predict and follow development sinkholes near lakes (Frumkin *et al*., 2011).

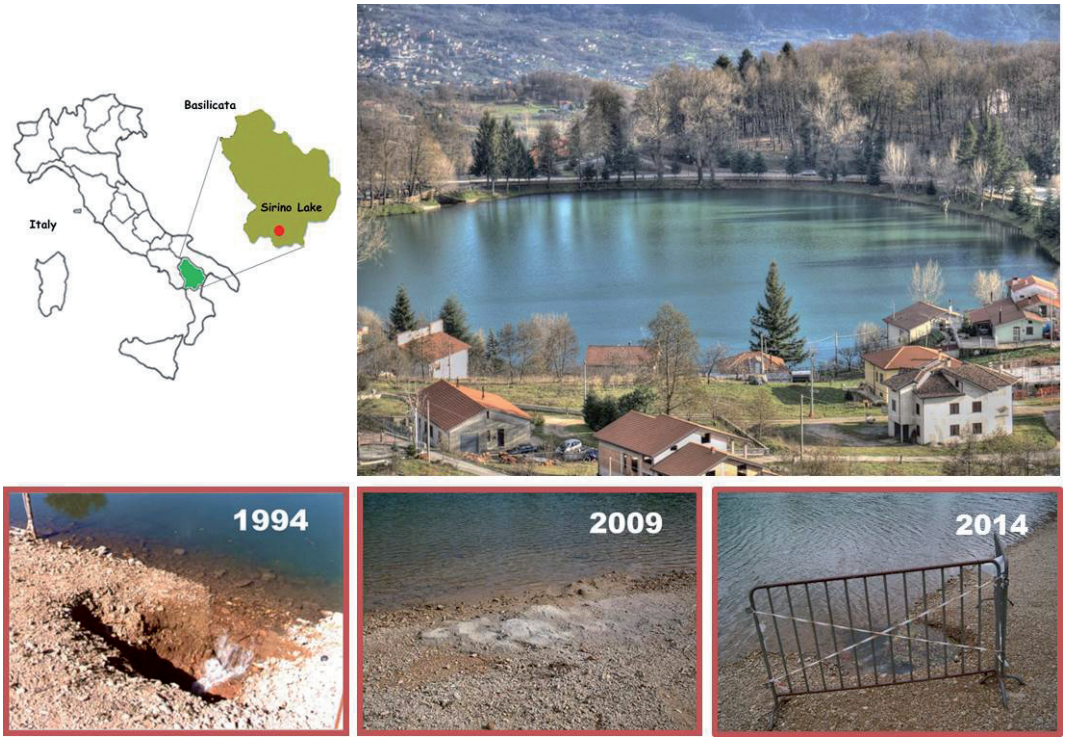


Fig. 1 – Sirino Lake affected by piping phenomena in 1994, 2009 and 2014.

Finally, the self-potential method (SP) is a passive geoelectrical technique and it consists in measuring the potential differences between two unpolarizable electrodes placed at the ground surface. These voltage differences result from the existence of an electric field produced by natural electrical sources distributed in the subsoil and generated by various phenomena (hydraulic, chemical, or thermal disequilibria). In particular, the SP method is sensitive to groundwater flow through the electrokinetic effect (Thony *et al.*, 1997; Revil, 1999; Darnet and Marquis, 2004; Rizzo *et al.*, 2004). Therefore, detecting electrokinetic effect based on SP survey can allow zoning of infiltrating water recharge and run-off areas, and can determine the extent of effects of subsurface drainage works.

**Site description.** The Sirino Lake (Fig.1), placed at 784 m above sea level is a major tourist place in the middle of a naturalistic interesting area, between the towns of Lauria, Lagonegro and Maratea (south Basilicata region, Italy). Almost elliptical in shape, the Lake Sirino extends for about 3 hectares with a 300 m length and a 150 m width; the depth varies according to the season but it doesn't exceed 6 m depth. The landscape surrounding the lake is characterized by a complex orography, mostly mountainous with a steep morphology. Furthermore, the studied area is affected by severe and permanent landslides, involving relevant sectors of infrastructure systems, and a pervasive network of minor entity gravitational phenomena (Grassi *et al.*, 2001a, b; Guida and Siervo, 2005; Guida *et al.*, 2006).

The Sirino Lake is placed on the SE side of the Mount Sirino tectonic window at the base of the Costa del Capraro ridge**.** The area is characterized by a calcareous-siliceous marly succession attributable to Lagonegro I Unit (Flinty Limestone, Siliceous Schists and Galestrino Flysh), which constitutes the backbone of the Monte Sirino. Moreover, massive glacial debris accumulations, refer to the last Wurm glacial phase, and slope and/or landslide debris are present (Cotecchia *et al.*, 1993). The Sirino Lake rests on silty-clay sediments accumulated in the depression that houses the lake. These reddish clay deposits, due to the dissolution of

the cherty limestone, were detected above the bedrock (Siliceous Schists) and they probably contributed to waterproofing the bottom of the lake.

The Flinty Limestone and Siliceous Schists are the main reservoir of the Monte Sirino aquifer system. The cherty limestone are characterized by a relatively mid-high permeability, mainly due to the widespread cracking and\or layering and to the major fracture systems oriented N-S and NNE-SSW; instead, the Siliceous Schists can be appreciably permeable along the stratification planes and\or along bands of intense fracturing. All around, the system is wholly or partially buffered by a belt of less permeable soils (Galestrino Flysch) which constitute the main waterproof of the carbonate aquifer formed by Monte Sirino (D'ecclesiis *et al*., 1990). Locally, for anisotropy of the structure, also the Siliceous Schists act as impermeable soils (Grassi *et al*., 2001a, 2001b).

In the last century, the Sirino Lake was affected by many pipings, as a result of sudden openings of sinkholes, which have resulted in the almost total lake depletion. For these reasons, a series of local waterproofing remediation actions were carried out. These, however, did not prevent the phenomenon to recur at different times and in adjacent areas. Moreover, these measures have been often of environmental and especially visual strong impact.

The opening of these sinkholes occurs with a not predictable multi-yearly frequency. However, a written record of all the episodes that took place over time lacks. Among the most recent episodes, there are those occurred in 1994, 2009 and 2014. In July 1994, a sinkhole opened in the SW side of the lake, about 3 meters from the shore, with a collapse area of 1 meter in diameter. The water was poured into the hole and in a short time the lake level dropped about 2 m. Simultaneously, there was a sudden increase in the flow rates of underlying sources: in particular the *Sotto il Lago II* source reached a flow rate value of about 300 l/s. The siphoning stopped naturally, following the collapse of a shore section, with the consequent closure of the hole and the returning, after a few days, at normal flow rates values (Grassi *et al*., 2001a, 2001b).

In the episode occurred in the summers of 2009 and 2014, a sinkhole opened on the same shore that was affected in the 1994 episode, a few tens of meters away. In this case, the hole was closed artificially with concrete.

**Geophysical data acquisition and processing.** For the study of sinkhole phenomena along the Sirino lake shores an electrical resistivity tomography (ERT) was carried out both on land and water-covered area and a ground penetrating radar and a self-potential surveys (SP) were carried out around the lake shores (Fig. 2).

The ER profile was carried out between the northwester and the southeastern lake shores, with a total length of approximately 450 m of which 210 m into the lake with electrodes floating on the water surface.

The geoelectrical tomography was performed using the georesistivity meter Syscal Junior (IRIS Instrument) coupled to a multi-electrode system, consisting of two measuring cable at 24 channels with an electrodes spacing of 10 m. For the geoelectrical data acquisition in water, the only measuring cable, floating on the lake surface by means of a series of PVC bottles equally spaced along the cable, was used. For the ground measures, standard stainless steel electrodes were used connected to the cable. The Syscal Junior resistivity meter was placed on board of a small boat, held steady in the lake centre for the whole duration of measures. The ERT was acquired using the Wenner, Wenner-Schlumberger and Dipole-Dipole arrays, with an electrodes spacing of 10 m. Furthermore, water electrical conductivity and temperature were measured along ERT profile.

The ETR was inverted by means of the res2Dinv software that uses the smoothness-constrained least-squares inversion method based on the quasi-Newton method (Loke and Barker, 1996). In particular, water electrical resistivity and bathymetry constrains were included in the inversion processes, using a distorted finite element grid, where the upper part of the mesh was used to model the water layer at the assigned electrical resistivity value of 50 Ωm.

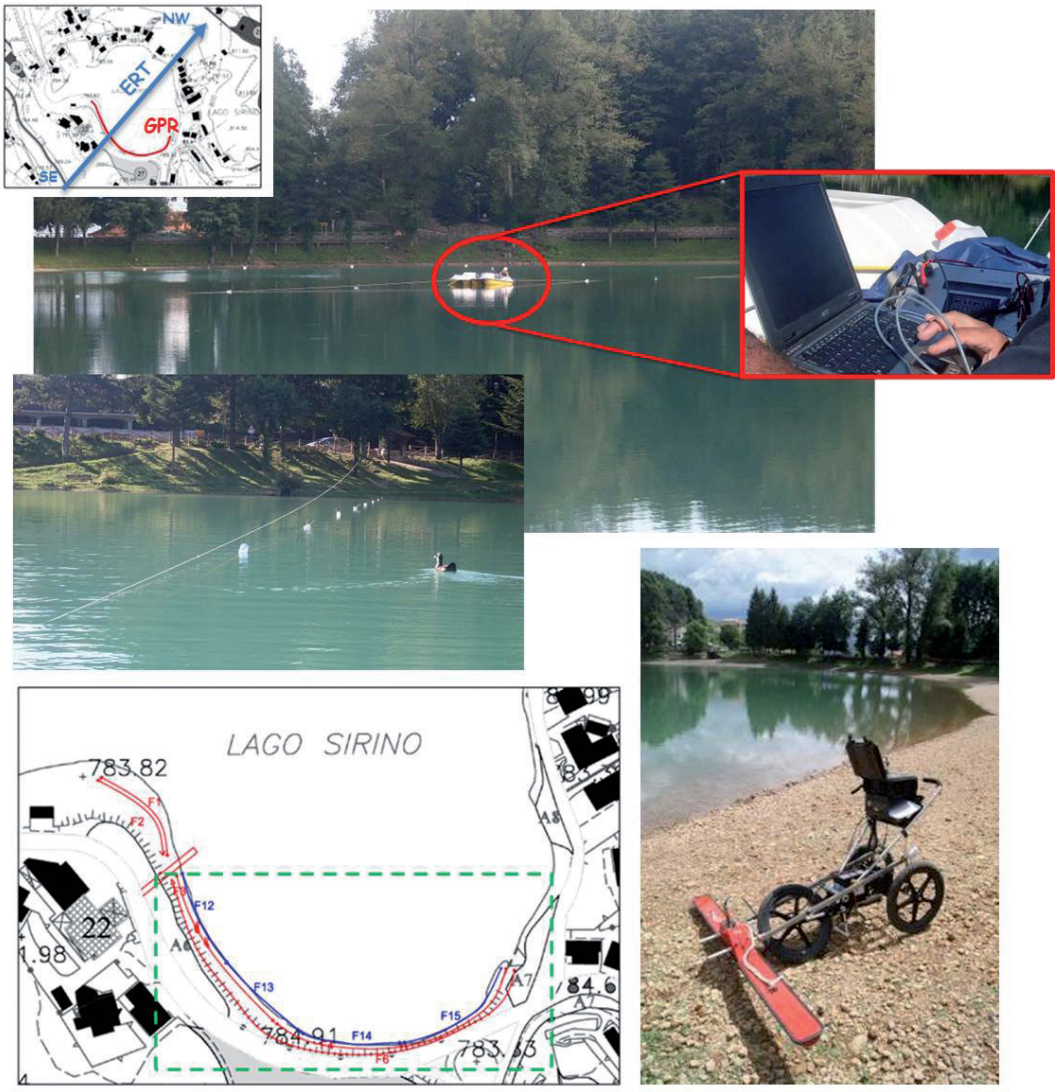


Fig. 2 – Electrical resistivity and GPR profiles acquired with 400 (red line) and 40 MHz antennas (blu line) carried out both on water covered area and lake shores.

GPR surveys were carried out using GSSI SIR-2000 Instruments equipped with the two high-frequency antenna 40 and 400 MHz, characterized by different resolution and investigation depth. The two antennas were used to investigate the lake shores to find possible areas affected by sinkhole phenomena. For this purposes, on the south lake shore, two long acquisition profiles (about 180 m) were performed (Fig. 1): 400 MHz antenna: red line composed by F1÷F11 segments in step mode with survey-wheel coupled to the antenna; 40 MHz: blue line composed by F12÷F15 segments in continuous mode.

The raw-data acquired in field without gain and other filters were processed in order to, compensate the attenuation of GPR signal, eliminate noise and associate the GPR information with the real depth of reflectors after an assessment of electromagnetic velocity propagation (migration).

Finally, self-potential measurements (for a total of 226 points) were acquired along closed loops, around the lake shores and the surrounding areas, by alternating the leading and following

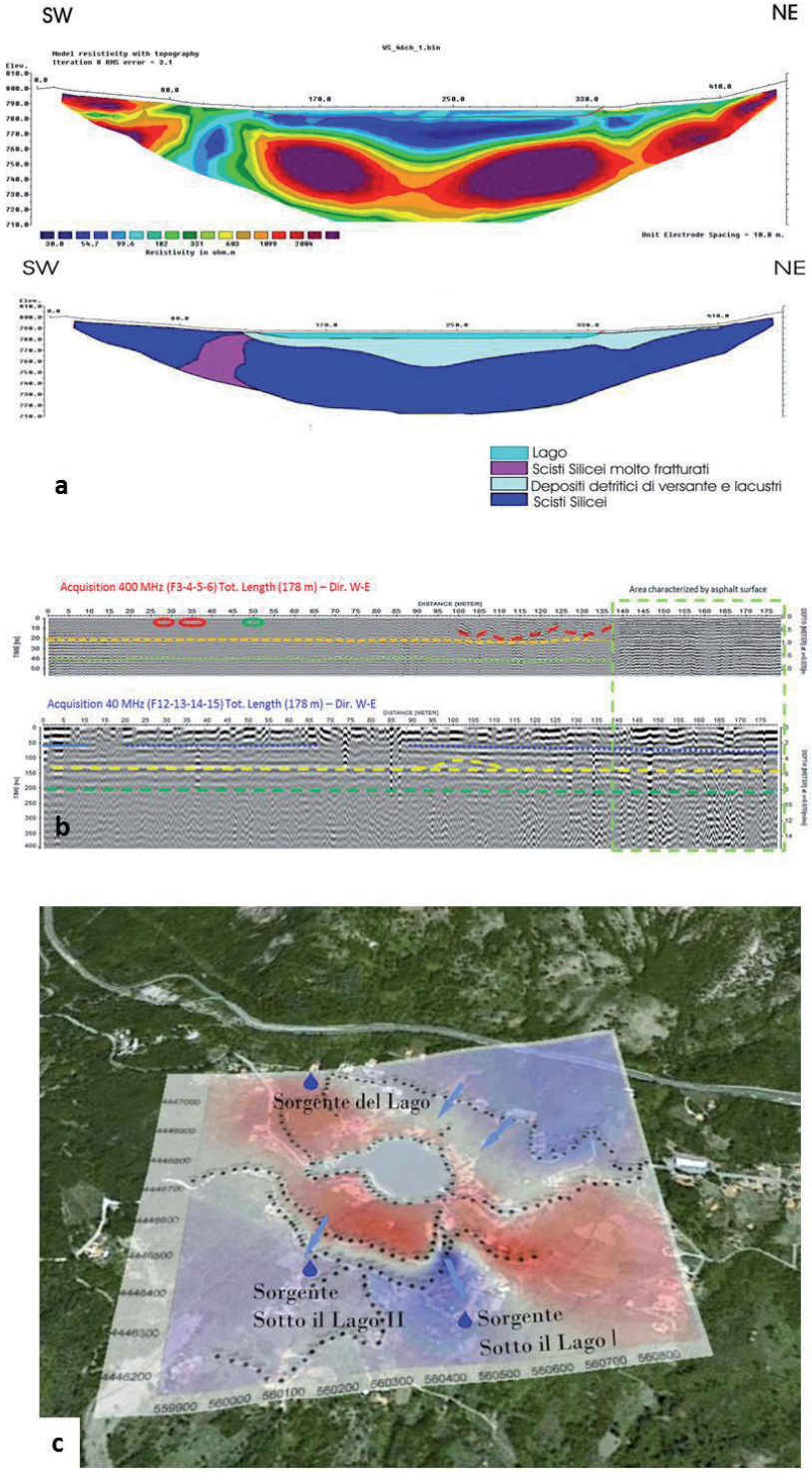


Fig. 3 – Geophysical surveys result: a) ERT and lithological model; b) GPR results (dotted lines: sub horizontal continuous reflectors; red and green circle: anomalies individuate in correspondence of sinkholes; red line: strong and chaotic reflections probably due to the presence of filling material; yellow line: an hyperbolic anomaly located between 90 and 110 m of the radargram); c) SP map and reconstruction of water flux direction.

electrodes (leap-frog technique) in order to reduce cumulative errors caused by electrode polarization. The distance between the measuring electrodes was 25 m. The SP values in the measuring net were obtained by adding readings after establishing a SP arbitrary zero value as a point of reference in the area. Moreover, SP measurements were corrected in order to compensate for cumulative errors and the topographic effect. Finally, we obtained a SP map using Surfer 8 for a contour line representation of the distribution of the potential field.

**Results and conclusions.** Fig. 3 shows the results of the integrated geophysical survey carried out at the Sirino Lake.

The ERTs acquired with different electrode arrays shows similar results. In particular the Wenner-Schlumberger one (Fig. 3a) is characterized by relatively low electrical resistivity values (< 100 Ωm) down to - 20 m depth and by higher electrical resistivity values (> 700 Ωm) in the lower portion. In the right the ERT shows a low resistivity zone, connected to the lake that crosses the underlying resistive body. The comparison between the electrical resistivity data with the lithostratigraphy obtained by a geognostic drilling investigation and a gamma-ray log (Grassi *et al*., 2001b) allows us to reconstruct the complex geological situation beneath the Sirino Lake. In particular, the shallower low electrical resistivity body represents the debris and lacustrine deposits characterized by an inhomogeneous downwards infiltration. The deeper resistive area denotes the presence of a Siliceous Schists body not fractured and therefore with a generally low hydraulic permeability. Moreover the ERT underline the presence of a low resistivity area, on the southern shore of the lake, interpreted as a highly fractured portion of Siliceous Schists involved into mass movements, with a medium-high relative permeability. This area may represent a possible water route escape because is characterized by more permeable soil layers.

Results of GPR survey are shown in Figure 3b. In particular, the 40 MHz acquisition shows three main sub-horizontal continuous reflectors probably due to presence of interfaces with different physical properties. An interesting hyperbolic anomaly is located between 90 and 110 meter of the radargram (yellow line). The 400 MHz radargram shows two horizontal reflectors located respectively at an estimated depth of 0.8 and 1.6 meter. At a distance of 27 and 35 meter from the origin of the acquisition there are the two sub-surface anomalies due to the seepage phenomena occurred in the past (red circle). A zone with a similar electromagnetic behaviour is located to 50 m from the origin (green circle). Moreover between 100 and 125 m there is a zone characterized by strong and chaotic reflections, probably due to deposits of filling material.

Finally, the obtained SP map (Fig. 3c) shows negative values upstream (down to -350 mV), while there are positive ones (up to 200 mV) in the lower area surrounding the lake. In particular, the SP negative values identify the areas characterized by a downward water flow, while SP positive values represent water accumulation zones.

In conclusions the integration of GPR, SP and ERT techniques allowed to identify possible causes of sinkhole problem and characterize the hydro-geological structure of the area. Moreover, joint interpretation of geophysical, geological, hydrogeological and geomorphological data allowed us to estimate the thickness of the lacustrine deposits, describe the main patterns of the subsurface fluid flows in the area, and identify possible water escape routes causing the piping phenomena.

**Acknowledgements.** The authors are grateful for the geological and logistical support the “Micromondo”, the first theme park on the geology, in order to create an impetus to the dissemination of knowledge concerning the Earth Sciences (geologists Patrizia Magnotti and Dario Rizzo, *http://www.ilmicromondo.com*).

## References

Baumgartner F.; 1996: *A new method for geoelectrical investigations underwater*. Geophysical Prospecting **44**, 71–98.

Binley A. and Kemna A.; 2005: *Electrical Methods*. In: Hydrogeophysics by Rubin and Hubbard (Eds.), 129-156, Springer.

Binley A., Winship P., West L.J., Pokar M. and Middleton R.; 2002: *Seasonal variation of moisture content in unsaturated sandstone inferred from borehole radar and resistivity profiles*. Journal of Hydrology **267**, 160–172.

Cotecchia V., D'Ecclesiis G. and Polemio M.; 1993: *High pressure artesian wells to tap Torbido Spring (Italy)*. In: International Conference on Environmental Management, Geo-water and Engineering Aspects (February, 1993, Wollongong, Australia) Edited by: Chowdhury & Sivakumar editors. Balkema, Rotterdam.

D'Ecclesiis G., Grassi D., Sdao F. and Tadolini T.; 1990: *Potenzialtà e vulnerabilità delle risorse idriche sotterranee del monte Sirino (Basilicata)*. Geologia Applicata e Idrogeologia **25**, 195-219.

Daily W., Ramirez A., Labrecque D. and Nitao J.; 1992: *Electrical resistivity tomography of vadose water movement*. Water Resources Research **28**, 1429-1442.

Dam D. and Christensen S.; 2003: *Including geophysical data in groundwater model inverse calibration*. Ground Water **41**, 178-189.

Darnet M. and Marquis G.; 2004: *Modelling streaming potential (SP) signals induced by water movement in the vadose zone*. Journal of Hydrology **285**, 114–124.

Darnet M., Marquis G. and Sailhac P.; 2003: *Estimating aquifer hydraulic properties from the inversion of surface Streaming Potential (SP) anomalies*. Geophysical Research Letters **30**, doi: 10.1029/2003GL017631.

Frumkin A., Ezersky M., Al-Zoubi A., Akkawi E. and Abueladas A.R.; 2011: *The Dead Sea sinkhole hazard: geophysical assessment of salt dissolution and collapse*. Geomorphology **134**, 102–117.

Gómez-Ortiz D. and Martín-Crespo T.; 2012: A*ssessing the risk of subsidence of a sinkhole collapse using ground penetrating radar and electrical resistivity tomography*. Engineering Geology **149-150**, 1–12.

Grassi D., Grimaldi S., Sdao G. and Spilotro G.; 2001a: *Ambiente idrogeologico e fenomeni di sifonamento relativi al Lago di frana Sirino (Basilicata)*. Atti del convegno Geoitalia 2001, 320-322, Chieti.

Grassi D., Grimaldi S., Sdao G. and Spilotro G.; 2001b: *Geologia, geomorfologia, idrogeologia e stabilità idraulica del lago Sirino (Basilicata)*. Atti del Dipartimento Strutture, Geotecnica, Geologia Applicata all'Ingegneria - Università della Basilicata **3**, 20 pp, Lamisco-Spes, Potenza.

Guida D., Nocera N. and Siervio V.; 2006: *Analisi morfoevolutiva sulla riattivazione di sistemi franosi a cinematismo intermittente in Appennino campano-lucano (Italia meridionale)*. Giornale di Geologia Applicata **3**, 114-122.

Guida D. and Siervo V.; 2005: *La Carta Inventario dei Fenomeni Franosi del Foglio 521"Lauria"*. Giornale di Geologia Applicata **2**, 58-64.

Kosinski W.K. and Kelly W.E.; 1981: *Geoelectric soundings for predicting aquifer properties*. Ground Water **19**, 163-171.

Loke M.H. and Barker R.D.; 1996: *Rapid least-sqares inversion of apparent resistivity pseudosections by a quasi-Newton method*. Geophysical Prospecting **44**, 131–152.

Loke M.H. and Lane J.W.; 2004: *Inversion of data from electrical resistivity imaging surveys in water-covered areas*. Exploration Geophysics **35**, 266-271.

Mansoor N. and Slater L.; 2007: *Aquatic electrical resistivity imaging of shallow-water wetlands*. Geophysics **72**, F211–F221.

Naudet V., Lazzari M., Perrone A., Loperte A., Piscitelli S., Lapenna V.; 2008: *Integrated geophysical and geomorphological approach to investigate the snowmelt-triggered landslide of Bosco Piccolo village (Basilicata, southern Italy)*. Engineering Geology **98**, 156–167.

Nuzzo L., Leucci G. and Negri S.; 2004: *GPR survey in the karstic area Vore di Spedicaturo near Nociglia (Lecce, Italy)*. Tenth International Conference on Ground Penetrating Radav, Delft, The Netherlands.

Revil A.; 1999*: Ionic diffusivity, electrical conductivity, membrane and thermoelectric potentials in colloids and granular porous media: a unified model*. Journal of Colloid Interface Science **212**, 503–522.

Rizzo E., Suski B., Revil A., Straface S. and Troisi S.; 2004: *Self-potential signals associated with pumping tests experiments*. *Journal of Geophysical Research **109**: doi: 10.1029/2004JB003049*.

Slater L., Binley A. and Brown D; 1997: *Electrical imaging of fractures using ground-water salinity change*. Ground Water **35**, 436-442.

Straface S., Fallico C., Troisi S., Rizzo E. and Revil A.; 2007: *An inverse procedure to estimate transmissivity from heads and self-potential signals*. Ground Water **45**, 420–428.

Thony J.L., Morat P., Vachaud G. and Mouel J.L.L.; 1997: *Field characterization of the relationship between electrical potential gradients and soil water flux*. Comptes rendus de l'Académie des Sciences de Paris Série IIa **325**, 317–321.

Yang C., Tong L.T. and Yu C.Y.; 2006: *Integrating GPR and RIP Methods for Water Surface Detection of Geological Structures*. TAO **17**, 391-404.

Zajc M., Pogačnik Ž. and Gosar A.: 2014: *Ground penetrating radar and structural geological mapping investigation of karst and tectonic features in flyschoid rocks as geological hazard for exploitation*. International Journal of Rock Mechanics and Mining Sciences **67**, 78–87.

# GRAVITY ANOMALY CONSTRAINTS FOR A CRUSTAL MODEL OF THE NORTHERN APENNINES

**C. Girolami, C. Pauselli, M.R. Barchi**
*Dep. of Physics and Geology, University of Perugia, Italy*

**Introduction.** In the last 50 years the structure of the deep crust and of the upper mantle of the northern Apennines was intensely investigated through different geophysical surveys, such as seismic refraction experiments (e.g. Scarascia *et al*., 1994; Ponziani *et al*., 1995), NVR deep seismic profiles (Pialli *et al*., 1998; Pauselli *et al*., 2006), analysis of the teleseismic waveforms (Piana Agostinetti *et al*., 2002; Mele and Sandvol, 2003) and, more recently, passive seismic tomography (Cannarate *et al*., 2013). Most of these surveys are focussed on a WSW-ENE trending transect, approximately following the alignment Grosseto-Perugia-Ancona.

All these models agree on the general picture, highlighting the presence of a relatively thin Tyrrhenian crust, contrasting a thicker Adriatic crust, separated by a sharp Moho step beneath the Perugia area. In more detail, however, the model also shows significant differences in the attitude and depth of the two crustal domains: in particular the attitude of the Adriatic Moho [see Barchi *et al*. (2006) for a discussion].

Along the same transect, a complex geological and geophysical data-set has been progressively made available, mainly consisting of surface geology survey, commercial seismic profiles and well data, highlighting the details of the relatively shallow, upper crust structures (e.g. Pialli *et al*., 1998; Brogi and Liotta, 2006).

In this paper we present the preliminary results of a research project, aimed to propose new gravimetric modelling of both deep and surface structures of the northern Apennines. In the past, different Authors have already proposed gravimetric models of this region, at both regional (e.g. Larocchi *et al*., 1998; Scarascia *et al*., 1998; Marson *et al*., 1998) and local (e.g. Di Filippo and Toro, 1980; Orlando *et al*., 1991; Barberi *et al*., 1994) scale. The novelty of our project is essentially based on:

- the use gravimetric data as an independent data-set, aimed to compare the suitability of the different available crustal models;
- the integration of both shallow and deep structures along regional transects.

The studied area is located in the southern part of the northern Apennines, crossing Tuscany, Umbria and Marche regions. The northern Apennines consists of different tectonic units, pertaining to both oceanic (Thetys) and passive margine (Adria) environments. Top to bottom we find Liguride, Tuscan and Umbria-Marche units, covered by syn-orogenic units consisting of turbidites, deposited in foreland basins.

The present-day crustal structure of the northern Apennines envisages two different crustal domains: a western Tyrrhenian domain, where extensional deformation destroyed the pre-existing compressional belt; and an eastern Adriatic domain where the compressional structures are still preserved.

The upper crust of the Tyrrhenian domain is thinned by a set of east-dipping low-angle normal faults, driving the onset and evolution of the syn-tectonic hinterland basins. The age of the syn-rift deposits testifies the regular eastward migration of the extensional deformation. The shallow structures of the Adriatic domain correspond to the arc-shaped Umbria-Marche fold and thrust belt where the timing of deformation is marked by the onset and evolution of syntectonic foreland basins. The transition between these two domain is sharp and occurs along a narrow and arcuate strip that define the "transition zone" (Barchi, 2010).

**Characteristics of the Data-set and location of the transect.** For this project we use a large data set, already published by ISPRA, in their "Carta gravimetrica digitale dell'Italia alla scala 1:250000" (Ferri *et al*., 2006). The original data points were kindly made available by ENI.

The data set is made of 50000 stations, which cover central Italy with an average spacing less than 1 km (Fig.1). Bouguer gravity anomaly was calculated using a constant density of 2.67

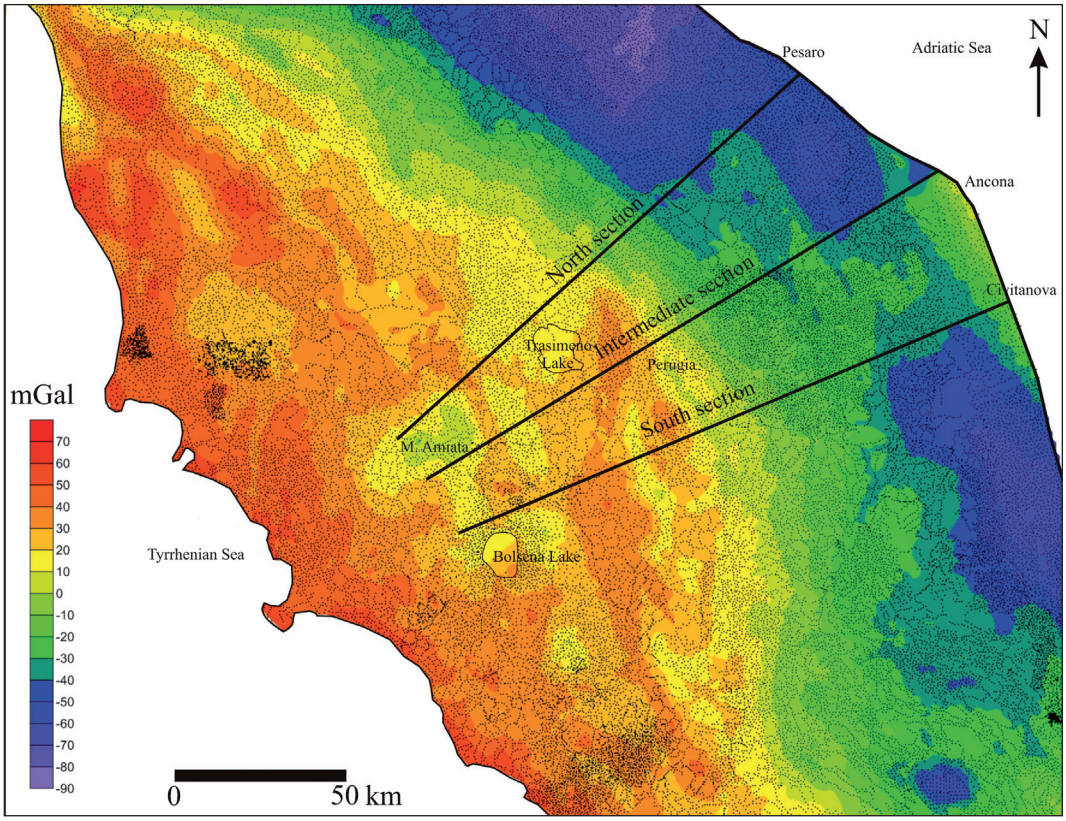


Fig. 1 – Gravity anomaly Bouguer map for central Italy, showing the data set we used for this study and the traces of the three studied sector.

g/cm$^3$. The close spacing of stations and the wideness of the covered area give us the chance to use the gravimetric data to obtain information on both the deep and the shallow geological structures.

From these randomly distributed data we generated a Bouguer gravity map of central Italy, using Minimum Curvature interpolation method, with a grid cell size of 1 km. The map shows two different gravity anomaly signals that characterize Tyrrhenian and Adriatic Domains, which show long-wavelenght positive (+70 mGal) and negative (-70 mGal) Bouguer gravity anomalies respectively, separated by a sharp arc-shaped step below the transition zone.

In the Tyrrhenian Domain short-wavelenght relative minima are also observed, related to syn-tectonic basins (Radicofani Basin, Val di Chiana Basin, Tiber Basin) and volcanic complexes (M. Amiata, Roman volcanic district). By contrast, in the Adriatic Domain two wide gravity minima can be observed, NW-SE trending, separated by a relative maximum, corresponding to the Conero area. These anomalies are related to Po Plain-Adriatic foredeep (Royden and Karner, 1984), but also to the stacking of slices of continental crust beneath the adjacent mountain ridge.

These general features were already well represented in the ISPRA (2006) map.

For this first experiment we considered a regional transect, consisting of three WSW-ENE trending sections, radiating from the M. Amiata area towards the Adriatic coast (Fig. 1). The Northernmost section reaches the coast at Pesaro; the intermediate few km north of Ancona; and the third approximately at Civitanova. Along these traces, a large amount of data, mainly acquired for industrial purposes (oil and geothermal exploration) is available, constraining both the surface

and shallow subsurface geology (e.g. Brogi and Liotta, 2006; Mirabella *et al*., 2011). We used these data to build-up the shallow sections, to be incorporated in our geological models.

Since the traces are spaced each other less than 20 km, we can assume that the deep (i.e. lower crust and upper mantle) structures are the same for the three sections: so we projected the available data on the three sections along the arcuate trace, depicted by both gravimetric and regional geological structures.

**Stratigraphy and density data.** We used GM-SYS program to calculate the gravity response of the 2D geologic models. This program considers the method of Talwani *et al*., (1959) and Talwani and Heirtzler (1964) and makes use of the algorithm described in Won and Bevis, (1987). The curvature of the Earth was not considered because of the short length of the profile. The model extends more than the real length of the section to eliminate edge effects.

We dedicated a strong effort in selection of the density data following this path:

- definition of the stratigraphic model (i.e. definition of the main litho-mechanical layers within the sedimentary cover and the upper crust);
- collection of density data from the literature for each of the layers of the model, as well as for the lower crust and for the mantle;
- calculation of a new data-set of density data, derived from the velocity data collected by active seismic surveys;
- integration of stratigraphic, literature and new data in a comprehensive model.

Our stratigraphic model can be schematically divided into two sections: a) sedimentary cover and upper crust basement; and b) lower crust and upper mantle.

*Sedimentary cover and basement*. The shallow part of our models is characterized by a great lateral and vertical variability, comprising a large number of different geological units. For our purposes, we grouped these rock bodies in a limited number of representative lithological units, briefly described in the following.

Pliocene-Pleistocene Units include continental and shallow marine sediments deposited in both hinterland and foreland recent basins.

Liguride Units include a complex assemblage of sandstone, marls, limestones and ophiolites (Cretaceous- Miocene).

Tuscan turbidites include Macigno Sandstones and the lithologically complex Scaglia Toscana fm (Cretaceous-Early Miocene).

Umbrian turbidites include Marnoso-Arenacea and the other flysch-like successions exposed in the Umbria and Marche region (Early to Late Miocene).

Carbonate Units include the marine Mesozoic-Early Tertiary multilayers of both Tuscan and Umbria-Marche successions.

Evaporite Units include alternated anhydrites and dolomites (Burano fm.) and the overlaying marls of Raetavicula contorta Fm., in both Tuscan and Umbri-Marche realms (Late Triassic).

Basement s.l. units include both terrigenous (Verrucano) and meta-sedimentary (mainly phyllites) rocks of the shallower part of the basement (Late Paleozoic-Early Triassic).

Upper crust corresponds to the crystalline basement.

*Lower crust and upper mantle*. Many seismic refraction studies investigated crustal structure of Northern Apennine and adjacent region. The results where synthesised on Moho isobath maps (e.g. Scarascia *et al*., 1994; Scrocca *et al*., 2003). They highlight the presence of a thin Tyrrhenian crust (20-25 km), contrasting a thicker Adriatic crust (30-35 km), separated by a sharp Moho step.

In this work we analyzed the crustal models that present different estimation of Moho depth accross the studied regional transect (Ponziani *et al*., 1995; Piana Agostinetti *et al*., 2002; Mele and Sandvol, 2003).

Ponziani *et al*. (1995) reconstruct a detailed velocity model for the P waves for the crust and the mantle, considering an attenuated velocity for the Tuscan Moho in the Tyrrhenian Domain (7.7 km/s) and a velocity of 8.0 km/s for the Moho in Adriatic Domain. They propose also a

Moho doubling in correspondence with the zero-Bouguer anomaly where Tuscan Moho overlaps the Adriatic one for 30 km. The Moho depth below Apennine Chain is approximately 32 km.

Piana Agostinetti *et al*. (2002) do not show a doubling of Moho and do not give information about the thickness and velocity of the upper and lover crust. They estimated the depth of the crust below Apennine Chain of about 35-38 km.

Mele and Sandvol (2003) consider a doubling of Moho beneath the Val Tiberina and the partial overlapping between the shallow Tuscan Moho and the deeper Adriatic Moho. They also consider a deep crustal root beneath Apenninic Chain to a depth of 49±3 km.

*Density data*. We decided to calculate density values of lithologic units, considering density, ϱ, as function of seismic P waves velocities, $V_P$. In particular we used the polynomial regression (Brocher, 2005) that fits the Nafe-Drake empirical curve (Ludwig *et al.*, 1970), where $V_p$ is in m/s.

$$\varrho(g/cm^3) = 1.6612V_P - 0.4721V^2_P + 0.0671V^3_P - 0.0043V^4_P + 0.000106\,V^5_P$$

We choose $V_P$ for the lithologic units on the base of the literature for the studied area. In particular for the sedimentary cover we used Amato *et al.*, (1994) and Mirabella *et al*. (2011). As regard of $V_P$ velocities for the crust and the mantle we take in to account the detailed velocity

Tab. 1 - Densities values used in this study calculated follow the emipirical relation of considering density, ϱ, as function of seismic P waves velocities, VP, (Brocher, 2005).

| Lithologic Unit | References | P waves velocity $V_P$ (m/s) | Calculated density ρ (g/cm³) | This model ρ (g/cm³) |
|---|---|---|---|---|
| Plio-Pleistocene Units | Mirabella *et al.*, 2011 | 2000 | 1.91 | 1.91 |
| Amato et al., 1994 | 2750-2900 | 2.16-2.20 | 2.18 | |
| Ligurids Units | Amato *et al.*, 1994 | 3900 | 2.38 | 2.38 |
| Tuscan-Umbrian turbidites | Mirabella *et al.*, 2011 | 4000-4300 | 2.39-2.43 | 2.41 |
| Carbonates Units | Mirabella *et al.*, 2011 | 5600 | 2.64 | 2.64 |
| Evaporites Units | Mirabella *et al.*, 2011 | 6100 | 2.74 | 2.74 |
| Basement s.l. | Mirabella *et al.*, 2011 | 5100 | 2.55 | 2.55 |
| Upper crust | Ponziani *et al.*, 1995 | 6000-6300 | 2.72-2.78 | 2.75 |
| Tuscan lower crust | Ponziani *et al.*, 1995 | 6300-6700 | 2.78-2.88 | 2.83 |
| Adriatic lower crust | Ponziani *et al.*, 1995 | 6500-6700 | 2.83-2.88 | 2.85 |
| Tuscan Mantle | Ponziani *et al.*, 1995 | 7800 | 3.22 | 3.22 |
| Adriatic Mantle | Ponziani *et al.*, 1995 | 7900-8000 | 3.26-3.29 | 3.27 |

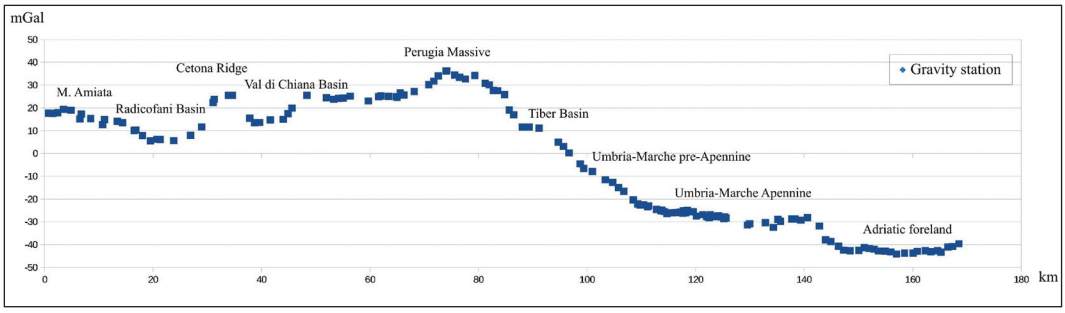


Fig. 2 – Intermediate sector (see trace in Fig. 1) which extends from M. Amiata to Adriatic coast. This figure shows the original data points of Bouguer gravity anomaly and the gravity signal of the main tectonic structures of the studied area.

Tab. 2 - Densities used by several authors for gravity modelling.

| Lithologic Unit | References | (g/cm³) |
|---|---|---|
| Marine and continental Plio-Pleistocene sediments | Barberi *et al.*, 1994 | 2.2-2.3 |
| | Manzella *et al.*, 1998 | 2.3 |
| | Mostardini *et al.*, 1986 | 2.25-2.35 |
| | Orlando, 2005 | 2.1-2.4 |
| Ligurides and turbidites | Barberi *et al.*, 1994 | 2.5 |
| | Manzella *et al.*, 1998 | 2.5 |
| | Mostardini *et al.*, 1986 | 2.50-2.60 |
| | Orlando, 2005 | 2.55 |
| Carbonates | Mostardini *et al.*, 1986 | 2.65-2.75 |
| | Barberi *et al.*, 1994 | 2.7 |
| | Manzella *et al.*, 1998 | 2.6 |
| Evaporites | Barberi *et al.*, 1991 | 2.95 |
| | Manzella *et al.*, 1998 | 2.7 |
| Basement s.l. | Barberi *et al.*, 1994 | 2.65 |
| | Manzella *et al.*, 1998 | 2.65 |
| Magmatic Intrusion | Murace *et al.*, 1973 | 2.55 |
| | Soula, 1982 | 2.35 |
| | Barberi *et al.*, 1994 | 2.4 |
| | Manzella *et al.*, 1998 | 2.55 |
| | Orlando, 2005 | 2.45-2.55 |
| Upper crust | Bernabini *et al.*,1995 | 2.65-2.7 |
| | Cassano *et al.*, 1998 | 2.65 |
| | Larocchi *et al.*, 1998 | 2.62 |
| | Marson *et al.*,1998 | 2.68-2.73 |
| | Orlando, 2005 | 2.67 |
| | Scarascia *et al.*, 1998 | 2.7 |
| Tuscan lower crust | Bernabini *et al.*,1995 | 2.74 |
| | Larocchi *et al.*, 1998 | 2.79 |
| | Marson *et al.*,1998 | 2.8 |
| | Orlando, 2005 | 2.8 |
| Adriatic lower crust | Bernabini *et al.*,1995 | 2.8 |
| | Larocchi *et al.*, 1998 | 2.79-2.98 |
| | Marson *et al.*,1998 | 2.85 |
| Tuscan mantle | Bernabini *et al.*,1995 | 3.26 |
| | Larocchi *et al.*, 1998 | 3.28 |
| | Marson *et al.*,1998 | 3.05 |
| | Orlando, 2005 | 3.2-3.4 |
| Adriatic mantle | Bernabini *et al.*,1995 | 3.32 |
| | Larocchi *et al.*, 1998 | 3.28 |
| | Marson *et al.*,1998 | 3.21 |

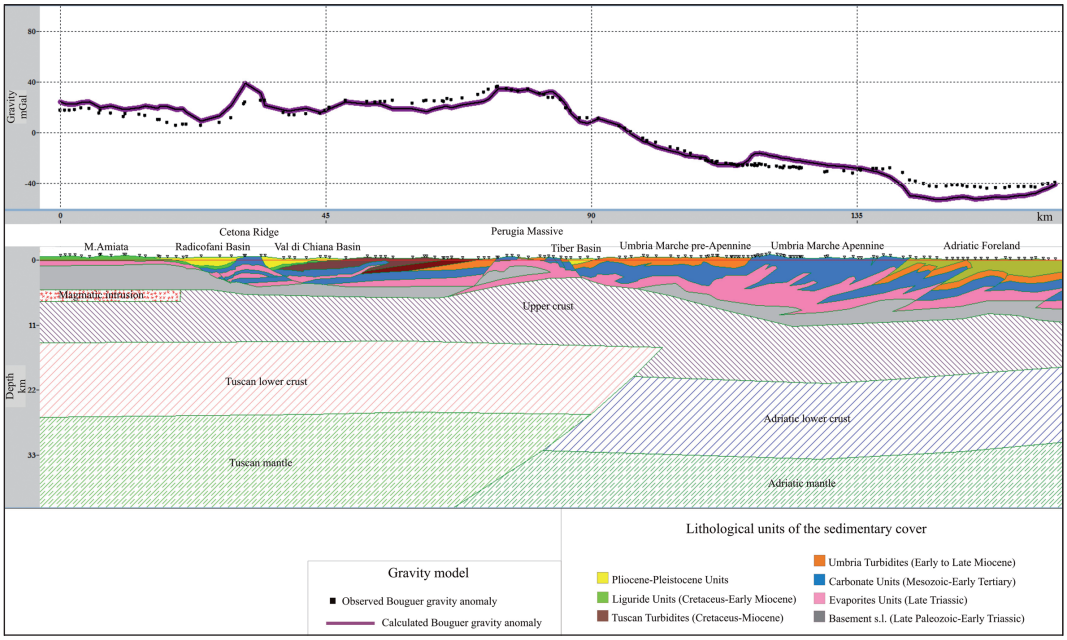


Fig. 3 – Preliminary gravimetric model of the intermediate section, see text for details.

model of Ponziani *et al*., (1995) (Tab. 1). The density values obtained were compared with the density for the same crust used by many authors for gravity modelling at regional and local scale (Tab. 2). We used these values for estimating the reliability of calculated densities.

**Gravity Section.** In this work in order to compare the suitability of the crustal models we made a first attempt studying the intermediate 2D section that extends for 170 km from the southern slope of M.Amiata to the Adriatic coast. It contains 144 gravity stations and shows the gravity signal of the main tectonic structures of the studied area (Fig. 1). Moving from the eastern part of the profile to Perugia regional gravity anomaly is positive with a maximum value of +40 mGal in correspondence of Perugia Massive, and negative with a minimum value of - 44 mGal in the Adriatic coast (Fig. 2).

In the east side of the section, four relative gravity minimum are present: one located to the southern slope of M. Amiata (with a wavelength of about 20 km), and other in correspondence with the Radicofani Basin and Val di Chiana Basin (with a wavelength of about 10 km), and Tiber basin (with a wavelength of about 5 km).

Our 2D section is close to M. Amiata and we had to consider the presence of an intrusive body. According to the following studies (Barberi *et al*., 1994; Orlando *et al*., 1994; Acocella, 2000) we defined in our model an intrusive body at a depth of about 5 km with a lenght of 15 km and a density of 2.4 g/cm$^3$.

In the section, we fixed the geometries of the sedimentary cover and we performed many gravity models changing the depth of lower crust and upper mantle following the information given by Ponziani *et al*. (1995), Piana Agostinetti *et al*. (2002) and Mele and Sandvol (2003).

**Summary and conclusion.** The model presented is a preliminary result of a research project aimed to propose new gravimetric modelling of both deep and surface structures of northern Apennines (Fig. 3). The model shows how the two different crustal domains are recognizable in the gravimetric signals. The feature of the regional gravity response of this model and particularly the wide deficit mass observed beneath the western part of the section are caused by the doubling of Moho and the crustal root beneath the Apennine Chain.

As pointed out in the introduction our project is essentially based on the use of gravimetric data set to compare the suitability of the different available crustal models, integrating both shallow and deep structures.

We have dedicated a strong effort on using appropriate constraints in order to obtain reliable results to reduce the high degree of indetermination of the gravity interpretation.

The first constraint used concerns a strong selection of density values for the formation involving in the modelling: after defining a stratigraphic model characterized by litho-mechanical layers, we calculated a density value for each layers on the base of P seismic velocities. These values were then compared with those present in literature.

The second constraint regards the geometries of shallow and deep structures. In particular, the shallow section was built using the large amount of data coming from oil exploration and surface geology whereas several gravity models are performed to analyze the different depth estimation of Moho across the regional transect as inferred from teleseismic receiver functions and from the interpretation of seismic refraction study.

**Acknowledgement.** We are thankful to ENI, which made available the original data points of gravity data and to Dott. Carlo Ungarelli, for helpful suggestion to improve this study.

## References

Acocella V., 2000: *Spacing accomodation during pluton emplacement*. Terra Nova, Vol. 12, n.4, 149-155.

Amato A., Biella G., Chiesa S., De Franco R., Malagnini L., Minelli G., Ponziani F., Vezzoli L.; 1994: *Tuscania Pienza seismic rifraction profile, geophysical model and geological interpretation*. Mem. Descr. Carta Geol. d'It XLIX, 23-36.

Barberi F., Buonasorte G., Cioni R., Fiordelisi A., Foresi L., Iaccarino S., Laurenzi M.A., Sbrana A., Vernia L., Villa I.M.; 1994: *Plio-Pleistocene geological evolution of the geothermal area of Tuscany and Latium*. Mem. Descr. Carta Geol. d'It XLIX, 77-134.

Barchi M., Pauselli C., Chiarabba C., Di Stefano R., Federico C & Minelli G., 2006: *Crustal structure, tectonic evolution and seismogenesis in the Northern Apennines (Italy)*. Bollettino di Geofisica Teorica e Applicata. Vol.47, n.2, 249-270.

Barchi, M. (2010), *The Neogene-Quaternary evolution of the Northern Apennines: Crustal structure, style of deformation and seismicity* [online], J. Virtual Explor., 36, paper 11.

Bernabini M., Di Bucci D., Orlando L., Parotto M. & Tozzi M., 1995: *Gravimetric evidence of deep structure in mountain building: subducted Adriatic Crust beneath he Tyrrhenian Moho in Central Italy*. Geodynamics Vol.21, N.3, 223-234.

Brocher T., 2005: *Empirical Relations between Elastic Wavespeeds and density in the Earth's Crust*. Bullettin of the Seismological Society of America, Vol. 95, N. 6, 2081-2092.

Brogi A. and Liotta D., 2006: *Understanding the crustal structures of southern Tuscany: The contribution of the CROP18 Project*. Bollettino di Geofisica Teorica ed Applicata Vol. 47, n. 3, 421-423.

Cannarate S., Monachesi G., Cattaneo M, Amato A., Chiarabba C., 2013: *Deep structure and tectonics of the northern-central Apennines as seen by regional-scale tomography and 3-D located earthquakes*. Journal of Geophysical Research: Solid Earth. Research: Solid Earth, Volume 118, Issue 10, 5391–5403.

Cassano E., Anelli L., Cappelli and La Torre P.; 1998*: Interpretation of Northern Apennine Magnetic and gravity data in relation to the profile Crop 03*. Mem. Soc. Geol. It. Vol LII, 413-425.

Di Filippo M. and Toro B., 1980: *Analisi gravimetrica delle strutture geologiche del lazio meridionale*. Geol. Rom. 19, 285-294.

Ferri F., Porfidia B., Ventura R., 2006: *Gravimetria: la banca dati ed il progetto di cartografia 1:250.000 del Dipartimento Difesa del Suolo - A.p.a.t.*, Atti XXV Convegno GNGTS, 141-143.

Larocchi L., Gualtieri L., Cassinis R., 1998: *2D lithosperic gravity modelling along the Crop 03 profile*. Mem. Soc. Geol. It. Vol LII, 225-230.

Ludwig W. J., Nafe J. E., Drake C. L., 1970: *Seismic refraction, in The Sea*. A. E. Maxwell (Editor), Vol. 4, Wiley-Interscience, New York, 53–84.

Manzella A., Ruggeri G., Gianelli G. & Puxeddu M., 1998*: Pluton geothermal system of Southern Tuscany a review of the crustal models*. Mem. Soc. Geol. It. Vol LII, 283-294.

Marson I., Cernobori L., Nicolich R., Stoka M., Liotta D., Palmieri F., & Velicogna I., 1998: *Crop 03 Profile: a geophysical analysis of data and results*. Mem. Soc. Geol. It. Vol LII, 123-137.

Mele G. and Sandvol E., 2003: *Deep crustal beneath the Northern Apennines inferred from teleseimic receiver functions*. Earth Planet. Sci. Lett., 211, 69-78.

Mirabella F., Brozzetti F., Lupattelli A. & Barchi M.R., 2011: Tectonic evolution of a low angle extentional fault system from restored cross-section in the Northern Apennines (Italy). Tectonics, Vol. 30, TC6002.

Mostardini F., and Merlini S., 1986: *Appennino Centro Merdionale sezioni geologiche e proposta di modello strutturale*. Mem. Soc. Geol. It., Vol. 35, 177-202.

Orlando L., Bernabi M., Bertini F., Camenli G.M., Dini L., 1991: *Il bacino di Radicofani*. Studi Geologici Camerti, Vol.1 199-206.

Orlando L., Bernabini M., Cameli G.M., Dini I., Bertini G., 1994: *Interpretazione preliminare del minimo gravimetrico del Monte Amiata*. Studi Geologici Camerti Vol. speciale 1994/1, 175-181.

Orlando L., 2005: *Interpretation of Tuscan gravity data*. Boll.Soc. Geol. It. Volume Speciale n.3, 179-186.

Pauselli C., Barchi M.R., Federico C., Magnani M.B. and Minelli G.; 2006*: The crustal structure of the Northern Apennines (Central Italy): An insight by the CROP03 seismic line*. Am. J. Sci., 306, 428-450.

Pialli G., Barchi M., Minelli G. (Eds.), 1998: *Results of the CROP-03 Deep Seismic Reflection Profile*, Mem. Soc. Geol. Ital., 52, 654.

Piana Agostinetti N., Lucente F.P., Selvaggi G., Di Bona M., 2002: *Crustal structure and Moho geometry beneath the Northern Apennines (Italy)*. Geophys. Res. Lett. 29, 60-63.

Ponziani F., De Franco R., Minelli G., Biella G., Federico C., Pialli G., 1995: *Crustal shortening and duplication of thr Moho in the Northern Apennines: a view from seismic refraction data*. Tectonophysics, 252, 391-418.

Royden L., Karner G.D., 1984: *Flexure of Lithosphere Beneath Apennine and Carpathian Foredeep Basins: Evidence for an Insufficient Topographic Load*. AAPG Bulletin, 68, 704-712.

Soula J.C., 1982: *Charecteristic and mode of emplacement of gneiss domes and plutonic domes in central-eastern Pyrenees*. J.Structural Geology, Vol.4, 313-342.

Scarascia S., Cassinis R., Federici F., 1998: *Gravity modelling of deep structures in the Northern-Central Apennines*. Mem. Soc. Geol. It. Vol LII, 231-246.

Scarascia S., Lozej A., and Cassinis R., 1994: *Crustal strucrures of Ligurian, Tyrrhenian and Ionian seas and adjacent onshore areas interpreted from wide-angle seismic profile*. Boll. Geog. Teor. Appl., 36, 141-144.

Scrocca D., Doglioni C., Innocenti F., Manetti P., Mazzotti A., Bertelli L., Burbi L., D'Offizi S., (eds), 2003: *CROP Atlas: seismic reflection profiles of the Italian crust*. Mem. Descr. Carta Geol. It., 62, 194 pp, 71 plates.

Talwani M. and Heirtzel J.R., 1964: *Computation of magnetic anomlies caused by two-dimensional bodies of arbitrary shape, in Parks, G. A., Ed., Computers in the mineral industries, Part 1*. Stanford Univ. Publ., Geological Sciences, 9 464-480.

Talwani M., Worzel J.L., Landisman M., 1959*: Rapidy gravity computations for two-domensional bodies with application to the Mendocino submarine fracture zone*. J. Geophys. Res. 64 49-59.

Won I.J. and Bevis M., 1987: *Computing the gravitational and magnetic anomalies due to a polygon: Algorithms and Fortran subroutines*. Geophysics 52 232-238.

# MEMBRANE POLARIZATION BY CONSTRICTIVITY OF PORES: ITS EFFECTS ON DC AND TEM GEO-ELECTROMAGNETIC MEASUREMENTS

**V. Hallbauer-Zadorozhnaya[1], G. Santarato[2], N. Abu Zeid[2], S. Bignardi[2]**
[1] *Council for Geoscience, South Africa*
[2] *University of Ferrara, Italy*

**Introduction.** It is well known that the induced polarization (IP) phenomenon is due to at least four known mechanisms, i.e. the so-called electrode polarization, electro-osmosis polarization, Maxwell-Wagner effect, although very weak, and membrane polarization due to presence of clay minerals in rock pores and/or by constrictivity, i.e. the polarization effect is due to change in pore size (Schön, 1996). Of course freshwater saturated pores is essential for the occurrence of the IP phenomena, on the contrary, increased concentration of dissolved salts affects negatively membrane polarization until its complete nullification at elevated concentrations.

In general, traditional practice for IP data collection is done by commercial geo-resistivity meters while acquiring subsurface resistance data, for example by means of the Electrical Resistivity Tomography (ERT: Barker, 1989) technique. In this case, the IP information is measured in Time-domain by observing the IP decay curve over one or several time windows after current switch-off and the measured quantity determines the value of the chargeability (M).

The chargeability M provides additional independent information, which in many circumstances helps to better understand the subsurface. For instance, it is used, since its discovery, for metallic minerals explorations, nowadays, the method is used for solving environmental issues related to the presence of pollutants in the subsurface, both of inorganic (e.g. Abu-Zeid and Santarato, 2004) and of organic origin (see e.g. the review paper by Atekwana and Atekwana, 2010).

Throughout the seventies of the past century, together with the increasing use of the Transient (or Time-Domain) Electro-Magnetic (TEM or TDEM) technique, also, for mineral exploration, geophysicists become aware of the fact that IP may affect the observed decay curve observed after current switch-off of the inducing magnetic field (Sidorov and Yakhin, 1978; Walker and Kawasaki, 1988). Their presence was dealt with by developing specific algorithms being implemented in computer codes to both model this behavior (Ingeman-Nielsen and Baumgartner, 2006) and consequently to remove it (Antonov and Shein, 2008).

Nevertheless, geo-electromagnetic community agrees that the IP phenomenon is "linear", i.e. not dependent neither on intensity nor on charging time length.

Recently, while conducting intensive resistivity and chargeability measurements on freshwater saturated samples of different rock types, Zadorozhnaya, discovered that both chargeability and resistivity depend on time and intensity of the polarizing direct current (Zadorozhnaya, 2008; Zadorozhnaya and Maré, 2011), although at values that are generally above charging times and current densities which are commonly used in the field. In particular, she observed that chargeability always decreases with increasing current intensity, while resistivity can assume both behaviors. The effect of increasing time of current feeding increased both resistivity and chargeability values. The observed non-linearity of chargeability increase with time is known to be a common occurrence and can be easily understood; however, the remaining non-linear phenomena were quite surprising. That IP could be, under specific conditions, a non-linear phenomenon due to current increase, was a circumstance of which, in early times of the method, scientists were aware of (Bleil, 1953), although the reasons were not investigated further. Few decades later, one of the authors of this paper was involved in laboratory IP measurements on samples of loose sediments (Iliceto *et al.*, 1982), where it was claimed that all the measurements were performed in the range of supplied currents that ensured the linear behavior.

To our knowledge, nobody has published field observations related to the observed remaining non-linear phenomena, in particular, on the dependence of resistivity on charging time and

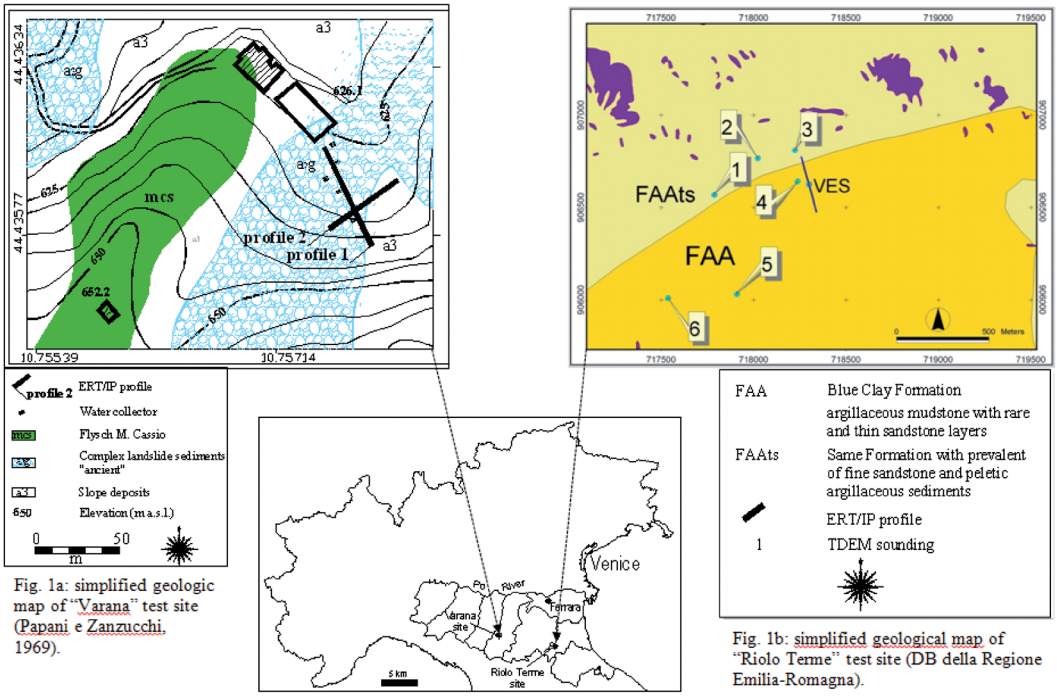


Fig. 1a: simplified geologic map of "Varana" test site (Papani e Zanzucchi, 1969).

Fig. 1b: simplified geological map of "Riolo Terme" test site (DB della Regione Emilia-Romagna).

Fig. 1 – Simplified geological maps of the two test sites tackled in the text.

intensity of the injected current. A reason could be the fact that its specific behavior is observed only in the lab where employed current densities are orders of magnitude greater than those normally available in field measurements, mainly for safety and portability of current sources. In addition, the non-linearity dependence on charging time was observed using longer charging times than those normally used in field resistivity surveys.

In the above-cited papers, Zadorozhnaya published a physical-mathematical model which accounts for the observed non-linear behavior in the tested rock samples. She showed that the non-linearity can be explained by a specific solution of the equations governing the phenomenon of membrane polarization invoking the concept of constrictivity of pores. In her solution, the observed non-linearity depends on the pore-size spectrum, which, if extended successfully to field-scale surveys, shall gain relevance especially for hydrogeological studies (i.e. to be able to indirectly measure porosity from the analysis of the non-linear behavior of specific geoelectric surveys).

In this paper, we show that the non-linearity can be observed in the field too, provided a suitable setup of field measurements. Some hints to the (partly) published model by Zadorozhnaya shall be given in the following.

**Direct current experiment.** Laboratory studies of Zadorozhnaya were focused on clay-free samples so as to avoid any IP contribution due to the well-known mechanism of membrane polarization. Therefore, our field experiment was carefully planned, firstly by selecting a site where a clay-free, saturated aquifer of very shallow depth (i.e. nearly outcropping), so that measurements certainly involve it and the reduced investigation depth allows that current densities, available from a common, portable geo-resistivity meter, could approach the lab conditions. The test site was found in the northern Apennines, where fresh potable water is exploited from a sandstone aquifer. This site is located in the municipal territory of Serramazzoni (Modena Province, N. Italy, Fig. 1a). The acquiclude layer is represented by fine-grained sediments (clay) underlying the sandstone rocks. The hydrogeological unit belongs to the flysch

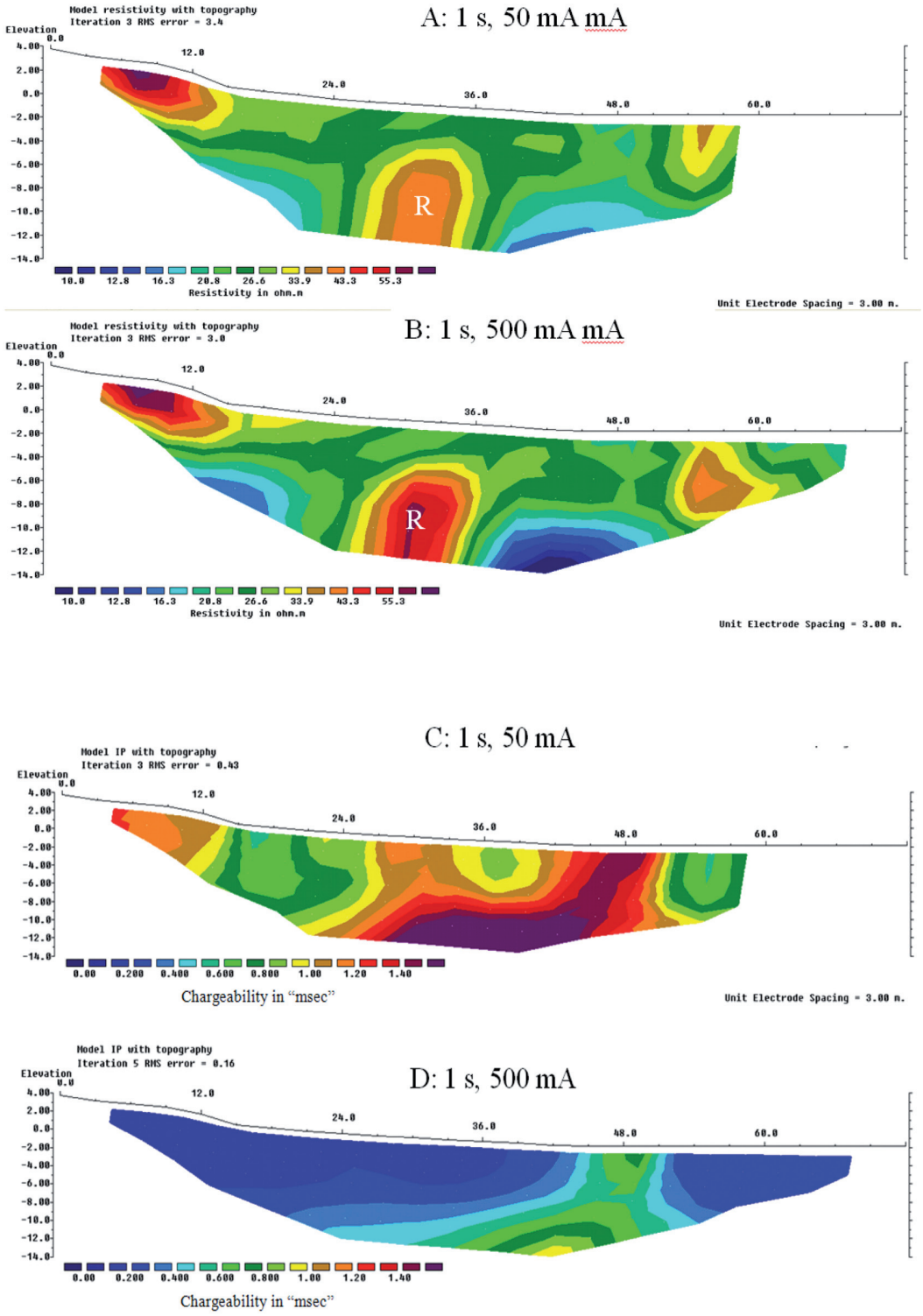


Fig. 2 – 2D inversion resistivity sections obtained using 50 mA (A) and 500 mA of injected current (A,B) and the corresponding chargeability ones obtained using 50 mA (C) and 500 mA (D).

formation (mcs) of Monte Cassin [Campanian-Maastrichtian epoch of the Upper cretaceous period, Papani and Zanzucchi (1969)]. There, an experiment of electrical resistivity and time-domain IP tomography was conducted, using a commercial geo-resistivity meter capable of transmitting controlled current intensities, in the range of 1 mA to 1 A (ABEM SAS4000/ES464, Sweden). To this end, a profile of 72 m long and 3 m electrode spacing was laid out. Along this profile two data subsequent datasets were acquired using the Wenner-Schlumberger electrode array and two current intensities: 50 mA and 500 mA.

The 2D inversion sections of both resistivity and chargeability distributions were obtained using the commercial software RES2DINV$^{tm}$, based on the Gauss-Newton inversion method (Loke and Barker, 1996) (Figs. 2a to 2d). While chargeability strongly decreases with increased current intensity, some increase of resistivity is observed in those more resistive volumes (the red color resistivity body indicated with the letter "R" in Figs. 2a and 2b) that, given the local geology and locations of water collectors, certainly correspond to the sandstone aquifer. The authors are glad to provide a copy of this data set to who is interested.

**The TEM experiment.** In the framework of the EU financed project "Cities on Power" (www.citiesonpower.eu, report 3.4.5) where a number of TEM measurements were performed at and around the RioloTerme town (Province of Ravenna, Northern Italy). The aim of the survey was to aid in the reconstruction of the subsurface conceptual model for hydrogeological assessment of the test site. In this site, a pilot low-enthalpy geothermal plant was planned to be installed in a 100 m deep borehole. The subsurface geology, as given by the simplified geological map and by the visual inspection of the cutting, consists mainly of clayey layers, with some inclusions of sandstone layers and blocks; the local outcropping formations together with the locations of TEM soundings are shown in Fig. 1b. As can be seen, three soundings (1, 2 and 3) were performed over the FAAts geological formation, composed mainly of fine sandstone and pelitic argillaceous sediments, while the remaining 4, 5 and 6 where located on sediments belonging to the FAA formation: a Blue Clay formation composed of gray argillaceous mudstones with rare and thin sandstone layers. The TEM equipment model GDP-3224 by Zonge Ltd was used for data acquisition.

Multi-Function receiver was used to collect the data at the center of a square loop of 50x50 m dimensions. Data were acquired at three different repeating time cycles, at frequencies of respectively 4, 8 and 32 Hz, to get both the maximum resolution in the shallow surface and the maximum investigation depth in accordance with the loop dimensions.

Tab. 1 - 1D petrophysical models of soundings 4, 5 and 6.

| Sounding | layer No. | ρ Ohmm | Thickness m | η | τ s |
|---|---|---|---|---|---|
| 4 | 1 | 18 | 13 | 2.8°-3 | 0.0125 |
| | 2 | 3.5 | 25 | - | - |
| | 3 | 0.75 | 25 | - | - |
| | 4 | 0.5 | 45 | - | - |
| 5 | 1 | 18 | 13 | 2.7°-3 | 0.01 |
| | 2 | 3.5 | 25 | - | - |
| | 3 | 0.75 | 25 | - | - |
| | 4 | 0.8 | 45 | - | - |
| 6 | 1 | 18 | 13 | 2.9°-3 | 0.02 |
| | 2 | 1.7 | 22 | - | - |
| | 3 | 0.5 | 35 | - | - |
| | 4 | 0.7 | 35 | - | - |

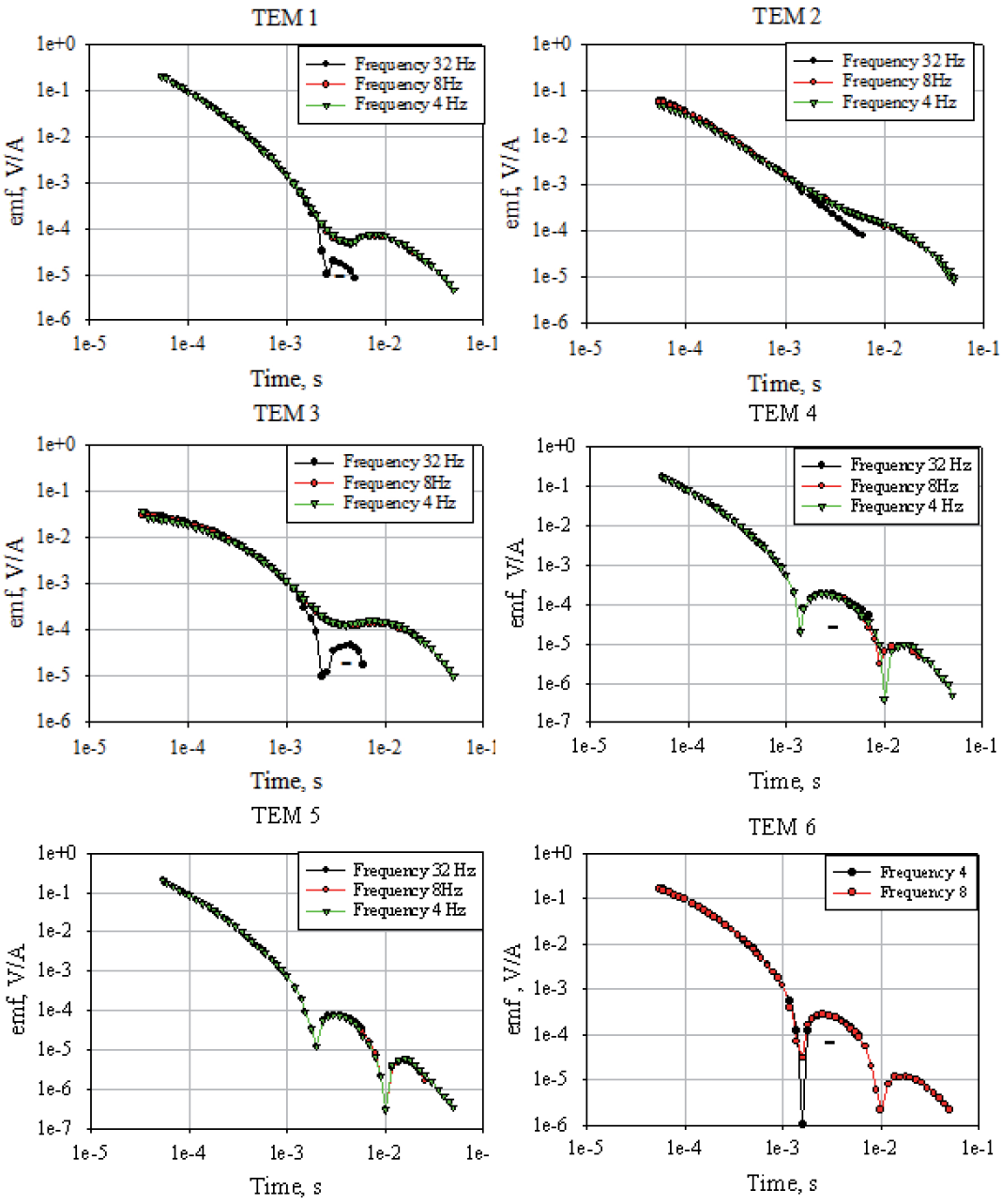


Fig. 3 – Experimental decay curves of the acquired TEM soundings 1 to 6 at the second test site located at RioloTerme town (Ravenna, N. Italy). The curves refer to the used frequencies.

All TEM soundings were perturbed by IP, but, surprisingly, in a quite different way: as shown in Fig. 3. This IP perturbation was found to depend on the repeating frequency in soundings 1, 2 and 3, while it was identical at all frequencies in the remaining 4, 5 and 6. It is worthwhile to specify that this behavior has never been reported before in the literature, at least to the knowledge of the authors.

Of course we can try to invert these data by merging the IP effect into the constitutive TEM

equations. We can use the well-known Cole-Cole model (Pelton *et al.*, 1978), as expressed in eq. 81):

$$\rho(\omega) = \rho_0 \left\{1 - \eta \left[1 - \frac{1}{1 + (i\omega\tau)^c}\right]\right\}, \quad (1)$$

(Where, $\varrho$: is the frequency-dependent resistivity, $\varrho_0$: the resistivity at zero frequency, $\omega$: the angular frequency, $\eta$: the chargeability at 0 time after current switch-off, $\tau$: the relaxation time and 0< c <= 1 a suitable exponent) and implement its Fourier transform in the time-domain into a suitable computer program. If c=1 in this equation, in time domain the function can be expressed as in eq. 2):

$$\sigma(t) = \frac{\sigma_0}{1+\eta}\left[1 - \eta \cdot exp\left(-\frac{1-\eta}{\tau}\, t\right)\right], \quad (2)$$

where $\sigma$: indicates the electrical conductivity $\sigma=1/\varrho$. Using a proprietary Matlab code, written by Zadorozhnaya and described by Zadorozhnaya and Lepyoshkin (1998), we obtain reasonable model parameters (i.e. solution) when we invert soundings 4, 5 and 6 (Tab. 1), while we obtain a similar solution for soundings 1, 2 and 3 only if we invert the data pertaining to the repeating frequency of 32 Hz (Tab. 2, model on left). If we try to invert, with the same algorithm, data pertaining to the repeating frequency of 4 Hz, we obtain nonrealistic low resistivity at depth. As an example we show, in Tab. 2, both models obtained for TEM-3.

Tab. 2 - Model parameters obtained.

1D petrophysical model parameters of sounding 3 using the Cole-Cole formula at 32 Hz repetition rate

| Layer No. | ρ Ohmm | Thickness m | η | τ s |
|---|---|---|---|---|
| 1 | 90 | 15 | - | - |
| 2 | 12 | 25 | - | - |
| 3 | 2.3 | 19 | - | - |
| 4 | 0.5 | 20 | 0.25 | 3.5°-3 |
| 5 | 0.5 | 25 | 0.25 | 3°-3 |
| 6 | 0.6 | 24 | 0.25 | 3°-3 |

1D petrophysical model parameters of sounding 3 using the Cole-Cole formula at 4 Hz repetition rate

| Layer No. | ρ Ohmm | Thickness m | η | τ s |
|---|---|---|---|---|
| 1 | 30 | 30 | - | - |
| 2 | 8 | 45 | - | - |
| 3 | 0.92 | 45 | 0.25 | 3°-3 |
| 4 | 0.05 | 45 | 0.99 | 3.5°-3 |
| 5 | 0.05 | 45 | 0.99 | 3°-3 |
| 6 | 0.05 | 45 | 0.99 | 3°-3 |

How to explain both the time-dependent behavior and the obtained very low resistivity values? If we are successful to explain and model it, we should obtain coherent TEM inverted models throughout. Perhaps we could be so lucky to find second order parameters linked to hydrogeology. Moreover, is this time-dependent behavior correlated with observed time- and current-dependence of resistivity in the (more usual) geo-electrical method? In both reported cases geology suggests the presence of membrane polarization linked to saturated sandstone, which is more abundant in the FAA formation, i.e. below soundings 1, 2 and 3. We remember that sandstone is the same rock type where these phenomena were clearly observed in the lab.

**Non linearity of DC and TEM data: preliminary common model.** The foundation of membrane polarization caused by constrictivity of pores is as follows: when the electrical current flows through a porous channel with pores of different radii (transfer numbers), an excess/loss of ions accumulates at the boundaries (Marshall and Madden, 1959). Obviously captions have higher mobility (transfer more electrical charges) when in a large capillary because in narrow capillaries some of the anions are absorbed by the double electric layers (DEL) hence they become immobile. When a steady state current is applied, concentration of ions at one side of a

Tab. 3 - 1D models of sounding 3 using the Cole-Cole formula and eq. (4) at 4 Hz repetition rate.

| # of layer | ρ Ohmm | h m | $\eta_1$ | $\tau_1$ s | $\eta_2$ | $\tau_2$ s | $\alpha_2$ |
|---|---|---|---|---|---|---|---|
| 1 | 50 | 28 | 4.0e-3 | 0.032 | 2.0e-2 | 0.5 | 0.17 |
| 2 | 1.5 | 25 | - | - | - | - | - |
| 3 | 1.1 | 25 | - | - | - | - | - |
| 4 | 2.0 | 29 | - | - | - | - | - |

capillary increases while at the opposite side it decreases. Decreasing of concentration cannot continue infinitely: it will reach zero causing a rupture of the electrical circuit. No electrical current flows through the capillaries any more, since the current pass is blocked.

Calling $t_0$ the time of blockage, i.e. the time when rupture of the electrical circuit occurred, it has been shown (for more details we address the reader to the above-cited papers by Zadorozhnaya) that, for cations and anions respectively the following equation apply:

$$t_0 = -\frac{u_{0k} FzDS_1S_3\sigma_k}{I^2 M_k (n_{1k} - n_{3k})}, \quad -\frac{u_{0a} FzDS_1S_3\sigma_a}{I^2 M_a (n_{1a} - n_{3a})}: \tag{3}$$

$t_0$ is controlled by current $I$ and it depends on transfer numbers $n_a$ and $n_k$, i.e. on pore radii of the connected pores and on the conductivity of pore fluid $\sigma_k$ and $\sigma_a$. In Eq. (3) $S_1$: is the surface area of the central pore, $S_2$: and $S_3$: are surface areas of left and right pores/channels respectively, $F$: the Faraday number, $z$: valence, $u_0$: ion's salinity of free solution. Subscripts $k$ and $a$ indicate captions and anions, respectively. The amplitude of the potential difference (voltage) also depends on the mobility's of both anions $M_a$ and cationes $M_k$ and on the diffusion coefficient D too. The process of polarization continues up to time $t_0$, after which the rupture of the electrical circuit occurs and the potential difference between the ends of the pore becomes constant. During the polarization process all contacts between pores of different transfer numbers will be blocked and the electrical current will flow through the remaining pore channels.

This brings us to define the phenomenon of membrane polarization as the successive blockage of inter-pore connections due to the excess/loss distribution of ions during current flow. Under these premises, it can be shown that both resistivity and chargeability of a model built by many capillaries of different diameters depend on current intensity, which means that the electrical behavior is not linear.

Moreover, since the response of the model depends on the pore-size parameterization, i.e. the amount of non-linearity can be predicted, the inverse path is also possible, i.e. it becomes possible to estimate the pore-size distribution using measurements made in the non-linear range of the supplied electrical current.

Another consequence of the mechanism, which produces the excess of ions concentration at the boundary between pores, is that it depends on time of the applied current: if the pulse length is short, then the excess of the ions is small and time of levelling (discharging) is also short. However, increasing current pulse length the membrane effect increases. The direction of accumulation of ions along the boundaries is the same as the current flow; therefore the direction of discharge is also the same as the direction of transient emf. That is why the resistivity of bodies, where this membrane IP effect occurs, can considerably decrease.

To account for the time-dependence of the phenomenon, the solution of the constitutive diffusion equation:

$$\frac{\partial u}{\partial t} = -D\frac{\partial^2 u}{\partial x^2}, \tag{4}$$

which led to Eq. (3), consists of numerous exponentials. For a preliminary interpretation we assumed that the membrane IP effect could be modelled using Cole-Cole model [Eq. (2)] with

opposite sign and we added a new function, which takes into account also of the amplitude of the above-described membrane effect as expressed in Eq. (5):

$$p_{ME} = \alpha \frac{\eta_2}{\tau_2} exp\left(-\frac{1-\eta_2}{\tau_2} t\right). \quad (5)$$

where $\eta_2$: is Chargeability and $\tau_2$: is relaxation time for membrane polarization, $\alpha$: is a coefficient referred to attenuation. In this way, re-interpreting the low-frequency curves of TEM 3, resulted in a 1D model that is consistent with the "normal" soundings, as is shown in Tab. 3. Obviously, TEM1 and 2 show coherent 1D models with TEM3.

**Acknowledgements.** Authors acknowledge HERA S.p.A. for authorizing the access to the Varana test site where groundwater collectors are found. Province of Ravenna, partner of the project Cities on Power,, implemented through the Central Europe Program Co-Financed by the ERDF is also acknowledged for the financial support of the geophysical survey at RioloTerme test site.

## References

Abu-Zeid N. and Santarato G.; 2004: On the correspondence between resistivity and texture of loose sediments, saturated with salt water. Near Surface Geophysics, **2**, 144-149.

Antonov E.Yu., Shein A.N.; 2008: *Improving inversion quality for IP-affected TDEM data*. Russian Geology and Geophysics, **49**, 790–802.

Atekwana E.A. and Atekwana E.A.; 2010: Geophysical signatures of microbial activity at hydrocarbon contaminated sites: a review. Surveys in Geophysics, **31**, 247-283.

Barker R.D.; 1989: Depth of investigation of collinear symmetrical four-electrode arrays. Geophysics, **54**, 1031-1037.

Bleil D.F.; 1953: Induced polarization: a method of geophysical prospecting. Geophysics, **18**, 636–661.

Iliceto V., Santarato G. and Veronese S.; 1982: An approach to the identification of fine sediments by Induced Polarization laboratory measurements. Geophysical Prospecting, **30**, 331-347.

Loke M.H. and Barker R.D.; 1996: Rapid least-squares inversion of apparent resistivity pseudosections using a quasi-Newton method. Geophysical Prospecting, **44**, 131-152.

Ingeman-Nielsen T. and Baumgartner F.; 2006: CR1Dmod: A Matlab program to model 1D complex resistivity effects in electrical and electromagnetic surveys. Computers & Geosciences, **32**, 1411–1419.

Marshall D.J. and Madden T.R.; 1959: *Induced polarization, a study of its cases*. Geophysics, **24**, 790–816.

Papani G. and Zanzucchi G.; 1969: *Le argille di Viano: nuove unita litostratigrafiche dell'Appennino emiliano*. L'Ateneoparmense, Actanaturalia, 5, 19–28.

Pelton, W.H., Ward, S.H., Hallof, P.G., Still, W.R. and Nelson, P.H.; 1978: *Mineral discrimination and removal inductive coupling with multifrequency IP*. Geophysics, **43**, 588–609.

Schön J.H.; 1996: *Physical properties of rocks:-fundamentals and principles of petrophysics*.K. Helbig and S. Treitel Editors, Handbook of Geophysical Exploration – Seismic Exploration, vol. 18, Elsevier Scientific Ltd, pp. 583.

Sidorov V.A, and Yakhin A.M.; 1979: *Induced polarization occurred due to induction excitation*.Izvestiya, Physics of the Solid Earth, **26**, 46-52.

Sumner J.S.; 1976: Principles of induced polarization for geophysical exploration. Elsevier Scientific Ltd, pp.277.

Walker, G.G. and Kawasaki K.; 1988: Observation of double sign reversals in transient electromagnetic central induction soundings. Geoexploration, **25**, 245-254.

Zadorozhnaya, V.Yu.; 2008:Resistivity measured by direct and alternating current: why are they different? Advances in Geophysics, 19, 45-59.

Zadorozhnaya V. and Maré L. P.; 2011:*New model of polarization of rocks: theory and application*. ActaGeophysica59, 262-295, DOI: 10.2478/s11600-010-0041-6s.

# ANALYTIC SIGNAL AND MAGNETIC FIELD MODULI ANALYSIS IN EUROPE

**M. Milano, M. Fedi**
*Università degli Studi Federico II di Napoli, Italy*

**Introduction.** Working with a two-dimensional magnetic field data, an important goal is to process the data in order to better evidence the complex information of the original data. One of these procedures is to produce a map in which the shape of the anomalies is more directly linked to the physical properties of the sources. In this work we studied the European magnetic field at different levels from the Earth surface in order to analyze the different components of the magnetic field related to lithospheric sources by the application of methods removing the dipolar shape of the anomalies: the field modulus and the analytic signal modulus. This is important to get a rapid distinction among anomalies of normal or reversed polarization.

**Methods.** In the last decades the analytic signal modulus and magnetic field modulus have been of great utility to interpret potential field data, helping to localize in a very simple way the edges of the sources and their horizontal position without specifying a priori information about source parameters and. We define the modulus of the magnetic field (|**F**|) as:

$$|\mathbf{F}| = \sqrt{F_x^{\,2} + F_y^{\,2} + F_z^{\,2}} \tag{1}$$

where $F_x$, $F_y$ e $F_z$ are the three components of the total magnetic field along *x*, *y* and *z* respectively. The advantage of this operator is the removal of the dipolar behavior of the magnetic anomaly field, placing its maximum amplitude toward the barycenter of the anomaly sources.

The analytic signal is defined by:

$$|A(x,y)| = \sqrt{\left(\frac{\partial T}{\partial x}\right)^2 + \left(\frac{\partial T}{\partial y}\right)^2 + \left(\frac{\partial T}{\partial z}\right)^2} \tag{2}$$

where $\frac{\partial T}{\partial x}$, $\frac{\partial T}{\partial y}$ and $\frac{\partial T}{\partial z}$ are the derivatives of the total-intensity component of the magnetic field ($T$) with respect to the directions *x*, *y*, and *z*. The advantage of this method, compared to the calculation **F** modulus, is to have a complete independence from the variation of magnetic inclination ($I$) (Nabighian, 1972) in the case of 2D fields (profiles). In the 3D case such independence has not been proven mathematically, but we can assume that it is only weakly dependent on the direction of **F**. |**A**| has a higher resolution than |**F**|, and this is very useful when some problematic phenomena make more difficult the interpretation of anomalies, for example the effect of coalescence between single anomalies.

**Aeromagnetic data and main European magnetic field features.** The area covered by the data has an extension of: 20°W, 57°N; 45°E, 57°N; 35°E, 37°N; 5°W, 37°N.

Aeromagnetic data used in this work are extracted from the European and Mediterranean Magnetic Project (Fletcher *et al.*, 2011). The EMMP aimed at bringing together all the available magnetic data (ground, air and marine, profiles and data network) to obtain a 1 km high-resolution grid of total-intensity magnetic field (TMI).

In order to observe the various contributions of lithospheric sources placed at different depths, the aeromagnetic data were upward continued at many levels from the Earth surface. Since the aeromagnetic data are originally gridded at a 1 km surface from the topography, the first step was to upward continue the data at 5 km altitude from the Earth surface using a DEM SRTM30. Than data were upward continued up to satellite altitudes (400 km) (Fig. 1) using the following level-to-level formula:

$$U(x,y,z) = \frac{1}{2\pi}\int_S U(\xi,\eta,0)\,\frac{z}{[(x-\xi)^2+(y-\eta)^2+z^2]^{3/2}}\,d\xi\,d\eta \tag{3}$$

where $U(x,y,z)$ is the potential upward continued field at the scale *z*, $U(\xi,\eta,0)$ is the potential of

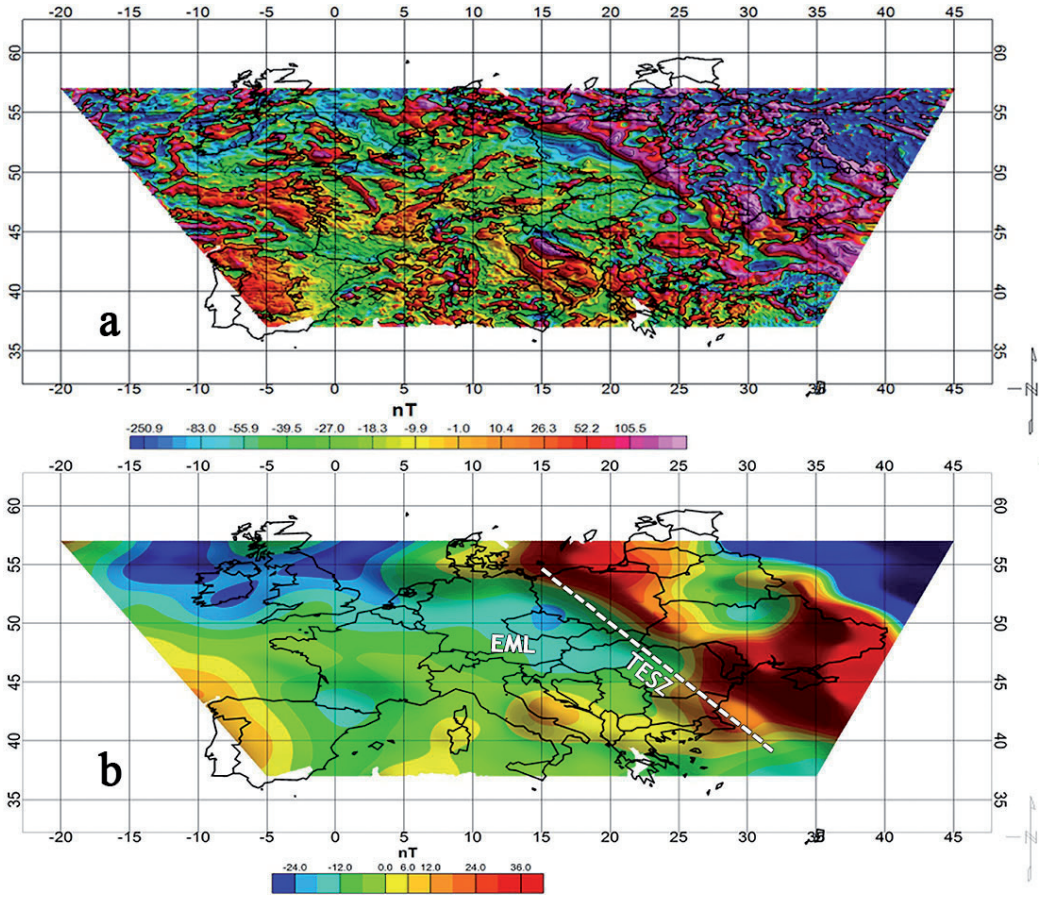


Fig. 1 – European magnetic field maps at 5 km (a) and 200 km (b) of altitude.

the field at level $z$=0 and $z/[(x-\xi)^2+(y-\eta)^2+z^2]^{3/2}$ is the upward continuation operator. It is known that, approaching or moving away from the Earth's surface, we can see that the contributions of individual sources change considering being, those related to shallow sources, most visible at lower scales and viceversa. In fact, considering the aeromagnetic map of Europe at low altitude, we observe a complex magnetic field characterized by little and local high-frequency anomalies, that describe the presence of localized and shallow sources in the upper-crust (Fig.1a).

The complexity of the geological structures of Europe leaves many questions and interpretations related to the meaning and validity of the measurements of the magnetic field. In addition to magnetic anomalies with a "standard" behavior at our latitudes (the high south and the low north), in Europe there are other anomalies that do not meet these characteristics presenting a reverse dipolar aspect, due either to negative magnetic contrasts or to a reversed inducing field. These formations are made up of large deposits of the Permian quartz-Porfiry. Henkel (1994) has shown that the metasedimentary rocks containing pyrrhotite may have magnetic susceptibility greater than 2 x 10-3 (cgs), while the values of the Koenisberger Q ratio, between the residual component and that of induced magnetization, is around 100. In particular, a complex district of high-frequency magnetic anomalies dominates above the central Europe and especially the Czech-Polish area. In this area the magnetic field derives mainly from metamorphic rocks and deep basic and ultrabasic intrusions. In western Europe the most significant magnetic features are defined by the Paris basin anomaly, whose structures' nature and composition are still unknown (Pham *et al.*, 2000), and, in general, by anomalies

related to structures located in the Variscan orogen or older continental lithospheric basements, such as dioritic bodies and calc-alkaline volcanics (Thébault, 2006). In northern Spain, we may observe the magnetic anomaly located in the southern part of the Cameros Basin. This anomaly, with a 26 nT maximum and a weak minimum to the north (14 nT), could be caused by Triassic intrusions placed along the northern margin of the Cameros Basin (Del Río *et al*., 2013). At higher altitudes, the European magnetic field is defined mainly by an intense and extended magnetic low placed above the Central Europe with an intense magnetic high northeast of it. Such anomaly of Europe has been studied and interpreted by many authors in the last decades (Von Frese *et al*., 1981; Ravat, 1989; Ravat *et al*., 1993; Taylor and Ravat, 1995; Pucher, 1994). From a geological point of view, the European magnetic low (EML) is placed exactly above the Trans-European Suture Zone (TESZ) (Fig. 1b), which is the most prominent geological boundary in Europe, separating mobile Phanerozoic units in the south and west from the Precambrian East European Craton. TESZ is oriented NW-SE from the North Sea to the Black Sea, along a distance exceeding 2000 km, and, in the northern part, the most important feature of this fan zone is the Teisseyre-Tornquist fault. Moho depths increase across the TESZ from 30 km, beneath Phanerozoic Europe, to 45 km, beneath the craton (Guterch *et al*., 1986). A relatively high heat flow characterizes the Palaeozoic western Europe, in contrast with the thick, relatively cold, Precambrian eastern craton. Thus, this important fan zone separates the "cold" western lithosphere with a low heat flow of 30-40 mW/m$^2$ from the "hot" Eastern lithosphere that is characterized by a higher heat flow of 40-70 mW/m$^2$ (Majorowicz and Plewa, 1979; Cermák *et al*., 1989; Cermák and Bodri, 1998; Plewa, 1998; Majorowicz *et al*., 2003; Królikowski, 2006).

The Palaeozoic structures are largely obscured by Mesozoic and younger strata of the North Sea-Danish-North German-Polish Basin. A detailed analysis of this basin complex and its partial inversion is required to unravel the enigmatic early Phanerozoic history of this major suture zone. Many authors tried to interpret the EML using different approaches. Von Frese *et al*. (1981) and Ravat (1989) considered a prismatic blocks modeling with three-dimensional spherical coordinates, while Nolte and Hahn (1992) used a three-dimensional block consisting of smaller prisms extended one degree in latitude and three degrees in longitude. Nolte and Hahn (1992) also noted that the component of residual magnetization is much smaller than that induced (low Q) for the source rocks. Ravat *et al*. (1993) interpreted this anomaly as an effect of the structural features and of changes in the thickness of the crust, assuming a non-magnetic upper mantle. Taylor and Ravat (1995) added an alternative explanation for the origin of this anomaly, based on the effect of crustal sources with reverse magnetization at medium and shallow depths of the Paleozoic European platform. The regional directions of magnetization were chosen in relation to those found by palaeomagnetic studies of the sedimentary basins of Germany. Thus, it would be the direction of the remanent magnetization vector to determine the shape of some of the magnetic anomaly. Pucher (1994) inferred a model that causes the effect of the magnetic anomalies generated by the orientation of metamorphic pyrrhotite rocks of Paleozoic age. The results indicated directions of reverse magnetization, probably due to re-magnetization, with a wide minimum to the South and maximum to north. Taylor and Ravat (1995) have thus interpreted the EML as a result of the coalescence of the magnetic field, measured at satellite altitudes, of a large number of reversely magnetized bodies.

**Application methods and interpretation.** We first studied the error related to |**F**| method (eq.1), by considering magnetic inclination changes. In the large area of study, the magnetic field inclination varies from 50° to 70° and the influence of the variation anomalies positioned at different latitudes, has been calculated by taking as an example the anomaly of the central Adriatic, for which two synthetic-sources maps of |**F**|, were generated by considering, respectively, the average value of inclination Europe ($I$=65°) and its local value ($I$=60°) (see Fig. 2a). Then we calculated their difference, which ranges from -11 to 6 nT. This implies that the amplitude variation in the area concerned is equal to only 3.3% of the signal amplitude.

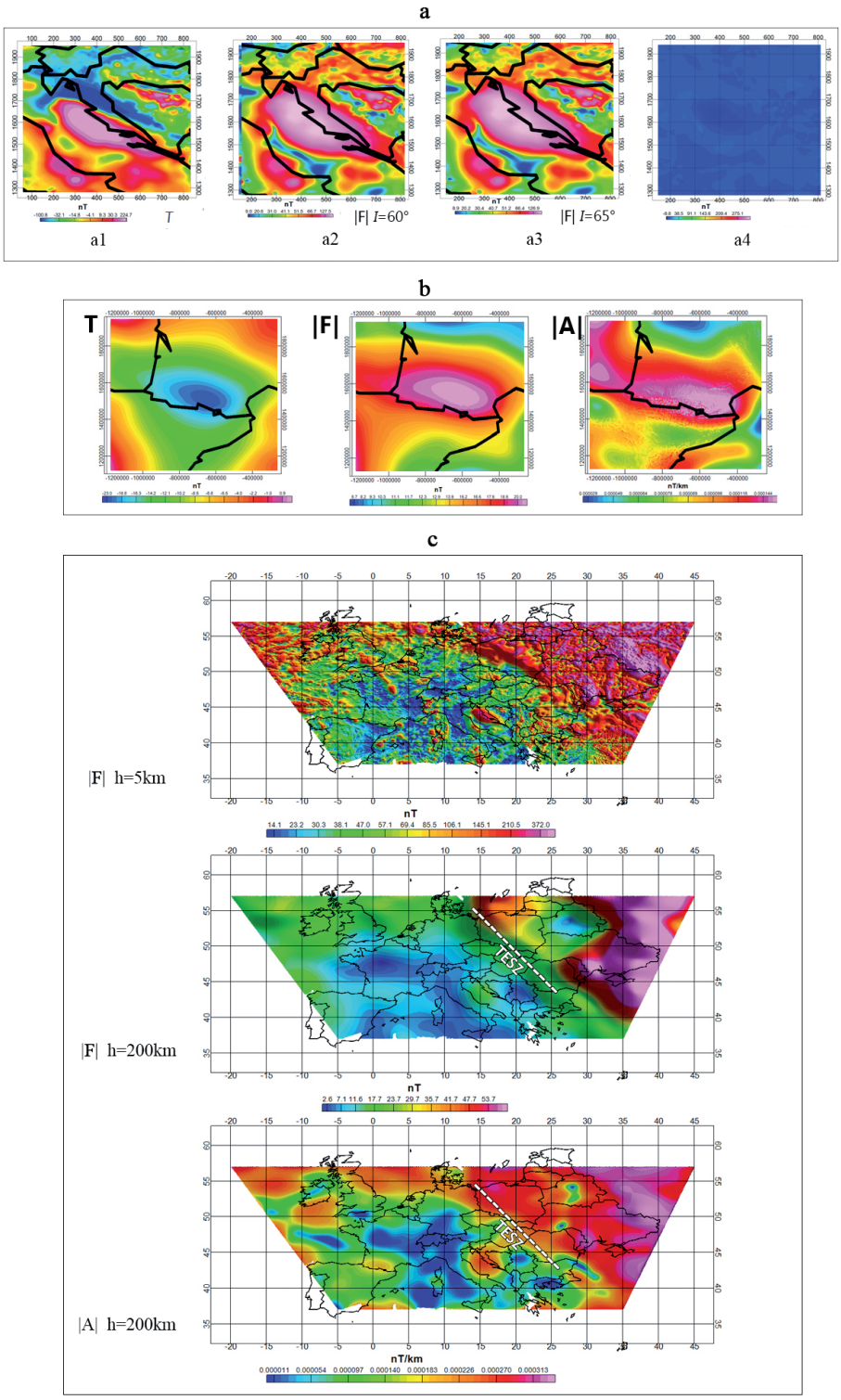


Fig. 2 – a): Adriatic magnetic anomaly (a1) and |**F**| considering $I = 60°$ (a2) and $I = 65°$ (a3), on the right the difference between the two |**F**| maps (a4); b): Pyrenees magnetic anomaly, |**F**| and |**A**| maps at 100 km of altitude; c) |**F**| of Europe at h = 5 km, h = 200 km and analyic signal at h = 200 km.

Then the analytic signal and the field moduli methods have been applied to the aeromagnetic data at different levels. The dipolar shape disappears and the maxima are positioned nicely on the different geological structures. The results obtained by applying the two methods are coincident in most of the areas of anomaly. In particular, the map at 5 km shows the complexity of the distribution of sources in the upper part of the crust, thanks to the positioning of the maximum of the amplitudes at small scales. With increasing altitudes the amplitudes decrease and the maximum was moving, so localizing the position of deeper crustal structures (Fig. 2c).

Even at higher altitudes (5-10 km), after calculating the modules of the field and of the analytic signal, the dipolar aspect of the anomalies disappears, and the maximum amplitudes of |**F**| and |**A**| are positioned above the anomaly sources, such as the anomaly of the center Adriatic. In addition to these types of anomalies with a "standard" behavior at our latitudes, we also recognized anomalies with reverse dipolar aspect. An example could be the magnetic field in the area close to the Pyrenees orogens, where the anomalies have the lows positioned exactly on top of the mountain range. Rising to an altitude of 100-150 km this area is characterized by a single large minimum which extends for several hundred kilometers (Fig. 2b). This could be interpreted as being due to a negative magnetic contrast caused by the deep roots of the Pyrenees mountain chain.

These results are useful for giving a valid interpretation of the EML above the TESZ. The maps shown in Fig. 2c describe a strong amplitude difference between the central-western and the central-eastern Europe, near the suture between the two platforms. The shape and extent of the maximum amplitudes in the maps seem to give a more complex explanation than that proposed in the previous works. On the one hand, the extension of the maximum amplitude of |**F**| and |**A**| along the NW-SE direction can be interpreted by a source localization exactly occurring along the TESZ, which represents an area of separation between two platforms of different nature and depths. In literature there are many geological and geophysical studies that describe the difference in thickness between the Precambrian and Paleozoic platforms and, probably, this different depth could be the cause of the reverse dipolar aspects of many anomaly. To demonstrate this type of interpretation a simple test was performed in which, considering a discontinuity that puts two bodies in contact, K1 and K2, with different thickness (Fig. 3a), were calculated the values of the total-intensity magnetic field *T*, by considering a inclination of magnetization of 65° and the analytic signal |**A**|. It can show a low above the shallow body K1 and a high at NE of the fault, where the thick body K2 is greater, while the analytic signal is positioned exactly above the main discontinuity. The profile obtained from this test seems to be plausible than a profile extracted from real data at 200 km of altitude and passing through the fault line. In Fig. 3b we see that the maximum amplitude of |**A**| is slightly shifted towards the high of the anomaly, probably due to the inclination of the fault plane. The amplitudes of |**F**| and |**A**|, however, are positioned not only along the suture zone, but they have an extension which also occupies a large part of central Europe, in which is located the magnetic low EML (Fig. 3c). This shows that the sources are not placed exclusively along the fault line, but also within the Paleozoic platform.

From these results it appears that the contributions responsible for the nature of this anomaly are to be reconnected to both the presence of the fault of Teisseyre-Tornquist, which puts in contact two different platforms with different depths and thicknesses and both to the presence of bodies with a strong remanent component, which characterize large part of the Central European crust, as argued by Taylor and Ravat (1995). Moreover, also from the combined effect of these two types of different sources derive the large extent and the reverse dipolar aspect of the anomaly. Among the main anomalies that give a contribution to this kind of phenomenon, there is one placed above the Bohemian Massif (Czech Republic). Observing the total magnetic field, we note that this anomaly continues to be visible even at higher altitudes, (Fig. 3c). In addition, the analysis of the analytic signal of this anomaly showed the positioning of the maximum just above its magnetic low, indicating the source position.

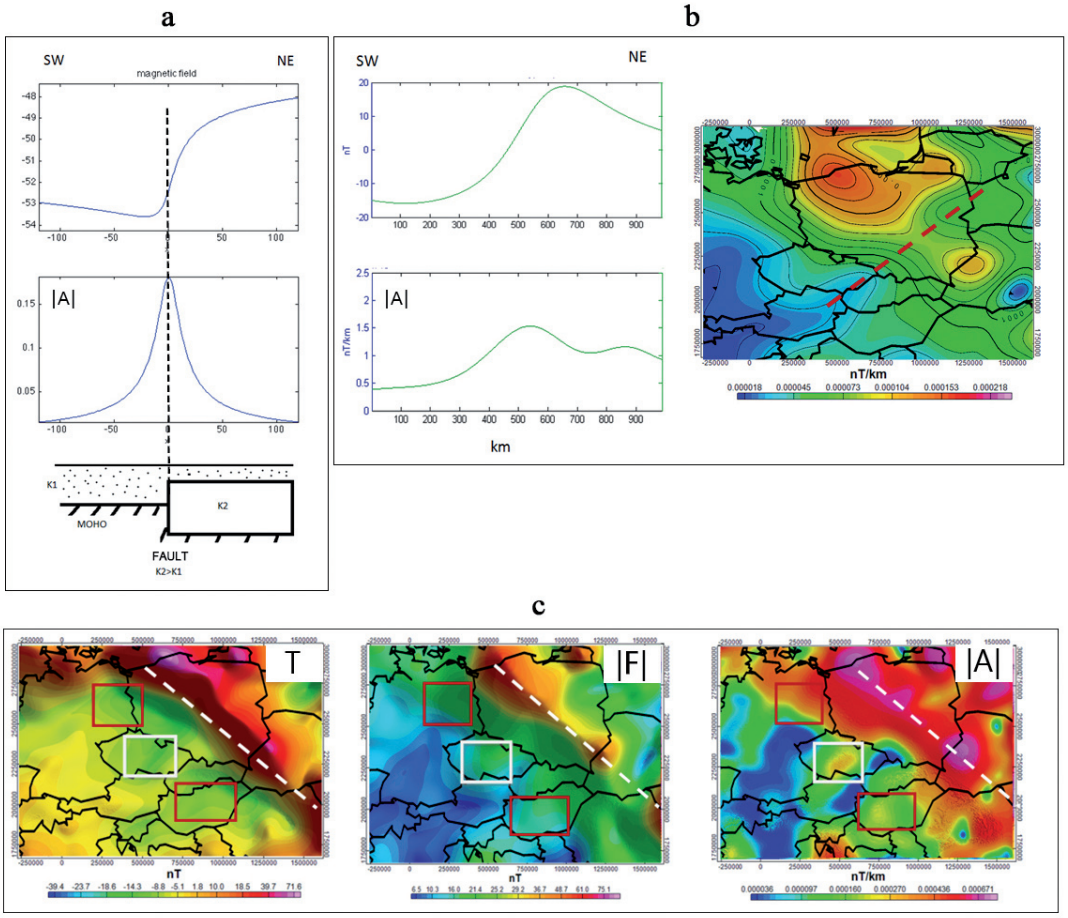


Fig. 3 – Synthetic exemple of discontinuity between two bodies (K1,K2), magnetic field and analytic signal profile (a); magnetic field and analytic signal profile through the TESZ (b); magnetic field, field modulus and analytic signal modulus of central Europe at 100 km altitude (c). The TESZ is indicated by the dashed line, T magnetic lows by white and red squares.

**Conclusions.** In this work we analyzed the magnetic field of the lithosphere above Europe using aeromagnetic data at different altitudes in order to study the European geological-structural feature mainly characterized by the wide suture range of Teisseyre-Tornquist or Trans-European Suture Zone (TESZ), bringing together the two main European platforms: the Paleozoic and Precambrian to the West to the East. The analytic signal and field moduli methods have been used for this analysis. These methods allow suppression of the dipolar aspects of the total intensity component of the magnetic field and the location of the maximum amplitude values above the source baricenter. These methods have been useful in the phase of interpretation of the central European anomaly (EML), which over the years has been described as the effect of a different depth between the Cambrian and Paleozoic platform (Ravat *et al.*, 1993), or caused by the coalescence of several sources with a high remanent component of magnetization in the central Europe and in contact at N-E with the Precambrian crust, which would also explain the nature of its polarity inversion (Taylor and Ravat, 1995), or, finally, as the effect of a single body reversely magnetized adjacent to the Teisseyre-Tornquist fan zone (Pucher and Wonik, 1998). The maps of the field and analytic signal moduli show that the maximum amplitudes in this area are positioned either along the fault line in the direction NW-SE, and along large

part of central Europe, allowing us to interpret the EML as caused by the union of the effect of Teisseyre-Tornquist dislocation and of the anomalies due to bodies with a strong reverse magnetization within the Paleozoic platform. In particular, the anomaly linked to the Bohemian orogenic complex, in the Czech Republic, continues to make contributions to the magnetic field even at high altitudes from the Earth's surface. The results obtained from this work show how the analysis of potential fields through the operators of the field and the analytic signal moduli present high reliability and stability without the requirement of source parameters and information or filtering. These methods are, therefore, leading tools for the interpretation of anomaly fields and to obtain information about location and depth of the sources.

**References**

BARANOV, V., 1957. A new method for interpretation aeromagnetic maps: pseudo-gravimetric anomalies, Geophysics, 22, pp. 359-383.

CERMÁK, V. and BODRI, L., 1998. Heat flow map of Europe revised. Deutche Geophysikalische Gesellschaft e.V., 2: 58–63.

CERMÁK, V., ŠAFANDA, J. and GUTERCH, A., 1989, Deep temperature distribution along three profiles crossing the Teisseyre-Tornquist tectonic zone in Poland. Tectonophysics, 164 (2–4): 151–163.

DEL RÍO, P., CASAS, A., VILLALAÍN, J.J., MOCHALES, T., SOTO, R., OLIVA-URCÍA., B., 2013. Interpretation of gravimetric and magnetic anomalies in the Cameros Basin (North Spain): combination of deep and shallow sources. Studia Geophysica et Geodetica, 57, 442-459

FLETCHER, K. M. U., FAIRHEAD, J. D., SALEM, A., LEI, K, AYALA AND CABANILLAS, P. L. M, 2011. Building ahigher resolution magnetic database for Europe for resource evaluation. First Break,v29, pp. 96-1 GUTERCH, A., GRAD, M., MATERZOK, R. and OERCHUC E., 1986. Deep structure of the earth's crest in the

contact zone of the Palaeozoic and Preecambrian platforms in Poland (Tournquist-Teisseyre Zone), Tectonophysics,128, 251-279.

HENKEL, H., 1994. Standard diagrams of magnetic properties and density--a tool for understanding magnetic petrology. J. Appl. Geophys., 32: 43-53.

KRÓLIKOWSKI, C., 2006. Crustal-scale complexity of the contact zone between the Palaeozoic Platform and the East European Craton in the NWPoland. Geol. Quart., 50 (1): 33–42.

MAJOROWICZ J. and PLEWA S., 1979. Study of heat flow in Poland with special regards to tectonophysical problems. In: Terrestrial Heat Flow in Europe (eds. V. Èermák and L. Rybach): 240–252. Springer. Berlin.

MAJOROWICZ J. A., ÈERMÁK V., ŠAFANDA J., KRZYWIEC P., WRÓBLEWSKA M., GUTERCH A. and GRAD M., 2003. Heat flow models across the Trans-European Suture Zone in the area of the POLONAISE'97 seismic experiment. Phys. Chem. Earth, 28: 375–391.

NABIGHIAN, M. N., 1972. The analytic signal of two-dimensional magnetic bodies with polygonal cross-section: its properties and use for automated anomaly interpretation, Geophysics, 37(3), 507–517.

NOLTE, H.J. and HAHN, A., 1992. A model of the distribution of crustal magnetization in central Europe compatible with the field of magnetic anomalies deduced from Magsat results. Geophys. Jour. Int., l 11 : 483-496.

PHAM, V. N., D. BOYER, and J.L. LE MOUEL, 2000. Nouveaux arguments sur L'origine de L'anomalie Magnetique du bassin Parisien (AMBP) d'aprés les propriétés électriques de la croûte, C.R. Acad. Sci., 331, 443 – 449.

PLEWA, S., 1998. Map of heat flow in Poland. In: Tectonic Atlas of Poland (ed. J. Znosko). Pañstw. Inst. Geol. Warszawa.

PUCHER, R., 1994. Pyrrohotite-induced aeromagnetic anomalies in western Germany. J. Appl. Geophys., 32: 32-42.

PUCHER, R., WONIK, T., 1998. A new interpretation of the Magsat anomalies of central Europe. Phys. Chem. Earth. 23, 981–985.

RAVAT, D.N., 1989. Magsat Investigations over the Greater African Region. Ph.D. Thesis. Purdue Univ., West Lafayette, IN, 234 pp.

RAVAT, D.N., HINZE, W.J., TAYLOR, P.T., 1993. European tectonic features obselwed by Magsat. Tectonophysics, 220: 157-173.ROEST, W. R., J. VERHOEF, and M. PILKINGTON, 1992. Magnetic interpretation using the 3-D analytic signal, Geophysics, 57(1), 116–125.

TAYLOR, P.T. & RAVAT, D., 1995. An interpretation of the MAGSAT Anomalies of Central Europe, J. Appl. Geophys., 4, 83-91.

THÉBAULT, E., 2006. Global lithospheric magnetic field modeling by successive regional analysis. Earth Planets Space 58, 485–495.

VON FRESE, R.R.B., HINZE, W.J., BRAILE, L.W. and Luca, A.J., 1981. Spherical-earth gravity and magnetic anomaly modeling by Gauss-Legendre quadrature integration. J. Geophys., 49: 234-242.

# HIGH-RESOLUTION MAGNETIC AND GAMMA-RAY AIRBORNE SURVEY AT SOCORRO ISLAND, MEXICO

**V. Paoletti[1], M. D'Antonio[1], R. Supper[2], S. Gruber[2], K. Motschka[2]**
[1] *Dipartimento di Scienze della Terra, dell'Ambiente e delle Risorse, University Federico II, Naples, Italy*
[2] *Geological Survey of Austria, Vienna, Austria*

**Introduction.** The Island of Socorro (Fig. 1) is located 700 km off the western coastline of Mexico at the northern Mathematicians Ridge, an abandoned mid-ocean ridge spreading centre. Together with several other islands (e.g., San Benedicto and Clarion) and numerous seamounts, the so called Revillagigedo archipelago represents post-abandonment alkaline magmatism [e.g., Taran *et al*. (2002) and references therein]. The last volcanic event in the area of Socorro took place in 1993 (e.g., Siebe *et al*., 1995), when a submarine basaltic eruption threatened the small settlement on the island. Until today, due to the remote location of the island, little knowledge is available concerning the subsurface structure of the volcanic edifice.

In support of plans of the Mexican government to enlarge the settlement on the island, a combined geophysical survey was conducted in February 2009 to open up new resources for local groundwater supply. Investigations were focused on determining the resistivity structure of the shallow subsurface of the volcanic edifice, as this parameter is directly related to the water content of subsurface structures. However other parameters such as clay content, fluid conductivity and temperature control the subsurface resistivity and these parameters normally show significant variations in volcanic areas. Thus, we conducted other investigations/analyses over the island, such as airborne magnetic, electromagnetic and gamma-ray measurements in order to have an overall view of the main structural/lithological features of the island.

The aim of this work is to retrieve information about the surface and subsurface geology of the island based on the analysis and interpretation of magnetic and gamma-ray airborne data, integrated with available geo-volcanological information.

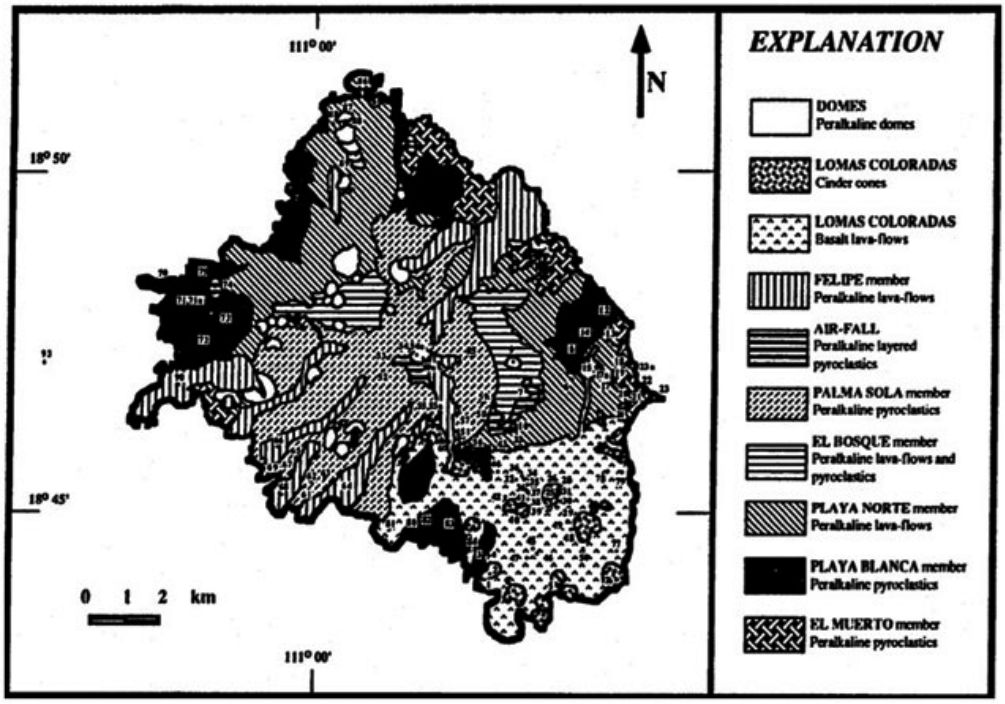


Fig. 1 – Geologic sketch-map of Socorro Island (Carballido-Sanchez, 1994).

**Geo-Volcanological Outlines of Socorro.** Socorro Island is located in the eastern Pacific Ocean at 18°47'N and 110°58'W, 700 km off the coast of mainland Mexico at the intersection of the Clarion Fracture Zone and the Mathematician Ridge System. With an extent of 130 $km^2$ it is the largest island of the Revillagigedo Archipelago, which consists of the four islands Socorro, Clarión, San Benedicto and Roca Partida, all of them being volcanic in origin. These four islands as well as a group of several seamounts make up the Mathematician Ridge, an abandoned mid-ocean ridge spreading centre which was active from 6.5 Ma to 3.15 Ma before present (Siebe *et al*., 1995).

Socorro Island is the emergent portion of a large shield volcano, Volcán Evermann, which rises from the seafloor at a depth of about 3 km to the summit of the volcano at 1050 m above sea level (Carballido-Sanchez, 1994) and has a submarine slope of a little less than 10 degrees (Siebe *et al*., 1995). With a basal radius of 24 km and the assumption that the volcano is a perfect cone, the total volume of the volcano makes up approximately 2400 $km^3$. Hence the subaerial portion of Volcán Evermann makes up about 2 vol. % of the total edifice.

Volcanism in the Revillagigedo Archipelago produced primarily alkali olivine basalts, followed by eruptions of soda-rich rhyolite (Siebe *et al*., 1995). Therefore, Volcán Evermann could be better described as a composite volcano, with an early shield-building stage, characterized by basaltic effusive eruptions, and late extensive pyroclastic peralkaline eruptions (Carballido-Sanchez, 1994). The domination of subaerial silicic peralkaline eruptions makes Socorro Island virtually unique in the Pacific Ocean. Peralkaline volcanic rocks show a molar excess of ($Na_2O$ + $K_2O$) over $Al_2O_3$ whereas the opposite characteristic is usual in the Earth's crust (Carballido-Sanchez, 1994). Samples from Socorro Island have a peralkalinity index, i.e. molar ($Na_2O$ + $K_2O$)/$Al_2O_3$, of 1.1 – 2.2 (Bohrson and Reid, 1998). According to Carballido-Sanchez (1994), almost 90% of the peralkaline products on Socorro Island are of pantelleritic[1] composition. It is supposed that peralkaline rocks make up 80-90% of the total subaerial volume of rocks exposed on Socorro Island. With the assumption that the submarine portion of the volcano is composed mainly of basalts, peralkaline rhyolitic rocks make up only 1.5 vol. % of the volcanic edifice. Only little is known about the submarine part of the volcano.

The eruptive history of Socorro Island has been divided into pre-, syn- and postcaldera stages (Bohrson *et al*., 1996), whereas the postcaldera stage has been subdivided by Bryan (1966) into Cerro Evermann eruptives and Lomas Coloradas eruptives. A geological sketch-map of the island (Carballido-Sanchez, 1994) is shown in Fig. 1.

The bulk of the volcanic edifice, which is submarine, erupted before the formation of a small caldera and is basaltic in origin. The precaldera units on Socorro Island erupted in two episodes of activity. The first episode of eruptions was mainly effusive. The volcano built up from the seafloor, which corresponds to the shield-building stage of volcanism. The second stage of precaldera activity was dominated by explosive eruptions and deposition of peralkaline pyroclastics (Carballido-Sanchez, 1994). The oldest subaerially exposed units of Socorro Island are precaldera alkaline basalts to comendites[2], which are confined to the base of a sea cliff at the eastern part of the island (Bohrson and Reid, 1998; Taran *et al*., 2002). Most of the subaerially exposed pre- and syncaldera rocks are silicic peralkaline ignimbrites, which are commonly holocrystalline non-vesicular lava-like deposits that lack inclusions or lithic fragments (Bohrson *et al.,* 1996). These authors found some evidence that silicic pre- and syncaldera phases on Socorro Island were dominated by explosive eruptions with low eruption columns. The products of pre- and syncaldera activity range in age between 540 and 370 ka.

The remainder of a former caldera wall can be found on the southeastern side of the summit at approximately 600 m elevation. The size of the steep escarpment is consistent with a former caldera dimension of about 4.5 x 3.8 km, which is typical for peralkaline volcanoes (Bohrson

1 Pantellerite: peralkaline rhyolite, FeO-richer than comendite

2 Comendite: peralkaline rhyolite less FeO-rich than pantellerite

*et al*., 1996). Caldera formation occurred probably around 370 ka and was followed by up to 200 kyr of quiescence. The presence of a small summit caldera on Socorro suggests that the silicic magma reservoir was shallow, probably located within the volcanic edifice or the upper oceanic crust. Caldera formation was followed by a change in eruptive style from predominantly explosive to predominantly effusive (Bohrson *et al*., 1996).

Rocks of the postcaldera stage had been subdivided into the Cerro Evermann Formation and Lomas Coloradas Formation, which erupted between 180 and 15 ka (Cerro Evermann) and 150 and 70 ka (Lomas Coloradas), respectively (Bohrson *et al*., 1996). Rocks of the Cerro Evermann Formation are pyroclastics, lava flows, and lava domes of peralkaline composition, exposed in the caldera and at the northern, western and southern flanks of the volcano. These are primarily trachytes, comendites and pantellerites (Carballido-Sanchez, 1994). The lava flows and cinder cones of the Lomas Coloradas Formation are exposed at the south-eastern part of the island and are composed of basalt, hawaiite and mugearite (Carballido-Sanchez, 1994). Eruption of peralkaline-rhyolitic and basaltic magmas during the same time interval of post-caldera phase has been explained by a stratified magma chamber composed of soda-rhyolite overlying basaltic magma (Siebe *et al*., 1995).

Morphologically, the subaerially exposed rocks on Socorro Island can be classified as lava-flows, domes, pyroclastic flows, air-fall pyroclastics and cinder cones. The lava-flows on Socorro Island can be of both basaltic and peralkaline composition, whereas the pyroclastic flows are exclusively peralkaline (Carballido-Sanchez, 1994). Cinder cones are generally basaltic in composition (except for one) and are confined to the Lomas Coloradas unit. The domes, on the other hand, are exclusively peralkaline. Air-fall pyroclastics are both peralkaline and basaltic, whereas the basaltic ash, cinder, spatter and bomb deposits are all (except for one deposit in the Bahia Academy area) restricted to the Lomas Coloradas area (Carballido-Sanchez, 1994).

Bryan (1966) identified three major zones of fractures that intersect on Socorro Island. One zone has a north-south orientation and extends from the summit of Volcán Evermann to Bahia Academy, which is located in the northern part of the island. A second zone is orientated in east-west direction and extends from the western coast of the island (Cabo Henslow, Punta Tosca, Caleta Grayson) to the summit area of Volcán Evermann. The third zone is located in the southern part of the island and shows approximately NW-SE orientation.

Bohrson and Reid (1997) found three different conditions that are required for the formation of silicic peralkaline magmas: a mildly extensional tectonic setting, a shallow magma reservoir and availability of parental transitional to mildly alkalic basalt. The formation of silicic peralkaline magmas can be explained by three different mechanisms: fractional crystallization of transitional to mildly alkalic basalt, partial melting of mafic intrusive rock and volatile complexing and transport in association with one of these (Bohrson and Reid, 1997). According to these authors, the most likely mechanism of silicic peralkaline magma formation for Socorro Island is a moderate degree of partial melting of intrusive alkalic basalt and associated crystal cumulates followed by crystal fractionation.

Calculation of eruption rates for submarine and subaerial parts of the volcanic edifice suggests that either subaerial eruption rates are less than submarine eruption rates, or the growth of the volcano has continued to be dominantly submarine. Comparison of eruption rates of other isolated ocean islands suggests that the source of alkaline magmatism associated with Socorro may be consistent with a mantle plume (Bohrson *et al*., 1996).

Volcanic activity on Socorro Island has continued to the present. The first historically reported eruption took place in 1848, but no detailed description of the event exists. Another eruption was observed in 1896, but also no further information on the eruption is available. Further small eruptions were reported in 1947 and 1951. The so long last eruption occurred in 1993 and was submarine. At the moment, fumarolic activity can be observed near the summit of Volcán Evermann (Carballido-Sanchez, 1994).

Siebe *et al*. (1995) carried out a geochemical study on the 1993 submarine eruption near Socorro Island. Further work was done to investigate the genesis of silicic peralkaline magmas (Bohrson *et al*., 1996; Bohrson and Reid, 1998). In 1999, a seismic survey was carried out in the south-eastern part of Socorro Island with the use of five portable broadband seismometers (Valenzuela *et al*., 2005). The intention was to install a seismic T-phase station on Socorro, as part of the International Monitoring System (IMS) of the Comprehensive Nuclear-Test-Ban Treaty Organization (CTBTO). The geochemistry of hydrothermal fluids on Socorro was investigated by Taran *et al*. (2010).

The airborne geophysical and ground geoelectric survey of the Geological Survey of Austria (GSA) in 2009 was the first detailed geophysical survey on Socorro Island.

**Airborne and Gamma-ray Survey at Socorro.** Airborne geophysics has been intensively applied for exploration of raw materials within the last decades, however so far it was hardly ever used to investigate the groundwater resources of volcanic islands. One of the big advantages of airborne geophysical measurements is that large areas can be surveyed within relatively short survey times. Furthermore, airborne geophysics is the only remote sensing method yielding information not only about the surface but also about the subsurface structures.

To perform the airborne measurements we used the complex airborne system of the Austrian Geological Survey (Motschka, 2001). Its instrumentation consists of a frequency domain electromagnetic bird operating at four different frequencies, a magnetic sensor and a gamma spectrometer. Positioning was performed using the data of a laser altimeter, two differential GPS sensors and flight path recordings from a downward looking digital video camera. For correction of altitude raw values for variations in vegetation thickness we employed advanced algorithms. The survey covered an area of 200 km$^2$, with an average line spacing of 100 m. The use of the electromagnetic system required the distance between terrain and sensor ("bird") to be less than 100 m, in order to yield a reliable subsurface resistivity mapping.

*Airborne Magnetics*. With this methodology the total intensity of the Earth's magnetic field is measured. Deviations from a reference earth magnetic field (IGRF) are considered as anomalies and assist e.g. in the discovery of differently magnetized bodies (i.e. ore bodies, young volcanic rocks, metallic contents of waste repositories) or fracture zones. The results are given in Fig. 2, which shows a high resolution map of the magnetic field anomalies reduced

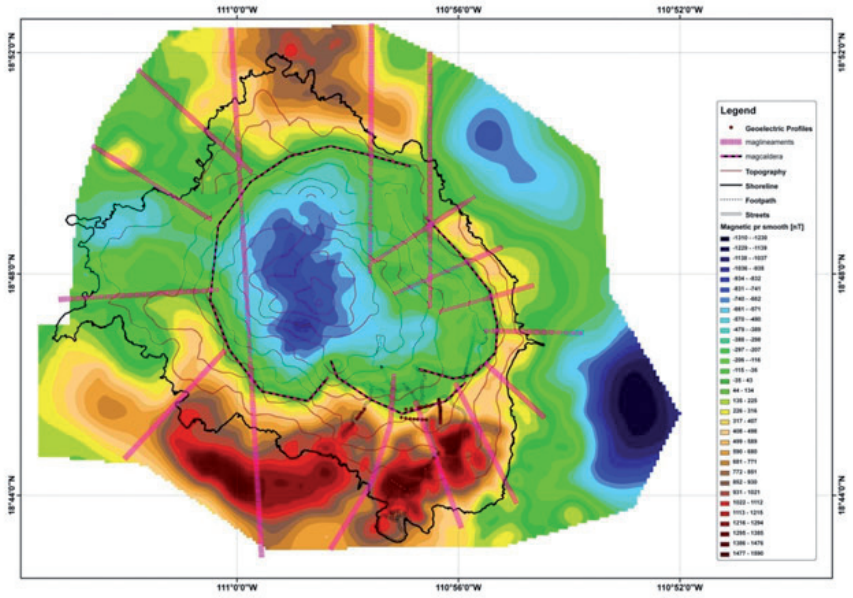


Fig. 2 – Preliminary interpretation of the pole-reduced magnetic data: magnetic lineaments and structures.

to the pole. Interestingly, the central part of the map, corresponding to the of the summit of the island, shows a very large negative anomaly which is extended to the eastern part of the island. A preliminary *DEXP* analysis of magnetic data (Fedi, 2007) pointed out the presence of a low magnetization volume, which may be connected to: may be connected to: a high temperature (above the Curie temperature) in the deeper part of the volcano, a low total remanent magnetization of pyroclastic caldera sediments due to non-aligned sedimentation, and/or the influence of hydrothermal alteration within the caldera. In the latter case the caldera structure would extend further to the southern part of the island than assumed before.

*Gamma-ray spectroscopy.* This methodology determines the natural and artificial radioactivity, which depends on the content of radioactive minerals within the first decimeters of the subsurface. Natural gamma radiation is essentially derived from three sources: the radioactive elements thorium (energy peak: 2.62 MeV), uranium (energy peak: 1.76 MeV) and potassium (energy peak: 1.46 MeV). These elements occur in different rocks and soils at various concentration levels. The measuring sensor consists of several sodium-iodide crystals, which convert gamma radiation into flashes of light. Appropriate survey instruments determine their energies. With conventional measuring systems the energy spectrum between 0.2 to 6.0 MeV is resolved in 256 channels.

Since the air layer between helicopter and ground is absorbing gamma radiation (depending on the physical condition of the air), the exact flight altitude, air pressure, air temperature as well as air moisture have to be taken into consideration when correcting survey data.

Prior to processing, data were inspected for incorrect values and in particular all samples which were taken at altitude higher than 400 m were deleted.

The following calibration constants and coefficients were used for the processing of gamma-ray data of Socorro Island (Tab. 1):

Tab. 1 - Calibration constants and coefficients used for the gamma-ray processing.

| | K40 | U238 | Th232 | TC |
|---|---|---|---|---|
| Aircraft Background | 28.32 | 13.408 | 7.078 | 40.02 |
| Cosmic Background | 0.083 | 0.043 | 0.059 | 1.9 |
| Attenuation by air | -0.0057333 | -0.0058056 | -0.0070921 | -0.0061463 |
| Sensitivity | 47.2 | 7.3 | 3.4 | 29.5 |
| Stripping Coefficients | 0.2 | 0.26 | 0.74 | 0.05 |
| SC altitude increase | 0.00049 | 0.00065 | 0.00069 | 0 |

Processing was performed both with and without the use of PCA smoothed spectra. Radon removal was first run with the full-spectrum method, but this seemed to remove too much and so radon removal was run for a second time with the spectral-ratio method.

The best gridding results could be achieved with the gridding-method kriging. Since flight line spacing at Socorro was approximately100 m, the grid-node spacing was also chosen to be 100 m, with a search radius of 150 m. The results for potassium, shown in Fig. 3, provide valuable information for geological and volcanological research. They show a good correlation between the maxima of the potassium map and the peralkaline trachytes dated approximately at 15 ka (Bohrson *et al*., 1996) belonging to the Felipe member (Fig. 1).

Interpretation of gamma-ray data of Socorro Island is being performed with the combined use of radioelement maps, ternary maps, a detailed satellite image and several pre-existing geological maps.

**Conclusions.** Through this work we aim at retrieving information about the surface and subsurface geology of the volcanic island of Socorro based on the analysis and interpretation

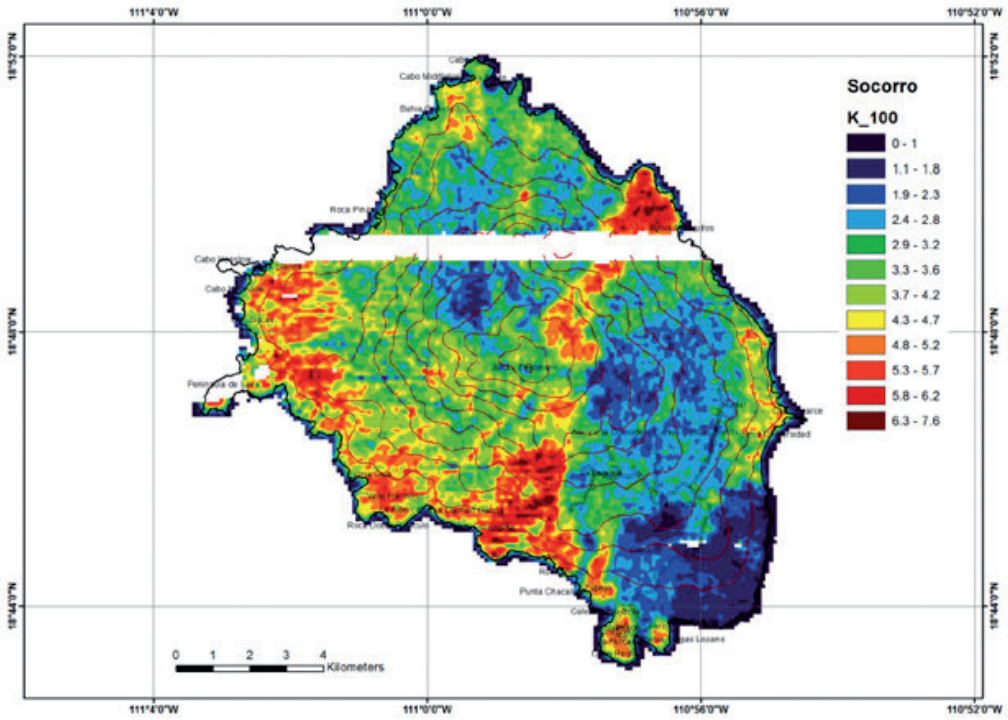


Fig. 3 – Gamma Ray Spectroscopy: Potassium content (%).

of high-resolution magnetic and gamma-ray airborne data. The data were measured in 2009 in the frame of a combined geophysical survey including also EM and ground resistivity data. A comparison of these data with available geological information and rocks composition is being carried out in order to put some constrain on the surface and subsurface geology of specific areas of the island.

A preliminary analysis of magnetic data (Fig. 2) performed through the DEXP method shows the presence of a low magnetization volume below the surface of the island, possibly connected to high temperatures in the deeper part of the volcano, a low total remanent magnetization of pyroclastic caldera filling due to non-aligned sedimentation, and/or the influence of hydrothermal alteration within the caldera. The airborne gamma-ray data (Fig. 3) show a good correlation between the maxima of the potassium map and the 15 ka old peralkaline trachytes of the Felipe member (Fig. 1).

## References

Bohrson W.A., Reid M.R., Grunder A.L., Heizler M.T., Harrison T.M. and Lee J.; 1996: *Prolonged history of silicic peralkaline volcanism in the eastern Pacific Ocean.* Journal of Geophysical Research, **101,** 11457–11474.

Bohrson W.A. and Reid M.R.; 1997: *Genesis of silicic peralkaline volcanic rocks in an ocean island setting by crustal melting and open-system processes: Socorro Island, Mexico*. Journal of Petrology, **38,** 1137–1166.

Bohrson W.A. and Reid M.R.; 1998: *Genesis of evolved ocean island magmas by deep- and shallow-level basement recycling, Socorro Island, Mexico: constraints from Th and other isotope signatures.* Journal of Petrology, **39**, 995–1008.

Bryan W.B.; 1966: *History and mechanism of eruption of soda-rhyolite and alkali basalt, Socorro Island, Mexico.* Bull. Volc., **29**, 453–480.

Carballido-Sanchez E.A.; 1994: *The geology and petrology of Socorro Island, Revillagigedo Archipelago, Mexico*, PhD Thesis, Tulane University, 253 pp.

Fedi M.; 2007*: DEXP: a fast method to determine the depth and the structural index of potential field sources*. Geophysics, **72**, 1–11.

Motschka K.; 2001: *Aerogeophysics in Austria*. Bulletin of the Geological Survey of Japan, **2/3**, 83–88.

Siebe C., Komorowski J.C., Navarro C., McHone J., Delgado H., and Cortes A.; 1995: *Submarine eruption near Socorro Island, Mexico: geochemistry and scanning electron microscopy studies of floating scoria and reticulite*. Journal of Volcanology and Geothermal Research, **68**, 239–271.

Taran Y.A., Fischer T.P., Cienfuegos E. and Morales P.; 2002: *Geochemistry of hydrothermal fluids from an intraplate ocean island: Everman volcano, Socorro Island, Mexico*. Chemical Geology, **188**, 51– 63.

Taran Y.A., Varley N.R., Inguaggiato S. and Cienfuegos E.; 2010: *Geochemistry of H2- and CH4-enriched hydrothermal fluids of Socorro Island, Revillagigedo Archipelago, Mexico. Evidence for serpentinization and abiogenic methane*, Geofluids, **10**, 542–555.

Valenzuela R.W., Galindo M., Pacheco J.F., Iglesias A., Terán L.F., Barreda J.L., Coba C.; 2005: *Seismic survey in southeastern Socorro Island: background noise measurements, seismic events, and T phases*. Geofísica Internacional, **44**, 23–38.

## PROSPEZIONE GEOFISICA PER LA RICERCA ARCHEOLOGICA SU LARGA SCALA: IL SITO DI MONTE PRAMA (CABRAS, ITALIA)

**G. Ranieri[1], A. Trogu[1], M. Zucca[2], A. Usai[3]**

*[1] DICAAR – Dipartimento di Ingegneria Civile, Ambientale e Architettura, Cagliari*

*[2] DSSUF – Dipartimento di Storia, Scienze dell'Uomo e della Formazione, Sassari*

*[3] Soprintendenza Archeologica per le Provincie di Cagliari e Oristano*

**Premessa. La necropoli della prima età del ferro di Monte Prama (Sardegna centro occidentale).** Il celebre sito archeologico di Monte Prama, caratterizzato da una necropoli con sculture monumentali della prima età del ferro (IX- VIII sec. a.C.), è localizzato nel Sinis di Cabras (Oristano), a 2 km ad oriente della laguna di Cabras (*Mar'e Pontis*) e a 4 km ad occidente del Mare Sardo. Il complesso archeologico, individuato casualmente nel 1974, è stato fatto oggetto di scavi nel 1975, 1977, 1979 ( Bedini *et al*., 2012; Lilliu, 1997) ripresi nel maggio 2014 e ancora in atto.

La Sardegna è caratterizzata durante l'età del Bronzo, nella seconda metà del secondo millennio a.C. dalla cultura nuragica, così denominata dal monumento più caratteristico, il nuraghe.

Con la Prima età del ferro dal IX secolo a.C. non si costruiscono più nuraghi, ma la cultura dei Sardi vive tra IX e VIII secolo nella memoria della grande civiltà architettonica dei nuraghi, ora riprodotti in pietra, bronzo e terracotta (modellini miniaturistici) che eternano il ricordo di un'età ormai mitica.

Il complesso di Monte Prama è probabilmente un santuario, unico nel suo genere in tutto il Mediterraneo centrale e occidentale, nato da una monumentalizzazione di una necropoli a tombe individuali a inumazione, caratterizzato dalla scultura monumentale.

Al di sopra del sepolcreto delle tombe a pozzetto del IX sec. a.C. / prima metà dell'VIII secolo a.C., viene costituita una vasta area lastricata per giochi funebri, presumibilmente disposta su due livelli, inferiore quello più occidentale, superiore l'area orientale.

L'area lastricata poté ospitare un complesso di betili troncoconici in arenaria e calcare e di statue colossali in calcare del miocene superiore, alte fino a m 2,20, di cui sono state finora rinvenute ventotto esemplari, di cui 16 pugilatori, 6 arcieri e 6 guerrieri, inoltre 16 modelli di nuraghe, di cui 8 monotorre, 5 a otto torri laterali ed una centrale e 3 ad torre centrale cinta da un bastione a 4 torri. Tale complesso di statue è il più grandioso di tutto l'Occidente protostorico.

Le sculture furono investite da un volontario intervento distruttivo attuato simultaneamente entro la fine del IV sec. a.C., forse ad opera dei Cartaginesi, che curarono l'obliterazione dei 5178 frammenti statuari in una discarica sopra le tombe più occidentali e, soprattutto,

all'interno di una strada funeraria, profondamente incassata, parallela all'estremo filare ovest di sepolture.

La fine di queste prime campagne di scavo ha lasciato insoluti alcuni interrogativi di particolare rilievo:

1. Che cosa rappresentano le statue e gli altri ritrovamenti, e perché si trovano in questo sito?
2. Le statue sono di produzione locale (nuragica) o sono state realizzate da culture orientali?
3. Perché guerrieri, pugilatori e arcieri?
4. Perché betili e modelli di nuraghe?
5. Erano dei testimoni della cultura nuragica?
6. Erano a guardia ...di un santuario? ...di un tempio delle acque? ...o di che altro?
7. Erano poste a guardia di un villaggio? Dovevano spaventare le altre tribù? …
8. Quale è la reale estensione della necropoli?
9. La necropoli è stata interamente scavata come sembrerebbe dai suoi confini meridionale e occidentale?

Per rispondere in parte a queste domande, nell'ambito di una intesa tra le Università di Cagliari e di Sassari e la Soprintendenza per i Beni archeologici di Cagliari e Oristano, con il finanziamento della Regione Sardegna (L.R. 7 / 2007), nel 2013 si è avviato un progetto di indagine geofisica e archeologica (Archeologia di Monte Prama) che ha visto coinvolte insieme alle tre Istituzioni promotrici, la Casa Circondariale di Oristano, il Comune di Cabras e il Consorzio Uno per la promozione universitaria di Oristano.

**La prospezione geofisica. Premessa.** Preliminarmente a qualunque nuovo intervento di scavo nell'area di Monte Prama è stata condotta un'ampia indagine geofisica che ha coinvolto complessivamente circa 6,6 ettari. La prospezione geofisica è stata realizzata in due tempi: nel 2013, da luglio a ottobre sono state oggetto di indagine le aree circostanti il sito scavato negli anni 70 (circa 5,7 ettari); nel 2014 (maggio-agosto) è stato lo stesso sito delle precedenti indagini archeologiche, di proprietà della Curia arcivescovile di Oristano, ad essere oggetto della prospezione geofisica (circa 0,9 ettari).

Gli obiettivi delle due campagne si possono così riassumere:

- nel 2013 l'indagine sulle aree circostanti ha mirato a determinare l'effettiva estensione del sito archeologico per meglio poterne interpretare il significato, poiché le aree interessate sono tutte di proprietà privata al momento non è stato possibile procedere con saggi di scavo;
- nel 2014 invece la campagna geofisica è stata concentrata sull'area degli scavi degli anni 70 dove, grazie agli accordi con la Soprintendenza e con la Curia arcivescovile di Oristano, è stato poi possibile procedere con i nuovi scavi. In questo caso l'obiettivo delle indagini è stato più mirato e volto a determinare con precisione la posizione e profondità di eventuali resti ancora sepolti per pilotare l'ubicazione dei successivi saggi di scavo.

In effetti l'indagine geofisica su un sito già indagato dagli archeologi può apparire ridondante ma l'esigenza di una verifica preliminare ai nuovi scavi nasceva proprio dalle conclusioni dei precedenti lavori di indagine archeologica che avevano verificato l'arresto della discarica delle sculture in corrispondenza della tomba più meridionale, e pertanto era opinione diffusa che il sito non avesse più nulla da rivelare.

**Metodi.** Tra i vari metodi impiegati nel campo della ricerca archeologica quello magnetico (Chianese *et al*., 2004; Ciminale, Gallo, 2008), quello elettromagnetico (Ranieri *et al*., 2013; Welham *et al*., 2014), quello elettrico (Ranieri *et al*., 2007; Trogu *et al*., 2014) e il georadar (Goodman, 1994; Sternberg and McGill, 1995; Leckebusch, 2000; Whiting *et al*., 2001; Jol, 2008; Conyers, 2013; Piga *et al*., 2013; Urban *et al*., 2014) sono sicuramente i più diffusi.

Nel caso del presente studio la scelta del metodo più idoneo doveva soddisfare i seguenti criteri: velocità di acquisizione, precisione nel posizionamento delle anomalie, elevata

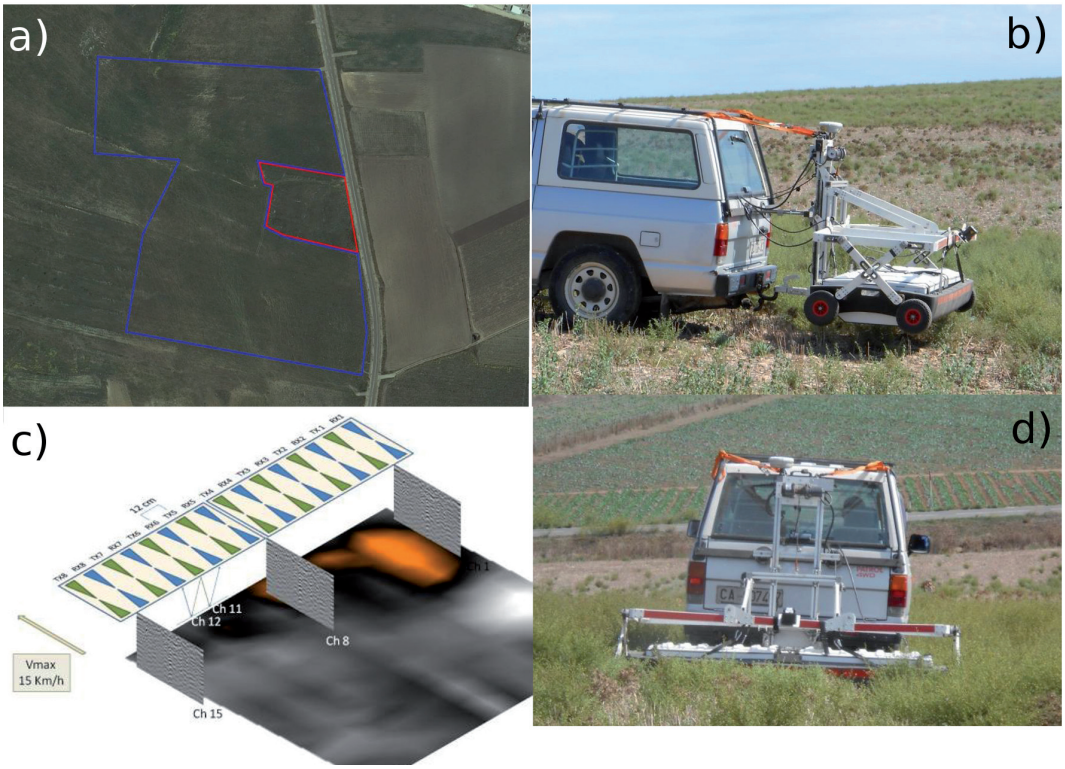


Fig. 1 – a) Le aree indagate: in blu l'area del 2013 in rosso l'area del 2014; b) d) lo Stream-X al lavoro; c) Schema concettuale dello Stream-X: Tx = antenne trasmittenti; Rx = antenne riceventi; Ch = canali di acquisizione.

risoluzione (sia verticale che orizzontale) e profondità di indagine di almeno 1,5-2 metri.

Considerando la natura del terreno da indagare, costituita da campi arati su di un versante collinare con un dislivello massimo di una ventina di metri, una superficie complessiva di quasi sette ettari e la mancanza di capisaldi fissi ai quali riferire il posizionamento delle anomalie rilevate, nessuno dei dispositivi normalmente in uso poteva soddisfare contemporaneamente tutte i requisiti richiesti.

La scelta del metodo principale di indagine è pertanto caduta sul nuovo apparato georadar multicanale con frequenza di 200 MHz "Stream-X" (IDS Italia). Questo GPR è dotato di 16 antenne da 200 MHz ciascuna che consentono l'acquisizione simultanea di 15 canali paralleli distanziati di 12 cm. L'apparato viene trainato da un veicolo e può operare ad una velocità effettiva, su un terreno come quello in esame, di circa 10 km/h. Il dispositivo è completato da un doppler con funzione di odometro e da un GPS differenziale che consente un posizionamento con precisione centimetrica delle tracce GPR (Fig. 1).

L'utilizzo di questo apparato ha consentito di soddisfare tutti i criteri richiesti, infatti la velocità di 10 km/h unita alla larghezza dell'area indagata ad ogni passaggio dell'antenna (15 canali ogni 12 cm = 168 cm) ha consentito di eseguire la prospezione su tutte le aree in soli 8 giorni lavorativi; il GPS differenziale ha consentito di posizionare esattamente le anomalie rilevate senza necessità di capisaldi di appoggio sul terreno garantendo, inoltre, la "riservatezza" dell'informazione; la risoluzione sia verticale che orizzontale (circa 9 cm nella direzione di trascinamento e 12 cm trasversalmente ad essa); una profondità utile di indagine effettiva maggiore di 1,5 metri.

Certamente anche questo apparato presenta dei limiti d'utilizzo, particolarmente su terreni sconnessi come quello in esame. Infatti poiché l'antenna viene trascinata a pochi centimetri di

distanza dal suolo, benché sia supportata da un sistema parzialmente ammortizzato, essa non è utilizzabile in presenza di ostacoli come pietre e cespugli o comunque oggetti sporgenti dal terreno; la direzione d'acquisizione è stata fortemente condizionata dall'andamento delle arature obbligando a procedere parallelamente ad esse per evitare un eccessivo effetto di saltellamento dell'antenna; poiché per la correzione differenziale del dato GPS è stata utilizzata la rete di stazioni fisse SarNet (http://www.sarnet.it) tramite connessione GPRS, occasionali problemi sulla rete hanno comportato la sospensione dell'acquisizione fino al ripristino del servizio; la dimensione complessiva dell'apparato che tra veicolo e antenna raggiunge quasi sette metri di lunghezza e due di larghezza (chiaramente la lunghezza può variare in funzione della vettura utilizzata per il rimorchio) non permette di operare su aree ristrette e quindi piccole porzioni ai bordi delle aree da investigare non sono state completamente indagate.

Limitatamente all'area dei vecchi scavi, oltre all'indagine GPR, sono state eseguite anche una prospezione magnetica e una prospezione FEM. Ulteriori 29 Tomografie elettriche (ERT) sono state condotte su una piccola area test di 28x11,75 m, con 48 elettrodi spaziati di 25 cm in modalità Wenner-Schlumberger, sempre all'interno dell'area degli scavi degli anni 70.

Preliminarmente all'inizio delle indagini sul terreno è stata eseguita un'analisi delle foto aeree e satellitari.

L'elaborazione dei dati GPR è stata eseguita mediante il software dedicato GredHD e i dati ERT sono stati invertiti mediante il software Res2DInv. I dati magnetici ed elettromagnetici sono stati preliminarmente ripuliti degli spikes e quindi rappresentati mediante vari software di visualizzazione.

**Discussione dei risultati.** La discussione dei risultati ottenuti da questa campagna geofisica parte dai dati della campagna del 2014, nell'area di proprietà della Curia arcivescovile di Oristano dove sono stati successivamente eseguiti i saggi di scavo che hanno consentito di interpretare le varie tipologie di anomalie registrate per poi estendere l'interpretazione ai dati del 2013, dove non è stato ancora possibile eseguire gli scavi. Di seguito vengono illustrati e discussi i risultati della prospezione GPR.

**L'area di proprietà della Curia arcivescovile di Oristano (prospezione 2014).** Le indagini condotte sull'area di proprietà della Curia arcivescovile di Oristano hanno chiaramente mostrato la presenza di anomalie estese ben oltre i limiti dei precedenti scavi. Sia i dati GPR che quelli FEM hanno mostrato la presenza di anomalie allineate secondo direttrici ben precise, che in alcuni casi sono perfettamente coerenti con i dati provenienti dagli scavi archeologici degli anni '70. L'indagine magnetometrica non ha purtroppo restituito risultati di particolare interesse nelle aree ancora non scavate probabilmente per via della diffusa presenza di blocchi di basalto sepolti, provenienti dal piccolo nuraghe presente nel sito, mentre ha ben definito i bordi e i resti dei vecchi scavi che attualmente sono nuovamente sepolti. Sono state identificate anche altre direttrici di anomalie che restano di dubbia interpretazione. I risultati delle tomografie elettriche, eseguite parallelamente a distanza di un metro l'una dall'altra, in alcuni casi hanno evidenziato la presenza di anomalie isolate alla profondità di circa 50-100 cm.

Sulla base dei risultati della prospezione GPR sono stati effettuati saggi di scavo nell'ambito di cinque quadrati (di 100 mq ciascuno) nel settore meridionale dell'area.

I dati più rilevanti sono stati acquisiti nei quadrati SE-B3-79 e SE-B3-89 dislocati immediatamente a sud dell'area precedentemente scavata e dove, fino a questo momento, si riteneva non ci dovessero essere ulteriori sviluppi della necropoli.

L'analisi geofisica ha verificato, lungo un'asse NNE / SSO dei citati quadrati 79 e 89, per una lunghezza di m 15 ed una larghezza di circa m 3, una sequenza di anomalie a quote varie.

Due anomalie inclinate sovrastanti le altre, di piano trapezoidale di circa m 2,25 di lunghezza x 0,60 di larghezza, si sono rivelate pertinenti a due betili troncoconici; l'anomalia trapezoidale più meridionale del quadrato 89 si è definita come appartenente ad un betilo in arenaria. Un secondo betilo, di dimensioni analoghe al precedente, corrispondente alla seconda anomalia trapezoidale, è stato individuato nel quadrato 79.

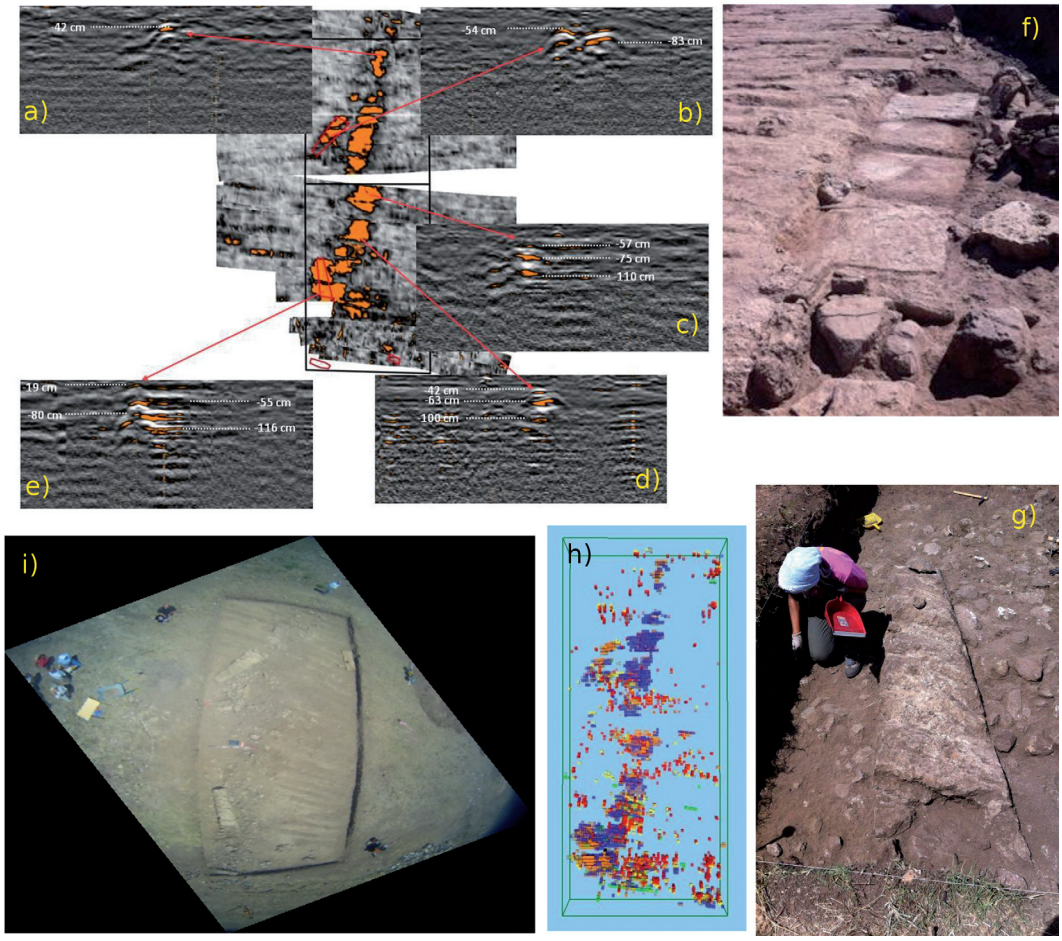


Fig. 2 – Area di proprietà della Curia (indagini 2014). Time-Slice a 60 cm di profondità. I rettangoli neri delimitano i due saggi di scavo. a) lastra con sottostante tomba?; c) d) lastre con tombe sottostanti; b) e) betili e lastre con tombe sottostanti; f) la parte settentrionale dello scavo con le quattro lastre di copertura delle tombe; g) il primo betilo rinvenuto nella parte meridionale dello scavo; h) ricostruzione 3D delle anomalie GPR realizzata selezionando le anomalie con ampiezza maggiore del 20% del massimo valore registrato. I colori si riferiscono alla profondità: verde da 0 a 30 cm, arancio da 30 a 60 cm, blu da 60 a 100 cm, giallo da 100 a 150 cm, rosso da 150 a 200 cm; i) foto aerea dello scavo realizzata da un drone. Sono ben visibili i betili mentre le tombe a pozzetto e le lastre non erano ancora state evidenziate al momento della ripresa.

Varie anomalie quadrate sono risultate riferite dallo scavo a lastroni di copertura di tombe; anomalie più caotiche, di varia estensione, sono risultate appartenenti a frammenti di sculture in calcare, a lastre e a pietre brute corrispondenti alla discarica.

Al di sotto dello strato della discarica, sono stati evidenziate due serie di quattro lastroni in arenaria (m 1,15 x 1,10) ciascuna, disposte parallelamente ed orientate NNE-SSO con la serie più settentrionale spostata di circa 90 cm a ovest rispetto a quella meridionale, pertinenti, con probabilità, a due filari di tombe a pozzetto, del genere di quelle del settore settentrionale della necropoli [scavi degli anni '70, Bedini *et al.* (2012)]. Sono inoltre venute alla luce diverse tombe a pozzetto.

Il confronto tra i dati di scavo e i risultati delle indagini GPR ha consentito di classificare almeno tre tipi di anomalie differenti: betili o comunque oggetti massivi (busti di statue?) di dimensioni medio-grandi; lastre di copertura delle tombe; frammenti di statue o di lastre.

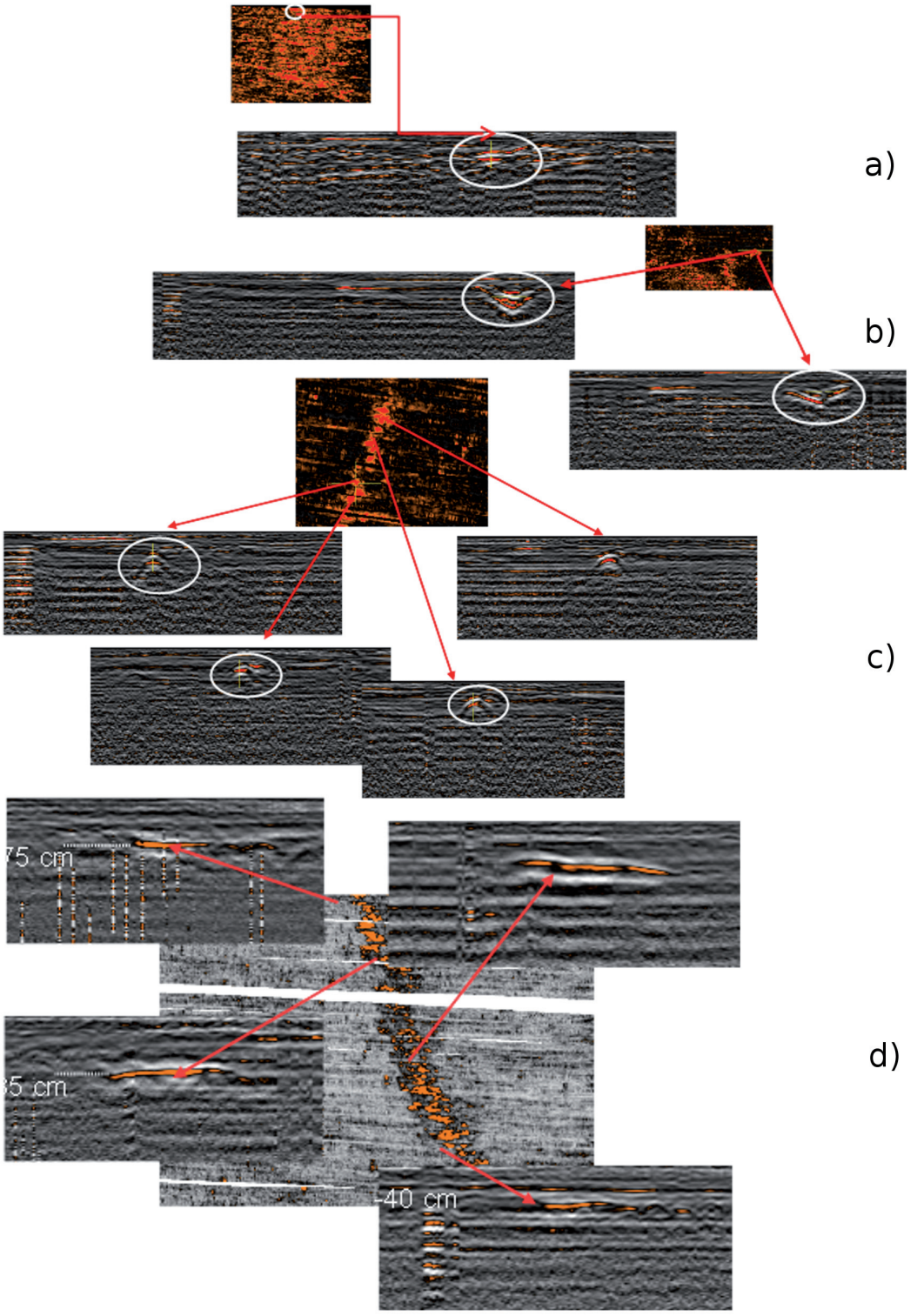


Fig. 3 – Aree esterne alla proprietà della Curia (indagini 2013). Alcuni esempi di anomalie: a) strada?; b) canali riempiti da accumuli di frammenti di statue?; c) tombe?; d) strada?

Altri due tipi di anomalie piuttosto caratteristici, benché ancora non verificati dagli scavi archeologici, possono essere ragionevolmente attribuiti, sulla base delle attuali conoscenze del sito, a canali con riempimenti di discarica (frammenti di statue, betili?) e strade (Fig. 2).

**Le aree circostanti la proprietà della Curia arcivescovile di Oristano (prospezione 2013).** Sulla base dell'interpretazione dei risultati ottenuti nelle indagini 2014, nelle aree circostanti indagate nel 2013 sono state riconosciute diverse aree variamente orientate dove si sono potute identificare alcune anomalie probabilmente riconducibili a tombe, strade e discariche di frammenti (Fig. 3).

**Conclusioni.** Dai risultati delle indagini geofisiche e degli scavi archeologici fin qui condotti si possono trarre alcune conclusioni, che rispondono solo in minima parte alle domande poste in premessa:

1. l'area della necropoli è certamente molto più vasta di quanto prima ipotizzato, estendendosi ben oltre il terreno di proprietà della Curia arcivescovile di Oristano dove vennero alla luce i primi reperti;
2. i risultati dello scavo nei settori 79 e 89, selezionati sulla base dei dati GPR, hanno accertato la prosecuzione verso sud della necropoli rinvenuta nei precedenti scavi;
3. lo scavo ha messo in evidenza l'ottima corrispondenza tra l'ubicazione e la profondità delle anomalie GPR e i rinvenimenti archeologici;
4. sulla base della comparazione tra rinvenimenti archeologici ed anomalie GPR è stato possibile riconoscere almeno tre tipi di anomalie relative a: oggetti massivi di medio-grandi dimensioni (betili, busti di statue...); lastre in arenaria di copertura tombale; accumuli di frammenti di statue, lastre ecc.. Altri due tipologie di anomalie caratteristiche e ben distinguibili, sulla base delle conoscenze attuali del sito, possono essere con molta probabilità attribuite a accumuli di discarica (di frammenti di statue) e a strade.

L'utilizzo di un apparato veloce, affidabile e ad alta risoluzione come lo Stream-X apre nuovi scenari per la prospezione archeologica. Infatti, senza l'uso di questo strumento non sarebbe stato possibile eseguire una prospezione GPR su di un'area di più di 6 ettari in soli 8 giorni. Inoltre la spaziatura di soli 12 cm tra ciascun canale consente di ottenere una copertura molto accurata dell'area e delle time-slices di ottima qualità. L'accurato posizionamento dei dati mediante GPS differenziale consente un rapido e preciso posizionamento delle anomalie sul terreno permettendo un'accurata selezione dei siti di saggio con un sensibile risparmio di tempi e costi.

**Riconoscimenti.** Si ringraziano Marcello Ciminale, Giovanni Montrone, Sergio Calcina, Luca Piroddi, Francesco Loddo, Luigi Noli e Mario Sitzia che hanno partecipato ai lavori di prospezione geofisica e Emina Usai, Paolo Bernardini, Piergiorgio Spanu, Luciana Tocco, Adriana Scarpa e Barbara Panico che hanno condotto gli scavi. Si ringraziano inoltre il Consorzio UNO di Oristano e Pierluigi Farci per il loro aiuto. Questo studio è stato finanziato dalla Regione Autonoma della Sardegna, L.7/2007.

## Bibliografia

A. Bedini, C. Tronchetti, G. Ugas, R. Zucca (2012). Giganti di Pietra - L'Heroon che cambia la storia della Sardegna e del Mediterraneo. Fabula Editore, Cagliari.

D. Chianese, M. D'Emilio, S. Di Salvia, V. Lapenna, M. Ragosta, E. Rizzo (2004) Magnetic mapping, ground penetrating radar surveys and magnetic susceptibility measurements for the study of the archaeological site of Serra di Vaglio (southern Italy). Journal of Archaeological Science, 31(5), 633-643.

M. Ciminale, D. Gallo (2008). High-resolution magnetic survey in a quasi-urban environment. Near Surface Geophysics, 6, 97-103. ISSN: 1569-4445.

L.B. Conyers (2013) Ground-penetrating radar for archaeology, AltaMira Press.

D. Goodman (1994) Ground-penetrating radar simulation in engineering and archaeology. Geophysics, 59, 224-232.

H. M. Jol (2008) Ground penetrating radar theory and applications, Elsevier.

J. Leckebusch (2000) Two-and three-dimensional ground-penetrating radar surveys across a medieval choir: a case study in archaeology. Archaeological Prospection, 7, 189-200.

G. Lilliu. (1997). La grande statuaria nella Sardegna nuragica. Atti Accademia dei Lincei. Memorie Sc. Mor. Stor. Filol., ser. IX, vol. IX, 281-385.

C. Piga, L. Piroddi, E. Pompianu, G. Ranieri, S. Stocco, A. Trogu (2013). Integrated geophysical and aerial sensing methods for archaeology: a case history in the Punic site of Villamar, (Sardinia – Italy).Remote Sens., 5, 1-x manuscripts; doi:10.3390/rs50x000x

G. Ranieri, D. Schirru, A. Trogu, A. Saba (2013). Towards an integration of laser scanner survey and geophysical prospection: an example from the Nuragic Site of Mont 'e Nuxi – Esterzili (Sardinia, Italy). Proceedings of the 10th International Conference on Archaeological Prospection 2013. Vienna, 29 Marzo-2 Giugno 2013.

G. Ranieri, L. Sharpe, A. Trogu, C. Piga (2007). Time-lapse electrical resistivity tomography to delineate mud structures in archaeological prospections. Near Surface Geophysics, 5, 375-382. ISSN: 1569-4445.

B.K. Sternberg, J.W. McGill (1995) Archaeology studies in southern Arizona using ground penetrating radar. Journal of Applied Geophysics, 33, 209-225.

A. Trogu, G. Ranieri, S. Calcina, L. Piroddi, (2014). The Ancient Roman Aqueduct of Karales (Cagliari, Sardinia, Italy): Applicability of Geophysics Methods to Finding the Underground Remains. Archaeological Prospection, 21 (3), 157-168, doi: 10.1002/arp.1471

T.M. Urban, J.F. Leon, S.W. Manning, K.D. Fisher (2014). High resolution GPR mapping of Late Bronze Age architecture at Kalavasos-*Ayios Dhimitrios*, Cyprus. Journal of Applied Geophysics, 107, 129–136, DOI: 10.1016/j.jappgeo.2014.05.020.

K. Welham, J. Fleisher, P. Cheetham, H. Manley, C. Steele, S. Wynne-Jones, (2014) Geophysical Survey in Sub-Saharan Africa: magnetic and Electromagnetic Investigation of the UNESCO World Heritage Site of Songo Mnara, Tanzania. Archaeological Prospection, doi:10.1002/arp.1487.

B.M. Whiting, D.P. McFarland, S. Hackenberger (2001) Three-dimensional GPR study of a prehistoric site in Barbados, West Indies. Journal of Applied Geophysics, 47, 217-226.

## FINAL RESULTS OF "TERME CARONTE" GEOTHERMAL AREA (CALABRIA, ITALY)

**E. Rizzo[1], G. Iovine[2], F. Muto[3], A. Caputi[1], L. Capozzoli[1], V. Giampaolo[1], L. Pizzino[4], A. Manzella[5]**

*[1] CNR-IMAA, Tito (PZ), Italy*
*[2] CNR-IRPI U.O.S. of Cosenza, Italy*
*[3] University of Calabria, Rende, Italy*
*[4] INGV, Roma, Italy*
*[5] CNR-IGG, Pisa, Italy*

**Introduction.** The VIGOR project is aimed at assessing the geothermal potential and exploring geothermal resources of four regions in southern Italy, and it is part of the activities of the Interregional Programme "Renewable Energies and Energy Savings FESR 2007-2013 – Axes I Activity line 1.4 "Experimental Actions in Geothermal Energy".

During the final stage of the project, a bore-hole has been realized and reached a depth of more then 900 m. This direct investigation is the last part of the investigation of the low-medium enthalpy geothermal resources at "Terme Caronte", in the Lamezia Terme territory (Calabria - Southern Italy). The assessment work, characterized by geophysical, geochemical and geological investigation around the localized hot springs,in the Terme Caronte area, has defined the subsurface and the deep structures correlated to the deep geothermal fluid circulation.

**Geological, geochemical and geophysical previous data: first part of Vigor project.** The studied area is located at the westernmost edge of the Catanzaro Graben (Fig. 1), one of the most important cross-dislocations of the Calabrian Arc (hereafter referred to CA), where metamorphic and crystalline Alpine rocks and Hercynian rocks (Calabrian basement Complex) cropping out in the Sila massif (upperplate), overthrust on apennine carbonate units (underplate). In the frame of the Mediterranean mobile belt, the Calabrian Arc is an arc-shaped continental fragment located between the E-W trending Sicilian Maghrebides, to the south, and the NW–SE trending Apennines, to the north (Ogniben, 1973; Amodio-Morelli *et al*., 1976; Bonardi *et al*., 2001, and references therein). All these rocks are dissected by a complex assemblage of high-angle faults, which can be ordered in a number of major systems and patterns, partly related to transcurrent faulting. As a whole, the regional structural framework is characterized

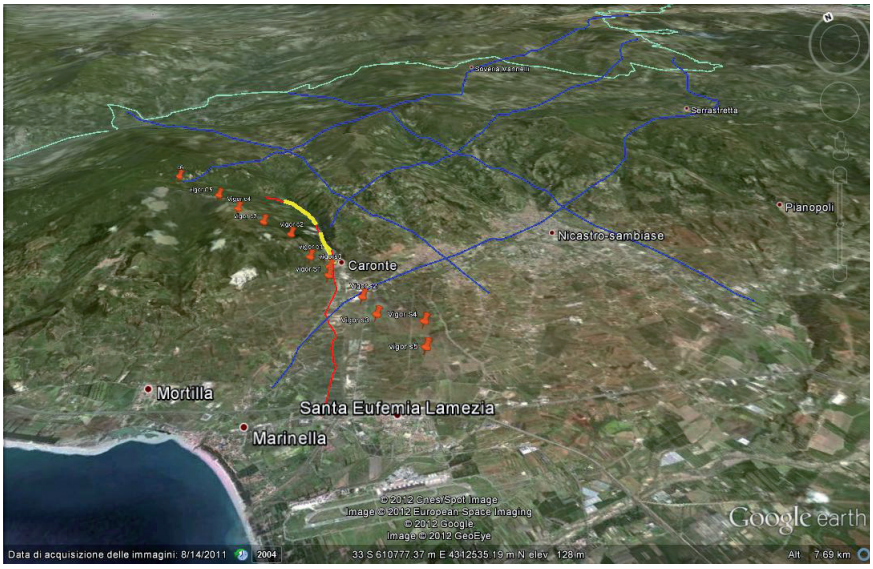


Fig. 1 – The location of the geophysical profiles. Red marks indicate the MT stations, red lines the DERT stations and the blue lines the seismic profiles.

by a low-angle thrust sheet assemblage, dissected by high-angle faults with normal/oblique kinematics. After the deformations associated to tectonic evolution of Calabrian Arc, during an intense post-orogenic extensional tectonic phase, several marine sedimentary basins were developed corresponding to main segments of the faults, arranged both parallel and transverse to the direction of the Arc and raised in blocks, giving a typical structure at horst and graben (Ghisetti, 1979; Ghisetti and Vezzani, 1979).

In the study area, a Plio-Pleistocene marine succession of clays, sands, sandostones and conglomerates outcrops. In the northeastern sector of Terme Caronte, a terrigenous, evaporitic and carbonate mio-pliocenic sedimentary succession overlies the igneous-metamorphic basement of the Sila Unit. These deposits are strongly controlled by NW- strike-slip system, arranged in a right-hand en´echelon pattern (Tansi *et al*., 2007). Slate and metapelite crop out in test area, in particular belonging to the Paleozoic Bagni Unit. The lowest group of the orogenic tectonic piling is formed by a Mesozoic carbonate complex. In literature, their outcrops are traditionally considered as "tectonic windows" of the Apennine Chain (e.g. Amodio-Morelli *et al*., 1976; Tortorici, 1981; Tansi *et al*., 2007). The Mesozoic-Tertiary continental-margin carbonates, outcropping in Terme Caronte district, were extruded within transpressional areas. The uplift the deep-seated units of the Chain can in fact generally be ascribed, at a regional scale, to reverse-oblique strike-slip movements along NW-SE regional shear zones (Tansi *et al*., 2007). From hydrogeological point of you, the Terme Caronte area should be divided by three hydrogeological sectors. The recent debris deposits complex, along the main rivers and coastal plain, shows the most interesting geological characteristics in terms of resource volumes stored and favourable logistical conditions. The Plio-Pleistocene sandstone and conglomerate is characterized by high permeability and great thickness and, finally, the Mesozoic carbonate complex has a deepwater circulation mainly occurs in high-permeability fractured zones associated to the main faults.

Geochemical data provided in the Terme Caronte district were acquired in order to define the origin and interactions of the circulating fluids and to investigate possible relationships with the local faults. Thermal and cold waters were sampled during the field work in the last year, showing outlet temperature ranging between 10°C and 39°C. The thermal waters sampled near

Fig. 2 – A picture of the drill machine.

Terme Caronte are close to intersection of two faults: a NS trending fault, along the Bagni River, and a WNW-ESE-trending regional strike-slip fault system (Ghisetti and Vezzani, 1981; Tansi *et al*., 2005; Tansi *et al*., 2007). The low heat flow measured both in the Caronte area (50 mW/m$^2$, Cataldi *et al*., 1995), and in the whole Calabria rules out magma intrusions at shallow depth in the crust. This implies that the thermal character of the investigated waters is a consequence of the deepening of the hydrological circuit in fractured areas marked by a normal geothermal gradient (~30°C/km) allowing the existence of low to medium-enthalpy aquifers at a depth of about 1-3 km. For some of the thermal waters, the temperatures calculated by different geothermometers show a limited cooling as a result of a fast uprise through highly permeable discontinuities (namely the local faults). Classical geothermometric relations applied on thermal waters of Caronte (Na/K and K/Mg in Fig. 2, from Italiano *et al*. (2010) to test their suitability to be used for the estimation of deep temperature conditions provided contrasting and unreal values. This is mainly due to the particular geological and hydrochemical settings of the area; as a result, chemistry of thermal waters is due to isochemical dissolution of country rock-forming minerals rather than a real equilibrium with them. The only reliable geothermometer for the Caronte system (Marini *et al*., 1986) indicates a deep reservoir temperature in the range 55-65°C, confirming the low to medium enthalpy of the geothermal system.

Moreover, in the Terme Caronte area new deep geophysical investigations were carried out and old seismic lines were re-elaborated (Fig. 1). The main target zones for geothermal utilization is the Carbonate basement rocks, made of limestone/dolomite of Mesozoic age. This kind of layers is thought to have the highest permeability, and its thickness and extent are also significant. The mentioned targeted reservoir is below the Calabrian Terranes. The seismic available VIDEPI data was used to trace the lateral extent of these rock types and to locate fault zones within them. The seismic lines all came with Two-Way-Time (TWT) in ms as a depth reference. Seismic interpretation was focused on to identify the following seismostratigraphic horizons: slate and metapelite (bottom of Calabrian Terranes) horizon and Mesozoic carbonate horizon. Easy identification is reflected by the observed continuity, of Slate and metapelite layers and of tectonic features. Mesozoic carbonate seismic unit consists of low continuity, moderate amplitude and low frequency reflectors with chaotic configuration, poor quality is attributed to seismic lines showing this layers and their tectonic features controlling the permeability and flow patterns. The E-W seismic profile shows low-angle overthrust contacts with basement units (Mesozoic Carbonate and bottom of Calabrian Terranes) obliterated by subsequent overprinting of high-angle faults. Seismic profiles covering the Terme Caronte area demonstrate the presence of a fractured carbonate reservoir, which is deformed to shape a partly buried positive flower structure.

One Deep Electrical Resistivity Tomography (DERT) and one magnetotelluric (MT) profile were carried out in the investigated area. The Deep Electrical Resistivity Tomography carried out in the Terme Caronte did not allow to reach an investigation depth of 1000 m. On the contrary, the Magnetotelluric (MT) investigation allowed to retrieve information on the distribution of the electrical properties from hundred meters down to five kilometers. Under this point of view, the MT method can be considered a useful and non-invasive tool to investigate the Earth interior. In the framework of the project, DERT and MT data show clearly the contact between different electrical layers which should be associated to the geological formations.

Moreover, the main structure associated to the geothermal system and the connection with the hot springs of Terme Caronte are detected.

Finally, in the plain of the town of Lamezia Terme (CZ) reflection and refraction seismic surveys were carried out at high resolution. A seismic profile was acquired and reached a total of 2975 m of investigation depth. The seismic reflection section shows structures related to sub-horizontal stratification on an inclined base and displaced by faults. On the migrated section, in the northern part of the section a series of strong reflectors is evident at a depth of 600-800 m. By the geological characteristics and seismic velocity (> 3000 m/s), these reflectors most probably represent the top of the bedrock. These reflectors deepen toward south, where they are found at a depth of 1200-1400 m. The deepening of the bedrock top and corresponding reflectors at the southern edge of the profile is most probably related to tectonic dislocations, which are evident at surface.

**Data coming from a new deep bore-hole.** Due to the lack of geothermal gradient data in the area of Terme Caronte only an approximate estimate of the depth reached by the thermal waters was possible. A deep borehole integrated with geophysical measurements was therefore planned, in order to improve the assessment of the geothermal potential of the area, and to increase the current knowledge on the relationship between heat flow and deep tectonics, particularly complex in this sector of the Calabrian Arc.

The borehole was drilled about 5 km south of the Terme Caronte hot spring, on the Catanzaro Graben. The location of the well was designed combining logistic aspects with the geophysical results obtained by DERT, MT and reflection seismic acquisitions.

The well was drilled in the summer 2014 and reached a depth of about 900 m. Several drilling problems, due to the different confined aquifer located in the various geological layers, constrained the company to change the type of coring several times.

From geological point of view, the deposits down to 350 m should be associated to late Pleistocene - lower??? units. Below them, down to a depth of about 600 Gelasian (formerly Upper Pliocene) - Early Pleistocene units can be found. From 500-600 m to 800 m Pliocene (Piacenziano-Zanclean) units have been drilled. The final part, from about 800 until the bottom, the cores show conglomeratic terms that are the base of the Pliocene and the roof of the Messinian. The detailed stratrigraphy of the geological formations was obtained and a comparison with the seismic and geoelectrical data was defined using a constrained approach. Therefore, the well data provided more useful information on the geological and hydrogeological complexes in the area and on the potential geothermal in the plain of Lamezia.

**Conclusion.** By integrating geological, geochemical, indirect and direct data, the potential geothermal reservoirs of the study area has been investigated indicating the target depth, expected outflow temperature, and yield of the expected reservoir. The integrated interpretation of surface geology, geochemical analysis, seismic reflection profiles, and Electrical and Electromagnetic data integrated with the borehole stratigraphy, allowed to defining the main features of the overall reservoir/caprock system and its structural-stratigraphic setting. Moreover, the electric and electromagnetic results, calibrated with surface geology, focused on the structural contact between Mesozoic carbonate and alluvial fans that is marked by most of the thermal spring clusters of the area. Thermal water, outcropping at Terme Caronte, resulted to rise along the NW-SE-trending left-lateral strike-slip fault system that separates the Plio-Quaternary Catanzaro Graben from the southern edge of the Sila Massif, i.e. where the entire pile of the Calabrian Terranes and underlying Mesozoic Carbonate Complex crop out, and the oldest N-S fault system. Also, the area of contact with the impermeable Neogene deposits constitute a threshold permeability which tends to hinder the transfer to the Plains of Lamezia Terme. The geochemical studies have demonstrated that the water of the springs of Terme Charon not have elevated shuffles with those surface, demonstrating the presence of a rapid ascent along the two indicated main fault system. Furthermore, considering a thermal gradient of 30-33 °C/km, it can be assumed a depth of the circuit between 2 and 3 km, taking into account the estimated

temperature in depth (55-60 ° C). Finally, given the presence of elements that describe the waters of the spring Terme Caronte exchange of meteoric origin with water-carbonate rock type, it is assumed that the geothermal reservoir is fed by rainwater that infiltrates in the southern sector of the Sila Massif, penetrating into the metamorphic units showing a surface permeability for billing especially along the areas affected by regional tectonic. Once infiltrated, the water will deepen in the geothermal reservoir in the complex carbonate below a depth of about 2-3 km.

**Acknowledgements.** The present activity has been performed in the frame of the VIGOR Project, aimed at assessing the geothermal potential and exploring geothermal resources of four regions in southern Italy. VIGOR is part of the activities of the Interregional Programme "Renewable Energies and Energy Savings FESR 2007-2013 – Axes I Activity line 1.4 "Experimental Actions in Geothermal Energy". The authors acknowledge the management of VIGOR Project, and in particular Dr. Piezzo of MiSE-DGENRE (Directorate General for Nuclear Energy, Renewable Energy and Energy Efficiency of the Ministry for Economic Development) and Dr. Brugnoli, Director of CNR-DTA (National Research Council of Italy, Department of Sciences of the EarthSystem and Environmental Technologies). The authors warmly thank citizen of Lamezia Town and the staff of the mayor for its istutional help and the Region Calabria energy office,. Morevoer, the authors thank the water company SORICAL for the support during the sampling. Moreover, the authors thank the President of Thermal spa Dott. Cataldi for Terme Caronte springs historical data and the interesting narrations about the spa history, belonging to his family since three centuries. Finally, authors thank ENI that supported this research providing the seismic reflection stack sections available for the studied area

## References

Amodio-Morelli L., Bonardi G., Colonna V., Dietrich D., Giunta G., Ippolito F., Liguori V., Lorenzoni S., Paglionico A., Perrone V., Piccarreta G., Russo M., Scandone P., Zanettin-Lorenzoni E. and Zuppetta A.; 1976: *L'Arco Calabro-Peloritano nell'orogene appennino-maghrebide*. Mem. Soc. Geol. Ital., **17**, 1–60.

Bonardi G., Cavazza W., Perrone V. and Rossi R.; 2001: *Calabria-Peloritani Terrane and northern Ionian Sea*. In: Vai G.B. and Martini J.P. (eds), Anatomy of an Orogen: The Appennines and the Adjacent Mediterranean Basins, Kluwer Acad., Norwell, MA, pp. 287–306.

Bousquet J.C. and Dubois R.; 1967: *Decouverte de niveaux anisiens et caracteres du metamorphisme alpin dan la region de Lungro (Calabre)*. Comptes rendus des seances de l'Academie des Sciences, **264**, 204–207.

Bousquet J.C. and Gradjacquet J.C.; 1969: *Structure de l'Apennin Calabro-Lucanien (Italie meridional)*. Comptes rendus des seances de l'Academie des Sciences, **268**, 13–16.

Cataldi R., Mongelli F., Squarci P., Taffi L., Zito G. and Calore C.; 1995: *Geothermal ranking of Italian territory*. Geothermics, **24**, 115–129.

Dubois R.; 1966: *Position des granites de l'axe Decollatura-Conflenti-Martirano dans une structure probablement hercynienne (Calabre centrale, Italie)*. Comptes rendus des seances de l'Academie des Sciences, **262** (D), 1331–1333.

Egbert G.D. and Booker J.R.; 1986: *Robust estimation of geomagnetic transfer functions*. Geophysical Journal. Royal Astronomical Society, **87**, 173-194.

Ghisetti F.; 1979: *Evoluzione neotettonica dei principali sistemi di faglie della Calabria Centrale*. Bollettino della Società Geologica Italiana, **98**, 387-430.

Ghisetti F. and Vezzani L.; 1979: *The geodynamic evolution of the crustal structures of Calabria and Sicily*. I.G.U. Commission on Geomorphological Survey and Mapping. 15th Plen. Meeting, Proceedings, pp. 1-12.

Ghisetti F. and Vezzani L.; 1981: *Contribution of structural analysis to understanding the geodynamic evolution of the Calabrian Arc (Southern Italy)*. J. Struct. Geol., **3**, 371–381.

Italiano F., Bonfanti P., Pizzino L. and Quattrocchi F.; 2010: *Geochemistry of fluids discharged over the seismic area of the Southern Apennines (Calabria region, Southern Italy): Implications for Fluid-Fault relationships*. Applied Geochemistry, **25**, 540–554.

Marini L., Chiodini G. and Cioni R.; 1986: *New geothermometers for carbonate- evaporite geothermal reservoirs*. Geothermics, **15**, 77-86.

Ogniben L.; 1973: *Schema geologico della Calabria in base ai dati odierni*. Geol. Romana, **12**, 243–585.

Tansi C., Iovine G. and Folino Gallo M.; 2005: *Tettonica attiva e recente, e manifestazioni gravitative profonde, lungo il bordo orientale del graben del Fiume Crati (Calabria Settentrionale) (Present and recent tectonics, and deep-gravitational phenomena, along the eastern boundary of the R. Crati graben (Northern Calabria)*. Bollettino della Società Geologica Italiana, **124** (3), 563–578.

Tansi C., Muto F., Critelli S. and Iovine G.; 2007: *Neogene-Quaternary strike-slip tectonics in the central Calabrian Arc (Southern Italy)*. Journal of Geodinamics, **43**, 393-414.

Tortorici L.; 1981: *Analisi delle deformazioni fragili dei sedimenti postorogeni della Calabria settentrionale (Analysis of fragile deformations in the post-orogenic sediments of northern Calabria)*. Bollettino della Società Geologica Italiana, **100**, 291–308.

# CASE HISTORY: A MAGNETIC AND GPR PROSPECTION ON A ROMAN RURAL VILLA IN WESTERN PIEDMONT (ITALY)

**L. Sambuelli[1], D. Elia[2], V. Meirano[2], C. Colombero[3]**
*[1] Dipartimento di Ingegneria dell'ambiente, del Territorio e delle Infrastrutture – Politecnico di Torino, Italy*
*[2] Dipartimento di Studi Storici – Università di Torino, Italy*
*[3] Dipartimento di Scienze della Terra – Università di Torino, Italy*

**Foreword.** Since the half of the past century the use of geophysical methods for archaeological prospection has been proposed (Segre, 1958; Rees, 1962). However only in the few past decades the evolution of theory, software and instrumentation has allowed for the possibility of adopting multi methods prospection with reasonable execution times and costs. New technologies, such as ERT and GPR, have been added to the traditional ones (Pasquinucci and Trément, 2000; Gaffney and Gater, 2003). On the occasion of exploring an archaeological site in western Piedmont, we then decided to proceed to a multimethod survey using fast methods and taking also into account the information achievable after a 2D or 3D data processing and/or rendering. This choice restricted the methodologies to magnetic and GPR prospecting. The non contact resistance imaging, in our opinion, still gives too smeared results even if indicative of resistivity anomalies. We selected the magnetic prospecting because of the remarkable size of some of the walls actually excavated even if, as we explain in the geological context, the probability of collecting a significant amount of noise was high.

**The geological context.** The village of Costigliole Saluzzo (CN) is located in north-western Italy, at the end of the Varaita Valley, at the edge between north-western Alps and the wide piedmont's plain. The Varaita Valley elongates in WE direction from the Monviso Massif and the administrative border with France (Fig. 1).

From a geological point of view, two main tectono-metamorphic units outcrop in this area: the Dora-Maira Massif, in the lower part of the valley, and the Piedmontese Zone with the Monviso Ophiolitic Massif in the upper part, from the town of Sampeyre to France.

The Dora-Maira Massif is a continental crust unit mainly constituted by ercinic and pre-ercinic methamorphites (mainly gneiss and micascists). On the other hand, the upper part of the valley is characterized by oceanic lithologies (Calcescists with Green Stones, Jurassic-Cretaceous) overthrusted on the Dora-Maira Unit. The Monviso ophiolite complex is a north-trending body, 35 km long and up to 8 km wide, sandwiched structurally between the underlying Dora-Maira thrust units and the tectonically higher, dominantly metasedimentary, units of the Piedmontese Zone (Lombardo *et al.*, 2002).

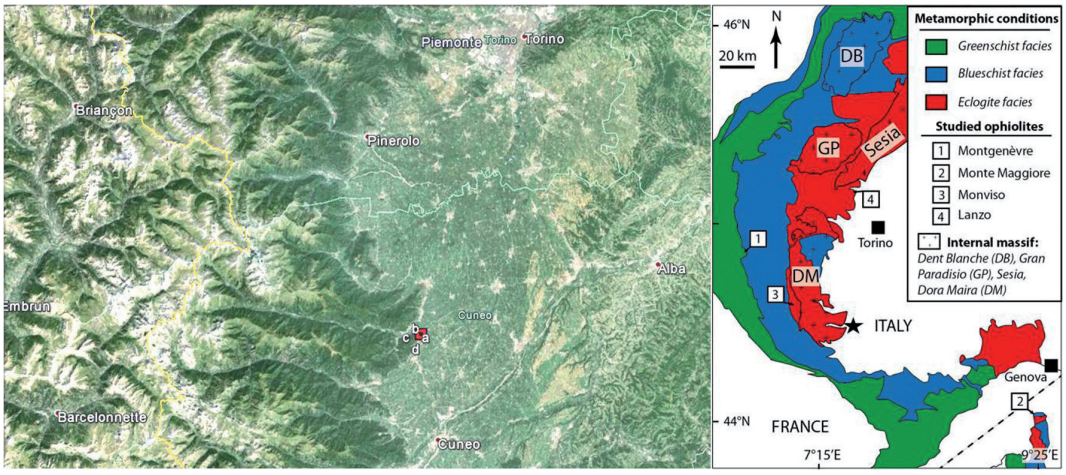


Fig. 1 – On the left the geographical location of the archaeological site: the white letters refer to the surveyed area. On the right the geological map of western Alps; the black star refers to the surveyed area.

The municipal area of Costigliole Saluzzo mainly lies on quaternary deposits mainly consisting of fluvioglacial and fluvial sediments (Pleistocene-Holocene) of the big alluvial fan apparatus of the Varaita River that opens towards the plain with slight slop (about 1%). The deposits are mainly made by medium-to-coarse gravels with a sandy matrix and a wide variety of pebbles and blocks of variable size, resulting from the erosion of the lithologies of the whole valley, can also be found.

The alluvial deposits in the archaeological site show on the surface the presence of centimetric to decimetric pebbles. In the exploratory trenches and excavations, however, the soil seems mainly consisting of silt and clay down to about 3 m. Therefore most of the pebbles are likely due to the destruction of the ancient walls and structures. The Roman remain walls, in fact, are largely made up of these natural pebbles and blocks. From a visual expeditious analysis on the field, the pebble lithology is largely represented by serpentinites and metabasites, probably outcoming from the Monviso Massif. Monviso serpentinites consist of antigorite and magnetite, with subordinate brucite, Mg-chlorite, tremolite, diopside, Ti-clinohumite and haematite (Balestro *et al*., 2011; Castelli and Compagnoni, 2007). Magnetite grains are generally heterogeneously distributed in the serpentine matrix but locally they appear aligned to form thin bands that cross rocks following preferential directions (Compagnoni and Fiora, 1976). Geochemical analysis of the bulk rock composition shows a very high percentage of iron oxides, variable from 6% to more than 13% (Hattori and Guillot, 2007).

**The archaeological context.** The ruins of a wide *villa rustica* (Fig. 2) belonging to the Roman imperial period (Ist to IIIrd centuries AD) were unearthed by the University of Turin at the southern periphery of modern Costigliole Saluzzo and are still under excavation (Barra Bagnasco, 2003, 2005; Barra Bagnasco and Elia, 2007; Elia and Meirano, 2008, 2008-2009, 2012a, 2012b; Elia, *et al*., 2013). After the destruction and the abandonment of the settlement, an occupation of the site is attested during the late-antique period (IVth-Vth centuries AD). The area, showing structures and erratic ancient materials, extends over ca 3 hectares. Measuring ca 56 x 85 m in its major phase, the main building reaches an extent of around 5000 m$^2$.

The explorations carried out in the last few years allow for the identification of a "U-shaped" villa characterized by a clearly-defined plan which represents an *unicum* in western *Gallia Cisalpina* so far. The evidence recovered supports the identification of the functions of the different sections of the building, with regard to both the *pars rustica* and the *pars urbana*. The main body is situated in the eastern part and shows an anomalous extent for this kind of buildings. The western part consists in a wide court (more than 1200 m$^2$) delimited by two long wings. These wings were destined to stocking agricultural products and to housing the


Fig. 2 – Plan of the villa (left) and picture of the walls unearthed after earlier excavation campaigns (right).

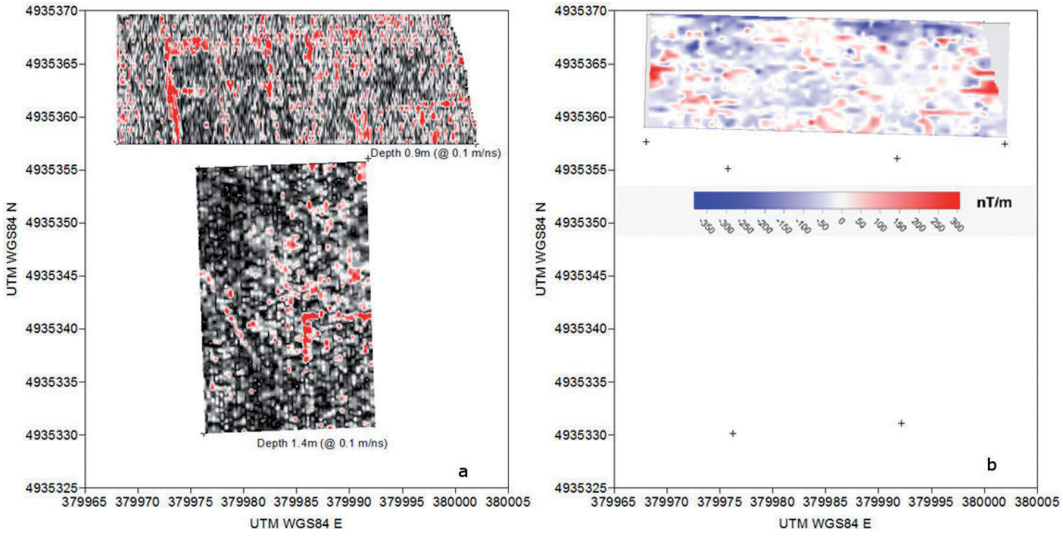


Fig. 3 – a) GPR timeslices on the south and north areas. b) Map of the vertical gradient of the TMF. Near the northern side of the area a metallic fence, that could not be removed, strongly influenced the measurements.

productive units (namely, a wine press room), while the central body had a residential function. The villa also shows a southern area including a small paved court which probably acted as a *taberna deversoria* for housing merchants and voyagers travelling on the way to ancient Gallia. The building had a water supply line and a sewer system.

The walls of the *villa* show socles in *opus caementicium* or dry rubble with pebbles and fragmentary tiles and bricks, while the elevations were basically in perishable materials, like sun-dried bricks, pisé or *opus craticium*. The roofs, sometimes covering wide surfaces, were made of large rectangular tiles and cover-tiles.

The building complex described is the result of a long series of enlargements and modifications, starting during the Augustan period.

Near the main construction, other contemporary buildings are known, probable dependencies to the *villa*. The characteristics and destination of these partially explored evidences are still under evaluation. The geophysical investigation programme started from the immediate surroundings of some of these structures, south of the "trincea F" (north area). Moreover, to test the effectiveness of the methods in the given geological context, another area was selected for a blind test (south area) where some structures were already unearthed and later covered .

**Data acquisition and processing.** We made the survey on two areas within the archaeological site: the North area and the south area (Fig. 3). In the north area, on May 2014, we made both a magnetic and GPR survey while in the south area only a GPR survey was performed on July 2014, after the processing of North area data which lead us to exclude the magnetic method.

In the North area we used a Radar K2 from IDS with a 500 MHz IDS antenna. On the whole we made 31 profiles, each one about 32 m long. The profile interval was 0.4m while the trace interval was 0.035 m. The trace's length was 50 ns and they were digitized with 512 samples. All the profiles show, on average, a quite broad band spectrum with a -3dB band ranging from 200 to 700 MHz. Raw radargrams showed a lot of clutters and there were no evidences of clear coherent reflections in the x-twt domain. The processing flow was very reduced and it consisted of: move start time, to set properly the zero time; dewow to remove low frequency effects and a non linear manual gain, increasing with time, to recover energy in the deeper radar section. Time slices, on the envelope of the Hilbert transform of the radargrams, have then been made summing up the samples over 1 ns window length.

In the north area we also made a magnetic survey with a GSM-19GF Overhauser magnetometer in walk-grad mode, setting an acquisition frequency of 2 readings/s. Both the total magnetic field (TMF) and the vertical gradient of the TMF were acquired with lower and upper sensors at 0.2m and 0.8 m above the ground respectively. On the whole we acquired 5093 raw readings along 51 profiles with a profile interval of 0.2 m. A further interpolation showed that, along any profile, on average, we had a 0.3 m reading interval. After outliers rejection and bad quality data removal we worked on 4647 readings. Data were then destriped and the gradient and TMF maps were obtained with a triangular interpolation.

In the south area we used a Radar K2 from IDS with a 200 MHz GSSI antenna. On the whole we made 41 profiles, each one about 25 m long. The profile interval was 0.25 m while the trace interval was 0.075 m. The trace's length was 100 ns and they were digitized with 512 samples. All the profiles show, on average, a spectrum with a -3dB band ranging from 100 to 250 MHz. Raw radargrams showed again a lot of clutters and there were no or little evidences of clear coherent reflections in the x-twt domain. The processing was reduced and it consisted of: move start time, to set properly the zero time; dewow to remove low frequency effects; a Butterworth 4 poles bandpass filter (100-500 MHz); a non linear manual gain, increasing with time, to recover energy in the deeper radar section and a time cut to 50 ns. The choice of the filter bandwidth, larger than the -3dB band, has been done to preserve shorter wavelets. Indeed in the average spectrum there is still a platform of energy at -9dB up to about 600 MHz, Time slices, on the envelope of the Hilbert transform of the radargrams, have then been made summing up the samples over 2 ns window length.

**Results.** Results are shown in Figs. 3a and 3b.

The vertical gradient map, as the total field one, is noisy and it is likely pervasively influenced by the serpentine pebbles and blocks. A simulation run with the software POTENSOFT (Ozgu Arısoy and Dikmen, 2011) showed that a cube having 0.2 m side with a magnetic susceptibility of 0.05 (SI), 0.2 m below the lower sensor, gives a total field and an vertical gradient anomaly compatible, both in amplitude and wavelength, with some of the high spots found in the field. Such a spread noise hinder the recognition of any alignment. The magnetic map does not seem to have any relation with the underlying structures revealed by the GPR despite the noticeable size of the structures themselves. It should however be observed that the walls are built randomly assembling blocks of serpentine and other lithologies in such a way that they might also give a magnetic signal similar to an incoherent noise. In every GPR time slice clutters are thoroughly in evidence. All the top of the walls are very irregular and there are not flat surfaces in agreement with the ones already dug up. Clutters concentration between and aside the walls let us suppose that there could be a remarkable amount of ruined material. The tops of reflecting walls in the North area are more shallow than the one in the South area. A long diagonal reflecting body, with an incoherent direction with respect to the others, appears in the western part of the South area. Looking at raw data both magnetic and GPR surveys failed to find any structure. Only time slice processing of GPR data revealed a frame of buried walls limiting rooms with dimensions comparable to the ones already dug up.

**Comments and conclusions.** Once again this case history pointed out the importance of the information on the target and surrounding environment materials in the early stage of the design of a geophysical prospection (Sambuelli and Strobbia, 2002). The results of the prospection allow for important preliminary evaluations concerning an unexplored area and are crucial in order to plan further excavations. In this area, anomalies showing straight lines have emerged, which confidently belong to two different buildings. The North area, in particular, shows the south continuation of two parallel structures already unearthed in trench F for a very short part. They respectively correspond to the outer west wall and to a inner wall of the same building and they both can be traced for more than 12 m. Other structures, approximately perpendicular to these ones, apparently delimitate two rows of quadrangular rooms showing recurrent dimensions (4-5 m). Further anomalies in the south-east corner of the North area and

in north-east corner of the South area are probably related to a second building. Short parts of east-west orientated walls belonging to this construction had already emerged in a limited sounding made in the modern irrigation canal crossing the archaeological area. In this case, the presence of a rectangular building (11 x 7 m) can be inferred.

At this stage of research, prospection allows for a better knowledge of the dependencies of the villa in the area north to the main building, and offers new data about the extent and inner plan of these constructions, which will be verified by means of further archaeological investigations.

**Acknowledgements.** The Authors would like to thank Diego Franco and the students of the Ph. D. course on "Theory and application of GPR" for the help in data acquisition. The logistic support of the municipality of Costigliole Saluzzo is also gratefully acknowledged.

## References

Balestro G., Fioraso G. and Lombardo B.; 2011: Geological map of the upper Pellice Valley (Italian Western Alps). Journal of Maps, 2011, pp. 637-654, doi:10.4113/jom.2011.1213.

Barra Bagnasco M.; 2003: Recenti indagini a Costigliole Saluzzo (CN): una nota. Orizzonti. Rassegna di Archeologia, IV, pp. 33-42.

Barra Bagnasco M.; 2005: Nuovi documenti romani nel Cuneese occidentale: Costigliole Saluzzo. *In* Sapelli Ragni M. (ed.), Studi di Archeologia in memoria di Liliana Mercando. Torino, pp. 19-31.

Barra Bagnasco M. and Elia D.; 2007: Un contributo alla conoscenza della romanizzazione del Piemonte: l'insediamento di Costigliole Saluzzo. *In* Brecciaroli Taborelli (ed.), Forme e tempi dell'urbanizzazione nella Cisalpina (II secolo a.C.-I secolo d.C.), Atti delle giornate di Studio, Torino 4-6 maggio 2006. Borgo S. Lorenzo, pp. 275-282.Castelli D. and Compagnoni R.; 2007: Guide-book to the pre-Conference Field Excursion on HP Monviso metaophiolites and UHP Dora-Maira continental rocks (Western Alps). Quaderni di Geodinamica Alpina e Quaternaria, 9, pp. 1-33.

Compagnoni R. and Fiora L.; 1976: Sopra una sequenza ofiolitica metamorfica di ultramafiti, gabbri con layering magmatico e basaliti a pillow nel Massiccio del M. Viso (Alpi Occidentali). Rendiconti Soc. Italiana di Mineralogia e Petrologia, 32 (2), pp. 699-714.

Elia D. and Meirano V.; 2008: Costigliole Saluzzo, loc. Cimitero. Insediamento di età romana. Quaderni della Soprintendenza Archeologica del Piemonte, 23, pp. 204-207.

Elia D. and Meirano V.; 2008-2009: Scavi dell'Università di Torino a Costigliole Saluzzo (CN): l'insediamento di età romana in Località Cimitero. Bollettino della Società Piemontese di Archeologia e Belle Arti, LIX-LX, pp. 27-31.

Elia D. and Meirano V.; 2012a: Costigliole Saluzzo, loc. Cimitero. Insediamento di età romana. Campagne di scavo 2009-2011. Quaderni della Soprintendenza Archeologica del Piemonte, 27, 2012, pp. 218-224.

Elia D. and Meirano V.; 2012b: La villa di Costigliole Saluzzo (CN). Contributo alla conoscenza del territorio piemontese in età romana. Orizzonti. Rassegna di Archeologia, XIII, pp. 43-65.

Elia D., Meirano V., and Russo D. 2013: Costigliole Saluzzo, località Cimitero. Insediamento di età romana. Interventi di scavo e di restauro: campagna 2012, Quaderni della Soprintendenza Archeologica del Piemonte, 28, pp. 220-223.

Gaffney G. and Gater J.; 2003: Revealing the buried past: geophysics for archaeologists. Tempus Publishing, Gloucestershire, 192 pp.

Hattori K.H. and Guillot S.; 2007: Geochemical character of serpentinites associated with high-to ultrahigh-pressure metamorphic rocks in the Alps, Cuba, and the Himalayas: Recycling of elements in subduction zones. Geochemistry Geophysics Geosystems, 8 (9), Q09010, doi:10.1029/2007GC001594.

Lombardo B., Rubatto D. and Castelli D.; 2002: Ion microprobe U-Pb dating of Zircon from Monviso Metaplagiogranite: implications for the evolution of the Piedmont-Liguria Tethys in the Western Alps. Ofioliti, 27 (2), pp. 109-117.

Ozgu Arısoy M. and Dikmen U.; 2011: Potensoft: MATLAB based software for potential field data processing, modeling and mapping. Computer & Geoscience, 37, pp. 935-942.

Pasquinucci M. and Trément F.; 2000: Non-destructive techniques applied to landscape archaeology. Oxbow Books, Oxford, 276 pp.

Rees A. I.; 1962: Electrical prospecting method in archaeology, Antiquity, n.36, Cambridge.

Sambuelli L. and Strobbia C.; 2002: The Buffon needle problem and the design of a geophysical survey. Geophysical prospecting, 50, 4, pp. 403-409.

Segre E.; 1958: Mezzi tecnici ausiliari nella prospezione archeologica: Lerici, Roma

# STIMA DELLA PROFONDITÀ DELLA MOHO NEI BALCANI OCCIDENTALI DA OSSERVAZIONI DI GRAVITÀ DEL SATELLITE GOCE

**D. Sampietro**
*GReD s.r.l., Como*

**Introduzione.** L'area dei Balcani occidentali, ovvero la zona che si estende tra la Bulgaria e il Mar Adriatico, è una delle regioni europee più complesse e attive dal punto di vista tettonico. L'area si trova in corrispondenza della collisione tra la placca africana e quella eurasiatica ed è caratterizzata dalla presenza della cintura orogenetica alpino-himalayana e dall'apertura del bacino pannonico. Infatti, la spinta della placca Adriatica nella litosfera europea, ha causato la formazione di importanti catene montuose come le Alpi, le Dinaridi e le Albanidi. Secondo studi più recenti, basati principalmente sull'analisi delle velocità da reti GNSS permanenti, e da metodi di sismica passiva la placca Adriatica può essere suddivisa in una serie di due o anche tre unità più piccole in movimento verso nord con velocità dell'ordine di 35 mm/anno (Herak *et al.,* 2005; Ivančić *et al.,* 2006). Al contrario la parte meridionale dei Carpazi e la parte orientale della penisola balcanica mostrano un movimento orientato verso sud di circa 3 mm/anno. Oltre che per l'estrema complessità geologica i Balcani occidentali rappresenta anche una zona interessante anche da un punto di vista "storico": infatti i primi studi sulla litosfera e in particolare sulla determinazione della Moho sono stati condotti in questa regione da Mohorovičić che per primo, studiando il terremoto avvenuto nella valle di Kupa nel 1909 (Mohorovičić, 1992), individuò la presenza di una discontinuità tra crosta e mantello terrestre, la cosiddetta discontinuità di Mohorovičić o Moho. Nel suo lavoro Mohorovičić, sulla base delle registrazioni di una serie di terremoti, osservava la presenza di due distinte coppie di onde P e S una delle quali generata a una discontinuità strutturale sotto la superficie della Terra. Nel suo articolo Mohorovičić stimò la profondità di questa discontinuità nella zona croata in circa 54 km. Da allora sono stati condotti molti altri studi per comprendere meglio la struttura litosferica sotto i Balcani occidentali: a partire dai lavori di Dragaševií e Andric (1968) che utilizzarono due profili di sismica profonda lungo le Alpi Dinariche, al lavoro di Aljinović *et al*. (1984) che suggerisce, sulla base di altri tre profili sismici che vanno dalla costa adriatica al continente in direzione sud est-nord ovest, uno spessore della crosta di 45 km sotto le Dinaridi rapidamente decrescente fino ad arrivare a soli 20 km nel bacino pannonico e in corrispondenza del mar Adriatico.

In aggiunta è importante ricordare qui l'analisi della velocità di propagazione delle onde sismiche nella regione circum adriatica di Herak e Herak (1995) che ha mostrato uno spessore crostale media di 40 km nelle Dinaridi crescente verso sud-est e fino a raggiungere 55 km nella loro parte più meridionale, il lavoro di Van der Meijde *et al*. (2003) e di Stipčević *et al*. (2011) che hanno analizzato i tempi d'arrivo delle onde sismiche in corrispondenza di stazioni sismologiche per stimare modelli semplici della struttura della crosta terrestre.

In particolare in Van der Meijde *et al*. (2003) due stazioni lungo la costa croata sono stati indagate stimando uno spessore crostale di 47 e 41 km, con una incertezza dell'ordine di 1.6 km mentre in Stipčević *et al*. (2011), una serie di 8 stazioni è stata utilizzata per trovare uno spessore medio della crosta sotto le stazioni dell'Adriatico settentrionale in linea con i risultati pubblicati dai recenti esperimenti DSS [profilo Alp07: Šumanovac *et al*. (2009)], mentre nelle Dinaridi centrali e nel nel sud della Croazia hanno osservato una Moho significativamente più profonda delle stime precedenti.

È importante notare che tutti questi studi derivanti da osservazioni sismiche soffrono ancora di mancanza di osservazioni nella regione delle Dinaridi e nelle aree circostanti, che si traduce inevitabilmente in elevate incertezze nelle stime della profondità Moho. Infatti, mentre la struttura crostale del bacino pannonico è ragionevolmente ben conosciuta grazie all'esplorazione delle compagnie petrolifere, si veda ad esempio Dolton (2006) la disponibilità di osservazioni in Croazia e nella vicina Bosnia-Erzegovina è abbastanza limitata.

Nel presente lavoro i dati di gravità, e in particolare la quinta release del modello di gravità globale ottenuto da osservazioni GOCE applicando il metodo Time-Wise (Pail *et al.,* 2010) sono stati utilizzati per dedurre informazioni sulla struttura crostale e sulla profondità della Moho nei Balcani occidentali. La procedura può essere divisa in due fasi principali: la prima consiste nel riconoscere e isolare le diverse province geologiche nell'area di studio sfruttando le informazioni provenienti dal modello globale del campo gravitazionale stesso, mentre la secondo consiste nell'invertire il campo gravitazionale per stimare la profondità della Moho e alcune informazioni sulla densità della crosta.

Nel secondo capitolo l'algoritmo e i risultati della classificazione in province geologiche saranno descritti e discussi, mentre nel terzo capitolo verrà presentato l'algoritmo di inversione. Infine nell'ultimo capitolo verranno esposti e analizzati i principali risultati numerici.

**Definizione delle province geologiche.** Per poter stimare la profondità della Moho da osservazioni del campo gravitazionale è necessario conoscere le principale variazioni di densità all'interno della crosta e nei primi strati del mantello. Infatti una volta che tali variazioni sono note è possibile calcolarne l'effetto in termini di campo gravitazionale e quindi isolare e rimuovere dai dati il segnale dovuto alla discontinuità di Mohorovičić. Per questo è necessario modellizzare la geometria e la densità dei sedimenti, della crosta cristallina, di eventuali mari o ghiacci presenti e del mantello superiore. Per quanto riguarda la crosta cristallina, una possibilità per modellizzare almeno le principali variazione di densità laterali, studiata e applicata recentemente a livello globale in Reguzzoni e Sampietro (2014), consiste nel suddividere la crosta in regioni geologicamente omogenee, ognuna delle quali classificate come una di otto tipi di crosta (i.e. scudi, piattaforma continentale, bacini sedimentari, crosta in estensione, zone orogenetiche, crosta oceanica, ridge oceanici e province ignee). Per ogni classi di crosta viene quindi definita una funzione empirica [basata sul lavoro di Christensen and Mooney (1995)] che descriva variazioni di densità rispetto a variazione di profondità. È importante notare che tali funzioni sono richieste oltre che per la riduzione dei dati anche per definire il contrasto di densità tra crosta e mantello terrestre necessario per l'inversione del segnale gravitazionale residuo.

In questo contesto la definizione dei limiti geografici delle province geologiche è un tema cruciale per ridurre correttamente i dati e invertire il segnale residuo. Nel presente lavoro è proposto un approccio bayesiano per classificare a partire da un funzionale del campo gravitazionale, la regione indagata in province geologiche.

In dettaglio consideriamo una griglia di anomalie di gravità $\delta g$ ad una certa altitudine $h$ costante, possibilmente vicina alle masse topografiche, ottenuta applicando un operatore di

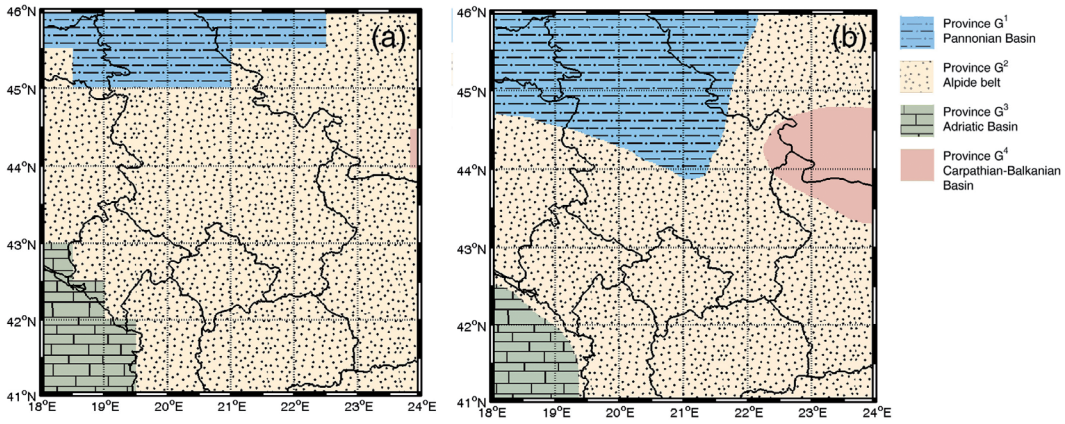


Fig. 1 – Mappa delle province geologiche a-priori digitalizzata a 1°x1° (a) e risultato dell'algoritmo di classificazione proposto (b).

sintesi armonica (Moritz, 1980) a un modello di campo gravitazionale globale e supponiamo di conoscere un modello approssimato, ad esempio da una mappa a-priori delle province geologiche (Exxon, 1995), di province geologiche $G_i$ per ogni nodo $i$ della griglia. In generale, $G_i$ può assumere $n$ valori dove $n$ è il numero delle province geologiche nella zona di interesse. Si veda ad esempio la mappa delle province geologiche dei Balcani occidentali con una risoluzione di 1°x1° ottenuta digitalizzando la mappa delle province geologiche sviluppata dall'U.S. Geological Survey riportata in Fig. 1. Dal momento che solo quattro province geologiche sono presenti, $n = 4$, $G_i$ può assumere solo un valore nel set delle province disponibili, i.e. : $G^1$, $G^2$, $G^3$, $G^4$.

Per ogni pixel $i$ inoltre viene selezionato un intorno $\Delta_i$, ad esempio formato dagli 8 pixel adiacenti a quello considerato. La probabilità a priori che $G_i$ assuma un certo valore $G^k$ con $k = 1,2,\ldots,n$, cioè $P(G_i = G^k)$ è calcolata per mezzo di una matrice peso W:

$$P(G_i = G^k) \propto \sum_{j=\{i,\Delta_i\}} \chi_j^k W \quad dove \quad \begin{cases} \chi_j^k = 1 \; if \; G_j = G^k \\ \chi_j^k = 0 \; if \; G_j \neq G^k \end{cases} \qquad (1)$$

La matrice dei pesi $W$ è definita in base alla distanza tra ciascun pixel in $j = \{i,\Delta_i\}$ e il pixel $i$. Ad esempio, supponendo che in un intorno di un certo pixel $i$ il modello a priori abbia solo due province geologiche con la geometria e la matrice dei pesi W di Fig. 2 le due probabilità a priori sono $P(G_i = G^1) \propto \sum_{j=\{i,\Delta_i\}} \chi_j^k W = 2\beta + \gamma$ e $P(G_i = G^2) \propto \sum_{j=\{i,\Delta_i\}} \chi_j^k W = \alpha + 2\beta + \gamma$.

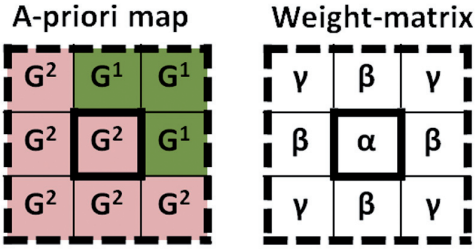


Fig. 2 – Esempio di matrice dei pesi. Il pixel $i$ è posto nel centro della matrice.

Per calcolare la *likelihood*, i.e. $P(\delta g_i | G_i = G^k)$ supponiamo che la crosta sia in perfetto equilibrio isostatico (secondo il modello di Airy) è che l'effetto gravitazionale ad ogni nodo della griglia sia in prima approssimazione dovuto ad una *slab* di Bouguer con spessore pari allo spessore della crosta. Considerando queste approssimazioni è possibile scrivere una relazione lineare tra $\delta g_i$ e la densità della crosta $\rho_{Gi}$. A questo punto, partendo dal modello a-priori di province geologiche è possibile stimare ai minimi quadrati $\hat{\rho}_{Gi}$ per ogni provincia geologica e la relativa varianza $\hat{\sigma}^2_{\rho_{Gi}}$. Infine per ogni *pixel* la *likelyhood* è calcolata come la probabilità che la densità di un certo *pixel i* appartenga a una distribuzione normale con media $\hat{\rho}_{Gi}$ e varianza $\hat{\sigma}^2_{\rho_{Gi}}$. La probabilità a posteriori è calcolata applicando il noto teorema di Bayes come il prodotto tra la probabilità a-priori e la *likelihood*. La provincia geologica del singolo *pixel i* è quindi scelta in modo da massimizzare la probabilità a posteriori.

A questo punto due osservazioni sono necessarie: in primo luogo è importante sottolineare che le approssimazioni introdotta dall'ipotesi di crosta perfettamente isostatica e dal calcolo del segnale gravitazionale utilizzando la semplice *plate* di Bouguer non consentono una corretta determinazione della densità crostale, tuttavia questa prima fase ha come scopo finale solamente quello di individuare regioni omogenee (dal punto di vista della struttura della crosta) all'interno dell'area di studio. In secondo luogo va anche notato che l'uso della *plate* di Bouguer permette di considerare $G_i$ come una realizzazione di un campo di Markov con correlazione significativa solo con i vicini più prossimi permettendo l'applicazione di un metodo come il *Gibbs sampler* per massimizzare la probabilità a posteriori (Smith e Roberts, 1993; Sansò *et al*., 2011) e quindi facilitando notevolmente la classificazione delle zone omogenee.

Il metodo è stato applicato per migliorare la modellazione dei principali confini delle province geologiche nei Balcani occidentali. In particolare è stato utilizzato come punto di partenza dell'algoritmo di classificazione il modello a priori mostrato in Fig. 1, considerando come osservazioni una griglia di *gravity disturbances* sintetizzate dal modello globale GO_CONS_GCF_2_TIM_R5 (Pail *et al*. 2010) ad una quota di 3000 m con risoluzione di 1' e

considerando una matrice peso W (come in Fig. 2) definita da $\alpha = 0.3$ e $\beta = \gamma = (1 - \alpha)/8$.

Va sottolineato come questa configurazione della matrice dei pesi obblighi l'algoritmo a scegliere la provincia geologica per il *pixel i* solo tra le province geologiche adiacenti andando quindi a modificare solamente i confini tra due (o più) province.

Il risultato finale è mostrato in Fig. 1 dove si può vedere come il metodo sia in grado di modificare correttamente i confini delle province geologiche ottenendo una mappa molto più dettagliata rispetto a quella di partenza e sostanzialmente guidata solamente dalle osservazioni del campo gravitazionale.

**Stima della Moho.** L'algoritmo di inversione si basa sulla soluzione locale sviluppata all'interno del progetto GEMMA (GOCE Exploitation for Moho Modeling and Applications) finanziato dal programma dell'Agenzia Spaziale Europea Support To Science Element (STSE). Nel seguito sono riportati solamente i concetti principali, rimandando il lettore a consultare Sampietro (2011), Reguzzoni e Sampietro (2012) e Sampietro *et al*. (2014) per dettagli.

Prima di descrivere l'algoritmo di inversione è importante sottolineare il sistema di riferimento utilizzato nel presente studio. Essendo l'area di interesse abbastanza ridotta la soluzione si basa su un'approssimazione planare del problema. Infatti è stato dimostrato che per regioni con estensione inferiore a 10°x10° la differenza tra l'approssimazione planare e l'approssimazione sferica è trascurabile essendo inferiore a 0.5 km in termine di profondità della Moho (Sampietro, 2011). La prima operazione consiste quindi nel mappare il sistema di riferimento globale geodetico (i.e. latitudine, longitudine e quota ellissoidica) in un sistema di coordinate cartesiane locali. Questo *mapping* è definito dalle seguenti equazioni:

$$\begin{aligned} x &= R\cos(\bar{\varphi})(\lambda - \bar{\lambda}) \\ y &= R(\varphi - \bar{\varphi}) \\ z &= h \end{aligned} \qquad (2)$$

dove $\varphi$, $\lambda$ e $h$ sono la latitudine, longitudine e altezza ellissoidica, rispettivamente, di un certo nodo della griglia delle osservazioni, $\bar{\varphi}$ e $\bar{\lambda}$ e sono la latitudine e la longitudine del centro della regione considerata, R è il raggio della sfera locale e infine x, y, e z sono le coordinate mappate. Si noti che questa operazione è solo un cambiamento di coordinate e che il nuovo sistema di riferimento è solo approssimativamente quello definito da una terna locale con origine nel centro della griglia e tangente all'ellissoide (Sansò, 2006).

Considerando il sistema di riferimento di cui sopra, è possibile applicare l'algoritmo di inversione basato su un processo di deconvoluzione di Wiener nel dominio delle frequenze che filtra gli errori delle osservazioni e rende numericamente efficiente la risoluzione del problema [per dettagli si veda Reguzzoni e Sampietro (2012)]. L'unicità della soluzione è garantita dall'approssimazione della struttura crosta-mantello con un semplice modello a due strati (Sampietro e Sansò, 2012), quest'approssimazione è resa valida rimuovendo, a monte dell'inversione del campo gravitazionale, gli effetti dovuti alle principali variazioni di densità (e.g. topografia, batimetria, sedimenti e mantello superiore). La soluzione è stata quindi migliorata adattando la strategia globale proposta in Reguzzoni e Sampietro (2014) all'inversione locale. In sintesi tale miglioramento permette, conoscendo informazioni derivanti ad esempio da profili sismici, di stimare la profondità media della Moho, un fattore di scala per la funzione profondità-densità di ogni provincia geologica e di considerare nella soluzione eventuali variazioni di profondità della densità della crostale.

Per quanto riguarda la riduzione del segnale gravitazionale è stato utilizzato il modello ETOPO1 (Amante e Eakins, 2009) per la topografia e la batimetria, un modello di sedimenti a 1°x1° (Laske e Master, 1997) e il modello GyPSuM per il mantello superiore (Simmons et al., 2010). Come informazione sismica per la stima della profondità media della Moho è stato utilizzato il modello CRUST1.0 (Laske *et al*., 2013 ). I risultati dell'inversione in termini di profondità della Moho sono presentati in Fig.3

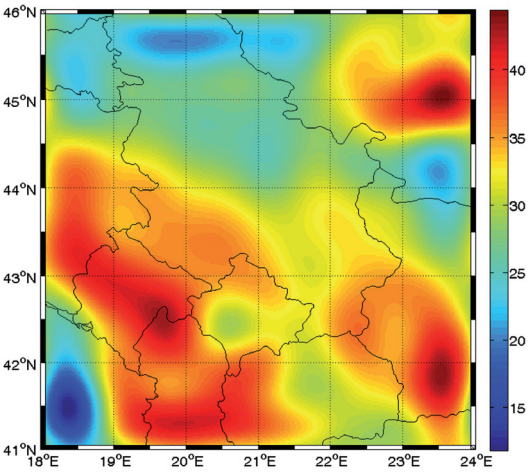


Fig. 3 – Stima della profondità della Moho (in km) nell'area di studio.

**Conclusioni.** La Moho stimata sembra presentare tutte le caratteristiche note in letteratura quali l'elevato spessore in corrispondenza delle maggiori regioni orogenetiche e la riduzione dello spessore della crosta in corrispondenza della placca adriatica e dei bacini sedimentari. Lo spessore della crosta in corrispondenza della Pannonia, compreso tra 20 e 30 km è consistente con diversi modelli di crosta (e.g. Grad e Tira, 2009). Questi risultati mostrano in primo luogo la capacità dell'osservazioni della missione GOCE di classificare regioni omogenee di crosta terrestre anche in presenza di geologie complesse. Inoltre dimostrano la bontà dell'algoritmo di inversione utilizzato e l'elevata accuratezza e risoluzione che si può ottenere sfruttando localmente le osservazioni globali del campo gravitazionale.

## Bibliografia


Amante, C., & Eakins, B. W. (2009). *ETOPO1 1 arc-minute global relief model: procedures, data sources and analysis* (p. 19). US Department of Commerce, National Oceanic and Atmospheric Administration, National Environmental Satellite, Data, and Information Service, National Geophysical Data Center, Marine Geology and Geophysics Division.

Aljinović, B., Blašković, I., Cvijanović, D., Prelogović, E., Skoko, D., & Brdarević, N. (1984). Correlation of geophysical, geological and seismological data in the coastal part of Yugoslavia. *Boll. Ocean. Teor. Appl*, *2*, 77-90.

Christensen, N. I., & Mooney, W. D. (1995). Seismic velocity structure and composition of the continental crust: A global view. *Journal of Geophysical Research: Solid Earth (1978–2012)*, *100*(B6), 9761-9788.

Dolton, G. L. (2006). *Pannonian Basin Province, Central Europe (Province 4808)--petroleum Geology, Total Petroleum Systems, and Petroleum Resource Assessment*. US Department of the Interior, US Geological Survey.

Dragaševií, T., & Andric, B. (1968). Deep Seismic Sounding of the Earth's Crust in the Area of the Dinarides and the Adriatic Sea. *Geophysical Prospecting*,*16*(1), 54-76.

Exxon, 1995. Tectonic Map of the World, 18 sheets, scale 1: 10,000,000. 594 Technical Report. Exxon, Houston , Texas.

Grad, M., & Tiira, T. (2009). The Moho depth map of the European Plate. Geophysical Journal International, 176(1), 279-292.

Herak, D., & Herak, M. (1995). Body-wave velocities in the circum-Adriatic region. *Tectonophysics*, *241*(1), 121-141.

Herak, D., Herak, M., Prelogović, E., Markušić, S., & Markulin, Ž. (2005). Jabuka island (central Adriatic Sea) earthquakes of 2003. *Tectonophysics*, *398*(3), 167-180.

Ivančić, I., Herak, D., Markušić, S., Sović, I., & Herak, M. (2006). Seismicity of Croatia in the period 2002-2005. *Geofizika*, *23*(2), 87-103.

Laske G. & Masters G. (1997). A Global Digital Map of Sediment Thickness, EOS Trans. AGU, 78, F483.

Laske, G., Masters, G., Ma, Z., & Pasyanos, M. (2013). Update on CRUST1.0 - A 1-degree Global Model of Earth's Crust, Geophys. Res. Abstracts, 15, Abstract EGU2013-2658.

Mohorovičić, A. (1992). Earthquake of 8 October 1909. *Geofizika*, *9*(1), 3-55.

Moritz, H. (1980). Advanced physical geodesy. *Karlsruhe: Wichmann; Tunbridge, Eng.: Abacus Press, 1980. 1*.

Pail, R., Goiginger, H., Mayrhofer, R., Schuh, W. D., Brockmann, J. M., Krasbutter, I., & Fecher, T. (2010). GOCE gravity field model derived from orbit and gradiometry data applying the time-wise method. In *Proceedings of the ESA Living Planet Symposium, ESA Publication SP-686, ESA/ESTEC, ISBN (Online)* (pp. 978-92).

Reguzzoni, M., & Sampietro, D. (2012). Moho estimation using GOCE data: a numerical simulation. In *Geodesy for Planet Earth* (pp. 205-214). Springer Berlin Heidelberg.

Reguzzoni, M., & Sampietro, D. (2014). GEMMA: An Earth crustal model based on GOCE satellite data. *International Journal of Applied Earth Observation and Geoinformation*.

Smith, A. F., & Roberts, G. O. (1993). Bayesian computation via the Gibbs sampler and related Markov chain Monte Carlo methods. *Journal of the Royal Statistical Society. Series B (Methodological)*, 3-23.

Sampietro, D. (2011). GOCE exploitation for Moho modeling and applications. In *Proc. of the 4th International GOCE User Workshop* (Vol. 31).

Sampietro, D., Reguzzoni, M., & Braitenberg, C. (2014). The GOCE estimated Moho beneath the Tibetan Plateau and Himalaya. In *Earth on the Edge: Science for a Sustainable Planet* (pp. 391-397). Springer Berlin Heidelberg.

Sansò, F. (2006). *Navigazione geodetica e rilevamento cinematico*. Polipress.

Sampietro, D., & Sansó, F. (2012). Uniqueness theorems for inverse gravimetric problems. In *VII Hotine-Marussi Symposium on Mathematical Geodesy* (pp. 111-115). Springer Berlin Heidelberg.

Simmons, N. A., Forte, A. M., Boschi, L., & Grand, S. P. (2010). GyPSuM: A joint tomographic model of mantle density and seismic wave speeds. *Journal of Geophysical Research: Solid Earth*, *115*(B12).

Stipčević, J., Tkalčić, H., Herak, M., Markušić, S., & Herak, D. (2011). Crustal and uppermost mantle structure beneath the External Dinarides, Croatia, determined from teleseismic receiver functions. *Geophysical journal international*, *185*(3), 1103-1119.

Šumanovac, F., Orešković, J., & Grad, M. (2009). Crustal structure at the contact of the Dinarides and Pannonian basin based on 2-D seismic and gravity interpretation of the Alp07 profile in the ALP 2002 experiment. *Geophysical Journal International*, *179*(1), 615-633.

Van Der Meijde, M., Van Der Lee, S., & Giardini, D. (2003). Crustal structure beneath broad-band seismic stations in the Mediterranean region. *Geophysical Journal International*, *152*(3), 729-739.

## 4D MONITORING OF SEA WATER INTRUSION BY ELECTRICAL RESISTIVITY TOMOGRAPHY: CASE STUDY IN THE COASTAL ALLUVIAL PLAIN OF THE VOLTURNO RIVER, ITALY

**D. Tarallo, V. Di Fiore, G. Cavuoto, N. Pelosi, M. Punzo, L. Giordano, E. Marsella**
*IAMC - CNR, Institute for Coastal Marine Environment, National Research Council, Naples, Italy*

**Introduction.** A common problem of coastal aquifers is saltwater intrusion, induced by the flow of seawater into freshwater aquifers due to the groundwater development near the coast. Several factors affect the ingression of sea water. Among these, the most important are the coastal subsidence, the lowering of the sea level, coastal erosion and excessive pumping of groundwater. In fact, where the groundwater is pumped from coastal aquifers, the induced gradients may cause the migration of salt water from the sea to the well, making the freshwater unusable; being the fresh water less dense than salt water, it floats on top.

According to the Integrated Coastal Zone Management (ICZM) of the European Commission, coastal areas are of great environmental, economic, social and cultural relevance. Therefore, the implementation of suitable monitoring and protection actions is fundamental for their preservation and for assuring the future use of this resource. Such actions have to be based on an ecosystem perspective for preserving coastal environment integrity and functioning and for planning sustainable resource management of both the marine and terrestrial components. Planning and management of natural resources through a dynamic process has to set, as its objective, the promotion of economic and social welfare of coastal zones.

Unfortunately coastal plains are often contaminated by sea water intrusion, and the vulnerability to salinization is probably the most common and diffused problem in an aquifer. The boundary between salt water and fresh water is not distinct; the dispersion and transition zone, or salt-water interface are brackish with salt water and fresh water mixing. Under normal conditions fresh water flows from inland aquifers and recharge areas to coastal discharge areas to the sea. In general, groundwater flows from areas with higher groundwater levels (hydraulic head) to areas with lower groundwater levels. This natural movement of fresh water towards the sea prevents salt water from entering freshwater coastal aquifers (Barlow, 2003).

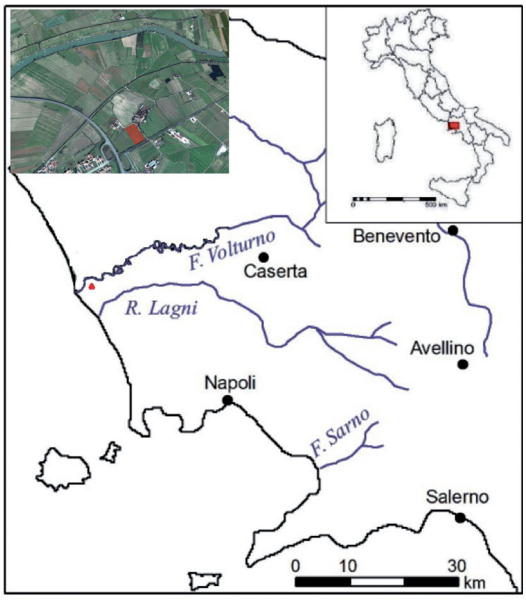


Fig. 1 – Location of the study area. Red lines are the 3D ERT grid.

Sea water intrusion in the water table can cause significant worsening in vegetation status. A likely related soil salinization would cause detrimental environmental and socio-economic impacts. Hence, monitoring the sea water intrusion represents a priority for the safeguard of coastal areas. Identify changes in the freshwater-saltwater interface position can be a useful element for the rationalization of water resources and to guide the choice of use of these areas.

Among the geophysical method applied for the location and movement of saltwater intrusion, best results were obtained by electrical methods (Al-Sayed and Al-Quady, 2007; Chitea *et al.*, 2011). Many hydrological processes can be expected to provide significant contrasts in resistivity, consequently, Electrical Resistivity Tomography (ERT) has been adopted as a tool for new research within the hydrology field. Previous workers have demonstrated the ability of ERT to visualize hydrological structure within laboratory cores (Binley *et al.*, 1996a, 1996b), monitor fluid or contaminant migration at the field scale (Daily *et al.*, 1992, 1995; Schima *et al.*, 1993), and to ascertain the efficiency of new contaminant remediation processes (Daily and Ramirez, 1995; LaBrecque *et al.*, 1996).

This paper outlines the results of a 3D ERT experiment obtained in the coastal alluvial plain of the Volturno river to assess changes in the freshwater-brine interface. The main aim was to investigate spatial and temporal variations of groundwater salinity. Acquisitions have been carried out in the months of May and October 2013 and in May 2014. This acquisition has allowed to obtain a monitoring 4D salt wedge in a "volume" specific subsurface.

**Geological and hydrogeological setting.** The investigated area is located in the northern sector of the Campania Plain, near to the mouth of Volturno river (Fig. 1). It is the main river in southern Italy: it crosses Molise and Campania regions, for a total length of 175 km with a watershed of 545 km$^2$. The Volturno is characterized by minimum flow in summer and overflow in autumn and spring. The area is characterized by a sub-horizontal morphology with main level similar to the sea level.

The geomorphology of the Campania Plain corresponds to a structural depression which is formed during the Lower Pleistocene. Until to 130.000 years ago the plain of the Volturno was regulated by a phenomenon of subsidence (Cinque and Romano, 2001) and fell in a marine environment. Afterwards, the area was affect by pyroclastic fall-out and flow from Campi Flegrei and Roccamonfina (Ortolani and Aprile, 1978, 1985).

In general, the stratigraphic sequence of the area is characterized by continental deposits (Romano *et al.*, 1994; Corniello *et al.*, 2010), a surface layer of silt and clay, an underlying sand layer and a basal layer characterized by clayey peat and reworked pyroclastics. River-borne sediments discharged in the sea in the past caused the river mouth to prograde. However, in the last 150 years, the latter has progressively retreated due to the dams built along the river and the extraction of gravel from the river bed (Biggiero *et al.*, 1994).

All these sediments have a lenticular pattern that determines a groundwater flow in layered aquifers. This determines, in conditions of excessive pumping and for a greater thickness of the sedimentary body that houses the sweet aquifer, a mixture of fresh water with the salt water. In

addition, the rising salt water also occurs along the bed of the river Volturno as the bottom of the river is located at the mouth, about 3.5 m below the sea level (Corniello *et al*., 2010).

**Geophysical methods and data processing.** The Electrical Resistivity Tomography (ERT) consists of the experimental determination of the apparent resistivity ϱ of a given material, by joint measurements of electric current intensity and voltage introduced into the subsoil through separate couples of electrodes, driven in the ground surface. All natural rocks can conduct electricity when subjected to an electric field. The measure with which the rocks are crossed through the current depends on the type of resistivity that they present. The resistivity parameter is influenced by: texture and porosity, degree of cementation, the temperature of the rock, clay content, water content and its temperature and salinity. Furthermore, under equal lithological conditions, there are some geological processes that cause an immediate variation of resistivity because they change the porosity. In general, many of these processes lead to a reduction of the resistivity as: clay alteration, dissolution, billing rock, saltwater intrusion.

The instrumentation used for the measurement of the resistivity consists of two parts: one for the measurement of the current intensity $I$ injected into the ground through the electrodes A and B and one for the measurement of the potential difference $\Delta V$ between the electrodes $M$ and $N$. In the experimental surveys reported hereafter, the ERT data have been gathered through electrodes of length equal to 40 cm.

The electrodes were then connected through multichannel cables, adopting the Wenner-Schlumberger array configuration. This type of arrangement is hybrid between the Wenner and Schlumberger arrays (Pazdirek and Blaha, 1996): during the acquisition, the wiring is continuously changed so that the spacing $a$ between the 'potential electrodes' remains constant, while that between the 'current electrodes' increases as a multiple $n$ of $a$. The value of $n$, in this case is given by the ratio between the distance of the electrodes $A$-$M$ (or $N$-$B$) and the spacing between the electrodes of potential $M$-$N$. For this array the distribution of the measurements is comparable with the Wenner array, but the horizontal coverage is better. The choice of such arrangement was due to the necessity to study areas in which both lateral and vertical variations of resistivity are present. The resulting horizontal distribution of the underground data points in the pseudo-section, in fact, is comparable with that typical of the Wenner array, but their vertical resolution is better. Moreover, this type of array is a fair compromise between the device Wenner and the dipole-dipole. The intensity of the signal is smaller than the Wenner but is higher than the dipole-dipole axial. At constant distance between the current electrodes, the depth of investigation that can be achieved with the device Wenner-Schlumberger is 10% higher than the Wenner device.

The geoelectric measurements of resistivity were executed with the georesistivimeter "SYSCAL Pro" of Iris Instrument. Within the chosen area for 4D monitoring of the salt wedge, geometrically similar to a rectangle of about 4600 square meters (length 115m and width 40 m), the geoelectric surveys performed by acquiring 9 geoelectric profiles. These profiles are arranged parallel to each other and with a spacing of 5 m and the multi-electrode resistivity measurements used 24 electrodes, for a total of 216 electrodes. Data acquired have been processed using 3D inversion technique performed with *ERTlabplus* software.

Data inversion started from a discretized model of the investigated area, constructed starting from average apparent resistivities on measured pseudosection. The inversion procedure uses a smoothness-constrained least-squares routine implemented into Occam's optimization algorithm (La Brecque *et al*., 1996b), which allows determining iteratively a 3D resistivity model for the subsoil.

**Result and discussion.** The results of the inversion procedure are three high resolution ERT 3D models in different periods, more specifically in May and October 2013 and in May 2014. These acquisitions have allowed to obtain a 4D monitoring of saline intrusion in a specific subsurface "volume". Resistivity data processing within that volume has therefore defined the electrical characteristics and geometry of the subsurface going to spatially delimit the intrusion

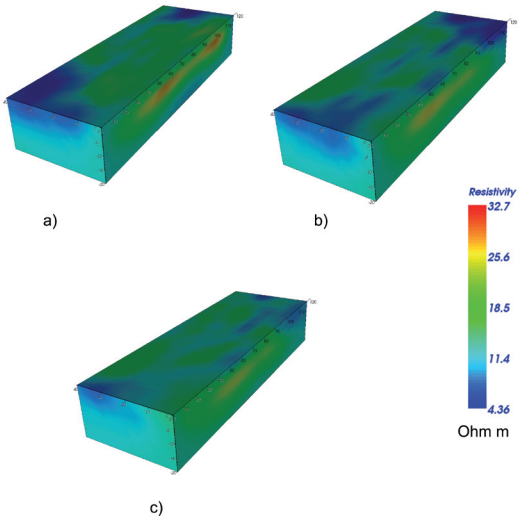


Fig. 2 – 3D ERT tomography models determined for different periods: a) May 2013; b) October 2013; c) May 2014.

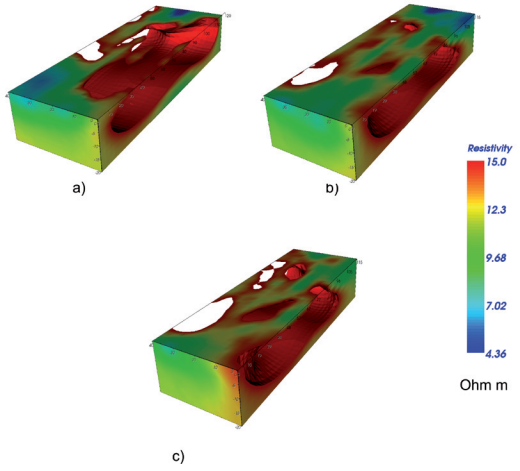


Fig. 3 – 3D resistivity contour plot referred to salt water (resistivity 4-15 Ωm): a) May 2013; b) October 2013; c) May 2014.

of salt water and the relationship with the sweet water. 3D models obtained by the inversion also showed seasonal variation (in time) of these relationships. Analyzing the three models (Fig. 2) it is possible to notice variations of resistivity very small (a) 4,36-31,2 Ωm; b) 4,66 – 30,36 Ωm; c) 7,45 – 32,7 Ωm).The low resistivity zone (Fig. 3), located in the lower and side part of the models, is interpreted as salt water related to marine intrusion. The middle sector of the models presents resistivity values compatible with the fresh aquifer. In detail, it is possible to observe changes between the volumes of brackish water and fresh-water during the spring and autumn seasons. In particular, the results highlight lower resistivity values in autumn (October 2013) in the shallow sector, ascribed to an increase of salt intrusion. This phenomenon is attributed to a lower contribution of fresh water in the aquifer of the plain due to the reduction of rainfalls during the summer season. The comparison, instead, with the two resistivity models acquired in May 2013 and 2014 showed no significant changes. The results of this study have led to a reconstruction of a three-dimensional model of the water bodies in the areas of flat in order to understand the extent of the phenomenon of saltwater intrusion in time and space, resulting in qualitative and quantitative analysis of the volume of water used. This analysis shows that the shallow fresh-water should not be used because the pumping could determine greater intrusion of sea water, not allowing the accumulation of fresh water necessary in the natural suction of native species of plants. This monitoring program, supported by a careful management of resources, would prevent the worsening of the intrusion of the wedge with a difficult chance to return to the initial equilibrium conditions.

**Acknowledgements.** The authors wish to thank Dr. Paolo Bonasoni, Scientific Responsible of I-AMICA project (High technology infrastructure for Integrated Climatic-Environmental monitoring), PON a3_00363.
In addition, the authors wish to thank Paolo Scotto di Vettimo, Michele Iavarone, Dr. Rodolfo Baculo and Dr. Ivan Granata, for their help during data acquisition.

## References

Al-Sayed E.A., El-Quady G.; 2007: *Evaluation of sea water intrusion using the electrical resistivity and transient electromagnetic survey: case study at Fan of Wadi Feiran, Sinai; Egypt*. EGM 2007 International Workshop, Italy.

Barlow P.M.; 2003: *Groundwater in fresh water-salt water environments along the Atlantic seaboard*. Circular 1262 USGS.

Biggiero V., Fiorentino M., Pianese D.; 1994: *Analisi dell'evoluzione d'alveo del tronco vallivo del fiume Volturno*. Atti del Meeting Annuale UU.OO. MURST 40% "Processi Fluviali: osservazioni analisi e controllo", Padova 10/1992.

Binley A., Henry Poulte S., Shaw B.; 1996a: *Examination of solute transport in an undisturbed soil column using electrical resistance tomography*. Water Resources Research, v.32, pp. 763-769.

Binley A., Shaw B., Henry Poulte S.; 1996b: *Flow pathways in porous media: elettrical resistance tomography and dye staining image verification*. Measurement Science Technology, v.7, pp. 384-390.

Chitea F., Georgescu P., Ioane D.; 2011: *Geophysical detection of marine intrusion in black sea coastal areas (Romania) using VES and ERT data*. Geo-Eco-Marina 17/2011, pp. 95-102.

Cinque A., Romano P.; 2001: *Evoluzione geomorfologica e caratterizzazione oro-idrografica della Regione*. In: L'ambiente geologico della Campania, a cura di A. Vallario, CUEN, pp. 59-90

Corniello A., Ducci D., Trifuoggi M., Rotella M. and Ruggieri G.; 2010: Hydrogeology and hydrogeochemistry of the plain between Mt. Massico and river Volturno (Campania region, Italy). Italian Journal of Engineering Geology and Enviroment, 1, pp. 51-64, doi: 10.4408/IJEGE.2010-01.O-04.

Daily W., Ramirez A., LaBrecque D., Nitao J.; 1992: *Electrical resistivity tomography of vadose water movement*. Water Resources Research, v.28, pp. 1429-1442.

Daily W. and Ramirez A.; 1995: *Electrical resistance tomography during in-situ trichloroethylene remediation at the Savannah River site*. Journal of Applied Geophysics, v. 33, pp. 239-249.

Daily W., Ramirez A., LaBrecque D. and Barber W.; 1995: *Electrical resistance tomography experiments at the Oregon Graduate Istitute*. Journal of Applied Geophysics, v. 33, pp. 227-237.

LaBrecque D. J., Ramirez A., Binley A. and Schima S. A.; 1996a: *ERT monitoring of environmental remediation processes*. Measurement Science Technology, v.7, pp. 375-383.

LaBrecque D. J., Miletto M., Daily W., Ramirez A, Owen E.; 1996b: *The effects of noise on Occam's inversion of resistivity tomography data*. Geophysics, v.59, pp. 1839-1848.

Ortolani F., Aprile A.; 1978: Nuovi dati sulla struttura della Piana Campana a sud est del fiume Volturno. Boll. Soc. Geol. It., 97, 591-608.

Ortolani F., Aprile A.; 1985: Principali caratteristiche stratigrafiche e strutturali dei depositi superficiali della Piana Campana. Boll. Soc. Geol. It., 104, 195-206.

Pazdirek O., Blaha V.; 1996: *Examples of resistivity imaging using ME-100 resistivity field acquisition system*. In: EAGE 58th Conference and Technical Exhibition Extended Abstracts, Amsterdam, P050.

Romano P., Santo A., Voltaggio M.; 1994: *L'evoluzione morfologica della pianura del Fiume Volturno (Campania) durante il tardo Quaternario (Pleistocene medio-superiore/ Olocene)*. Il Quaternario, 7(1), pp. 41-56

Schima S., LaBrecque D. J. and Miletto M.; 1993: *Tracking fluid flow in the unsaturated zone using cross-borehole resistivity and IP*. Proceedings of the Symposium on the Application of Geophysics to Engineering and Enviromental Problems 1993, San Diego, CA, pp. 527-543.

# sessione 3.3

## Metodi integrati

**Convenor: V. Sacco e E. Cardarelli**

**co-organizzata con Sezione Italiana Eage-Seg**

# NEW SEISMOSTRATIGRAPHIC AND TEPHROSTRATIGRAPHIC DATA IN THE CONTINENTAL SHELF OFFSHORE THE VOLTURNO BASIN: STRATIGRAPHIC CONSTRAINTS ON THE OCCURRENCE OF NEW VOLCANIC STRATIGRAPHIC MARKERS

**G. Aiello[1], D.D. Insinga[1], M. Iorio[1], E. Marsella[1], M.R. Senatore[2]**
*[1] Istituto per l'Ambiente Marino Costiero (IAMC), Consiglio Nazionale delle Ricerche (CNR), Napoli, Italy*
*[2] Dipartimento di Scienze Biologiche, Geologiche ed Ambientali, Università degli Studi del Sannio, Benevento, Italy*

A volcanic stratigraphic marker in the continental shelf offshore the Volturno river (northern Campania, southern Tyrrhenian sea) has been recovered and discussed through seismostratigraphic and tephrostratigraphic data. The seismostratigraphic data include a Subbottom Chirp and Sparker seismic grid collected in the frame of research programs on marine geological mapping of the continental shelf off the Campania Region. Cores have also been collected and their sedimentological study, coupled with seismostratigraphic analysis has recently evidenced the occurrence of a volcanic stratigraphic marker, corresponding to a highly continuous and parallel reflector on the seismic sections. Seismo-stratigraphic analysis has evidenced that the volcanic level, interpreted as a tephra deposit is interlayered in transgressive system tracts deposits, pertaining to the Late Quaternary depositional sequence, well detected in the whole Campania Tyrrhenian margin. The volcanic level, which has been mapped in six different seismic profiles, is located at different depths, ranging between 70 and 155 m below the sea bottom, interrupting in correspondence to the shelf break (Fig. 1).

Although several tephrostratigraphic studies have been carried out in southern Italy, concealing, in particular, the Somma-Vesuvius, Ischia and Procida offshore (Pyle *et al*., 2006; Rolandi *et al*., 2007; Turney *et al*., 2008; de Alteriis *et al*., 2010; Insinga *et al*., 2010), only few of them have linked the geological aspects on tephrostratigraphy detected through geochemical, sedimentological and SEM analyses with high resolution seismic profiles (de Alteriis *et al*., 2010). Tephrochronology of the Ischia island has been recently discussed (Insinga *et al*., 2010). The stratigraphic succession of the Gulf of Naples slope offshore Ischia is dated back through a time interval spanning 40 ky B.P., deduced by $^{14}C$ AMS dating and tephrostratigraphy. It has been attributed, based on the calcareous nannofossils assemblages to the Emiliana huxleyi Acme Zone (Rio *et al*., 1990), during the Late Pleistocene-Holocene time interval. This succession is characterized by coarse-to-fine-grained ashes alternating with volcaniclastic turbidites along the whole succession. Four ash layers have been characterized and correlated with several eruptions occurring in the Ischia island in a time interval spanning between 17 ky B.P. and the Middle Ages and Roman times. The deposits related to the explosive activity of the Procida island have also been found and dated at about 23 ky B.P.

In the Ischia stratigraphic succession the oldest tephra layers are distinguished by a well-preserved layer, thick about 30 cm, which is correlated with the Phlegrean products of the Campanian Ignimbrite event [39 ky B.P.; De Vivo *et al*. (2001)]. The marine counterpart layer correlated with the Campanian Ignimbrite is named the C13 tephra layer in the Tyrrhenian sea (Thon-That *et al*., 2001; de Alteriis *et al*., 2010; Insinga *et al*., 2010). The stratigraphic position of two other main marker tephras recognized in the succession have allowed to correlate them with two other marker tephras, such as the Schiava and Codola layers (Paterne and Guichard, 1993; Sulpizio *et al*., 2003; Giaccio *et al*., 2009).

The Volturno offshore has been intensively studied based on deep multichannel seismic data and marine magnetic data (Aiello *et al*., 2000, 2005, 2011a, 2011b) coupled with high resolution seismics and gravity cores (Iorio *et al*., 2014). A new geological approach based on multi-proxy analysis has been recently applied to the northern Phlegrean Fields offshore aimed at defining the sedimentary processes in recent prodelta deposits based on the geological interpretation of seismic profiles coupled with petrophysical and sedimentological analysis of cores (Iorio *et al*., 2014). A Holocene unit has been characterized through Subbottom Chirp profiles coupled with

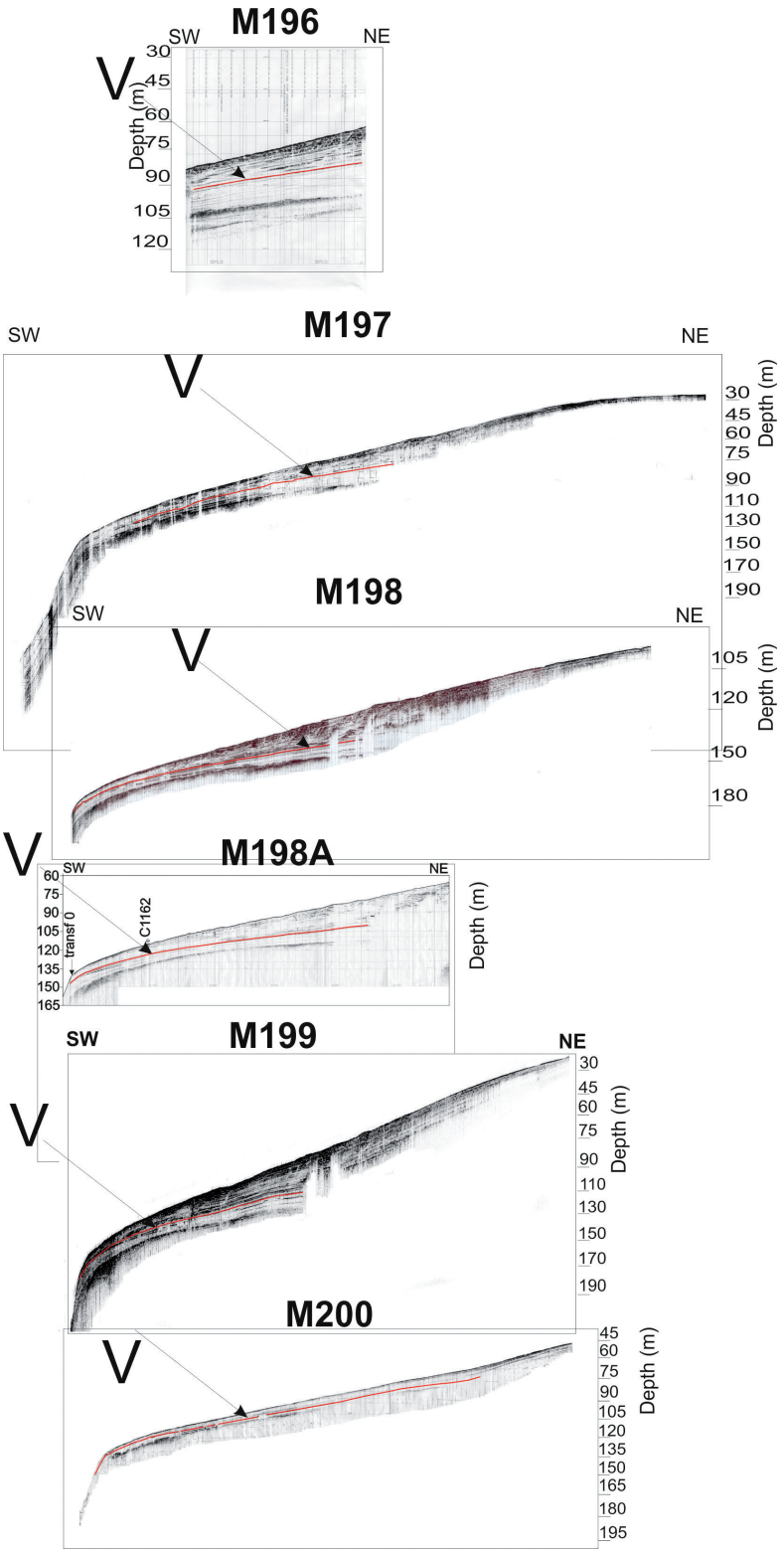


Fig. 1 – Correlation of the volcanic stratigraphic marker, namely V in different seismic profiles.

sedimentological and petrophysical data. The chronostratigraphic framework was achieved by means of a colorimetric parameter calculated through petrophysical analysis with nearby dated marine sediments. A time interpretation of about 2300 years B.P. has been estimated for the sedimentary record collected in the cores. The seismic interpretation of high resolution data has shown that the Late Holocene highstand shelf deposits are affected by undulation phenomena. The undisturbed sedimentation and the preservation of an internal geometry at a decimetric scale, as detected by the sedimentological and the petrophysical analysis indicates a sliding of sediments without sediment reworking for this sedimentary body. Small normal faults have also been identified, related to high water content, fluid escape features and triggered by the occurrence of seismic activity. The depth-age conversion of the detected lithological features has evidenced a regular climatic change in the depositional environments of the Volturno sedimentary prodelta. The detection of spectrophotometry correlations of Holocene shelf margin sediments has also confirmed for the Volturno continental shelf the potential value of spectrophotometer data in high resolution stratigraphic correlations.

The volcanic deposits, including the lava flows, the ash flows, the ash layers and the tuffs represent important stratigraphic markers providing excellent stratigraphic correlations through sedimentological, seismo-stratigraphic and petrophysical constraints (Self and Sparks, 1981; Sarna-Wojcicki, 2000; Giaccio *et al*., 2009; Iorio *et al*., 2014). The volcanic eruptions usually represent brief events and the erupted materials are usually emplaced during short geological times. The volcanic units, often the pyroclastic units, can be distinctive and laterally continuous: in these cases the field geological surveys can be used as stratigraphic markers and physically correlated among geographically separated stratigraphic sections (Di Vito *et al*., 1999; Amorosi *et al*., 2012). One aim of this paper is to demonstrate that the basic approach of tephrochronology and tephrostratigraphy in field studies, already applied in the Neapolitan volcanic district (Insinga *et al*., 2005; Sacchi *et al*., 2005; de Alteriis *et al*., 2010; Insinga *et al*., 2010) may be applied also in studying the seismic sections, if they provide highly continuous seismic reflectors correlating to tephra layers and perhaps representing useful stratigraphic markers, as in the case of the Volturno offshore (Aiello *et al*., 2011a, 2011b; Iorio *et al*., 2014).

Moreover, in tephrochronological and tephrostratigraphic studies the volcanic units can be dated through numerical methods, as the fission tracks; in these cases they become chronostratigraphic markers, providing a chronostratigraphic control everywhere they can be identified. This concept may be applied also to seismic reflectors if they are calibrated by piston and gravity cores studied through sedimentological and petrophysical methods, as it happens in our case study. The tephra layers are usually represented by volcanic ash layers and usually cover large areas, so representing the most useful markers among the volcanic materials in order to reconstruct their stratigraphic relationships. The term “tephra” derives from a Greek word meaning ash and is used for all the pyroclastic materials erupted from a volcanic vent, particularly referring to ash-fall deposits, ash-deposits and pumice flow deposits. These volcanic materials are usually transported by air and gas and, after being deposited, form tephra layers or tephra beds (Simkin and Siebert, 1994). The tephrochronology is divided into two fundamental disciplines, such as the tephrostratigraphy and the tephrochronometry. The tephrostratigraphy is represented by the correlation of the tephra layers distinguishing their physical and chemical characteristics and corresponding stratigraphic sequences. The tephrochronometry is represented by the numerical age determination of tephra layers, either from the tephra itself through the K/Ar or the fission track methods or indirectly, from the ages of the associated layers or deposits. The tephra deposits may consist of three main components, such as the volcanic glasses generated during the rapid cooling of the eruption, the lithic fragments, being pieces of pre-existing rocks becoming incorporated into the tephra layers during the volcanic eruption and consequent phases of transport and deposition and finally, the mineral crystals of crystal fragments, which have been formed in the magma prior to the

eruption (Sarna-Wojcicki, 2000). The tephra layers may be in the form of pumice, usually light coloured and siliceous or scoriaceous, represented by solidified rock froths of glass containing various amounts of crystals, crystal fragments, vescicles and sometimes lithic fragments. The pumice clasts deposited near the eruptive vent are quite large, decreasing in size with the increase of the distance from the vent. At the distal locations, the tephra may consist of small pumice fragments, solid glass fragments and fine-grained lithic fragments. The mineralogic composition of the tephra layers varies with the composition of the parent magma, being mainly siliceous or dacitic and often including accessory minerals.

The identification and the correlation of tephra layers is one fundamental step in tephrostratigraphic studies. The identification is carried out by using several characteristics, such as the colour, the texture, the stratigraphic context of their deposition, the occurrence of comagmatic mineral grains and the chemistry of the glasses. The correlation of such a volcanic deposits is carried out through the analysis of the petrographic characteristics. Their reconstruction in different depositional basins and over long distances requires the chemical analysis of a glass or of the associated comagmatic minerals. The time range of applicability of tephrochronology has also been discussed and is commonly applied to Neogene and Quaternary deposits.

The characteristics of tephra useful for their identification include the field characteristics, the mineral grains, the volcanic glass, the magnetic and magneto-stratigraphic properties and the numerical age dating. The field characteristics are represented by the physical continuity, the thickness, the bedding characteristics, the grain size and grading, the colour, the stratigraphic context, the site location and the reflectivity, all investigated through standard field geological techniques. The mineral grains include the presence or relative abundance of mineralogic species, the characteristics of a particular species and the chemistry of a particular species, analyzed through standard petrographic techniques and electrone microprobes. The property of glasses include the refractive index, the morphology, the degree of hydration and the chemical composition, including major, minor and trace elements, analyzed through the petrographic microscope examination or binocular microscope, the chemical analysis and the X-ray fluorescence. Other significant properties to be investigated include the determination of magnetic and magnetostratigraphic properties, including the core petrophysical measurements, such demonstrated in the present paper. The interpretation in data analysis of tephrochronology includes the age estimates which are represented by correlated ages, based on the correlation of tephra deposits with tephra deposits of known age. These ages may be considered to be numerical if the tephra layers have been dated through numerical methods, such as K-Ar, $^{40}Ar/^{39}Ar$ or fission track methods, such providing a certain datum to which other deposits can be related due to their stratigraphy and providing an age estimate good for numerical age dating.

The Volturno valley fill has been intensively investigated through the analysis of depositional facies, ostracod and foraminiferal assemblages of onshore cores drilled at the Volturno river mouth (Amorosi *et al*., 2012). The Late Quaternary stratigraphic architecture is offered beneath the modern coastal plain of the Volturno river. An important stratigraphic marker has been identified in the Volturno plain, such as the Campanian Ignimbrite. Its top has been reconstructed and therefore it has been traced in the subsurface a Late Quaternary palaeovalley incised by the Volturno river and filled by Quaternary marine sediments. A stratigraphic cross-section across the Volturno coastal plain (Amorosi *et al*., 2012) has been re-drawn in order to show the geometry of the Volturno coastal plain. The geological section shows the geometry of the Volturno incised valley cut into the deposits of the Campanian Ignimbrite. The section has been calibrated, concealing its basin fill by the cores drilled respectively in the Mondragone area, in the Castelvolturno area and in the Phlegrean Fields area. Apart the Campanian Ignimbrite deposits, another important volcanic stratigraphic marker, corresponding to the deposits of the Neapolitan Yellow Tuff (Orsi *et al*., 1991; Deino *et al*., 2004; Di Fiore *et al*., 2011), dated back at 15 ky B.P. has been identified only in the Phlegrean Fields area. A terraced palaeotopography

of the valley flanks has been reconstructed based on core data. The basal fluvial deposits are separated by the Early Holocene transgressive facies by a suite of estuarine deposits. These are separated from overlying transgressive barrier sands by a ravinement surface. Upwards, a distinctive shallowing upward succession of Middle-Late Holocene age is interpreted to reflect the beginning and the consequent progradation of a wave-dominated delta system, produced as a response to a reduced rate of sea level rise.

A detailed tephrochronological study has been carried out in three deep sea cores drilled in the Tyrrhenian and Ionian seas (Paterne *et al*., 2008). The age and the origin of the marine tephra were inferred from oxygen isotope records of foraminifera and from major element composition of glass fragments. Seventy-one eruptions have been detected during the time interval spanning from 90 to 200 ky B.P., during which the volcanoes of the Roman-Campanian comagmatic region were in activity. This evidence is confirmed by the geochemical compositions of marine and terrestrial deposits. The study tephra layers consist of trachytes and phonolites: several of them have been purposed as marker horizons for proximal and distal sediments (Paterne *et al*., 2008). Eight tephra markers have been purposed within marine isotope stage 5 from MIS5.2 (87 ky B.P.) to sapropel S5 [122 ky B.P.; Paterne *et al*. (2008)]. Sixteen ash layers of trachytic composition have been purposed to be stratigraphic markers between the sapropel S5 and the MIS 6.6 (183 ky B.P.). In the Tyrrhenian sea five tephra layers, trachytic in composition, have been recognized between the MIS 6.6 and the MIS 7.2 [205 ky B.P.; Paterne *et al*. (2008)]. In addition, other five tephra layers have been distinguished due to their chemical composition and stratigraphic location. The tephrochronological analysis of three deep sea sediment cores collected in the Tyrrhenian sea and in the Ionian sea extends a stratigraphic record of the volcanic history of the southern Italy volcanology up to 200 ky B.P. The marine tephra layers are well representative of the volcanic activity of the central (Campanian and Roman provinces) and southern Italy (Aeolian and Pantelleria islands, Etna Mount), in agreement with the dating of the terrestrial proximal deposits (Paterne *et al*., 2008). In the deep sea sediments the ash layers have mainly a trachytic and phonolitic composition, since they originate both the Campanian and Roman provinces. Moreover, the marine tephra layers originating from the Pantelleria island are better represented than those from the Aeolian islands. The activity of the Pantelleria island is well represented in the cores drilled in the northern Tyrrhenian sea. The marine tephrochronological study has pointed out that frequent explosive events occurred in Italy over the past 200 ky B.P., enhancing the important role of the tephra layers as chronological marker horizons.

A sketch diagram of the stratigraphic relationships between the seismic units and the unconformities offshore Cuma (northern Campania) based on the geological interpretation of Subbottom Chirp profiles has been constructed. In this scheme three main seismic units have been indicated (A, B and C) in both continental shelf and slope domains. A detailed geologic interpretation has allowed to distinguish the sub-units in the continental shelf, coeval to seismic units pertaining to slope depositional environment. The A unit, i.e. the most recent one, is composed of two sub-units in the shelf (A1 sub-unit and A2 sub-unit) coeval with the AC unit on the continental slope. The A1 and A2 sub-units are bounded below by the R2 unconformity, while the AC unit is bounded below by the S2 unconformity. The B unit is composed of two sub-units in the continental shelf (B2 sub-unit and B1 sub-unit), separated among them by the R2a unconformity. The B2 and B1 sub-units are bounded at their base by the R1a unconformity, while the BC unit is bounded at its base by the S1a unconformity. Finally, the C unit, i.e. the oldest one, is composed by the C2 and C1 sub-units, separated by the R1 unconformity. These units, pertaining to the shelf, are coeval with two different sub-units on the continental slope, namely the Cc2 and Cc1 sub-units, separated by the S1 unconformity.

## References


Aiello G., Marsella E., Sacchi M.; 2000: *Quaternary structural evolution of the Terracina and Gaeta basins*. Rend. Lincei, **11**, 41-58.

Aiello G., Angelino A., D'Argenio B., Marsella E., Pelosi N., Ruggieri S., Siniscalchi A. 2005: *Buried volcanic structures in the Gulf of Naples (southern Tyrrhenian sea, Italy) resulting from high resolution magnetic survey and seismic profiling*. Annals of Geophysics, **48 (6)**, 883-897.

Aiello G., Cicchella A.G., Di Fiore V., Marsella E.; 2011a: *New seismo-stratigraphic data of the Volturno Basin (northern Campania, Tyrrhenian margin, southern Italy): implications for tectono-stratigraphy of the Campania and Latium sedimentary basins*. Annals of Geophysics, **54 (3)**, 265-283.

Aiello G., Marsella E., Cicchella A.G., Di Fiore V.; 2011b: *New insights on morpho-structures and seismic stratigraphy along the Campania continental margin (Southern Italy) based on deep multichannel seismic profiles*. Rend. Lincei, **22**, 349-373.

Amorosi A., Pacifico A., Rossi V., Ruberti D. (2012) *Late Quaternary incision and deposition in active volcanic setting: the Volturno valley fill, southern Italy.* Sedimentary Geology, **282**, 307-320.

De Alteriis G., Insinga D.D., Morabito S., Morra V., Chiocci F.L., Terrasi F., Lubritto C., Di Benedetto C., Pazzanese M.; 2010: *Age of submarine debris avalanches and tephrostratigraphy offshore Ischia Island, Tyrrhenian sea, Italy.* Mar. Geology, **278**, 1-18.

Deino A.L., Orsi G., Piochi M., De Vita S. (2004) The age of Neapolitan Yellow Tuff caldera-forming eruption (Campi Flegrei caldera – Italy) ossesse by 40 Ar/39Ar dating method. Journ. of Volcanol. and Geoth. Res., **177**, 197-207.

De Vivo B., Rolandi G., Gans P.B., Calvert A., Bohrson W.A., Spera F.J., Belkin H.E.; 2001: *New constraints on the pyroclastic eruptive history of the Campanian volcanic plain (Italy)*. Mineralogy and Petrology, **73**, 47-65.

Di Fiore V., Aiello G., D'Argenio B. (2011) Gravity instabilities in the Dohrn canyon (Bay of Naples, Southern Tyrrhenian sea): potential wave and run-up (tsunami) reconstruction from a fossil submarine landslide. Geologica Carpathica, **62 (1)**, 55-63.

Di Vito M.A., Isaia R., Orsi G., Southon J., De Vita S., D'Antonio M., Pappalardo L., Piochi M. (1999) *Volcanism and deformation since 12.000 years at the Campi Flegrei caldera – Italy.* Journ. of Volcanol. and Geoth. Res., **91**, 221-246.

Giaccio B., Isaia R., Fedele F.G., Di Canzio E., Hoffecker J., Ronchitelli A., Sinitsyn A.A., Anikovich M., Lisitsyn S.N., Popov V.V.; 2008: *The Campanian Ignimbrite and Codola tephra layers:two temporal/stratigraphic markers for the Early Upper Palaeolithic in southern Italy and western Europe*. Journ. of Volcanol. and Geotherm. Research, **177**, 208-226.

Insinga D.D., Molisso F., Lubritto C., Sacchi M., Passariello L., Morra V. (2008) *The proximal marine record of Somma-Vesuvius volcanic activity in Naples and Salerno bays, Eastern Tyrrhenian sea, during the last 3 kyrs*. Journ. of Volcanol. and Geoth. Res., **177**, 170-186.

Insinga D.D., Sulpizio R., de Alteriis G., Morabito S., Morra V., Sprovieri M., Di Benedetto C., Lubritto C., Zanchetta G.; 2010: *Tephrochronology offshore Ischia Island, Tyrrhenian sea, Italy.* EGU General Assembly 2010, Abstract, held 2-7 May 2010 in Vienna, Austria, p. 15298.

Iorio M., Capretto G., Petruccione E., Marsella E., Aiello G., Senatore M.R.; 2014: *Multi-proxy analysis in defining sedimentary processes in very recent prodelta deposits: the northern Phlegrean offshore example (Eastern Tyrrhenian margin)*. Rend. Lincei, **25 (2)**, 237-254.

Orsi G., D'Antonio M., De Vita S., Gallo G. (1991) *The Neapolitan Yellow Tuff, a large magnitude trachiti phreatoplinian eruption: eruptive dynamics, magma withdrawal and caldera collapse*. Journ. of Volcanol. and Geoth. Res., **53**, 275-287.

Paterne M. and Guichard F.; 1993: *Triggering of volcanic pulses in the Campanian area, south Italy, by periodic deep magma*. Journal of Geophysical Research, **98** (B2), 1861-1873.

Paterne M., Guichard F., Duplessy J.C., Siani G., Sulpizio R., Labeyrie J. (2008) *A 90.000-200.000 yrs marine tephra recorded in Italian volcanic activity in the Central Mediterranean Sea*. Journ. of Volcanol. and Geoth. Res., **177**, 187-196.

Pyle D.M., Ricketts G.D., Margari V., Van Andel T.H., Sinitsyn A.A., Praslov N.D., Lisitsyn S.; 2006: *Wide dispersal and deposition of distal tephra during the Pleistocene Campanian Ignimbrite/Y5 eruption, Italy.* Quaternary Science Reviews, **25**, 2713-2728.

Rio D., Raffi I., Villa G.; 1990: *Pliocene-Pleistocene calcareous nannofossils distribution patterns in the western Mediterranean*. In: Kastens K.A. (Ed.) Proceedings of the Ocean Drilling Program Scientific Results, 107, Ocean Drilling Program, College Station, TX, 513-533.

Rolandi G., Paone A., Di Lascio M., Stefani G.; 2007: *The 79 A.D. eruption of Somma: the relationship between the date of the eruption and the southeast tephra dispersion*. Journ. of Volcanol. and Geoth. Res., **169**, 87-98.

Sarna-Wojcicki A. (2000) *Tephrochronology*. In: Quaternary geochronology: Methods and Applications. AGU Reference Shelf, **4**, 357-377.

Sacchi M., Insinga D., Milia A., Molisso F., Raspini A., Torrente M.M., Conforti A. (2005) *Stratigraphic signature of the Vesuvius 79 AD event off the Sarno prodelta system, Naples Bay.* Marine Geology, **222-223**, 443-469.

Self S. and Sparks R.J.S. (1981) *Tephra studies*. D. Reidel Publishing Company, pp. 552.

Simkin T. and Siebert L. (1994) *Volcanoes of the world*. Tucson Geoscience Press. for the Smithsonian Institution, ISBN 0 945005 12 1.

Sulpizio R., Zanchetta G., Paterne M., Siani G.; 2003: A review of tephrostratigraphy in central and southern Italy during the last 65 ka. Il Quaternario, **16**, 91-108.

Thon-That T., Singer B., Paterne M.; 2001: $^{40}Ar/^{39}Ar$ dating of latest Pleistocene (41 ka) marine tephra in the Mediterranean sea: implications for global climate records. Earth and Planetary Science Letters, **184**, 645-658.

Turney C.S.M., Blockley S.P.E., Lowe J.J., Wulf S., Branch N.P., Mastrolorenzo G., Swindle G., Nathan R., Pollard A.M.; 2008: Geochemical characterization of Quaternary tephras from the Campanian province, Italy. Quaternary International, **178**, 288-305.

## INTEGRATED GEOPHYSICAL AND HYDRAULIC METHODOLOGIES FOR THE STUDY OF CONTAMINANT TRANSPORT PROCESS IN THE SUBSOIL: A SAND BOX EXPERIMENT

**L. Capozzoli[1,2], G. De Martino[2],V. Giampaolo[2], S. Parisi[2], E. Rizzo[2]**

*[1] University of Basilicata, Potenza, Italy*

*[2] Istituto di Metodologie per le Analisi Ambientali, Consiglio Nazionale delle Ricerche, Tito (PZ), Italy*

**Introduction.** To analyze and study the problem of pollution and contamination of soil and groundwater due to industrial spills, landfills leakage or other accidents is very important understand the controlling contaminant transport processes.

For this reason is of crucial importance the environmental assessment of contaminated areas to minimize the risk to soil and groundwater health. There are a lot of hydrological and physical variables that play a key role into the fluid transport behavior such as, flow pathways, flow velocity and hydraulic conductivity. So, subsurface contaminant movement depends on both the site environmental, physical, chemical, and biological characteristics and the contaminant chemical properties. Generally, subsurface transport properties are affected by significant heterogeneity, depending on rock texture, pore-space geometry, and mineralogy, consequently, solute transport processes show a heterogeneous behavior, associated with strong spatial-temporal variability of solute concentrations.

The environmental geophysics provides a wide spectrum of tools to identify the most relevant hydrogeophysical parameters able to study the process occurring in the subsoil with good reliability at time and costs reduced. Moreover, obtained the physical characteristics of the soil, is possible define and optimize the simulated models to study and manage the contamination phenomenon.

A lot of geophysical research is based on the application of high resolution geophysical methods for the characterization of flow and transport. In particular, several works have shown the usefulness of coupling geophysical prospecting and tracer test as valuable tool for imaging solute transport processes in the subsurface (Binley *et al*., 2002; Slater *et al*., 2002; Martinez-Pagan *et al*., 2010; Boleve *et al*., 2011). The key feature of the geophysical approach is the non-invasiveness and repeatability of the methods with a high sampling density and different resolution. This is particularly true if geophysical imaging methods are applied in an automated, time-lapse manner, using modern data acquisition systems and processing techniques.

A sand box was built at the CNR-IMAA Hydrogeosite laboratory in Marsico Nuovo (PZ) where a controlled diffusion/infiltration experiment is performed in order to monitor in time lapse the contaminant flow with electromagnetics data. In this experiment we have simulated a salt infiltration in a sandy background where 84 steel electrodes are installed to investigate the

electrical behaviour of the sand. The main objective of this study is to analyse in time-lapse the contamination phenomenon with integration of electromagnetic data in presence of a constant water flow and evaluate the transport occurring in porous media in saturated and unsaturated conditions. Then the results obtained are compared with those obtained with a simulated model built with COMSOL multiphysics software to understand the results and consequently to optimize them.

**Cross-borehole ERT.** Electrical Resistivity Tomography based on cross-borehole configurations (Binley *et al*., 2002; Kemna *et al*., 2002; Cassiani *et al*., 2006; Deiana *et al*., 2007) is widely used to study and monitor fluid-dynamics and contaminant flow in the subsurface in the vadose and saturated zone. In cross-borehole ERT, quadripoles resistance measurements are made using electrodes in two or more boreholes. Maps of resistivity are obtained after inversion of the resistance data adopting finite element methods that allow computing the show resistivity values which satisfies both the measured dataset and some a priori constraints, in order to stabilize the inversion and constrain the final image (deGroot-Hedlin and Constable, 1990). The approach with cross borehole resistivity imaging provide a great advantage compared to more conventional surface electrical resistivity tomography, due to the high resolution at high depth (obviously depending on the depth of the well instrumented for the acquisition). Furthermore there are two critical issues; the first one is due to borehole electrodes characteristics that usually cause a high data noise levels, the second one is the reciprocal distance of the boreholes that reduce the sensitivity of the analysis.

Using the fundamental Archie's law (1942) that describes with an empirical relationship the complex electrical behaviour of the soil considering the formation factor F, porosity $\varphi$, matrix cementation m, pore geometry a, degree of saturation (s) and n saturation exponent, it's possible write:

$$\rho_0 = a\varphi^{-m}s^{-n}\rho_w \quad (1)$$

The equation may be rearranged considering the formation factor F defined as:

$$F = \frac{a}{\varphi^m} = \frac{\rho_0}{\rho_w} \quad (2)$$

to obtain in the saturated zone:

$$\rho_0 = F\,\rho_w \quad (3)$$

TDS of natural waters can be measured by standard gravimetric techniques or by the use of conductivity/ TDS meters. The specific conductance (electrical conductivity normalized to 25°C) of groundwater is directly related to the TDS based on the assumption that TDS in the water consist mainly of ionic constituents that conduct electricity (e.g., Wood, 1976; Hem, 1985; Lloyd and Heathcote, 1985). The relationship between electrical conductivity σ (or resistivity) and salt concentration in the water expressed as TDS (total dissolved solute, is a measure of the total ions in solution) is:

$$TDS\left[\frac{g}{l}\right] = \frac{F}{\rho_0} * 5 \quad (4)$$

After the evaluation of formation factor and resistivity values with the Eq. (4) is possible calculate the concentration of saline contaminant present in the subsoil. For a correct assessment of the TDS, is very important assess the formation factor. Resistivity maps in uncontaminated conditions can provide formation factor maps to be used subsequently to assess TDS concentrations in the water. For the case investigated the resistivity of formation water was equal to 0.3 mS/cm and the resistivity values of the soil are calculated according each maps acquired for the different sequences before the injection of NaCl solution.

**Experiment set-up.** At the CNR-IMAA "Hydrogeosite" laboratory in Marsico Nuovo a controlled system, equipped with an automatic system for the simulation of the water level fluctuations, was built to study the spatial and temporal dynamics of a phreatic aquifer through hydrogeophysical techniques.

The simulated aquifer consists of a sand box filled with about 1 mc of homogeneous silica

sand (95% SiO2) characterized by a diameter average equal to 0.09 mm (very fine sand), a porosity of about 45 ÷ 50% and hydraulic conductivity in the order of $10^{-5}$ $ms^{-1}$. In the Tab. 1 are presented the results of chemical, particle size and hydrogeological analysis obtained by laboratory tests.

Tab. 1 - Chemical analysis, Particle size analysis, Hydrogeological properties.

| **Chemical analysis** | | | | | | |
|---|---|---|---|---|---|---|
| | $SiO_2$ | $Al_2O_3$ | $Fe_2O_3$ | CaO | $K_2O$ | |
| % | 93.00 | 2.50 | 0.60 | 1.50 | 1.15 | |
| **Particle size analysis** | | | | | | |
| d (mm) | 1 – 0.5 | 0.50 - 0.25 | 0.250– 0.125 | 0.125– 0.063 | 0.063– 0.032 | > 0.032 |
| % | 0.00 | 0.14 | 3.70 | 86.34 | 7.92 | 1.08 |
| **Hydrogeological properties** | | | | | | |
| $d_m$ (mm) | | $K_{max}$ (m/s) | | $\rho$ (%) | | |
| 0.09 | | $4*10^{-5}$ | | 45 – 50 | | |

Fig. 1 shows the various components of the experiment and a view of the instrumented sand box. The box is height 90 cm and is an inverted truncated cone characterized by a base diameter of 90 cm and a top diameter of 120 cm. On the base where a drainage system was located, a steel slab was inserted near the interface between sand and gravel to have a strong reflection when GPR acquisition are made. Respectively ad a depth of 30 and 45 cm from the ground surface a pvc pipe (diameter 32 mm) and a steel rode (diameter of 12 mm) were inserted to have electromagnetics anomaly in GPR analysis.

Below the layer of sand, at the base of the vat, has been placed a layer of pebbles of height equal to 4 cm; the two materials were separated with a sheet of geotextile. With this layer was simulated a drainage system that allows to recharge the vat continuously during the pumpis process.

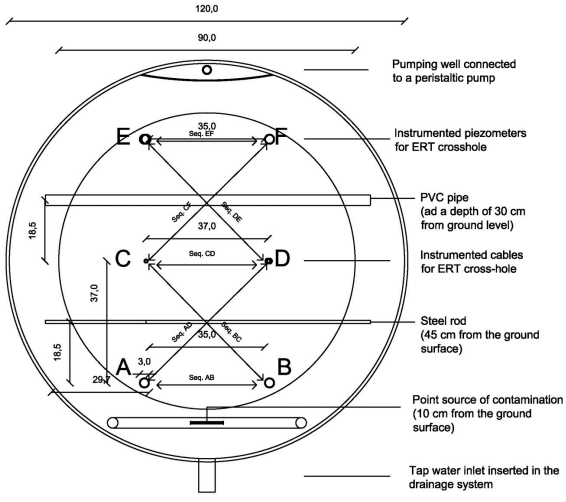


Fig. 1 – Plan of the test site and experimental set-up at CNR-IMAA "Hydrogeosite" laboratory in Marsico Nuovo (PZ-Basilicata).

The contamination phenomenon was simulated using a PVC pipe characterized by a hole in the middle of the diameter of 1 cm. Ten litres of saline solution (with a salt concentration of 100 g/l) were injected from the hole in ten days and a well, located on the opposite side, has generated a steady stream into the vat pumping 35 ml/minute of water for the entire experiment. The pumping well was inserted in a drainage system like that used to recharge the aquifer. The piezometric head was kept constant at a depth of about 30 cm from the surface with a hydraulic circuit consisting of two tanks connected to the column. Furthermore an integrated monitoring system was used to identify the contaminant flow consisting of geo-electrical cables (for ERT cross-borehole), piezometer (for groundwater measurements) and multi-parameter probes (for evaluation of water properties).

To perform ERT cross-borehole in the sand box, four piezometers instrumented with 48 steel plate electrodes and two cables with 24 steel electrodes are made in laboratory. With piezometer systems it was possible monitor the aquifer and analyse the water properties. All the cables were connected to the electrical resistivity meter Syscal Pro that provides electrical measurements with 96 electrodes and has ten channels to carry out up to 10 readings at the same time. The Syscal Pro, connected to a PC, allowed to acquire electrical resistivity data and to control them in real time. The 72 steel electrodes were used in order to perform the 2D cross-borehole resistivity measurements within 0.05÷0.65 m in depth. The cables were placed vertically in boreholes at a reciprocal distance of 0.35-0.37cm. A cross-borehole azimuthal dipole–dipole array was adopted using a current and potential dipole separation (D) of 0.15 m up to 0.30 m according seven different sequences. In order to define the electrical behaviour in uncontaminated and contaminated conditions seven ERT cross-borehole according to the sequences -AB-CD-EF-AD-BC-CF-ED- were performed and inverted each day where A-B-C-D-E-F are the borehole (see Fig.1) . For each one the reciprocal error was evaluated. Collection of measurements in the reciprocal configuration, which took approximately 180 minutes, permitted assessment of data errors (Binley *et al*., 2002a).

To investigate the effects caused by salt contamination several GPR acquisition were performed with SIR-3000 radar coupled to 400, 900 e 2000 MHz antennas also using a survey wheel. In this way the analysis are characterized by different resolution and depth. Three different acquisitions were made, two in the transverse direction with respect to the flow and one in longitudinal direction. To facilitate the estimation of the physical parameters of interest were placed anomalous bodies in the sand (steel rod, pvc pipe and steel plates already described).

The experiment was monitored for thirty-one days with two different multi-parameter probes, the Multi 340i WHW handheld meter and the HI 9828 multi-parameter system (Hannah Instruments). The first probe, thanks to the small size, was used to measurements into the piezometers; the second one was located in a tank with overflow placed at the water outlet. The Multi 340i WHW was used to carry out pH measurements and conductivity measurements in the instrumented piezometer during the experiment usually at time intervals of four hours. The HI 9828 probe allowed to analyse and record on internal memory measurement of dissolved oxygen, pH, ORP, conductivity and related parameters, temperature, atmospheric pressure, related on the outlet water.

Therefore, two different scenarios were analyzed:

a. Sand-box uncontaminated saturated for 60 cm from the bottom with tap water (Sc-1);
b. Sand-box contaminated with 10 litres of salt water (the concentration of NaCl was 100 g/l) and groundwater at 60 cm from bottom (Sc-2).

In uncontaminated conditions (Sc-1) the resistivity maps are performed in order to investigate the electrical starting behaviour of the sand and provide the data necessary to the assessment of the formation factor and the TDS concentrations.

The test started on June 24 2014 at 08:00 in uncontaminated scenario with the water table fixed to a depth of about 32 cm from the ground level. The tracer test injection started on June 24 2014 at 11:00 am (Sc-2). Ten litres of salt water solution, with a concentration of 100 g/l

of NaCl, were injected in ten days into the vat through the injection point located at ten cm from the surface with a system without pressure. In order to create a water flux longitudinal compared to boreholes a peristaltic pump pumped water at a velocity of 0.035 l/min for all the experiment. The test was monitored continuously with phreatimeter moved in the four boreholes instrumented for cross-borehole ERT. At the same time conductivity measurements were taken with the two probes.

A cross-borehole electrical resistivity survey, based on time-lapse geoelectrical prospecting methods, has been carried out in the investigated area during the tracer test. During the tracer injection, resistivity measurements were made every 6 hours. From the dataset collected, the data acquired every 3 days were inverted to study contaminant flow in the sand. A cross-borehole azimuthal dipole–dipole array, with reciprocal measurements, was adopted and apparent resistivity values were inverted using the R2 code (Binley, 2007). The data error was, for all the inversions, less than 10% and the RMS < 5%.

The laboratory test supported and at the same time was supported by a simulation performed with Comsol Multiphysics Version 4.4, a multiphysics software tool for the solution of partial differential equations based on the finite element method. Hydrogeophysical properties used in the model are listed in Tab. 2 and were assumed to be constant throughout the entire solution domain.

Tab. 2 - Hydrogeophysical parameter of simulation.

| | |
|---|---|
| Hydraulic permeability K | 4e-5[m/s] |
| Porosity $\vartheta$ | 0.45[dimensionless] |
| $\alpha$ van Genuchten (1980) | 0.22 [1/m] |
| n van Genuchten (1980) | 1.81 [dimensionless] |
| Bear coefficient | 9.2e-7[1/Pa] |
| Dispersivity | 0.1[m] |
| Diffusion coefficient | 1.5e-9[m^2/s] |
| Residual porosity | 0.1[dimensionless] |
| Tortuosity factor | 0.7 [dimensionless] |

The model uses the Richards' Equation interface to define nonlinear relationships with retention and permeability properties according to van Genuchten as well as Richards' equation governs the saturated-unsaturated flow of water in the soil and accounts for changes in the fluid volume fraction with time, and also for changes in the storage related to variations in the pressure head according to Bear.

The fluid flow is described by the equation:

$$(C + SeS)\frac{\partial H_p}{\partial t} + \nabla \cdot \left(-K\nabla\left(H_p + D\right)\right) = 0 \qquad (5)$$

where C denotes specific moisture capacity (m–1); Se is the effective saturation of the soil (dimensionless); S is a storage coefficient (m–1); Hp is the pressure head (m), which is proportional to the dependent variable, p (Pa); t is time; K equals the hydraulic conductivity (m/s); D is the direction (typically, the z direction) that represents vertical elevation (m).

**Results and discussions.** A dataset of about 840 ERTs was acquired to investigate the distribution of the tracer in the subsoil and several radargrams were recorded at different frequencies to analyse the variations in the e-m field due to the presence of a high conductivity substance.

Fig. 2 shows the results obtained for the scenario Sc-2 after 30 days from the tracer injection according the illustrated sequences A-B, C-D, E-F. The TDS values are more higher

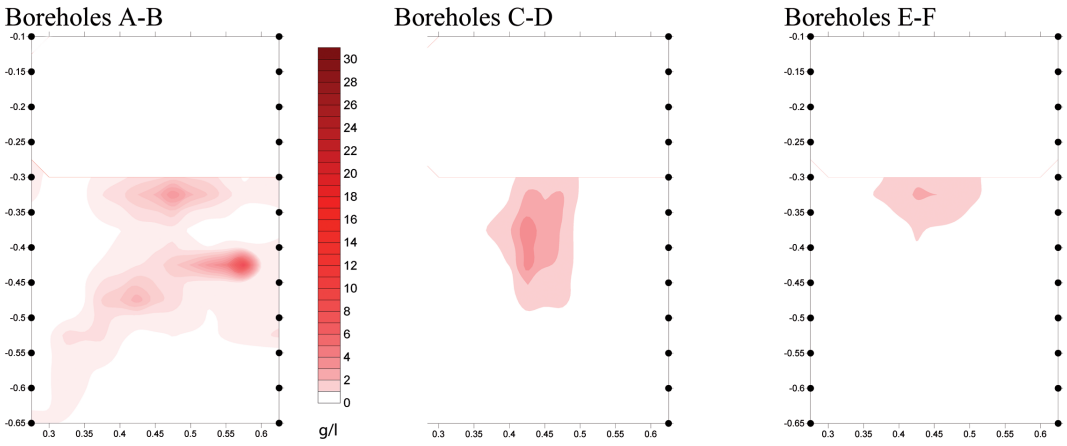


Fig. 2 – TDS concentration maps at the end of the experiment respectively between the boreholes A-B, C-D, E-F in the saturated zone.

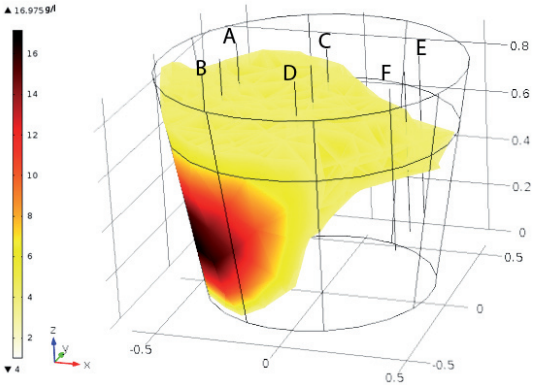


Fig. 3 – Volume concentration of solute injected after 30 days from contamination obtained with Comsol Multiphysics 4.4.

near the injection point (A-B sequence), then it's possible identify an alignment of the tracer near the groundwater level in according with the results obtained with the model simulated in Comsol Multiphysics as depicted in Fig. 3.

The capability of cross-borehole ERT as a tool to detect near-surface contaminants is illustrated through a test carried out under controlled conditions in the Hydrogeosite laboratory of the CNR-IMAA representing salt tracer infiltration in the subsoil. Tests showed that electrical resistivity tomography may provide a means of mapping contaminant in the saturated and unsaturated zone and consequently to understand the pathway of the contaminant. Furthermore with conversion of the resistivity values in TDS, it's possible provide high-density, quantitative data for investigations of vadose zone contaminant hydrogeology. Moreover the use of the resistivity data provides to define and optimize the physical parameters of the model that simulates the distribution of the contaminant in an aquifer.

**Acknowledgements.** The present activity has been performed in the frame of the TICaMoSC Project "Tecnologie Idrogeofisiche per la caratterizzazione ed il monitoraggio di siti contaminati", FSE Basilicata 2007-2013 funds.

## References

Archie G.E. (1942) - The electrical resistivity log as an aid in determining some reservoir characteristics. Trans. Am. Inst. Min. Metall. Pet. Eng. 146, 54–62.

Binley A. (2007a) - cR2: Summary. Lancaster University, Lancaster, UK.

Binley A. (2007b) - R2: Summary. Lancaster University, Lancaster, UK.

Binley A., Cassiani G., Middleton, R. and Winship P. (2002) - Vadose zone model parameterisation using cross-borehole radar and resistivity imaging. Journal of Hydrology, 267, 147-159.

Bolève A., Janod F., Revil A., Lafon A., and Fry J.J. (2011) - Localization and quantification of leakages in dams using time-lapse self-potential measurements associated with salt tracer injection. Journal of Hydrology, 403 (3), 242-252.

Cassiani G., Bruno V., Villa A., Fusi N. and Binley A.M. (2006) - A saline tracer test monitored via time-lapse surface electrical resistivity tomography. Journal of Applied Geophysics, 59, 244-259.

Deiana R., Cassiani G., Kemna A., Villa A., Bruno V. and Bagliani A. (2007) - An experiment of non- invasive characterization of the vadose zone via water injection and cross-hole time-lapse geophysical monitoring, Near Surface Geophysics, 5, 183-194.

de Groot-Hedlin C.D. and Constable S.C. (1990) - Occam's inversion to generate smooth, two-dimensional models from magnetotelluric data. Geophysics, 55, 1613-1624.

Hem, J.D. (1985) - Study and Interpretation of the Chemical Characteristics of Natural Water, 3rd ed. U.S. Geological Survey Water-Supply Paper, vol. 2254. Washington, DC.

Kemna A., Vanderborght J., Kulessa B. and Vereecken H., (2002) - Imaging and characterisation of subsurface solute transport using electrical resistivity tomography (ERT) and equivalent transport models. Journal of Hydrology, 267, 125-146.

Lloyd J.W., Heathcote J.A. (1985) - Natural Inorganic Hydrochemistry in Relation to Groundwater. Clarendon Press, Oxford, England.

Martinez-Pagan P., Jardani A., Revil A., and Haas A. (2010) - Self-potential monitoring of a salt plume. Geophysics, 75, 17–25.

Slater L., Binley A.M., Versteeg R., Cassiani G., Birken R., and Sandleberg S. (2002) - A 3D ERT study of solute transport in a large experimental tank. Journal of Applied Geophysics, 49, 211–229.

Van Genuchten M. Th. (1980) - A closed-form equation for pre- dicting the hydraulic conductivity of unsaturated soils. Soil. Sci. Soc. Am. ]. 44:892-898

Wood W.W. (1976) - Guidelines for collection and field analyses of groundwater samples for selected unstable constituents. Techniques of Water-Resources Investigations of the United States Geological Survey, Book 1, Chapter D2. U.S. Geological Survey, Washington, DC.

## INDAGINI GEOFISICHE INTEGRATE AD ALTA RISOLUZIONE PER LA DIAGNOSTICA DELLE PAVIMENTAZIONI AEROPORTUALI

**L. Di Giambattista, E. Cardarelli, M. Cercato, G. De Donno, L. Orlando, B. Renzi**
*DICEA, Area Geofisica, Università "Sapienza", Roma*

**Introduzione.** Nel corso della loro vita utile, le pavimentazioni aeroportuali devono garantire qualità, affidabilità e sicurezza, al fine di minimizzare eventuali rischi dovuti a fenomeni di rottura e cedimento strutturale. Tali pavimentazioni non devono altresì presentare irregolarità o caratteristiche che possano deteriorare le capacità di controllo direzionale dell'aeromobile, la capacità frenante dei sistemi antislittamento o condizionare la corsa di un velivolo (Manassero e Dominijanni, 2010).

È quindi necessario valutare lo stato di conservazione e individuare i parametri fisico-meccanici del complesso pavimentazione-terreno di fondazione, al fine di verificare da una parte la conformità al progetto originale in fase di collaudo, nonché individuare zone usurate, anomale o potenzialmente soggette a cedimento durante l'utilizzo dell'infrastruttura.

È pertanto di fondamentale importanza mettere a punto un'accurata e consistente attività di rilevamento e di monitoraggio dei principali parametri geometrici e fisico-meccanici della pavimentazione, che renda più affidabili le scelte manutentive da mettere in opera. In tal senso, i metodi non distruttivi ed in particolare i metodi geofisici permettono di effettuare test su pavimentazioni in maniera rapida, totalmente non invasiva e a basso costo.

Negli ultimi anni sono stati fatti significativi passi in avanti nel campo delle pavimentazioni stradali, utilizzando degli indicatori diretti della portanza strutturale attraverso una stima in sito dei valori tanto degli spessori quanto dei moduli elastici degli strati che costituiscono la pavimentazione (Goel e Das, 2008). Inoltre, tali proprietà possono essere anche monitorate nel tempo, fornendo così un utile strumento di valutazione nella fase di gestione e di progettazione di una pavimentazione stradale.

Poiché una singola tecnica geofisica spesso non è in grado di raggiungere la totalità degli obiettivi richiesti in termini di accuratezza e univocità interpretativa, in molti casi si opta per un approccio integrato di più metodologie, come è prassi comune nei rilievi geofisici degli ultimi anni (Piro *et al*., 2001; Cardarelli *et al*., 2014).

Il target richiesto per le indagini in ambito aeroportuale colloca le necessità diagnostiche nel campo dell'alta risoluzione. In particolare per la valutazione dell'integrità strutturale delle pavimentazioni aeroportuali sono necessari sia un grado di risoluzione elevato nel primo metro dal piano di campagna, al fine di individuare eventuali fratture nella pavimentazione, ma anche una buona penetrazione in profondità, per caratterizzare correttamente il suolo di fondazione.

Sulla base di quanto sopra descritto, si è eseguito un rilievo geofisico integrato con l'obiettivo di ricavare i parametri necessari alle verifiche delle condizioni attuali di un piazzale di sosta prospiciente un hangar aeroportuale e integrare le conoscenze dedotte dagli elaborati di progetto. In particolare sono state eseguite indagini georadar (GPR), elettromagnetiche a bassa frequenza (EM), di tomografia elettrica (ERT) e di tomografia sismica a rifrazione (SRT) per verificare le capacità diagnostiche e le potenzialità di integrazione dei vari metodi.

L'interprestazione integrata dei risultati delle indagini geofisiche eseguite nell'area d'indagine, ha costituito uno strumento utile per la determinazione di eventuali scostamenti tra il progetto originale e l'effettivamente costruito (*as-built*), per l'individuazione di eventuali anomalie relative a zone maggiormente deteriorate e conseguentemente per la pianificazione di successivi interventi di monitoraggio e/o messa in sicurezza delle piste aeroportuali.

**Descrizione del sito e metodi di indagine.** L'area di studio, collocata all'interno di un complesso aeroportuale situato nell'Italia centrale, è costituita dal piazzale di sosta di un hangar in costruzione, attualmente adibito alla sosta di aerei ed elicotteri per le periodiche prove di manutenzione. Tale piazzale è costituito da una pavimentazione rigida a piastre di dimensioni variabili per un estensione totale di circa 18 x 50 m (Fig. 1a). In Fig. 1b è riportata una sezione tipo della struttura con i tipi di materiali e spessori medi di ciascuno strato. Da un esame visivo si sono osservate fratture superficiali con andamento ricorrente in direzione x.

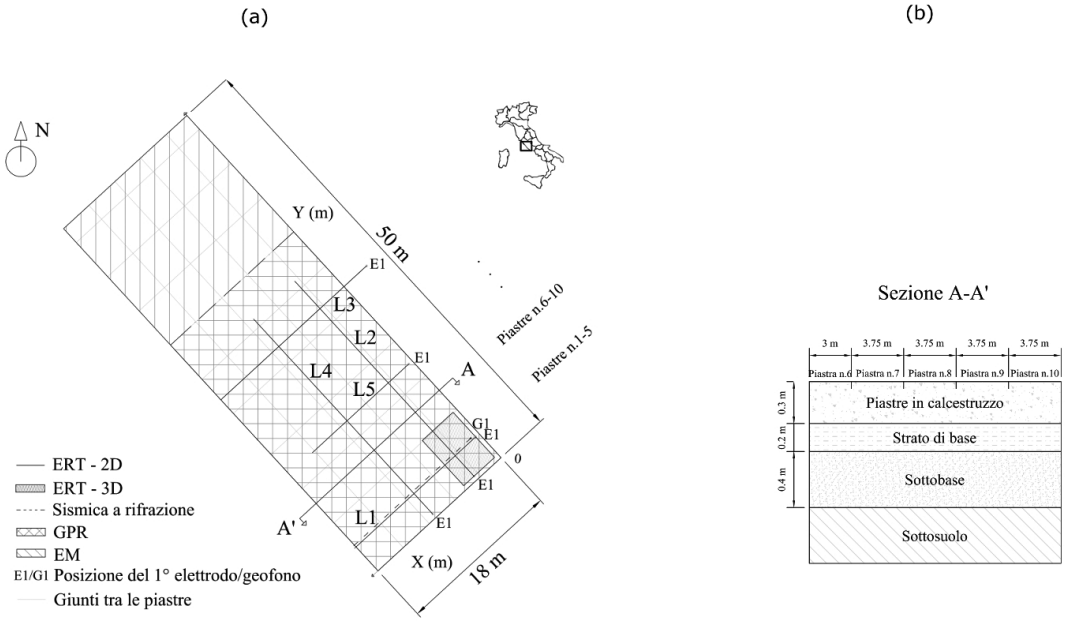


Fig. 1 – a) Planimetria dell'area indagata con indicazione delle indagini effettuate. b) Sezione A-A' della pavimentazione aeroportuale.

Sono state impiegate tecniche GPR, EM, ERT e SRT. I parametri utilizzati per l'acquisizione dei dati sono riportati in Tab. 1.

Tab. 1 - Parametri di acquisizione in sito.

| Tecnica | Parametri di acquisizione |
|---|---|
| Elettromagnetica a bassa frequenza (EM) | *Strumento:* Elettro-magnetometro GSSI Profiler EMP 400<br>*Frequenze:* 2, 8 and 16 kHz<br>*Grid spacing:* 0.5 m<br>*Area investigata:* 18 x 50 m |
| Ground Penetrating Radar (GPR) | *Strumento:* IDS antenna<br>*Frequenze:* 200, 600 e 900 MHz<br>*Grid spacing:* 0.5 m<br>*Area investigata:* 18 x 34 m |
| Electrical Resistivity Tomography (ERT) | *Strumento:* Iris Syscal Pro resistivimetro<br>*Array:* Polo-dipolo roll-along per le linee 2D, polo-dipolo 16x3 array (3D grid)<br>*Elettrodi:* 48 piastre in rame (10x10 cm)<br>*Spaziatura elettrodica:* 0.3 m |
| Seismic Refraction Tomography (SRT) - Onde P e S | *Strumento:* 2 sismografi Geode Geometrics<br>*Sorgente sismica:* mazza da 1 kg battente su barra di legno/alluminio<br>*Ricevitori:* 36 geofoni da 40 Hz (onde P) e 48 geofoni da 8 Hz (onde S)<br>*Spaziatura geofonica:* 0.3 m<br>*Distanza tra gli spari:* 0.3 m |

Per le indagini GPR si è scelto di realizzare un grigliato regolare in modo da coprire la zona d'interesse con un grado di risoluzione elevato. È stata così predisposta una maglia di dimensioni 18x34 m, a passo di 0.5 m nelle due direzioni, ed è stata effettuata l'acquisizione dei profili GPR in direzione x e y (Fig. 1a). A seguito di alcuni test preliminari e per conseguire la profondità d'indagine richiesta e la risoluzione desiderata, si è scelto di utilizzare le antenne da 200, 600 e 900 MHz. L'uso di antenne a diversa frequenza permette di investigare con diversa risoluzione le strutture costituite da strati di spessori limitati e caratteristiche elettromagnetiche simili (Saarenketo e Scullion, 2000). I dati acquisiti sono stati sottoposti ad un processing (amplificazione, filtraggio e migrazione) per eliminare eventuale noise sistematico (p.es. gli arrivi delle onde dirette in superficie) e aleatorio (p.es. i disturbi ambientali).

Per le indagini elettromagnetiche a bassa frequenza (EM) si è utilizzato un elettro-magnetometro GSSI Profiler EMP-400, che permette di acquisire a tre frequenze diverse, variabili tra 1 e 16 kHz. Per l'acquisizione si sono selezionate le frequenze pari a 2, 8 e 16 kHz. Anche per le indagini EM si è scelta una griglia regolare di dimensioni 18 x 50 m e spaziatura di 0.5 m nelle due direzioni (Fig. 1a). Sono state quindi ottenute delle mappe di conducibilità apparente e di suscettività magnetica per le diverse frequenze.

Le indagini ERT e SRT sono state invece focalizzate in zone specifiche, in cui le indagini GPR e EM avevano riscontrato anomalie. Come descritto nell'introduzione, i metodi sismici hanno lo scopo ulteriore, rispetto alle indagini elettriche ed elettromagnetiche, di permettere una stima delle proprietà elastiche della pavimentazione in termini di velocità delle onde P ed S con possibilità di una conseguente stima diretta delle costanti elastiche (modulo di Young, coefficiente di Poisson, ecc.).

Per le misure ERT è stato impiegato l'array polo-dipolo, che combina la potenza del segnale ad una buona risoluzione e profondità di indagine. L'inversione dei dati di resistività apparente

2D è stata effettuata utilizzando l'algoritmo VERDI (Cardarelli e Fischanger, 2006), basato su un'inversione alla Occam di tipo Gauss-Newton con la possibilità di inserimento di vincoli di disuguaglianza, per l'introduzione delle informazioni a priori nel processo di inversione. In questo caso, non è stata fatta alcuna ipotesi preliminare sulla stratificazione del terreno. I dati ERT 3D sono stati invertiti utilizzando il software commerciale ErtLab© della Multi-Phase Technologies, LLC e Geostudi Astier.

I dati sismici sono stati acquisiti impiegando un sistema a 36 canali con geofoni verticali a 8 Hz (vedi Tabella 1) per le onde P e un sistema a 48 canali con geofoni orizzontali a 50 Hz per le onde SH. Per consentire una ricostruzione tomografica ad alta risoluzione (HR), si è posta una distanza fra gli scoppi pari al doppio della distanze geofonica. Per l'acquisizione ad onde SH, si è impiegata una sorgente leggera in legno/alluminio che permette di migliorare il picking del tempo di arrivo delle onde S, tramite la polarizzazione dell'onda nei due versi opposti nella direzione trasversale rispetto alla linea sismica. L'inversione tomografica è stata effettuata utilizzando l'algoritmo sviluppato da Cardarelli e de Nardis (2001), impiegando il metodo (LTI) (Linear Traveltime Interpolation) per il ray-tracing (Asakawa e Kawanaka, 1993) e il gradiente biconiugato per la soluzione del problema inverso (Cardarelli e Cerreto, 2002).

**Risultati.** Lo screening preliminare, eseguito con l'elettromagnetometro a bassa frequenza (EM), ha evidenziato, considerando la frequenza di 16 kHz, due principali zone anomale (Fig. 2a): una zona rettangolare resistiva (A in Fig. 2a) situata a y = 6-18 m e x = 10-28 m ed una striscia conduttiva (B in Fig 2a) estesa lungo la direzione x a y = 0-3 m.

I dati GPR acquisiti su una griglia 18x34 m, confermano i risultati della prova EM rispetto alla forma delle anomalie, infatti il confronto mostra un'ottima sovrapposizione dell'anomalia B e una correlazione tra la resistività dell'anomalia A relativa alle mappe di conducibilità con l'alto scattering radar della zona centrale dei dati acquisiti con l'antenna da 600 MHz. Inoltre i dati GPR garantiscono maggiori informazioni circa la profondità delle stesse.

Infatti mappando i dati GPR tramite time-slices relative alla profondità di 0-30 e 130 cm (Figg. 2b e 2c, antenna 600 MHz), si può discriminare la diversa risposta dei vari materiali in termini di dispersione di energia. Le Figg. 2b (time-slice a profondità di 30 cm) e 2c (time-slice a profondità di 130 cm) evidenziano come la zona rettangolare resistiva (A) si trovi ad profondità di 30-40 cm, ovvero nella zona dello strato di base, e che la striscia conduttiva (B) sia legata a fenomeni che avvengono ad di sotto della profondità minima di posa della pavimentazione (circa 0.9 m), probabilmente correlati ad una struttura preesistente (strada, piattaforma di cemento, ecc.).

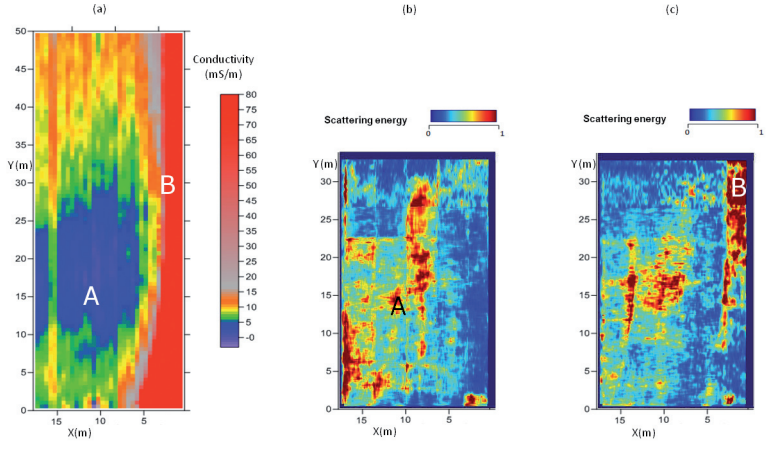


Fig. 2 – a) Mappa della conducibilità EM a 16 kHz. b) Time-slice GPR a una profondità di 30 cm dal p.c. ottenuta sommando l'energia per finestre di 30 cm c) Time-slice GPR a una profondità di 130 cm dal p.c ottenuta sommando l'energia per finestre di 60 cm. I dati GPR sono relativi all'antenna da 600 MHz.

Le sezioni verticali GPR confermano il dato progettuale: la pavimentazione risulta formata da un sistema a tre strati, in cui il primo, avente uno spessore di 30 cm, è sempre ben rilevabile, mentre il secondo (strato di base di circa 20 cm di Fig. 1a) spesso rimane indistinguibile dal terzo (sottobase di circa 40 cm in Fig.1b).

Partendo da questi risultati la seconda parte della campagna di indagini geofisiche è stata focalizzata nelle specifiche zone in cui sono state riscontrate anomalie significative. I modelli ERT 2D sono in grado di ricostruire solo due strati del pacchetto della pavimentazione (30-40 ohm×m fino a 30 cm e 200-600 ohm×m fino a 90-100 cm), mentre la sabbia limosa presente in sito ha un valore di resistività di circa 30-40 ohm×m. Tuttavia un migliore grado di risoluzione è stato ottenuto dai dati ERT 3D (11 array 3D formati ciascuno da 16 x 3 elettrodi spaziati 30 cm), ubicata nell'angolo SE dell'area di indagine in Fig.1a. Il modello risultante dall'inversione, mappato come sezione orizzontale a 20 cm di profondità (Fig. 3a), mostra sia il giunto tra le piastre n. 1 e n. 2 che una zona resistiva anomala situata all'interno della piastra n.1 ad x=0-1,2 m. Confrontando detta sezione orizzontale con la time-slices GPR a 30 cm di profondità in Fig. 2b, si può notare come quest'ultima anomalia resistiva risulti essere chiaramente sovrapposta ad una zona ad alta dispersione (in basso a destra in Fig. 2b). Queste evidenze potrebbero essere dovute ad una composizione disomogenea dello strato di base o ad una instabilità strutturale verificatasi al livello dell'interfaccia tra la piastra di calcestruzzo e lo strato di base.

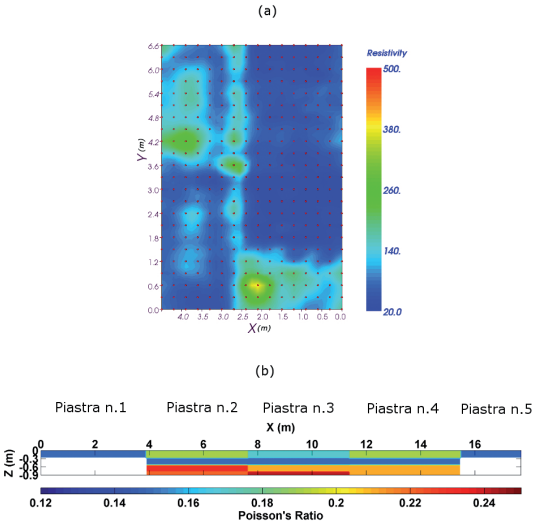


Fig. 3 – a) Sezione orizzontale del modello ERT 3D ad una profondità di 20 cm. La resistività è espressa in ohm·m. b) Sezione del coefficiente di Poisson risultante dall'inversione tomografica di dati sismici ad onde P ed S.

Oltre alla caratterizzazione geometrica della pavimentazione e all'individuazione di zone anomale, derivanti o da una difformità tra l'effettivamente costruito e il progetto originale o a un fenomeno di cedimento strutturale intervenuto a seguito della costruzione e verificatosi al di sotto delle piastre di cemento, l'autorità aeroportuale necessitava di una indicazione dei parametri elastici (ad es. i moduli elastici) per valutare la capacità di ciascuna piastra di sopportare il massimo carico verticale di progetto. La tomografia sismica a rifrazione può soddisfare tale obiettivo laddove i parametri meccanici varino sostanzialmente rispetto a quelli valutati in una zona indisturbata. Tuttavia questo tipo di indagine non presenta i caratteri di rapidità ed economicità richiesti per un'applicazione a larga scala, soprattutto per indagini ad alta risoluzione (griglia 30x30 cm), in quanto necessiterebbe di una meccanizzazione del sistema di acquisizione sismica. I risultati della tomografia sismica, eseguiti sulla linea denominata L1 in Fig. 1a, sono raffigurati in Fig. 3b come sezione del coefficiente di Poisson. Tramite l'inversione tomografica dei dati sismici si è ricostruito un range di velocità delle onde P ($V_p$) variabile dai 1100 m/s (piastre di cemento) ai 2700 m/s (sottobase) e un corrispondente range di velocità delle onde S (Vs) di 700-1600 m/s.

Il coefficiente di Poisson σ risultante è dato dalla seguente formula:

$$\sigma = 0.5\frac{\beta^2 - 2}{\beta^2 - 1}$$

dove β è il rapporto tra $V_P$ e $V_S$.

Le piastre n.1 e n. 5 sono caratterizzate da una scarsa o nulla densità di raggi sismici: di

conseguenza σ è stato valutato in queste zone solo per il primo strato. Considerando le piastre dal n.2 al n.4, si è riscontrata una distribuzione del coefficiente di Poisson coerente con la stratificazione della pavimentazione. Le piastre di cemento hanno un valore di σ di 0.17-0.18, mentre per lo strato di base e la sottobase σ è rispettivamente pari a 0.14-0.15 e 0.21-0.24. Questi valori sono coerenti con quelli proposti p.es. da Cruzado (2006) su materiali da costruzione simili.

**Conclusioni.** L'integrazione di metodi geofisici di comprovata affidabilità (georadar, elettromagnetici, elettrici e sismici a rifrazione) rappresenta un importante strumento per la valutazione dell'integrità e dell'affidabilità di una pavimentazione aeroportuale. Tali metodologie sono rapide ed economiche e possono essere utilizzate per mappare ampie aree durante la fase di collaudo, al fine di discriminare le aree critiche laddove il costruito differisca dal progetto originale.

In aggiunta al metodo GPR, che è una tecnica ormai consolidata per queste applicazioni, i metodi elettrici e sismici ad alta risoluzione possono fornire un ulteriore contributo al fine di determinare i parametri geometrici, fisici e meccanici della pavimentazione. In particolare, la campagna geofisica ha portato alla validazione della geometria di progetto della pavimentazione, costituita da tre strati aventi rispettivamente uno spessore medio di circa 30, 20 e 40 cm, ciascuno caratterizzato da un alto grado di variabilità sia in direzione x che y. Il primo strato, composto da piastre in cemento, è relativamente omogeneo e caratterizzato da bassa resistività (circa 30-40 ohm×m) e coefficiente di Poisson di circa 0.17-0.18. Lo strato di base che copre l'intera area ad una profondità di 30-50 cm è più disomogeneo restando, in alcune aree, non distinguibile dallo strato sottostante e presenta un diverso comportamento fisico-meccanico (resistività di circa 200-600 ohm×m e coefficiente di Poisson di 0.14-0.15). la sottobase presenta valori di resistività simili allo strato precedente, ma diverso Poisson (0.21-0.24). I coefficienti di Poisson dei tre strati sono coerenti con quelli desunti da lavori di letteratura su campioni di laboratorio. Al di sotto dei tre strati costituenti la pavimentazione, si rileva uno strato a bassa resistività (40-50 ohm×m) relativo alle sabbie limose presenti in-situ che coprono l'intera area, ad eccezione di alcune zone anomale dove gli alti valori di resistività indicano la presenza di una struttura preesistente.

Pertanto la procedura sperimentale adottata ha fornito modelli affidabili sia in termini di errore dei modelli ricostruiti che di ripetibilità dei risultati. Sebbene il primo strato sia stato ben rilevato e modellato utilizzando tutte le metodologie, la ricostruzione ERT ha lo svantaggio di perdere risoluzione in profondità mentre il GPR ha una penetrazione limitata del segnale in profondità. Qualora si renda necessaria anche una caratterizzazione meccanica per valutare il carico verticale massimo, la tomografia sismica a rifrazione ha il vantaggio sostanziale, rispetto a metodi quali il Falling Weight Deflectometer (FWD), di calcolare valori di velocità delle onde sismiche e conseguentemente il coefficiente di Poisson (o il modulo di Young o il modulo di taglio) per ogni strato e per ogni piastra. Questo ha portato ad una ricostruzione ad alta risoluzione della pavimentazione analizzata rispetto al valore singolo (ad esempio il modulo di taglio) ottenuto con il FWD su un volume d'interesse. D'altro canto, poiché i metodi sismici non sono sempre rapidi, soprattutto nel caso di tomografia ad alta risoluzione, è necessario un ulteriore sviluppo di un sistema meccanizzato per il rilevamento in continuo, comprendente la sorgente, gli streamer e i cavi.

Pertanto le tecniche GPR, EM ed ERT possono essere ampiamente utilizzate per ricavare informazioni sulla stratificazione, sia facendo riferimento allo spessore della piastra (il cui valore medio non deve essere inferiore di oltre il 5% rispetto al progetto originale) che allo spessore e al grado di conservazione dei materiali sottostanti (strato di base e sottobase). Più in dettaglio, gli array ERT 2D e/o 3D possono essere applicati per caratterizzare senza ambiguità interpretative le zone anomale precedentemente individuate da una fase di screening mediante indagini GPR e/o EM, in cui i valori di resistività più elevati possono essere associati a zone areate e/o con maggiore contenuto di inerte e quindi maggiormente soggette a rottura.

Successivamente un'indagine mirata sulle aree anomale, dovrebbe comprendere un rilievo SRT per la stima dei parametri meccanici. Un successivo sviluppo di questo approccio integrato potrà comprendere il monitoraggio dei parametri fisico-meccanici nel tempo, al fine di regolare le attività di manutenzione e di evitare il verificarsi di condizioni critiche sulla struttura.

**Ringraziamenti.** Questo lavoro è stato finanziato dall'Università "Sapienza" di Roma tramite un progetto di Ateneo 2012 dal titolo "Non destructive tests for the diagnosis of pavements and structures". Responsabile scientifico: Luciana Orlando.
Si ringraziano Francesco Pugliese e Stefano Pagano dell'Università "Sapienza" di Roma per il loro contributo all'acquisizione dei dati e la Prof.ssa Paola Di Mascio per il contributo nell'integrazione dei dati di progetto.

**Bibliografia**

Asakawa E., Kawanaka T.; 1993: Seismic ray tracing using linear travel time interpolation. Geophysical Prospecting, 41, 99–111.

Cardarelli E., Cercato M., De Donno G.; 2014: Characterization of an earth-filled dam through the combined use of electrical resistivity tomography, P-and SH-wave seismic tomography and surface wave data. Journal of Applied Geophysics, 106, 87-95.

Cardarelli E., Cerreto A.; 2002: Ray tracing in elliptical anisotropic media using linear traveltime seismic interpolation (LTI) method applied to traveltime seismic tomography. Geophysical Prospecting, 50, 55–72.

Cardarelli E., De Nardis R.; 2001: Seismic Refraction, isotropic and anisotropic seismic tomography on an ancient monument. Geophysical Prospecting, 49, 228–240.

Cardarelli E., Fischanger F.; 2006: 2D data modelling by electrical resistivity tomography for complex subsurface geology. Geophysical Prospecting, 54, 121-133.

Cruzado M.G.; 2006: Ingeniería Aeroportuaria. Editorial UPM, 3ª Edición, ETSI Aeronáuticos, Madrid.

Goel A., Das A.; 2008: Nondestructive testing of asphalt pavements for structural condition evaluation: a state of the art. A state of the art. Nondestructive Testing and Evaluation, 23, 121-140.

Manassero M., Dominijanni A.; 2010: Riqualifica Strutturale di un Sistema di Piste Aeroportuali, Rivista italiana di geotecnica, 21, 46-66.

Piro S., Goodman D., Nishimura Y.; 2001: High-resolution GPR survey in Forum Novum site (Vescovio, Rieti). Journal of Roman Archaeology, 14, 60-79.

Saarenketo T., Scullion T.; 2000: Road evaluation with ground penetrating radar. Journal of Applied Geophysics, 43, 119–138.

## INTEGRATION OF GEOPHYSICAL TECHNIQUES FOR SUSTAINABLE MANAGEMENT OF WATER RESOURCE IN AGRICULTURE

**A. Satriani[1], F. Soldovieri[2], M. Catalano[3], E. Scalcione[3], A. Loperte[1]**
*[1] Institute of Methodologies for Environmental Analysis (IMAA-CNR), Tito Scalo (PZ), Italy*
*[2] Institute for Electromagnetic Sensing of the Environment (IREA-CNR), Napoli, Italy*
*[3] Agency for the Agricultural Development and Innovation (ALSIA), Basilicata Region, Matera, Italy*

**Introduction.** The efficient use of water is one of the main objectives for the sustainable management of natural resources in agriculture. As well known, water is a fundamental resource for the metabolic activities of crops, but this resource is available in limited quantities and therefore optimizing the use of water in irrigation practice is very important for a sustainable management of it. A possible technological solution based on the integration between geophysical techniques for soil moisture measure and soil water spatial monitoring as time domain reflectometry (TDR), ground penetrating radar (GPR) and electrical resistivity tomography (ERT) technique can be used.

Of course, with the use of these technologies the opportunity to know the current soil moisture status and how it is distributed in the soil is useful to determine the actual water requirement of a crop, with the result of optimizing the use of water in irrigation practice for

a sustainable management of it, considering also the considerable water volumes required for the productive cycle of many crops. The method of Food and Agriculture Organization of the United Nations (FAO) for estimating crop water requirements, is based on the calculation of the crop evapotranspiration Etc as the product between the reference evapotranspiration (ET0) and the crop coefficient (Kc); where the evapotranspiration ET0 is defined as the loss of water due to the simultaneous processes of evaporation from the soil surface (E) and transpiration by the vegetation cover (T); while the crop coefficient Kc is a measure of the vegetative development of a specific crop in the various phenological phases (Allen *et al*., 1998).

Sensors for soil moisture estimation, as time domain reflectometry (TDR), can be used for verifying ET model applied in a given environments and for a given crop (Jeffrey, 2004; Thompson *et al*., 2007). In addition, the structural complexity of the soil has suggested the implementation of integrated geophysical investigations as Electrical Resistivity Tomography (ERT) and Ground Penetrating Radar (GPR) in order to gain information about the soil moisture content. In fact, the integration of ERT and GPR reduces the ambiguity in the data interpretation by means of a suitable integrated survey design and data processing. In particular, the data obtained from these geophysical surveys provides information with very high detail about the soil layers and this allows at monitoring undesired water losses for percolation into the deeper layers. In this way, it is possible to design a proper scheduling of the amount of irrigation water for a particular crop, which is not based on the only information about the estimated evapotranspiration. In some research, geophysical measurements to spatial and temporal monitoring of soil water on irrigated crop were applied (Parchomchuk *et al*., 1997; Michot *et al*., 2003; Dahlin *et al*., 2006; Pardossi *et al*., 2009; Kelly *et al*., 2011), and it appears that these geophysical measurements give a contribution on water irrigation management, moreover the measurements with integrated geophysical techniques have the advantage of being noninvasive, rapid and reproducible. A local population of dry bean (Phaseolus vulgaris L) named "fagiolo rosso scritto" has been cultivated at the Experimental Agricultural Farm "Pantano of Pignola" (40°33'31.34"N and 15°45'31.66"E); the farm is a facility of ALSIA (Agency for the Agricultural Development and Innovation of Lucania), Basilicata Region (Italy). Drip irrigation is a common practice worldwide, which compared to furrow or sprinkler irrigation, reduces deep percolation and evaporation and permits a more accurate control of the water within the crop root zone (Simsek *et al*., 2011).The drip irrigation system was installed after sowing and placed at each row with drippers spaced every 20 cm apart and delivering 2.1 L/h. The drip lines ran along the 25 m of the rows and were 1.5 m spaced each other. The present paper illustrates the preliminary results of the integration of geophysical applications on a specific dry bean crop, for monitoring the water content in the soil and its distribution.

**Geophysical investigation.** Eight waveguides long 20 cm were installed vertically along bean rows and distributed so to measure the average soil moisture in the depth profile 0-40 cm, corresponding basically to zone where the crop roots were present. During the growing season, a multiplexing time domain reflectometry system (TRASE, Soilmoisture Equipment Corp., California, USA) was deployed for a real-time monitoring of soil moisture content; the system was remotely controlled by a computer connected to internet network.

TDR provides an indirect measurement of the soil water content by measuring the travel time that the guided electromagnetic wave employs to propagate through the thickness L of the soil to be reflected at the end of probe and to return to the TDR probe. As well known, the velocity v of the electromagnetic wave is inversely proportional to the square root of the soil apparent dielectric constant *Ka*, and because the soil is composed by solid particles (*Ka*=3-5), air (*Ka*=1) and water (*Ka*=81), *Ka* varies significantly with soil volumetric water content. In particular, the relationship between *Ka* and soil water content is described using a calibration curve, which was established empirically by Topp *et al*. (1980). Field calibration of TDR system was performed with the gravimetric method; soil samples of known volume, using a metal cylinder sampler, were taken in the 0-40 cm soil depth range and heated at 105 degree centigrade for 72 hours,

after the samples were weighted and water content was estimated. A linear regression equation with R- square = 0.73 and RMSE = 2.23 % was used to calibrate the TDR readings.

Ground penetrating radar (GPR) and electrical resistivity tomography (ERT) provide observations at the spatial scale and resolution convenient to gain information about the hydrological processes of the topsoil. The use of these techniques has become ever more widespread for their ability to measure indirectly changes in soil moisture content and obtain images of soil water distribution during irrigation (Butnor *et al*., 2001, 2003; Hagrey *et al*., 2002, 2007; Huisman *et al*., 2003; Michot *et al*., 2003; Ursino *et al*., 2014) Geophysical surveys were performed at the soil surface along transects longitudinal and parallel with the bean rows with the aim to characterize the soil profile in correspondence of crop roots locations. In particular, electrical resistivity survey permits to determine the soil resistivity distribution, which provides an indirect measurement of various geological parameters such as the solid and fluid content, porosity and water content.

Electrical resistivity tomography (ERT) is an active sensing technique based on the injection of an electrical current I in the subsoil by means of a pair of electrodes (A and B) and the subsequent measurement of the electrical potential $\Delta V$ by using another pair of electrodes (M and N).

There are several possible electrode arrangements as Wenner, Schlumberger and dipole-dipole arrays. Whatever the used array, the ERT is based on the measure of the soil electrical potential while the current is injected. In this circumstance, it is possible calculate the apparent resistivity $\varrho a = k (\Delta V/I)$,where $\varrho a$ is expressed in $\Omega m$ and k is a geometrical factor depending on the adopted array configuration. The apparent resistivity value is not the true resistivity of the soil, but an "apparent" value that is the resistivity of a homogeneous soil which will give the same resistance value for the same electrode arrangement. The apparent resistivity provides, in fact, a first preliminary image of the electrical subsurface structure denominated as the 'pseudo-section' (Loke, 1999). The estimation of the true resistivity required the adoption of the inversion algorithm, RES2DINV, proposed by Loke (1999) and Loke and Barker (1996). For the surveys at hand, a Wenner-Schlumberger array survey were performed with the resistivity meter Syscal R1 (Iris Instruments, Orleans, France) equipped with 48 electrodes, aligned on the soil surface along a line parallel to the bean rows, with an electrode spacing of 0.15 m and a total length of 7.0 m.

Ground penetrating radar (GPR) is a powerful tool for subsurface remote sensing and in particular is a noninvasive geophysical technique that provides images space-time called radargram, of the subsoil. The ground-penetrating radar (GPR) is an active electromagnetic technique whose working principle is that of a common radar system. In particular, a transmitting antenna radiates an electromagnetic wave, usually a microwave pulsed signal The radar produces a short pulse of electromagnetic wave whose spectrum varies from 10 MHz to some GHz, it is transmitted into the soil generating a wave front which propagates downward through the sub-surface materials at the velocity determined by the soil dielectric permittivity. When this propagating wave encounters any change in the bulk electrical properties of different subsurface lithologies, mineralogy, and/or the character of the sediment interface, some of the energy is reflected back to the surface (Davis and Annan, 1989) The amount of energy that is reflected by an sediment interface is approximately proportional to the difference in dielectric constants of the two layers and these contrasts produce strong and identifiable reflections on radar records. The dielectric permittivity of soil materials is principally dependent upon moisture content (Annan *et al*., 1991). The GPR surveys in this experiment, were performed with an GSSI SIR 2000 acquisition unit equipped with a mono-static equipment, and two 400 MHz and 1500 MHz central frequency antenna was dragged along the same survey lines of the electrical resistivity survey; GPR data were post-processed with Reflex software (Sandmeier Scientific Software, Karlruhe, Germany). In order to display radargrams as a function of depth, the change of the time sections into depth was performed through a hyperbola approximation

with which the average velocity of the radar waves propagation through the media for the our soil was determined as v = 0.07 m/nsec (Daniels, 2004).

**Soil moisture monitoring.** Fig. 1 shows the soil moisture monitoring measured with TDR, outcomes in the first 40 cm of soil profile estimated through the integrated geophysical techniques. The peak of soil moisture is obtained three hours after the start of irrigation and the 0-20 cm soil moisture shows a larger variability compared to the 20–40 cm one, after with the pass of the hours the water is distributed into the soil.

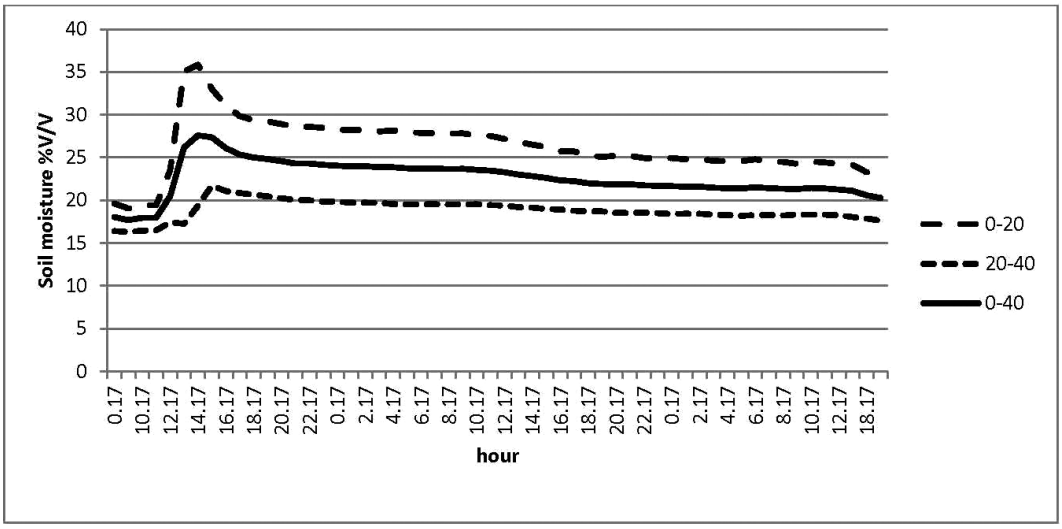


Fig. 1 – Soil moisture content in the first 40 cm of soil profile measured with TDR probes before, during and after irrigation. The peak was obtained three hours after the start of irrigation, and compared to the 20–40 cm , the 0-20 cm soil moisture profile shows a larger variability.

ERT and GPR surveys was performed to characterize soil horizon and soil water movement before and after an irrigation stage, as well as to determine the groundwater level and to assess its influence on crop. Soil images obtained were carried out before and after irrigation, so different images with a different soil moisture permit to gain information about the water diffusion trough the soil. ERT application permitted to point out the electrical resistivity changes in relation to soil moisture variations as a result of irrigation. ERT images are reported in Fig. 2 and refer to the situations before irrigation (higher panel) and 24 hours after the irrigation (middle panel); while, the lower panel depicts the change of the electrical resistivity corresponding to the two above cases.

The ERT1 survey carried out before the irrigation permitted to point out that the layer between the soil surface and 0.4 m depth exhibits resistive structures with values above 100 Ω m and an average moderate resistivity between 20 and 70 Ω m. Such a layer corresponds to the zone with higher root density and thus an increased root uptake, and a high porosity due to soil shallow tillage, as confirmed by GPR surveys shown below (see Fig. 3a).

On the basis of granulometric analysis, the first layer between 0 and 0.3 m was characterized by a content of silt and clay on the fine fraction of 55.0% and 29.0% , respectively. For the layer 0.3-0.6 m depth, the content of silt and clay was about 44.0% and 41.0% , respectively, and ERT1 image exhibited lowest resistivity values ($\varrho < 20$ Ω m). The higher clay content of this horizon and a lower root density with a more limited water uptake by bean roots is the cause of the soil electrical resistivity reduction (Michot *et al.*, 2003).

ERT2 survey was carried out 24 hours after the application of 38 mm of irrigation water in the experimental field. As can be seen, the water distribution during the moistening phase

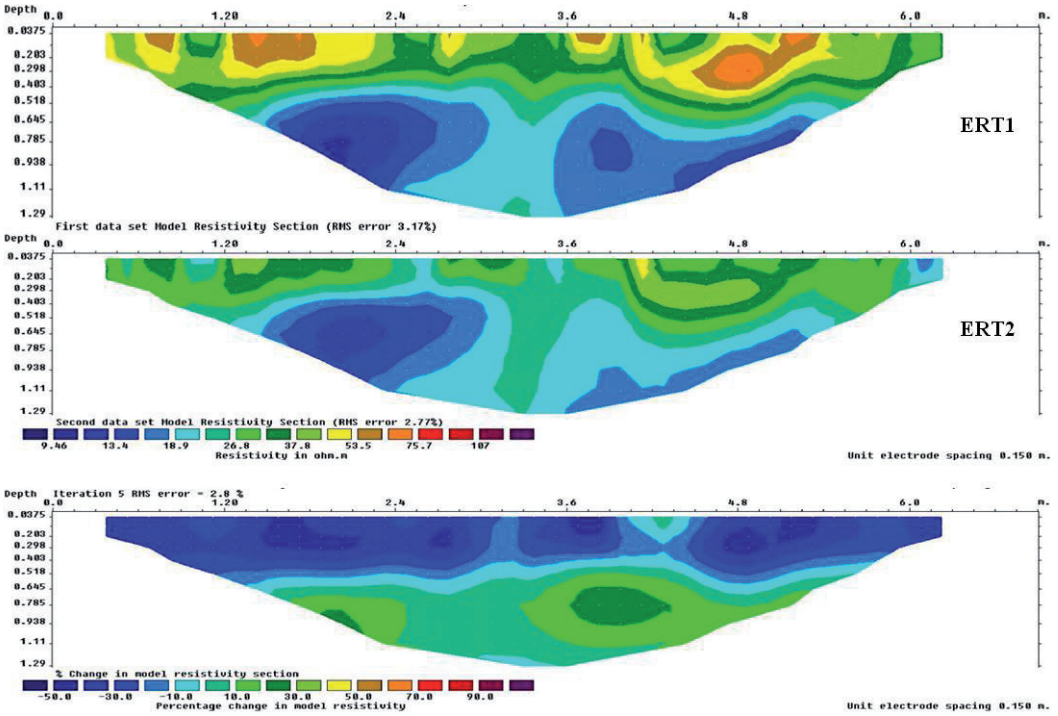


Fig. 2 – Soil section inverted electrical resistivity measured just before irrigation (ERT1) and 24 hours after irrigation (ERT2). Soil inverted resistivity section change between ERT2 and ERT1 (bottom).

has determined a decrease in soil electrical resistivity especially in the first layer; conversely, for the deeper layers, lowest electrical resistivity values were observed and consistent with the ones recovered at ERT1 survey. The ERT 2 outcome permitted to provide the indication that 38 mm of water irrigation was suitable to satisfy the needs of the crop avoiding undesired waste water by infiltration. The percentage relative changes between resistivity sections ERT2 and ERT1, shown in the lower panel of Fig. 2, is negative in the first layer between 0 and 0.4 m, and positive in the deeper layers. This confirms that only a limited percolation of irrigation water occurred. Moreover, the transition from negative to positive resistivity change is observed in correspondence of the middle soil layer (0.5-0.6 m depth). We compared the radargrams obtained by GPR surveys with ERT images performed at the soil surface in transects longitudinal and parallel with the bean rows so to characterize the same soil profile. A SIR 2000 Radar System equipped with a monostatic antenna at 400MHz central frequency was deployed for the GPR surveys. GPR data were acquired in continuous mode, with a time range equal to 100 ns for the 400 MHz antenna. GPR datasets were first analysed using the REFLEX- Win Version 5.0.5 program (Sandmeier, 2001). Standard data processing has the aim to improving the "imaging" by correctly locating and focusing all the reflectors. The processing was performed according to several steps and the result of the standard data processing is shown in Fig. 3 for the same profile shown by the ERT images in Fig. 2.

In Fig. 3a, the GPR radargram acquired with antenna of 400 MHz before irrigation, shows horizontal and parallel layers in the tilled shallower zone, between 0.0 m and 0.30 m depth. At about 0.30 m depth, radargram shows an horizontal and continuous reflector attributed to the presence of a more compacted soil layer and identified as plow layer created by repeated tillage at same depth. In the deeper layers, many distinguishable reflectors are visible, probably due to the presence at vary levels of stoniness; finally, the water table was observed at about 1.0 m depth.

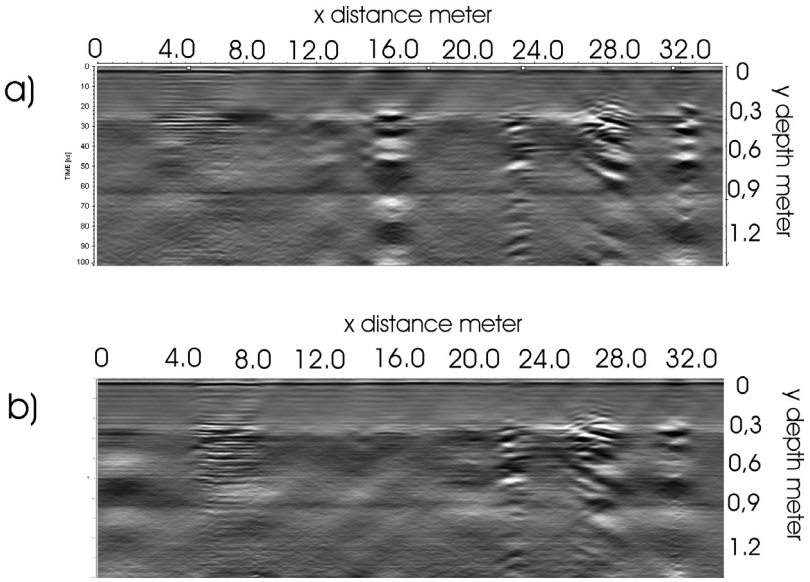


Fig. 3 – GPR radargrams acquired with antenna 400MHz before irrigation (a) and after irrigation (b).

Radargram of Fig. 3b, acquired 24 hours after irrigation, shows the area between 0 and 0.3 m depth characterized by a significant attenuation of the electromagnetic signal, which is associated to the increased presence of water. Conversely, in the deeper layers no significant variations are observable compared to the radargram of Fig. 3a, confirming when obtained with the ERT surveys that the water is distributed, mainly in the first 30-40 cm of the soil, where was observed a higher root density.

**Conclusions.** The availability of water more than any other environmental factor is important for the physiological activity of the plants and thus for crops productivity. It is necessary, therefore, that water supplies are available for root uptake, and at the same time reduce losses due percolation of water given to excess. In this context the use of an integrated system through a network of sensors, allows monitoring of the soil moisture content for a specific crop in a given soil. Moreover, the application of these non-invasive geophysical technologies to irrigation were used in the most varied application fields, and have several advantages as such being fast techniques, their measurement systems utilize technologies proven with consequent cost reduction and are not dangerous for the operators.

**Acknowledgements.** The authors wish to thank the Agency for the Agricultural Development and Innovation of Lucania, Basilicata Region ,Italy (ALSIA) for the technical support and the availability during the field activities.

## References

Allen, R.G., Pereira, L.S., Raes, D., Smith, M.; 1998: *Crop Evapotranspiration Guidelines for Computing Crop Water Requirements. FAO Irrigation and drainage*. Paper **56**. Rome, Italy: Food and Agriculture Organization of the United Nations.

Annan, A.P., Cosway, S.W., Redman, J.D.; 1991: Water table detection with ground penetrating radar. Society of Exploration Geophysicists, Expanded Abstracts 61st Annual Meeting, **1**, 494–495.

Butnor J.R, Doolittle JA, Johnsen KH, Samuelson L, Stokes T, Kress L ; 2003: *Utility of Ground-Penetrating Radar as a Root Biomass Survey Tool in Forest Systems*. Soil Sci Soc Am J, **67**, 1607–1615.

Butnor J.R, Doolittle JA, Kress L, Cohen S, Johnsen KH ; 2001: *Use of ground-penetrating radar to study tree roots in the southeastern United States*. Tree Physiol, **21**, 1269–1278.

Dahlin, T., Aronsson, P., Hagevi, A., Wall, E. and Thörnelöf, M.2006: *Resistivity monitoring of an irrigation experiment at Högbytorp*, Sweden, Procs. Near Surface 2006 - 12th European Meeting of Environmental and Engineering Geophysics,Helsinki, Finland.

Daniels D.J.; 2004: *Ground Penetrating Radar*. 2nd Ed. The Institution of Electrical Engineers, London.

Davis, J.L., Annan, A.P.; 1989: *Ground penetrating radar for high resolution mapping of soil and rock stratigraphy*. Geophysical Prospecting, **37**, 531-551.

Hagrey S.A al, Michaelsen J ; 2002: *Hydrogeophysical soil study at a drip irrigated orchard*. Eur J Environ Eng Geophys Soc **7**,75-93.

Hagrey S.A al; 2007: *Geophysical imaging root-zone, trunk and moisture heterogeneity –Structures and processes in plant stress studies*. J Exp Bot, **58** (4), 839-854, doi:10.1093/jxb/erl237.

Huisman J.A., Hubbard S.S., Redman J.D., Annan A.P.; 2003: *Measuring Soil Water Content with Ground Penetrating Radar: A Review.* Vadose Zone Journal **2**, 476–491.

Jeffrey, P. Walker, Garry R. Willgoose1, Jetse D. K.; 2004: *In situ measurement of soil moisture: a comparison of techniques* , Department of Civil, Surveying and Environmental Engineering, The University of Newcastle, Callaghan, NSW 2308, Australia.

Kelly, B. F. J., Acworth R. I. and Greve A. K.; 2011: *Better placement of soil moisture point measurements guided by 2D resistivity tomography for improved irrigation scheduling*. Soil Research,**49**,504-512.

Loke, M.H.; 1999: *Electrical imaging surveys for environmental and engineering studies, user manual for Res2dinv* .Electronic version available from http://www.geometrics.com.

Loke, M.H., Barker, R.D.; 1996: *Rapid least-squares inversion of apparent resistivity pseudosections by a quasi-Newton method*. Geophysical Prospecting, **44**, 131-15.

Michot, D., Benderitter, Y., Dorigny, A., Nicoullaud, B., King, D., and Tabbagh, A.; 2003: *Spatial and temporal monitoring of soil water content with an irrigated corn crop cover using surface electrical resistivity tomography*. Water Resour. Res., **39**, 1138-1158.

Parchomchuk, P., Tan, C.S., Berard, R.G.; 1997: *Practical use of time domain reflectrometry for monitoring soil water content in microirrigated orchards*. HortTechnology **7**, 17–22.

Pardossi, A., Incrocci, L., Incrocci, G., Malorgio, F., Battista, P., Bacci, L., Rapi, B., Marzialetti, P., Hemming, J. and Balendonck, J.; 2009: *Root zone sensors for irrigation management in intensive agricolture*. Sensors, **9**, 2809–2835.

Sandmeier, K.J.; 2001: *Program for Processing and Interpretation of Reflection and Transmission data Reflex-Win version 4*. copyrights © Sandmeier Software Zibse strasse 1,D-76227 Karlsruha, Germany.

Simsek M., Comlekcioglu N., Ozturk I. ; 2011: *The effects of the regulated deficit irrigation on yield and some yield components of common bean (Phaseolus vulgaris L.) under semi-arid conditions* African Journal of Biotechnology, **10** (20), 4057-4064, doi: 10.5897/AJB10.2012.

Thompson, R.B., Gallardo, M., Valdez, L.C., Fernández, M.D.; 2007: *Using plant water status to define soil water thresholds for irrigation management of vegetable crops using soil moisture sensors*. Agric. Water Manage. **88**, 147–158.

Topp, G.C., J.L. Davis, Annan, A.P.; 1980: *Electromagnetic determination of soil water content, Measurements in coaxial transmission lines*.Water Resource. Res.,**16**, 574–582.

Ursino N., Cassiani G., Deiana R., Vignoli G., J. Boaga; 2014: *Measuring and modeling water-related soil–vegetation feedbacks in a fallow plot*. Hydrol. Earth Syst. Sci., **18**, 1105–1118.www.hydrol-earth-syst-sci.net/18/1105/2014/ doi:10.5194/hess-18-1105.

# Indice degli autori